Centre for
Energy Research

# Progress Report on Research Activities

2021

# CENTRE FOR ENERGY RESEARCH

29-33 KONKOLY-THEGE MIKLÓS ÚT

1121 BUDAPEST, HUNGARY

# PROGRESS REPORT

# ON RESEARCH ACTIVITIES

# IN 2021

# DEAR READER

Welcome to the 2021 yearbook published by the Centre for Energy Research (EK), summarizing the scientific achievements of its three institutes and the highlights in 2021. This booklet provides a summary of the research personnel and capacities of the research groups working in the Centre.

The year 2021 had been greatly influenced by the COVID-19 pandemic, forcing many of us to work in home office. Conferences could not be organized in the usual form due to the travel restrictions.

In 2021 the National Research, Development and Innovation Office (NKFIH) launched an updated survey version of national research infrastructures. In this survey the EK management registered two infrastructures, the Budapest Neutron Centre and the Aberration Corrected Transmission Electron Microscope Laboratory. Both have been elected members of the TOP 50 excellent research infrastructures in Hungary.

Three important research works are selected for highlights this year:

i) Under a contract with the fusion experiment ITER, one of the world's largest scientific collaboration, the Centre has designed, built and commissioned a laboratory to test a key machine safety technology, the shattered pellet injection. The requirements were extreme: hydrogen and neon gases have to be frozen at 5 Kelvin temperature to a 3 cm x 5 cm (diameter x length) cylinder and accelerated with a high-pressure gas pulse to several hundred m/s velocity. These pellets hit an oblique plate and the resulting fragments will supply large amount of material in short time to the ITER plasma, to cool it in case of an instability. The pellet injector, gas valve and fragment diagnostic equipment were fully designed and built by the EK team, and the first hydrogen pellet launch was achieved 13 months after start of the project.

ii) The growing energy needs of mankind stimulate the utilization of unconventional methane resources such as shale gas, methane hydrates and renewable biogas. Furthermore, environmental regulations world-wide focus on the effective decrease of greenhouse gases in the atmosphere like methane and $CO_2$. Combining these two important issues, methane conversion using $CO_2$ oxidant seems to be a sustainable way of getting value-added products from these abundant and relatively cheap starting materials. The so-called dry reforming reaction (DRM) converts methane/biogas with high $CO_2$ content and yields synthesis gas over appropriate catalysts. Our goal in DRM is to develop a novel generation of NiIn catalysts that can withstand detrimental coking during the reaction.

iii) Engineering nanoscale structural corrugations in graphene enables the scaling up of the resonance frequency of its plasmonic optical excitation from native THz into the commercially relevant visible range, as directly evidenced by Scanning Near-field Optical Microscopy (SNOM) imaging. Visible frequency graphene plasmons facilitate orders of magnitude stronger Raman enhancements than previously achieved with graphene, allowing the detection of molecules well below part per trillion level sensitivity, and high selectivity. Surface Enhanced Raman Scattering (SERS) substrates based on nanocorrugated graphene offer a series of practical advantages over conventional nanoparticle films, such as simpler and cheaper fabrication, better reproducibility, and highly improved environmental stability, up to several months. The results have been published in Nature Nanotechnology.

The research strategy of the Centre has also been updated according to the instructions of the Governing Board of the Eötvös Loránd Research Network. In parallel to the discussions on the new research directions, the support has significantly been increased. The new concept in the financial model promotes the participation in international research projects, higher level of innovation and the direct support of research infrastructures.

***Ákos Horváth***
***Director General***
***horvath.akos@energia.mta.hu***

# CONTENTS

# MISSION STATEMENT OF THE CENTRE FOR ENERGY RESEARCH

- Research and development in the field of nuclear science and technology for facilitating the adoption and the safe use of nuclear technology in Hungary.
- To participate in international research effort aiming at the establishing a new generation of nuclear power plants and closing the fuel cycle.
- Maintaining and improving competence in nuclear science and technology, especially in the field of nuclear safety, security, health physics, nuclear and isotope chemistry.
- To guarantee the safe operation of Budapest Research Reactor (BRR), and to ensure the open access to the research facilities around the reactor operated by the Budapest Neutron Centre.
- Research activities to improve nuclear analytical and imaging methods and their applications for energy and materials science.
- Perform studies in the field of environmental physics related to energy generation, renewable energies, energy storage and their impact on public health, and on environmental safety.
- Research and development in the field of low carbon energy technologies and of energy saving in industrial technologies.
- Development of nuclear energy production processes based on nuclear fusion, research and development of related technological and physical issues.
- Development of manned mission space dosimetry and space weather measurement systems, furthermore, improvement of devices for space-biological, -chemical and -material science experiments.
- Interdisciplinary research on complex functional materials and nanometer-scale structures, exploration of their physical, chemical, and biological principles, exploitation their operations in integrated micro- and nanosystems, and in the development of characterization techniques.
- Dissemination of the results in international programs, education and industrial research.

# ORGANIZATION STRUCTURE OF THE CENTRE FOR ENERGY RESEARCH (2021)

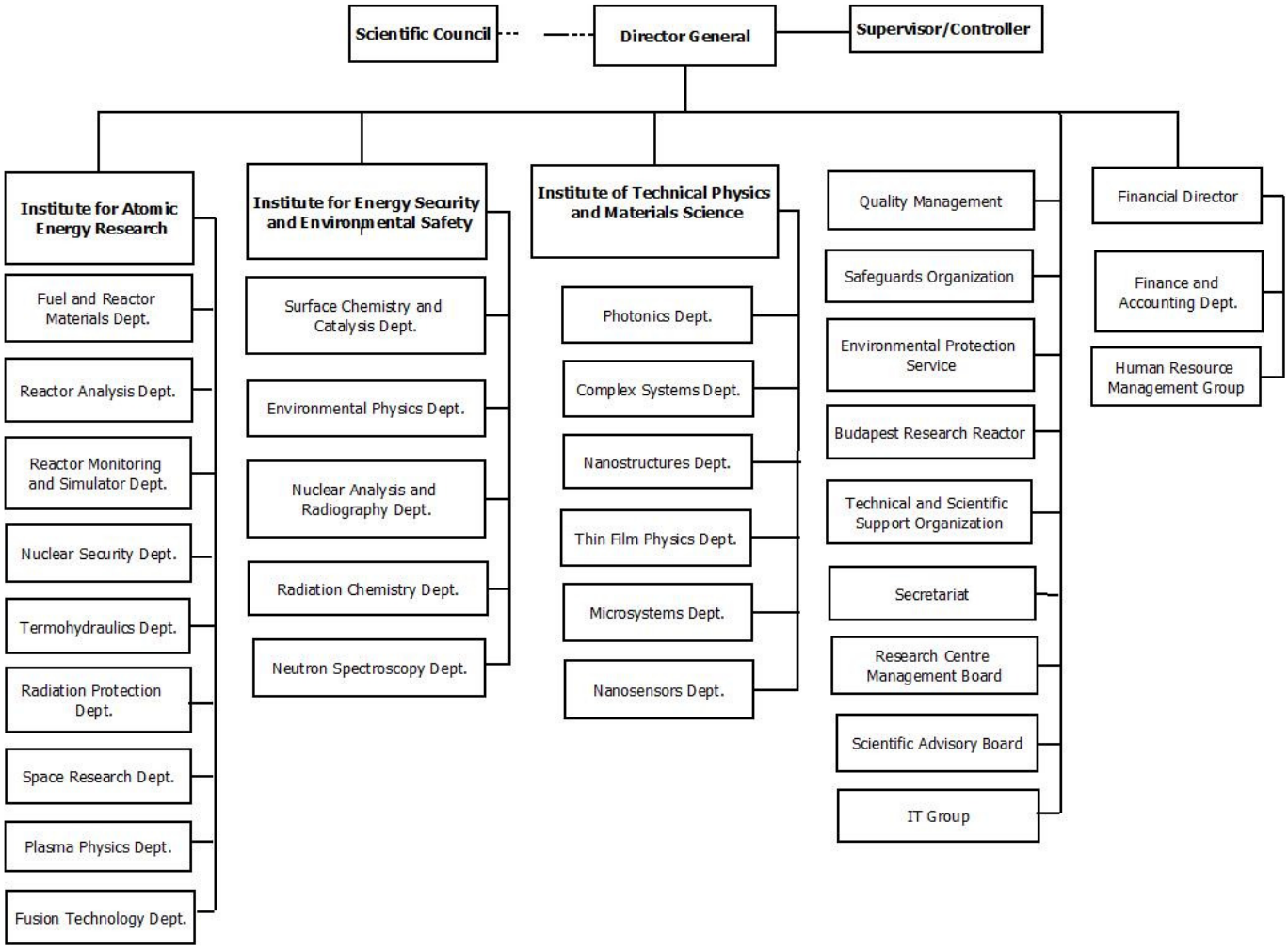

# QUALITY MANAGEMENT

In order to achieve the highest quality of research, development, design, condition monitoring and valuation, engineering, contracting and managing in design, production, implementation and inspection, the Research Centre's quality management system has continuously been upgraded by the recommendations of ISO 9001 standard since 1994. Reviewing our QM system by integral audits and management reviews, evaluating improvement opportunities, maintaining project documentation, infrastructure, supporting communication, ensuring the competence of workers the management improves the Centre's QM system. For the new organization structure, our Quality Policy has been renewed. Many new employees induced a need to upgrade our QM tuition practice. We organized the work and fire safety educations. Our QM system has been certified by Hungarian Standards Institution, IQNet, MVM Paks NPP, PaksII and Public Limited Company for Radioactive Waste Management.

MAGYAR SZABVÁNYÜGYI TESTÜLET
HUNGARIAN STANDARDS INSTITUTION
H-1082 Budapest, Horváth Mihály tér 1.

TANÚSÍTÁSI OKIRAT
CERTIFICATE

Tanúsítjuk, hogy a
We certify that the Management System of

**Energiatudományi Kutatóközpont**
**(kivéve az MFA és a Reaktorüzem)**
**H-1121 Budapest, Konkoly-Thege Miklós út 29-33.**
**Tanúsított székhely: H-1121 Budapest, Konkoly-Thege Miklós út 29-33.**

irányítási rendszere megfelel a szabvány követelményeinek a következő alkalmazási területen:
kutatás, fejlesztés, tervezés, állapotfelmérés és szakvéleményezés, mérőkszolgálat, fővállalkozási tevékenység tervezési, gyártási, kivitelezési és vizsgálati munkák irányítására, atomenergia alkalmazása körében eljáró független műszaki szakértői tevékenység

meets the requirements of the standard for the following activities:
research, development, design, condition monitoring and valuation, engineering, contracting and managing in design, production, implementation and inspection, independent technological expert activity in the field of application of nuclear energy

**MSZ EN ISO 9001:2015 (ISO 9001:2015)**

A tanúsítási okirat érvényes / The certificate is valid: **2020. 06. 25. – 2023. 06. 24.**
Ez a tanúsítvány az MSZT által évente kiadott fenntartási határozattal együtt érvényes.
This certificate is valid together with the maintenance decision annually issued by MSZT.
A tanúsítási okirat száma / Reg. number: **503/0309(7)**
Budapest, **2020. június 25.**
Az első tanúsítás dátuma / Date of the first certification: **1999. 06. 22.**

Pónyai György
ügyvezető igazgató

IQNet
THE INTERNATIONAL CERTIFICATION NETWORK

*CERTIFICATE*

*MSZT has issued an IQNet recognized certificate that the organization:*

***Centre for Energy Research***
***(except Institute of Technical Physics and Materials Science (MFA) and Reactor Department (Reaktorüzem))***
**H-1121 Budapest, Konkoly-Thege Miklós út 29-33.**
**Certified headquarters: H-1121 Budapest, Konkoly-Thege Miklós út 29-33.**

has implemented and maintains a

***Quality Management System***

for the following scope:

***research, development, design, condition monitoring and valuation, engineering, contracting and managing in design, production, implementation and inspection, independent technological expert activity in the field of application of nuclear energy***

which fulfils the requirements of the following standard:

**ISO 9001:2015**

Issued on: **25-06-2020**
First issued on: **22-06-1999**
Expires on: **24-06-2023**

*This attestation is directly linked to the IQNet Partner's original certificate and shall not be used as a stand-alone document*

*Registration Number:* **HU-MSZT-503/0309(7)-97(7)**

*Alex Stoichitoiu*
*President of IQNet*

*György Pónyai*
*General Director of MSZT*

IQNet Partners*:
AENOR Spain AFNOR Certification France APCER Portugal CCC Cyprus CISQ Italy CQC China CQM China CQS Czech Republic Cro Cert Croatia DQS Holding GmbH Germany EAGLE Certification Group USA FCAV Brazil FONDONORMA Venezuela ICONTEC Colombia Inspecta Sertifiointi Oy Finland INTECO Costa Rica IRAM Argentina JQA Japan KFQ Korea MIRTEC Greece MSZT Hungary Nemko AS Norway NSAI Ireland PYCE-SIGE Mexico PCBC Poland Quality Austria Austria RR Russia SII Israel SIQ Slovenia SIRIM QAS International Malaysia SQS Switzerland SIQAC Romania TEST St Petersburg Russia TSE Turkey YUQS Serbia
* The list of IQNet partners is valid at the time of issue of this certificate. Updated information is available under www.iqnet-certification.com




AZ MVM PAKSI ATOMERŐMŰ ZRT. IGAZOLJA, HOGY
KÖVETELMÉNYEINEK AZ

**ENERGIATUDOMÁNYI KUTATÓKÖZPONT**

**MINŐSÉGIRÁNYÍTÁSI RENDSZERE**

**MEGFELEL.**

*MINŐSÍTETT TERÜLET:*

ABOS 1, 2, 3 biztonsági osztályokba sorolt technológiai rendszerek és rendszerelemek átalakításával, javításával, karbantartásával és üzemeltetésével összefüggően főkonzulensi, tervezői, szakértői, valamint független műszaki szakértői tevékenységek végzése.

**A MINŐSÍTÉS ÉRVÉNYESSÉGI IDEJE: 2023.07.31.**

**A MINŐSÍTÉS SZÁMA: KM 67/2020**

EZEN MINŐSÍTŐ LAP A MELLÉKLETTEL EGYÜTT ÉRVÉNYES.

Paks, **2020. július 31.**

**PUSKÁS LÁSZLÓ**
főosztályvezető

**HORVÁTH GYÖRGY**
osztályvezető

atom erőmű
m v m

MINŐSÍTŐ LAP

PAKS II. PROJEKT

A MINŐSÍTÉS SZÁMA: NSZM/001/2019

Az MVM ERBE Zrt. igazolja,
(1117 Budapest, Budafoki út 95.)
hogy követelményeinek a

Energiatudományi Kutatóközpont
címe: Budapest, Konkoly-Thege Miklós út 29-33.

minőségirányítási rendszere
MEGFELEL.

Minősített terület:

1. Az új atomerőművi blokkok megvalósításához kapcsolódóan tanulmányok, elemzések, műszaki tervek készítése.
2. Az új atomerőművi blokkok megvalósításával kapcsolatban az orosz féllel megkötésre került szerződések végrehajtásával kapcsolatos mérnökszolgálati feladatok ellátása.
3. Az új atomerőművi blokkok megvalósításával összefüggő, magas szintű nukleáris biztonság megvalósításával kapcsolatos mérnökszolgálati feladatok ellátása.
4. Engedélyezési folyamatok támogatása.

A MINŐSÍTÉS ÉRVÉNYESSÉGI IDEJE: 2021.12.04.

Ezen minősítő lap a melléklettel együtt érvényes.

Budapest, 2020. május. 14.

dr. Korom Norbert Lajos
vezérigazgató

dr. Walter Géza
Paks II. igazgató

Minősítő Lap

A RADIOAKTÍV HULLADÉKOKAT KEZELŐ NONPROFIT Kft. IGAZOLJA, HOGY A

Magyar Tudományos Akadémia Energiatudományi Kutatóközpont

(cím: 1121 Budapest, Konkoly-Thege Miklós út 29-33.)

minőségirányítási rendszere megfelel a beszállítói követelményeknek.

Minősített terület

Radioaktív hulladéktárolókkal, nukleáris létesítményekkel kapcsolatos mérnökszolgálati tevékenység végzése az alábbi területeken:

- biztonsági elemzés készítése;
- szakértés;
- kísérletek tervezése, kivitelezése és kiértékelése;
- szoftverfejlesztés (tervezés, kivitelezés, validálás);
- kutatás-fejlesztés.

Biztonsági Osztály: KF,F,NF
Beszerzési Kategória: 1.,2.,3.

MINŐSÍTETT TEVÉKENYSÉG ÉRVÉNYESSÉGI IDEJE: 2022.03.20.
MINŐSÍTÉS KEZDETE: 2019.03.20.
A MINŐSÍTÉS SZÁMA: RHK 2019/02
MINŐSÍTŐ LAP A MELLÉKLETEKKEL EGYÜTT ÉRVÉNYES.
BUDAÖRS, 2019.03.22.

Horváth Attila
osztályvezető

Gémesi Csaba
biztonsági Főmérnök

*Certifications by Hungarian Standards Institution, IQNet, MVM Paks NPP, Paks II and Public Limited Company for Radioactive Waste Management*

Centre for Energy Research has complied with the requirements of the Hungarian Academy of Sciences which follow international standards. The Hungarian Academy of Sciences thereby authorized the Centre for Energy Research to use the label MTA Centre of Excellence.

CERTIFICATE
OF EXCELLENCE

The Hungarian Academy of Sciences (hereinafter: MTA) certifies that pursuant to the evaluation of the MTA research network, which was conducted in the period between 21 December 2018 and 31 March 2019, as approved by Decision 11/2018 (XII. 6.) of the General Assembly of MTA and in accordance with the evaluation criteria set by Decisions 2/2018 (XI. 16.) KTEB and 2/2018 (XII. 15.) KTEB of the MTA Presidential Committee for the Research Network (KTEB), the

Centre for Energy Research

has complied with the requirements of the Hungarian Academy of Sciences which follow international standards.

The Hungarian Academy of Sciences hereby authorises the Centre for Energy Research to use the label:

Hungarian Academy of Sciences Centre of Excellence;

short version: MTA Centre of Excellence,

as well as to use, in conjunction with this label, the logo of the Hungarian Academy of Sciences as defined in Annex 1 to this Certificate until 30 September 2020.

Done at Budapest, on October 2019.

Dr László Lovász
President
Hungarian Academy of Sciences

4495/5/2019/ET

Annex 1 to the Certificate of Excellence

The coloured figurative mark protected and registered under the name "MAGYAR TUDOMÁNYOS AKADÉMIA 1825" registration number 196064 at the Hungarian Intellectual Property Office, may be used as shown below, concurrently with the designation "Hungarian Academy of Sciences Centre of Excellence" or "MTA Centre of Excellence", or concurrently with a reference thereto.

Any re-editing, extension, completion or alteration in substance of the mark, or its use in any other way than what is described herein shall be prohibited and shall entail the revocation of the use of this mark.

MAGYAR TUDOMÁNYOS AKADÉMIA · 1825 ·

*Certificate of Excellence* (*This certificate was extended annually in 2020 and 2021*)

# BUDAPEST RESEARCH REACTOR

One of the most important strategic large scale research facilities in Hungary is the Budapest Research Reactor (BRR). It serves the needs of an extensive and diverse scientific community by supporting R&D opportunities, helping innovation and providing a strong foundation for training and education.

*Birdeye view of the Budapest Research Reactor*

BRR is a VVR-type reactor that uses light water as moderator and cooling fluid. The power of the reactor is 10 MW provided from low enrichment uranium fuel, and its main purposes – as established during the feasibility/functionality study – are radioisotope production, production of thermal and cold neutron beams for research and applications in all areas, primarily development of new functional materials and neutron activation analysis.

The core is designed to have about 120 reactor-days per year, having time-spans of 10 days or 4 days in a week. We are committed to long-term safety and responsible operations, taking care of the wastes from the spent fuel coming from the reactor. Besides the temporary spent fuel storage pool, we also operate a long-term spent fuel storage building for the physical and environmental separation between the reactor and the spent fuel storage.

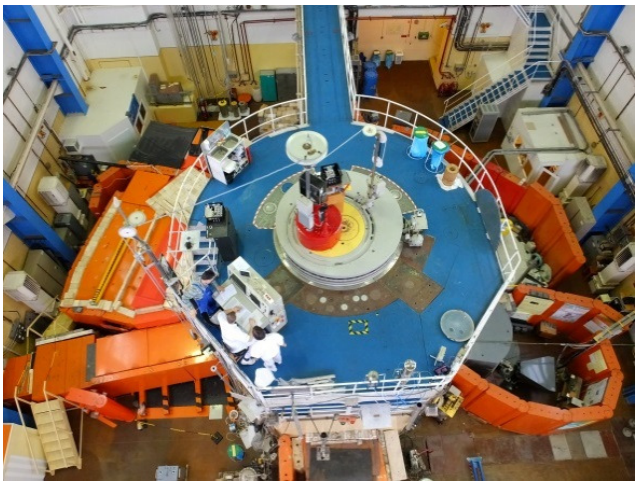

*Top view of the research reactor*


*Layout of the BRR's facilities*

The reactor hosts three kinds of activities: research activities utilizing neutron beams, production of radioisotopes for industrial and research purposes, and providing national and international training. We are proud of our innovative flagship research topics, which are carried out with a network of neutron beam stations, including beam-lines of thermal neutrons, experiments on powder and residual stress diffractometry, TOF neutron spectroscopy, radiography, biological irradiations and beam-lines of cold neutrons for experiments on small angle neutron scattering, reflectometry, prompt gamma activation analysis and nuclear data measurements. In accordance with recent worldwide trends, we are open to establishing new industrial relations, and supporting innovation. The BRR's experimental facilities are open to science based on excellence for researchers from all around the world. We aim to increase our competence on special topics, to implement new technologies and develop new materials, to promote and exploit our R&D capacity at the national and regional/international level. During the past years BRR hosted several international schools on various technical and research topics, special trainings in the field of reactor physics, reactor operation, nuclear measurement techniques, and safety and environmental issues. Typical research topics are: physics, chemistry, material sciences, engineering, life sciences and biotech.

BRR is used by groups of different scientific communities from medical, environmental, material, archaeological, nuclear sciences and industry, as well as several Hungarian Universities. Neutron beams are uniquely suited to study the structure and dynamics of materials at the atomic level. The Budapest Neutron Centre (BNC) coordinates the scientific utilization of the research reactor. Some of the main research topics currently are:

- neutron scattering, used to examine changes of sample properties under different conditions such as variations in vacuum or pressure, high and low temperature and magnetic field, modelling real-world conditions.
- using prompt and delayed neutron activation analysis, it is possible to measure the concentration of elements in ppm and ppb levels even for small samples. Atoms of a sample become radioactive by exposure to neutrons from the reactor. They decay by gamma-rays characteristic for each element that can be detected by suitable detectors.
- neutron activation is also used to produce different radioisotopes, widely used in industry and medicine. For example, Y-90 microspheres to treat liver cancer are produced by bombarding Y-89 with neutrons, which capture them. Production of radioisotopes for different applications such as medicine, sterilization and industrial use.
- testing reactor materials; they are subjected to intense neutron irradiation which cases radiation damage of their crystalline structure. For instance, some steels become brittle. Thus, the so-called high-entropy alloys resisting embrittlement are to be used in nuclear reactors.
- applied research using neutron beams to produce images of material interior. Examples are the visualization of porosities in materials or changes of density inside the sample. Dynamic neutron radiography of cooling system of refrigerator or visualization of fuel burn in engine system of a car and tomography of different materials and items.

BNC provides researchers with 15 neutron instruments; 13 of them are installed directly on the horizontal beam ports of the reactor or to the thermal and cold neutron guides, while the other 2 are placed at the vertical irradiation channels. The instruments are supported by a variety of sample environments and data analysis and visualization capabilities.

BNC provides access to the international neutron user community through a peer-review system. Local scientists assist researchers and industrial users to find the appropriate neutron techniques that meet their research needs. The various neutron scattering instruments in BNC cater to a large number of users from Europe and have grown in strength and stature over the years. Due to the COVID-19 pandemic, BNC accepts only so called remote users, which means that samples are sent by mail and the measurements are performed by the instrument scientists without the user and the results are forwarded to the users via electronic ways.

BNC is a member of the League of advanced European Neutron Sources and CERIC-ERIC, and partner in recent EU Framework Programme projects (H2020 IPERION HS, CREMLIN+, ARIEL and TOURR).

BNC is strongly committed to the training of future professionals inland and all over the world in co-operation with the International Atomic Energy Agency. We cooperate with several Hungarian universities (Budapest University of Technology and Economics, Eötvös Loránd University (ELTE), Pannon University, Óbuda University and University of Pécs). BNC accommodates students for laboratory practice for studying nuclear-based techniques. A specialized course was developed for geology students of ELTE to introduce nuclear analytical techniques into their education. BNC organizes the Central European Training School on Neutron Scattering annually, which was cancelled this year due to the pandemic. The school provides insight into neutron scattering, element analysis and imaging techniques and their applications to study the structure and dynamics of condensed matter.

The Budapest Research Reactor is open to the public. Members of the local communities and high school and university students visit us regularly and learn more about the amazing nuclear science possibilities available at BRR.

# I. RESEARCH ACTIVITIES SUPPORTED BY DOMESTIC AND INTERNATIONAL PUBLIC AGENCIES

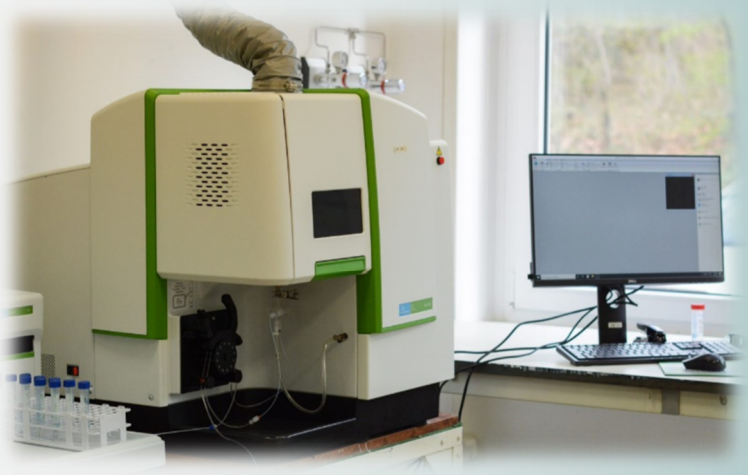

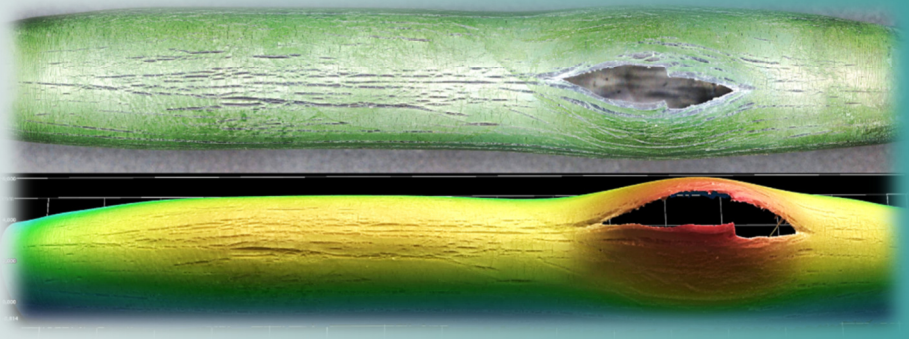

# DEVELOPMENT OF ALLEGRO GAS-COOLED FAST REACTOR DEMONSTRATOR

*János Gadó, Zoltán Hózer, Bálint Batki, Gusztáv Mayer*

## *Objective*

ALLEGRO is a small power helium-cooled fast spectrum demonstrator reactor. Its primary goals are to demonstrate the technology and to test a new type of refractory carbide fuel in a fast neutron spectrum and at high core outlet coolant temperature. Two starting core configurations are developed. Because of the transportability and proliferation issues of the Mixed Oxide (MOX) fuel in Europe, a Uranium Oxide (UOX) core is being developed parallel. The starting core's outlet coolant temperature is about 520 °C, and dedicated positions will be used for the refractory fuel subassembly qualification with a helium coolant outlet temperature of around 800 °C. The final selection between the MOX and the UOX starting core will be done in a later phase of the project. When the new refractory fuel is validated, a fully refractory core is envisaged with a helium outlet coolant temperature of around 800 °C. Currently, EK actively participates in the Euratom SafeG project, which aims to improve the safety of the Gas-cooled Fast Reactor (GFR) technology. It has several work packages. One of its tasks is dedicated to ALLEGRO core safety and core optimization. EK also participates in the recently launched Euratom PUMMA project dedicated to investigate the behaviour of fuel with high plutonium content and to study fuel recycling possibilities.

## *Methods*

An iterative method was used between the thermal-hydraulics and the neutronic calculations to achieve an optimized ALLEGRO core. As a first step, we selected the most enveloping transients for the current ALLEGRO design, based on the previous categorization carried out for the Experimental Technology Demonstration Reactor (ETDR), CATHARE thermal-hydraulics calculations and engineering considerations. These transients are the total hot duct break with Decay Heat Removal (DHR) bypass, 10-inch Loss of Coolant Accident (LOCA) with DHR bypass, unprotected 3-inch LOCA and unprotected control rod group withdrawal. As a next step, a suitable reactor physics calculation tool - KIKO3DMG macroscopic code using group constants from SERPENT and with special Cusping effect treatment - was developed and validated on the ALLEGRO CEA 2009 concept. The Pu content of the fuel assemblies was varied in the radial direction. The newly optimised core has 111 MOX assemblies, and it meets the SiC Displacement per Atom (DPA) rate requirement (> 8 DPA/year) and satisfies the preliminary requirement for the maximum power density. The $Pu_{239}$ content of the assembly is varied in the range of 4.95 – 3.96% atomic ratio. The maximal MOX assembly power is decreased by 32% compared to the CEA concept.

Euratom has recently launched the PUMMA project to investigate the behaviour of fuel with high plutonium content and to study fuel recycling possibilities. Experiments made earlier will serve for the validation of fuel behaviour codes.

The main steps of the fuel qualification process for GFR fuel assembly with $SiC_f/SiC$ cladding and carbide fuel pellets were identified in the framework of EU SafeG project using the Technolgy Readiness Level (TRL) methodology and taking into account the categories introduced by the OECD Working Group on the Safety of Advanced Reactors.

## *Results*

The CATHARE safety analyses of the newly defined MOX core were performed with both best estimate and conservative calculations. The best estimate analyses showed that the maximum cladding temperatures stay below the criteria for the selected transients. Nevertheless, the peak cladding temperatures are above the given limits if the conservative frame parameters are used, which indicates that further investigations are necessary.

The following decision-making points could be identified in the framework of fuel qualification:

a) The selection between Uranium Carbide (UC) and mixed carbide pellet could be made taking into account fabrication capabilities and proliferation issues. Oxide fuel has to be considered as a near term solution.
b) In the design process, the main core parameters and some of fuel assembly design and fuel criteria will be set, but they can be changed based on qualification results. And vice versa, any change in reactor design will influence the fuel qualification requirements.
c) The decision on the fabrication process and the selection of a fuel supplier will have an important impact on the whole qualification process. The products of the given supplier produced by the agreed technology will have to be checked, even if similar products were already tested.
d) Decision on the necessity of irradiation testing of a full fuel assembly in a separate He cooled loop in a fast reactor, or testing the full assembly only in the ALLEGRO reactor has to be done.
e) The selection of computer codes and their application strategy will be an integral step of fuel qualification.

## *Remaining work*

The following pivotal step in the SAFEG project is to define a new optimized refractory core.

The fast reactor fuel behaviour code FUROM-FBR developed by EK will be validated with experiments in the framework of the PUMMA project. The qualification process will be extended for refractory fuel with UOX pellets and $SiC_f/SiC$ cladding.

## *Related publication*

[1] Z. Hózer, E. Slonszki, J. Klouzal: *D4.1 GFR refractory fuel qualification options,* Version 1.0 EU SafeG project (2021)

# STRATEGIC RESEARCH GROUP FOR THE CHALLENGES OF RENEWABLE ENERGY BASED SYSTEMS

*Bálint Hartmann, Attila Kazsoki, Bálint Sinkovics, Viktória Sugár*

## *Objective*

The cornerstone of Hungary's energy independence is the decentralized renewable-based energy production. Funding schemes primarily focus on the facilitation of the spread of photovoltaic (PV) systems. According to the present plans, the built-in PV capacity to be installed in Hungary by 2030 is 6400 MW, while by 2040 it should reach 12,000 MW. As a result of this development, at least 21% of gross energy demand in 2030 will be produced from Renewable Energy Sources (RES). In order that these units could be connected to the electric grid properly, the existing medium voltage distribution network and the voltage control mechanisms should also be developed.

The ever-changing performance of weather-dependent energy producing units makes it difficult for the Distribution System Operators (DSOs) to ensure appropriate power quality. In order that the integration of RES-based energy producing units could be achieved without a loss in power quality, the possible effects of this process on the distribution network should be analyzed. This can successfully be achieved by the application of a simulation framework, which allows the analysis of various weather changes on computer models of real-life systems with high PV penetration.

## *Methods*

The central component of the simulation framework is a stochastic simulation, which can map the possible event horizons based on both static inputs and data changing in every running cycle. The model on which the simulation is run was built up from electric and GIS parameters in DIgSILENT PowerFactory environment. The emerging topography is mapped onto a coordinate system fixed by us, while special attention is paid to network nodes and the connection points of PV panels. Solar irradiation data enter the simulation framework as the output of a cloud movement simulation. The framework chooses the load profile of Medium Voltage/Low Voltage (MV/LV) transformers from a database of real measurement data from real areas in 1-minute resolution. Load profiles are updated by the stochastic simulation at each run, including the load of the MV/LV transformer (30–35%, with future load projections based on the estimated increase of residential consumption), the power factor (in the 0.95–1 range), and time series data. The production profiles of PV panels are also included. The number of PV units connected to the network is changed according to the simulated scenario, while the nominal capacity of each PV unit is 500 kVA and operates with a power factor of one according to the present Hungarian practice, which does not require reactive power compensation. Consequently, only active power is fed into the grid. The modelled PV units do not have any control device; thus the modelled cases can be regarded as worst-case scenarios from the perspective of voltage control.

## *Results*

The results have shown that current limitations of rapid voltage changes could be violated even in case of moderate PV penetration levels, which is likely to be observed in the short-term. The results have also highlighted the importance of placement strategies, namely that knowing climatic parameters (most importantly wind distribution) and topography of the supply area, the DSO is able to minimize adverse grid effects.

It is important to highlight that the question of rapid voltage changes is only one aspect of challenges concerning voltage control, which arise for DSOs owing to the increasing solar panel capacity. In our view, the 2% limit must be examined in all cases by considering the whole voltage profile of the line, as the technical problem to be solved is how those future PV capacities could be included.

## *Future work*

The authors are working on the further development of the simulation network. The aim is to make the possibility of validation of simulation results by measurements of weather data and the power produced by solar panels. The ongoing setting up of a demonstration system at the Centre for Energy Research, Hungary will use several solar panels with different material structures, with a weather station and also the recordings of a total sky imager for validation.

## *Related publications*

[1] B. Turóczi, A.S. Kazsoki, V.O. Groma, B. Hartmann: *Effects of Cloud Movements on the Rapid Voltage Changes of PV Rich Distribution Networks*, IEEE Access, under review (2022)

[2] B. Sinkovics, B. Hartmann: *Flexibilis tartaléktervezési módszertan bemutatása az időjárásfüggő termelők figyelembevételével: Esettanulmány, in Proc. XI. MAIT*, (2021)

# CORTEX – CORE MONITORING TECHNIQUES AND EXPERIMENTAL VALIDATION AND DEMONSTRATION

*Sándor Kiss and Sándor Lipcsei*

## *Objective*

The CORTEX project has been a four-year long, wide cooperation between 20 institutes, universities and companies of 11 countries in several working packages. The consortium was strategically structured around the required core expertise from all the necessary actors of the nuclear industry, both within Europe and outside. The project aimed at developing an innovative core monitoring technique that allows detecting anomalies in nuclear reactors, such as excessive vibrations of core internals, flow blockage, coolant inlet perturbations, etc. The technique is based on primarily using the inherent fluctuations in neutron flux recorded by in-core and ex-core instrumentation, from which the anomalies are differentiated depending on their type, location and characteristics. The method is non-intrusive and does not require any external perturbation of the system. The project was planned to result in a deepened understanding of the physical processes involved. This allows utilities to detect operational problems at a very early stage and to take proper actions before such problems have any adverse effect on plant safety and reliability.

## *Methods*

The project work was divided into several working packages covering specific objectives:

- Development of modelling capabilities for reactor noise analysis,
- Validation for the modelling tools against experiments in research reactors,
- Development of advanced signal processing and machine learning methodologies for analysis of plant data,
- Application and demonstration of the developed modelling tools and signal processing techniques against plant data,
- Knowledge of the dissemination and education.

## *Results*

The four years of the project have resulted in more than 65 publications, 30 conference presentations, and 8 training courses. For more details see: https://cortex-h2020.eu/

Here we focus on our research contribution to the analysis and enhancements of the coolant velocity estimation method in Pressurized Water Reactor (PWR) core [1]. This paper investigates analytically the method that has been proven so far for coolant velocity estimation in PWRs and demonstrates its various features through measurements performed at a VVER-440 unit. Presence of the background noise makes the evaluation of the measurements quite difficult, but the disturbing effects can be eliminated.

A model was set up in order to help separating the fractions of the measured signals coming from the propagating perturbation and the background noise, and the spectra of these signal fractions were produced. Then the cross-spectrum of the propagating perturbation freed from background noise was reconstructed and the components of the transfer function between the detectors were produced. It was proven that the similarity of the spectra of the background noise and the propagating perturbation makes a sharper peak in the impulse response function than in the cross-correlation function.

The transit time is usually read from the cross-correlation and impulse response functions estimated as the inverse Fourier transform of the cross-spectrum and the transfer function, respectively. We found that resetting the real part (which also contains the background) before performing the inverse Fourier transform produces functions from which the transit time can be read more easily (this helps the automation of measurement evaluation).

It was also investigated how the size of the detector with finite length influences the transfer of the propagating perturbation by the detector. The effect of the non-constant neutron flux distribution along the measurement chain was also investigated and analyzed.

Finally, the peaks appearing in the correlation functions at the transit time were investigated and it was found that the slope of axial distribution of the neutron flux makes them asymmetrical and slightly shifts the maximum of the peak.

## *Acknowledgement*

The research leading to these results has received funding from the Euratom research and training programme 2014-2018 under grant agreement No. 754316.

## *Related publications*

[1] S. Kiss and S. Lipcsei: *Analysis and enhancements of the coolant velocity estimation method in PWR core*, Annals of Nuclear Energy **174** (2022) https://doi.org/10.1016/j.anucene.2022.109146

[2] C. Montalvo, L. Pantera, S. Lipcsei, L.A. Torres: *Signal processing applied in CORTEX project: from noise analysis to OMA and SSA methods*, Annals of Nuclear Energy **175** (2022) https://doi.org/10.1016/j.anucene.2022.109193

# PARTICIPATION TO THE SIMULATION BENCHMARK IN THE ATLAS+ PROJECT

*Levente Tatár*

## *Objective*

In the ATLAS+ project experiments and simulations were strongly interconnected. As much of the experimental work done in the framework of the project involved Finite Elements (FE) simulation using damage mechanics, a Gurson-Tvergaard-Needleman (GTN) type damage mechanics [1] benchmark has been organized to increase confidence in simulations, by identifying strengths and weaknesses of the methods used by the participants.

## *Methods*

Every participant involved in the benchmark used exactly the same FE mesh, material properties (including plastic flowcurve and Gurson parameters) for 3 types of specimens: Notched Tensile (NT), Single Edged Notched Tensile (SENT) and Compact Tension (CT). The applied boundary conditions were also the same. Axisymmetric simulations had been performed for the NT specimens, 3D simulations were used for the SENT and CT specimens. For comparison, a simple elasto-plastic analysis had been performed for each case.

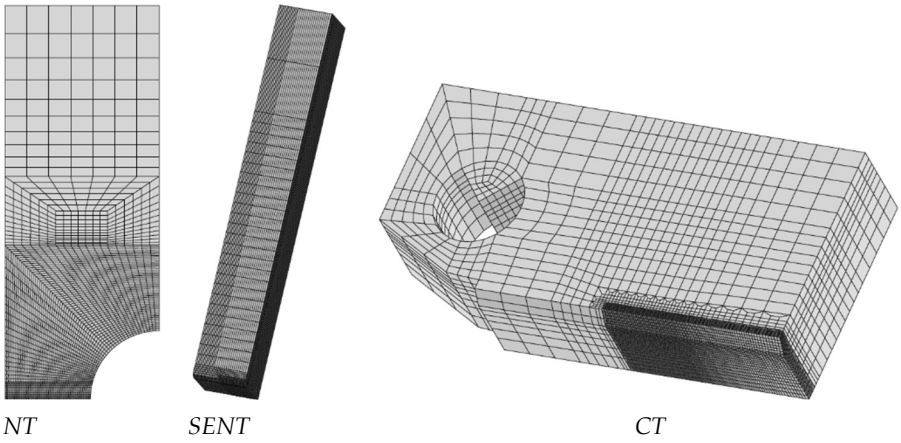


*Figure 1: Specimens used in the benchmark*

## *Results*

The benchmark revealed differences between the codes used and the approaches of the participants.

For all participants, the elasto-plastic reference case for all specimens produced very little differences, of the order of 0.1 %.

For all participants, the axisymmetric computations for NT specimens produced acceptable differences (of the order of 1-2 %), but to obtain these results several runs with different time-steps were needed. As the model was small, rerunning the job several times was not problematic.

For the SENT computations a good agreement has been found between partners, except EK, where there was a remarkable overestimation of the Crack Mouth Opening Displacement (CMOD) with regard to the other results. In general, the scatter for all partners was higher than for the NT specimen.

EK results for CT specimens were in satisfactory agreement with the partners' results, however an oscillatory behaviour has been found for one of the stress components at a predefined node.

## *Remaining work*

Rerunning the analysis outside the ATLAS+ benchmark gave results, which were more in line with the partners'.

The ATLAS+ project has been finished, however, work involving damage mechanics will most probably be the subject of more research in the framework of other upcoming projects. As a main remark it can be stated, that although damage mechanics has already several decades of history and was/is very promising, practical application for complex 3D structures requires very highly skilled professionals and it is still quite far from being useable in everyday practice. An elasto-plastic analysis requires considerably more effort than a simple elastic one, and an analysis involving damage mechanics needs much more effort than an elasto-plastic one. This requires weeks for running an analysis, where a single wrong job parameter (like convergence testing, time step, solver type etc.) can multiply the time needed to finish and can lead to unacceptable results.

## *Related publication*

[1] A. Needleman, V. Tvergaard: *An analysis of ductile rupture in notched bars*, Journal of the Mechanics and Physics of Solids **32.6,** 461-490 (1984)

# RADONORM: TOWARDS EFFECTIVE RADIATION PROTECTION BASED ON IMPROVED SCIENTIFIC EVIDENCE AND SOCIAL CONSIDERATIONS – FOCUS ON RADON AND NORM

*Árpád Farkas, Balázs G. Madas*

## *Objective*

The RadoNorm project under EURATOM Horizon 2020 aims at managing risk from radon and Naturally Occurring Radioactive Materials (NORM) exposure situations to assure effective radiation protection based on improved scientific evidence and social considerations. EK coordinates the Dosimetry Work Package (WP3) and contributes to the Effects and Risks (WP4), Education and Training (WP7), and Communication, Dissemination and Exploitation of Results (WP8) WPs. The project lasts for five years. Specific objectives for 2021 were i) to quantify the *in vivo* dose distributions in human lungs in order to provide realistic exposure conditions for *in vitro* experiments with cell cultures and organotypic tissue models, ii) to support such experiments with dosimetry, iii) to collect experimental data on low dose hyper-radiosensitivity and induced radioresistance (see 129_PR2021), iv) to support the evaluation of a training course, and v) to organize the 1st Annual Meeting of the project.

## *Methods*

Two computational modelling approaches were combined in order to estimate absorbed doses in different cell nuclei in case of several exposure conditions including home and uranium mine environments. Taking into account the spatially inhomogeneous dose distribution, average doses in the bronchial airways and maximum doses in the deposition hot spots were estimated. Computational microdosimetry was applied to determine dose rates and dose distributions in *in vitro* experiments. An online survey was applied to collect feedback from course participants. Due to COVID 19 pandemic, the 1st Annual Meeting was held virtually.

## *Results*

Based on the simulations, the following recommendations could be made to investigate the effects of one Working Level Month (WLM) exposure in the bronchial airways. In the deposition hot spots, cells should be irradiated with 500 mGy dose and 0.7 mGy/h dose rate corresponding to home conditions, while cells should be irradiated with 860 mGy dose and 15.5 mGy/h dose corresponding to mine conditions. Outside the deposition hot spots, cells should be irradiated with 5 mGy dose and 0.007 mGy/h dose rate corresponding to home conditions, and cells should be irradiated with 8.6 mGy dose and 0.16 mGy/h dose rate corresponding to mine conditions. Besides this, support was provided successfully to WP4, WP7, and WP8.

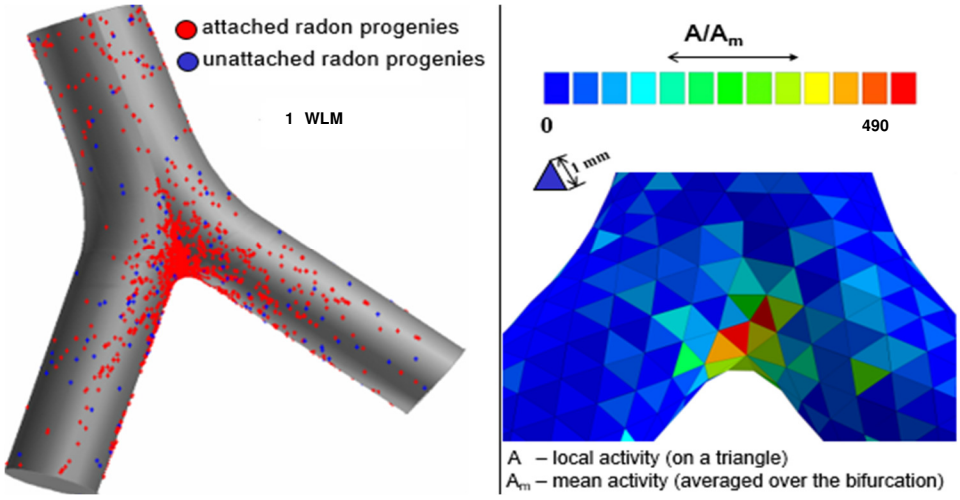


*Figure 1: Deposition pattern of the inhaled radon progenies in a central bronchial airway bifurcation (left) and colour map of the deposition enhancement factors (right)*

## *Remaining work*

The RadoNorm project runs until mid-2025. Important tasks for 2022 are to determine dose distributions in rat lungs on radon exposure, and to quantify the effects of smoking on absorbed doses from radon exposure.

## *Related publication*

[1] Á. Farkas and B. G. Madas: *Milestone 40: Dose distributions in human lungs* (2021)

# CHEMICAL EVOLUTION AND RADIONUCLIDE RETENTION STUDIES FOR HIGH-LEVEL RADIOACTIVE WASTE DISPOSAL

*Margit Fábián, István Tolnai, János Osán, Ottó Czömpöly*

## *Objective*

The interface between carbon steel and cementitious materials is a key issue in the design of a disposal cell for vitrified High-Level radioactive Waste (HLW) and Intermediate Level Waste (ILW) in argillaceous and crystalline rock formations for the Hungarian national waste disposal program. The designs rely upon steel-containers (S235JR) containing the HLW encased in a prefabricated cylindrical concrete/clay buffer material. The concrete is made from CEM II cement and limestone aggregates. The clay is from the Boda Claystone Formation (BCF), the host rock considered for the final disposal program in Hungary. The pH has to be kept at high values during the thermal phase, and for a much longer period after, in order to keep the carbon steel container passivated, to limit corrosion and ultimately to prevent radionuclide release. The aim of the planned experiments is to gain information on chemical-physical alterations of the steel/concrete and steel/clay interfaces, for different environmental conditions (temperature, groundwater) using different characterization methods. The planned work is an attempt to simulate the conditions which cause the corrosion, whose intensity we plan to measure in laboratory tests. All experimental results will serve as input parameters for modellers. The modelling calculations will be carried out by SCK CEN (Centre d'Étude de l'énergie Nucléaire, Belgian) in a later stage of the project.

Quantifying the long-term entrapment of radionuclides (RN) in the solid phases of the host rock around the radioactive waste repository is a crucial step toward understanding diffusion and transport mechanisms. Sorption and diffusion characteristics of RNs in anionic form ($SeO_3^{2}$) are studied on clay-rich rock sections of BCF in both crushed and intact forms. Diffusion experiments involving inactive $SeO_3^{2-}$ are especially performed for later microscopic investigations of the diffusion front on both the oxidative (albitic claystone) and on the reductive (pyritic) sections of a recent BCF core. These studies may deliver information on the possible formation of nanocrystalline precipitates due to redox reactions.

## *Methods*

The "Assessment of the Chemical Evolution of ILW and HLW Disposal Cells Work Package" is dedicated to identify and model the main reactive processes at the steel/cement and steel/clay interfaces and their consequences in terms of element transfers and the evolution of microstructures. All data (from modelling and experiments) have to describe geochemical behaviours as a function of the environmental constraints which are representative of the conditions expected to be encountered in geological storage facilities. Two parallel sets of laboratory experiments were conducted to gain information on the corrosion intensity at the interfaces between carbon steel and concrete and of carbon steel and clay. A temperature of 80°C was used for the sake of consistency and comparison with the other experiments performed earlier. Synthetic groundwater of the Boda Claystone was used for hydrating the clay and conditioned cementitious water for the cement to set the boundary environmental conditions. After 3, 7 and 12 months a container was opened for post-mortem characterization. With Scanning Electron Microscopy / Energy Dispersive X-ray spectroscopy (SEM/EDX) investigations we focused on the composition and nature of the alteration products formed on the steel and within the clay/cement, and these results were further checked by micro-Raman investigations. The surrounding liquid was characterized using Inductively Coupled Plasma - Optical Emission Spectrometry (ICP-OES) [1] and Ion Chromatography (IC). The initial physical and chemical properties of the concrete and the Boda water chemistry have been compiled to further define the initial states of the reactive transport model.

The "Fundamental Understanding of Radionuclide Retention Work Package" is dedicated to experimental and modelling studies to give a deeper insight into radionuclide retention. Our research group focuses on sorption and diffusion experiments on the BCF host rock. Sorption of $SeO_3^{2-}$ is studied on crushed rock samples with a particle diameter less than 63 μm using conditioned synthetic BCF groundwater. Sorption isotherms (sorbed amount as a function of the equilibrium concentration, $C_{eq}$(M), in the liquid phase) are recorded through batch experiments in the $10^{-10}$-$10^{-3}$ M equilibrium concentration regime using both $^{75}$Se tracer and inactive Se. Diffusion cells accommodating 4-8 mm thick slices of full diameter (62 mm) core sections and small hexahedral pieces (10×10×30 mm$^3$) are used. To monitor the diffusion in the rock, the changes in concentration of the RN during the experiment lasting several months are measured in the liquid phase. At the end, the rock will be cut and the concentration profile which has developed inside the rock will be mapped. Equilibrium concentrations in the liquid phase are determined using ICP-OES and Liquid Scintillator Counting (LSC) for inactive Se and $^{75}$Se tracer, respectively. On the solid samples microscopic X-Ray Fluorescence (μXRF), microscopic X-Ray Diffraction (μXRD), Scanning Electron Microscopic (SEM) and X-ray Absorption Near-Edge Structure (XANES) investigations will be performed.

## *Results*

For the cement samples the corrosion potential had positive values close to zero, while for clay samples, the potentials were negative throughout the experiment. Local corrosion was not observable based on potentials for both cases. After 3, 7 and 12 months, the clay/concrete phases were still well saturated. Formation of 30-40 μm long Fe-oxide ingrowths were detected and confirmed by micro-Raman investigations. The main corrosion products contain hematite, magnetite and ferrihydrite in different ratios. On the steel/clay interface, as early as 7 months, a FeO -> $Fe_2O_3$ (e.g. hematite) partial transformation was found (see Figure 1). The B, Ca, K and Na concentrations measured in the soaking liquid increased, while the Mg, and Si concentration decreased with time. Concentrations of $Cl^-$ and $SO_4^{2-}$ ions in the final porewater are close to the starting concentrations; the increase was less than 10% for chloride but higher for sulphate.

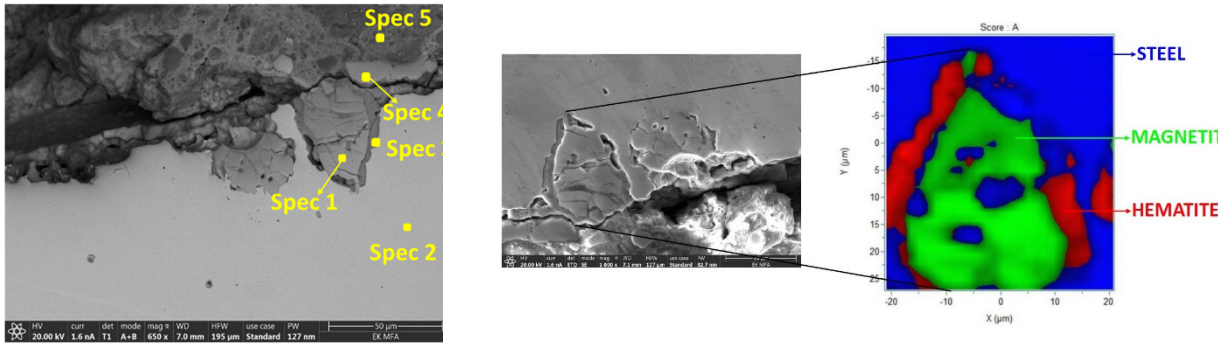


*Figure 1: Steel/clay surface after 7 Month, SEM image (left), and micro-Raman map (right). In our opinion the objects are easy to be identified in the original figures.*

*Table 1: SEM/EDX elemental composition after 7 months (at %)*

| **Elements** | **Spec 1** (Corrosion prod.) | **Spec 2** (steel) | **Spec 3** (Corrosion prod.) | **Spec 4** (Corrosion prod.) | **Spec 5** (clay) |
|---|---|---|---|---|---|
| O | 48,04 | | 64,90 | 61,42 | 67,07 |
| Na | | | | | 0,64 |
| Mg | | | | | 2,47 |
| Al | | | | | 4,11 |
| Si | | 0,36 | 0,38 | 1,49 | 9,82 |
| K | | | | | 0,64 |
| Ca | | | | | 0,78 |
| Mn | 1,08 | 0,65 | 0,53 | 0,88 | |
| Fe | 50,74 | 98,99 | 34,18 | 35,68 | 14,47 |

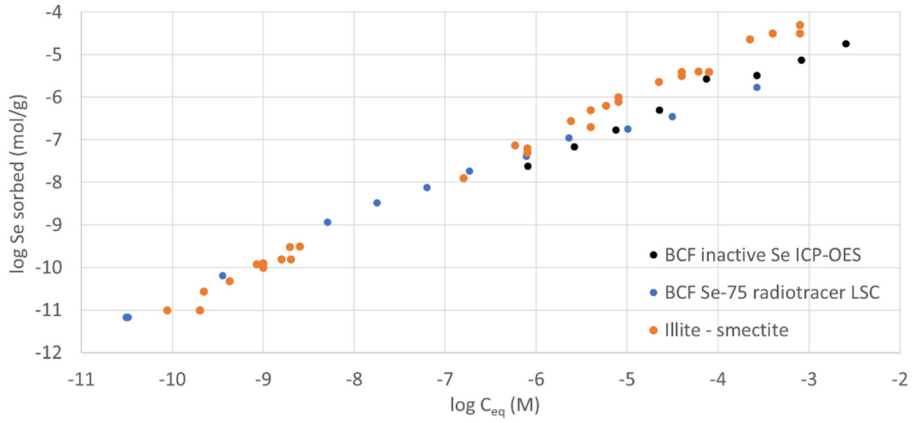


*Figure 2: Comparison of $SeO_3^{2-}$ sorption isotherms obtained for BCF and data available in the literature for illite/smectite. Sorption isotherm was already defined in the "Methods" section.*

Results obtained from batch sorption experiments of $SeO_3^{2-}$ on crushed Boda Claystone are in line with sorption isotherms reported in the literature for pure illite and illite-smectite minerals (Fig. 2) [1]. The diffusion experiments are currently ongoing, the decrease of $SeO_3^{2-}$ concentration indicates uptake, but so far no breakthrough of $SeO_3^{2-}$ was experienced. The BCF core sections which have undergone diffusion studies are being prepared for microscale characterization. No change of the Se oxidation state was detected in the liquid phase during sorption/diffusion experiments. Synchrotron radiation XANES revealed that the majority of Se was found to remain as Se(IV) for BCF both in dispersed (crushed) and compact (thin section) forms.

*This work was supported by the H-2020 European Joint Program on Radioactive Waste Management (EURAD) – 847593.*

## *Remaining work*

This is the third year of a five-year project; we continue the well-prepared schedule.

## *Related publication*

[1] O. Czömpöly, M. Fábián, I. Tolnai and J. Osán: *Application of TXRF and ICP-OES in studies related to radioactive waste management,* 1st International Summer School on TXRF, 20-24 09 2021, Bari, Italy (virtual), poster (2021)

# TESTING OF CLADDING MATERIALS FOR ACCIDENT TOLERANT FUEL DESIGNS

*Zoltán Hózer, Márton Király, Richárd Nagy, Erzsébet Perez-Feró, Balázs Peidl, Anna Pintér-Csordás, Levente Illés, Márta Horváth*

## *Objective*

In the framework of the IAEA project "Testing and Simulation for Advanced Technology and Accident Tolerant Fuels" (ATF-TS) several cladding samples arrived from foreign partners to EK laboratories in order to carry out different tests and examinations for the characterization of different designs. The EK's experimental work focuses on the investigation of ATF cladding behaviour under accident conditions.

## *Methods*

High temperature furnace was used for the execution of oxidation tests in steam. The Cr-coated and uncoated zirconium ring samples with 8 mm length were oxidized in steam mixed with 12 vol.% argon under isothermal conditions at 1000 °C and 1200 °C for 3600 s and 1800 s, respectively. A high temperature tube furnace with a quartz tube was used for the oxidation of the samples. The experimental setup consisted of a steam generator, a three-zone horizontal furnace with temperature control system and a condensing system.

Ballooning tests were carried out with linear pressure increase of samples at high temperatures up to 945 °C. The tests were conducted at isothermal conditions. The samples were heated up to high temperatures in inert atmosphere in a three-zone tube furnace. A self-modified National Instruments LabView Virtual Instrument (VI) was used to control the pressure increment and also for data acquisition. The samples were cut by lathe to 85 mm and were closed at one end by a welded zirconium plug. An iron sealing adapter was welded to the other end of all the tubes, which were then connected to an argon feeder tube by a cutting ring tube connector. 99.999% pure argon gas was used for the internal pressure increment during these tests.

Metallography and scanning electron microscopy were applied for the examination of cladding microstructure before and after oxidation. A scanning electron microscope (ThermoScientific Scios 2 type) was used for morphological studies. Both secondary- (SEI) and backscattered electron images (BEI) were taken on the cross sections of each sample at 5 keV. The elemental composition and the distribution of the most interesting elements were investigated by an Oxford X-MAX20 type energy dispersive X-ray microanalyzer (EDX) with silicon drift detector. Energy dispersive X-ray spectra were recorded on some interesting areas of the different layers of cross sectional samples.

## *Results*

The two-sided oxidation resulted in much higher mass gain for the uncoated reference Zr samples than for the coated ones. Table 1 summarizes the results of oxidation tests expressed in ECR (Equivalent Cladding Reacted) on the basis of mass gain measurements. The specific mass gain on the Cr surface was several times less than that on the Zr surfaces.

*Table 1: Oxidation in steam of uncoated and Cr-coated Zr alloys*

| Material | Ox. temp. (°C) | Ox. time (s) | Oxidation ratio (ECR%) |
|---|---|---|---|
| uncoated Zircaloy-4 | 1000 | 3600 | 14.5 |
| Cr-coated Zircaloy-4 | | 3600 | 7.5 |
| Cr-coated optZirlo™ | | 3600 | 6.0 |
| uncoated Zirlo™ | | 3600 | 13.5 |
| Cr-coated optZirlo™ | | 3600 | 6.9 |
| uncoated Zircaloy-4 | 1200 | 1800 | 33.6 |
| Cr-coated Zircaloy-4 | | 1800 | 25.4 |
| Cr-coated Zirlo™ | | 1800 | 20.2 |
| uncoated optZirlo™ | | 1800 | 42.3 |
| Cr-coated optZirlo™ | | 1800 | 21.6 |

Burst tests series were started for the benchmark exercise in the ATF-TS project. Several preliminary ballooning and burst tests were carried out on uncoated and Cr-coated Zircaloy-4 and optZirlo™ samples, supplied by Karlsruhe Institute of Technology (KIT) and Czech Technical University, Prague (CTU). Slight degree of oxidation due to air ingress was visible on the surface

of the samples, green $Cr_2O_3$ was formed. Significant cracking of the coating was observed close to the burst location in the first tests (Fig. 1 left), which was done at 945 °C with 20 kPa/s pressurization rate.

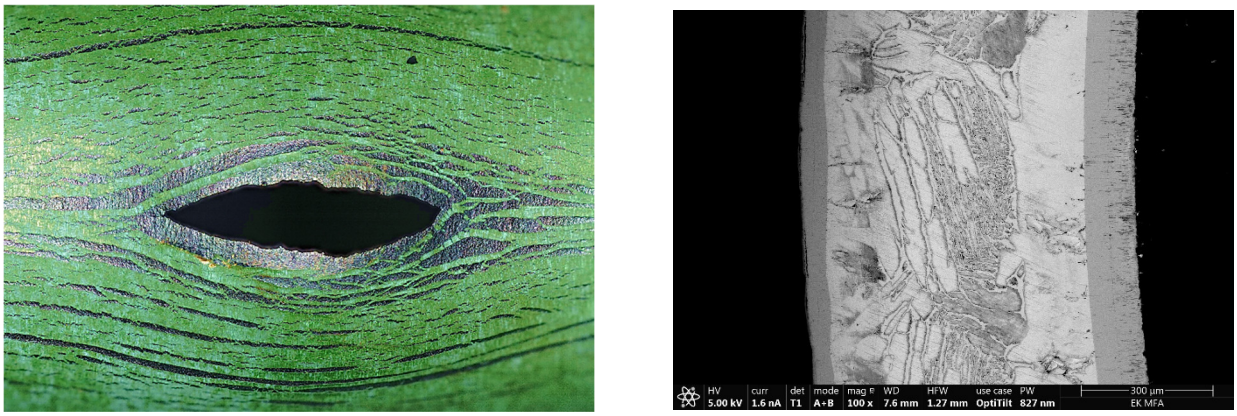


*Figure 1: Burst opening of Cr-coated Zircaloy-4 sample at 945 °C, $p_{burst}$= 1,88 MPa ( left) and microstructure of Cr-coated Zircaloy-4 cladding after oxidation in steam at 1200 °C for 1800 s (right)*

Cross sectional samples were prepared from the cladding samples uncoated and coated with chromium and oxidized at 1000 °C and 1200 °C. The main observations were the followings:

- It was established that the outer Cr–oxide layer was mostly detached from the cladding samples oxidized at 1000 °C and it was missing from a lot of places for the Cr-coated Zircaloy-4 sample. At 1200 °C thinner or thicker cracks could be revealed between the Cr-oxide and the Cr, or the Cr layer and the Zr metal.
- For cross sectional sample of Cr-coated Zircaloy-4 sample after oxidation at 1000 °C the thickness of the Cr layer was 10-12 µm and that of the inner side Zr–oxide layer 45-60 µm.
- For cross sectional Cr-coated Zircaloy-4 sample, oxidized at 1200 °C, the Cr–oxide layer has 0.8–1.2 µm, the Cr layer 4–5 µm thickness and there was a Zr-oxide layer even at the outer edge of the cladding sample. The thickness of this layer was 40-45 µm. In the Cr layer small Zr–oxide inclusions could be found. At the inner side of the sample the thickness of the Zr–oxide layer was about 120 µm (Fig. 1 right)
- In case of Cr-coated Zirlo™, oxidized at 1000 °C, the Cr-oxide layer was slightly detached from the Cr layer. The thickness of the Cr–oxide layer was 2.8–3 µm, while that of the Cr layer was 9-10 µm. At the inner side of the sample the thickness of the Zr–oxide layer was 20–40 µm.
- In the cross section of Cr-coated Zirlo™, oxidised at 1200 °C, the Cr–oxide was partly detached from the Cr and two Cr-oxide layers could be found at some places with different O content. The thinner (1–1.2 µm) layer had 17.3 wt% O, while the thicker one (about 4.5 µm) had 28.6 wt% O. The thickness of the Cr layer was 5- 8 µm. Between the Cr and the Zr there was a Cr-Zr mixed layer with about 0.4–0.6 µm. At the inner side of the sample, the thickness of the Zr–oxide was about 110 µm.
- It seems that the Cr–oxide layer, which was thin in most of the studied samples, was detached from the Cr layer. In some samples, two types of Cr–oxides were produced probably due to the high temperature oxidation. The presence of Cr in the Zr metal and that of the $ZrO_2$ in Cr shows intensive diffusion processes.
- The presence of gap(s) between the Cr–oxide and the Cr, or the Cr layer and the Zr metal is not advantageous. In some samples oxidized at 1200 °C, Zr-oxide layer was also detected beside Cr–oxide and Cr layers. The presence of cracks especially the ones perpendicular to the surface of the ring samples, can help the oxygen to admit even to the Zr metal accelerating the corrosion rate.

## *Remaining work*

Further testing and examination of ATF cladding tubes will be continued according to the IAEA ATF-TS project plan.

## *Related publications*

[1] B. Peidl, E. Perez-Feró: *High temperature oxidation of accident tolerant fuels*, EK-FRL-2021-120-1-3-M0

[2] A. Pintér Csordás, L. Illés: *Electron beam studies of oxidised and Cr-coated zirconium alloys Part 2*, EK-FRL-2021-120-1-2-M0

[3] Z. Hózer, M. Király, R. Nagy, E. Perez-Feró, B. Peidl, A. Pintér-Csordás, L. Illés, M. Horváth: *Planned activities of EK in the framework of IAEA ATF-TS Coordinated Research Project*, First Coordination Meeting on Testing, Modelling and Simulations for Accident Tolerant and Advanced Technology Fuels (ATF-TS), 23-27 August 2021, IAEA Headquarters, Vienna, Austria

# PROGRESS ON THE EURAD SCF EUROPEAN JOINT PROGRAMME

*Márton Király, Márta Horváth, Richárd Nagy, Nóra Vér, Zoltán Hózer*

## *Objective*

The European Joint Programme on Radioactive Waste Management (EURAD) project began in 2019. The Centre for Energy Research Fuel and Reactor Materials Department is involved in the Spent Fuel Characterization (SFC) work package to develop characterization techniques that will allow us to more fully understand the physicochemical evolution of irradiated spent fuels (pellets and cladding) under normal and credible accident scenarios following reactor discharge, during (wet and dry) interim storage, transport to and emplacement in a geological displacement facility.

## *Methods*

In the five years of the project, two separate experiments are conducted on two zirconium-niobium fuel cladding alloys used in WWER-type NPPs, the E110 and the E110G. The first task is to study the creep of cladding samples near the operating temperature under internal pressure. The samples are either untreated as-received claddings, or heat treated and hydrogenated up to 1000 ppm at 600 °C. The second task is to study the ductility and embrittlement of claddings under various hydrogen treatments using the mandrel method to simulate pellet-cladding mechanical interaction. The upper limit of the hydrogen content of the samples is 3200 ppm.

## *Results*

Only the first creep and mandrel tests have been performed in 2020. Two sets of creep test were completed, in which samples heat treated and hydrogenated at 600°C were subsequently tested at 400°C in inert atmosphere with 11 MPa inner pressure. The diameter change was registered with laser scanner micrometre at regular intervals. The result confirmed a decrease in creep velocity for the hydrogenated samples compared to the heat treated and as-received samples. This might be caused by the hardening effect of the hydrogen that was first absorbed and then precipitated in the zirconium lattice as zirconium hydrides. The two tested alloys behaved in a similar manner.

The mandrel ductility tests were conducted at room temperature in the apparatus designed in the EK laboratory. The as-received cladding samples were very ductile, the 8 mm long cladding ring samples reached over 80% increase in inner diameter before failure. As the hydrogen content of the samples increased, so did the maximum measured force, but before failure, the diameter increase lessened. The mode of failure changed after 1500 ppm hydrogen, as the ductile necking and large plastic deformation was replaced with ruptures along definite axial cracks. The least ductile samples were those containing around 3000 ppm of hydrogen, as these samples hardly showed plastic deformation and ruptured into several pieces at twice the force as the as-received samples. The gradual decrease in ductility can be seen in Figure 1. The decrease in ductility is almost linear up to 2000 ppm hydrogen, after that a plateau is reached. This is well in line with our ring compression ductility tests where the change in ductile to brittle behaviour was reported at 2000 ppm hydrogen as well.

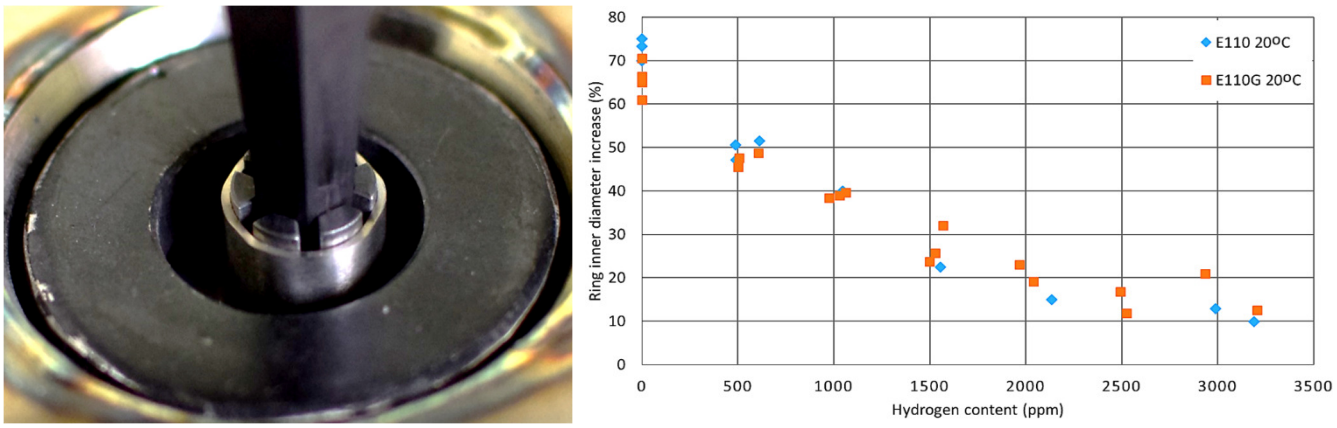


*Figure 1: The mandrel test on a zirconium cladding sample (left) and the decrease in ductility (maximum reached inner diameter before failure) with the growing hydrogen content for the two tested cladding types (right)*

## *Remaining work*

In the following years, additional creep tests will be carried out on different cladding materials, and the mandrel tests will be continued at higher temperatures. The project ends with a Deliverable Report towards the European Commission in 2024.

## *Related publication*

[1] M. Király, M. Horváth, R. Nagy, N. Vér, Z. Hózer: *Segmented mandrel tests of as-received and hydrogenated WWER fuel cladding tubes,* Nuclear Engineering and Technology, Available online 26 March 2021

# IMPROVEMENT OF IODINE SPIKING SIMULATION IN THE FRAMEWORK OF EU R2CA PROJECT

*Zoltán Hózer, Berta Bürger*

## *Objective*

During a Steam Generator Tube Rupture (SGTR) event the system parameters will change and activity release associated with iodine spiking is expected from defective fuel rods. The amount of released activity from those fuel rods has to be estimated. The objective of the present work was to improve the iodine spiking model in the RING code by extension of the scope of simulation with caesium isotopes.

## *Methods*

Fitting of the new coefficients of the spiking model in the RING code was performed using reactor shutdown, power change and start-up transients of a VVER-440 Nuclear Power Plant (NPP). After running calculations on all data sets with the old coefficients, the measured and calculated activity concentrations were compared and this procedure was repeated with the new coefficients. Several iterations were needed to reach acceptable agreement between the measured and the calculated data.

## *Results*

The iodine spiking model of the RING code was updated against new NPP measured data. Both power transients and reactor shutdown cases were used. The results showed that the effect of power change was underestimated by the previous version of the code.

The introduction of the new caesium spiking model was based on the available measured data. The correlation for $^{134}$Cs and $^{137}$Cs is similar to that of $^{131}$I, and takes into account the effects of power, pressure and boric acid concentration changes during the transient.

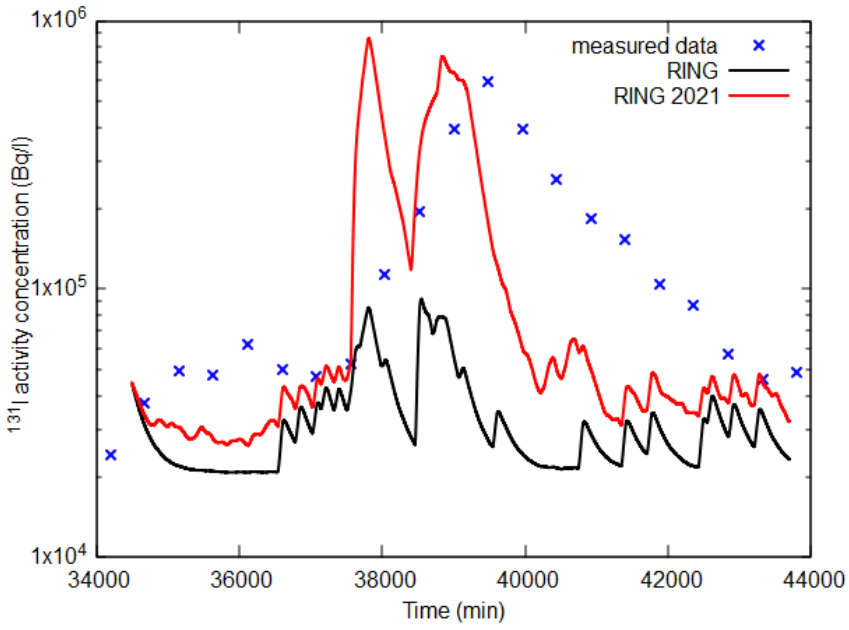


*Figure 1: Measured and calculated coolant $^{131}$I activity concentrations using the original (RING) and improved (RING 2021) code versions*

## *Remaining work*

The new model will be applied to the simulation of iodine and caesium spiking effects in steam generator tube rupture and collector cover opening incidents. This model will allow to estimate the activity release according to the specific power and pressure histories of the two events more precisely.

## *Related publication*

[1] B. Bürger, Z. Hózer: *Improvement of the iodine and caesium spiking models in the RING code,* EK-2021-437-1-4-M0 (2021)

# HYDROGEN UPTAKE TESTS WITH ZIRCONIUM ALLOYS IN THE FRAMEWORK OF EU R2CA PROJECT

*Péter Szabó, Zoltán Hózer*

## *Objective*

In the present work the measurement of the hydrogen uptake by two Zr alloys was addressed. There are a large number of results available on hydrogen uptake tests of Zr, but most of the tests were carried out at high temperatures. The typical cladding temperatures in defective fuel rods, under normal operational conditions, are in the range of 300-400 °C and the main objective of this work was to produce new experimental data in this range.

## *Methods*

The investigated cladding materials were E110G and Zircaloy-4. E110G is a sponge base Zr-1%Nb alloy while Zircaloy-4 (Zry-4) is a tin-bearing alloy with 1.4-1.6 wt% Sn content. The E110G (outer diameter: 9.10 mm; wall thickness: 0.67 mm) and the Zry-4 (outer diameter: 10.75 mm, wall thickness: 0.73 mm) fuel cladding tubes were cut into 8 mm long specimens. The specimens were open tube segments. Prior to the experiments the tube segments were degreased and cleaned by acetone in ultrasonic bath and weighed carefully.

The experimental set-up consists mainly of an electrically heated three-zone tube furnace with a quartz tube put in it that joins to a pipe-line system. The quartz tube contains the sample holder and can be evacuated or filled up with argon or hydrogen gas. The hydrogen pressure was measured by a Vacuubrand type DVR 5 pressure gauge and recorded by a computer during the experiments. The decreasing of the pressure meant that the samples were absorbing the hydrogen. After 23 hours the recording of the pressure was stopped and the sample holder was fully pulled out from the furnace. After it has cooled down to room temperature, the system was filled with argon gas up to around 1000 mbar and after opening the samples were carefully collected and weighed.

The samples were weighed both before and after the hydrogenation using a Mettler Toledo XP2U type ultra microbalance having a readability of 0.1 µg. Based on the weight of the samples the approximate hydrogen content of the samples could be estimated.

## *Results*

The experimental series with hydrogen charging of Zircaloy-4 and E110G alloys were successfully completed. The tests covered the temperature range of 300-400°C. The experimental data showed the increase of hydrogen uptake with the increase of temperature (Fig. 1). The hydrogen uptake of the two tested alloys was significantly different.

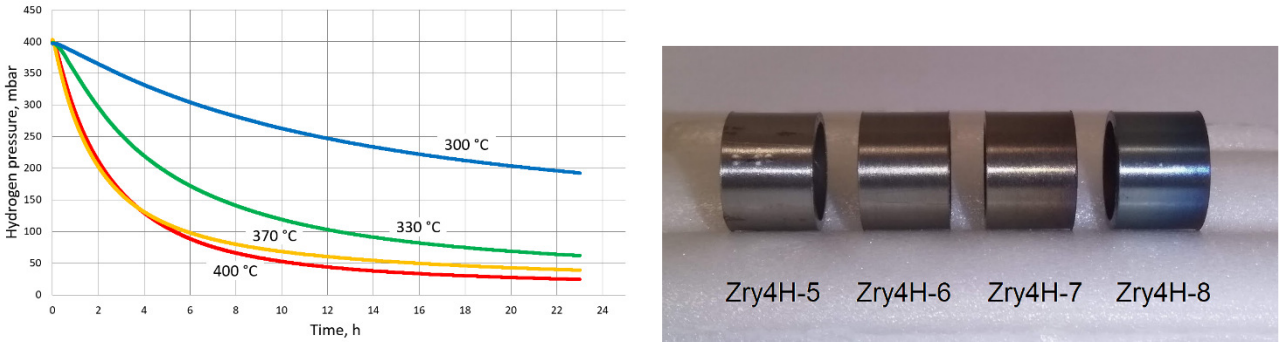


*Figure 1: The hydrogen pressure during the experiments with Zircaloy-4 samples at different temperatures (left) and view of the samples after the hydrogen uptake test at 400 °C (right)*

## *Remaining work*

The experimental database will be used for the development of hydrogen uptake numerical models for the TSKGO computer code which is used for the simulation of defective fuel rods.

## *Related publication*

[1] P. Szabó, Z. Hózer: *Hydrogen uptake tests with zirconium alloys at reactor operational temperatures,* EK-2021-437-1-1-M0 (2021)

# POTENTIAL REFERENCE SAMPLES FOR ELEMENTAL ANALYSIS OF AEROSOL PARTICLES COLLECTED BY CASCADE IMPACTORS

*János Osán, Csaba Dücső, Ottó Czömpöly, Veronika Groma*

## *Objective*

Direct Total-reflection X-Ray Fluorescence (TXRF) analysis of aerosol particles collected by means of cascade impactors is a valuable method for size-resolved elemental analysis. Detection limits below 100 pg/m$^3$ can be reached by laboratory or portable equipment for sampling durations of a few hours [1]. Having an appropriate size and time resolution, the combination of cascade impactor sampling and TXRF results in size distribution of chemical elements, which is reliable for identifying sources of short-term pollution episodes [2]. The non-destructivity of TXRF has also the advantage that the collected samples are available for complementary characterization methods, e.g. Scanning Electron Microscopy (SEM), Raman spectroscopy and X-ray absorption spectrometry. Internal standardization generally performed for droplet residues is not straightforward for direct TXRF analysis of cascade impactor samples, since the deposition pattern of the collected particles is generally different for various impactor types that can even have a stagewise variation. For example, May-type and Sioutas impactors collect the aerosol particles deposited as thin stripes, while Dekati impactors have series of round nozzles distributed in a rotational symmetry around the centre of impactor plates.

## *Methods*

The AEROMET II project aims at the development of potential reference samples for the TXRF analysis of aerosol particles collected by cascade impactors. These reference samples are designed to have known elemental composition and mass distributed along a lateral pattern similar to the aerosol particle deposits expected in the impactors. Based on previous experience on Cr pads distributed onto 20×20 mm$^2$ Si wafers using optical lithography along a thin stripe in the centreline, similar samples have been prepared on round Si wafers of around 30 mm in diameter to be suitable for measurements in most commercial TXRF equipment. Deposition patterns of both May-type and Dekati impactors were considered, distributing metallic pads of a few μm in diameter and 50-120 nm in height taken randomly within the deposited areas.

## *Results*

Since the deposition pattern is different for each stage for the 13-stage Dekati impactor, reference-free synchrotron-radiation XRF revealed that stagewise correction factors are necessary for appropriate elemental quantification [1]. The amount of particulate matter deposited on the impactor stages is also critical for TXRF quantification [3], therefore the potential reference samples were designed to contain low but quantifiable mass of the elements of interest. The shape and diameter of the pads and their uniformity were verified by electron microscopy (Dekati stage 5, Fig. 1). The test samples prepared so far were found to be promising with excellent production repeatability. Further developments are on-going to obtain reliable reference samples that can be used as external standards for calibration of table-top TXRF equipment.

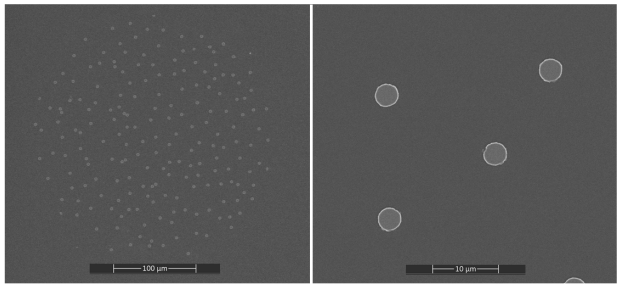


*Figure 1: SEM images of Cr pads randomly distributed within one of the 27 circular spots of Dekati stage 5*

*This work was supported by the EMPIR programme, co-financed by the Participating States and from the European Union's Horizon 2020 research and innovation programme, through grant agreement 19ENV08 AEROMET II.*

## *Remaining work*

Development of calibration procedures for laboratory TXRF equipment used in elemental analysis of aerosol particles.

## *Related publications*

[1] S. Seeger, J. Osán, O. Czömpöly, A. Gross, H. Stosnach, L. Stabile, M. Ochsenkuehn-Petropoulou, L. A. Tsakanika, T. Lymperopoulou, S. Goddard, M. Fiebig, F. Gaie-Levrel, Y. Kayser and B. Beckhoff: *Quantification of element mass concentrations in ambient aerosols by combination of cascade impactor sampling and mobile total reflection X-ray fluorescence spectroscopy*, Atmosphere **12**, 309 (2021)

[2] O. Czömpöly, E. Börcsök, V. Groma, S. Pollastri and J. Osán: *Characterization of unique aerosol pollution episodes in urban areas using TXRF and TXRF-XANES,* Atmospheric Pollution Research **12**, 101214 (2021)

[3] Y. Kayser, J. Osán, P. Hönicke and B. Beckhoff: *Reliable compositional analysis of airborne particulate matter beyond the quantification limits of total reflection X-ray fluorescence*, Analytica Chimica Acta **1192**, 339367 (2022)

# FUEL CYCLE AND FUEL BEHAVIOUR SIMULATION IN THE FRAMEWORK OF EU PUMMA PROJECT

*Zoltán Hózer, János Gadó, Berta Bürger*

## *Objective*

The EU PuMMA project aims to outline various options for plutonium management in Generation-IV systems, to assess their impact on the full fuel cycle, with regard to safety and performance. EK will contribute to the simulation of fuel behaviour and analyses of fuel cycle scenarios. Furthermore, EK coordinates a work package on fuel properties with high Pu content – measurements and modelling.

## *Methods*

The FUROM-FBR-2 code is applied for the simulation of fast reactor fuel behaviour simulation. The FUROM code was developed in EK for calculating reactor fuel behaviour in the quasi-static approximation. The code was validated for VVER and Light Water Reactor (LWR) conditions and it is widely applied for VVER reactor studies. The code was now rewritten for gas cooled fast reactor conditions.

The nuclear fuel cycle simulation code called SITON (SImulation TOol for modelling the Nuclear fuel cycle) is a result of a co-operation between EK and BME NTI. The fuel cycle model was developed in EK; the burnup module to evaluate the discharge composition in the 2400 MW thermal power design of the Gas-cooled Fast Reactor (GFR2400) was developed in BME NTI.

## *Results*

Input data sets were collected for the TRABANT and CAPRIX irradiation experiments. The requested output data were agreed with the EU PuMMA project partners. The first runs with the FUROM-FBR-2 codes were successfully completed.

Fuel cycle scenarios with LWRs and fast reactors were specified together with EU PuMMA project partners. The contribution of EK will focus on gas-cooled fast reactors. The first runs with the SITON code were successfully completed.

A meeting of the EU PuMMA WP3 was organized in on-line manner and the progress in the following tasks was reviewed:

Task 3.1: Evaluation at atomic scale or meso-scale of thermal properties,

Task 3.2: Evaluation of mechanical properties,

Task 3.3: Evaluation of thermodynamic properties of the fuel,

Task 3.4: Measurements of thermal properties.

## *Remaining work*

The activities in the EU PuMMA project will be continued as described in the detailed work plan.

## *Related publication*

[1] Z. Hózer: Minutes of the EU PuMMA WP3 meeting, 18th May, 2021 (on-line) *"Fuel properties with high Pu content: Measurements and modelling"*

# STRUMAT: STRUCTURAL MATERIALS RESEARCH FOR SAFE LONG TERM OPERATION OF LIGHT WATER REACTOR NUCLEAR POWER PLANTS

*Ildikó Szenthe, Ferenc Gillemot, Márta Horváth, Balázs Hargitai*
*Kristóf Andor Csikós, Szilvia Móritz, Dávid Cinger*

## *Objective*

One of the critical issues of long-term operation of pressurized water reactors is the embrittlement of the reactor pressure vessel wall caused mainly by neutron irradiation. The goal of the project is understanding the unfavourable synergy between Nickel, Manganese and Silicon on the microstructure and mechanical properties of the reactor pressure vessel at high neutron fluences. This is needed to elucidate the irradiation effects toward the end of the life of the vessel. Existing embrittlement trend equations tend to underpredict the reactor vessel material embrittlement at higher fluence regimes. The suitability of a master curve approach at high fluences together with the use of small/sub-sized test specimens to characterize irradiation induced shifts in reference curves for bulk materials needs to be further investigated.

## *Methods*

An international collaborative research project with the participation of 18 European countries + Ukraine was set up to study these issues. The project is led by our institute. An irradiation campaign had been performed in the High Flux Reactor, Petten, Netherlands. A variety of different reactor vessel steel samples with systematic variations in Nickel, Manganese and Silicon contents have been irradiated to high fluence resembling reactor operation for greater than 60 years. Post irradiation study of these specimens will allow a better understanding of the above problems. EK undertook the management of the manufacturing and testing possibilities of small specimens, which played a key role in carrying out the study. Round-Robin measurements of non-irradiated specimens was initiated to enhance the testing quality of the participants.

## *Results*

Un-irradiated and irradiated specimens were received, and the irradiated ones were stored in a hot cell. New facilities have been built for testing them and new extensometers were ordered. EK participated in the elaboration of the project test matrix and designed the detailed testing plan for its share of the testing. According to the test matrix, the half thickness Charpy specimens have been recut for three-point bend specimens and pre-fatigued. All the specimens were hardness tested. The testing of the 32 un-irradiated specimens is going on. After the ongoing mechanical testing, fractography, metallography and small angle neutron scattering measurements will be performed.

EK also leads the work package related to tests of the mini compact tension specimens, small punch tests and the supplementary testing. The result of the un-irradiated sample small punch tests is shown in Figure 1.

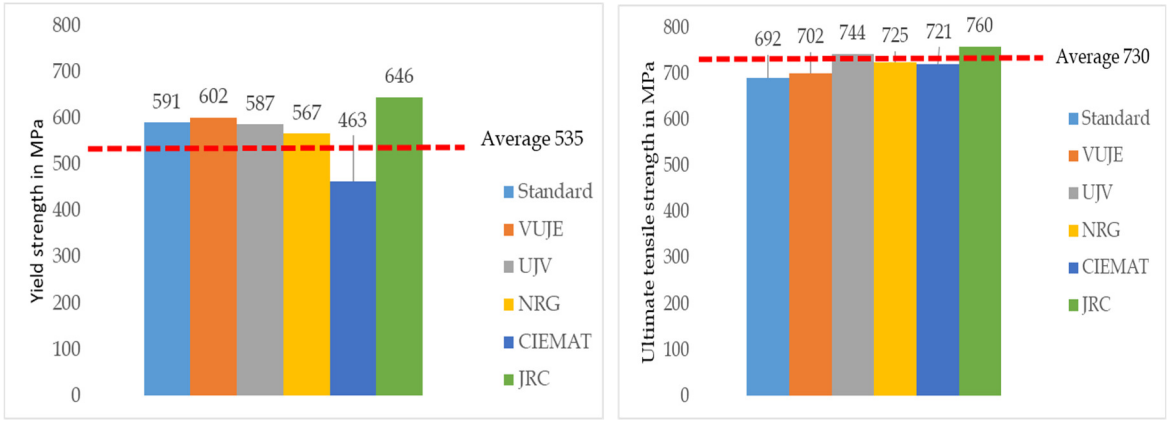


*Figure 1: Small punch test results: yield strength and ultimate tensile strength in MPa, per participants (JRC European Joint Research Centre, Belgium, VUJE Vujjini Consultancy Services Ltd., Slovakia, UJV Institute of Nuclear Research Czech Republic), NRG Nuclear Research and Consultancy Group, Netherlands, CIEMAT Centre for Energy, Environmental and Technological Research, Spain)*

## *Remaining work*

After the un-irradiated specimen tests are complete, the irradiated samples will be machined from the half thickness remnants and will be tested. Reactor vessel surveillance data will be collected and used to develop enhanced embrittlement trend equations. The results will increase the knowledge of the role of the Nickel and Manganese in the aging of steel reactor materials.

## *Related publication*

[1] F. Gillemot, Á. Horváth, M. Kollury, I. Szenthe, M. Horváth: *The project "STRUMAT-LTO"*, OATK (2021)

# INVESTIGATION OF CHEMICAL REACTIVITY OF HIGH-LEVEL RADIOACTIVE WASTE STORAGE MATERIALS

*Margit Fábián, Ottó Czömpöly, István Tolnai, János Osán*

## *Objective*

According to international experts, the most suitable material for stabilizing High-Level radioactive Waste (HLW) is glass, which is produced by vitrification and then moulded into a metal container. As the host rock of the deep geological repository, which serves as a natural barrier, argillaceous rock has been chosen for radionuclide retention in several countries. The Boda Claystone Formation (BCF) is considered as the potential host rock in Hungary. We concentrate on extending existing HLW concepts in Europe through the study of the "glass/steel/clay" system. The glass alteration rate strongly depends on the chemistry (pH, concentration of waste material in a silica matrix) of the aqueous phase in the buffer material, and on the nature of the products formed during the corrosion of the containment package before its breakdown. The present work is designed to investigate (i) the interaction of the materials used to form the engineering barrier system, especially on the contact interfaces, and (ii) the sorption and diffusion properties of the selenite anion for the evaluation of the radionuclide retention capacity of the BCF, which functions as the external natural barrier.

## *Methods*

In order to study the chemical evolution of a glass/steel/clay system and to compare it with other different HLW systems, a long term experiment was performed. A recently developed borosilicate glass composition which was found to efficiently incorporate lanthanides/actinides [1] and Boda claystone were used as the glass and clay components, respectively. Our experiment started on 29 June 2020 and finished on 30 June 2021. We completed a set of three glass/steel/clay experiments using groundwater/porewater for saturation. The initial water phase considered in the experiment is a synthetic BCF porewater (SBPW) with the following composition (mol/L): $Na^+$: $1.7\times10^{-2}$, $Ca^{2+}$: $3.1\times10^{-3}$, $Mg^{2+}$: $2.3\times10^{-3}$, $K^+$: $1.8\times10^{-4}$, $Cl^-$: $2.3\times10^{-2}$, $HCO^{3-}$ $6.1\times10^{-4}$, $SO_4^{2-}$ $1.9\times10^{-3}$ pH: 8.1, Eh= -300 ± 10 mV (measured at RT). Double walled Teflon containers were constructed: an external vessel and an internal vessel, which contains the mixture of powdered glass, steel and claystone. The container dimensions were: external Teflon container: height: 160 mm, diameter: 90 mm and an internal Teflon container: h: 100 mm, d: 50 mm. The internal Teflon vessel contained a mixture of 1.4 g of powdered glass (borosilicate powder, 50-86 µm, 0.083 $m^2$ surface area), 0.7 g of steel (Fe powder, 50-86 µm, 0.008 $m^2$ surface area) and 27.9 g of claystone (crushed Boda claystone, <100 µm fraction), and the external vessel contained the internal vessel surrounded by 75.36 ml of SBPW. The experimental setup was kept at 80°C. After 3, 7 and 12 months one of the containers was removed from the incubator, opened and emptied (samples were denoted as 3M, 7M and 12M). Pellets were pressed from the solid phase and then polished to reveal the glass/steel, glass/clay and steel/clay interfaces which were characterized with Scanning Electron Microscopy (SEM) and micro X-Ray Fluorescence (µ-XRF) methods. The initial and final liquid phases were studied using Inductively Coupled Plasma Optical Emission Spectroscopy (ICP-OES) and Ion Chromatography (IC) analyses.

The concentration dependence of the partition coefficient ($R_d$) of $SeO_3^{2-}$ between the solid and liquid phases – the sorption isotherm – was recorded on crushed BCF core samples ($d_p$> 63µm) in the region of $10^{-3}$-$10^{-8}$ M. Diffusion characteristics of $SeO_3^{2-}$ through BCF were studied by long-term in- and through diffusion experiments at a $SeO_3^{2-}$ concentration of $2\cdot10^{-5}$ M. The selenium concentration and speciation in the liquid phase was investigated using Total-Reflection X-ray Fluorescence (TXRF) and ICP-OES [2], while in the solid phase this was studied by µ-XRF and X-ray Absorption Near-Edge Structure (XANES) spectroscopy.

## *Results*

The SEM investigations of all three polished glass/steel/clay samples revealed that the glass and steel grains were well isolated in the clay matrix. Concentrations of major ions in the final porewater are 782.0±3 ppm (3M) and 841.2±4.4 ppm (7M) for $Cl^-$ which are close to the starting concentration (816.5 ppm); 296.1±4 ppm (3M) and 246.4±1.3 ppm (7M) for $SO_4^{2-}$ which are significantly higher than the starting concentration (182.4 ppm). Higher Si, Na and K concentrations were found by ICP-OES in the final pore water of the glass/steel/clay system compared to those of the initial conditioned pore water. Elevated Si and Na concentrations can be traced back to the glass content, based on our study on leaching behaviour [1]. The concentration of the bivalent cations (Mg and Ca) decreased, while the concentration of K jumped up one order of magnitude.

The results obtained from batch sorption experiments of $SeO_3^{2-}$ on crushed Boda Claystone are in line with sorption isotherms reported in the literature for pure illite and illite-smectite minerals. The diffusion experiments are currently ongoing. The decrease of $SeO_3^{2-}$ concentration indicates uptake, but so far no breakthrough was experienced. No change of the Se oxidation state was detected in the liquid phase during sorption/diffusion experiments. Synchrotron radiation XANES revealed that the majority of the Se was found to remain as Se(IV) for Boda Claystone both in dispersed (crushed) and compact (thin section) forms.

*This work was partly supported by the H-2020 European Joint Program on Radioactive Waste Management (EURAD) - 847593.*

## *Remaining work*

Intense research efforts are underway to understand the corrosion activity on the glass/steel/clay interfaces. Synchrotron radiation microspectrometry investigations are planned to study the distribution of Se in the BCF samples subjected to diffusion experiments.

## *Related publications*

[1] M. Fabian, F. Pinakidou, I. Tolnai, O. Czompoly and J. Osan: *Lanthanide (Ce, Nd, Eu) environments and leaching behaviour in borosilicate glasses*, Sci. Rep. **11**, 13272 (2021)

[2] O. Czömpöly, M. Fábián, I. Tolnai and J. Osán: *Application of TXRF and ICP-OES in studies related to radioactive waste management,* 1st International Summer School on TXRF, 20-24 09 2021, Bari, Italy (virtual), poster (2021)

# STRUCTURE OF LI-ION OXY-HALIDES FOR SOLID STATE ELECTROLYTES

*Margit Fábián, István Tolnai*

## *Objective*

These novel inorganic and thermally stable oxides are potential substitutes for the toxic and flammable organic liquid electrolytes that are currently used in Li-ion batteries. The oxy-halide solids are derived from the precursors of crystalline anti-perovskites of metal hydroxides and have the highest reported $Li^+$ conductivity, $\sigma>10^{-2}$ S·cm$^{-1}$ at room temperature.

## *Methods*

Li-ion based oxy-halide materials with compositions $A_{3-2x}M_xO_{1+y}Cl_{1-2y}$ (A=Li; M=Ca,Ba,Mg; x=0.005; y=0) have been prepared. Neutron diffraction experiments were performed at 100°C temperature using the 2-axis PSD diffractometer (Neutron Diffractometer with a Position Sensitive Detector system) of the Budapest Neutron Centre. The short-range order of samples, bond lengths/nearest neighbour distances was determined using the Reverse Monte Carlo (RMC) simulation. Magic Angle Spinning (MAS) Nuclear Magnetic Resonance (NMR) spectra were recorded on a 600 MHz spectrometer equipped with the 3.2 mm double resonance MAS probe setup with $^1$H tune and X tune Magic-Angle Spinning at the Slovenian NMR Centre.

## *Results*

The structure factors (S(Q)) calculated from RMC simulations agree very well with the experimental ones for the three samples, and are shown in Figure 1. We identified micro-crystallinity with amorphous phases, the presence of crystalline $Li_3ClO$ is clear, and two broad peaks indicate structural disorder which can enhance ion conduction. The interatomic distances obtained from the RMC modelling are presented in Table 1.

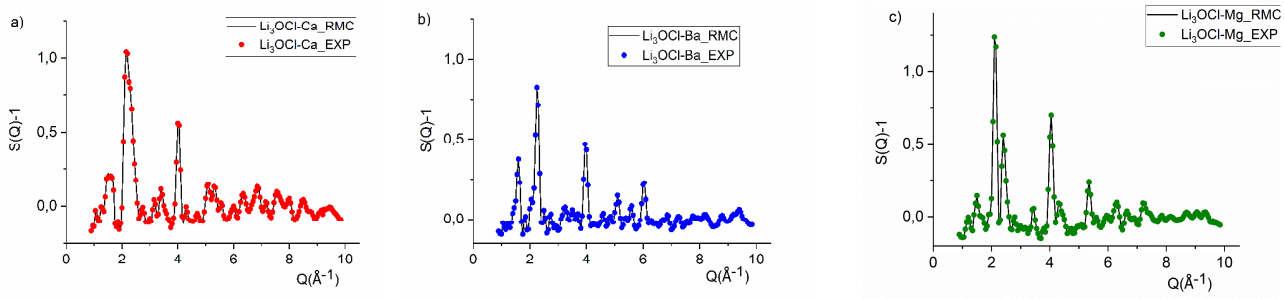


*Figure 1: Neutron diffraction structure factors for $Li_3OCl$-Ca (a), $Li_3OCl$-Ba (b) and $Li_3OCl$-Mg (c) samples*

We have found very compact structures with characteristic first (X-O) and second neighbour (X-Y) distributions, which predict that even though it's not a perfect structural configuration, the atomic connections are in the range of tabulated literature data.

*Table 1: Interatomic distances in Li-based samples obtained from RMC simulation*

| **Samples** | **Interatomic distances, $r_{ij}$ (Å)** | | | | | | | | |
|---|---|---|---|---|---|---|---|---|---|
| | **Li-Li** | **Li-Ca** | **Li-Cl** | **Li-O** | **Ca-Cl** | **Ca-O** | **Cl-Cl** | **Cl-O** | **O-O** |
| **$Li_3OCl$-Ca** | 2.10±0.03 | 2.20 ±0.05 | 2.30/2.90 ±0.03 | 1.80/2.32 ±0.02 | 2.55±0.05 | 2.30±0.05 | 2.80/3.25 ±0.03 | 1.75±0.02 | 2.50±0.03 |
| | **Li-Li** | **Li-Ba** | **Li-Cl** | **Li-O** | **Ba-Cl** | **Ba-O** | **Cl-Cl** | **Cl-O** | **O-O** |
| **$Li_3OCl$-Ba** | 2.25±0.05 | 2.55 ±0.05 | 2.30/2.85 ±0.03 | 1.81±0.02 | 2.75/3.25 ±0.05 | 2.50±0.05 | 2.65±0.03 | 1.70/2.25 ±0.02 | 2.45±0.03 |
| | **Li-Li** | **Li-Mg** | **Li-Cl** | **Li-O** | **Mg-Cl** | **Mg-O** | **Cl-Cl** | **Cl-O** | **O-O** |
| **$Li_3OCl$-Mg** | 2.30±0.05 | 2.85 ±0.05 | 2.30±0.03 | 1.84±0.02 | 2.20±0.05 | 1.76±0.05 | 2.80±0.03 | 1.70/2.15 ±0.02 | 2.45±0.05 |

$^7$Li MAS NMR spectra show that the relative intensities of the different contributions vary among the samples. All three spectra exhibit three or four contributions, see Figure 2. The $^7$Li nuclei are quadrupolar nuclei with a spin of 3/2. They have a small quadrupole moment, because of which their NMR signals can usually be adequately modelled by symmetric Gaussian/Lorentzian lines. The signals #1, #2, and #4 are quite well defined, the broad signal #3 is not.

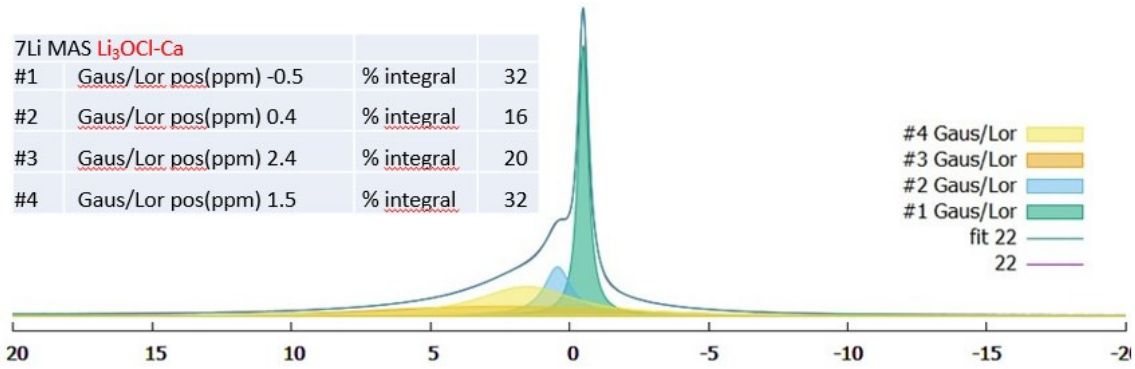


*Figure 2: NMR spectra of $Li_3OCl$-Ca sample*

## *Remaining work*

This work was supported by the NKFIH, Nr. 2017-2.3.7-TÉT-IN-2017-00023, the project was completed.

## *Related publication*

[1] M. Fabian et al: *Structural characterization of oxy-halide materials for solid state batteries,* Phys. Stat. Sol. **A 218,** 9 (2021) http://doi.org/10.1002/pssa.202000682

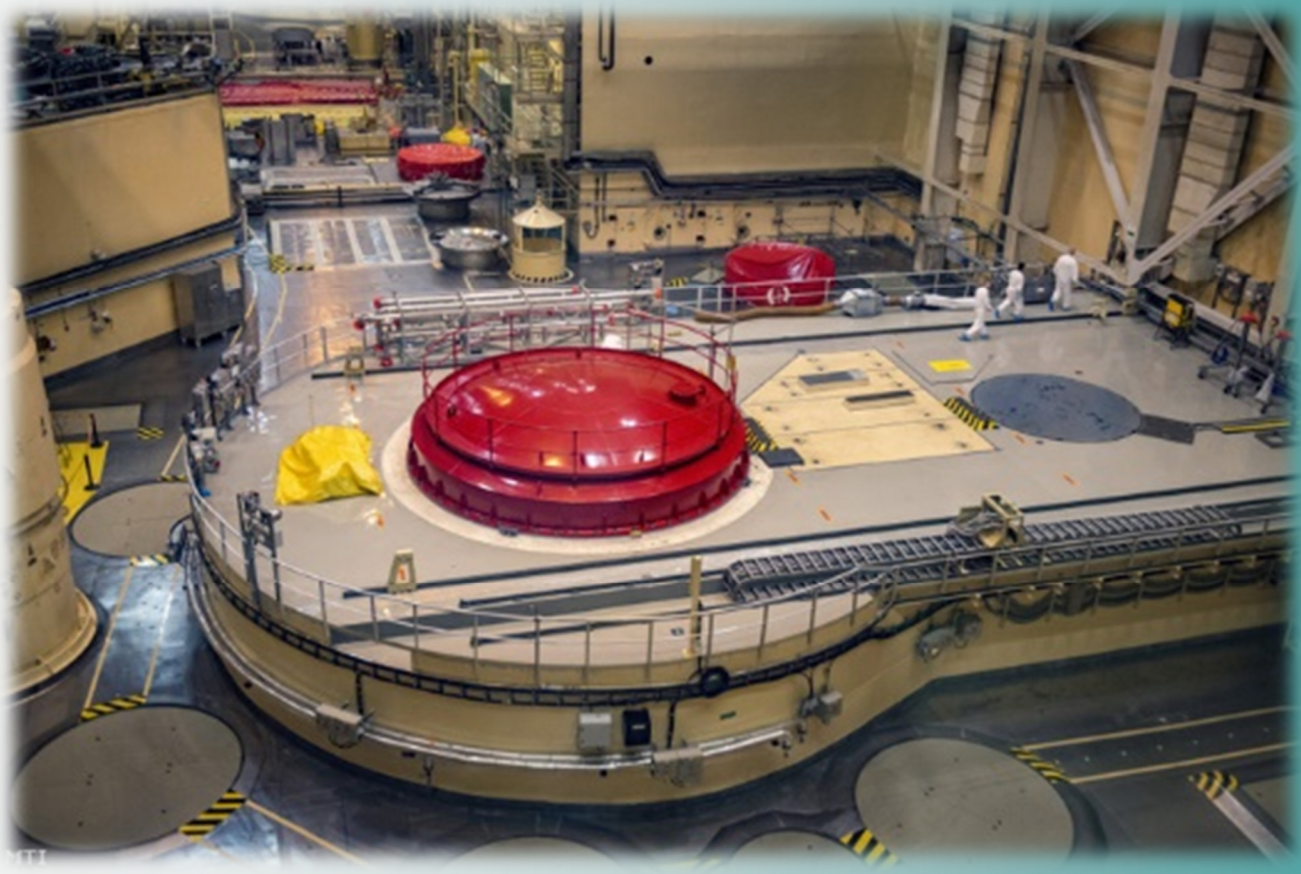

# II. RESEARCH AND DEVELOPMENT RELATED TO NUCLEAR POWER PLANTS

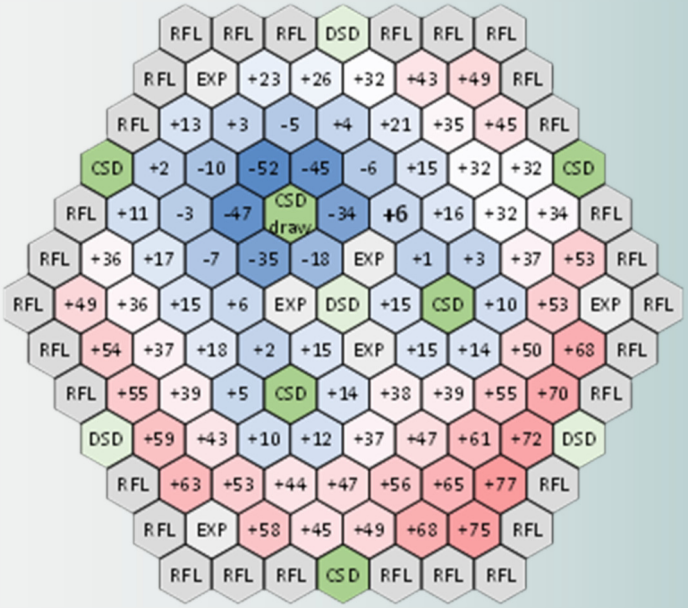


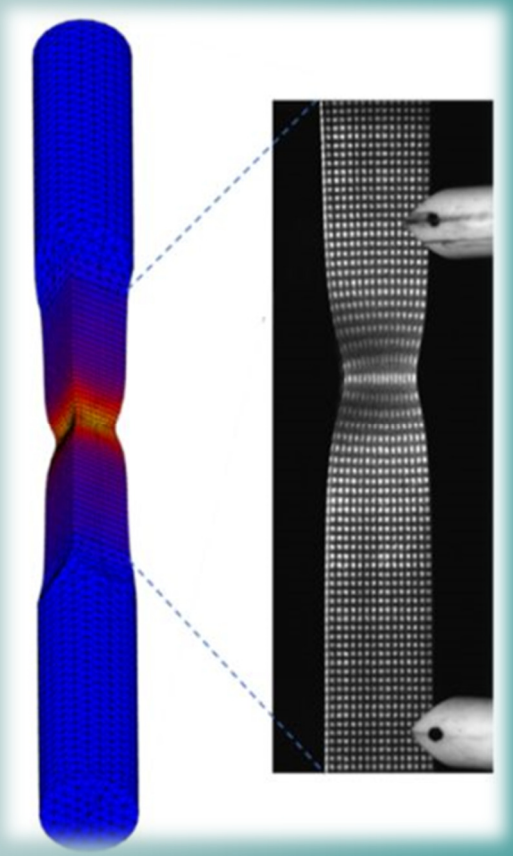

# ACTIVITIES OF EK AS MAIN CONSULTANT OF PAKS NPP

*Katalin Kulacsy, Zoltán Hózer, Berta Bürger*

## *Objective*

EK, together with NUBIKI (Nuclear Safety Research Institute), has been the main consultant of Paks Nuclear Power Plant (NPP) for many years. The main consultant supports the NPP in solving safety-related technical issues and helping with strategic planning. The work is done by the most experienced and highly qualified members of the staff on the basis of individual orders. In 2021 EK undertook the following separate tasks, performed by different (groups of) experts:

- evaluation of the effect of extended reduced-power operation and the ensuing rise back to power on fuel rods;
- handling of iodine spiking related to the changes in reactor power.

## *Methods*

Each task required a different method, which can be summarized as follows.

During normal operation at a burnup sufficiently high for the pellet and cladding to come into contact, an equilibrium state is established where the cladding experiences some moderate, approximately constant hoop stress (about 100 MPa on the left-hand side of Fig. 1). When the power is reduced (to 65% in the case of Fig. 1) the contact pressure between the pellet and the cladding decreases and can even become zero. If the power goes back to the original level right away, the stress goes back to some value, in the present case the original one (pink '0' line, covered by the red one). However, if the reduced-power operation lasts long enough, the cladding creeps towards the pellet, and when the power rises back to the original level, a higher hoop stress will build up in the cladding. The coloured lines are the stresses after 16, 32, etc. days of reduced-power operation. This phenomenon is called deconditioning.

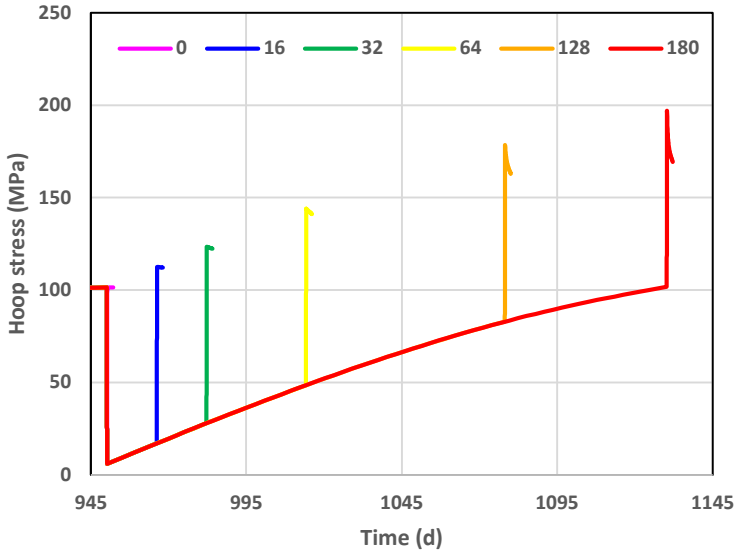


*Figure 1: Example of cladding hoop stresses reached after 0, 16, 32, etc. days of reduced-power operation*

In order to study deconditioning, the methodology established in 2020 was used again: 10 cm-long fictive rodlets, each representing one axial node of a VVER-440 fuel rod, were subjected to a constant-power irradiation followed by a power decrease, a certain time at reduced power and an increase back to the initial power at the highest allowed rate, in simulations performed with the steady-state fuel behaviour code FUROM-2.2. The linear heat rates during irradiation and at the reduced power, the final burn-up, the duration of the reduced-power operation and the axial position (through cladding temperature and the ratio of the local burn-op to the average) were varied within the possible limits. Both the fuel rods used since the beginning of the 15-month cycles in the Paks reactors ('old' design) and those of the lead-test assemblies representing the fuel rods loaded starting from autumn 2021 ('slim' design) were simulated. The linear heat rate changes and times at reduced power were recorded when the hoop stress exceeded the design limit.

The basic mechanisms of activity release from leaking fuel rods during steady state and transient conditions were described. The effects of fuel rod power and temperature were evaluated on the basis of full-core fuel behaviour calculations performed by the FUROM code. The potential effect of gap closing and opening were also analyzed using the FUROM code for the simulation of 100%-50%-100% type power transients. The flux tilt method applied in Boiling Water Reactors (BWR) to limit activity release from leaking fuel assemblies was reviewed. The integrated $^{131}$I activity release from fuel rods was determined on the basis of activity concentration measurements at the NPP. The iodine spiking phenomenon was simulated for power change transients considering different power change scenarios and water purification flowrates.

## *Results*

The individual results of the tasks were as follows.

For a general transient from 100% power to reduced power and back to 100% there was no limit violation with the 'old' rods as long as the reduced-power operation did not exceed 40 days. For the 'slim' rods this value was 24 days. For a transient representing a turbine trip (100%-50%-100%) there was no limit violation with the 'old' rods as long as the reduced-power operation did not exceed 46 days. For the 'slim' rods this value was 30 days. This means that as long as the repair works of a turbine trip do not last longer than 30 days the reactor can be brought back to power with no extra limitation of the power increase rate.

The analyses of iodine spiking lead to the following conclusions:

- The $^{131}$I activity release from a leaking fuel rod is in the order of $10^{11}$ Bq for a 100%-50%-100% power transient. Similar values were obtained for other (e.g. reactor shutdown) transients, too. This means that some activity deposited on the surface of fuel pellets and cladding was washed out during such power transients.
- The increase of power transient duration by applying slower or faster power change rates or two-step changes with intermediate power levels slightly changed the maximum activity concentration in the coolant, but had no effect on the integrated value of released activity.
- The analyses of transients indicated the importance of operating the water purification system (Fig. 2).
- The calculations showed that the size of the defects is controlled by thermal expansion, causing a change of only a few microns during the power change, which is not significant for activity release.
- The potential application of the flux tilt method in VVER reactors needs more detailed studies.

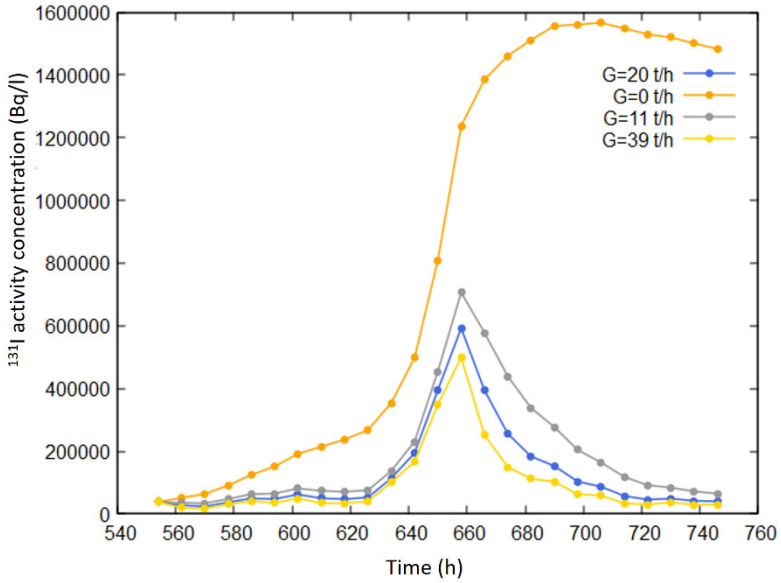


*Figure 2: Coolant $^{131}$I activity concentration during a 100%-50%-100% power transient with different purification flowrates*

## *Remaining work*

The 2021 tasks have been completed.

## *Related publications*

[1] K. Kulacsy: *Evaluation of the effect of extended reduced-power operation and the ensuing rise back to power on fuel rods*, EK TFO-2021-751-04-01-M1, in Hungarian (2021)

[2] Z. Hózer, K. Kulacsy, B. Bürger, P. Szabó, E. Slonszki: *Treatment of iodine spiking related to the changes in reactor power*, EK-TFO-2021-751-5-1-M1, in Hungarian (2021)

# THE EFFECT OF HEAT TREATMENT ON OXIDIZED CLADDING SAMPLES

*Eszter Barsy, Anna Pintér Csordás, Lászlóné Horváth, Zoltán Hózer*

## Objective

This PhD research is aimed to model the azimuthal distribution of oxidation of the Zr-1%Nb cladding. For this purpose, a standalone code (numerical model) is developed, which simulates the oxidation of a ruptured cladding in steam [1, 2]. This kind of modelling is crucial for supporting the planned redefinition of acceptance criteria.

In this phase of the project the objective was to continue the experiments and conduct post-test examinations. The results can be used to assist the model development.

## Methods

Last years oxidized E110G samples were used in the following steps:

- Heat treatment: the samples were inserted into a furnace (1000 °C) for different durations (0 – 10 800 s),
- Sample preparation: the ring samples were moulded into epoxy and then polished,
- Metallography: the oxide layer thicknesses were determined by using an optical microscope,
- SEM: the radial oxygen distribution was measured by an energy dispersive X-ray microanalyzer applied to a Scanning Electron Microscope (SEM).

## Results

At room temperature the oxide layer and the oxygen-rich zone are in thermodynamic equilibrium. At higher temperature (and in vacuum) this equilibrium is disturbed: the non-uniform oxygen profile drives the diffusion, the oxygen migrates deeper into the metal and in consequence the equilibrium at the oxide-metal interface is also disturbed leading to the partial dissolution of the oxide. The experimental results (Figure 1) confirm this effect, the heat treatment modified the oxygen distribution: the longer the sample remained at high temperatures the thinner the oxide layer got, it was dissolved and the oxygen diffused deeper into the metal thus forming a Diffusion Hardened Zone (DHZ).

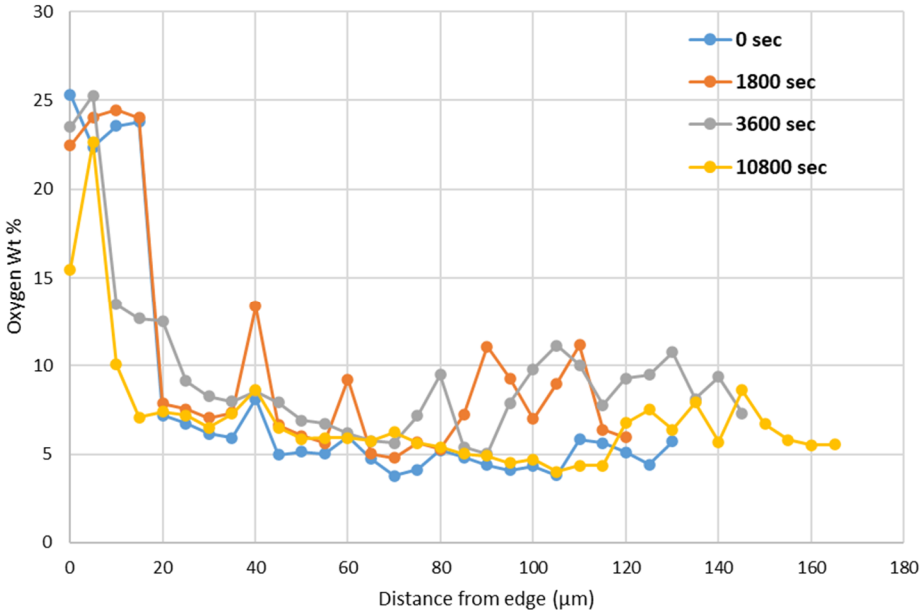


*Figure 1: Change of radial oxygen distribution due to heat treatment*

## Remaining work

The work can be extended with further model development.

## Related publications

[1] E. Barsy, P. Szabó, K. Kulacsy, Z. Hózer: *The non-uniform high-temperature oxidation of Zr–1%Nb cladding – A numerical model*, Progress in Nuclear Energy **133,** 103613 (2021) ISSN 0149-1970

[2] E. Barsy, Z. Hózer: *Simulation of Zr-1%Nb alloy high temperature oxidation on the basis of microstructure examinations*, Anyagvizsgálók lapja, 2021/III., 36-41, in Hungarian (2021)

# OXIDATION OF CR COATED ZR CLADDING TUBES AT DIFFERENT TEMPERATURES

*Zoltán Hózer, Péter Petrik, Alekszej Romanenko, Emil Agócs, Miklós Serényi, Erzsébet Perez-Feró, Balázs Peidl, Anna Pintér-Csordás, Levente Illés*

## *Objective*

The characterization of the oxidation process on the Cr coated surfaces of Zr alloys under different conditions was the main goal of this work. The comparison with reference uncoated Zr alloys was also addressed.

## *Methods*

In-situ ellipsometry was applied for the investigation of oxidation up to 600 °C using small segments of Zr tubes. The samples were annealed in an isolated quartz tube (Fig. 2/A). The optical measurements were made by a Woollam M-2000DI rotating compensator spectroscopic ellipsometer at the angle of incidence of 70° with temporal resolutions of a few seconds and thickness resolution under 1 nm. The spectra were recorded and evaluated real-time every 10 s during thermal treatment.

Two-sided oxidation of 8 mm long cladding tube samples were carried out in high temperature furnaces in steam atmosphere at 1000-1200 °C. The mass gain was measured. The oxidized surfaces were examined using SEM technique.

## *Results*

Five different samples were used in this study. Two of them were reference samples made of two different Zr alloys (Karlsruhe Institute of Technology (KIT) and Czech Technical University, Prague (CTU), see Fig. 2). Three samples were coated by Cr in different laboratories (Fig.2).

The SEM investigations showed that the Cr oxide layer formed at 1000-1200 °C, which was thin in most of the studied samples, was detached from the Cr layer (Fig. 1). In some samples, two types of Cr oxides were produced probably due to the high temperature oxidation in steam atmosphere.

In-situ ellipsometry was successfully applied for the investigation of cylindrical geometry. The thermal treatment with 20 °C/min heat-up rate was feasible from room temperature up to 850 K. The results illustrated well the significant differences between the oxidation of Zr and Cr surfaces during the oxidation process. Some differences could also be identified between the three Cr coated samples (Fig. 2/D).

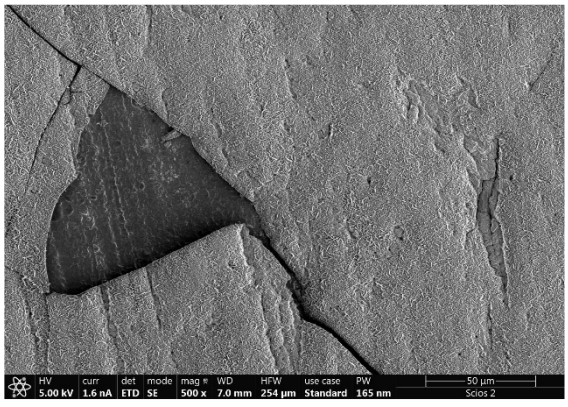


*Figure 1: Cracked oxide scale on the surface of Cr-coated Zr sample after 1000 °C oxidation in steam for 3600 s (left)*

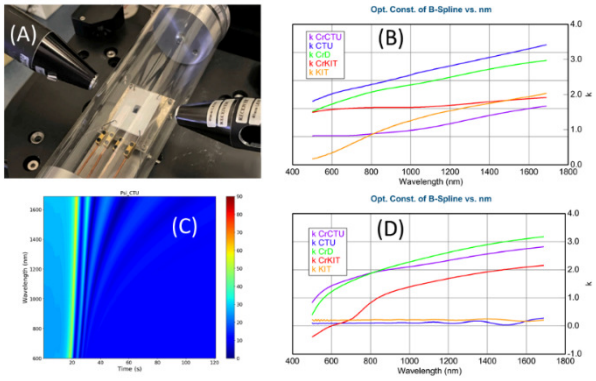


*Figure 2: (A) Developed in-situ ellipsometry cell for high temperature measurements, (B) extinction coefficients before thermal treatment, (C) refractive index during thermal treatment, (D) extinction coefficients after thermal treatment*

## *Remaining work*

The planned experimental work was completed. The measured data will be used for further quantitative analyses. The new measurement cell can be applied for further examinations with different materials.

## *Related publications*

[1] A. Pintér-Csordás, L. Illés: *Electron beam studies of oxidized and Cr-coated zirconium alloys, Part 1*, EK-FRL-2021-161-1-1-M0

[2] A. Romanenko, E. Agócs, Z. Hózer, P. Petrik, M. Serényi: *Concordant element of the oxidation kinetics – Interpretation of ellipsometric measurements on Zr*, Applied Surface Science **573,** 151543 (2022)

# IDENTIFICATION AND HANDLING OF DEFECTIVE FUEL RODS

*Zoltán Hózer, Imre Szalóki*, Péter Szabó, Gábor Radócz*, Anita Gerényi*, Berta Bürger, Emese Slonszki*

**BME NTI*

## Objective

It was requested by the Paks NPP that the experience on identification and handling of defective fuel rods should be summarized in a handbook type report, including basic theoretical considerations and typical operational data on the related phenomena. Some recent events at the Paks NPP were also analyzed and included in the handbook. Several proposals arrived from the Paks NPP experts and the handbook was extended to cover those subjects.

## Methods

The experts of EK and BME NTI were involved in the analyses of defective fuel rods' behaviour for the Paks NPP. Large number of technical reports and publications were produced during the last decades and those documents served as the basis for the comprehensive report. Measured data were supplied by the Paks NPP on campaigns with defective fuel rods. The data were evaluated and the conclusions were documented in the handbook.

## Results

The first part of the handbook was produced in 2020. The following changes and additions were done in 2021:

- New chapter was introduced on the estimation of number and characteristics of defective fuel rods.
- New chapter was added on the identification of fuel assemblies with defective fuel rods by sipping technique.
- Some old illustrations were changed to acquaint us with measured data from the NPP dated after 2020.
- The chapter on "activity release during transients" was significantly extended. There are illustrations and evaluations for the following cases:
  - power decrease and increase transients,
  - reactor shutdown,
  - start-up after refuelling,
  - fuel failure,
  - change of the operation of water purification system.
- The role of longer (15 months) campaigns on the primary coolant activity concentrations is discussed.
- Fuel assembly types were reviewed and the main design changes were illustrated.
- Regulatory aspects, including short history of operational limits were added in a special chapter. Reference is given on the relation between the number of defective rods and the activity concentrations, taking into account the water purification flowrates.

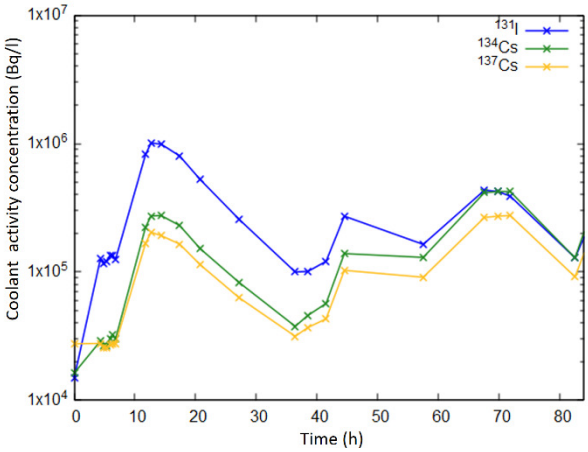


*Figure 1: Iodine and caesium activity concentrations during reactor shutdown*

## Remaining work

The work has been completed.

## Related publication

[1] Z. Hózer, I. Szalóki, P. Szabó, G. Radócz, A. Gerényi, B. Bürger, E. Slonszki: *Review of Experience on Identification and Handling of Defective Fuel Rods*, EK-FRL-2021-701-1-1-M0, in Hungarian (2021)

# SURET SUBCHANNEL CALCULATION INTEGRATION TO VERONA ON-LINE MONITORING SYSTEM

*Áron Vécsi, Gábor Házi*

## *Objective*

A new type of fuel assembly has been introduced at Paks Nuclear Power Plant (NPP) in order to improve its fuel economy. The new fuel rods and their cladding are thinner than the ones used before and some of the spacer grids have been supplemented by mixing vanes to intensify the mixing in the assembly. To simulate the behaviour of mixing vanes we used our SURET (SUbchannel REactor Thermohydraulics) subchannel analysis code, which has been developed based on COBRA 3c. SURET differs from COBRA by the solution of the energy equation and it makes possible to locally modify the resistance factors of the spacer grids to model the effect of mixing vanes.

SURET has also been developed for online calculations applying more efficient algorithms for matrix inversion and optimizing the so-called inner calculations. With these changes, we could significantly speed up the calculations which was required for the application of SURET subchannel calculation in the online VERONA application.

## *Methods*

SURET input file has been created to model the new fuel design, and benchmark calculations have been carried out to prove that SURET is able to provide reasonably accurate solutions for the new geometry. Calculations were verified by separate effect tests and validated by comparing their results with the ones obtained by Computational Fluid Dynamics (CFD) calculations. We demonstrated that the calculation results of SURET follow reasonably well the temperature field calculated by CFD.

SURET was originally developed for offline calculation. After performing some tests, it became clear that it is suitable for online monitoring applications, too. The new aim was to improve the accuracy of temperature field calculations of VERONA (VVER On-Line Analysis) on-line core monitoring system of Paks NPP by applying SURET as a detailed thermohydraulic model. For this purpose, we had to reduce the computational time of SURET because in the online systems a full calculation has to be done in less than 2 seconds without any accuracy degradation.

The most time-consuming function of SURET is the calculation of the diversion crossflow. We have to solve a system of equations, which depends on the subchannels' parameters (flow, pressure) and it has to be solved for every single connection between the subchannels. In order to make the solution efficient, we replaced the approach adopted from COBRA by a new one, which solves a band matrix with reduced bandwidth. Applying this new approach, we were able to reduce the computational time to almost half of the original one.

Each assembly of a VVER-440 type reactor has a wall so it is possible to calculate these assemblies in parallel because the assemblies are independent i.e. they do not interact with each other. After we made calculations with the band-matrix optimized matrix inversion and parallelization, where each assembly had its own thread, the running time was around 1 minute, which was still not sufficiently low for online calculations.

The most important result of the online SURET calculation is the value of the outlet water temperature which can be obtained by solving the energy equation. Its value depends on a number of calculated parameters, which have different rates of change. The flow rate, crossflow rate, and pressure change slowly and their calculation is the most time-consuming. Therefore the recalculation of these parameters was detached from the overall computation.

The calculation of all thermohydraulic variables are completed only in asynchronous mode and it gives the pressure, flowrate, and crossflow rate to the synchronous calculations. The sync mode gets data from the async mode and from the VERONA (inlet water temperature, inlet water flowrate, power distribution). It solves only the energy equation to obtain the results of the distribution for the outlet water temperature. While async needs 1 minute to run a cycle, sync runs around 0.3 seconds.

After many tests, it was demonstrated that using only one async calculation and providing stable flowrate parameters for the sync mode, the accuracy of the solution is reasonable throughout an overall campaign. We made several calculations, and the maximum outlet water temperature of sync calculations differed less than 0.02 Celsius degree from the measured temperature.

## *Results*

We have shown that we could reduce the computational time of SURET from 5 minutes to 0.3 seconds using a specific matrix inversion method and separating the calculations into a synchronous and an asynchronous part. The application of these modifications did not lead to significant reduction of accuracy of the results computed.

## *Remaining work*

The design of the integration of the SURET to the VERONA system is done and the new approach has already been introduced in the 2nd unit of Paks NPP. We have to install the new approach in the other units of the plant before the upcoming campaigns. We also designed a new graphical interface for SURET to support the user's offline calculations, especially during the input preparation process and evaluation of results. The implementation of this new interface is an ongoing process.

## *Related publication*

[1] Á. Vécsi, G. Házi: *SURET calculation of a new type of nuclear fuel assembly having spacer grid with mixing vane*, Proceedings of the 20th International Conference on Modelling and Applied Simulation (MAS 2021), pp. 72-76.

# DEVELOPEMENT OF RECONSTITUTION TECHNOLOGY OF IRRADIATED SPECIMENS

*Ildikó Szenthe, Márta Horváth,*
*Dávid Cinger, Balázs Hargitai, Kristóf Andor Csikós*

## *Objective*

Our task was the development of laser welding reconstruction technology for irradiated specimens and process validation for irradiated Charpy inserts with 5x10 mm and 10x10 mm cross section. Validation of the technology had two main objectives: to prove that the welds will not suffer plastic deformation of failure during the standard testing of the reconstituted specimens, and the heat affected zone of the welding is narrow enough to remain at least 10 mm wide unaffected middle zone for testing in accordance with the requirement of the relevant standard.

## *Methods*

Remote controlled laser welding technology had been developed for reconstitution of remnants Charpy size fracture toughness specimens from 18 mm length irradiated austenitic steel inserts. The welds are only 2 mm wide with a very narrow heat affected zone. The new technology required verification tests, proving that the reconstituted specimens fully replace the standard ones. The following tests had been used to validate the reconstitution technology: hardness testing, Charpy test, slow bending test on tensile machine, tensile tests, fracture toughness test, temperature measurement near the welds (2 and 3 mm away from the welding) and microstructural evaluation of the joint. The developed technology and the device fully satisfy the relevant regulations and special requirements related to the handling of irradiated materials.

## *Results*

During the year, the first experimental equipment was redesigned to increase the controllability of the system, thus performing a radiation protection analysis to make it suitable for installation in its final location. As part of the qualification of the technology, hardness tests performed before and after welding proved that the hardness of the weld and the heat affected zone only slightly differ from the unirradiated base material. Bending tests of the reconstituted specimens verified that the strength of the welds is satisfying the standard requirements, even more since the specimens are loaded without notch in the middle section (see Figure 1 left side). Standard reconstituted fracture toughness specimens have also been tested to prove that the welds and the heat affected zone don't absorb deformation energy during the test. Thermocouple measurement 2 and 3 mm away from the laser welding ensured that the middle zone of the specimens wasn't overheated during welding.

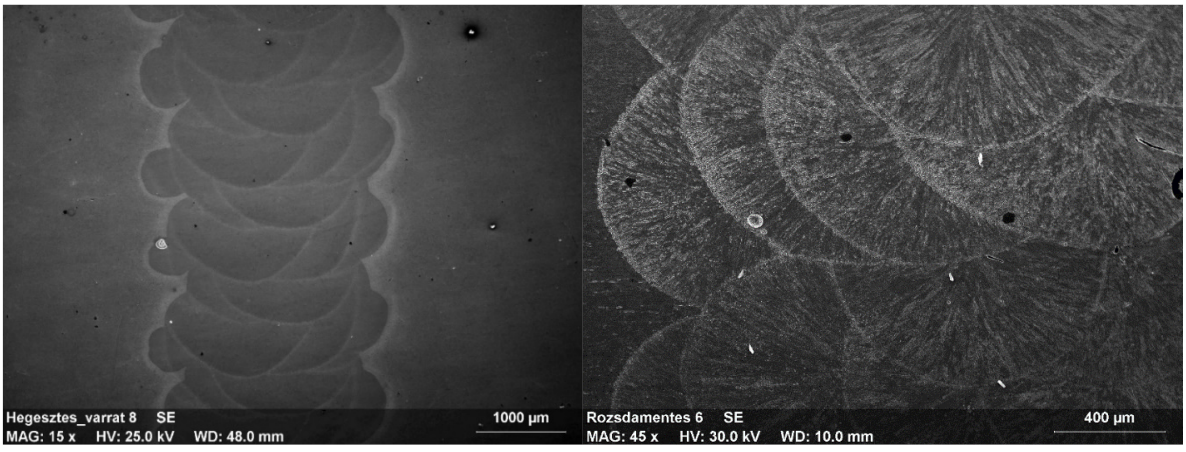


*Figure 1: SEM result of laser beam welded joint with pulse marks*

## *Remaining work*

The developed laser welding reconstruction technique is suitable for the conversion of irradiated and in advance tested surveillance specimen residues into standard test specimens thus allowing the re-use of them. It is planned to use it in the next years for several projects: the STRUMAT project, the FRACTESUS project, and the developed materials for fusion purposes, too.

## *Related publications*

[1] D. Cinger, I. Szenthe, F. Gillemot, M. Horváth: *Reconstruction of irradiated Charpy specimens*, RAKK-AGY (2021)

[2] D. Cinger, M. Horváth, B. Hargitai: *Grain structure changes in steels during laser welding*, OATK (2021)

# OXIDATION, BALLOONING, BURST AND MECHANICAL TESTS WITH THE CLADDING OF SLIM FUEL

*Márton Király, Erzsébet Perez-Feró, Balázs Peidl, Richárd Nagy, Barbara Somfai, Márta Horváth, Péter Szabó, Zoltán Hózer*

## *Objective*

The objective of the work was the testing of E110 cladding tubes with thinner wall under high temperature accident conditions, focusing on potential fuel failure mechanisms.

## *Methods*

The high temperature oxidation and burst tests were performed in special furnaces. The burst tests were carried out between 660-877 °C, under isothermal conditions and linear pressure increase. The temperature range of oxidation in steam covered 600-1200 °C.

Ring compression tests were carried out at room temperature with 8 mm long samples using a standard tensile test machine.

The FRAPTRAN transient fuel behaviour code was used for the simulation of burst tests.

## *Results*

The ballooning tests showed that the burst of thin wall E110 cladding took place at 20% lower pressure compared to the standard thickness cladding tubes. It is a reasonable result, since the thickness ratios would give 17% increase in the cladding wall.

The post-test calculations by the FRAPTRAN code well reproduced the measured pressure history (Fig. 1, left) and confirmed the reliability of this code for carrying out predictive calculations for NPP accident scenarios.

The thin wall cladding was produced from sponge raw material. For this reason, it showed very good oxidation behaviour without the signs of breakaway oxidation. Furthermore, the results of ring compression tests showed that the ductile to brittle transition takes place later for the oxidized thin E110 samples compared to the standard E110, which was produced by the traditional electrolytic method (Fig. 1, right).

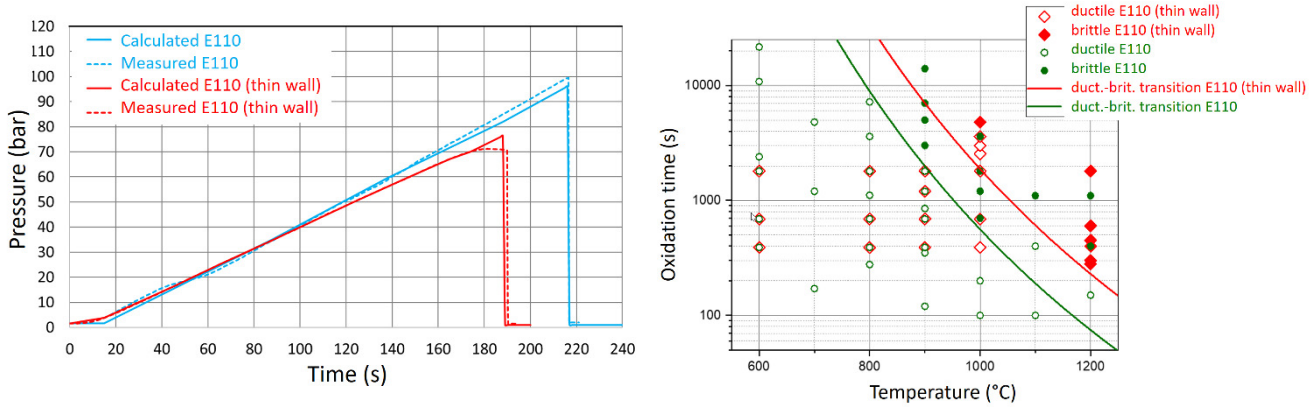


*Figure 1: Measured and calculated pressure during isothermal burst tests with normal and thin wall E110 cladding (left) and ductile to brittle transition of oxidized claddings (right)*

## *Remaining work*

The second series of burst tests will be performed at higher temperatures. The ASTM method will be applied for additional oxidation and the ring compression testing will be done at 135 °C.

## *Related publication*

[1] M. Király, E. Perez-Feró, B. Peidl, R. Nagy, B. Somfai, M. Horváth, P. Szabó, Z. Hózer: *Burst, oxidation and ring compression tests with thin wall E110 cladding*, EK-FRL-2021-709-1-1-M0, in Hungarian (2021)

# SAFETY ANALYSES FOR LICENSING NEW, OPTIMIZED FUEL TYPE AT PAKS NPP

*István Panka, Bálint Batki, Áron Brolly, Attila Guba, György Hegyi, Gábor Hordósy, András Keresztúri, Csaba Maráczy, Tamás Pázmándi, Csilla Rudas, Barbara Somfai, Emese Temesvári, István Trosztel*

## *Objective*

Some years ago, Paks Nuclear Power Plant (NPP) has decided to introduce new, modified fuel type optimized to water to uranium ratio. The average enrichments of the new fuel assemblies remained the same to the earlier ones: 4.2% and 4.7%, but some essential changes were made: reduced clad thickness, reduced pin outer diameter, modified pellet geometry (solid pellet in fuel rod without Gd burnable absorber). The application of the new assembly modifies the power distributions essentially at the level of the pin-wise and the assembly-wise calculations. The reloading schemes are modified to a great extent, too. The relevant parts of the Design Basis Analyses – where modified distributions are important – were repeated. Additionally, the subcriticality of the transport and storage devices of the NPP was investigated by using an advanced burnup credit methodology.

## *Methods*

Safety analyses with coupled codes, subcriticality by using Monte Carlo Method.

## *Results*

The following DBA (Design Basis Accident) initiating events were analyzed in the last years:

- Steam line break,
- Inadvertent closure of 6 MSIV (Main Steam Isolation Valve),
- Seizure of one MCP (Main Coolant Pump),
- Inadvertent withdrawal of a control rod group,
- Control rod ejection,
- Stuck control rod in upper and lower position,
- Inadvertent connection of one closed loop,
- Large break LOCA (Loss of Coolant Accident),
- Erroneous loading of one fuel assembly or erroneous loading of one fuel pin,
- Inadvertent withdrawal of a control rod group without scram.

For checking the fulfilment of the PCI (Pellet-Cladding Interaction) requirement, the following analyses were performed in cooperation with the Russian fuel supplier for licensing purposes:

- Loading up to the nominal power after refuelling,
- Operation in the 100-0-100 %, 100-50-100 % power ranges,
- Variation of the power in the 10 % range,
- Inadvertent opening of one closed loop,
- Control rod withdrawal.

Additionally, the dose conditions were also assessed:

- Environment dose estimations for the large break LOCA using the conservative isotopic inventory,
- Dose estimations of the transport and storage devices in case of abnormal events,
- Thermal hydraulic analysis of the spent storage pool.

Furthermore, the application of burnable poison makes it necessary to analyze the subcriticality of the storage and transport devices also for the burnt out fuel and as a consequence to apply burnup credit methodology, similarly to the previous fuel project. In case of all the above analyses, the acceptance criteria are fulfilled.

## *Related publications*

60 EK inner reports (in Hungarian).

# ANALYSES OF HOMOGENEOUS BORON DILUTION SCENARIOS AT DIFFERENT PLANT OPERATION STATES FOR PAKS NPP

*Bálint Batki, György Hegyi, András Keresztúri, István Panka*

## Objective

As a consequence of the recent Probabilistic Safety Assessment (PSA) study of initial events of homogenous boron dilution scenarios in Paks Nuclear Power Plant (NPP), it was found that some supplementations of the existing boron dilution safety analyses are needed to enhance the safety assessment of the current VVER-440 units. The following initial events were selected for these purposes:

- Malfunctioning of the Boron and Water Makeup System at Plant Operation State (POS) 2, homogenous boron dilution,
- Malfunctioning of the Boron and Water Makeup System at Plant Operation State (POS) 0, homogenous boron dilution, ATWS (Anticipated Transient Without SCRAM (emergency shutdown of the reactor)) analysis
- Malfunctioning of the Boron and Water Makeup System at Plant Operation State (POS) 1, homogenous boron dilution, ATWS analysis.

## Methods

Safety analyses were carried out with three-dimensional neutron dynamics: KIKO3D code with its own built-in thermal hydraulics and with coupled code named KIKO3D-ATHLET. In case of POS 2, a Design Basis Accidents (DBA) scenario was analyzed according to the conservative DBA rules and the fulfilment of the related DBA criteria were investigated, while, in case of the ATWS events, (due to the very small probability of the ATWS events) the systems were modelled in a best-estimate manner. Nevertheless, in order to cover a large number of the possible fuel loadings, the enveloping values of the main determining reactor physics 'frame parameters' were applied, e.g. in all cases the followings were assumed:

- Maximum reactivity reserve,
- Minimum (mostly negative) boron concentration reactivity coefficient.

## Results

In case of the POS 2 state, the transient was initiated by continuous injection of pure condensate during the shutdown process. It was found that after the SCRAM - initiated by the falling of the control rods into the core – the recriticality was not reached after 30 minutes. In cases of POS 0-1, the KIKO3D-ATHLET calculations were supplemented with detailed hot channel analyses. It was concluded that not only the DBC-4 (Design Basis Condition category 4) but also the DBC-2 criteria are fulfilled in the investigated POS 0-1 cases. The relatively mild consequences of the ATWS events are mainly due to the automatic injection of concentrated boron (it happened with some delay after SCRAM signal was activated, but the control rods didn't fall into the core, we assumed their mechanical jamming), see e.g. the time evaluation of the reactor power in Figure 1 for the POS 0 case.

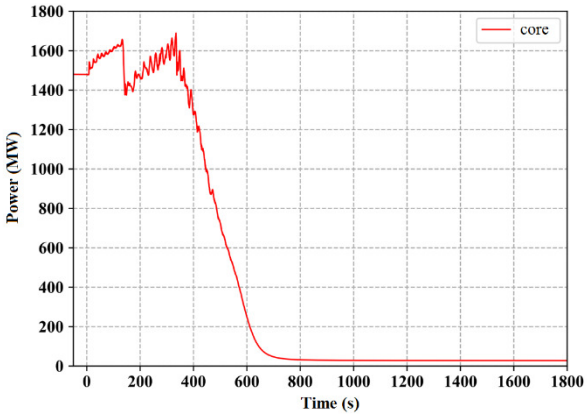


*Figure 1: Reactor power in case of POS 0, ATWS analysis*

## Related publications

[1] A. Keresztúri, I. Panka: *Malfunctioning of the Boron and Water Makeup System at Plant Operation State (POS) 2, homogenous boron dilution*, EK RAL-2020-723-01-02-M1, in Hungarian (2021)

[2] B. Batki, Gy. Hegyi, A. Keresztúri, I. Panka: *Malfunctioning of the Boron and Water Makeup System at Plant Operation State (POS) 0, ATWS analysis*, EK RAL-2020-723-01-05-M1, in Hungarian (2021)

[3] B. Batki, Gy. Hegyi, A. Keresztúri, I. Panka: *Malfunctioning of the Boron and Water Makeup System at Plant Operation State (POS) 1, ATWS analysis*, EK RAL-2020-723-01-06-M1, in Hungarian (2021)

# PRE-TREATMENT OF THIN WALL E110 CLADDING TUBES FOR TENSILE AND MANDREL TESTS

*Márton Király, Erzsébet Perez-Feró, Balázs Peidl, Richárd Nagy, Barbara Somfai, Márta Horváth, Péter Szabó, Zoltán Hózer*

## *Objective*

As part of a longer experimental series, the objective of this work was the production of pre-treated thin wall samples for mechanical testing. The test parameters had to be selected in such a way that the results of mechanical tests could be used for numerical model development. Beyond the preparation of samples, investigation of creep behaviour was also targeted.

## *Methods*

Creep tests with internally pressurized specimens were carried out at 400 °C for 103 effective days in a high temperature furnace in inert atmosphere. The internal pressure was 92.5 bar.

2 mm long ring samples for tensile tests were oxidized in steam at 800 °C with moderate Equivalent Cladding Reacted (ECR) values of 1-4%.

8 mm long ring samples for mandrel tests were oxidized in steam at 800 °C and 1000 °C with ECR values of 1-7%.

2 mm and 8 mm long ring samples were treated in inert atmosphere at 700-1000 °C temperature (Fig. 1).

*Figure 1: Ring samples prepared for thermal treatment in inert atmosphere*

Large number of 2 mm and 8 mm long rings were charged with hydrogen. The samples with the requested H contents were selected after mass gain measurements.

## *Results*

According to the creep tests results the creep rate of the thin wall E110 was higher than that of the standard E110 under the same hoop stress in the cladding tube.

The pre-treatment for mechanical tests was successfully completed and the following samples are available for the mandrel and tensile tests:

- 12 pieces of 2 mm long rings were oxidized in steam for tensile tests,
- 16 pieces of 8 mm long rings were oxidized in steam for mandrel tests,
- 36 pieces of 2 mm long rings were treated at high temperature in inert atmosphere for tensile tests,
- 24 pieces of 8 mm long rings were treated at high temperature in inert atmosphere for mandrel tests,
- 16 pieces of 2 mm long rings were selected from the hydrogen charged samples for tensile tests with 100-600 ppm H content,
- 12 pieces of 8 mm long rings were selected from the hydrogen charged samples for tensile tests with 500-3000 ppm H content.

## *Remaining work*

The mechanical tests will be performed with the pre-treated samples. Additional creep tests are suggested to check the current results.

## *Related publication*

[1] M. Király, R. Nagy, E. Perez-Feró, B. Peidl, P. Szabó, Z. Hózer: *Creep test with thin wall cladding tubes and pre-treatment of samples for tensile and mandrel tests*, EK-FRL-2021-741-1-1-M1, in Hungarian (2021)

# THE CODEX-SLIM EXPERIMENT

*Róbert Farkas, Péter Szabó, Eszter Barsy, Álmos Roland Mischl, Zoltán Hózer, Berta Bürger, Imre Nagy*

## Objective

The simulation of thin wall E110 cladding tubes under Loss of Coolant Accident (LOCA) conditions was the main objective of the integral test.

## Methods

Electrically heated bundle with thin wall E110 claddings was used in the experiment. Alumina pellets with tungsten heaters were applied. The bundle was covered by hexagonal shroud made of E125 zirconium alloy. Internal pressurization was used to simulate the internal gas pressure in the fuel rod simulators.

The inlet coolant was provided by the steam generator unit, which had a precision pump for water injection. The outlet of the test section was connected to the condenser. The data acquisition was performed with LABVIEW program and the same program was used to control the heating power. The temperature, pressure and coolant level data were recorded during the test. The composition of the outlet gas was measured by a Pfeiffer OmniStar GSD 320 O2 type mass spectrometer.

Commissioning tests were performed in inert atmosphere to check the operation of facility components. The recorded data provided useful information on the thermal response of the test section at different power levels and on the leak tightness of the fuel rod simulators.

## Results

The CODEX-SLIM experiment was successfully completed on 28th September 2021. The maximum temperature reached in the test was 921.8 °C (Fig. 1, left). On the basis of Nuclear Power Plant (NPP) analyses, the temperature had to be kept above 900 °C for three minutes and that was done. The final cool-down was performed by water quench from the bottom of the bundle simulating the injection by the emergency core coolant system.

One of the fuel rods burst during the tests at 14.3 bar pressure. The other six rods, in which the internal pressure was lower, kept their integrity.

The oxidation of Zr components could be observed by the mass spectrometer. The total mass of the hydrogen produced during the test was 0.678 g, which indicated modest oxidation compared to other similar tests.

After the test, visual observation was carried out using an endoscope camera. There was no spalling oxide layer on the surface of the cladding. The spacer grids remained intact. Beyond the burst tube, ballooning of an intact tube could also be observed.

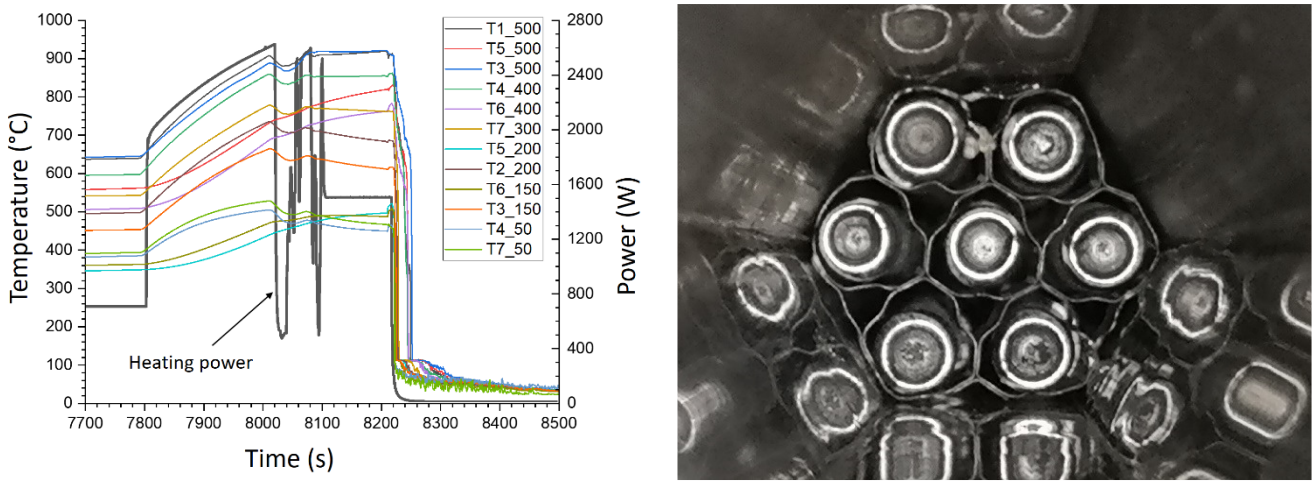


*Figure 1: Temperature and power history in the CODEX-SLIM experiment (left) and view of the top of the bundle after the test (right)*

## Remaining work

Post-test examination of the bundle will be performed in order to characterize the bundle geometry, oxidation state, mechanical strength and hydrogen uptake.

## Related publication

[1] R. Farkas, P. Szabó, E. Barsy, R. Mischl, Z. Hózer, B. Bürger, I. Nagy: *CODEX-SLIM: integral LOCA test with new fuel type*, EK-FRL-2021-743-1-1-M1, in Hungarian (2021)

# EVALUATION FRAMEWORK FOR TENSILE MEASUREMENTS

*Tamás Fekete, Dániel Antók, Levente Tatár, Péter Bereczki, Endre Kocsó*

## *Objective*

Structural Integrity (SI) refers to a branch of engineering science that deals with '*the safe operation of engineering components, structures and materials, and addresses the science and technology that is used to assess the margin between safe operation and failure*' – as specified by the European Structural Integrity Society (ESIS).

In case of an actual engineering system that is specifically designated to perform certain technological functions, SI is the technical term that describes both the load-carrying characteristics as well as the stability conditions of the load-bearing solid structure. In other words, SI is the capability of the solid structure to keep all technological aspects together that serve the objectives of the design, assuring that the construction will be safe up to the technically allowable service lifetime of the system, during normal operation and also in accidental situations that have a probability to occur at or above a certain level, taking into account the ageing of structural materials and their defective character.

In the scientific domain, SI denotes a relatively young field of engineering science, which deals with the evaluation of engineering solid structures from the safety point of view; that is, how and for how long they can operate under various conditions without catastrophic damage (e.g. brittle fracture, tearing or collapsing), taking into consideration the ageing processes occurring in the structural materials and their stability-reducing effects.

The objective of SI of large-scale, high-performance energy generating and chemical systems – with a particular focus on their pressure systems, called Large-Scale Pressure Systems (LSPSs) – is to assure the fail-safe operation during their entire Service Lifetime (SL). The Design Service Lifetime (DSL) of an LSPS is the SL '*that the designer intends*' the system '*to achieve when subject to the expected service conditions …*' (Nireki 1996). DSL and expected service conditions are laid down in the design specification that serves as basis for the design. The DSL of an LSPS is justified by the Design Safety Calculations (DSCs) that simulate the long-term behaviour of the system, considering the effects of its expected load history. The Technically Allowable Lifetime (TAL) of a system is the time-period – calculated from the start of its operation –, during which it can perform its intended functions safely, under normal working conditions and in case of various – very low probability and mainly hypothetical – accidents. The expected TAL of these systems is predicted by Structural Integrity Calculations (SICs). SICs are computations that simulate the long-term behaviour of the systems by considering the combined effects of past actual operating history and expected future load history. Usually, for a system, DSL ≤ SL ≤ TAL.

Supporting the safe operation of LSPSs for long-term operation (LTO) is a growing challenge for the scientific and engineering community, making the need to increase the accuracy of SICs ever more urgent. The efficacy of SICs is highly dependent on: (1) the predictive potential of the methodology's underlying theoretical and numerical framework; (2) the amount and quality of information obtained from the material tests supporting the computations; (3) the amount and quality of information processed from materials testing results.

## *Methods*

In the theoretical part of the project, a methodology development – based on a systematic theoretical study – is being conducted to elaborate state-of-the art measurement and evaluation method for tensile measurements that seems promising for applications in future industrial SI projects. In the practice-oriented part, digital twins of the measurements are being developed first for special problems. The models will further be developed towards more advanced material models and for future industrial applications.

## *Results*

The main goal during the theoretical part of the project is the elaboration of the Measurement and Evaluation *Framework*. The *Framework* architecture follows the well-established material testing methodology: first performing experiments and then evaluating them. The *Framework* is a combination of two (sub)systems, *Measurement* and *Evaluation/Simulation*, with a suitable coupling, which implement the experiment → evaluation procedure. The most striking improvement over traditionally instrumented systems is the integration of an optical system into the data acquisition. The major enhancement in the evaluation methodology is the introduction of the Digital Twin (DT) concept into it that paves the way for a process-based understanding of measurements beyond the metrology-based understanding. Furthermore, the use of DT simulations permits, on a conceptual level, to understand measurement evaluation not just as parameter's determination for a given constitutive model, but also identifying the constitutive model of the material under examination. The conceptual architecture of the *Framework* is sketched in Figure 1.

The test system is based on a Gleeble 3800 thermomechanical simulator. Tensile tests are based on standard test setups, using square cross-section specimens. Force and crosshead displacement are measured by in-system sensors; standards-compliant elongation is measured by clip-type extensometers. The testing machine is equipped with an optical system that provides spatial geometric images of the test specimens during measurements, allowing beyond-standard measurements to be made. The active part of the test specimens has initially a regular mesh along the gauge length. During measurements, the optical system takes images of the specimen at times synchronized with the sampling, controlled by the machine's trigger signal.

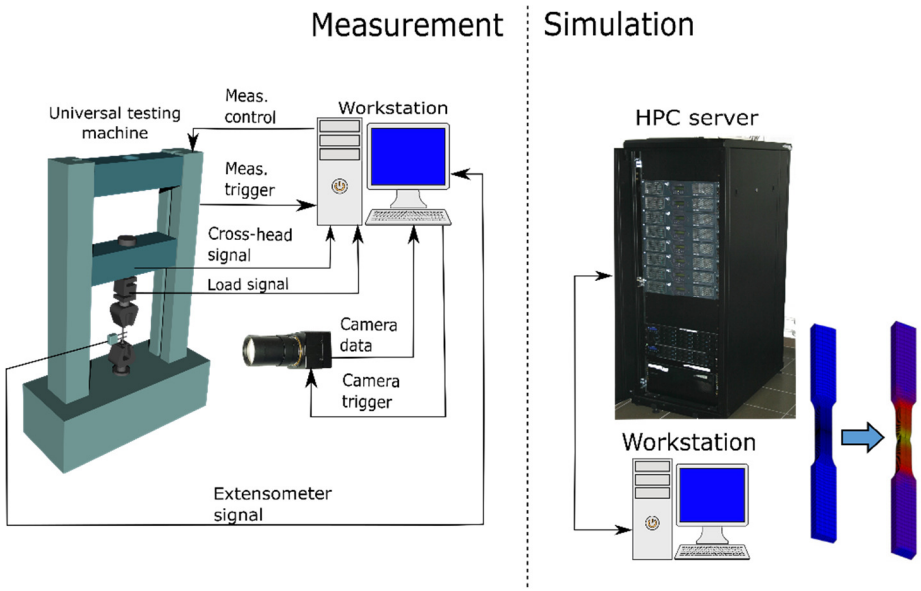


*Figure 1: Architecture of the Framework: The Measurement and the Evaluation/Simulation subsystems*

DTs of the tensile tests are implemented using Finite Element (FE) modelling technology. The DTs of the specimens are modelled in the MSC Marc-Mentat FE system, corresponding simulations are performed using that system respectively. The modelling strategy is guided by the principles of targeting accuracy of evaluation rational and economical use of resources. The specimen models were designed as 3D models, one being a *simple* model, exploiting the symmetry properties of the specimen geometry, the other being a *full* geometric model of the specimen. Only *1/8th* of the sample is modelled in the simple model, considering all three planes of symmetry, so reducing both number of nodes and computation time. The full model is more resource intensive but can also be used in situations where the symmetries of the simple model cannot be exploited. Gauge sections are meshed using hexahedron elements, with increased mesh density around the contraction zone and tetrahedron elements around the heads. Von Mises plasticity theory is used with strain-hardening material response. The material is considered initially homogeneous and isotropic. Boundary conditions are provided by the corresponding kinematic constraints. The calculations use large strain large displacement kinematics in updated Lagrangian setting.

The adequacy of the developed DTs for the problem is illustrated in Figure 2. The image of a specimen near its final failure is compared to the simulated geometry on a full model: the two results show good qualitative agreement; however, a more accurate tracking of the asymmetry detectable on the image requires further refinement of the full model.

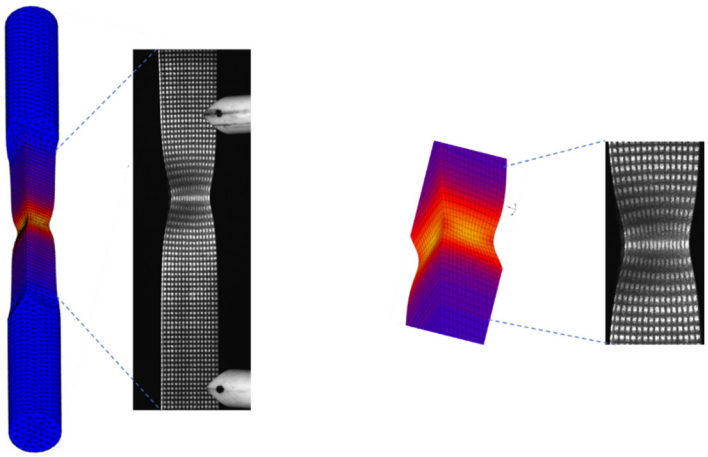

*Figure 2: The image of a specimen near its final failure, compared to the simulated geometry, using full 3D geometry model*

## *Remaining work*

The presented methodology and the models developed for the evaluation of the measurements will further be developed towards more advanced material models and later for industrial applications.

## *Related publication*

[1] D. Antók, T. Fekete, L. Tatár, P. Bereczki, E. Kocsó: *Evaluation Framework for Tensile Measurements, based on Full-Field Deformation Measurements and Digital Twins,* In: ICSI 2021 The 4th International Conference on Structural Integrity, Structural Integrity Procedia **37,** 796–803 (2022)

# ENERGY STORAGE AND LOW-TEMPERATURE HEAT SOURCE UTILIZATION – TWO WAYS TO SUSTAINABILITY

*Attila R. Imre, Kristóf Kummer*

## *Objective*

The present energy crisis requires better utilization of the existing sources. There are several ways to do that; here, two alternatives will be discussed: firstly the utilization of low-temperature heat sources for power production and secondly, the high-capacity seasonal storage of energy; the latter would enable us to use during winter solar-based surplus energy produced in summer.

## *Methods*

For efficiency calculations, thermodynamic data were taken from RefProp database and NIST Webbook; the calculation itself was done by our own codes. For storage-related calculations, own codes were developed to estimate time-dependent energy losses.

## *Results*

In several cases, one can access heat sources with sufficiently high heat flow, but the temperature might be too high to utilize this source for power production. In this case, one of the ways to solve the problem is the addition of a secondary heat source (hybrid system) with a higher temperature. The maximal cycle temperature increase is considered one of the best tools to increase cycle efficiency for all thermodynamic cycles, including Organic Rankine Cycles (ORC). This kind of improvement has technical difficulties and added costs; therefore, increasing efficiency by increasing the maximal temperature might have technical and/or financial limits. It has been shown that there is an additional thermodynamic limit caused by the existence of a previously unknown maximum in the efficiency *vs* maximal cycle temperature function. The existence of this maximum has a great influence on the design of hybrid systems [1,2]. Traditional power cycles use saturated steam or vapour to drive the turbines/expanders and the generators. It is usually a very good solution, but due to the previously mentioned efficiency maximum, there are cases when the expansion of the partial evaporated high-pressure fluid is more efficient than the evaporation of the fully evaporated one [3].

To utilize the various heat sources, one should have a set of ORC-design, when two building blocks can be varied to fit the system into the given heat sources to obtain maximal efficiency and power. One of these components is the expander; the other one is the working fluid. We are focusing on the working fluid in our study. Because most of the traditional working fluids (halogenated alkanes) are already phased out by their unfavourable GWP (Global Warming Potential) and ODP (Ozone Depletion Potential), it is necessary to utilize the so-called "natural" working fluids. Expansion of the hot, pressurized vapour is a crucial step for power production cycles because this is the case when part of the added heat turns to work, which can be used to produce power. As part of this project, we started to build a database of natural alkanes, which can help engineers to find the proper fluid based on its expansion property [4].

In case of some special working fluids – namely some of the medium alkanes – the efficiency with partially evaporated ORC-like cycle with zero evaporation rate (i.e. the expansion of the saturated hot liquid, instead of the saturated hot vapour) proved to be more efficient than their partially or fully evaporated ORC counterpart [1,2]. The cycles with zero evaporation are called Trilateral Flash Cycles (TFC). It has been shown that with the addition of a heat recovery system (where part of the residual heat was removed from the already expanded vapour and used to pre-heat the pressurized liquid), the ratio of the recovered heat can cause remarkable efficiency increase for TFC and ORC cycles The gain for the ORC cycles are bigger, although the cost of these systems is quite high, compared to basic TFC systems. Therefore, careful optimization for cost can be necessary to pick the proper design when medium alkanes are used as working fluids [5].

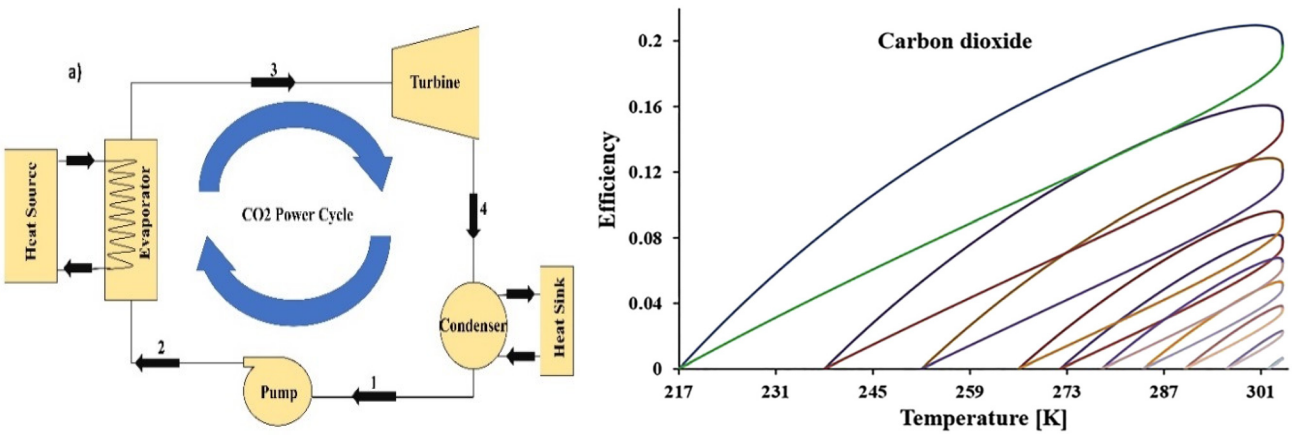


*Figure 1: Schematic layout of a $CO_2$ power cycle (left) and the change of efficiencies in Rankine (upper part of the loops) and Trilateral Flash cycles (lower part of the loops) with different minimal and maximal cycle temperatures*

An additional "natural" working fluid, namely carbon dioxide is gaining more and more attention. Due to the very high critical temperature, one can realize so-called trans-critical cycles with this working fluid. In this case, heat addition happens in the supercritical region, while heat removal happens in the two-phase sub-critical range. The efficiencies of these cycles using various maximal and minimal temperatures were studied; some anomalies were found in the near-critical region, requiring further research [6].

The other way for better energy utilization is the introduction of high capacity energy storage devices with seasonal storage ability. The present way – to use batteries to store solar-based excess electricity – is not suitable for this purpose, partly because of the relatively low capacity of these systems and the relatively high self-discharges. Power-to-Methane technology is a promising new way to store excess energy of a great amount [7]. We defined a new function for the simple comparison of energy-storage methods to find the proper range for the application. According to our study, the Power-to-Methane storage method can be better than most battery-based methods for storage times exceeding four months. At the same time, it is still less expensive than other long-term storage methods (like pumped hydro) [8,9].

## *Related publications*


[1] A. M. Ahmed, L. Kondor, A. R. Imre: *Thermodynamic Efficiency Maximum of Simple Organic Rankine Cycles.* Energies **14,** 307 (2021)

[2] A. M. Ahmed, A. R. Imre: *Effect of heat source temperature on ORC and TFC efficiency*, Pollack Periodica **16**, 73–79 (2021)

[3] S. Daniarta, P. Kolasiński, A. R. Imre: *Thermodynamics Efficiency of Trilateral Flash Cycle, Organic Rankine Cycle and Partially Evaporated Organic Rankine Cycle*, Energy Conversion and Management **249,** 114731 (2021)

[4] A. M. Ahmed, R. Kustán, A. Groniewsky, A. R. Imre: *Alkanes as natural working fluids for organic Rankine cycles*, AIP Conference Proceedings **2323,** 080001 (2021)

[5] A. M. Ahmed, A. R. Imre: *The effect of recuperator on the efficiency of ORC and TFC with very dry working fluid*; MATEC Web of Conferences **345,** 00012 (2021)

[6] S. Daniarta, A. R. Imre, P. Kolasiński: *The Efficiency of Transcritical $CO_2$ Cycle Near Critical Point and with High Temperature*; MATEC Web of Conferences **345,** 00005 (2021)

[7] M. Zavarkó, A. R. Imre, G. Pörzse, Z. Csedő: *Past, Present and Near Future: An Overview of Closed, Running and Planned Biomethanation Facilities in Europe*, Energies **18,** 5591 (2021)

[8] A. Imre, K. Kummer: *Szezonális és hosszútávú energiatárolási lehetőségek*, Energiagazdálkodás **62,** 24-31 (2021) különszám

[9] K. Kummer; A.R. Imre: *Seasonal and Multi-Seasonal Energy Storage by Power-to-Methane Techn*ology. Energies **14,** 3265 (2021)

# IMPROVEMENTS AND VALIDATION OF THE IN-HOUSE DEVELOPED KARATE AND KIKO3DMG CODES

*Bálint Batki, György Hegyi, Csaba Maráczy, István Panka, István Pataki, Emese Temesvári*

## Objective

Applying new fuel and reactor types implies continuous improvements and validation of our in-house developed reactor physics codes. The Russian fuel supplier has a new fuel design named RK3+, having higher fuel lattice pitch, more uranium content, thinner clad thickness, etc., as against the standard Russian-type fuel assemblies of VVER-440. Our goal was to validate the KARATE code system against the RK3+ two-dimensional benchmark problem defined by the Atomic Energy Research Cooperation. In addition, the simulation of xenon transients of VVER-1200 reactors against the available measurements in the literature was also aimed by using KARATE-1200. In the case of KIKO3DMG, our goal was to elaborate and test a new solver for the solution of the Bateman equations during the burnup processes and to validate the code against the rod drop measurements of China Experimental Fast Reactor (CEFR), which are fast dynamic transients.

## Methods

For the RK3+ benchmark, a new nodal and pin-wise cross-section library has been developed by the MULTICELL transport code, and nodal and pin-wise calculations were performed by the KARATE code system. In the case of VVER-1200, some reasonable assumptions were surmised concerning the input data because of lacking some information on the xenon measurements performed during the first load of Novovoronezh NPP. For the simulation, the global calculation module of KARATE-1200 was used. For the validation of KIKO3DMG, rod drop measurements of individual control assemblies were simulated. The reactivity and the power (assumed to be proportional to the measured neutron flux) were calculated.

## Results

In the case of the RK3+ benchmark, it was found that some calculation error is appearing due to the different pin lattice pitch of normal assemblies next to the RK3+ fuel assembly in the mixed core loading. However, the deviation of the assembly-wise radial power peaking factor (Kq) was smaller than 3%, and the deviation of the Kk pin-wise 2-D peaking factor averaged over rows of fuel pins in the assembly was smaller than 3.5%, which are acceptable [1]. Concerning the xenon transients of VVER-1200 reactors, it was concluded that the information obtained could be effectively used to verify the code system under development. Based on our simulations of the available experimental data, rather good agreements (see Fig. 1) were gained by the KARATE-1200 code system [2]. The Padé approximation was selected and implemented in the KIKO3DMG code for the solution of Bateman equations, and compared to the results of the MULTICELL code good agreement was observed. The KIKO3DMG simulation results agree well with the rod drop measurements (see Fig. 2), which validates the code in a dynamic case of a fast reactor [3].

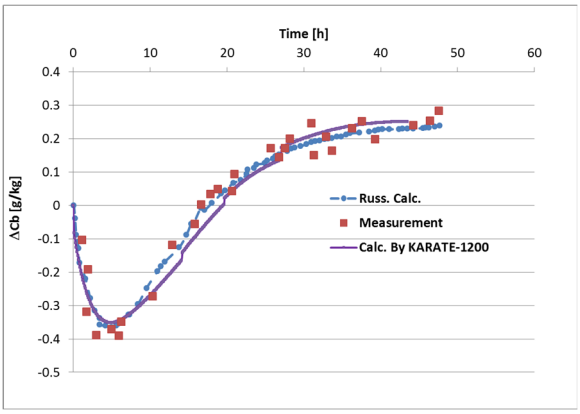


*Figure 3: The xenon transient for 75-40% power variation, KARATE-1200 results against the Russian calculation and measurements [2].*

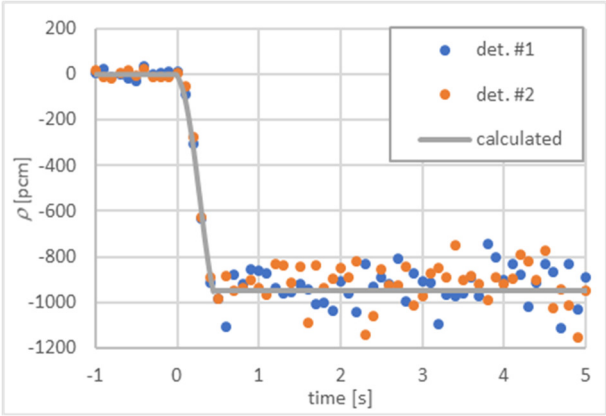


*Figure 4: Measured (det. #1 and #2) and calculated dynamic reactivity during the rod drop measurement of one safety assembly of the CEFR [3].*

## Remaining work

The results of RK3+ benchmark and the rod drop transients should be published in 2022.

## Related publications

[1] E. Temesvári, Gy. Hegyi, Cs. Maráczy, L. Kovács: *Solution of the RK3+ Benchmark by KARATE*, AER Working Group A&B meeting, 15 June 2021

[2] Gy. Hegyi, Cs. Maráczy, E. Temesvári: *Simulation of Xenon transients in the VVER-1200 NPP using the KARATE code system*, Submitted to Annals of Nuclear Energy

[3] I. Pataki, B. Batki: *Simulation of the rod drop measurements of the China Experimental Fast Reactor using the KIKO3DMG code*, EK internal report, EK RAL-2021-103-01-01-M0, November, 2021

# INVESTIGATION OF DYNAMIC BEHAVIOUR IN GENERATION IV FAST SPECTRUM REACTORS DURING UNPROTECTED TRANSIENTS – PHD THESIS SUMMARY

*Bálint Batki, István Pataki, András Keresztúri, István Panka*

## Objective

1) The essential core safety parameters (e.g. reactivity coefficients, power peaking factors) of fast reactors are loaded with significant uncertainties originating from nuclear data and modelling uncertainties. Because of the uncertainties and the complex processes, it was not apparent what the relevant core safety parameters are during unprotected transients.

2) Neutronics modelling of fast reactors must include thermal expansion of fuel and structural elements due to significant reactivity effects, which are practically negligible in thermal reactors. The reactivity effect of the (radially non-uniform) axial fuel thermal expansion is a defining prompt negative feedback in fast reactors.

3) The application of a three-dimensional neutronics code instead of the point-kinetics methodology is essential for the dynamic behaviour of fast reactor transients, especially when the nuclear power distribution changes significantly.

4) A reliable calculation tool needs to be validated by measurements. The IAEA Coordinated Research Project on the Neutronics Benchmark of the China Experimental Fast Reactor (CEFR) Start-Up Tests provided an excellent opportunity to validate the criticality calculations of the KIKO3DMG nodal neutronics code by experimental measurements.

## Results

1) The ALLEGRO gas-cooled fast reactor's most important core safety parameters were determined during unprotected transients by performing sensitivity and uncertainty analyses using the ATHLET thermal-hydraulics code with point-kinetics methodology [1]. The results adumbrate that additional safety shutdown systems are to be applied to mitigate the consequences of reactivity transients (Figure 1).

2) A methodology for modelling the radially non-uniform axial thermal expansion of fuel was developed for the KIKO3DMG using mixed nodes [2]. The new model was validated on the ALLEGRO reactor by comparison with Serpent Monte Carlo calculations. It was shown that volume-weighted group constants and inverse volume-weighted diffusion coefficients provide correct results in the introduced small mixed nodes.

3) The first-ever analysis of an unprotected control rod withdrawal transient of the ALLEGRO reactor core was performed using a coupled neutronics/thermal-hydraulics code [3]. It was found that the classic point-kinetics approach significantly underestimates the assembly-wise peak temperatures nearby the withdrawn control assembly compared to the KIKO3DMG/ATHLET results (Figure 2).

4) The KIKO3DMG code and the developed group constant generation method proved to be applicable for the precise calculation of the CEFR start-up tests.

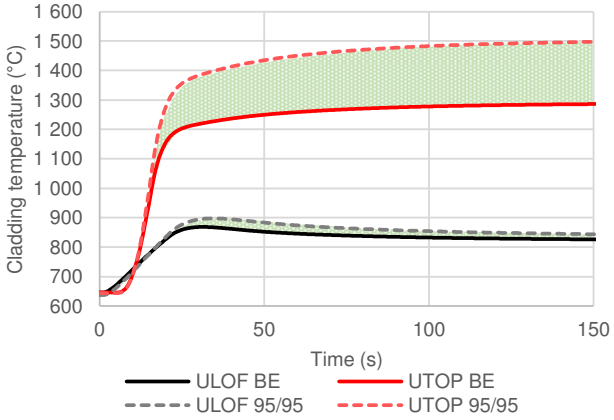


*Figure 5: The best estimate of the maximum cladding temperature and the 95%/95% one-sided upper tolerance interval during the unprotected transients for the ALLEGRO [1]*

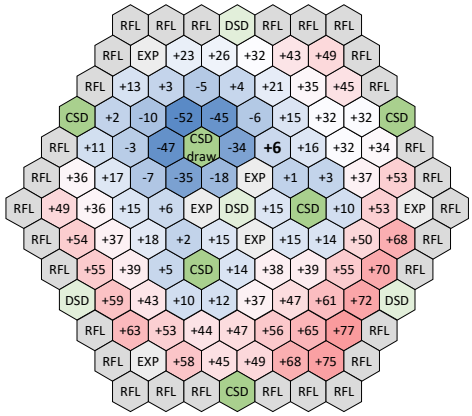


*Figure 6: Peak fuel temperature (°C) differences between the point-kinetics results and the KIKO3DMG/ATHLET results at the end of the transient [3]*

## Related publications

[1] B. Batki, A. Keresztúri, I. Panka: *Calculation of core safety parameters and uncertainty analyses during unprotected transients for the ALLEGRO and a sodium-cooled fast reactor,* Annals of Nuclear Energy **118,** 260-271 (2018)

[2] B. Batki, I. Pataki, A. Keresztúri, I. Panka: *Extension and application of the KIKO3DMG nodal code for fast reactor core analyses,* Annals of Nuclear Energy **140,** 107295 (2020)

[3] B. Batki, I. Pataki, A. Keresztúri, I. Panka: *Simulation of an unprotected transient of the ALLEGRO reactor using the coupled neutronics/thermal-hydraulics system code KIKO3DMG/ATHLET3.0,* Annals of Nucl. Energy **154,** 108086 (2021)

# III. NUCLEAR SECURITY, DOSIMETRY AND SPACE RESEARCH

# IAEA COLLABORATING CENTRE FOR NUCLEAR FORENSICS

*Csaba Tóbi, György Nagy, Gergely Dósa, Péter Kirchknopf, Krisztián R. Soós, Mihály Óvári, Emese Csipa, Vivien Sós, István Almási, Péter Völgyesi*

## *Nuclear Forensic Collaborating Centre in the Centre for Energy Research*

The Centre for Energy Research (EK) was designated to be the first Collaborating Centre for nuclear security (nuclear forensics) of the International Atomic Energy Agency (IAEA) for 4 years in 2016. Recently, in 2021, the EK has been redesignated for the period of 2021 – 2025. The tasks of EK as a nuclear forensics collaborating centre includes the development of non-destructive and destructive analytical methods (e.g. in IAEA collaborating research projects), conduction of trainings and demonstrations, cooperation with national and international organizations and strengthening the nuclear security in the region and all over the world.

## *Nuclear forensic research activities in the Collaborating Centre*

- Nuclear forensic method development and research projects,
- Research related to Radiological Crime Scene Management (RCSM),
- Education, trainings, demonstrations.

The nuclear forensic method development and research projects activities in 2021:

- Nuclear forensic characterization of uranium ore concentrates by Fourier-Transform Infrared Spectroscopy (FTIR),
- Development of new capabilities for EK in nuclear forensics by using FTIR and analytical dataset development for the National Nuclear Forensic Library, FTIR measurements of different nuclear materials,
- PhD research at ELTE TTK HKDI (Hevesy György PhD School of Chemistry): Title: "Development of nuclear forensic analytical methods for determining the origin of confiscated materials". The focus of this PhD research is to further develop new or existing nuclear forensic analytical methods (e.g. Scanning Electron Microscopy - Energy-Dispersive X-ray Spectroscopy (SEM-EDS), Positron Annihilation Spectroscopy (PAS), Inductively Coupled Plasma Mass Spectrometry (ICP-MS), Alpha-spectroscopy).
- MSc diploma thesis at BME TTK: Title: "In-field categorization and origin assessment of unknown radiological materials using nuclear forensics analytical methods". Main activities: measurement of sealed Cm-244 sources by hand-held X-Ray Fluorescence (XRF) analysis, physical characterization, gamma-spectrometry and X-ray radiography.

Radiological crime scene management in 2021:

- Development of a procedure for the safe removal of contaminated Personal Protective Equipment (PPE) during the work in a radiological crime scene in cooperation with the National Bureau of Investigation, Criminal Forensic Department.
- On-site investigation of nuclear and other radioactive materials by different types of hand-held Raman-spectroscopes in cooperation with the National Bureau of Investigation, Criminal Forensic Department.

*Figure 1: Radiological Crime Scene Management (RCSM) demonstration in the 65th IAEA General Conference (Vienna, Austria)*


*Figure 2: Demonstration of the contaminated evidence collection in the 65th IAEA General Conference (Vienna, Austria)*

Education, trainings, demonstrations in 2021:

- In June 2021, a safe dressing/undressing video was filmed with the cooperation of EK Mobile Expert Support Team (MEST) in the IAEA (Vienna, Austria) for educational purposes in radiological crime scene management.
- In September 2021, in the 65th IAEA General Conference (Vienna, Austria) a full scale radiological crime scene management demonstration was performed by the EK MEST team in cooperation with the National Bureau of

Investigation, Criminal Forensic Department (Figures 1 and 2.).

## *Results of Nuclear Forensic research in 2021*

Nuclear Forensic characterization of uranium ore concentrates by FTIR:

- The main and the trace element composition of uranium ore concentrates has successfully been identified qualitatively by FTIR.
- Origin assessment method of uranium ore concentrates has been developed for FTIR.

PhD research at ELTE TTK HKDI:

- It has been proved that PAS is capable to determine different origin of nuclear materials (e.g. between uranium ore concentrates and nuclear fuel pellets), based on the positron lifetime measurements. Therefore, PAS can be a novel methodology for nuclear forensics; however, a nuclear forensics library is required for sample identification and comparison.
- A rapid and simple particle size distribution method was developed for SEM measurements.
- Morphological characteristics of uranium ore concentrates and nuclear fuels pellets were identified by SEM.

MSc diploma thesis at BME TTK:

- Eight Cm-244 sealed sources were investigated from nuclear forensics aspect using non-destructive methods (physical characterization, X-ray radiography, handheld XRF and mainly gamma-ray spectrometry) in two campaigns. Age dating method based on the gamma-rays of Cs-137 & I-132 (Cm-244 fission products), as well as activity-, isotopic composition and impurity determination were performed during multiple measurement sets. Some isotopic activity ratios were also determined (Cm-243/Cm-244, Np-239/Cm-244, Np-239/Cm-243), the results of which were consistent in both campaigns.

Radiological crime scene management research:

- Based on the PPE contamination experiments, a dress removal procedure was developed. The procedure showed that the PPE, used by the MEST team, is suitable to protect the crime scene personnel even in case of a high surface contamination risk. Similarly, the procedure can prevent the possible radioactive contamination of the crime scene personnel during the removal of the PPE.
- Based on the results of the measurements, the hand-held Raman-spectroscopes can detect nuclear fuel pellets, uranium ore concentrates and other radioactive materials (e.g. Th-glass) but a Raman-spectra library is needed for the identification and comparison.

## *Future research projects*

Future FTIR measurements:

- Other nuclear and radioactive materials will be measured by FTIR for explore the possible applicability of the technique.

Development of quantitative identification method for trace elements and for chemical composition ratio of uranium. PhD research at ELTE TTK HKDI:

- Further development of existing radiochemical separation techniques (rare earth elements, trace element) for ICP-MS measurements,
- Sample preparation method development for alpha-spectrometry.

Radiological crime scene management research:

- Development of on-site sample preparation technique and measurement method for hand-held Raman-spectroscopes. Furthermore, measurement of more nuclear and other radioactive materials by the spectroscopes will be performed to explore the applicability of the technique.
- Simulation of radioactive contamination spreading in and outside of the radiological crime scene during the investigation.

## *Related publication*

[1] R. Zhang, K. Nadeau, E. A. Gautier, P. A. Babay, J. L. Ramella, M. Virgolici, A. E. Serban,V. Fugaru, Y. Kimura, C. Venchiarutti,S. Richter, Y. Aregbe, Zs. Varga, M. Wallenius, K. Mayer, H. Seo, J. Y. Choi, Cs. Tobi, M. Fayek, R. Sharpe, K. M. Samperton, V. D. Genetti, R. E. Lindvall, J. D. Inglis, J. S. Denton, A. A. Reinhard, B. F., Xiaolei Zhao, W. Kieser, J. He, Y. Gao, J. Meija, A. El-Jaby, L. Yang, Z. Mester: *Certification of Uranium Isotope Amount Ratios in a Suite of Uranium Ore Concentrate Certified Reference Materials*, Geostandards and Geoanalytical Research **46**, 43-56 (2021)

# THE PARTICIPATION OF THE CENTRE FOR ENERGY RESEARCH IN THE INTERNATIONAL PARTNERSHIP FOR NUCLEAR DISARMAMENT VERIFICATION

*István Almási, Zoltán Hlavathy, Péter Völgyesi*

## *Objective*

The International Partnership for Nuclear Disarmament Verification (IPNDV) is an ongoing initiative, which includes more than 25 countries with and without nuclear weapons. In this initiative the partners are identifying the challenges associated with nuclear disarmament verification, and are developing potential procedures and technologies to address those challenges.

The initiative was founded in December 2014, when the U.S. Department of State announced that the U.S. government will lead the IPNDV, in cooperation with the Nuclear Threat Initiative (NTI). The Partnership is organized around three working groups (Hosts, Inspectors, Tech Track) that meet several times a year and report their progress to an annual Plenary Meeting. The plenary meetings bring together senior government officials and technical experts to monitor the progress of the working groups, discuss common themes and challenges, and increase the understanding of other relevant research that may inform on the overall work of the Partnership.

## *Results*

The Centre for Energy Research has been involved in the work of IPNDV Phase II since 2018 to help politicians and military experts in the technical parts of the verification activities. The Centre took part in the meetings of the Tech Track and the plenary in 2018-2019, including a general presentation in Seoul (South-Korea) about our capabilities. The main focus of this working group was to identify a limited number of key verification technologies. This working group was co-chaired by Sweden and the United States.

The result was an executive summary of the series of presentations and papers on key activities and lessons learned from partners related to dismantlement, monitoring and verification technologies and approaches covering the IPNDV's 14-step dismantlement framework. Also, a summary of lessons learned was made from the development and execution of two technology demonstrations—one on high explosives and the other on the detection of special nuclear material using muon tomography—and one measurement campaign related to detecting the presence or absence of nuclear material from a nuclear weapon. In collaboration with Working Group 5, an assessment was conducted on existing and potential technical capabilities necessary to enable monitoring and verification over the IPNDV's 14-step dismantlement framework with a list that identifies capabilities and weaknesses. In this assessment a review was also included about the monitoring technology gaps to help future research.

Experts at the Belgian Nuclear Research Centre (SCK•CEN) in Mol, Belgium, organized a technology experiment to investigate methods for verifying the presence or absence of a special nuclear material. Over two weeks in September 2019, 30 participants from 10 IPNDV partner countries used non-destructive, passive methods to investigate the detector performance on unirradiated mixed-oxide (MOX) fuel pins with various types of shielding materials. The number of pins and the isotopic ratio of Pu has been changed during the assay, so it was possible to test the sensitivity of the different methods and the effect of the different shields. In addition to the standard detectors, special detector systems like gamma cameras were tested as well. The EK group tested the spectral features of a Symetrica neutron detector[1]. The summary of the measuring campaign appeared in 2021[2].

## *Remaining work*

The Initiative continues with the NuDiVe22 exercise in Jülich and the JUNEX22 tabletop exercise in Brussels and it will be reported in the next progress report.

## *Related publications*

[1] Oral presentation at Esarda-INMM Joint Meeting 23rd Aug – 1st Sep 2021, https://inmmesarda.vfairs.com/en/

[2] https://www.ipndv.org/wp-content/uploads/2021/11/IPNDV_Report_2021_TechDemoSCK_FINAL.pdf

# SOURCE-ACTIVITY MEASUREMENT WITH SCINTILLATION CRYSTAL BASED DETECTORS UNDER FIELD CONDITIONS

*Attila Gulyás, Gergely Dósa, Zsolt Csalótzky, Péter Völgyesi*

## Objective

A research and test campaign was carried out by the Detector Testing Laboratory of the Centre for Energy Research in the frame of a Coordinated Research Project (CRP J02012) supported by the International Atomic Energy Agency (IAEA). The title is „Advancing Radiation Detection Equipment for Detecting Nuclear and Other Radioactive Material out of Regulatory Control". During the third research year (2021), the analysis of scintillation crystal based Radioisotope Identification Detectors (RID) was in the focus. The aim was to investigate the possibility of activity estimation of unknown radiation sources under field conditions and support its development with methods, algorithms and specifications. The typical case of real field condition can be a radioactive source found in a closed barrel or container which presents many difficulties in contrast with laboratory conditions: for example, insufficient information about source distribution in the barrel (one or more sources), source dimensions (point or extended), source barrel wall distance, quality and thickness of the filling material (shielding) between the source and the barrel wall. These data and their uncertainties need to be estimated and used as input to the formulas. The easy solutions described below make the estimate more reliable and reasonable.

## Methods

The research project includes a number of activities related to nuclear security needs, such as radioisotope identification and calibration/application of instruments. Measurements with calibrated sources related to laboratory and modelled field conditions, and analysis of handheld RID spectra were carried out. Our self-developed, responsive web software (Figure 1a), which handles the calculation, depiction and analysis was used to help the investigation of the source-activity measurement method through an easy, specially designed experimental setup (Figure 1b). We strived for the theoretical formulas, practical implementation and measurements to be as simple as possible and at the same time metrologically correct.

## Results

Based on the experiences of test campaigns performed in the second and third year, $LaBr_3$ detectors have good capabilities for source-activity measurement under field conditions. For a handheld RID, the base theory, the practice of activity determination as well as the estimation, evaluation and reduction of uncertainties were presented. Several experimental conditions were created in test measurements to demonstrate and verify the method. As the barrel is not allowed to be open under real field conditions, a "gamma camera" experimental setup is worth assembling a scintillation detector and a lead collimator mounted on a rotatable and tiltable table, like a real camera on a tripod. With the possibility of horizontal and vertical rotation, and with the lead collimator in front of the crystal, the effect of angular deviation can easily be taken into account. Thus, the gamma radiation for the scintillation crystal is only visible from a solid angle allowed by the combination of horizontal and vertical orientation of the lead collimator. Hence, a gamma heat map can be recorded, quasi pixel by pixel, by several consecutive measurements. The heat maps recorded by this gamma camera setup from different directions (front and side) allow a much better estimation to be made for not adequately known data and uncertainties (Figure 1). An activity estimation case study was also prepared for a quasi-unknown radioactive source to compare the two methods from several distances, and the results are the same within their measurement uncertainties: one method used unshielded H*(10) dose-rate measurement with ion chamber, and the other used $LaBr_3$ scintillation spectrum measurement with lead shielding.

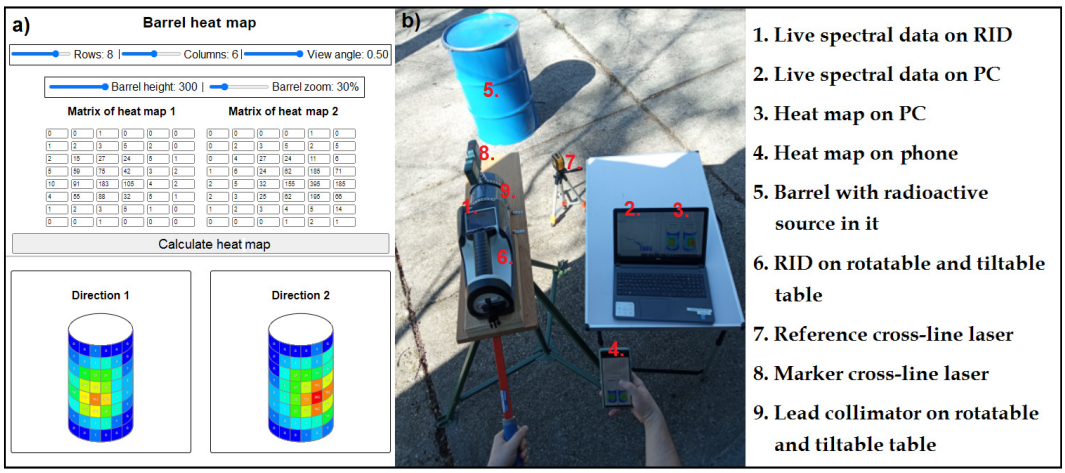


*Figure 1: a) The user interface of the self-developed gamma heat map calculation (responsive web software) b) Modelled field condition measurement with handheld RID in "gamma camera" setup*

## Remaining work

The technical report, the conference presentation and publication of this RID method are expected in the final year (2022).

# GAMMA-RAY MEASUREMENT AND ANALYSIS OF SPENT FUEL ASSEMBLIES OF PAKS NPP (2021)

*Péter Kirchknopf, István Almási, Péter Völgyesi*

## *Objective*

For safety reasons, the fuel manufacturer must set a maximum burnup limit for its assemblies. To guarantee operational safety, the NPP staff decreases this limit by a so-called 'engineering factor'. This factor accounts for the uncertainty of the NPP's reactor physics calculations. The long-term goal of this project is to prove that the uncertainty of the burnup calculated by the NPP is well within the scope of the currently used engineering factor. This would allow the staff to increase the burnup limit, thus achieving better fuel utilization while maintaining operational safety.

## *Methods*

We performed in-situ High-Resolution Gamma-ray Spectrometry (HRGS) measurements on ten selected spent fuel assemblies with 3.82%, 4.2%, or 4.7% average initial enrichments (see table 1). All assemblies were measured from three sides that were rotated by an angle of +/-120° relative to each other and they were also scanned axially at 9-10 points to record the burnup profile. The spectra were collected with an Ortec GEM10P4-70 coaxial type High-Purity Germanium (HPGe) detector connected to an Ortec digiDART 16k channel Multi Channel Analyser (MCA). We measured the $^{134}Cs/^{137}Cs$ and $^{154}Eu/^{137}Cs$ fission product activity ratios which correlate well with the fuel burnup, as well as the novel $^{134}Cs^2/(^{106}Ru^{137}Cs)$ activity ratio which can yield even more accurate burnup predictions [1]. After calculating the net peak areas with the Ortec GammaVision software, we used an intrinsic efficiency calibration method to obtain the mentioned activity ratios. Lastly, we calculated the activity ratio values at the end-of-operation dates using the known cooling times of the assemblies.

## *Results*

The results (Table 1) were sent to the NPP, so that the reactor physicists can compare them with their own calculations. Figure 1 shows this year's measurement results in comparison with fitted curves obtained in earlier measurement campaigns. With the analysis done, we have completed our objectives for 2021.

*Table 1: Measured activity ratios calculated at the end-of-operation dates. Each measurement lasted for 9,000 s (live time). The 2σ relative uncertainties for $^{134}Cs/^{137}Cs$, $^{154}Eu/^{137}Cs$, and $^{134}Cs^2/(^{106}Ru^{137}Cs)$ are 1%, 2.1%, and 5.1%, respectively.*

| Assembly ID | Initial Enrichment [%] | Declared Burnup [GWd/MTU] | $^{134}Cs/^{137}Cs$ | | | $^{154}Eu/^{137}Cs$ | | | $^{134}Cs^2/(^{106}Ru^{137}Cs)$ | | |
|---|---|---|---|---|---|---|---|---|---|---|---|
| | | | 0° | -120° | +120° | 0° | -120° | +120° | 0° | -120° | +120° |
| **470_1** | 4.7 | 48.59 | 2.01 | 2 | 2.03 | 0.07 | 0.072 | 0.071 | 0.89 | 0.89 | 0.95 |
| **470_2** | 4.7 | 48.59 | 2 | 2.03 | 2.02 | 0.07 | 0.072 | 0.072 | 0.89 | 0.92 | 0.9 |
| **470_3** | 4.7 | 52.09 | 1.72 | 1.55 | 1.7 | 0.068 | 0.65 | 0.72 | 0.96 | 0.91 | 0.96 |
| **470_4** | 4.7 | 52.09 | 1.68 | 1.73 | 1.54 | 0.069 | 0.069 | 0.064 | 0.99 | 1.02 | 0.86 |
| **420_1** | 4.2 | 45.09 | 1.7 | 1.62 | 1.51 | 0.067 | 0.066 | 0.065 | 0.83 | 0.82 | 0.76 |
| **420_2** | 4.2 | 47.71 | 1.58 | 1.68 | 1.8 | 0.065 | 0.068 | 0.07 | 0.86 | 0.87 | 0.95 |
| **420_3** | 4.2 | 43.79 | 1.65 | 1.64 | 1.64 | 0.071 | 0.071 | 0.07 | 0.78 | 0.76 | 0.79 |
| **420_4** | 4.2 | 44.08 | 1.86 | 1.87 | 1.82 | 0.071 | 0.07 | 0.07 | 0.76 | 0.79 | 0.82 |
| **420_5** | 4.2 | 44.11 | 1.57 | 1.56 | 1.57 | 0.071 | 0.073 | 0.073 | 0.76 | 0.75 | 0.76 |
| **382_1** | 3.82 | 37.5 | 1.52 | 1.52 | 1.5 | 0.07 | 0.073 | 0.068 | 0.6 | 0.61 | 0.57 |

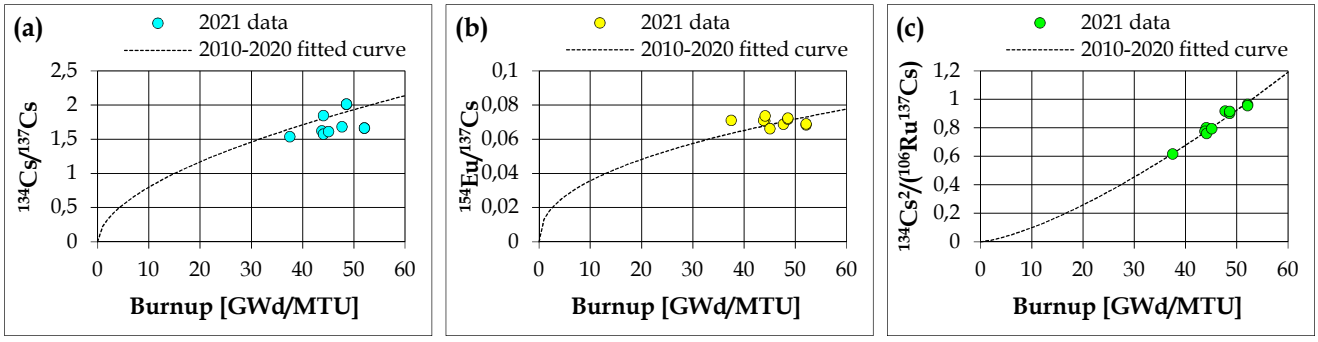


*Figure 1: Measurement results for (a) $^{134}Cs/^{137}Cs$, (b) $^{154}Eu/^{137}Cs$, and (c) $^{134}Cs^2/(^{106}Ru^{137}Cs)$ activity ratios compared to previous data*

## *Remaining work*

The work for the year 2021 has been completed. A new contract for this project in the year 2022 is in preparation.

## *Related publication*

[1] P. Kirchknopf, I. Almási, G. Radócz, I. Nemes, P. Völgyesi, I. Szalóki: *Determining burnup, cooling time and operational history of VVER-440 spent fuel assemblies based on in-situ gamma spectrometry at Paks Nuclear Power Plant*, Annals of Nuclear Energy **170,** (2022)

# EVALUATION OF THE PERFORMANCE CHARACTERISTICS OF ENVIRONMENTAL RADIATION MEASUREMENTS

*Dorottya Jakab, Tamás Pázmándi, Péter Zagyvai*

## *Objective*

Approval criteria for environmental radiation monitoring services generally include the need for conformity with quality assurance systems, which require the evaluation of measurement uncertainty for ensuring the validity and metrological traceability of the results [1]. Additionally, the characteristic limits, such as the decision threshold, the detection limit and the limits of coverage interval are also important performance characteristics of the measurement processes and should be determined in line with the objective of achieving a reasonably low level of detection capability so that the measurement systems would retain sufficient precision [2].

The above mentioned performance characteristics have been assessed using different evaluation methods for the most prevalent environmental radiation measurements that are also used in the environmental monitoring system operated at our site, such as the active gamma dose rate and the passive gamma dose measurements [3], air, deposition [4], soil [1], vegetation and water sampling and subsequent laboratory measurements with total beta counting and gamma spectrometry. For such characterization of these measurements, on-site measurement data have been used. Here, as an example, we summarize the main findings concerning the sampling and measurement of radioactive deposition (fallout).

## *Methods*

Uncertainty arising from sampling has been estimated empirically through parallel sample collections performed at the same location [4]. Such results of parallel sampling were available from a series of experiments conducted over several years to measure radioactive deposition. The samplers used in these series of experiments are suitable for combined sampling of the total deposition, but additionally we installed a collector equipped with a rain sensor, hence capable of separate sampling of wet and dry deposition (both types of collectors are shown in Figure 7) to facilitate the examination of the deposition processes and the validation of dry and wet deposition models and model parameters.

The empirical estimation of the uncertainty associated with the analytical measurement (here the gamma spectrometric analysis) has been performed by replicate measurements of the same samples. Additionally, the analytical (i.e. measurement) uncertainty has been estimated using uncertainty evaluation methods such as uncertainty propagation and stochastic approach (i.e. Monte Carlo Method-based propagation of distributions, the used methods are described in [1]). The characteristic limits have similarly been determined using both uncertainty propagation-based and stochastic evaluation methods [2], [4].

*Figure 7: Radioactive deposition collectors at Station 1 of the environmental radiological monitoring system operated at the KFKI Campus – collectors used in parallel for combined deposition sampling (on the left), and collector for separate sampling of wet and dry deposition (on the right)*

## *Results*

The comparative analysis of parallel samples showed occasionally noticeable differences, which justified quantifying and accounting for sampling uncertainty. Sampling uncertainties were in most cases substantially larger than the empirically estimated analytical uncertainties, and their contribution dominated the overall uncertainty (the distribution ratio of the two types of uncertainty's contribution was about 80%-20%). Such uncertainties can be reduced in statistical term by increasing the number of replicates. The empirically determined measurement uncertainty was typically exceeded by the measurement uncertainty estimated using evaluation methods, while the relative value of the former remained below 5.0%, the latter averaged around 20%, occasionally exceeding 50% for small activities in the samples. In most cases the error in the net peak area was the dominant contributor to the analytical uncertainty, with other significant contributors being detection efficiency and sample volume (i.e. the collector surface area). The uncertainty of net peak area could effectively be reduced by extending the counting time, whereas the sample volume uncertainty was decreased with combination and collective measurement of samples collected simultaneously during a given sampling period. For the typical values of analytical uncertainty and the quantities contributing to it we found no violation of the validity of the uncertainty propagation-based calculations, despite the fact that the activity concentration as a measurand is inversely proportional to the quantities other than net peak area (resulting in a non-linear measurement model). This was due to the relatively small uncertainty associated with a $w$ conversion factor involving these quantities ($u_{rel}(w)$~4.0% on average). We showed, however, as $u(w)$ increases – for example due to the additional introduction of self-attenuation and true coincidence summing correction factors, where necessary – both the measurement uncertainty and the characteristic limits increase as well (as shown in *Figure 8*). This also results in an

increasingly appreciable skewness in the output and detection limit distributions, which ultimately leads to a significant deviation between the results obtained using the uncertainty propagation-based and the stochastic evaluations (see *Figure 9*). In addition, in this particular measurement example there is a difference in principle that in the uncertainty propagation-based determination of characteristic limits, $u(w)$ influences only $a^{\#}$ detection limit but not $a^{*}$ decision threshold, unlike in the stochastic approach where $u(w)$ will have an impact on $a^{*}$ as well.

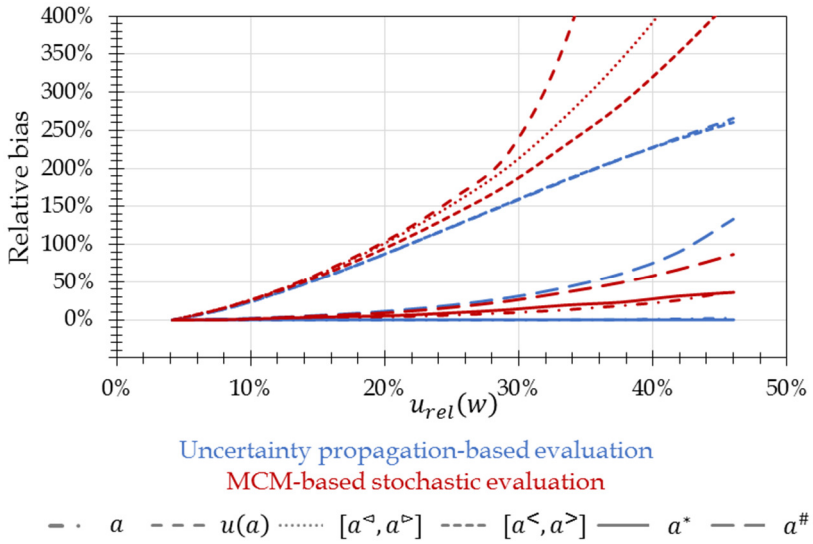


*Figure 8: Relative bias of performance characteristics ($a$ best estimate of the measurand, $u(a)$ measurement uncertainty, $a^{*}$ decision threshold, $a^{\#}$ detection limit, limits of $[a^{\triangleleft}, a^{\triangleright}]$ probabilistically symmetric and $[a^{<}, a^{>}]$ shortest coverage intervals, respectively) from their typical values as a function of $u_{rel}(w)$*

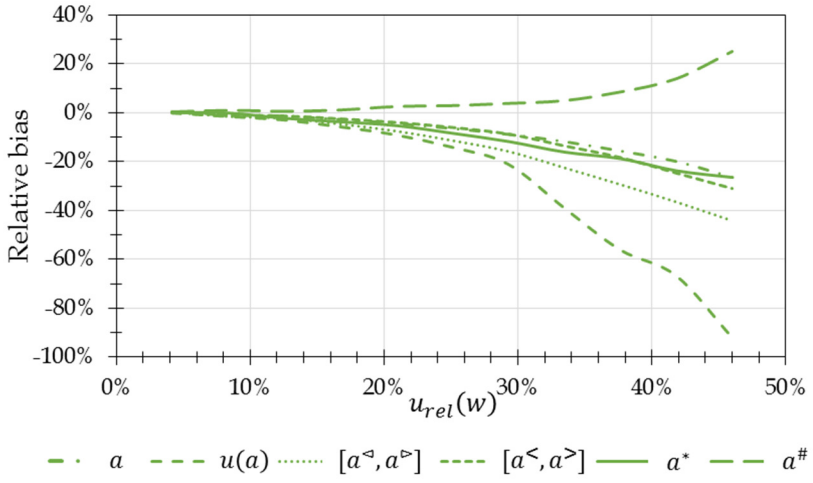


*Figure 9: Relative bias between performance characteristics ($a$ best estimate of the measurand, $u(a)$ measurement uncertainty, $a^{*}$ decision threshold, $a^{\#}$ detection limit, limits of $[a^{\triangleleft}, a^{\triangleright}]$ probabilistically symmetric and $[a^{<}, a^{>}]$ shortest coverage intervals, respectively) obtained using the uncertainty propagation-based and the Monte Carlo Method (MCM)-based stochastic evaluations as a function of $u_{rel}(w)$*

## *Related publications*

[1] D. Jakab, T. Pázmándi, P. Zagyvai: *Effects of the uncertainty contributions on the methods used for measurement uncertainty evaluation,* Applied Radiation and Isotopes **173**, 109704 (2021)

[2] D. Jakab, Zs. Endrődi, T. Pázmándi, P. Zagyvai*: Methods for improving the detection capabilities of environmental radioactivity measurements in the light of increased atmospheric radioactivity levels in 2020*, IRPA15, Seoul, South Korea (2021)

[3] D. Jakab, Zs. Endrődi, S. Deme, T. Pázmándi, L. Tósaki: *Comparative analysis of the environmental radiation monitoring systems used in the KFKI Campus*, Radiation Protection online **XIV (1)**, 80–97 (2021) (in Hungarian)

[4] D. Jakab, Zs. Endrődi, T. Pázmándi, L. Tósaki, P. Zagyvai: *Evaluation of the precision of radioactive deposition measurements*, RAD 2021, Herceg Novi, Montenegro (2021)

# OPTIMIZATION OF THYROID MEASUREMENTS WITH MONTE CARLO SIMULATION IN IN-VIVO MONITORING

*Annamária Pántya, Tamás Pázmándi, Péter Zagyvai*

## Objective

In case of *in-vivo* measurements of low activities in the human body, the non-standard geometries and the limited measurement times considerably increase the measurement uncertainty [1]. The thyroid measurements are also influenced by various parameters such as the age of the individual, the shape of thyroid glands, the distribution of the activity within the organ, the position of the thyroid inside the human body or the detector distance from the body surface. Supplementing the efficiency calibration of the thyroid counter with physical phantoms [2], efficiency calibration was performed by numerical methods to optimize the measurements taking the parameters into account as accurately as possible. In order to consider the uncertainties introduced by the above mentioned factors in the estimation of dose attributed to different radioactive isotopes of iodine, numerical simulations based on Monte Carlo photon transport techniques were performed, the detector response and the corresponding detection efficiencies were calculated.

## Methods

Thyroid activity could be measured by lead shielded NaI(Tl) scintillation detector, standing on a vertically adjustable stand making possible the optimal adjustment of the equipment. An additional lead collimator, having a truncated cone shape with a 4.5 cm inner diameter and 11 cm outer diameter window entrance, could be placed. For the empiric efficiency calibration, the ANSI thyroid phantom available at the laboratory was used. This phantom was made of a plexi-glass cylinder with a diameter of 150 mm and a height of 146 mm. It has one cavity (20 ml) modelling the thyroid of an adult with 3 calibration sources having different $^{131}$I activities [2]. The SURO phantoms with three different sizes (adult, teenager and child) were also used in this project. These phantoms contained three pairs of holes with different wall thicknesses. The activities to be measured were filled in two vials, each containing $^{133}$Ba in gel form. Figure 1 shows the used phantoms.

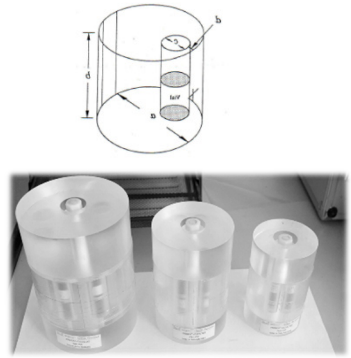

*Figure 1: Thyroid phantoms: ANSI (above); SURO (below).*

The Monte Carlo simulation was performed by MCNP version 6 to obtain pulse height spectra from the NaI(Tl) spectrometer for various phantoms. The spectrometer with a crystal size of 40 mm diameter was modelled (as realistically as possible based on the information provided by the manufacturer). The crystal is covered with an aluminium alloyed Mg-Si layer and is mounted inside a lead collimator. Figure 2 represents two phantoms modelled for the simulation and the used detector geometry [3]. The ANSI phantom was defined with a material of (Poly)methyl methacrylate (PMMA), the SURO phantom with polystyrene. The uncertainties of the efficiency calibration of the thyroid monitoring system were analyzed based on the experimental measurements and simulation with several assumptions:

1) The phantom geometry (1 hole, or 2 holes) was set to represent the adult anatomy.
2) The distance between the body surface and the detector was set to various values (d=3.5, 7.5, 15.5 cm without collimator, and d= 19.5, 23.5, 31.5 cm with collimator).
3) The thyroid mass and size were varied depending on age, ranging from 4.7 g to 20 g for children and adults, respectively.
4) The distance between the thyroid and the body surface was varied between 1.2 cm and 3.4 cm, as a function of age.

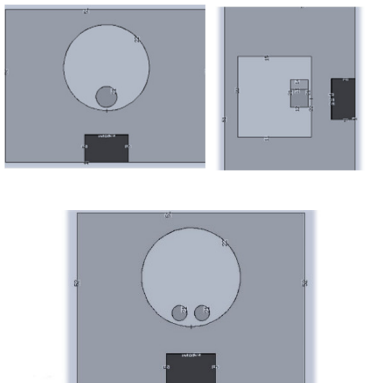

*Figure 2: The thyroid geometry and detector model with MC simulation.*

## Results

It was found that the parameter that had the most significant effect on the detection efficiency was the distance of the body surface to the detector both for the measurements and the simulation [3]. The difference between the measurements and the simulation was the most significant for small thyroid mass and greater thyroid distance from the surface in case of adults and teenagers. The computed uncertainties due to various parameters should be taken into account while estimating the activity of iodine isotopes in the thyroid. All these factors affect the accuracy of the dose estimation as well.

## Related publications

[1] A. Pántya, A. Andrási, T. Pázmándi, P. Zagyvai: *Dose assessment of thyroid in accidental situation*, Radiation Protection online **Vol. X.**, No. 1. (2017) (in Hungarian).

[2] A. Pántya, A. Andrási, D. Jakab, T. Pázmándi, P. Zagyvai: *Uncertainty estimation of thyroid activity measurements and its consequences in dose assessment*, 5th European IRPA Congress (2018)

[3] A. Pántya, T. Pázmándi, L. Horváth, P. Zagyvai*: Optimization of thyroid measurements with Monte Carlo simulation in in-vivo monitoring,* 9th International Conference on Radiation in Various Fields of Research, Herceg Novi, Montenegro (2021)

# NEW METHOD FOR CONFIRMING COMPLIANCE WITH RELEASE CRITERIA FOR NUCLEAR FACILITIES

*Csilla Rudas, Tamás Pázmándi, Péter Zagyvai*

## *Objective*

There are high level requirements for avoiding large and early atmospheric releases from nuclear facilities, but practical guidance on details of application has not been established yet. For ensuring better transparency and comparability of the application of release requirements in practice, we developed an improved methodology by enhancing the already existing computational formulae. The method was implemented in the Calculations for Atmospheric Release Criteria (CARC) software [1].

## *Methods*

The basic concept of the improved methodology is that with appropriate boundary conditions the release source term, the environmental transport and the exposure of the public can be regarded as independent factors. Consequently, the dose attributed to the radiation exposure can be computed as a product of these three factors. The method is capable of considering site-specific meteorological data as well as habit and consumption data of the population in the surrounding area of the nuclear facility. The evaluation of the methodology was conducted by comparing the CARC calculations with the results obtained with commercially available codes for a simple release scenario. Practical application of the method was demonstrated through a hypothetical case study [2]. Sensitivity analysis of the parameters that characterize the habit and consumption of local population around the nuclear facility was investigated [3].

## *Results*

Air and ground activity concentrations at distances between 1 and 10 km from the release point were computed with CARC and PC-COSYMA codes for unit release of a few nuclides and different meteorological conditions kept constant for the modelled time period. The results obtained with CARC for different sets of meteorological conditions (ranges of parameters: wind velocity 1 m/s to 5 m/s, rain intensity 0 mm/h to 10 mm/h, Pasquill stability class A to F) were in the same order of magnitude but always higher than those of PC-COSYMA, implying that our method is more conservative. The external exposure factor for cloudshine and groundshine were compared with similar quantities obtained with MicroShield software. The difference between the results for energies ranging from 100 keV to 10 MeV fell between -5% and +13%. The internal exposure factors of CARC were compared with corresponding values generated using PC-COSYMA, the relative inhalation doses were almost in perfect agreement (with <1% difference), and the food-chain dose factors were in the same order of magnitude (with difference ranging from -33% to +58%). Overall, the results obtained with CARC showed acceptable agreement with the values computed by MicroShield and PC-COSYMA considering the differences between the codes.

During the sensitivity analysis of the habit data, the effect of using different values for outdoors residence time, building type (shielding), activity intensity (breathing rate), and local food consumption were investigated. A realistic release scenario was considered with fixed meteorological conditions (5 m/s wind velocity, 5 mm/h rain intensity, Pasquill stability class D) and a 1 year-long meteorological database. The annual effective dose and its 95$^{th}$ percentile was computed at 800 m distance with the fixed and the one year-long meteorological data, respectively. The default values were 0.4 shielding, 0.735 m$^3$/h breathing rate and no local food consumption, which were perturbed throughout the calculations (Table 1).

*Table 1: The annual effective dose (for fixed meteorology) and its 95$^{th}$ percentile (for 1 year-long meteorological data) with different shielding factors, breathing rates and food consumption*

| | Meteorological data | Shielding factor | | | | Breathing rate [m$^3$/h] | | | Consumption of one food product | | |
|---|---|---|---|---|---|---|---|---|---|---|---|
| | | 0.4 | 0.2 | 0.05 | 0.01 | 0.735 | 1.59 | 2.96 | 20 kg/y leafy veg. | 70 kg/y potatoes | 115 kg/y milk |
| Eff. dose [mSv] | fixed | 9.22 | 8.16 | 7.36 | 7.15 | 9.22 | 9.88 | 10.94 | 21.42 | 11.22 | 16.02 |
| | 1 year long | 8.82 | 8.61 | 8.47 | 8.43 | 8.82 | 9.67 | 11.1 | 10.96 | 9.23 | 11.31 |

In case of the fixed meteorological data, the consumption of different foodstuff had the largest effect on the results. With the use of long-term meteorological measurement data and the 95$^{th}$ percentile, the result of the dose assessment was more robust and was not affected as much by the perturbations of the habit data as with fixed meteorology.

## *Related publications*

[1] Cs. Rudas and T. Pázmándi: *Consequences of selecting different subsets of meteorological data to utilize in deterministic safety analysis*, Journal of Environmental Radioactivity **225** (2020)

[2] Cs. Rudas, T. Pázmándi and P. Zagyvai: *Evaluation of an improved method and software tool for confirming compliance with release criteria for nuclear facilities*, Annals of Nuclear Energy **159** (2021)

[3] Cs. Rudas and T. Pázmándi: *Case Study with CARC software for Verifying Compliance with Atmospheric Release Criteria of Nuclear Installations*, Poster, RAD 2021 Conference, Herceg Novi, Montenegro (2021)

# SMARTPHONE APPLICATION FOR THE KFKI CAMPUS'S DOSE RATE MEASUREMENTS

*Attila Gábor Nagy, Gáborné Endrődi*

## *Objective*

On the KFKI Campus, there are 17 GM counters for dose rate measurements. The GM counters' data are transmitted via RS485 network and collected by a PC. On this PC there is a program that calculates the dose rate from the counts in 10 minutes average time, it detects if the dose rate is above the warning or emergency limit, and it also creates an 'index.html' file. You can see this file on the internet with the help of a web server (URL: 'http://adatgyujt.svl.kfki.hu/index.html'). On this webpage, the data of all the GMs are shown. Our research goal was to supplement this system by an additional feature. When using our new app you have to move close to a GM tube, the application detects your GPS position, from the GPS data it calculates the closest GM probe and shows its actual data on your smartphone. This application can be useful at the calibration by an isotope etalon. One can either immediately check the measured data, or after maintaining or repairing the correct working status can easily be checked.

## *Methods*

For achieving our goal, we had to know the GPS positions of all the GM tubes, the position of the user, and we had to be able to calculate distances between GPS positions. To solve this problem, we used the Haversine formula, because it is good for short distances. The formula is:

$$d = 2r \cdot arcsin\left(\sqrt{sin^2\left(\frac{\varphi_2-\varphi_1}{2}\right)+\left(1-sin^2\left(\frac{\varphi_2-\varphi_1}{2}\right)-sin^2\left(\frac{\varphi_2+\varphi_1}{2}\right)\right)\cdot sin^2\left(\frac{\lambda_2-\lambda_1}{2}\right)}\right)$$

Where **d**: distance, **r**: radius of the earth, $\varphi_1$, $\varphi_2$ are the latitudes of point 1 and point 2, $\lambda_1$, $\lambda_2$ are the longitudes of point 1 and point 2. Using this formula, the program calculates all the GM tubes' distances from the user whenever the smartphone GPS data changes. It chooses the nearest one of them. The actual dose rates data are downloaded and extracted from a file. It is downloaded in every minute and the dose rates are taken out of it. All the features of the program are based on this data.

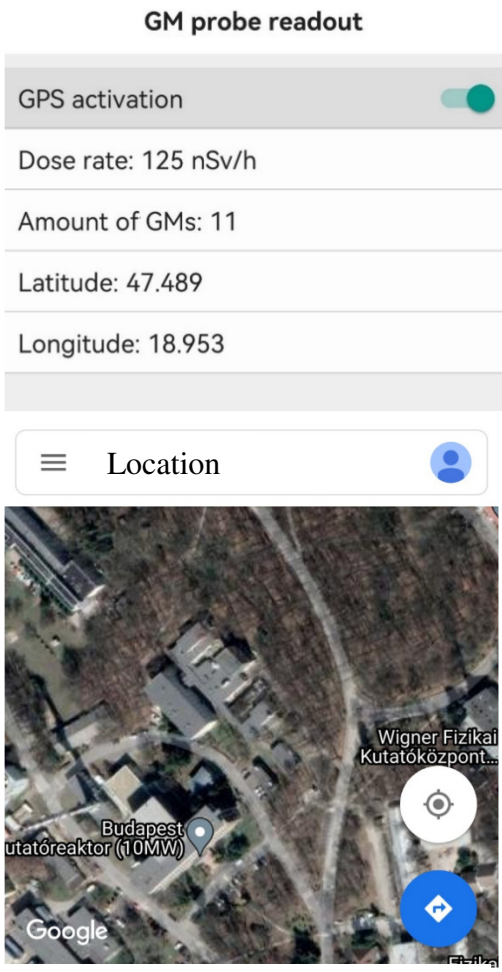


*Figure 1: The GUI of the application*

## *Results*

We tested the application on an Android-based smartphone (Huawei P30 Pro). On this phone, we could achieve 4-5 m precision in the GPS data since the GM tubes are (apart from the entrance point) much further than 5 m, the application can detect which GM tube is the nearest. It can pair the actual GM tube with its dose rate data several times. If we are moving, the GPS position of the user is always updated, and all the distances are recalculated. Thus, if we approach another GM tube, the data becomes actual. The program has sometimes issues with the data downloaded from the http://adatgyujt.svl.kfki.hu/ address. It is not clear whether it is the application's fault or it is caused by other problems. The Graphical User Interface (GUI) of the application is quite simple (see Figure 1), it is focused on the functionality, on the bottom of the screen Google maps are added that helps the user in orientating.

## *Remaining work*

[1] Make dose rate/time graphs

[2] Add warning functions on dose rate rise

[3] Fix the downloading problems

[4] Design more sophisticated GUI

# DOSE ASSESSMENT AT A PROTON ACCELERATOR BY SIMULATIONS

*Dávid Hajdú, Péter Zagyvai*

## *Objective*

For the accelerator-driven neutron source currently under construction in Martonvásár (LvB project) there are several radiation safety issues, including the dose consequences of primary and secondary radiations and later handling of the activated components as radioactive waste. The aim of the current study was only to estimate the dose consequences of the expected high energy proton losses in the accelerator and in the guide and to evaluate one shielding option against this radiation.

## *Methods*

Monte Carlo N-Particle Transport (MCNP) 6.2 was used as a simulation tool. The simplified model of the studied shielding structure is plotted in Figure 1. The geometry consists of a 40 cm thick heavy concrete shield, a 3 m long, 2.4 cm thick copper tube (representing the accelerator) and a 4 m long, 0.5 cm thick aluminium tube (representing the beam tube that conducts protons to the target where the neutrons are generated). The radiation source was a line source in the middle of the tube, separated to 2 parts. The first part was at the last 70 cm of the accelerator assuming a continuous 3.5% proton beam loss in the copper, while in the second part, along the aluminium tube a 3% loss was assumed for the 2.5 MeV, $6.25*10^{15}$ proton/s current, leading to around $3*10^{8}$ photon/s. Cross sections of gamma producing proton reactions were obtained from the Ion Beam Analysis Nuclear Data Library (IBANDL): https://www-nds.iaea.org/exfor/ibandl.htm.

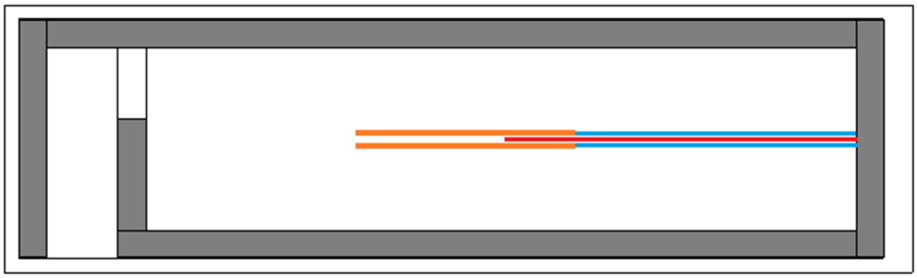

*Figure 1: The MCNP model used in the simulations. The colours are referring to the following materials: white – air, grey – 40 cm thick heavy concrete shield, orange – copper accelerator, blue – aluminium guide, red – source of radiation.*

## *Results*

The resulting dose map is plotted in Figure 2. Dose rates were tallied in 20x20x20 $cm^3$ boxes. As the area inside the shield will be closed during operation, the areas outside the walls are the most interesting. The highest dose rates in this area were around 5 nSv/h with 1% standard deviation. As can be seen in the figure, the highest values appeared around the entrance of the labyrinth. It means that the shielding was very effective against the generated gamma-radiation, and the scattered radiation causes the highest dose rate in this region. Though some asymmetries in dose rates in Figure 2. are the consequences of statistical uncertainties (the previously mentioned '1% standard deviation' was only characteristic to dose rates in the order of nSv/h magnitude or higher, as lower dose rates were meant to be only indicative values), the higher dose rates outside the long wall on the bottom of the figure are caused by the radiation scattered on the walls of the labyrinth. For this reason, the dose rates are not symmetric along the long walls.

The obtained 5 nSv/h dose rate value was compared to the anticipated dose constraint as well. 50 µSv/year dose constraint is a widely used value in similar facilities for personnel categorized as non-radiation workers. Assuming 2000 working hours per year the derived hourly dose constraint is 25 nSv/h. The 5 nSv/h is 5-times lower than the derived dose constraint, so the applied shielding concept was appropriate. A door at the entrance of the labyrinth would result in a further improvement of the shielding effect.

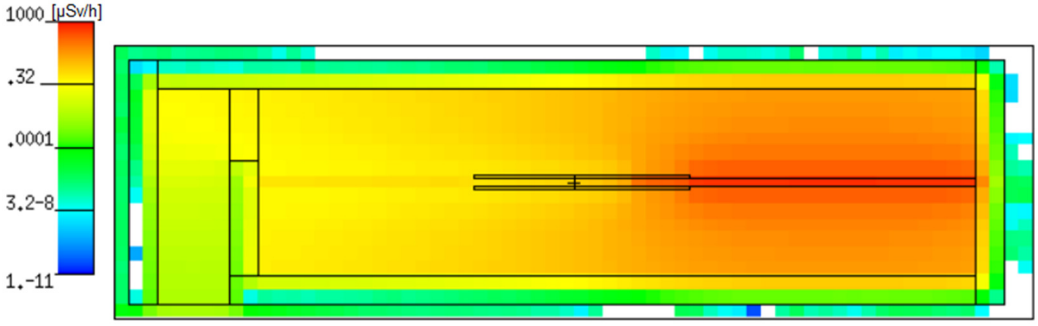


*Figure 2: Dose rate distribution at the height of the proton beam deriving from proton losses*

## *Remaining work*

As the plans are still developing, the anticipated modifications must be implemented in the model. Other sources of radiation must be evaluated together with the proton losses, like neutron and gamma radiation of the target.

## *Related publications*

Publication is intended only after the entire safety planning and licensing has ended.

# MATHEMATICAL MODELLING OF LOW DOSE HYPER-RADIOSENSITIVITY AND INDUCED RADIORESISTANCE

*Szabolcs Polgár, Balázs Madas*

## *Objective*

When developing mathematical models, it is important to have experimental data of good quality for validation. In case of low dose hyper-radiosensitivity, raw data are rarely available. The aim of this work was to collect datasets from the literature, integrate them into a single database, and make them freely available. In the future, it will also be used to validate our models.

## *Methods*

Literature review was performed by searching for the following keywords: "low-dose hyper-radiosensitivity", "low-dose hrs", and "induced radioresistance" in Google Scholar, and also by searching the reference lists of the articles found. The last search was performed on 2nd August, 2021. Additional criteria for a dataset to be included were the followings:

- there is a clear region of low-dose hyper-radiosensitivity in the graphs,
- the standard deviations of surviving fractions are also provided (except for the background),
- the axes and the data points are clearly readable from the graphs,
- when multiple datasets are plotted on the same graph, the individual data points with their standard deviations have to be clearly visible.

In order to obtain numerical values of the data points and their standard deviations in the graphs, WebPlotDigitizer4.2 (GNU Affero General Public License v3.0) and OriginPro2018 (OriginLab Corporation) were used. First the x and y axis had to be defined with the scale (linear or logarithmic) and then by identifying two known points on each axis the size of one unit. After that, data points could be read from the graph along with the standard deviations. Standard deviation was determined as half of the difference between the maximum and minimum values of the whiskers belonging to a specific point. In order to exclude the possibility of incorrect reading, every dataset collected was checked for a second time with another program. If there was difference, the dataset was read for the third time, too.

It was also tested how a mathematical model, the Induced Repair (IR) model, fit the datasets. The obtained parameters were compared to the published ones if they were available. For fitting, OriginPro2018 was used applying the Levenberg – Marquardt method to minimize $\chi^2$ with instrumental weighting of the errors.

## *Results*

Applying this procedure, 46 articles containing 101 datasets were found. The oldest articles were published in 1993, while the most recent ones in 2021, so the datasets were taken from a time span of over 25 years.

It was found that the clonogenic survival assay was not performed uniformly in the articles, partly because there was big variety among the cell types, and different radiation types and dose rates were applied. The method of counting the surviving colonies was also different. It was uniform, however, that those colonies were counted as survivors, which consisted of more than 50 cells after irradiation. Although there were three articles without this statement, it can be presumed that the same definition was also used in these cases, as the authors defined the colony forming in the same way in their other publications. If plating efficiency was mentioned, it was always stated that surviving fractions were calculated by dividing the fraction of surviving cells by the mean plating efficiency of the non-irradiated control.

The database itself is an Excel file, which contains the title of the articles, its authors, the figure which the dataset was collected from, the dataset, i.e. doses and surviving fractions with standard deviations, the characteristics of the irradiation, and the name of the cell line. If mathematical models were fitted in the original publication (the IR model or the linear quadratic model), then the parameters of these functions were also recorded in our database. There were 59 datasets where the authors published such parameters. In three cases, the same parameters could not be obtained again by reanalysis of the data. The most probable reason for that was mistyping in the original article; in one case, a negative sign may be missing.

The database has been uploaded to the STORE Database [1].

## *Remaining work*

The manuscript which will serve as a reference publication for the database has to be finalized [2].

## *Related publications*

[1] Sz. Polgár, P. N. Schofield, B. G. Madas: *Data collection and analysis on low dose hyper-radiosensitivity and induced radio-resistance*, STOREDB (2021) https://doi.org/10.20348/STOREDB/1163

[2] Sz. Polgár, P. N. Schofield, B. G. Madas: *Experimental database for research on low dose hyper-radiosensitivity and induced radioresistance* (in preparation)

# CHARACTERIZATION OF RADIATION EXPOSURE AND ITS BIOLOGICAL EFFECTS AT DIFFERENT SPATIAL SCALES

*Tariq Hailat, Balázs Madas*

## *Objective*

Ionizing radiation dosimetry is a well-developed discipline of physical science with several applications in biology and medicine. In particular, radiation therapy relies on dosimetry for optimizing cancer treatment and avoiding severe toxicity. The improvement of the accuracy of the procedures for measuring spatial dose distributions is of great importance. The objectives of this research were i) to measure the average number of alpha particles per unit surface with different exposure times and different distances from alpha sources using CR-39 detectors, ii) to know if the Fricke gel dosimeters such as ferrous–methylthymol blue (MTB)–polyvinyl alcohol (PVA) cross-linked chemically with glutaraldehyde (GTA) (Fricke-MTB-PVA-GTA dosimeter) [1] can be applied for alpha-particle dosimetry as potential indicators of spatial inhomogeneties in dose distributions, and iii) to compare the effect of alpha tracks between CR-39 detectors and Fricke-MTB-PVA-GTA dosimeters. Perceptible colour change of the gel dosimeter could make it possible to instantly recognize spatial inhomogeneities in case of alpha-particle exposure.

## *Methods*

CR-39 detectors, also known as Solid-State Nuclear Track detectors (SSNTDs), are thin plastic sheets capable of recording alpha tracks. The principle of SSNTDs is that charged particles such as alpha particles hitting the detector surface produce damage within nanometres along the track in such a way that the track can be etched many times faster than the undamaged material. The process of etching needs several hours to enlarge the damage to conical pits of micrometre dimensions. These tracks can be observed by using an optical microscope.

The Fricke gel dosimeters are 3D tissue-equivalent systems. They are based on adding gelling agents (such as agarose, gelatine, or polyvinyl alcohol (PVA)) to the Fricke solutions which are considered acidic oxygenated aqueous solutions of ferrous ions ($Fe^{2+}$). The oxidation of ferrous ions ($Fe^{2+}$) into ferric ions ($Fe^{3+}$) during irradiation is the basis for Fricke gel dosimeters. By utilizing Magnetic Resonance Imaging (MRI) techniques or measuring the optical density of the solution, the concentration of ferric ions can be evaluated and correlated to dose.

Fricke-MTB-PVA-GTA gel samples were prepared and poured into suitable small Transwell-like containers and sealed using suitable covers and parafilm. The containers include a very thin transparent layer at the bottom (food packaging bags) which allows the penetration of alpha particles to the gel. The gel samples and CR-39 detectors were exposed to an Americium-241 source with an activity 3.3737 kBq for different exposure times (1, 4, 30 and 60 minutes) and at different distances (1 mm, 4 mm, 1 cm and 5 cm) between the source and the target. Three gel samples were left for three days at a distance of 1 mm from the alpha source in a dark refrigerator at 10 °C in order to maintain the properties of the gel. After the exposure, the gel samples and CR-39 detectors were collected and evaluated. The CR-39 detectors were washed in distilled water and chemically etched. Then an optical microscope was used to identify and count alpha particle tracks on the surface of each of the CR-39 detectors.

## *Results*

As expected for the measurements of CR-39 detectors, the results show that the average number of alpha tracks on the surface of CR-39 detectors increases with the exposure time. The average number of alpha tracks on the surface of a CR-39 detector decreases with the distance between the CR-39 detector and the alpha source (see the left four panels of Figure 1).

In case of the gel measurements, no tracks of alpha particles were observed on the surface of the gel samples even with the closest distance from the alpha source and with the longest exposure time (see Figure 1). The colour change in the gel sample is due to auto-oxidation. The main reason for this could be that the gel dosimeters are not as sensitive to alpha particles as the CR-39 detector. However, the potential shielding effect of the plastic bag and the size of the source were not quantified.

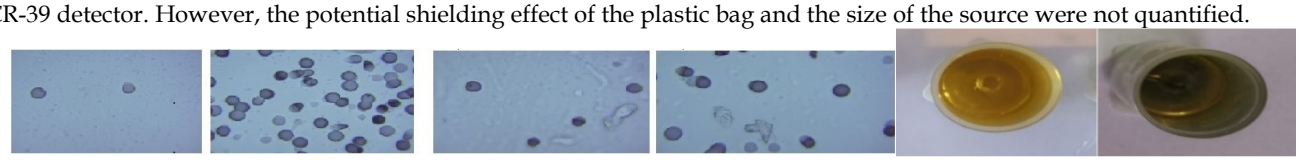

*Figure 1: Views of alpha particle tracks on a CR-39 detector surface viewed by an optical microscope (the four panels on the left). The CR-39 detectors of these views were exposed to Am-241 activity of 3.3737 kBq for 1 min and 60 min at a fixed distance of 1 mm, and for fixed exposure time of 60 min at a distance of 1 cm and 4 mm, shown from left to right. The fields presented were selected randomly, and do not necessarily correspond to the average track density. Two photographs of the unexposed (second from the right) and exposed (first from the right) samples to Am-241 source of Fricke-MTB-PVA-GTA gel.*

## *Remaining work*

The next question is whether alpha particles can be accelerated to penetrate a very thin layer of gel to record the alpha tracks on the gel surface, and using an optical microscope to see these tracks.

## *Related publication*

[1] K. A. Rabaeh, M. M. Eyadeh, T. F. Hailat, B. G. Madas, F. M. Aldweri, A. M. Almomani, S. I. Awad: *Improvement on the performance of chemically cross-linked fricke methylthymol-blue radiochromic gel dosimeter by addition of dimethyl sulfoxide*, Radiation Measurements **141**, 106540 (2021)

# USE OF RETROSPECTIVE DOSIMETRY METHODS FOR NUCLEAR SECURITY AND FOR CONSERVATION OF CULTURAL HERITAGE OBJECTS

*Péter Völgyesi, András Kovács, András Kelemen, Vivien Sós, Attila Hirn, Andrea Strádi, Tamás Pázmándi, Dorottya Jakab, László Szentmiklósi, Zsolt Kasztovszky, Tünde Tóth, Krisztina Kovács*

## *Objective*

The aim of retrospective dosimetry is the determination of absorbed dose after a certain „radiological event" (e.g. accidents or terrorist attacks), when no dosimeters were used. These measurements are usually performed by applying thermoluminescence (TL) or Optically Stimulated Luminescence (OSL) dosimetry methods. Retrospective dosimetry methods, among others, are used in nuclear security and for dating and studying the potential former irradiation of Cultural Heritage (CH) artefacts. Due to the importance of retrospective dosimetry both at national and international levels, five departments of the Centre for Energy Research (Nuclear Security, Radiation Chemistry, Radiation Protection, Nuclear Analytics and Radiography, and Space Research) decided to start a joint project with two topics, i.e. (1) the use of TL and OSL methods for retrospective dosimetry purposes and (2) the use of ionizing radiation for the preservation of cultural heritage artefacts.

## *Methods*

In order to better do retrospective dosimetry, the capabilities of our Freiberg Instruments GmbH lexsyg smart type TL reader was extended with an OSL unit from the same firm. The introduction and use of the new OSL system was performed by the firm on-line. Beryllium oxide (BeO) chips, as standard OSL dosimeters, were purchased for initial tests. The first experimental measurements were performed using these chips irradiated with different doses using a Cs-137 irradiation source.

Irradiation treatments of CH objects for conservation purposes have not yet been performed in Hungary. Therefore, as a starting step, a pilot experiment has been designed in cooperation with several research institutes (EK, Research Centre for Natural Science), irradiation companies (Institute of Isotopes Ltd. Co., Agroster Ltd. Co.) and end users such as the Hungarian National Museum and the Semmelweis Medical History Museum. The cooperation aims to introduce gamma-, X-Ray- and electron irradiation methods for the conservation of pre-selected CH artefacts consisting of wood, textile, paper, leather, bone, metal, etc. One industrial and one pilot gamma irradiation facility are planned to use for the gamma irradiations. In addition, an R&D-type linear electron accelerator will be used for electron and X-Ray irradiations. Additionally, various liquid and solid phase dosimetry systems have been selected and will be introduced and tested for quality control. Moreover, the introduction of the potential for use of retrospective dosimetry to decide whether a CH object has been irradiated earlier will be investigated. For testing the irradiations' effects, archaeological animal bone samples (horse and cow bones, 7th century AD) have been selected and artificially contaminated with microorganisms prior to the irradiation (see Table 1).

*Table 1: Experimental design of archaeological animal bone samples artificially contaminated with microorganisms*

| **Effect of radiation on bone structure** | Irradiation (kGy) | FTIR | **Effects of radiation on microbes** | Micro-biology | FTIR | Irradiation (kGy) | Micro-biology | FTIR |
|---|---|---|---|---|---|---|---|---|
| Biologically "pure" samples | **0** | + | Samples "contami-nated" with microbes | + | + | **0** | - | - |
| | **10** | + | | + | + | **10** | + | + |
| | **25** | + | | + | + | **25** | + | + |
| | **50** | + | | + | + | **50** | + | + |

The microbiological analysis (by Wessling Hungary Ltd.) of the bones, as well as structural analysis by Fourier transform infrared (FTIR) spectroscopy prior to the irradiation have been performed.

## *Results*

A short visit was paid in October to the Belgian Nuclear Research Centre (SCK•CEN). At the Dosimetry Laboratory of SCK•CEN it was demonstrated, in a large-scale experiment in collaboration with Public Health England (PHE) and Helmholtz Zentrum München (HMGU), that smartphones can serve as 'casual dosimeters' in radiological incidents. We visited the OSL laboratory (equipped with a Risø TL/OSL reader) and obtained detailed information on sample preparation of resistors and OSL data evaluation, as well as the determination of different types of correction factors. Our host, Olivier Van Hoey kindly supplied us with literature, procedure descriptions and a sufficient amount of standard components to test basic measurement settings, irradiation and readout configurations in the future. In addition, a collaboration was established with the Mining and Geological Survey of Hungary, which has long term experience in OSL measurements, in order to collect information regarding laboratory construction and sample preparation.

The first results of the FTIR spectroscopy investigation revealed some variability in the spectral features of different bone samples as a function of their origin and/or contamination (Figure 1).

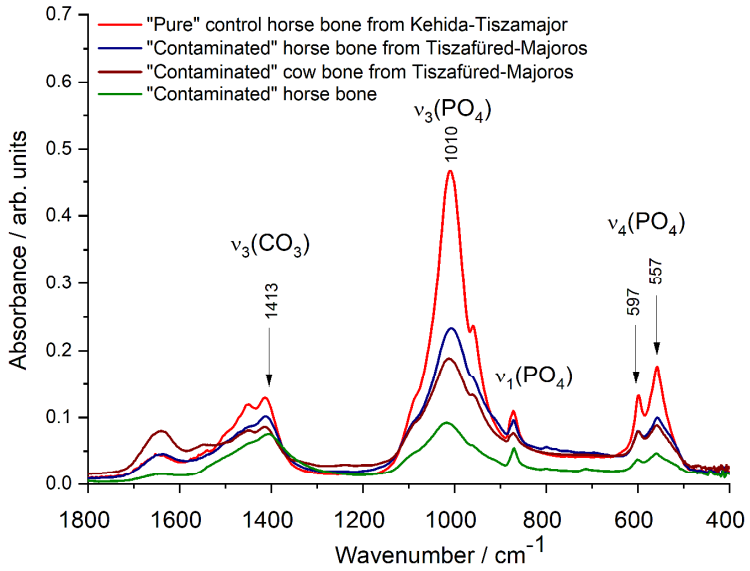


*Figure 1: FTIR spectra of the selected bone samples*

To characterize the possible alteration/damage in the carbonated apatite bone structure upon irradiation, two parameters will be monitored: i) the carbonate content through the $CO_3/PO_4$ ratio obtained from the band intensity at 1413 $cm^{-1}$ ($\nu_3(CO_3)$ and the intensity of phosphate band at 597 $cm^{-1}$, and ii) the crystallinity of the apatite calculated from the splitting of the $\nu_4PO_4$ bands.

One of the biggest outcomes of this project in 2021 was the building of capacity within the Centre for Energy Research related to dosimetry and cultural heritage research fields. As a result, a new methodology was established by procuring an OSL measurement unit and by creating a group of scientists to fulfil the requirements related to these two main topics.

## *Remaining work*

The retrospective dosimetry program continues with the preparation and analysis of potential devices, materials and samples. After completing the test investigations, the cultural heritage program will start with the selection of various objects to be irradiated, followed by the evaluation procedures.

# EFFECTIVE USE OF DOSE PROJECTION TOOLS IN THE PREPAREDNESS AND RESPONSE TO NUCLEAR AND RADIOLOGICAL EMERGENCIES: PART 2

*Tamás Pázmándi, Csilla Rudas*

## *Objective*

The research in this 3-years long project is focused on the assessment and application of dose projection software, and the main objective is the evaluation of uncertainties in atmospheric dispersion modelling and dose estimation in case of accidental radiological releases. In the second phase of the project [1], the dose assessment calculations were performed with deterministic input parameters, the results were compared and the uncertainty bands for the perturbation of the most important input parameters were selected. The work was carried out in cooperation with the Nuclear Safety Research Institute (NUBIKI).

## *Methods*

A benchmark analysis was carried out with two different dose projection tools, the SINAC decision support system developed in the Centre for Energy Research and the MACCS engineering-level computer code developed at Sandia National Laboratories. A simple release scenario was assumed for the benchmark study with consideration of spatially and temporally constant meteorological conditions and using a release source term taken from literature [2]. Simulations of the radioactive dispersion were carried out by a Gaussian Puff model built in SINAC and by a Gaussian plume segment model built in MACCS using the same parametrization and meteorological data, and the results were compared. Receptor points were selected at 5.0 km, 7.5 km, 10.0 km, 12.5 km and 15.0 km from the release point along the plume centreline.

## *Results*

A comparison of the output quantities from the basic benchmark study was conducted. The time integrated air activity concentrations at ground level and the ground concentrations for a selected number of nuclides are shown in Figure 1 and Figure 2, respectively. All things considered the activity concentration results show good agreement (are in the same order of magnitude), the air activity concentrations obtained with SINAC are only about 1.2-2.0 times higher than the corresponding values of MACCS, and ratio of the ground deposition in SINAC and in MACCS is around 90%-120%.

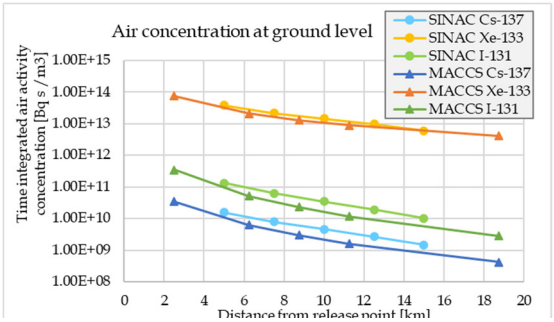


*Figure 1: The time integrated air activity concentrations at ground level for selected nuclides*

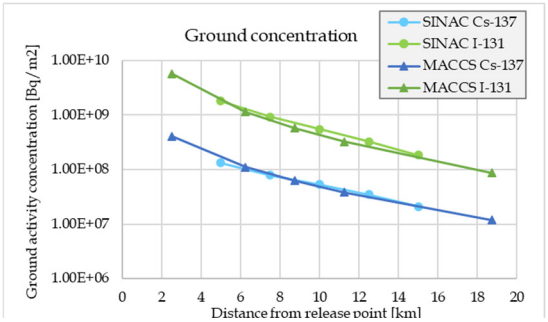


*Figure 2: Ground activity concentrations for Cs-137 and I-131*

The effective committed lifetime doses for cloudshine, groundshine (with 7 days residence time) and inhalation were also compared. Cloudshine and inhalation doses are about 20%-90% higher in SINAC than in MACCS, resulting from the higher plume air concentrations obtained with the former software. However, the groundshine dose in MACCS is 2-3 times higher than in SINAC, due to the difference in the built-in dose conversion factors for groundshine of MACCS and SINAC.

## *Remaining work*

In the third and final phase of the work, input parameters considered for uncertainty assessment will be selected, perturbation ranges will be established, and the uncertainties will be estimated. Assessment and visualization of output uncertainties of the dose projections will be carried out and the performance and effectiveness of the two software will be compared.

## *Related publications*

[1] T. Pázmándi, Cs. Rudas, A. Bareith, G. L. Horváth, G. Lajtha: *Second Phase: Comparison of SINAC and MACCS calculations for the basic benchmark scenario,* EK-SVL-2021-345-01-01-00 (2021)

[2] I. Korsakissok et al.: *Uncertainty propagation in atmospheric dispersion models for radiological emergencies in the pre- and early release phase: summary of case studies*, Radioprotection 55 (2020)

# ASSESSMENT OF DOSE RATE IN THE BUILDINGS OF THE PAKS NUCLEAR POWER PLANT

*Dorottya Jakab, Annamária Pántya, Tamás Pázmándi, Csilla Rudas*

## *Objective*

Since the latest comprehensive assessment of the radiation conditions inside the buildings of Paks Nuclear Power Plant (NPP) in 2006, there have been several technological developments and changes (e.g. introduction of new fuel type, extension of fuel cycle), which affect the resulting dose rates in certain locations within the buildings. Since then a few assessments have been conducted to investigate the effect of these changes but a comprehensive analysis covering all (concerned) areas and operational scenarios has not yet been carried out. The aim of this work was the systematic development and improvement of the models with redefined input parameters to take into account the changes listed above, and the repetition of the whole chain of calculations to determine the dose rates around certain equipment and at certain locations within the NPP. [1]

## *Methods*

In the first phase of the work, the previous dose map assessments were reviewed, and the main conclusions and lessons learned were summarized. The previous methodology was enhanced to calculate the activity concentrations that occur, and in some cases, accumulate in certain equipment of the NPP. The models used for computing the dispersion of radioactive material in the air through the ventilation system and through a chain of rooms and areas of the NPP, as well as the deposition resuspension on and from surfaces were updated. The methods to calculate the dose rate arising from the activity inside certain equipment and in the air and deposited onto the walls were also developed to determine the resulting external and internal doses to which workers may be exposed.

In the next phase of the work, we examined all the equipment around which the dose rate calculations were necessary to perform with reviewing their functions and connections with other equipment or systems, and refined, if needed, the models taking into account operational aspects and specific attributes of these equipment. The input parameters to be used for these assessments were established, the available data on them were collected and organized, the missing data were obtained. All of the input data already used in previous calculations were updated to reflect the current operational practice, with the approval of the colleagues of NPP through several consultations. For certain equipment, more than one set of input parameters were defined to cover different operational aspects and scenarios: parameters typical and the worst case of the normal operation were selected. The areas and rooms around the selected equipment and potentially affected by its operation were determined and their relevant characteristics were reviewed. Dose rate values measured in the areas around the selected equipment were also collected from different sources and databases and they were organized.

Calculations were performed to estimate the accumulation of activity inside the selected equipment, and the dose rates due to direct radiation from it were determined in its surrounding area. The dispersion, deposition and resuspension of the activity released in the air was computed through several chains of linked rooms connected by openings or by the ventilation system. The time integrated activity concentrations in the air and the activity concentrations on the walls, ceiling and ground were determined and the external and internal inhalation dose rates due to residing in each of the considered areas were calculated.

In the final stage of the work, the computed and measured dose rate values were compared to assist the review of the potentially occurring radiation levels and the resulting radiation protection classifications of the locations within the buildings. The calculated values and the measurement data were collected and archived in a database.

## *Results*

Overall, the calculated dose rate values, the measurements and the classification limits were mostly in good agreement (i.e. in similar orders of magnitude). However, it is important to note that the calculations were made with numerous approximations and with considerably conservative assumptions in the composition, activity concentration, flow velocity of the radioactive medium moving through the equipment, as well as characteristics of the shielding. Additionally, it is important to highlight that as different operational states were considered (including highest permissible state), there can be a large difference between the dose rate results obtained for these various parameter sets.

As a results of the dose map assessment, the radiation levels of certain locations within the Paks NPP were reviewed. Suggestions were given to change the radiation protection classification of areas, where it was supported by calculated and measured values and by the operational experience.

## *Remaining work*

This project has been completed.

## *Related publication*

[1] D. Jakab, A. Pántya, T. Pázmándi, Cs. Rudas: *Development of Methods for Dose Rate Calculations Inside Buildings,* EK-SVL-2021-727-01-02-00, in Hungarian (2021)

# DEVELOPMENT OF THE CARC SOFTWARE CAPABLE OF CALCULATING ENVIRONMENTAL RADIOLOGICAL CONSEQUENCES

*Tamás Pázmándi, Csilla Rudas*

## *Objective*

The development of the first version of the Calculations for Atmospheric Release Criteria (CARC) software to calculate the environmental radiational consequences of atmospheric releases of radioactive material from nuclear facilities has been finished in 2017. The program was further developed from 2019 to 2021 with the goal of providing a detailed documentation of the software and to perform deterministic safety assessments for the new fuel type optimized for the water-uranium ratio with thinner cladding, referred to as SLIM fuel rods being introduced at the Paks Nuclear Power Plant (NPP). [1]

## *Methods*

The CARC software is capable of calculating environmental activity concentrations and public doses due to short-term atmospheric releases of radioactive material. The main advantage of the new developments is that consequences of large number of variant conditions can be evaluated and local, site specific meteorological and habit data can be considered.

The CARC software is capable of consideration of long-term meteorological measurement data and providing statistical variables of the result quantities. In the deterministic safety assessment for the SLIM fuel, 95$^{th}$ percentile of the various dose results obtained for different meteorological conditions was computed. The meteorological input data for the assessment was provided by the meteorological measurement tower of the Paks NPP. A 5 years-long database was used from 2014 to 2018, containing wind speed, wind direction, Pasquill stability category measured at 120 m height and precipitation values summed for 10 minutes.

The habit characteristics of the public concerned were considered in the assessment through dose reduction coefficients taking into account the decrease of exposure due to residing indoors for a given time while being shielded by the building from groundshine and cloudshine and reducing inhalation through insulation. Input parameters of contaminated food consumption were also taken into account, with the consideration that only a limited amount of the locally produced food is consumed by this public.

The deterministic safety assessment for the new SLIM fuels was conducted for scenarios originating from initiating events resulting in Design Basis Conditions 4 (DBC4) [2]. Release activities were provided for the SLIM fuels, based on release characteristics consistent with previous assessments. In the analysis, the Gaussian plume model of the CARC program was used for the atmospheric dispersion calculation with model parameters set to the same values as in the previous assessment conducted with PC-COSYMA software.

## *Results*

The resulted quantities of the assessment were the short-term committed effective doses for 2 days and 7 days residence time, which included exposure pathways of cloudshine, groundshine and inhalation, and long-term committed lifetime doses containing ingestion additionally to the previously mentioned pathways. These quantities were determined at fixed receptor points at 1 km and 3 km from the release point, assuming that the representative persons reside at locations at such distances. Additionally to the total dose, the contribution of different pathways was assessed as well as that of the different radionuclides.

The results were compared with the regulatory limits published in the Nuclear Safety Code of the Govt. Decree 118/2011 (VII. 11.) on the nuclear safety requirements of nuclear facilities and on related regulatory activities. The results of the assessment show that even with conservative calculation assumptions the committed effective lifetime doses are considerably below the acceptance criteria for DBC4, thus the application of the new SLIM fuels is in compliance with the regulatory limit with high degree of certainty.

## *Remaining work*

This project has been completed.

## *Related publications*

[1] T. Pázmándi, Cs. Rudas: *Development of the CARC Code Capable of Calculating Environmental Radiological Consequences, Assessment with CARC program*, EK-SVL-2021-731-01-01-00, in Hungarian (2021)

[2] T. Pázmándi, Cs. Rudas, B. Somfai, I. Trosztel: *Environmental dose assessment with previous and new methodology for zones containing second generation fuel type optimized for the water-uranium ratio*, RAL-2017-719-01-45-M2, in Hungarian (2021)

# IN-ORBIT DEMONSTRATION OF THE RADMAG (RM-S) SPACE WEATHER INSTRUMENT

*Balázs Zábori, Attila Hirn, Boglárka Erdős*

## *Objective*

There is already a heavy dependence of the human civilization on technology, e.g. in the fields of energy and telecommunication systems. A continuous increase in human presence and different space-based infrastructure is in progress in the Near-Earth region. They are seriously affected by changes in space weather, especially during coronal mass ejections and geomagnetic storms. Earth's cosmic environment is highly influenced by several physical parameters (magnetic field variability, cosmic ray intensity, solar activity, atmosphere, etc.) and, mainly due to the complexity of the magnetosphere, a very good spatial and time resolution is required in space weather monitoring. To achieve this goal, the European Space Agency (ESA) defined the Distributed Space Weather Sensor System (D3S) concept utilizing hosted primary and secondary payloads for operational space weather monitoring on board as many platforms as possible. In the framework of the ESA PRODEX, EK initiated the development of a space weather instrument suite, called D3S-RadMag (RM-L). The major goal of the development is to combine tools for radiation and magnetic field measurements into a single payload, which can be utilized within the D3S hosted payload concept. In parallel, a smaller version of the instrument has been developed (RM-S). For this version, the magnetometer was provided by Imperial College London, and the boom mechanism by Polish company Astronika.

## *Methods*

Ground visualization and on-ground post-processing of data are performed by the RADCUBE/RadMag Science Operation Centre (SOC). LEVEL-0 data (RadMag binaries in .bin and platform auxiliary data in .csv format) were shared with the RadMag consortium by the satellite operator via a dedicated ftp server. LEVEL-0 data in the EK database system were continuously synchronized with the data available on the FTP server. The EK database system used EK's Seafile file server in the period between the 29th of October 2021 and the 4th of January 2022.

SOC provides auto-interpretation of LEVEL-0 data to provide LEVEL-1A pre-processed data. LEVEL-1A data are distributed to Imperial College London (ICL, Magnetometer, MAG experiment) and ESA-TEC (Radiation Hardness Assurance, RHA experiment). ESA-TEC is also provided with LEVEL-0 data, and ICL with LEVEL-1A HK data according to their requests. RHA and MAG LEVEL-2 data provision is done offline by ESA-TEC and ICL, respectively. RAD LEVEL-2 Data Provision, for the moment, is done manually. After the calibration and data processing algorithms will have been frozen, the RAD LEVEL-1A to LEVEL-2 data conversion will be done automatically by the RadMag SOC. RAD/MAG/RHA combined science will be done manually to provide LEVEL-3 science data.

Data provision to the scientific community is planned through ESA's Open Data Interface (ODI). EK will share LEVEL-0, LEVEL-1A and LEVEL-2 RAD data in .csv format. Coordinate transformation will be realized either at SOC or at ODI.

## *Results*

Commissioning of the RadMag payload on RADCUBE started on the 5th of October 2021. After the commissioning phase and the corresponding ESA review have successfully been passed, the nominal operation phase started. Engineering data were all within their nominal ranges in 2021. Science data were also received, pre-evaluation started. A time spectrum measured with the RAD1D3 detector in RadMag is shown as example in Fig.1.

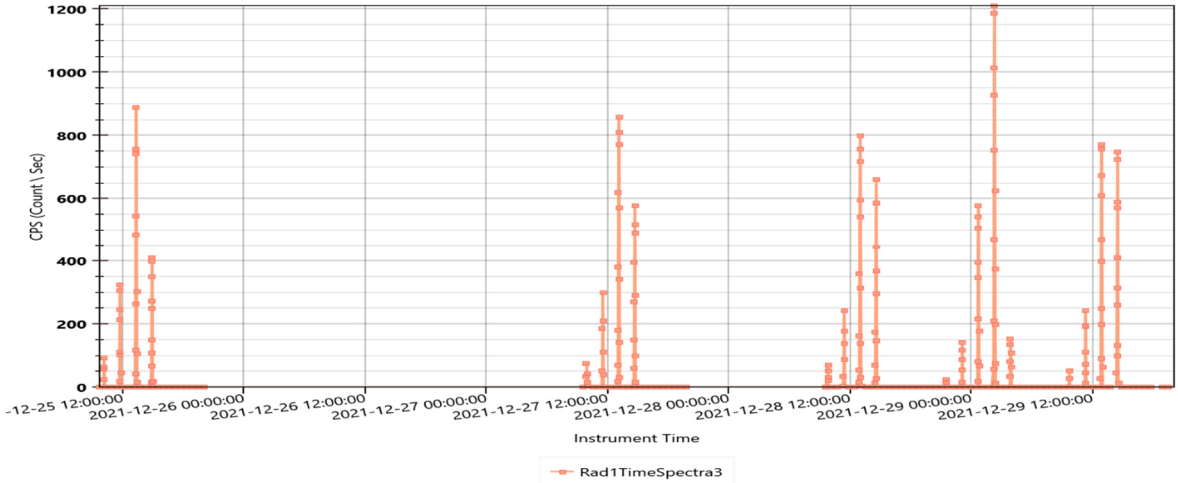


*Figure 1: Single detector time spectrum /count rate profile for RAD1D3 detector (Rad1TimeSpectra3) measured with RadMag on RADCUBE (zoomed for the period December 25 – 31, 2021 as example) shown by the Science Operation Centre software. The peaks correspond to time periods when the spacecraft crossed the South Atlantic Anomaly.*

The Elegant Breadboard Model (EBB) of RML-MAG (magnetometer unit) and the Engineering Model (EM) of RML-RAD (radiation detector unit) were manufactured (Fig. 2.) and tested against major functional and many of the performance instrument technical requirements in 2021, as part of the verification process.

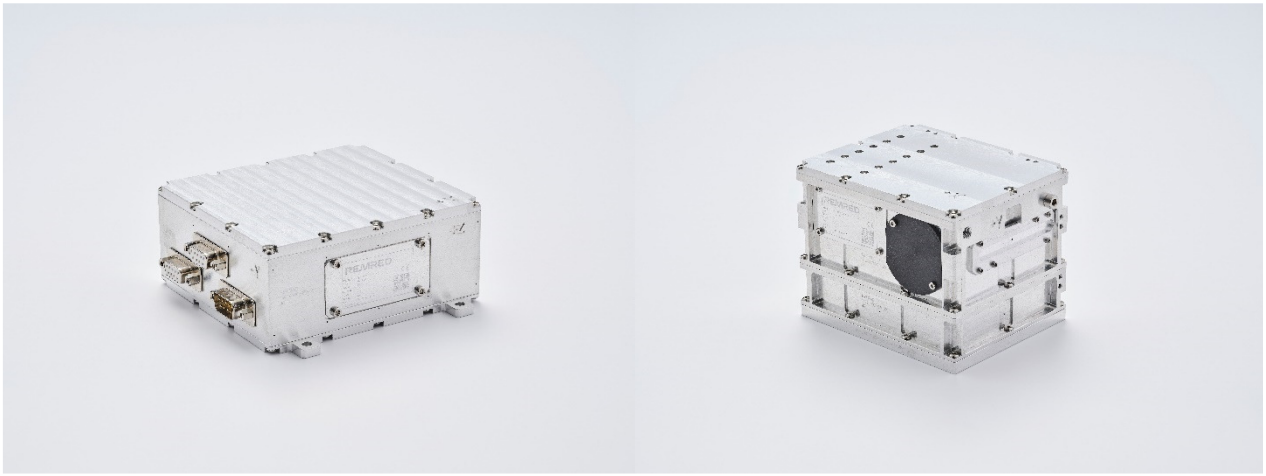

*Figure 2: The EBB of the RML-MAG (left) and the EM of the RML-RAD (right)*

## *Remaining work*

Nominal operation of RadMag on board RADCUBE finishes in 2022. Calibration measurements and performance testing of the radiation part of the RM-L instrument, as well as evaluation of RADCUBE flight data will be finished in 2022.

## *Acknowledgements*

The activity related to RadMag RM-L development was performed in the frame of the ESA Arrangement No. 4000124572/18/NL/CBi that of the RM-S implementation in ESA Arrangement No. 4000120860/17/NL/GLC

# DEFINITION STUDY FOR GATEWAY INTERNAL RADIATION DOSIMETRY UTILIZATION CONCEPT

*Balázs Zábori, Attila Hirn, Boglárka Erdős, Julianna Szabó*

## *Objective*

The Gateway space station, to be built in orbit around the Moon in the mid-2020s, will not be protected by the Earth's magnetic field or the atmosphere; hence, astronauts could be exposed to up to 700 times the radiation dose of an average human on Earth from space radiation. The main objective of Internal Dosimeter Array (IDA), the first internal payload by European Space Agency (ESA) for Gateway early utilization, is to monitor the internal space dosimetry environment with the combination of existing and proven instrument technologies in an international collaboration. The Space Research Department of the Centre for Energy Research was responsible for the definition and breadboarding of the IDA payload design consisting of a central electronics unit (eBox) being able to interface with the existing sensors TRITEL from EK, European Active Dosimeter (EAD) from the German Aerospace Centre (DLR), MediPix from Czech company Advacam, and Padles and D-Space from Japan Aerospace Exploration Agency (JAXA) as well as to connect and interface to the Gateway.

## *Methods*

To derive preliminary definition of the payload design, the interface requirements and the preliminary operational definition of IDA, the Interface Control Documents (ICDs) of the sensors to be integrated with the eBox to be developed and the major Gateway documentation were reviewed. In elaborating the conceptual design, the eBox, the sensors, the Gateway environmental conditions and operational constraints were considered. In view of a quick turn-over for utilization, the EK had to make as much as possible use of existing designs and technologies. To have a programmatic assessment, a preliminary schedule for the development of the payload including a first cost estimate was prepared.

## *Results*

All sensor ICDs and the major Gateway documentation was reviewed and assessed with respect to relevant measurement techniques and interfaces. The major challenges and drivers for the IDA design, development, integration, accommodation, and operation were identified and assessed as well as the environmental (radiation) conditions. The assessment resulted in the definition of preliminary payload engineering requirements, interface definitions (internal to the sensors and external to the Gateway), preliminary operational concept and the environmental reconstruction document. Based on the preliminary requirements agreed with the ESA regarding the definition of the interfaces and of the concept of operations, the conceptual design of the payload was established considering physical configuration, structural and mechanical design, thermal design, electrical design, required sensors and data handling. The breadboard of the eBox connecting with the sensors was developed and manufactured. The final assessment regarding cost and schedule of the full IDA development program was prepared with summary of open issues requiring clarification before entering the next phase of development.

## *Remaining work*

After successfully closing the definition study phase of the project and winning the call for the subsequent phases, the work will continue with the implementation of the IDA project.

## *Acknowledgments*

The IDA Definition Study was conducted in the frame of the ESA Contract No. 4000134497/21/NL/PA/eg.

# DEFINITION STUDY OF THE SPACE DOSIMETRY TELESCOPE FOR THE MARS SAMPLE RETURN MISSION EARTH RETURN ORBITER

*Balázs Zábori, Attila Hirn, Boglárka Erdős, Julianna Szabó*

## *Objective*

The Mars Sample Return (MSR) campaign led by NASA/JPL aims to convey soil and atmospheric samples from the Mars surface to Earth by 2031. An important contribution of the European Space Agency (ESA) to the program is the Earth Return Orbiter (ERO) spacecraft. The Space Dosimetry Telescope (SDT) experiment, composed of a space radiation monitor (RADTEL space radiation telescope system) and a dosimetry monitoring system (TRITEL 3-dimensional silicon detector telescope) was proposed for ERO to monitor space radiation and related dosimetry quantities during the Earth-Mars cruise, in orbit around the Mars and during the trip back from Mars to Earth to support future human Mars missions. In year 2021, the study work for MSR-ERO-SDT proceeded with the consolidation of the preliminary experiment requirements, the identification of experiment functions and associated performances, the baseline design approach, the system engineering plan, and the experiment roadmap for the upcoming project phases.

## *Methods*

To consolidate preliminary experiment requirements, the ERO Product Assurance and Safety Requirements for phases B2/C/D/E1, the ERO Assembly, Integration and Verification Requirements Document, and the ERO System Requirements Document were reviewed and assessed. Based on preliminary requirements, preliminary interfaces and the basic design were defined.

## *Results*

ERO system-level requirements were flown down to payload and unit level requirements. The assessment of the SDT science objectives and the ERO system level requirements resulted in preliminary functional, dosimetrical performance, space radiation (electron, proton, ion) measurement performance, technical performance, mission, interfaces, environmental physical properties, configuration, operational, and product assurance requirements. Electromagnetic compatibility and assembly integration and verification requirements are consolidated at latter phases of the project. The 3D model of the resultant preliminary design at the end of Phase B1 is shown in Fig.1.

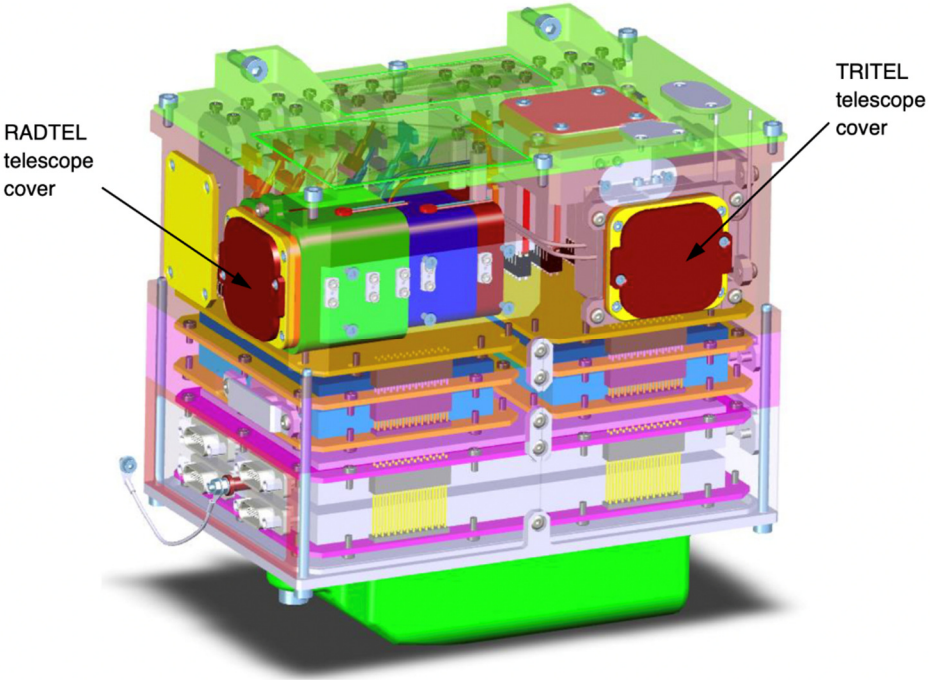


*Figure 1: Preliminary MSR-ERO-SDT design*

## *Remaining work*

After successfully closing the definition study phase of the project, the work continues with the implementation of the MSR-ERO-SDT project.

## *Acknowledgment*

The MSR-ERO-SDT Study was conducted in the frame of the ESA PRODEX Experiment Arrangement No. 4000132501.

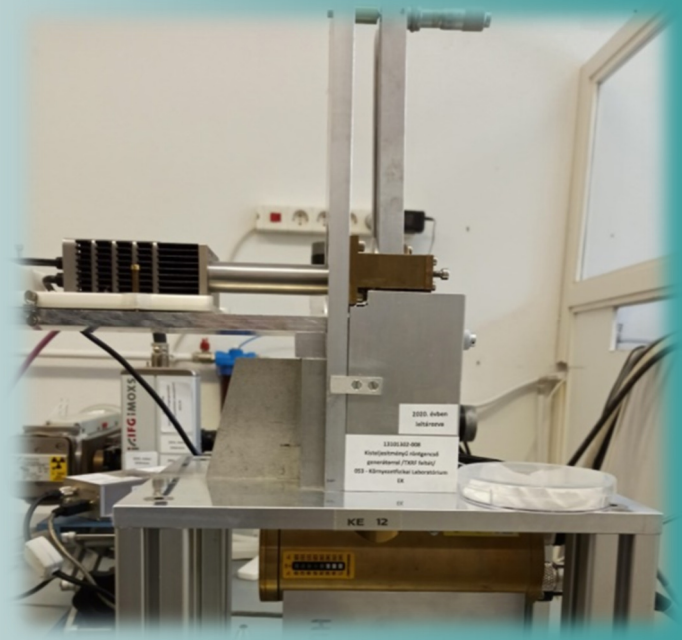

# IV. ENERGY SECURITY AND ENVIRONMENTAL STUDIES

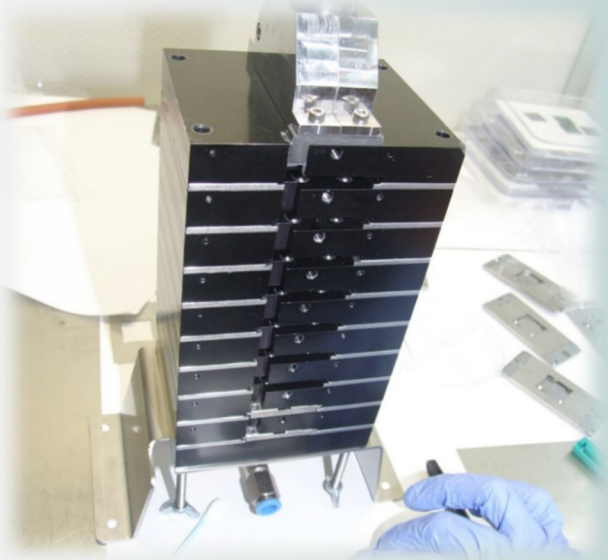

# CATALYTIC SYSTEMS FOR WATER ELECTROLYSIS

*Tímea Benkó, Krisztina Frey, Sahir M. Al-Zuraiji, Zsolt Kerner and József S. Pap*

## Objective

The electrolysis of water is an important technology worth investigating to replace the usage of fossil fuels since it can help to overcome the storage-reuse obstacles of renewable-based energy systems by producing the green energy carrier $H_2$. Progress in non-covalent/self-assembled immobilization methods on (photo)electrode materials for molecular catalysts could broaden the scope of attainable systems. While covalent linkage (though considered more stable) necessitates functional groups introduced by means of often cumbersome synthetic procedures, non-covalent assemblies only require sufficient propensity of the molecular unit for surface adsorption, and thus set less rigorous pre-requisites. Within the framework of the VEKOP 2.3.2-16-2016-00011 and the NKFIH 128841/2018 grants, Fe(III) complexes were prepared by Electrodeposition (ED), yielding stable adsorbtion-layers active in electrocatalytic Oxygen Evolution Reaction (OER).

## Methods

The different compounds to be used as catalytic materials were synthesized according to published procedures. Electrochemical analyses were carried out on a Bio-Logic SP-150 potentio-galvanostat. Boron-Doped Diamond (BDD), Glassy Carbon (GC), Indium Tin Oxide (ITO), Fluorine-doped Tin Oxide (FTO), or nanostructured $BiVO_4$/FTO were used as working electrodes. Quantitative gas analysis of the produced $O_2$ was done using a Shimadzu Tracera 2010 gas chromatograph equipped with a Barrier Ionization Discharge (BID) detector. The surfaces of the electrodes were analyzed by Scanning Tunneling Microscopy (STM), X-ray Photoelectron Spectroscopy (XPS), Scanning Electron Microscopy (SEM) with Energy Dispersive X-ray (EDX), and Raman and Infrared (IR) spectroscopy. Solution spectroscopy was performed using a Cary 60 UV-visible spectrophotometer.

## Results

We have successfully carried out efficient ED of two Fe(III) complexes prepared with closely related NN'N pincer ligands, yielding stable and active adsorption-layers for the electrocatalysis of the OER.

We compared how deposition techniques affected the OER performance. As shown in Figure 1, the considered methods included Drop-Casting (DC) and Dip-Coating (DIP), in combination with Nafion, a common additive for stable deposition of molecular catalysts, (methods A–C), as well as the ED technique (method D). In contrast to methods A–C which may be unsuited to fabricate catalytically active layers due to poor solubility of a complex in the obligate solvent mixtures, method D produced layers with better charge transfer properties and stability, in the most atom-efficient, additive-free way. The ED method is based on the utilization of a chloride precursor complex $[Fe^{III}Cl_2(NN'N)]$, which undergoes chloride/aqua ligand exchange in an organic electrolyte upon addition of water. ED provides a patchy distribution of a chloride-depleted catalyst layer on Indium Tin Oxide (ITO) and Fluorine-doped Tin Oxide (FTO) surfaces, which can then be used for long periods as OER electrocatalysts. Compared to drop-casting or layering of $[Fe^{III}Cl_2(NN'N)]$ with Nafion (a commonly used support for molecular electrocatalysts), the surface modification by ED is a material saving and efficient method to immobilize catalysts.

In sharp contrast to samples prepared by the DC and DIP methods, those made by ED showed distinctly better performance in the OER. Moreover, this method worked equally well for the different iron-complexes.

Following their use in the electrocatalytic OER experiments, the electrode surfaces were characterized by SEM, as well as SEM-EDX. In the SEM images, it was seen that the FTO surface is covered in patches by a solid material of random morphology but in a relatively even distribution on the scale of a few hundred µm. The average composition by EDX confirms the presence of the expected Sn, O and F for the substrate, and C, N, S and Fe for the complex, but Cl was found to be absent.

Our aim was also to reduce the amount of complex required for long-term operando stability. In the case of the first complex, the amount deposited by ED was an order of magnitude smaller compared to the self-supported system reported earlier (prepared by DC from methanol without Nafion). As for the second complex, which is practically insoluble in alcohols, i.e. making it unsuitable for DC, the electrodeposition worked just as well, resulting in a very stable complex-electrode combination.

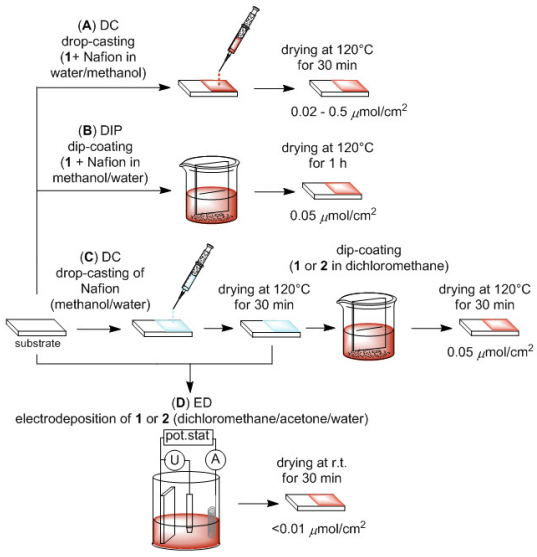


*Figure 1: Schematic view of the different sample preparation methods (methods A-D)*

## Related publication

[1] S. M. Al-Zuraiji, T. Benkó, K. Frey, Z. Kerner, J. S. Pap: *Electrodeposition of Fe-Complexes on Oxide Surfaces for Efficient OER Catalysis,* Catalysts **11,** 577 (2021)

# REDOX-INACTIVE METAL SINGLE-SITE MOLECULAR COMPLEXES AS NOVEL ELECTROCATALYSTS FOR OXYGEN EVOLUTION

*Tímea Benkó, Dávid Lukács, Krisztina Frey, Miklós Németh, Márta M. Móricz, József S. Pap*

## *Objective*

The utilization of first-row transition metals in molecular electrocatalysts for water oxidation (i.e. for the challenging Oxygen Evolving Reaction, OER) is a rapidly evolving topic. With the support of NKFIH NN128841 and the VEKOP-2.3.2-16-2016-00011 grants, our aim was to understand the behaviour of a copper molecular pre-catalyst complex immobilized on an Indium Tin Oxide (ITO) substrate, and study its performance to electrocatalytically generate $O_2$.

## *Methods*

Synthesis of the different compounds used was carried out according to published procedures. Electrochemical experiments were performed on a Bio-Logic SP-150 potentio-galvanostat. Boron-Doped Diamond (BDD), Glassy Carbon (GC), ITO, Fluorine-doped Tin Oxide (FTO), or nanostructured $BiVO_4$/FTO substrates were selected as working electrodes. Quantitative gas analysis of the produced $O_2$ and $H_2$ was done using a Shimadzu Tracera 2010 gas chromatograph equipped with a Barrier Ionization Discharge (BID) detector. The surface of the electrodes was analyzed by Scanning Tunnelling Microscopy (STM), X-ray Photoelectron Spectroscopy (XPS) and Scanning Electron Microscopy (SEM) with Energy Dispersive X-ray (EDX), and Raman and Infrared (IR) spectroscopy. Spectro-electrochemistry was carried out by a Cary 60 UV-visible spectrophotometer and a 3-electrode cell.

## *Results*

The molecular pre-catalyst complex $[Cu^{II}(indH)(OClO_3)(NCCH_3)](ClO_4)\cdot CH_3CN$ (**1**·$CH_3CN$) with the 3N pincer ligand 1,3-bis(2′-pyridyl)iminoisoindoline (indH) was immobilized on an indium tin oxide (ITO) transparent conducting substrate to electrocatalytically generate $O_2$. For over 20 hours at pH 10 in a carbonated buffer, reaching a turnover number of 139, no $CuO_x/Cu(OH)_2$ formation was identified at the surface. Further electrolysis experiments revealed that the catalyst was present in the aqueous phase, despite the poor initial solubility of the pre-catalyst. In order to identify the actual form responsible for this important catalytic reaction, the aquo complex $[Cu^{II}(ind)(OClO_3)(OH_2)]\cdot CH_3OH$ (**2**·$CH_3OH$) was structurally characterized. Spectroscopic investigations of a solid isolated from the buffer used in the electrolysis reaction and solution equilibrium studies indicated that the $[Cu^{II}(ind)(OH)]$ form occurs at pH 10. Electron Paramagnetic Resonance (EPR) spectroscopy and DFT calculations confirmed a distorted $\{3N,O\}_{eq}$ coordination plane in solution.

The buffer (i.e. bicarbonate/carbonate) may affect reactivity in two ways: as an external base facilitating the proton-coupled electron transfer steps; and/or displacing the inner-sphere solvent molecules from the favourable quasi-equatorial position, thus inhibiting the catalysis. Structural features of a tri-nuclear cluster $[Cu^{II}_3(ind)_3(\mu^3\text{-}CO_3)(CH_3OH)(OClO_3)]$ isolated under basic conditions confirmed that beside acting as an external base, the inhibiting effect of carbonate anions may also play a role.

In acetonitrile-water solutions, where both the aquo complex and the $[Cu^{II}(ind)(OH)]$ hydroxide forms exhibit reasonable solubility, experimental findings supported by DFT calculations suggest that it is the $ind^-$ ligand which is being oxidized while the cupric ion remains redox-inactive which is very unusual.

In the O–O bond formation step, the oxidized ligand is reduced by the electron from the attacking water molecule. The water molecule would release a proton in this process due to the interaction between the two oxygen atoms. Given the weak acidity of Cu–indH in water–acetonitrile mixtures determined by its acid–base equilibrium constant and the lack of an additional proton acceptor, this proton is expected to be finally attached to the ligand N like the N–H bond. Subsequently, this species would be oxidized twice to generate an $O_2$ molecule (species I6) and then replace it with $H_2O$ to close this catalytic cycle.

These findings are of great significance for a new synthetic strategy for the fabrication of a new generation of low-cost, redox-inactive, transition metal-based molecular electrocatalysts for the most challenging reaction of water oxidation, that is, the evolution of oxygen.

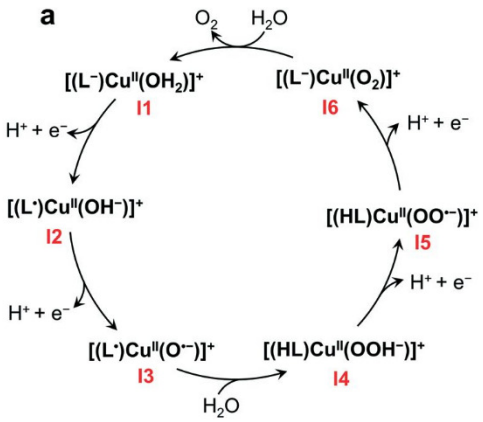


*Figure 1: The proposed catalytic cycle of water oxidation on [**2** –$ClO^{4-}$]+ in acetonitrile–water mixture, where L = ind*

## *Related publication*

[1] T. Benkó, D. Lukács, K. Frey, M. Németh, M. M. Móricz, D. Liu, É. Kováts, N. May, L. Vayssieres, M. Li, J. S. Pap: *Redox-inactive metal single-site molecular complexes: a new generation of electrocatalysts for oxygen evolution?*, Catal. Sci. Technol. **11,** 6411-6423 (2021)

# CATALYTIC METHANE CONVERSION TO HYDROGEN OR SYNGAS

*Andrea Beck, Miklós Németh, Tamás Korányi, Anita Horváth*

## *Objective*

Catalyst development for the $CO_2$-free exploitation of the abundantly available natural gas/biogas producing i) syngas by dry reforming of methane (DRM: $CH_4+CO_2 \rightleftharpoons 2CO+2H_2$) and (ii) $H_2$ and solid carbon products by methane pyrolysis ($CH_4 \rightleftharpoons C+2H_2$) were the aims of this work. The results concerning the actual dry reforming studies were already complete, and the manuscript exploring the potential of the novel indium promotion of a $Ni/Al_2O_3$ catalyst versus the usual ceria promotion was published [1]. As a new research direction – based on the emerging interests and perspectives of the natural gas conversion research area – methane pyrolysis studies were started that would allow the $CO_2$-free conversion of methane into pure $H_2$ and valuable nanostructured carbon using proper catalyst compositions. The establishment of the experimental setup (a pyrolysis reactor system) for this reaction and the synthesis of the first set of MgO supported Ni-based catalysts were the initial steps to be carried out together with some structural and catalytic characterisations.

## *Methods*

During catalyst synthesis, the Ni and Mo precursor salts were added to the suspension of a commercial MgO support at room temperature (RT) and held there for 1 hour (MoNi0.4_RT) or heated to 80 °C and kept there for 1 hour resulting in 7 wt% Ni/MgO samples with low (Mo/Ni=0.4) and high (Mo/Ni=1.2) Mo loadings. The three bimetallic (MoNi0.4_RT, MoNi0.4 and MoNi1.2) and the control monometallic samples were washed and centrifuged to keep only the strongly adsorbed metal precursor species. Inductively Coupled Plasma Optical Emission Spectrometry (ICP_OES) was used to determine the final catalyst composition. Catalyst characterizations by Temperature Programmed Reduction (TPR), X-ray diffraction (XRD), and Transmission Electron Microscopy (TEM) with elemental mapping were performed after different pre-treatments or catalytic reactions. The catalytic properties were investigated after reduction at 800 °C in a) 1% $CH_4$/He stream under temperature ramping or at an isothermal 700 °C in a Micrometrics AutoChem instrument with Quadrupol Mass Spectrometer (QMS) or b) in 50% $CH_4$/Ar flow at 800 °C in the newly built horizontal pyrolysis reactor attached to a Gas Chromatograph (GC). The methane decomposition rate was the measure of catalytic activity in both cases and $H_2$ was the sole gas phase product. The amount of coke was measured after pyrolysis and its structure was analysed by Raman Spectroscopy or High Resolution TEM (HRTEM).

## *Results*

The difference between the nominal and actual Mo loading of the catalyst suggested that the adsorption of the Mo precursor is limited, but can be enhanced at 80 °C, while the synthesis temperature did not influence the Ni loading and, in fact, the theoretical Ni concentration was achieved. This means that the surface anchoring sites and/or the strength of adsorption are different for Ni and Mo precursors. According to the TPR results, a hard to reduce Ni-Mo oxide phase strongly interacting with the MgO support and having a TPR peak maxima at around 800 °C was present. The amount of $H_2$ consumption corresponded to the full reduction of NiO and $MoO_3$ for the bimetallic samples, while for Mo/MgO and Ni/MgO it was lower (some oxidic Mo or Ni must remain after reduction pretreatment). XRD of the reduced catalysts showed small metallic Mo particles for Mo/MgO and bimetallic NiMo particles for the samples with Mo/Ni=0.4 and nothing but the MgO support for MoNi1.2. TEM also ascertained the alloyed NiMo composition for all the reduced bimetallic catalysts and mainly nice, well dispersed particles also for the monometallic samples, all having average particle size lower than 10 nm for all the samples. In the temperature ramped $CH_4$ decomposition experiments, $CH_4$ dissociation occurred on Ni/MgO only around 550 °C, on Mo/MgO only above 700 °C, while the bimetallic samples were active in both temperature ranges. In the $CH_4$ decomposition studies carried out in both the AutoChem and in the pyrolysis reactor, a synergetic effect was observed for the bimetallic catalysts, and the MoNi1.2 sample was the best one. According to Raman and High Resolution Transmission Electron Microscopy (HRTEM) results, the coke formed during pyrolysis on Ni/MgO was the most graphitic type but only in a 1-2 nm thick shell covering the Ni particles, while on Mo/MgO it was the most defective shell forming the same onion type graphitic layers around the Mo particles, but both experienced a very fast deactivation. Over the best MoNi1.2 catalyst, having a 300 % carbon yield, partially defective fine carbon nanotubes of maximum 10 nm in diameter were obtained. This is explained by the stable high dispersion of bimetallic NiMo particles of special composition stabilized over the Mg-oxide support. This means that the interaction of Ni with sufficient Mo partners assists the continuous nanotube formation and hence the good catalytic performance during $CH_4$ decomposition.

## *Remaining work*

Pyrolysis research will be continued with in situ X-ray Photoelectron Spectroscopic (XPS) and with Diffuse Reflectance Fourier Transform Infrared Spectroscopic (DRIFTS) investigations.

## *Related publications*

[1] A. Horváth, M. Németh, A. Beck, B. Maróti, G. Sáfrán, G. Pantaleo, L. Liotta, A. M. Venezia and V. La Parola: *Strong impact of indium promoter on $Ni/Al_2O_3$ and $Ni/CeO_2$-$Al_2O_3$ catalysts used in dry reforming of methane*, Applied Catalysis A: General **621,** 118174 (2021)

[2] Horváth A., Beck A.: *$H_2$ és CO előállítása a metán száraz reformálásával*, és Horváth A., Korányi T.: *Hidrogén előállítása a metán pirolízisével,* Nemzeti Hidrogéntechnológiai Platform, Fehér könyv, (2021)

# EFFECT OF ELECTRON BEAM IRRADIATION AND THE PRESENCE OF ANTIBIOTICS ON THE POPULATION RATIO OF RESISTANT/SENSITIVE BACTERIAL CULTURES IN A MODEL WASTEWATER MATRIX WITH ANTIBIOTICS AND BACTERIA ADDED PRIOR TO ADVANCED OXIDATION TREATMENT

*Renáta Homlok, András Kovács, Tünde Tóth, Viktória Dobó, Erzsébet Takács, Csilla Mohácsi-Farkas, László Wojnárovits, László Szabó*

## *Objective*

The objective was to clarify the population dynamics of resistant/sensitive Staphylococcus aureus co-cultures. On the one hand, we wanted to gain insight into the effect of trace amounts of antibiotics (piperacillin and erythromycin) on bacteria in different wastewater matrices, and on the other hand, to study the applicability of electron beam (EB) radiation to eliminate the antibacterial effect.

## *Methods*

Experiments were done on bacteria added to the wastewater matrix prior to EB treatment (Fig. 1). The synthetic wastewater matrix was prepared with (results are shown in Fig. 2) or without the antibiotic (results are shown in Fig. 3). The concentrations of antibiotics in the wastewater matrix were 2 μg $L^{-1}$. Control samples were treated in the same way as the irradiated samples but they were not subjected to the radiation treatment.

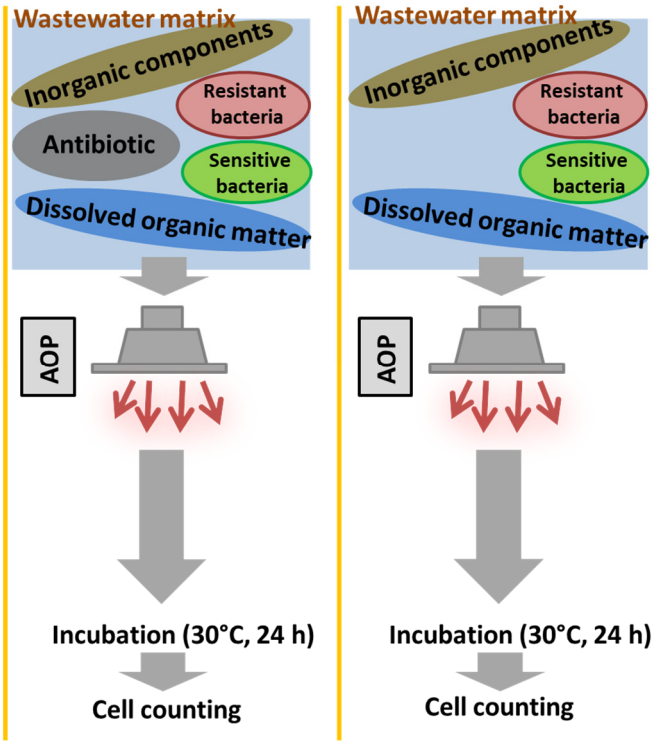


*Fig.1: Schematic representation of the model systems and the main processing steps applied in our study*

The EB treatment was performed using a Tesla Linac LPR-4 type linear electron accelerator. Our assessment method is based on a microbiological assay we developed previously. We selected sensitive and resistant Staphylococcus aureus (S. aureus) isolates (National Collection of Agricultural and Industrial Microorganisms, NCAIM, Szent István University) to monitor the change in antibacterial activity. In this test the dynamics of a mixed (sensitive/resistant) bacterial population gives information on the effects of antibiotics in a concentration well below the Minimum Inhibitory Concentration (MIC). Samples for testing were prepared from an overnight culture (incubated at 37 °C) in the case of the sensitive strain, and in the case of the resistant one, the cells to be inoculated were incubated at 72 h (at 37 °C) for the bacterial suspension preparation. This time difference was necessary to adjust the incubation sufficiently. The sensitive and resistant subtypes approximately in the same amounts were added to the wastewater matrix prior to irradiation. As the figures show 1:1 ratio was not achieved in none of the cases, the number of sensitive cells was always higher in the untreated cells than that of the resistant cells. E.g. as the blue columns in Fig. 2B show the fraction of the resistant cells was 21% in the population, corresponding to 17% resistant and 83% sensitive bacteria. After the irradiation, the samples were again incubated. The second incubation was necessary to grow visible colonies on the agar plates for cell counting. Colony counting was performed on trypto-casein soy broth (CASO) agar plates. After spreading 100 μL samples evenly on the surface, the inoculated plates were incubated and then the number of surviving colonies (resistant) were counted. The total colony count (sensitive + resistant) was determined on unspiked agar plates (no antibiotic), while resistant cells were counted on agar plates spiked with the corresponding antibiotic reaching a concentration well above the minimum inhibitory level. Only resistant cells grow on the surface of the agar plates containing the antibiotic above the MIC. Then the ratio of resistant colonies to the sensitive + resistant colonies was calculated.

## *Results*

The fraction of resistant bacteria in the population after irradiation is depicted in Fig. 2 and 3. As the dose increases, the ratio of bacteria R to R+S continuously decreases. Bacteria are not capable of growing on agar plates after 1 kGy or higher absorbed

dose (no orange columns). It was experienced that resistant bacteria are significantly more sensitive to radiation treatment over the entire dose range than sensitive bacteria when antibiotic is present in the matrix (orange columns).

Fig. 3 shows our results for the samples without antibiotics. In this case, the relative populations of surviving bacteria is not affected by low doses (e.g. the heights of the untreated (blue) and treated (orange) columns are the same). For Piperacillin there is no effect even at 0.6 kGy. Higher absorbed dose leads to significant changes in the relative fractions of the resistant and sensitive bacteria. The resistant bacteria disappear from the wastewater matrix without antibiotic (no orange columns). We think this is due to the effect of the toxic products formed by EB irradiation from the components of the wastewater matrix on bacteria. The lower relative survival of resistant bacteria (as shown on Fig. 2) does not appear in the samples without antibiotics (Fig. 3). It seems that the presence of the antibiotic makes the resistant subtype more sensitive to irradiation. This may be explained by some ongoing biological processes. The sensitive subtype is left intact at very low concentrations of the antibiotic. In contrast, the resistant subtype becomes weaker, less prepared to resist the attack of free radicals. In addition, it can be noted that a larger surviving resistant bacterial fraction was obtained on plates containing piperacillin (Fig. 3B) compared to the plates containing erythromycin (Fig. 3A). This observation may suggest that the resistant subtype that survived treatment in the effluent matrix eventually became more suitable for growing on piperacillin-containing plates. These experimental results need further investigations in the future.

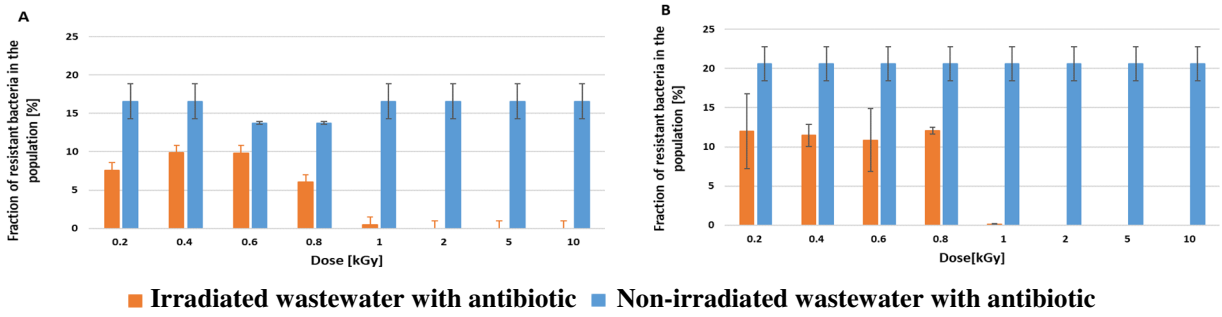


*Fig. 2: Fraction of resistant bacteria in the population after advanced oxidation treatment performed directly on a culture containing bacteria, wastewater matrix and either (A) erythromycin or (B) piperacillin at environmentally relevant concentrations (2 μg L$^{-1}$).*

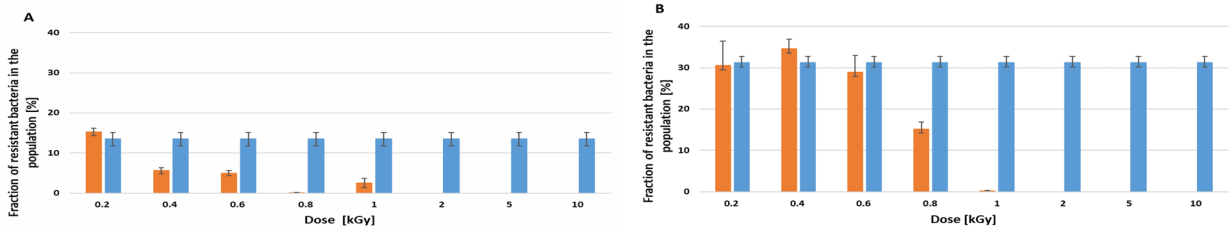


*Fig. 3: Fraction of resistant bacteria in the population after advanced oxidation treatment performed directly on a culture containing bacteria and wastewater matrix without antibiotics. Cell counting was performed on either (A) erythromycin or (B) piperacillin containing plates.*

## *Remaining work*

We would like to extend our studies to a sensitive and a resistant E. coli strain.

## *Related publications*

[1] V. Vogt, SI. Borrely, S. Shankar, HA. AbdEl-Rehim, F-H. Roegner, R. Homlok, HW. Bai, A. Abusam, S. Selambakkannu, M. Sudlitz, et al.: *Recent Achievements on the Removal of Biohazardous Pollutants by Radiation,* Report of the 2nd Research Coordination Meeting, 1-163 (2020) National Center for Nuclear Science and Technology, Tunis, Tunisia 2-6 March 2020.

[2] R. Homlok, G. Kisko, A. Kovacs, T. Toth, E. Takacs, Cs. Mohacsi-Farkas, L. Wojnarovits, L. Szabo: *Antibiotics in a wastewater matrix at environmentally relevant concentrations affect coexisting resistant/sensitive bacterial cultures with profound impact on advanced oxidation treatment.* Science of the Total Environment**, 754,** 142181 (2021)

[3] E. Takács, J. Wang, L. Chu, T. Tóth, K. Kovács, A. Bezsenyi, L. Szabó, R. Homlok, L. Wojnárovits: *Elimination of oxacillin, its toxicity and antibacterial activity by using ionizing radiation.* Chemosphere **286,** 131467 (2022)

# BIOGENIC CARBON CONTENT DETERMINATION OF CATALYTICALLY CONVERTED BIOMASS MATERIALS

*Tamás Korányi*

## *Objective*

The aim of this present study was the optimization of direct liquid scintillation counting (LSC) measuring conditions of biomass originated samples for the determination of the biogenic carbon content of catalytically converted biomass.

## *Methods*

The determination of the biomass content of biocarbon relative to fossil carbon in various materials (cellulose, lignocellulose and lignin derivatives) by radiocarbon ($^{14}C$) LSC was our goal. This determination depends on the fact that there is no $^{14}C$ in the fossil-carbon. The product mixture was dissolved directly in the scintillation cocktail and its biogenic carbon content was measured with a Tri-Carb 4810TR LSC equipment. This method is only applicable using colourless or slightly coloured samples.

## *Results*

Jenő Hancsók (Prof. Emeritus, Pannon University) provided to our group various gasoline, jet fuel and diesel fuel samples with 0-100 % biocarbon content. The aim of these investigations was to determine the reliability of biogenic carbon content determination on these samples by our radiocarbon LSC method. Altogether 65 samples were measured, the measuring conditions were varied systematically and they were optimized. Samples with 0.5-2 wt% biocomponent content did not provide reliable results. Others with 3-8 wt% biocarbon content were measured with less than a 10 % difference per mean (dpm) value, while those around 10 wt% with less than a 5 % dpm, and for pure biocomponent samples, results with 0.5 % dpm were determined.

## *Remaining work*

The accelerator mass spectrometry (AMS) method is recommended in ASTM standards for the determination of biogenic carbon content of fuels. We plan to measure the biocarbon content of some of these samples by AMS in cooperation with Mihály Molnár (Atomki, Debrecen) in order to compare the precision of $^{14}C$ detection from biomass originated samples by LSC and AMS.

## *Related publications*

[1] T.I. Korányi, B. Fridrich, A. Pineda and K. Barta: *Development of 'Lignin-First' Approaches for the Valorization of Lignocellulosic Biomass,* Molecules **25**, 2815 (2020)

[2] A. Deneyer, E. Peeters, T. Renders, S. Van den Bosch, N. Van Oeckel, T. Ennaert, T. Szarvas, T.I. Korányi, M. Dusselier and B.F. Sels: *Direct upstream integration of biogasoline production into current light straight run naphtha petrorefinery processes*, Nature Energy **3**, 969-977 (2018)

[3] J. Hancsók, T. Kasza and O. Visnyei: *Isomerization of n-C5/C6 bioparaffins to gasoline components with high octane number*, Energies **13**, 1672 (2020)

[4] J. Hancsók, O. Visnyei, A. Holló, L. Leveles, A. Thernesz, G. Varga and J. Valyon: *Alternative Diesel Fuels with High Hydrogen Content in their Molecular Structures,* Renewable Energy **142**, 239-248 (2019)

# HIGH ENERGY IONIZING RADIATION INDUCED DEGRADATION OF ATENOLOL AND PROPRANOLOL IN AQUEOUS SOLUTIONS

*Krisztina Kovács, Tünde Tóth, László Wojnárovits*

## *Objective*

Atenolol and propranolol are medicines used for blood-pressure control. Both appear in wastewater. The aim of the present work was to study the degradation reactions of atenolol and propranolol by high energy ionizing radiation [1], and determine the end-products.

## *Methods*

The samples in these end-product experiments were irradiated in a panoramic type $^{60}$Co-γ irradiation chamber (dose rate = 10 kGy $h^{-1}$) under various conditions. The initial concentration was 0.1 mmol $dm^{-3}$ for both atenolol and propranolol. The samples before and after irradiation were characterized using a JASCO 550 UV-Vis spectrophotometer with a 1 cm cell and applying appropriate dilutions before taking the spectra. The transient intermediates of degradation reactions were investigated by the pulse radiolysis technique using 4 MeV accelerated electrons with electron pulse length of 800 ns and utilizing kinetic spectrophotometric detection with a 1 cm path length cell. In order to identify and quantify the participating free radicals, radical scavenging experiments were used. The starting molecules and their end-products were characterized by chemical oxygen demand (COD), total organic carbon (TOC) content and toxicity (*Vibrio fischeri* was used as the test organism) measurements.

## *Results*

The pharma chromophore part of both molecules is the oxypropanolamine side chain. This side chain in atenolol is connected to a benzene, and in propranolol to a naphthalene unit (Figure 1). Degradation of atenolol and propranolol have been already studied in detail by Advanced Oxidation Processes [2]. In the present work, we investigated the reactions of these molecules in connection with their elimination from waste waters by applying high-energy ionizing radiation treatment. In pulse radiolysis we studied the intermediates of degradation, and in γ-radiolysis the final products. In these experiments the hydroxyl radicals (•OH) and the hydrated electrons ($e_{aq}^-$), produced in water radiolysis, induce the degradation of the target molecules. For both molecules, the •OH mainly reacted with the aromatic ring. Propranolol having a condensed ring showed higher reactivity compared to atenolol in both •OH and $e_{aq}^-$ reactions, and hence the oxidation and mineralization reactions also take place with higher rates in the case of propranolol. Neither atenolol nor propranolol did not show any toxic effect in the initial concentration. At low doses the toxic end-products, 1-naphthol and 2-naphthol, form in the degradation of propranolol. These toxic products disappear at higher doses. Removal of atenolol and propranolol, as well as abolishment of the toxicity can be achieved using appropriate doses.

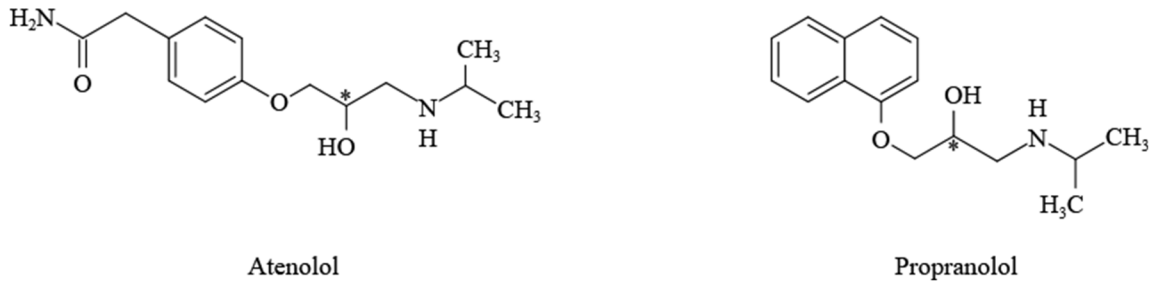


Atenolol Propranolol

*Figure 1: Structure of atenolol and propranolol (*: chiral carbon atom)*

## *Remaining work*

In order to get a comprehensive picture about the degradation processes of ß-blockers, we intend to investigate other ß-blockers predominantly by pulse radiolysis. Moreover, determination of the end-products will be an important task from the view of our research.

## *Related publications*

[1] K. Kovács, Á. Simon, T. Tóth, L. Wojnárovits: *Free radical chemistry of atenolol and propranolol investigated by gamma and pulse radiolysis*, Radiation Physics and Chemistry **196**, 110141 (2022)

[2] K. Kovács, T. Tóth, L. Wojnárovits: *Evaluation of Advanced Oxidation Processes for ß-blockers degradation: a review*, Water Science and Technology **85**:**(2)**, 685–705 (2022)

# MATRIX EFFECT ON THE HYDROXYL RADICAL INDUCED DEGRADATION OF β-LACTAM AND TETRACYCLINE TYPE ANTIBIOTICS

*László Wojnárovits, Jianlong Wang, Libing Chu, Tünde Tóth, Krisztina Kovács, Anikó Bezsenyi, László Szabó, Renáta Homlok, Erzsébet Takács*

## *Objective*

Due to the spread of antibiotic resistant bacteria, elimination of any remaining antibiotics from wastewater purified in the wastewater treatment plants is a highly important task. Purified wastewater contains a large variety of organic/inorganic compounds which strongly influence the efficiency of Advanced Oxidation Processes (AOP). In this work, we investigate the radiation-induced degradation of selected antibiotic contaminants (oxacillin and cloxacillin from the β-lactams; tetracycline and chlortetracycline from the tetracyclines) in four matrices: pure water, tap water, synthetic wastewater and purified wastewater received from a wastewater treatment plant. The selected matrices help us to understand the ongoing processes during practical application of the AOP method when purified wastewater is treated in advanced oxidation processes. The research was carried out in the frame of a National Office for Research and Development through the Hungarian-Chinese Industrial Research and Development Cooperation Project (No. 2017-2.3.6.-TÉT-CN-2018-00003).

## *Methods*

The experimental work was carried out using a $^{60}Co$ γ-radiation source (dose rate: 10 kGy/h). Most experiments were performed on $1 \times 10^{-4}$ mol $dm^{-3}$ (40-48 mg $dm^{-3}$) concentration aqueous solutions. The organic content of the solutions was characterized by the Chemical Oxygen Demand (COD), the Total Organic Carbon (TOC) content and the Biochemical Oxygen Demand (BOD) values. COD is the amount of $O_2$ (in $mg*dm^{-3}$) needed for complete oxidation of the organic molecules. The COD values were measured according to ISO Standard 6060:1989 in a Behrotest TRS 200 system using potassium dichromate for the oxidation. TOC is the carbon content of the solution in $mg*dm^{-3}$ unit. In these measurements a Shimadzu TOC-L CSH/CSN automatic analyser was used. In the BOD measurements, microbes from a wastewater treatment plant oxidize the carbon content. For this purpose, a tiny amount of activated sludge (mixed microbial population) was added to the test solution. The BOD experiments were performed by using an OxiTop® Control BOD Respirometer System according to DIN EN 1899-1 (1998). BOD is used in measuring the biodegradable waste loadings of the wastewater. The acute toxicity of the irradiated solution to *Vibrio fischeri* bioluminescent bacteria was determined by Microtox® tests according to DIN EN ISO 11348-2 (1999). The toxicity is evaluated based on the inhibition of bioluminescence. *Staphylococcus aureus* strains (S. aureus, B.01755) were used in the agar diffusion microbiological tests (Collection code in the American Type Culture Collection: ATCC1 6538PTM) to check for anti-bacterial activity of the irradiated solution. *Vibrio fischeri* and *Staphyloccous* are often used as a general method to measure toxicity. Degradation products of the irradiated structures may cause increased toxicity.

## *Results*

None of the four antibiotics were biodegradable in any of the four matrices, but after irradiation with relatively low doses the resulting products obtained were biodegradable. Oxacillin and cloxacillin were not toxic before irradiation in the *Vibrio fischeri* test, but the irradiation produced products did show considerable toxicity (Fig. 1). On the other hand, tetracycline and chlortetracycline showed toxicity before irradiation and it was strongly reduced by the irradiation treatment (Fig. 1).

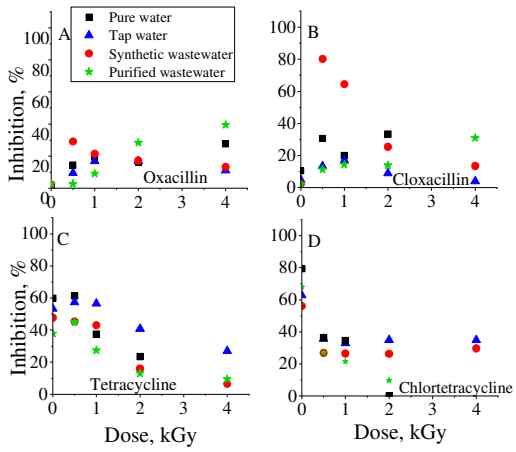


*Figure 1: Vibrio fischeri toxicity test measured in 0.1 mmol $dm^{-3}$ oxacillin, cloxacillin, tetracycline and chlortetracycline solutions in pure water, tap water, synthetic wastewater and purified wastewater matrices. Before the tests, catalase enzyme was added to the solutions in order to remove the toxic hydrogen peroxide formed during water irradiation.*

Both COD and TOC decreased after irradiation; but the decrease in COD was much larger than that in TOC. In purified wastewater matrices the decrease in COD was lower than in other matrices due to the presence of organic impurities in this matrix. We have no evidence here, but in our previous works we proved it and there are also literature data proving it. The antibacterial activity in most of the matrices was greatly reduced or completely disappeared at around 2-4 kGy. However, in purified wastewater matrices some antibiotic activity remained even at 4 kGy. Here the degradation of the antibiotic is slow (small ΔCOD/dose value), presumably because a large fraction of the reactive radicals is scavenged by the small, highly oxidized molecules in the solution. Although the water radiolysis product $H_2O_2$ affected some of the bioassays, this phenomenon was absent in the microbiological test indicating that *Staphylococcus aureus* is not sensitive to $H_2O_2$. The purified wastewater after ionizing radiation treatment can be safely released into the receiving lakes or rivers.

## *Remaining work*

Our further plan is to compare the degradability of various types of antibiotics.

## *Related publications*


[1] L. Wojnárovits and E. Takács: *Rate constants of dichloride radical anion reactions with molecules of environmental interest in aqueous solution, a review*, Environmental Science and Pollution Research **28**, 41552 (2021)

[2] L. Chu, J. Wang, S. He, C. Chen, L. Wojnárovits and E. Takács: *Treatment of pharmaceutical wastewater by ionizing radiation: Removal of antibiotics, antimicrobial resistance genes and antimicrobial activity*, Journal of Hazardeous Materials **415**, 125724 (2021)

[3] A. Bezsenyi, Gy. Sági, M. Makó, L. Wojnárovits and E. Takács: *The effect of hydrogen peroxide on the biochemical oxygen demand (BOD) values measured during ionizing radiation treatment of wastewater*, Radiation Physics and Chemistry **189,** 109773 (2021)

[4] A. Bezsenyi, I. Gyarmati, J. Oláh, E. Takács and M. Makó: *A Dél-pesti Szennyvíztisztító Telepen üzemelő nitrogéneltávolító bioszűrő-fokozat szerepe, teljesítménye és üzemeltetésének tapasztalatai,* Vízmű Panoráma **3,** 8 (2021)

[5] A. Bezsenyi, M. Makó and E. Takács: *Mit tehetünk, ha nincs pénzünk negyedik tisztítási fokozat kialakítására?* Hírcsatorna **4,** 5 (2021)

[6] A. Bezsenyi, I. Gyarmati, M. Makó and E. Takács: *Gyógyszermaradványok a szennyvízben – Csak a holnap kihívása?* Vízmű Panoráma **6,** 4 (2021)

[7] L. Chu, J. Wang, C. Chen, S. He, L. Wojnárovits and E. Takács: *Advanced treatment of antibiotic wastewater by ionizing radiation combined with peroxymonosulfate/H2O2 oxidation*, Journal of Cleaner Production **321,** 128921 (2021)

[8] L. Chu, J. Wang, C. Chen, Y. Shen, S. He, L. Wojnárovits, E. Takács and Y. Zhang: *Abatement of antibiotics and antimicrobial resistance genes from cephalosporin fermentation residues by ionizing radiation: From lab-scale study to full-scale application,* Journal of Cleaner Production **325**, 129334 (2021)

# MODELLING THE SOURCE COMPOSITION OF HUNGARIAN HEAT AND ELECTRICITY GENERATION WITH ROBUST OPTIMIZATION

*Endre Börcsök, Oláhné Groma Veronika*

## *Objective*

The research was motivated by the open questions of the forecasts about the Hugarian heating and electricity sectors. A methodology for portfolio optimization has been developed in order to identify the optimal energy mix in terms of technology alternatives and energy sources focusing on both the heating and electricity sectors. In our work we executed multiobjective optimization considering the investment costs, the operation and maintenance (O&M) costs, as well as carbon prices and the external costs of the environmental and human health (physiological) impacts. As the costs show a large variation, as well as the site-specific physical conditions, an extensive sensibility analysis is needed to obtain information about the stability of the results. Most models simply handle this problem using average values, from which oversimplified results are calculated that have no information about the uncertainty of the results. To overcome this weakness, we have done global sensitivity analysis with robust optimization.

## *Methods*

In our research, we developed a multiobjective optimization to establish the optimum energy and technology mix for the heating and electricity sectors in Hungary. Starting from a pure techno-economic assessment, the optimization was extended to the external costs of environmental impacts and human health, as well. Assumptions on realistic investment and O&M costs were based on the evaluation of benchmark projects. The modelling covered both heat (residential sector) and electricity supply (all sectors), as well as cogeneration among the heat and electricity supply alternatives. To reduce complexity, a typological approach was applied for location and building types. From the aspect of location, two categories were introduced: Budapest on the one hand and other regions on the other. The used three building typological groups consisted of large-scale, medium-scale multi-flat buildings and single family houses. For modelling the variations in the heat and electricity demand, typical seasonal, monthly and hourly load patterns were computed. The variability in solar and wind energy intake was considered by hourly generation patterns. Also, several technology choices have been implemented in the model including district heating and Combined Heat and Power (CHP) for heat and electricity supply generation. Among the supply alternatives, both low-carbon technologies and nuclear energy were considered. As shown by previous studies and by international literature, the costs exhibit a large variation, heavily influenced by the site-specific physical conditions and the closely interrelated number of full load hours. To deal with this problem a robust optimization was used on the randomly chosen starting parameters from the interval. The optimum was implemented as a linear programing problem in General Algebraic Modelling System (GAMS) environment. Stable formations were allocated using cluster analysis on the set of vectors determined by 1000 calculations.

## *Results*

Three central formations were found in the resulting vector set composed of scenarios, which showed great similarity from the aspect of energy sources, thus the difference appeared only in the proportions (Figure 1). It has to be noted, that the use of many energy sources was limited by the maximal available energy potential, especially in case of renewable sources. The resulting three central scenarios can be connected to different carbon prices. The portfolio related to low carbon price (20 €) is dominated by natural gas, while in case of higher carbon prices (47 and 55 €) natural gas is replaced by heating pump in the heating sector and nuclear energy in the electricity sector. Based on the current prices, biomass which has great potential wasn't found to be competitive even in the case when health effect is ignored.

## *Related publications*

[1] E. Börcsök, Z. Ferencz, V. Groma, Á. Gerse, J. Fülöp, S. Bozóki, J. Osán, S. Török and Á. Horváth: *Energy Supply Preferences as Multicriteria Decision Problems: Developing a System of Criteria from Survey Data,* Energies **13:(15)**, Paper: 3767, 21 p. (2020)

[2] E. Börcsök, Á. Gerse and J Fülöp: *Optimizing the use of renewable energy sources in the energy mix of Hungary,* 17th IEEE World Symposium on Applied Machine Intelligence and Informatics, SAMI 2019, Herlany, Slovakia

[3] E. Börcsök and Á. Gerse: *Sustainable nuclear-renewable hybrid systems: a case study for Hungary*, International Conference on Climate Change and the Role of Nuclear Power, IAEA 2019, Wien, Austria

[4] Á. Gerse and E. Börcsök: *Towards a Low-carbon Electricity Supply in Central Eastern Europe: Modelling the Role of Nuclear Power Plants*, International Conference on Climate Change and the Role of Nuclear Power, IAEA 2019, Wien, Austria

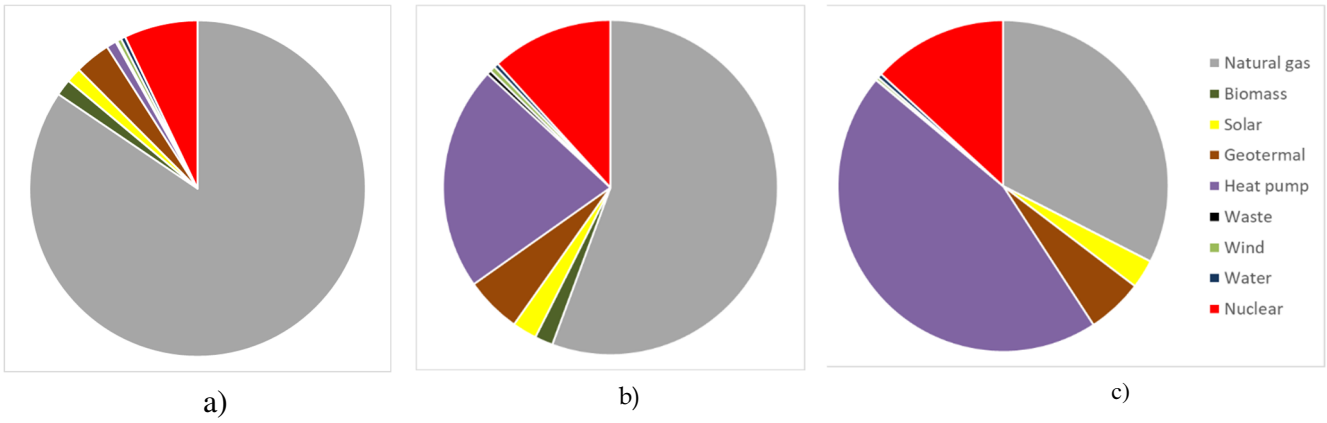


*Figure 1: Three central formations of the energy scenarios for a) low; b) medium and c) high carbon price based on energy sources.*

# SIMULATION OF INTELLIGENT ELECTRICITY SYSTEMS

*Attila Kazsoki, Bálint Hartmann*

## *Objective*

A simulation framework is constructed, in which the effects of the growing photovoltaic (PV) penetration on the rapid voltage change can be examined.

## *Methods*

In the framework, stochastic simulation is run on three Hungarian medium voltage reference network models. The load flow analysis is run in DigSILENT Power Factory. In addition to the network model, a 1-minute resolution of the production data is required as input to the simulation. The production data comes from the multiplication of the solar irradiation and the nominal output power of the PV power plants (in this case 500 kW(kVA) units). The solar irradiation data is the output result of the cloud movement simulation, calculated from the clear-sky model, the cloud shadow model (using cumulus clouds) and the cloud movement parameters (direction, velocity).

Network models, created by the authors' earlier research served as the basis for the clustering of medium voltage distribution networks. From the six Hungarian medium voltage Representative Network Models (RNM) three were selected, in which large-scale small power plants can be placed. The planned photovoltaic penetration in the Hungarian distribution network can be determined from the National Energy Strategy until 2030 and from a document published by the Ministry for Innovation and Technology at the beginning of 2020: for 2030 the expected capacity will be 6400 MW. Three scenarios were determined for the years 2019, 2025, and 2030, representing current and short-term future penetration levels. The number of PV units in those years are the following: 2019: ×1; 2025: ×5; 2030: ×8.

The network nodes are divided into three groups, based on their betweenness centrality values (minimum, average, maximum). In each simulation, the PV plants are placed in the same betweenness region. The topography of RNM5 can be seen in Fig. 1. PV penetrations for 2019, 2025, and 2030 are represented by connecting PV plants, respectively. Green, orange, and red colours represent connection according to minimum, average, and maximum betweenness centrality values, respectively.

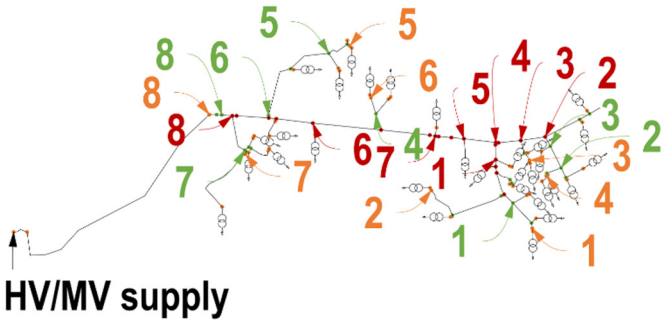


*Figure 1: Topography of RNM5*

Simulation scenarios: decentralized PV plant distribution (3 betweenness group × 3 PV penetration level), centralized (worst case: betweenness: minimum, PV penetration level: 2025). From these 10 simulation scenarios the maximum rapid voltage change values have been examined.

## *Results*

In the cases of decentralized PV generation, the maximum values of the rapid voltage changes are depending on the size of the feeder and the placement of the connection point. In the case of network RNM1 (primarily rural and sub-urban regions) the maximum value of rapid voltage change is under 1.5%, which does not exceed the limit defined in the EN 50160:2011 standard (2%). In the case of RNM5 (mainly rural area), the maximum value of rapid voltage change exceeds the 2% limit in 2025 and 2030 as well. In the case of RNM6 (loosely built-in suburban area) the maximum value of rapid voltage change is under 2%. In the case of centralized generation, the highest value of rapid voltage change proved to be 3.66% for RNM1, 4.68% for RNM5, and 3.37% for RNM6. Based on these findings, it can be stated that in the case of decentralized power generation, there is a connection point allocation that does not cause a limit value deviation in the rapid voltage change. In the case of centralized energy production, the voltage quality indicators specified in the standard cannot be maintained in the future. The distribution system operator does not investigate the rapid voltage change during the connection point license allocation. By performing such analyses, the time horizon of network development can be extended, its extent can be reduced in the case of a given PV penetration.

## *Related publication*

[1] B. Turóczi, A. Kazsoki, V.O. Groma, and B. Hartmann: *Effect of Cloud Movements on the rapid Voltage Changes of PV Rich Distribution Networks,* IEEE Transactions on Sustainable Energy (under preparation)

# QUALITATIVE ANALYSIS OF ELECTRICITY BALANCING SERVICES

*Bálint Sinkovics, Bálint Hartmann*

## *Objective*

The proposed research aims are to analyze and evaluate the temporal change of electricity balancing that needs in the Hungarian energy system.

## *Methods*

Due to the new directives derived from the Clean Energy Package the regulation framework of ancillary services is in transition. The expansion and standardization of these submarkets require uniform product definitions. Besides, the proliferation of intermittent energy producers implies the revision of previous electricity balancing capacity allocation methods. The new directives propose the elaboration of a unique capacity estimation method in regard to the national specialities of the energy system. In light of the reviewed issue the research set goals as follows:

- Review and summarize the main shifts in balancing capacity planning, legal changes and additional regulations,
- Evaluate the existing capacity allocation method and propose a new one in accordance with the new requirements,
- Validate and evaluate model performance in comparison with the recent method of the Hungarian Transmission System Operator (TSO).

The proposed balancing capacity estimation method follows a bottom-up approach to quantify each component and the possible negative synergies of various plant types. For this reason, the definition of system unbalance can be decomposed as follows:

$$\text{Unbalance} = \text{FRR} + \text{ACE}$$

where ACE is the area control error and FRR the activated balancing capacity.

ACE is a definite value that describes the temporal error of the balancing process measured by the Hungarian TSO. However, the activated balancing capacity is influenced by multiple reasons: (i) prediction error of photovoltaic (PV) systems and wind turbines, (ii) unplanned outage of conventional power plants.

Results

The annual dynamics of scheduled operation error of renewables and the unplanned power plant outages were investigated in the period of January 2019 - July 2021. The components are the following: (i) PV, (ii) wind, (iii) ACE. The required dataset was provided by the Hungarian TSO.

The study revealed that the scheduled power output of PV systems was overestimated in 2020. However, similar tendencies were not addressed in 2021. Moreover, there is a strong correlation between scheduling error and sunrise/sunset. Wind and ACE error does not have notable daily error patterns. The given results enabled to quantify the mutual error distribution of the mentioned three factors. As it was mentioned, all TSOs of Continental European areas shall determine the required reserve capacity. The estimation of FRR need is required to consider the consecutive historical records comprising at least the historical imbalance values. In accordance with the EU legislation a probabilistic estimation was applied to quantify the frequency restoration reserve FRR need of the system. This process considered that FRR is sufficient to cover the positive Load-Frequency Control (LFC) block imbalances for at least 99% of the time.

The proposed estimation model considers these needs and enables to quantify the annual (long term) tendencies of unbalanced needs of the system.

To achieve this goal, it was presumed that not only the distribution but also the dynamics of the unbalance is essential to consider. Therefore, the previous investigation of the various components was expanded that revealed the temporal tendencies and notable shifts in system unbalance. It is clearly seen that the PV penetration significantly increases the occurrence of sudden ramps. Finally, the FRR estimation method was supplemented with the ramping factor and long-term estimations were conducted in terms of PV penetration increase.

## *Remaining work*

The proposed research has been finished, further publication of the results are in progress.

## *Related publication*

[1] B. Sinkovics, B. Hartmann: *Flexibilis tartaléktervezési módszertan bemutatása az időjárásfüggő termelők figyelembevételével*, X. Mechwart András Ifjúsági Találkozó (2021)

# MULTI-VOLTAGE NETWORK MODEL DEVELOPMENT FOR EXAMINING THE STABILITY OF THE ELECTRICITY NETWORK WITH INCREASING PENETRATION OF PHOTOVOLTAICS

*Attila Kazsoki, Bálint Sinkovics, Bálint Hartmann*

## *Objective*

The research aims to develop a multi-voltage synthetic AC power system model that is suitable for the examination of desynchronization events (e.g. local service interruptions) caused by unexpected changes (e.g. sudden changes in the energy supply to the grid by renewable sources due to the weather).

## *Methods*

In this research a framework is developed in MATLAB environment, to generate a multi-voltage electricity system, in which the high voltage transmission network and a medium voltage distribution network are also appearing. The transmission network was mapped based on the topology of the Hungarian high voltage electricity system. In case of distribution network models the six sample networks developed in the previous research were used. In the graph representing the network, the distribution network connection points are the 2-degree nodes denoting the HV/MV substations. Among the substations, two types are distinct, underground and overhead ones, which are distributed randomly. Only the distribution network models with their characteristics are connected to each substation type. From the distribution network models, 4 overhead and 2 underground networks can be distinguished. The number of the sample networks varies between 25 and 40 randomly, thus ensuring the heterogeneity of the network. Each substation type is connected to its medium-voltage sample networks. In case of the underground substation, only cable Representative Network Models (RNMs) are connected to the node (RNM3 and RNM4). The proportion of the supply area number distributed among the RNMs is given by the probability of the networks (pRNM), which is formed by the size of the clusters. Its value on the RNMs is: pRNM1 = 0, pRNM2 = 0, pRNM3 = 0.1478, pRNM4 = 0.8522, pRNM5 = 0, pRNM6 = 0. In each substation of this type, the individual sample networks are distributed in the same proportion. In the case of the overhead substations, only overhead line RNMs are connected to the node (RNM1, RNM2, RNM5, and RNM6). Here the proportions of the RNMs are 0.3134, 0.0286, 0.2861, 0.4005, respectively. Network invariants (e.g. degree distribution) were performed using Gephi 0.9.2 and MATLAB software.

As the sample networks representing each voltage level can be replaced by the mathematical models used in the literature, they can be given by comparing the degree and betweenness distributions of the graphs representing the networks. For this comparison, the Kullback-Leibler divergence and Wasserstein metrics can be used. The two methods allow the comparison of continuous distributions. In this case, the examined distributions are approximated with normal distribution. Findings heve been taken into account during the description of the Hungarian electricity system with a synthetic topology: Hartmann et. al found that the domestic transmission network has small-world properties. In the present research, the application of other synthetic topologies at this voltage level has not been investigated. In the case of distribution networks, the applicability of the most commonly used mathematical models for the approximation of the electricity system was examined. These are the random graph, small world model, scale-free graph.

## *Results*

The number of nodes in the synthetic network is 443417, the number of edges is 443531, the average degree is 2.0005. The ratio of nodes to edges is close to 1, which is due to the topological feature of the large-scale distribution network (domestic medium-voltage distribution network is radial). On the generated network, the value of the synchronization (solution of the Kuramoto equations) is 0.002, which is much smaller than in Ódor and Hartmann's previous research (R=0.15). The reason for the difference is the structural difference in the synthetic networks.

Approximating the distribution network models with a synthetic topology, the normal distribution is not the most optimal choice for the approximation of the degree and betweenness distribution. In the degree distributions, it can be observed that the standard deviations of the distribution functions are in the same order of magnitude, so they can well be used in the comparison. Based on the comparison of the expected values, it can be stated that the Hungarian medium voltage network cannot be described with the mathematical models used so far. This is also confirmed by the Wasserstein metric values. The value of the Kullback-Leiber divergence between the distribution functions is infinite for small world and random graphs, regardless of the parameter setting. The value of the Kullback-Leiber divergence between the distribution functions is infinite for small world and random graph models, regardless of their input parameter setting.

## *Related publications*

[1] A. Kazsoki and B. Hartmann: *Distribution network approximation with synthetic network models* (under preparation)

[2] B. Hartmann and V. Sugár: *Searching for small-world and scale-free behavior in long term historical data of real-world power grid,* Scientific Reports **11,** 6575 (2021)

# SOLAR POTENTIAL ESTIMATION OF A DENSELY BUILT URBAN FABRIC

*Viktória Sugár, Bálint Hartmann*

## *Objective*

The aim of the current study was to be able to estimate the solar irradiation, the amount of the solar energy generation and its ratio compared to the energy utilization of the houses in the Budapest downtown urban fabric, considering the limitations due to the heritage protection rules.

## *Methods*

First, the downtown districts of Budapest were surveyed to find the characteristics of the building stock.

In the second step, a characteristic part of the urban fabric was chosen and modelled in Revit software (see the example picture in Figure 1). The modelling had to investigate the solar energy potential of an existing stock with its irregularities, and was aimed to find a connection between construction geometry and solar potential. Next and third, the irradiation data were acquired via software simulation.

The simulation results were used as input data for calculations. The average annual irradiation (kWh/m²a), the cumulative annual irradiation (kWh/a), the roof surfaces (m²), their orientation, the footprint of the building (m²) were acquired from the model. The net heated area of the building (m²) was calculated using the geometry input of the database.

To assess the ratio of energy produced by solar panels compared to the buildings' energy consumption, the Hungarian building energetics calculation system was used. Two scenarios of the building energy consumption were investigated.

The simple payback time of the Photovoltaic (PV) system application was calculated by using the household savings on electricity utility costs with solar panels installed compared to the construction and application cost of the system, resulting in the payback time in years. The $CO_2$ mitigation potential (kg/year) was calculated using the data of the Budapest power supplier.

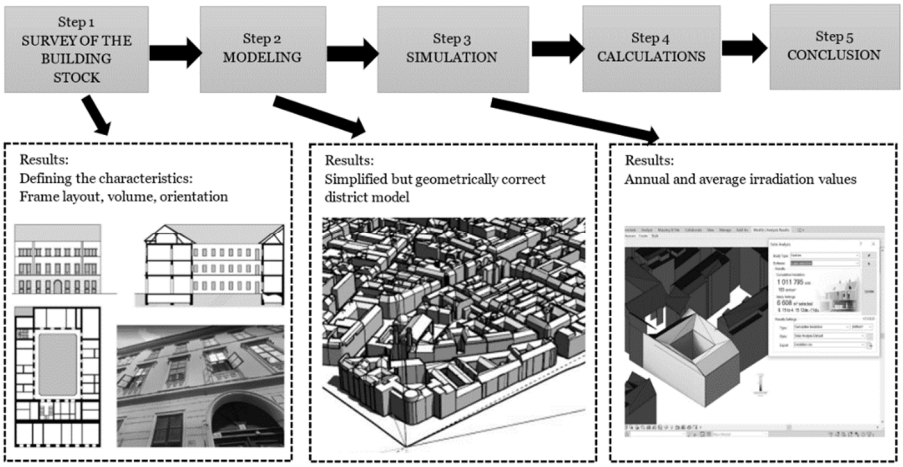


*Figure 1: Methodology of the Research*

## *Results*

Based on the results, it can be concluded, that using solar panels, 57.7 MWh electricity can be generated annually by an average building. This ratio covers 8.3% of the building's energy consumption. If the hypothetical retrofitted energy state is considered, 25.6% of the energy intake can be covered by the solar panels. In total, 37% of the investigated buildings above the renewable ratio criteria reach the 25% threshold in retrofitted state and another 32% of the buildings reach at least 20% of the renewable ratio. The average simple payback time for the solar panel system compared to the original system is 13.4 years. On average 18.9 t/year $CO_2$ mitigation could be reached by using panels in each building.

An annual solar irradiation and solar power generation estimation method for the traditional apartment building type is introduced, too, where the footprint of the building (easily acquirable from open-access satellite images) can be used to approximate the values [1].

## *Remaining work*

We continue the research, in which the above results will be compared to solar irradiation data based on Geographic Information System (GIS) software.

## *Related publication*

[1] V. Sugar: *Solar Potential Estimation of a Densely Built Urban Fabric*, OP Conference Series: Materials Science and Engineering (MSE) (under review)

# NANOCOMPOSITE ADSORBENTS FOR THE REMOVAL OF INDUSTRIAL AND NATURAL CONTAMINANTS

*László Almásy, Zsolt Endre Horváth, Zsolt Czigány, Zoltán Dudás*

## *Objective*

Due to the rapid development of the economy and industrial sectors, the water contamination by organic pollutants and heavy metal ions (toxic, non-toxic and radioactive) has become an important environmental problem. The aim of the present project is to obtain, characterize and test various types of composite nanostructured silica sorbents for contaminant removal.

## *Methods*

**Synthesis and characterization:** Mesoporous silica materials have been prepared using two approaches. In the first, the two-step sol-gel method was used to obtain silica xerogels, utilizing tetraethoxysilane (TEOS) or a mixture of vinyltriethoxysilane (VTES)/phenyltriethoxysilane (PhTES) with TEOS as precursors. Acid-base catalysts were used and the silica materials were obtained after drying and/or thermal treatment processes. Four series of samples have been made using NaF and $NH_4F$ as catalysts. In this way, non-ordered mesoporous silica materials have been produced with large surface areas and different chemical characteristics for the pore surfaces. The second approach consisted of utilizing cationic surfactants as pore forming agents, and in this way, ordered mesoporous silica of the MCM-41 type has been obtained in basic catalysis conditions. The pore structure and the surface chemistry of the materials was varied using various amounts of functionalized silica precursors in addition to the TEOS. The structural characterization of the materials produced has been carried out using traditional and well known methods of nitrogen sorption porosimetry, Small Angle Neutron Scattering (SANS), X-Ray Diffraction (XRD), Fourier-Transform Infrared Spectroscopy (FT-IR) and Scanning Electron Microscopy (SEM). Infrared spectroscopy has been utilized for characterization of the surfactant template removal from the ordered mesoporous silica materials.

**Adsorption experiments:** Batch sorption experiments at different pH and temperature values were conducted in order to test the affinity of the silica sorbents for variousmetal ions and dye pollutants.

## *Results*

1. **Mesoporous hybrid silica**

A graduated functionalization of the silica was observed with vinyl and phenyl groups. Three different samples have been chosen from each series in order to test the impact of the nature and amount of functionalizer on the pore sizes and types and the hydrophobic/hydrophilic profile on the sorption properties for the removal of coloured dye pollutants. With the gradual increase of the quantity of the vinyl/phenyl substituents, the pore size is decreasing. The surface areas are larger for the functionalized silica samples (400-850 $m^2/g$) than for bare silica (150-350 $m^2/g$). The morphology of the silica did not change much with the degree of functionalization (Figure 1). Similar layered-plate like silica particles were obtained. (Because of the pandemic situation, the sorption experiments were delayed but they are in progress now.)

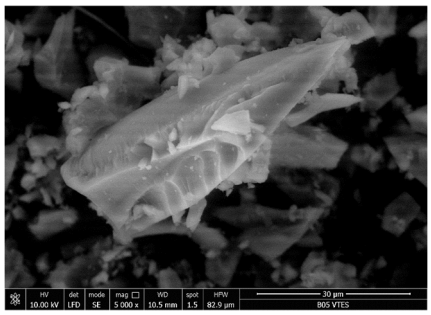

5% VTES/TEOS –$NH_4F$

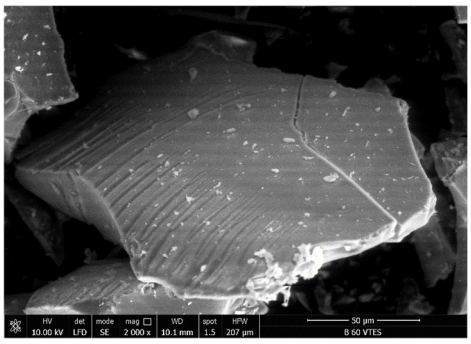

60% VTES/TEOS–$NH_4F$

*Figure 1: SEM images of hybrid silica particles obtained by 5% and 60% vinyl functionalization.*

**2. Ordered mesoporous silica sorbents**

Three series of ordered mesoporous silica materials have been prepared by the co-condensation method using the following precursors: mixtures of TEOS and 3-aminopropyl-triethoxysilane (APTES), TEOS and 3-aminopropyl-trimethoxysilane (APTMS), TEOS and 3-mercaptopropyl-trimethoxysilane (MPTMS). The volume ratios of functionalized precursors and TEOS ranged from zero to 0.25, 0.25 and 0.12, respectively. The apparent surfaces of the TEOS/APTES materials, as determined by nitrogen adsorption, ranged from 1170 to 650 $m^2/g$, monotonically decreasing with increasing amount of APTES, showing that all tested experimental conditions led to large effective surface materials, potentially suitable for contaminant sorption. The porosity in the other two series was similar, showing effective surfaces of 300 and 490 $m^2/g$ for the materials prepared with the largest amount of MPTMS and APTMS, respectively.

From the structural point of view, the prepared materials consist of submicron sized nearly spherical particles, as determined by SEM. The inner nanostructure of the particles was studied by SANS and XRD. The XRD patterns of two series of samples, prepared using APTMS and MPTMS functionalized precursors, are shown in Figure 2. The data show a typical hexagonal pore structure, characteristic for MCM-41 materials, for the samples containing a lesser amount of the functionalized precursor. The larger APTMS or MPTMS content leads to gradual destruction of the ordered porosity. At 15% and 20% of APTMS content, only the first diffraction peak remains visible, with substantial broadening, indicating that there is no long range periodicity in these materials, but only a certain degree of local order of the pores remains. Thus, variation of the synthesis conditions, by adding organic silica precursors in the studied concentration range results in the decrease of the pore ordering and of the specific surface. These effects cause a decrease of the sorption capacity of the materials, because of the diminishing of the contact interface. At the same time the parallel, hexagonally ordered pores presumably rearrange into a less ordered structure, in which the fraction of closed pores increases, reducing the effective mass transport of the larger organic pollutant molecules. On the other hand, the increase in the amount of functional groups on the pore surfaces increases the efficiency of the adsorption. The efficiency and the practical utility of the silica based sorbents will depend on the interplay of these two effects. Consequently, by further extending these investigations and optimizing the preparation conditions, the expected high performance can be reached.

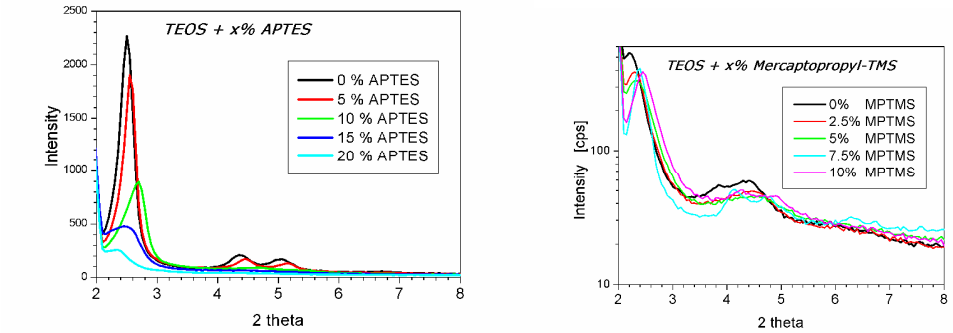


*Figure 2: XRD patterns of ordered mesoporous silica prepared by co-condensation of TEOS with APTES (a) and MPTMS (b)*

The investigations described above are based on the results of our recent studies on the different effects of functionalization of mesoporous silica materials prepared by co-condensation or post-grafting methods [1], and the influence of addition of magnetic nanoparticles on the structural and sorptive characteristics of silica nanocomposites [2]. Methyl-substituted ordered silica prepared in acidic conditions using different surfactants as pore forming agents have also been investigated as potential candidates for hydrogen storage [3]. Disordered silica xerogels with various degrees of methyl substitution have been studied for drug release applications [4]. Both methyl substituted silicas are good adsorbent candidate for heavy metals.

## *Remaining work*

Continuation of the work will consist of the preparation of further types of functionalized silica-based sorbents, and performing sorption experiments on the already synthesized materials with various organic and inorganic contaminants. Based on the comparative analysis of the synthesis methods and conditions, structural characteristics of the materials, and their adsorptive performance, optimized synthesis methods and structure-property relations will be identified which will lead to the development of sorbent materials characterized by the ease of preparation and high sorption capacities.

## *Related publications*

[1] A.-M. Putz, M. Ciopec, A. Negrea, O. Grad, C. Ianăşi, O. I. Ivankov, M. Milanović, I. Stijepović and L. Almásy: *Comparison of structure and adsorption properties of mesoporous silica functionalized with aminopropyl groups by the co-condensation and the post grafting methods,* Materials **14,** 628 (2021)

[2] C. Ianăşi, E.-M. Picioruş, R. Nicola, A.-M. Putz, A. Negrea, M. Ciopec, A. Len and L. Almásy: *Synthesis and characterization of magnetic iron oxide – silica nanocomposites used for adsorptive recovery of palladium (II),* Soft Materials *in press* (2022)

[3] A. Policicchio, A.-M. Putz, G. Conte, S. Stelitano, C. P. Bonaventura, C. Ianăşi, L. Almásy, A. Wacha, Z. E. Horváth and R. G. Agostino, *Hydrogen storage performance of methyl-substituted mesoporous silica with tailored textural characteristics,* Journal of Porous Materials **28**, 1049 (2021)

[4] A. Len, G. Paladini, L. Románszki, A.-M. Putz, L. Almásy, K. László, Sz. Bálint, A. Krajnc, M. Kriechbaum, A. Kuncser, J. Kalmár and Z. Dudás, *Physicochemical characterization and drug release properties of methyl-substituted silica xerogels made by sol-gel process,* International Journal of Molecular Sciences **22**, 9197 (2021)

# EFFECT OF CLOUD MOVEMENT ON THE POWER QUALITY OF DISTRIBUTION NETWORKS

*Bálint Hartmann, Attila Kazsoki, Veronika Oláhné Groma,*
*Bálint Sinkovics, Csaba Dücső, Erika Tunyogi*

## *Objective*

Variable power output of renewable energy sources makes keeping power quality of the network harder for distribution system operators, which may lead to violations of voltage limitations set in EN 50160 and regulations on Guaranteed Service. Such effects are typically examined through power simulations but fail to reckon with the dynamics of weather changes. Previously a simulation framework was developed by the researchers of the Centre for Energy Research, which could consider the effects of varying solar irradiation patterns on the models of distribution networks by using cloud shadow models. Objective of the present work was to extend the capabilities of this framework, to diversify the solar photovoltaic models and to validate the cloud shadow models through solar imaging.

## *Methods*

The central component of the simulation framework (Figure 1) is a stochastic simulation, which can map the possible event horizons based on both static inputs and data changing in every running cycle. The model on which the simulation is run was built up from electric and GIS (Geographical Information System) parameters in DIgSILENT PowerFactory environment. The emerging topography is mapped onto a coordinate system, while special attention is paid to network nodes and the connection points of photovoltaic (PV) panels. Solar irradiation data enter the simulation framework as the output of a cloud movement simulation. The framework chooses the load profile of Medium-Voltage/Low-Voltage (MV/LV) transformers from a database of real measurement data from real areas in 1-minute resolution. Load profiles are updated by the stochastic simulation at each run, including the load of the MV/LV transformer, the power factor, and time series data.

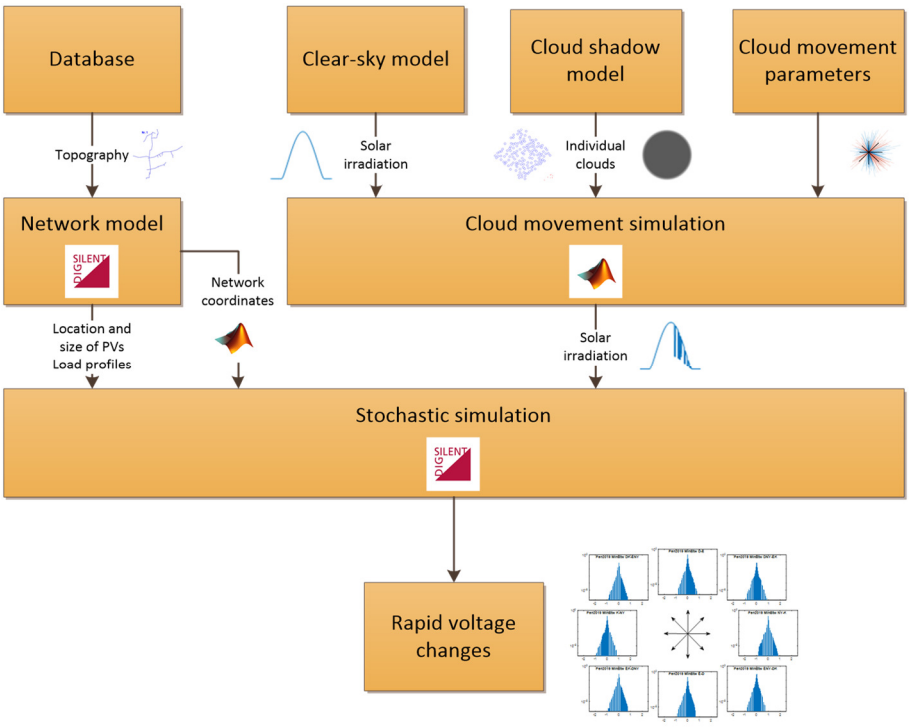


*Figure 1: Framework of the simulation*

The research team has purchased a Starlight Xpress Oculus sky imager camera (*Figure 2.a*), which is capable of recording colour pictures with 180° viewing angle. The camera is operated through a software of own development, based on the C# SxDotNet library of the camera. The software matches the special needs of the application, since successful determination of cloud parameters (such as cloud cover, cloud type, light transmission, direction and speed of cloud movements) necessitates the flexible handling of exposure time and frequency, according to the literature. The software is capable of capturing sky images with a pre-set frequency (e.g. one-minute), saving the results into a host machine. Furthermore, the ability to take series of images was also developed. Raw picture data (which are recorded for each colour channel) are combined with colour images before saving.

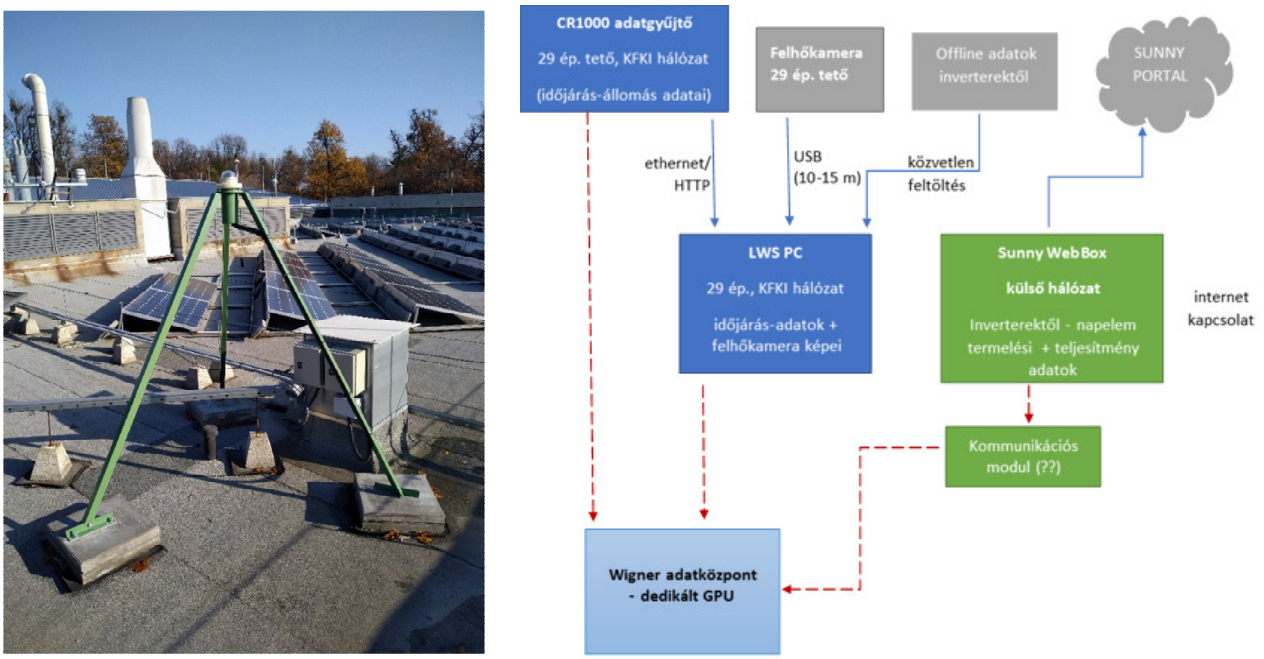


*Figure 2.a) The sky imager; 2.b) Architecture of the measurement and computation systems*

## *Results*

In 2021, the necessary maintenance and development works on the weather station were finished, including the repair of the humidity sensor, the deployment of the sky imager and the reconfiguration of the data collector. Power measurements of the solar photovoltaic units were also channelled into the data collector (Figure 2.b), thus effect of clouds on panels with different materials can be compared. Software of the sky imager was developed, operation has started (see Figure 3.).

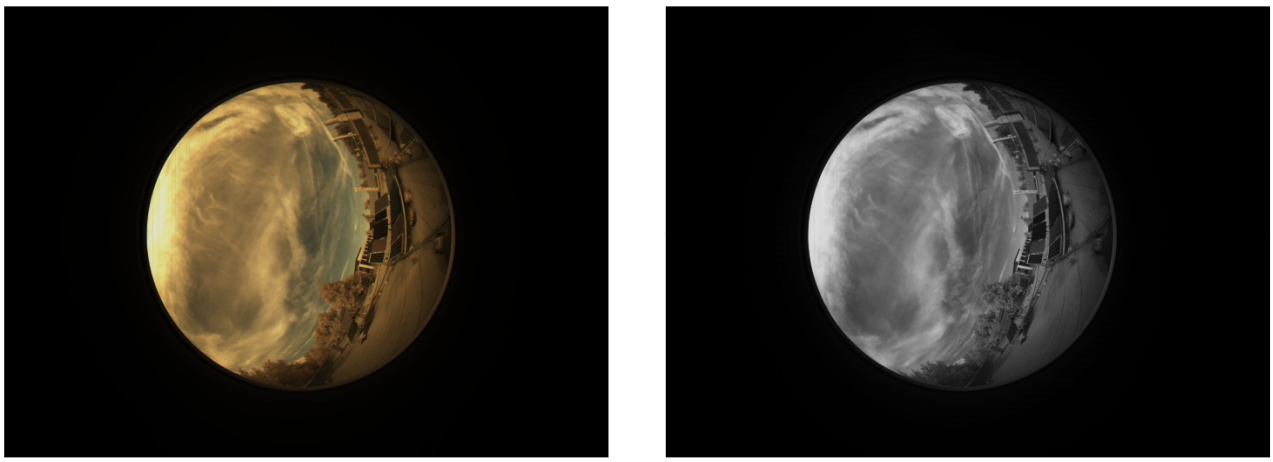

*Figure 3: Colour and monochrome images captured by the sky imager*
*(the use of different colour maps supports cloud movement analysis)*

## *Remaining work*

Remaining work focuses on the analysis of recorded data, including solar irradiation patterns, sky images, power output of the photovoltaic panels and the correlations between these various data.

## *Related publication*

[1] B. Turóczi, A. Kazsoki, V. O. Groma, B. Hartmann: *Effects of Cloud Movements on the Rapid Voltage Changes of PV Rich Distribution Networks*, IEEE Transactions on Sustainable Energy (under review)

# INCREASING THE STABILITY OF POWER SYSTEMS WITH HIGH RENEWABLE ENERGY SHARE BY THE USE OF COUPLED OSCILLATORS

*Bálint Hartmann, Géza Ódor, Shengfeng Deng, Lilla Barancsuk*

## *Objective*

Power-grids are among the largest man-made complex systems, staying in the synchronization state of billions of nodes. Formerly power-law tailed cascade size distributions have been found by outage statistics and DC (direct current) models. The spread of renewable resources poses unprecedented pressure on system stability. Our aim is to show how this can be modelled by Kuramoto-like synchronization models, which describe the real power flow in AC (alternating current) systems.

## *Methods*

The combination of swing equations with line threshold failures allows us to describe the dynamical avalanche-like blackout failures in different high voltage (HV) power-grid networks. In particular, we compare the stability and blackout statistics for the US- and the EU-HV networks, taking into account the feedback effects. We show that non-universal power-law size and duration distributions emerge below the first-order transitions of the Kuramoto model, thus we see an example for hybrid transition known in other branches of physics.

## *Results*

Regarding dynamical process and hysteresis behaviour in the thermalization process (600 samples), a larger damping force slows down the dynamics of $R$ (the Kuramoto order parameter describing the phase synchronization) and at the same time leads to a smaller frequency spread. Similar effects were observed following one line cut. Following one random line cut ($10^4$ samples), lower threshold $T$ (describing the relative maximal capacity of lines) leads to larger disruptions in the system, causing a more significant drop in $R$ and a larger increase in the frequency spread, therefore the system becomes less stable. Hysteresis behaviour in $R$ with respect to different initializations of the phase angles $\theta(0)$ is hinting a first-order phase transition. At a global coupling value $Kc \approx 80$ is for the EU-HV network and $Kc \approx 20$ is for the US-HV network.

As for cascade line failures, the EU-HV network appears to be more stable than the US-HV network in regard to both the $R$ and $\Omega$ (the frequency spread) changes after one line cut. Non-universal power laws are seen for cascade line failure sizes. A Dragon King bump is observed for an intermediate $T$ value. Greater exponent values in the EU-HV network once again suggest it to be more stable than the US-HV network.

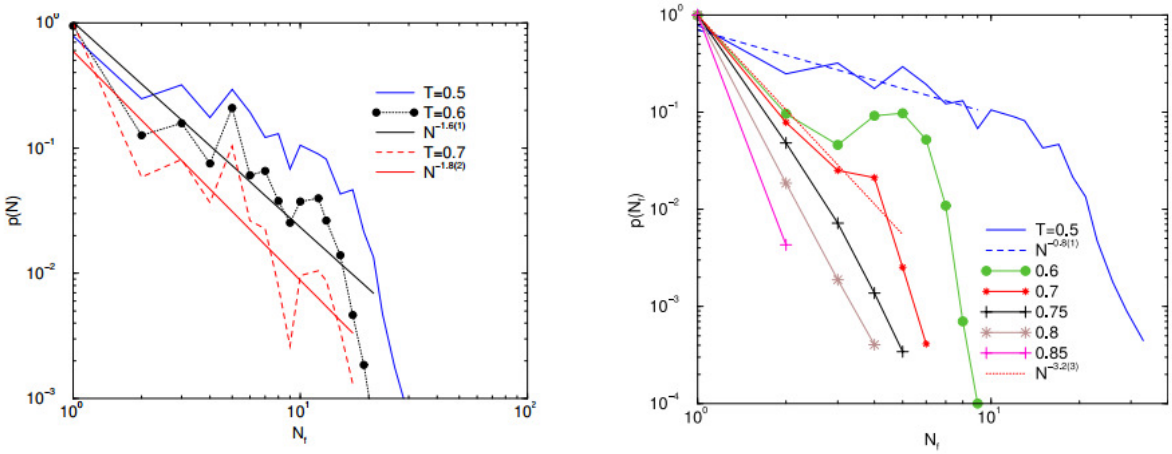


*Figure 1: Probability distribution of line failures for the US-HV network (Left: K = 30 and a = 0:4) and the EU-HV network (Right: K = 80 and a = 0:4) for different thresholds*

## *Related publications*

[1] S. Deng, G. Ódor, B. Hartmann, L. Barancsuk, J. Kelling: *Critical synchronization dynamics on power grids*, APS March Meeting (2022)

[2] L. Barancsuk: *Solving the Kuramoto Oscillator Model of Power Grids on GPU*, GPU Day 2021 (2021)

# MEASUREMENT OF SIZE FRACTIONATED CONCENTRATION OF THE NEW CORONAVIRUS IN CONJUNCTION WITH NUMERICAL MODELLING OF ITS INDOOR TRANSPORT AND AIRWAY DEPOSITION

*Árpád Farkas, Balázs G. Madas, János Osán, Péter Füri, Gábor Albrecht, András Deák*

## *Objectives*

The objectives of this work were:

- to monitor the size distribution of aerosol particles in hospital rooms of COVID-19 departments and identify nursing activities which are associated with high particle concentration and infection risk;
- to detect SARS-CoV-2 in the wards of COVID-19 departments and determine the size fractions of the aerosols the virus is attached to;
- to model the transport of virus-laden particles in different indoor environments and quantify the associated viral load;
- to simulate the lung deposition of the inhaled virus-containing aerosols in order to assess the risk of infection.

## *Methods*

A 24 h measurement of aerosol size distribution in the hospital room of a COVID-19 department (Semmelweis University's Department of Pulmonology) was carried out by an Optical Particle Counter (OPC, Grimm Aerosoltechnik). All the relevant medical visits and nursing activities were monitored. The sources of aerosol generation were identified.

A new impactor for size-fractionated aerosol sampling was developed by the extension of the original May impactor towards the range of ultrafine particle sizes. A method for the use of gelatin filter strips (Sartorius) on the cascade impactor plates was developed. Several aerosol samples from the air of hospital rooms of two COVID-19 departments (Semmelweis University's Department of Pulmonology, Budapest, Hungary and Pulmonology Hospital, Törökbálint, Hungary) were collected. The time of each sampling was 8 h with an air flow rate of 16.7 L/min. The size-fractionated aerosol samples were then tested by Polymerase Chain Reaction (PCR) techniques for E, $N_1$ and $N_2$ genes of SARS-CoV-2 virus by the DNS Laboratory of BIOMI Ltd. (Gödöllő, Hungary). The size distribution of aerosols was monitored simultaneously during each impactor sampling by the OPC.

The near-field far-field particle transport model [1] was applied to calculate the time-dependent spatial concentration of viable viruses after their emission by an infected person in indoor environments, such as the Pulmonary Function Test (PFT) and bronchoscopy laboratories of the Semmelweis University. Virus-laden particle transport and deposition within the human airways was simulated by the use of the Stochastic Lung Model [2]. The inputs of the model were the aerosol parameters measured in the COVID-19 ward.

## *Results*

Thirty-one human activities were recorded, and six representative ones were selected for deposition modelling, including patient activities (coughing, movements, etc.), diagnostic and therapeutic interventions (e.g., diagnostic tests, drug administration), as well as patient nursing care (e.g., bedding, hygiene). The left panel of Figure 1 shows the related particle concentrations. A big increase in particle concentration, more pronounced for the larger than the smaller particles, was associated with the number of healthcare personnel in the ward and the duration of activity (see activities), while submicron particles increased with all activities. The simulated particle deposition distribution within the airways corresponding to the selected activities is depicted in the right panel of Figure 1. Based on the simulations, the number of particles deposited in unit time was the highest in the acinar region, while deposition density rate (number/cm$^2$/min) was the highest in the upper airways [3].

The collection of the virus-laden aerosol particles on the plates of the cascade impactor in parallel with the measurement of particle size distribution by the OPC resulted in the size-fractionated virus concentration presented in the left panel of Figure 2. Based on the plot, particles between 1 μm and a few micrometres have the highest virus concentration.

Based on the simulations the viral load associated with exhalation during pulmonary function tests and bronchoscopy examination in comparison with virus emission during normal breathing and speaking is shown in the right panel of Figure 2. According to the calculation results, both lung function testing and bronchoscopy generate large numbers of aerosol particles. Although, the risk of infection associated with these activities is higher compared to everyday activities, stopping of these examinations is not recommended, as the information gained outweighs the excess risk [4], [5].

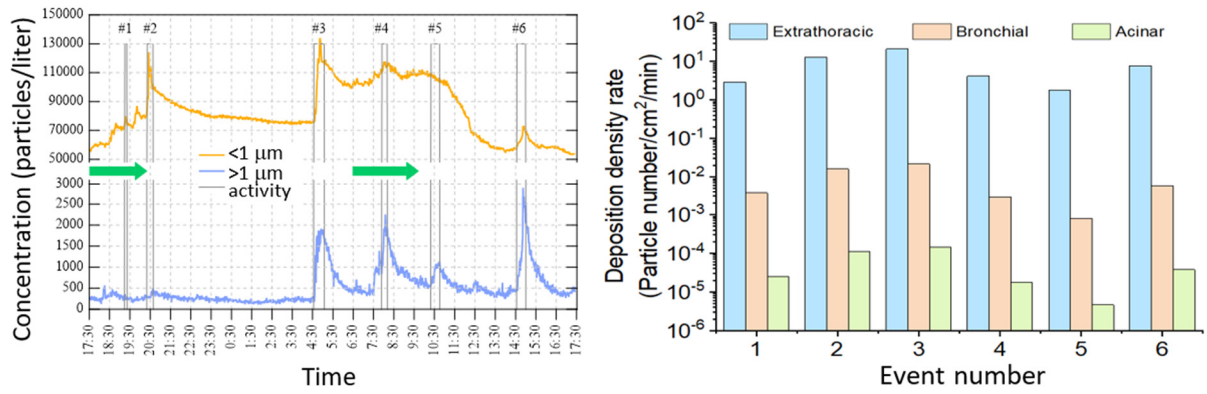


*Figure 1: Left panel: time series of the measured number concentrations in two size bins: below 1 µm (orange curve) and above 1 µm (blue curve); right panel: extrathoracic, bronchial, and acinar regional deposition density rates of the number of inhaled aerosol particles in the patient room studied. The numbered events are: 1 – patient's activity; 2 – diagnostic examination; 3 – nursing care; 4 – therapy administration; 5 – ultrasound; 6 – examination and bedding*

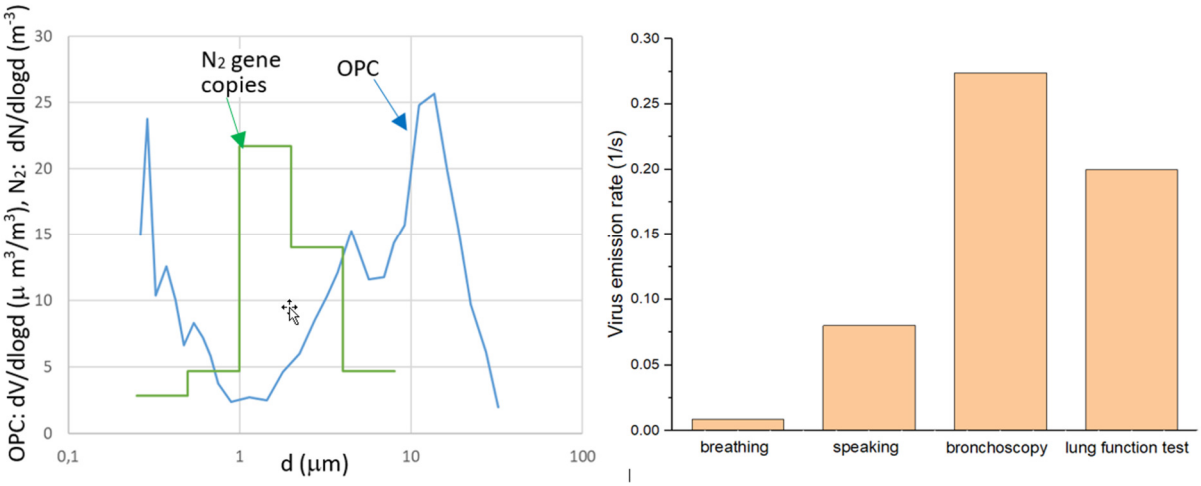


*Figure 2: Left panel: virus concentration and aerosol particle size distribution in the ward of a COVID-19 department; right panel: calculated virus emission rates corresponding to different activities.*

## *Remaining work*

The measurement of size-fractionated virus concentration in the hospital rooms of COVID-19 department will be continued in order to improve the statistical power of the results and to elucidate its dependence on the number of patients, their disease status and the type of activities of the healthcare personnel. All these measurements will take place in the frame of the AEROCOV project funded by Eötvös Loránd Research Network (ELKH).

## *Related publications*

[1] M. Nicas: *The near/far field model with constant application of chemical mass and exponentially decreasing emission of the mass applied.* Journal of Occupational Hygiene **13,** 519-528 (2016)

[2] B.G. Madas, P Füri, Á. Farkas, A. Nagy, A. Czitrovszky, I. Balásházy, G.G. Schay and A. Horváth: *Deposition distribution of the new coronavirus (SARS-CoV-2) in the human airways upon exposure to cough-generated droplets and aerosol particles*, Scientific Reports **10:** 22430 (2020)

[3] A. Nagy, A. Horváth, Á. Farkas, P. Füri, T. Erdélyi, B. G. Madas, A. Czitrovszky, Z. Ungvári and V. Müller: *Pathogen transmission by aerosol particles: time to rethink hospital- and nursing care-acquired airborne transmission of infections, new lessons from SARS-CoV-2*, GeroScience 44, 585-595 (2022)

[4] G. Tomisa, A. Horváth, Á. Farkas, A. Nagy, E. Kis and L. Tamási: *Real-life measurement of size-fractionated aerosol concentration in a plethymography box during the COVID-19 pandemic and estimation of the associated viral load*, Journal of Hospital Infection **118**, 7 (2021)

[5] Á. Farkas, A. Horváth, G. Tomisa and G. Gálffy: *A bronchoszkópiai vizsgálat, mint aeroszol generáló tevékenység és a hozzá kapcsolódó koronavírus terhelés*, Medicina Thoracalis **75,** 3-10 (2022)

# CHARACTERIZATION OF ELECTRONIC WASTE BY NUCLEAR ANALYTICAL AND IMAGING TECHNIQUES

*Noémi Buczkó, Boglárka Maróti, László Szentmiklósi*

## *Objective*

To determine the representative elemental composition of electrical and electronic equipment using analytical and imaging techniques. To quantify the amount of hazardous and/or valuable elements. To localize their spatial distributions. To create a suitable, validated analytical methodology.

## *Methods*

Different analytical techniques were used to characterize different memory cards. The major and minor components were identified using handheld X-Ray Fluorescence Analysis (XRF). To obtain the average bulk chemical composition the Prompt-Gamma Activation Analysis (PGAA) technique was used, combined with off-line counting measurements, e.g. in-beam Neutron Activation Analysis (NAA). PGAA and in-beam NAA measurements were carried out on the intact samples. Since the ideal sample geometry in PGAA is small and thin, to validate the position-sensitive measurements on the intact samples, the memory cards were ground to a powder and measured again with PGAA and in-beam NAA. To quantify other trace components, the powdered samples were measured with Instrumental Neutron Activation Analysis (INAA). Neutron radiography and tomography were used to visualize the intact samples in 2D and 3D.

## *Results*

The local PGAA measurements on the intact samples (Fig.1b) and on the powdered samples were in good agreement. A combination of consecutive PGAA, in-beam NAA, and INAA (Fig.1a) was found to be suitable to quantify most of the valuable and/or hazardous elements present in memory cards, such as Au, Ag, REEs (Rare Earth Elements), Br, Cd, etc. The PGAA concentrations we have measured so far were initially systematically higher than the INAA results. With the application of corrections for neutron self-shielding and gamma self-absorption, the differences are decreased significantly.

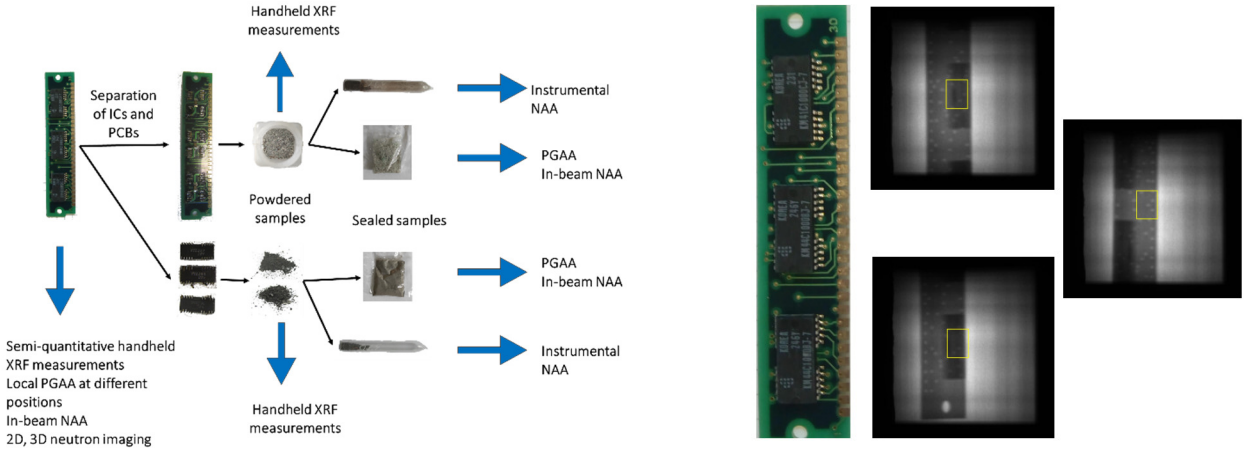


*Figure 1: a) flow-chart of the measurements carried out on the electronic waste*
*b) photo and the radiography images of the memory card together with the parts selected for elemental analysis*

## *Remaining work*

Implementing matrix-matched calibration to the handheld XRF spectrometer. To make absolute the in-beam NAA and PGAA results and to compare them with the INAA data. Do Monte Carlo N-Particle Transport (MCNP) computer simulations to determine the neutron self-shielding and compare to the other results.

## *Related publications*

[1] N. A. Buczkó, B. Maróti and L. Szentmiklósi: *Characterization of Electronic Waste with Neutron And X-Ray Based Techniques*, In: Jószai I. (szerk.) Őszi Radiokémiai Napok, 2021.10.18-20. ISBN 978-615-3018-07-6, pp. 68-73., Balatonszárszó, abstract and oral presentation

[2] N. A. Buczkó, B. Maróti and L. Szentmiklósi: *Characterization of Electronic Waste with Neutron And X-Ray Based Element Analysis Techniques*, Central European Training School on Neutron Techniques (2021), Budapest, poster presentation

# PHYSICAL AND CHEMICAL CHARACTERISTICS OF NEWLY FORMED AEROSOL PARTICLES DURING ADDITIVE MANUFACTURING

*Szilvia Kugler, Endre Börcsök, Árpád Farkas, Péter Füri, Veronika Groma, János Osán*

## *Objective*

Additive manufacturing is one of the most modern and improving of today's industrial technologies. Aerosol particles, mainly in the fine (<2.5 µm) and ultrafine (<100 nm) size range, are formed during 3D metal printing which is based on laser cladding. The majority of particle mass is below 0.5 µm as shown in Fig 1 and that is part of the fine fraction. There is still a lack of knowledge about the characteristics of the new particle formation processes. The goal of this study is the physical and chemical characterization of the emitted aerosol particles (particle size distribution, elemental content, shape) and the modelling of their possible deposition in the different parts of human lungs, providing information on the possible health effects for the operators of these printer machines.

## *Methods*

The properties of the aerosol particles emitted during the 3D metal printing process using different starting materials were determined. Feedstock powders made from two types of stainless steel (H13 and H15) and two types of nickel alloy (In 718 and In 625) were used. During the operation of the 3D printer, size fractioned aerosol samples were collected with a 9-stage May-type cascade impactor developed by us. The number and mass concentrations, and size distributions were measured simultaneously with a Scanning Mobility Particle Counter and Sizer (SMPS) and an Aerosol Particle Counter (APC). The elemental composition of the particles in the different size fractions was determined by Total-reflection X-Ray Fluorescence (TXRF) analysis and Scanning Electron Microscopy Energy Dispersive Spectroscopy (SEM/EDS). A stochastic lung deposition model was used to calculate the deposition rate of the newly formed particles in the human airways [1].

## *Results*

Size distributions determined by SMPS revealed that the vast majority of the emitted particles are 100 nm or smaller, which could be confirmed by the size-fractionated elemental concentrations determined by TXRF [2 3, 4]. Fig. 1. shows TXRF results for Cr (Panel A) and Mn (Panel B) concentrations on the different plates of the cascade impactor. In the original metal powders the Cr content varies from 5 to 20% and the Mn content is below 1%. High enrichment could be detected mainly in the lowest aerosol size fraction for both elements due to their high vapour pressure. The enrichment of Cr and Mn in ultrafine aerosols might increase their inhalation health impact compared to the original composition of the feedstock materials. The calculated fractions of the number of inhaled particles deposited in unit time (deposition rate) in different anatomical regions of the human respiratory system (extrathoracic, bronchial and acinar) show a monotonic decrease in time after the end of operation of the 3D metal printer (Fig. 1, Panel C). The decreasing tendency of the deposited amount is a result of the synergistic effects of particle fallout (decrease of particle concentration) and lower deposition by Brownian diffusion with increasing particle diameters.

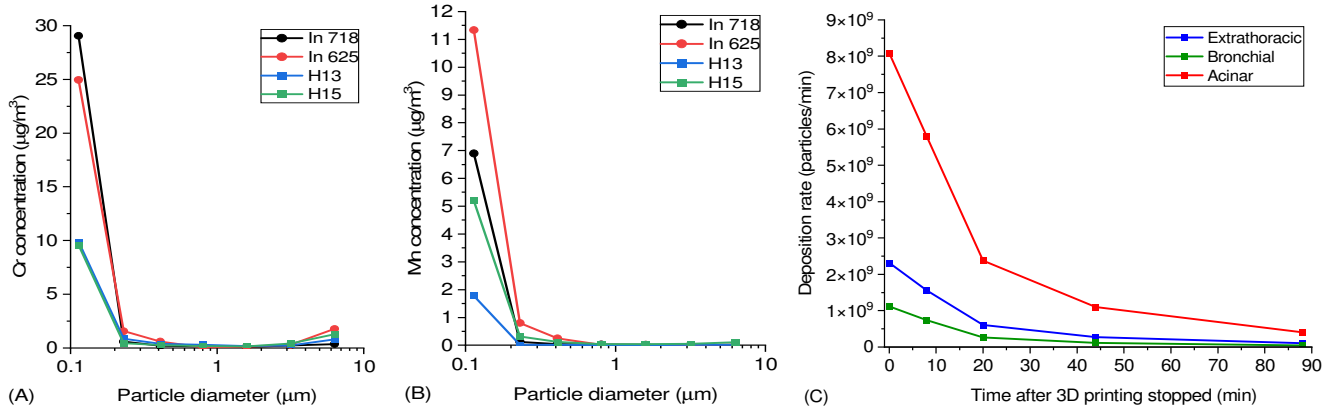


*Figure 1: Mass concentration of chromium (A) and manganese (B) at different size range during 3D printing, airway deposition of the particles in case of In 718 after 3D printing activity stopped (C)*

## *Related publications*

[1] B.G. Madas, P. Füri, Á. Farkas, A. Nagy, A. Czitrovszky, I. Balásházy, G.G. Schay and A. Horváth: *Deposition distribution of the new coronavirus (SARS-CoV-2) in the human airways upon exposure to cough-generated droplets and aerosol particles.* Scientific reports, 10(1), pp.1-8. (2020)

[2] Sz. Kugler, A. Nagy, J. Osán, L. Péter, V. Groma, S. Pollastri, A. Czitrovszky: *Characterization of the ultrafine and fine particles formed during laser cladding with the Inconel 718 metal powder by means of X-ray spectroscopic techniques,* Spectrochim. Acta - Part B, **177**, 106110 (2021)

[3] Sz. Kugler, A. Nagy, V. Groma, J. Osán and A. Czitrovszky: *Characteristics of the newly formed nanoparticles during 3D metal printing*, European Aerosol Conference, 30 08 – 03 09 2021, Birmingham, UK (virtual), AH 8-3_688 (2021)

[4] L. Péter, Sz. Kugler, V. Groma, J. Osán, and A. Nagy: *Comparison of two H13-type starting materials and their aerosol products formed in laser cladding process and the composition analysis of the cladded deposits* (in preparation)

# BORON LEACHABILITY FROM OXYDTRON CEMENTITIOUS MATRICES

*Margit Fábián, István Tolnai, Ottó Czömpöly*

## *Objective*

Cement is useful for solidifying wastes such as boric acid and borate salts, but borates tend to inhibit or retard the hydration of the cement powder. Boric acid, which is the precursor of the borates, is used as a moderator in Pressurized Water Reactors (PWR), and the borates which it forms are contained in both ion exchange resins and evaporation concentrates. This study was carried out on the immobilization of evaporator concentrate containing borates in a new cement matrix and evaluation of its long-term stability.

Borate waste concentrates vary in their content, ratios, and amounts of their salts according to conditions of operation, pretreatment, and coolant constituents. A simulated concentrated borate waste solution was used in the present study to evaluate the chemical characterization of the solidified Borate-containing cement. Part of this simulated waste solution was spiked with inactive CsCl to simulate the radioactive $^{137}Cs$ (but this preparation was unsuccessful). Based on the literature, boric acid waste could contain $^{90}Sr$, $^{137}Cs$, $^{51}Cr$, $^{60}Co$ and other radionuclides.

To ensure the radiological safety after the waste disposal, these solidified radioactive wastes are required to have some properties such as good mechanical strength, low leachability, good effects during water immersion, and good durability. Among these properties, the most difficult to determine is the leachability. Leaching is generally considered as the basic criterion to evaluate the safety, acceptability, and chemical behaviour of the final waste forms in the disposal sites.

## *Methods*

This study was aimed to understand the chemical stability of boric acid in cementitious structures, as the most common hosting matrix for low and intermediate level radioactive wastes. For the experiments, the simplest and the improved cement mixtures were used, with the names of Oxydtron and Oxydtron-B cements. We have studied the boron leachability from the cementitious matrices to compare the chemical sustainability of the solidified samples. The resulting information can provide initial data to compare the long-term durability of cements to that of the final waste-forms containing the cement mixture with the contained boric acid in different ratios. Simulated liquid boric acid wastes with 50 g/l, 100 g/l, 150 g/l, 200 g/l and 250 g/l boric acid concentrations were prepared. The cement powder was mixed with the liquid boric acid solution at room temperature until a homogeneous paste was obtained. The wet paste was filled into 2.5 cm diameter and 5 cm height Polyethylene cylindrical molds and put into an incubator with a fixed temperature of 20 °C and was cured for 28 days. Leaching tests followed the procedure described in ASTM C1308-08 standard. According to this standard, the cylindrical solid samples with 49.09 $cm^2$ contact surface were immersed in 500 ml demineralized (DM) water (leachant) and the resulting solutions (leachates) were changed at time intervals of 2, 5, 17 and 24 hours, and then daily for the next 10 days. All the leachates were filtered and acidified by 1 m/m% nitric acid. The treated samples were analysed by an inductively coupled plasma - optical emission spectrometer (ICP-OES; Perkin Elmer Avio 200).

## *Results*

For both cement samples and for all the boric acid concentrations, the boron dissolution shows dynamic activity between 0 and 24 h, followed by a slow rise, perhaps approaching a plateau (based on the data of Fig. 1). For both cement samples, the 150 g/l boric acid concentration shows the highest dissolution value. The lower and higher concentrations, for both types of cement, have a lower dissolution value more proportional to the concentration and all show a similar trend as a function of time.

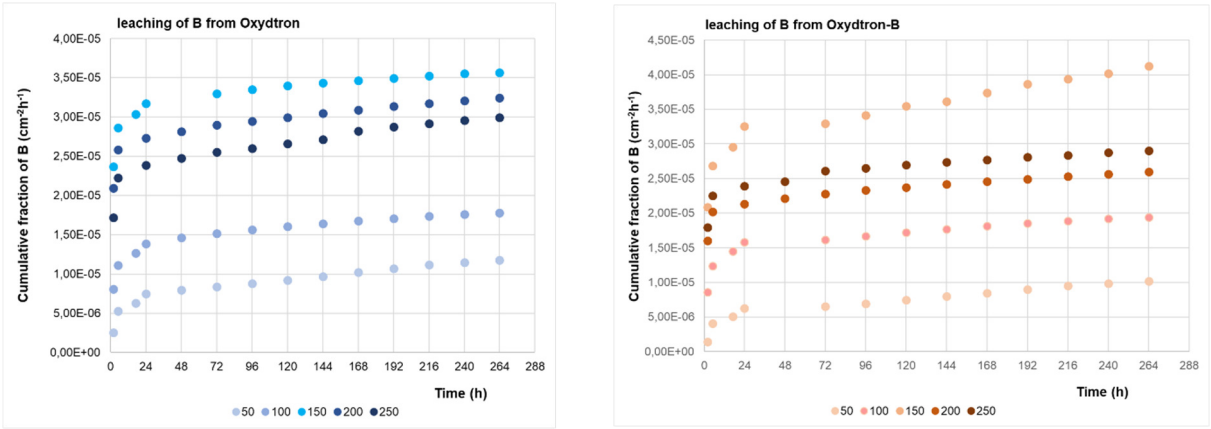


*Figure 1: Cumulative fraction of elemental B as a function of time from Oxydtron (a) and Oxydtron-B (b) samples*

The boron leachability is one of the most important parameters in the waste-form durability calculations. The Cumulative Fractions of boron Leaching (CFL) from the Oxydtron and Oxydtron-B are similar, and the dissolution rates are in the same range. Based on these measurements, cement mixtures could be a good choice for the stabilization of liquid boric-acid. Detailed results were presented in the Research Report, but some of the results are not public.

## *Remaining work*

The project was an external industrial assignment and was completed.

## *Related publication*

[1] M. Fabian, I. Tolnai and O. Czömpöly: *Sample preparation and dissolution test of inactive boric acid cement*, Research Report, EK-KFL-2020-344-1-1-M0, in Hungarian (2020)

# MESOPOROUS SILICA MATERIALS FOR ADSORPTIVE REMOVAL OF ORGANIC AND INORGANIC POLLUTANTS

*László Almásy, Zoltán Dudás, Adél Len*

## Objective

Silica based inorganic polymer materials and composites are used in numerous applications. They are produced by the sol-gel synthesis method, which allows easy modifications of the synthesis procedure and can produce materials with novel and desired properties. In this project we applied the sol-gel method to prepare mesoporous silica materials with high specific surfaces and ordered open porosity, suitable for applications as adsorbents for pollutant removal from an aqueous environment.

## Methods

**Synthesis and characterization.** Mesoporous silica materials have been prepared by the sol-gel method using different precursors and solvent conditions, in alkali catalysis conditions, and using a cationic surfactant as the pore forming agent. The pore structure and the surface chemistry of the materials was varied by changing the proportion of functionalized silica precursors. The structural characterization of the materials was performed by nitrogen adsorption porosimetry, small angle neutron and X-ray scattering, X-ray diffraction, infrared spectroscopy and scanning electron microscopy.

## Results

Ordered mesoporous silica materials have been prepared by the co-condensation method using mixtures of tetraethoxysilane (TEOS) with the functionalized silica precursors 3-aminopropyl-triethoxysilane (APTES), or 3-mercaptopropyl trimethoxysilane (MPTMS). Using nitrogen adsorption measurements and X-ray diffraction, we observed a monotonically decreasing specific surface with an increasing amount of the functionalized silica precursor, as well as the decrease of the pore ordering and finally the loss of the hexagonal pore arrangement. Thus, improving the affinity of the pore surface to potential contaminants, the usable surface and total pore volume are simultaneously decreasing. The optimal ratio of silica to functionalized silica precursor has to be determined for each specific application.

Diffraction patterns of two series of samples, prepared using different amounts of two different functionalized precursors, are shown in Figure 1. The data show a typical hexagonal pore structure, characteristic for MCM-41 materials. Increasing APTES or MPTMS content leads to gradual reduction of the ordered pore structure. At the highest APTES content, only the first diffraction peak remains, indicating the loss of the long range periodicity.

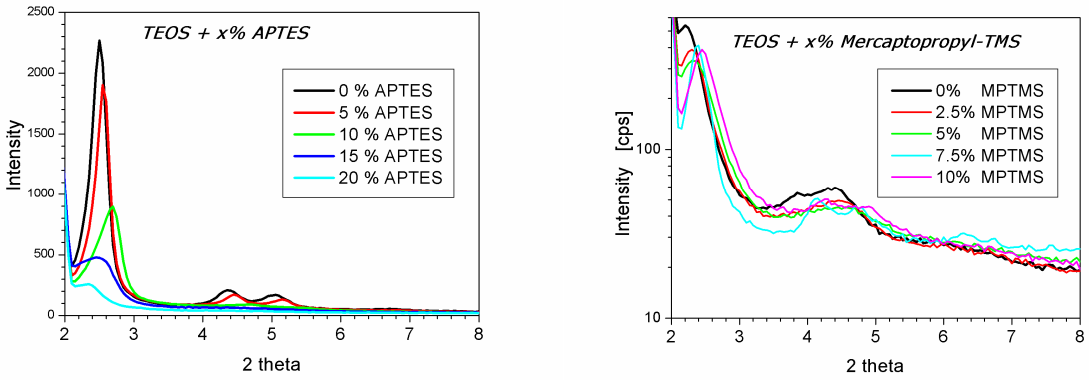


*Figure 1: Diffractograms of ordered mesoporous silica prepared by co-condensation of TEOS with APTES (left) and MPTMS (right)*

## Remaining work

The studies will be continued in the following years with exploring of new synthesis and characterization approaches.

## Related publications

[1] A.-M. Putz, M. Ciopec, A. Negrea, O. Grad, C. Ianasi, O.I. Ivankov, M. Milanovic, I. Stijepovic and L. Almásy: *Comparison of structure and adsorption properties of mesoporous silica functionalized with aminopropyl groups by the co-condensation and the post grafting methods,* Materials **14,** 628 (2021)

[2] C. Ianăşi, E.-M. Picioruş, R. Nicola, A.-M. Putz, A. Negrea, M. Ciopec, A. Len and L. Almásy: *Synthesis and characterization of magnetic iron oxide – silica nanocomposites used for adsorptive recovery of palladium (II),* Soft Materials *in press* (2021)

[3] A. Policicchio, A.-M. Putz, G. Conte, S. Stelitano, C. P.Bonaventura, C. Ianasi, L. Almásy, A. Wacha, Z. E. Horváth and R. G. Agostino, *Hydrogen storage performance of methyl-substituted mesoporous silica with tailored textural characteristics,* Journal of Porous Materials **28**, 1049 (2021)

# V. NUCLEAR ANALYSIS AND CHEMISTRY

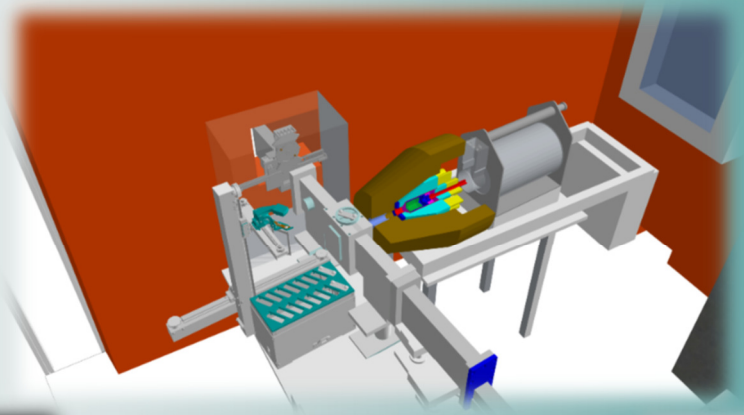

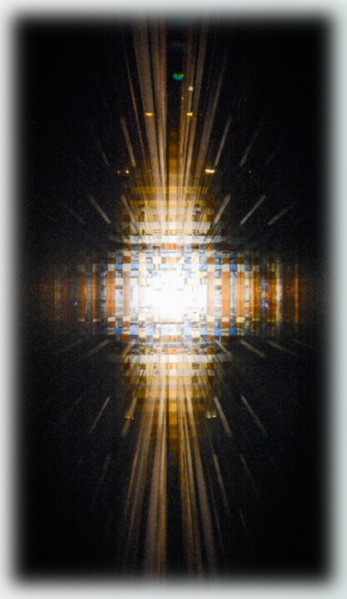

# NON-DESTRUCTIVE, SPATIALLY-RESOLVED ELEMENT ANALYSIS OF STRUCTURED SAMPLES

*László Szentmiklósi, Boglárka Maróti, Zoltán Kis*

## Objective

The aim of this present study was to develop Prompt-Gamma Activation Imaging (PGAI) and use it to study non-homogeneous and irregularly-shaped samples.

## Methods

We made composition measurements by PGAI-NT (Neutron Tomography), computer programming and Monte Carlo modelling.

## Results

Within the project K124068 funded by the NKFIH, we worked out a comprehensive matrix-effect correction method to extend the applicability of the Prompt-gamma Neutron Activation Analysis (PGAA) method to multi-layered objects, aiming at better analysing metallic cultural heritage objects covered with a corrosion layer, patina, metal coating, and multi-component cultural-heritage and industrial products or cast alloy items where in-depth segregation can take place.

We used the Monte Carlo N-Particle Transport (MCNP) 6.2 code with the nuclear data library Lib80x (based on the ENDF/B-VIII.0 database) for the modelling. The detailed geometries of the Budapest Neutron Centre's PGAA and NIPS-NORMA experimental stations, the energy distribution of the cold neutron beam, and the structure of the sample were implemented in the simulation environment to reproduce the real PGAA experiments. The beam hardening was studied for metal stacks using simulated and measured radiograms. Some typical results are shown in Fig. 1. Note how much better the corrected results agree than the uncorrected ones. It can be seen that the relative size of the two corrections for Neutron self-shielding and for Gamma self-absorption depends strongly on the ordering of the layers of the stack, as well as the direction of the correction. For the first time, we achieved consistent masses when changing the layer sequence of metallic double and triple stacks, or when incrementally rotating them. Finally, the method was applied to a real-world coated coin, the Kennedy half-dollar [1].

We further developed this approach to handle irregularly shaped and non-homogeneous objects using voxelization [2]. The detailed geometry of an articulated Japanese iron lobster was taken from segmented synchrotron CT data [3] (Fig 2. a), The material distribution was converted to a simulation geometry using a purpose-made utility. The regular mesh of 66×102×278 voxels had unit voxel sizes of 0.5×0.5×0.5 mm$^3$ and was filled with four materials: air, metal body, and two kinds of solder. This allowed us to correct for the neutron and gamma-related matrix effect even in this complex geometry, and provided the compositions of the two soldering materials, being brazing material (Cu63Zn37) and a eutectic alloy (Sn39Pb61) [3].

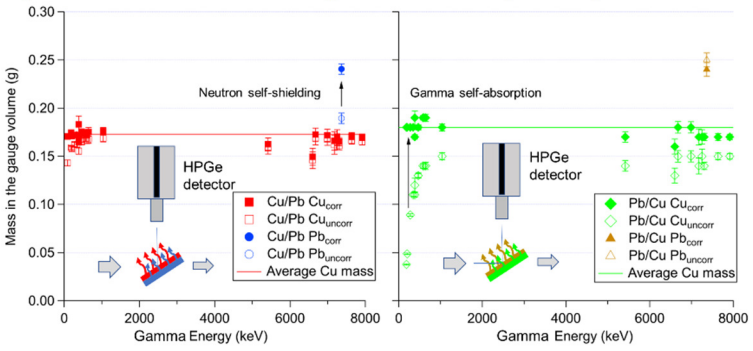


*Fig.1: (left) The masses of Cu and Pb in a Cu/Pb double stack became self-consistent after making the new matrix-effect correction [1].*

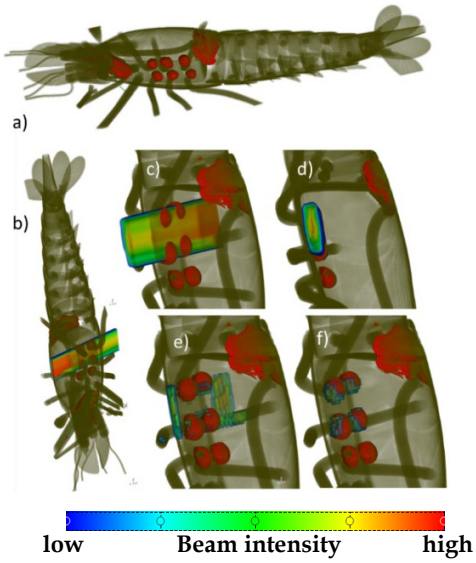


*Fig.2 (right): The non-destructive analysis of the structure and the soldering materials inside an iron lobster from Japan [3]. Red highlight shows the positions of the solder materials. The beam intensity is color-coded, ranging from red to blue.*

## Related publications

[1] L. Szentmiklósi, B. Maróti, Z. Kis: *Prompt-gamma activation analysis and neutron imaging of layered metal structures,* Nucl. Instr. Meth. A **1011,** 165589 (2021) DOI: 10.1016/j.nima.2021.165589

[2] L. Szentmiklósi, Z. Kis, B. Maróti and L. Z. Horváth: *Correction for neutron self-shielding and gamma-ray self-absorption in prompt-gamma activation analysis for large and irregularly-shaped samples,* Journal of Analytical Atomic Spectrometry **36,** 103–110 (2021) DOI: 10.1039/D0JA00364F

[3] L. Szentmiklósi, Z. Kis, M. Tanaka, B. Maróti, M. Hoshino, K. Bajnok: *Revealing hidden features of a Japanese articulated iron lobster via non-destructive local element analysis and 3D imaging,* Journal of Analytical Atomic Spectrometry **36,** 2439-2443 (2021) DOI: 10.1039/D1JA00261A

# NEUTRON OPTICS

*Márton Markó, Alex Szakál, Péter Kárpáti, László Bottyán, Gyula Török, László Rosta*

## *Objective*

Neutron optics research and development involves the basic development of neutron optical devices and the design, optimization and upgrade of neutron sources and neutron scattering instruments for use at the Budapest Neutron Centre (BNC) and at other neutron centres and at companies collaborating with the Neutron Spectroscopy Department. The work includes hardware and software upgrades as well.

## *Methods*

During our work we use optical considerations, and analytical, numerical, and Monte-Carlo calculations with the McStas software package. For instrumental alignment and background definition we use measurements on a reference sample, the Camera Obscura method, and simple geometrical considerations to define the orientation of the given neutron optical components of the instruments and the origins of the different instrumental backgrounds.

## *Results*

As a part of the development of the instrument suite of BNC, our group finished the alignment and calibration of the ATHOS instrument, upgraded to be a strain scanner last year, and, made the first demonstration of a residual stress measurement (Figure 1). We have developed a stress measurement reference method with a reliable calibration on the Time-Of-Flight (TOF) diffractometer and performed a demonstration measurement on an industrial sample. We analyzed the internal stresses in a sample of metal treated by different heat treatments. We determined the size and position of additional neutron shielding needs for the Grazing Incidence Neutron Apparatus (GINA) reflectometer and the Yellow Submarine small angle scattering instrument to reduce their own instrumental background originating from the scattering of the components in the vicinity of the sample. Using the Camera-Obscura method we determined the disorientation of the double monochromator system of the REF reflectometer. The results show that the accurate reorientations of the graphite monochromator elements will give at least a factor of two increase in the intensity.

It is planned to replace the cold source of the BNC by a new so-called low dimensional moderator. The new moderator geometry necessitates the redesign of the neutron guide system. Our investigations show that for some instruments a 1D moderator (flat, edge is facing to the neutron guides) can be more advantageous than the 0D pencil source. Alternatively, a pencil source combined with a round volume moderator similar to the present one can be used.

We defined the optimal instrument lengths and source frequencies for a pulsed Compact Accelerator-based Neutron Source (CANS) under consideration to replace the existing reactor source. CANS uses a pulsed proton beam to generate neutrons by irradiation of targets consisting low atomic number material. Two target stations irradiated with proton pulses of 100 Hz and 25 Hz frequency and equipped with 20 and 40m long instruments can give the neutron pulses with optimal resolutions and bandwidths the presently existing instrument suites at BNC. As a part of the theoretical neutron optics work, we studied the effect of the waviness of neutron supermirrors and implemented these effects in the McStas MonteCarlo ray-tracing package. The results of the McStas calculations are in agreement with our numerical model calculations. Publication is in progress. We investigated a quasi-parabolic beam extraction from a small-sized moderator, defined the maximal phase-space extraction and the geometrical constraints.

The relocation of the V14 horizontal polarized reflectometer is delayed due to the pandemic situation. We made extensive investigations to determine the optimal placing of the instrument in the cold neutron hall considering the geometrical constraints. The optimal solution is to build a double monochromator and replace the REF reflectometer being parallel to the first cold neutron guide to V14. This solution gives a factor of 2-4 increase in the intensity on the sample compared to the conventional solution with a single monochromator.

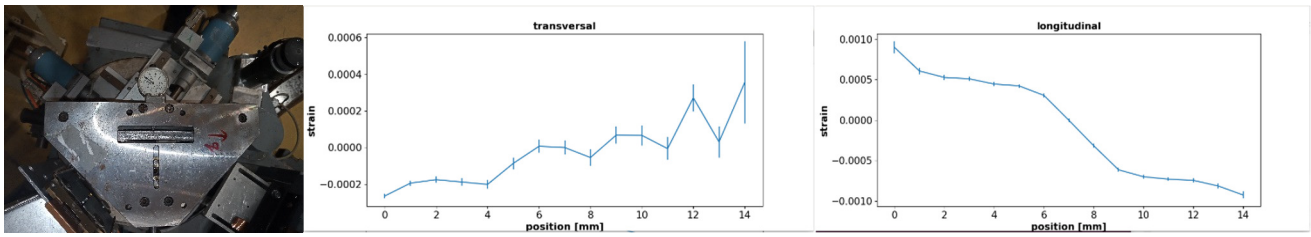


*Figure 10: Bent iron sample (left), and the longitudinal and transverse strain distribution in the transverse direction through the sample (middle and right)*

## *Remaining work*

The support for the local instrumental development is continuing: installing a reliable sample positioning system (3D) at the ATHOS instrument, finishing the control and data treatment software package, designing the monochromator and shielding

system of V14, developing of measurement methods, control and data treatment software package for the Focusing SANS (FSANS) instrument under development.

After finishing the cold source design and the definition of the instrument suite, we will finish the new guide system design for the low dimensional cold moderator.

The next step in the basic optical research is investigation of quasi-elliptic and hybrid beam extraction systems, comparison of the different geometries, and defining the optimal setup for each type of instrument.

## *Related publication*

[1] IAEA-TECDOC-1961: *Neutron scattering with low and medium flux neutron sources,* Processes Detections and Application ISBN 978-92-0-116721-7 (paperback), ISBN 978-92-0-116621-0 (PDF)

# TUNGSTEN-CARBIDE-RICH PROTECTIVE COATINGS PRODUCED BY NOBLE-GAS ION MIXING

*Adél Rácz, Zsolt Kerner, Zsolt Fogarassy, Miklós Menyhárd*

## *Objective*

Tungsten-carbide (WC) is known for its exceptional mechanical properties and good chemical resistance. In previous work [1], we have shown that it is possible to produce WC-rich coatings using ion beam mixing at room temperature. We have irradiated various C/W multilayer structures with noble gases in a wide range of fluences and energies. Due to ion beam mixing, WC was formed at the layer interfaces. A potentiodynamic corrosion test in 3.5 wt% NaCl solution has shown that the chemical resistance of the ion-mixed samples is better than a commercially available WC cermet.

For some applications, in addition to good chemical resistance, good mechanical resistance is also important. Here we show that, besides the corrosion resistance, it is also possible to tailor the mechanical resistance of the ion mixed samples. The application of simulation methods is essential for designing the layer structure which makes mechanical resistance tailoring possible. In the case of the W/C material pair, the mixing is governed by thermal spike processes. The fast and cheap TRIDYN simulation [2] is based on ballistic processes, and hence its application to the W/C system could be questioned. In principle, the main difference between the ballistic and thermal spike models is the very different effective diffusion constants. Our hope is that by simply increasing the value of the diffusion constant (decreasing the relocation threshold energy), the mixing will be estimated reasonably well when using the TRIDYN simulation.

## *Methods*

The samples, four different types of C/W multilayer systems, were produced by magnetron sputtering in the Jozef Stefan Institute, Ljubljana. The systems differed in the thickness (10-30 nm) and the order of layers. The actual layer thicknesses of the specimens, determined by cross sectional electron microscopy (XTEM), were the following: C 10.4 nm/W 24.5 nm/C 9.1 nm/Si substrate; C 8 nm/W 18 nm/C 8.7 nm/W 18.6 nm/C 7.1 nm/ Si substrate; C 15.8 nm/W 22.7 nm/C 17.2 nm/W 24.3 nm/C 21.1 nm/Si substrate. For easier reference we will label them 102010, 1020 and 2020. These layered samples were irradiated with medium energy argon and xenon ions. The argon ion energy was 40 – 110 keV and the fluence was 0.25 – 6 × $10^{16}$ $Ar^+/cm^2$, while for the xenon ions the energy was 40 - 120 keV and the fluence was 0.07 - 3 × $10^{16}$ $Xe^+/cm^2$. The irradiation took place in the Helmholtz Zentrum Rossendorf in Dresden in the framework of the RADIATE beam time project. AES depth profiling has been used to determine the component in-depth distribution of the samples before and after irradiation. We found that the low energy (1 keV) argon ions used in depth profiling caused more mixing of W and C, resulting in additional WC formation (e.g. artefact formation) besides that induced by the medium energy (argon and xenon) ions. This 1 keV artefact production has been simulated by the TRIDYN simulation. The effects caused by the medium energy irradiation has also been predicted also by this simulation method. The TRIDYN simulation can predict the in-depth distribution of elements (C, W) but does not know anything about compound (WC) formation. The amount of compound has been calculated by assuming that all minority components (C in W and W in C) form WC which is supported by previous AES measurements. The corrosion resistance of some samples has been tested in 1 molar $H_2SO_4$ solution. The mechanical resistance of the samples was tested by a scratch test in an Atomic Force Microscope (AFM) using diamond coated tips.

## *Results*

The scratch test has shown that, depending on the WC amount, the scratch resistance of the ion-mixed samples is sometimes better than that of WC cermet. Moreover, introducing the quantity of the effective areal density, we could predict the scratch resistance of the ion mixed layer. Figure 1.a shows the measured scratch depth for different samples as a function of the applied normal load, while Figure 1.b shows the scratch depth as a function of the calculated effective areal density for a given normal load. It can be seen that they are in good correlation even though the WC areal densities vary over an extremely large range. The corrosion test of some samples in $H_2SO_4$ solution shows that the corrosion resistance scales similarly with the areal density, as was found in the case of corrosion in NaCl solution. These findings enable the tailoring of the mechanical and corrosion resistance of the system.

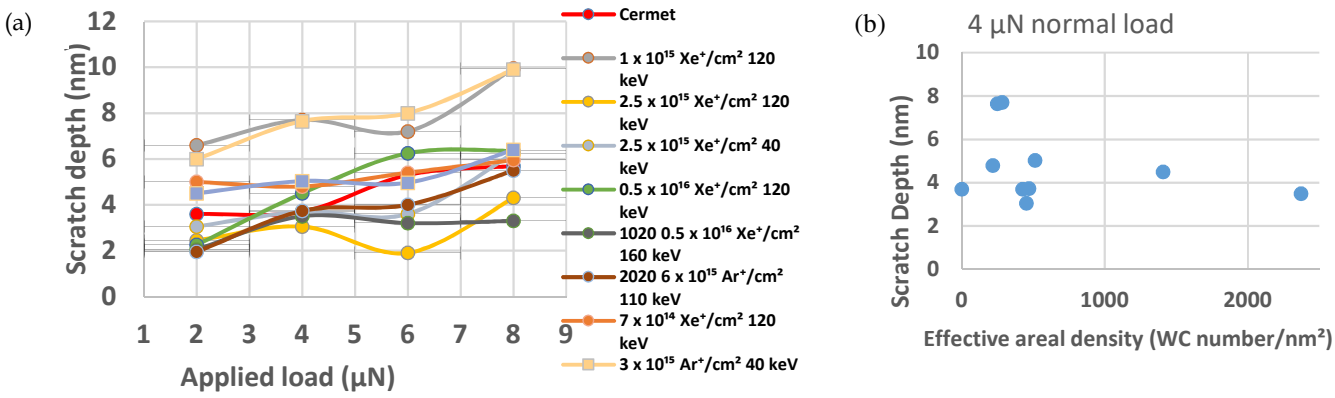


*Figure 1: a) Scratch depth vs applied normal load; the abbreviations of the layer structure are also labelled, except for 102010, which applies to all the other WC curves. b) Scratch depth vs effective areal density of WC for the variously irradiated different layer structures, the red point belongs to the WC cermet.*

The artefact production of the 1 keV argon ion sputtering during Auger Electron Spectroscopy (AES) depth profiling has been simulated by TRIDYN. Figure 2 shows an example for the reconstruction of the true depth profile for a 102010 sample (C 10 nm /W 24.5 nm / C 9.1 nm) irradiated by 120 keV, 0.5 x $10^{16}$ $Xe^+/cm^2$. An initial (ini) in-depth distribution is assumed, and then the 1 keV argon depth profiling is simulated (sim) by TRIDYN. If the simulated (sim) curve is in good agreement with the experimentally (exp) measured AES depth profile then the 'ini' curve is the original in-depth distribution [3].

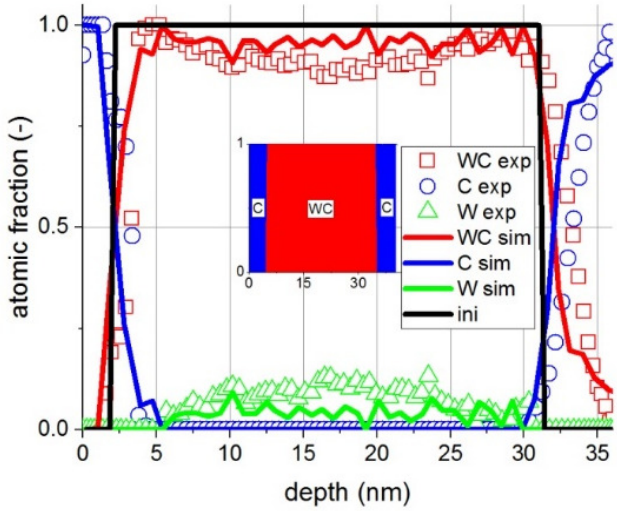


*Figure 2: The experimental (exp) and simulated (sim) depth profiles obtained from sample 102010 irradiated by 5x$10^{15}$/$cm^2$ $Xe^+$ of 120 keV and the WC distribution (ini) chosen for the simulation. The insert shows the sketch of the structure assumed for simulation.*

Concerning the possible design of the WC-rich layers by doing some parametrization – e.g. increasing the value of the diffusion constant - the TRIDYN simulation became able to estimate the in-depth distribution of the elements after ion irradiation. The agreement between the experimental and simulated depth profiles has been tested for a rich dataset differing in layer structures, projectiles, ion fluences and energies. The good agreement validates this method of designing the WC-rich layers which might act as protective layers. Figure 3 shows an example for the good agreement between the measured and simulated depth profiles for varying fluences in a 40 keV argon irradiated C 10 nm /W 24.5 nm / C 9.1 nm system [4]. The grey area is the measured AES experimental (exp) WC in-depth distribution which we want to predict. First we perform a TRIDYN simulation (sim) with the increased diffusion constant (decreased relocation threshold energy) to predict the in-depth distribution due to medium energy ion irradiation. We can see that the curves are not in good agreement. However, this red simulated curve is not corrected for the artefact production induced by the low energy ions during AES depth profiling. An additional simulation of the effect of the depth profiling is then performed – with the normal diffusion constant - resulting in the blue curve 'WC depth' which is in better agreement with the experimentally measured one. The figure also clearly shows that with increasing irradiation fluence, the produced WC increases and the artefact production of the AES depth profiling can be neglected. E.g. already in Fig. 3.c the difference between curve 'sim' and 'depth' can be neglected.

We see that these simulations provide a fairly good estimate of the WC in-depth distributions but it should be noted that there are deviations. It seems that the increased diffusivity is sufficient for producing higher intermixing - which is expected based on the thermal spike model. The systematic deviations show that the actual mixing process is a much richer phenomenon, but these additional processes could be more or less neglected from the point of view of layer formation.

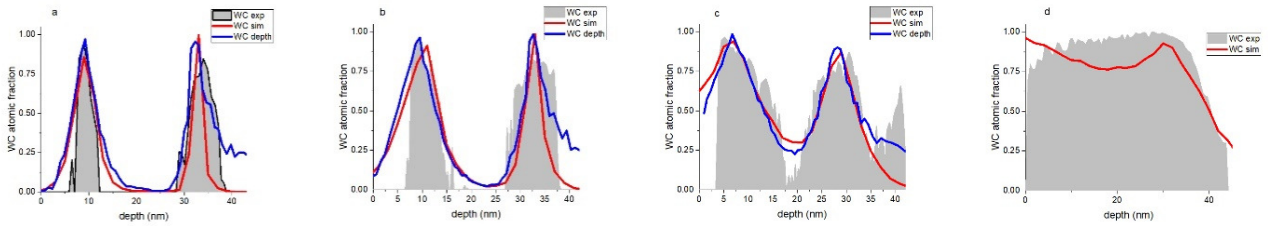


a. 1E15 *b.* 3E15 *c.* 1E16 *d.* 3E16

*Figure 3: Comparison of measured WC distribution with that of calculated for sample of C 10nm /W 24.5 nm / C 9.1 nm, irradiated by 40 keV $Ar^+$ applying various fluences*

## *Remaining work*

We would like to further investigate the mixing mechanism and compound formation of the C/W system. Additionally, further investigation of the mechanical properties of this system would be interesting as its thickness is below 100 nm.

## *Related publications*

[1] A. S. Racz, Z. Fogarassy, Z. Kerner, M. Menyhard: *Tungsten-carbide-rich protective coatings produced by noble-gas irradiation mixing,* Centre for Energy Research Progress Report 2020 91. (2021)

[2] W. Möller, W. Eckstein: *Tridyn – A TRIM simulation code including dynamic composition changes,* Nucl. Instrum. Methods Phys. Res. Sect. B Beam Interact. Mater. At. **2,** 814–818 (1984) https://doi.org/10.1016/0168-583X(84)90321-5

[3] A.S. Racz, Z. Fogarassy, P. Panjan, M. Menyhard: *Evaluation of AES depth profiles with serious artefacts in C/W multilayers,* Appl. Surf. Sci. **582,** 152385. (2022) https://doi.org/10.1016/j.apsusc.2021.152385.

[4] A.S. Racz, Z. Fogarassy, U. Kentsch, P. Panjan, M. Menyhard: *Design and production of tungsten-carbide rich coating layers,* Appl. Surf. Sci. **586,** 152818. (2022) https://doi.org/10.1016/j.apsusc.2022.152818.

# APPLICATIONS OF NUCLEAR ELEMENT AND STRUCTURE ANALYSIS TECHNIQUES TO HERITAGE SCIENCE

*Zsolt Kasztovszky, Ildikó Harsányi, Zoltán Kis, László Szentmiklósi, Veronika Szilágyi, Katalin Bajnok, György Káli, Adél Len and Boglárka Maróti*

## *Objective*

In this project, various, mostly non-destructive nuclear methods have been applied to archaeological and art objects, made of rocks, ceramics, glass, and metals. The studies aimed to provide analytical information on their provenance, production technology, or authenticity.

## *Methods*

The applied methods were Prompt-gamma Neutron Activation Analysis (PGAA), neutron and/or X-ray Radiography/ Imaging, Small Angle Neutron Scattering (SANS), Time-of-Flight Neutron Diffraction (TOF-ND), and handheld X-ray Fluorescence Analysis (XRF). The investigated objects have been provided by the Hungarian National Museum, Museum of Fine Arts, and Museum of Ethnography, Budapest. In case of the Aztec Mask study, the investigation was performed in cooperation with the Atomki, the Research Centre for Natural Sciences, and the Institute of Geography and Earth Sciences, Eötvös Loránd University (ELTE).

## *Results*

The sculpture "The Rider" (Museum of Fine Arts, attributed to Leonardo da Vinci)

We elaborated the self-absorption and self-shielding corrections of the Prompt-gamma Activation Imaging (PGAI) results taken at the head of the horse, using a recently developed, Monte Carlo N-Particle Transport (MCNP)-based approach. The complex geometry of the head part, including the casted bronze and the remains of the cast template inside, was taken from the neutron tomograms. Static neutron diffraction of selected inner and outer parts has been performed, too. The results are encouraging, but not yet quantitative. Further steps towards the final evaluation are needed.

19th-century Russian coins

These coins are of great scientific interest as the earliest pieces of bulk platinum materials, produced by chemical and mechanical methods in the St Petersburg mint in the mid-19th century, before the development of high-temperature furnaces for melting. The exact details of the process used at that time are not fully known.

Earlier investigations have shown that the coins contain around 1% iridium and 1-10% iron (trace elements: As Ti, Ni, Cu, Zn, Rh, Pd, and Au). Although our PGAA analyses on these specimens revealed roughly the same components and about 1.5% iron, the occasionally high iron content raises the possibility that the unknown process may have produced strongly magnetic substitutional Fe-Pt phases. Diffraction analysis failed to detect it. The platinum lattice shows extremely small (0.15% and 0.1%) isotropic contractions, perfectly consistent with the calculation based on the amount of the platinum group elements and mainly the copper. Thus, iron dissolution can be excluded. The amount of iron corresponding to the chemical iron content was detected as two-thirds hematite and only one-third magnetite, just above the limit of detection.

Identifying ancient pottery-forming techniques of prehistoric Nubia (Egypt/Sudan)

Neutron and X-ray tomography datasets and petrographic thin sections from experimental vessels have been analyzed using advanced image analysis and statistical techniques. By revealing patterns of preferential particle orientation, these techniques can successfully identify forming techniques, and offer a powerful, non-destructive method for investigating ancient pottery from Nubia and elsewhere. The results are currently being prepared for publication, together with further investigations of the application of machine-learning techniques.

On the authenticity of a Pre-Columbian Aztec Mask (with the Museum of Ethnography)

The wooden base was subjected to biological studies and C-14 dating, the organic glue fixing the tesserae and the inorganic mosaic tesserae were investigated by non-destructive chemical, Fourier-transform Infrared Spectroscopy (FT-IR), Raman, and Portable X-ray Fluorescence (pXRF) spectroscopic methods. Based on the results, the mask was made of an alder species of tree and its age is AD 1492-1653. The whitish covering mosaic plates were proved to be alabaster and claystone. Comparing the turquoise tesserae cover with reference materials, their chemical composition has clearly been differentiated from most of the known turquoise sources of the US Southwest. Based on our results, the Aztec mask proved to be an original piece of art from the 15th-17th century [1].

Analytical studies of Middle- and Late Bronze Age spirals (with the Hungarian National Museum)

A recently excavated Bronze Age burial site (Tumulus culture) near Sükösd shed new light on the potential function and significance of bronze spirals. Continuing our previous cooperation, eleven more objects (bronze spirals and other jewellery) from this newly excavated site (now part of the collection of Türr István Museum, Baja) were analyzed this year with handheld XRF, PGAA and 3D Light Emitting Diode (LED) scanner. The data evaluation is in progress, the results are planned to be published together with those on the bronze spirals measured earlier.

Multi-proxy analysis of ceramics from the Migration Period

Ceramic samples from the 6th-century cemetery of Szólád (Western Hungary) have been analyzed by polarizing light Optical Microscopy (OM), PGAA, Neutron Activation Analysis (NAA), and Scanning Electron Microscopy with Energy Dispersive Spectroscopy (SEM-EDS) to reveal the places of manufacture and the technological choices made during the production [2]. Marble tempered ceramics from Northern Italy have been analyzed to assess the geological origin of the marble used as an additive in 4–14th-century ceramics, using OM, C, and O isotope analysis by Inductively Coupled Plasma Mass Spectrometry (ICP-MS) and SEM [3]. Petrographic and SEM-EDS analysis have been carried out on 6th–7th-century ceramics from Bodajk and neighbouring archaeological sites aiming to better understand technological transfer connected to pottery production in Migration Period in Hungary [4].

In addition to the planned tasks, additional requests were also received and several exciting studies were already carried out. Elemental analysis on a fake late bronze age violin-bow fibula [5], on gold armlets from the Prehistoric Collection of the Hungarian National Museum [6, 7], and complex (imaging, elemental and structural) analysis on an unprecedently well-preserved, recently discovered Carolingian sword from the Thúry György Museum, Nagykanizsa have been done, too. Previous results on the identification of Roman Age glass making technology, based on PGAA, have been published or accepted for publication [8, 9].

## *Remaining work*

Further publications on the "Leonardo's Rider", on the Russian Pt coins, and on the bronze spirals are planned in 2022. Ad hoc cooperations are also foreseen when requests from colleagues of the Museums arise.

## *Related publications*


[1] J. Gyarmati, B. Maróti, Zs. Kasztovszky, B. Döncző, Z. Szikszai, L. E. Aradi, J. Mihály, G. Koch and V. Szilágyi: *Hidden behind the mask: an authentication study on the Aztec mask of the Museum of Ethnography, Budapest, Hungary*, Forensic Science International (submitted)

[2] K. Bajnok, Z. Kovács, J. Gait, B. Maróti, P. Csippán, I Harsányi, D. Párkányi, P. Skriba, D. Winger, U. von Freeden, T. Vida, Gy. Szakmány: *Integrated petrographic and geochemical analysis of the Langobard age pottery of Szólád, Western Hungary,* Archaeological and Anthropological Sciences, accepted manuscript (2021)

[3] L. Maritan, G. Ganzarolli, F. Antonelli, M. Rigo, A. Kapatza, K. Bajnok, C. Coletti, C. Mazzoli, L. Lazzarini, P. Vedovetto, A. Chavarría Arnau: *What kind of calcite? Disclosing the origin of sparry calcite temper in ancient ceramics,* Journal of Archaeological Science **129**, 105358 (2021)

[4] K. Bajnok, E. Pásztor, Gy. Szakmány: *II.9.1. Gyorskorongolt kerámia [Wheel-made pottery].* In: Frigyes Szücsi (ed.): *Avarok és magyarok Bodajkon* [Avars and Magyars in Bodajk]. A Szent István Király Múzeum Közleményei A sorozat 60. / Bulletin du Musée Roi Saint Etienne, Serie A. No. 60., Székesfehérvár 166–176 (2021)

[5] J. G. Tarbay, B. Maróti: *Brass brooch: the late bronze age violin-bowfibula from Esztergom-Dunapart (Komárom-Esztergom county) is a fake*, Archeometriai Műhely, 2021/XVIII./2 (accepted)

[6] J. G. Tarbay, B. Maróti, *Handheld XRF analysis of gold armlets with crescent-shaped terminals from the Prehistoric Collection of the Hungarian National Museum*, Communicationes Archaeologicae Hungariae (accepted)

[7] Several scientific reports

[8] R. Bugoi, A. Ţârlea, V. Szilágyi, I. Harsányi, L. Cliante, Zs. Kasztovszky: *Colour and beauty at the Black Sea Coast: archaeometric analyses of selected small finds from Histria*, Romanian Reports in Physics (accepted)

[9] R. Bugoi, G. Talmaţchi, V. Szilágyi, I. Harsányi, D. Cristea-Stan, S. Boţan, Zs. Kasztovszky: *PGAA analyses on Roman glass finds from Tomis,* Romanian Journal of Physics (accepted)

# APPLICATIONS OF NUCLEAR AND X-RAY ANALYTICAL TECHNIQUES TO CHEMISTRY, MATERIAL AND NUCLEAR SCIENCES

*Boglárka Maróti, László Szentmiklósi, Tamás Belgya, Ildikó Harsányi, Katalin Gméling*

## Objective

We determined the elemental compositions of various kinds of samples using PGAA, PGAI, NAA, and portable XRF methods. The data obtained were useful in catalysis, material-, and heritage science. Our task was the dissemination of these state of the art methods for students of numerous universities.

## Methods

- Prompt Gamma Activation Analysis (PGAA) and Neutron Activation Analysis (NAA) – to determine the bulk elemental composition,
- Portable X-ray Fluorescence instrument (pXRF) – to determine the elemental composition of near-surface regions,
- Education of university students, laboratory exercises, BNC Central European Training School (CETS), preparation of online training materials for Central European Research Infrastructure Consortium (CERIC).

## Results

A complex methodological study of a Sevres ceramic pot: A traditionally decorated porcelain has been manufactured at Sevres, France, and circulated amongst multiple facilities for method benchmarking. We analyzed the porcelain object with radiography, 3D optical scanning, position-sensitive PGAA, and pXRF techniques [1] at multiple positions according to the surface patterns on the porcelain, and additionally at paint-free areas. Besides the main components, such as Si, Al, K, Ca, Na, Fe, and possibly Mg, PGAA was capable to measure Gd, Ti, Mn, Cd, and Nd trace elements. We could differentiate between the blue paint that contained cobalt, the pink and brown manganese-based paints, the red paint which contained $Fe_2O_3$, the green paint which used $Cr_2O_3$, and the golden layers. The results of the pXRF measurements both supported and complemented the PGAA results. At appropriate measurement points, we could achieve almost identical porcelain bulk compositions. This mostly remained true even if we measured the different surface patterns on the porcelains. Most of the differences between the two technique's results could be explained by the differing probing volumes and the detectability conditions of the elements. Our data are found to be compatible with the results of the detailed Particle Induced X ray Emission (PIXE) element mapping made by our French partner at AGLAE (Association Générale Laboratoires Analyse Environnement).

Extension of the pXRF instrument suite: we used so far an Olympus Delta Premium pXRF device, that was found to be excellent for metallic matrices [2], but less capable of detecting light elements. The development of the method during the last decade significantly improved the analytical merits of these devices. After scrutinizing offers from the market-dominant suppliers, and thanks to the Infrastructure Grant of the Hungarian Academy of Sciences, we procured a Brucker Tracer 5g pXRF spectrometer, together with GeoExploration, GeoMining, and Obsidian calibrations, a Helium assembly with tubing, connector; flow-regulator, and a Desktop Stand Kit. In addition, we designed and realized an xyz sample stage, that will be used to create 2D X-ray fluorescence maps of flat objects.

*Figure 1: The new Brucker portable X-ray fluorescence spectrometer and the xyz sample stage*

Upgrade of the prompt-gamma spectroscopy: The internal infrastructure grant of the EK funded the purchased two state-of-the-art ORTEC DSPEC 502A digital gamma spectrometers for use at the PGAA and Neutron-Induced Prompt Gamma-ray Spectroscopy (NIPS) facilities. As they acquire spectra in 64k channels, the spectrum evaluation procedure has to be updated accordingly. The Hypermet-PC used for 25 years is being replaced with the Hyperlab 2021, where several improvements, we suggested to the developer, were implemented.

Catalysis: We contributed to a publication [3] with elemental concentration measurements of In, Ni, Al, Ce in catalysts used in dry reforming of methane. Zeolite catalyst samples provided by ETH Zurich are being measured by PGAA.

## Related publications

[1] *Characterization of decorated porcelain objects by X-ray and neutron-based element-analytical methods,* Master thesis of Sz. Csákvári, ELTE TTK Department of Analytical Chemistry, 2021, supervised by: L. Szentmiklósi, B. Maróti

[2] B. Maróti, G. Káli: *Non-destructive characterization of bronze objects from Ráksi and the Pusztasárkánytó depot find,* Acta Archaeologica Academiae Sci. Hung., **72(1)** http://dx.doi.org/10.1556/072.2021.00002

[3] A. Horváth, M. Németh, A. Beck, B. Maróti, G. Sáfrán, G. Pantaleo, L. F. Liotta, A. M. Venezia, V. La Parola: *Strong impact of indium promoter on Ni/Al2O3 and Ni/$CeO_2$-$Al_2O_3$ catalysts used in dry reforming of methane,* Applied Catalysis A: General, **621,** 118174 (2021)

[4] T. Belgya, L. Szentmiklósi*: Monte-Carlo calculated detector response functions to unfold radiative neutron capture spectra,* Nucl. Instr. Meth A. **991,** 165018 (2021) http://dx.doi.org/10.1016/j.nima.2021.165018

# MATERIALS SCIENCE APPLICATIONS OF NEUTRON SCATTERING

*Adél Len, Katalin Bajnok, Indu Dhiman, Zoltán Dudás, Bence Fehér, John Gait, György Káli, Dániel Merkel, Alex Szakál, Renáta Ünnep*

## Objective

Small Angle Neutron Scattering (SANS) has been applied to characterize the nanostructure of polyurethane and methyl substituted silica xerogel drug delivery systems, to study the hydration mechanism of calcium alginate aerogels, to study red fluorescent albumin proteins, to study photosynthetic membrane systems, and vessel forming techniques of archaeological interest. Neutron reflectometry has been used to study the nanostructure of functional thin films and membranes. Various neutron scattering studies have been performed as part of an international user program of the Budapest Neutron Centre.

## Results

*Nanostructure of drug delivery systems*

Polyurethane (PU) nanoparticles have been synthesized by using a polyaddition process. The samples of acyclovir-loaded and unloaded PU nanoparticles were investigated in terms of their encapsulation efficacy and their drug release profile using Fourier-transform Infrared Spectroscopic (FT-IR) spectra, Scanning Electron Microscopy (SEM), Small Angle Neutron Scattering (SANS), thermal analysis, and in vivo skin irritation. The inexpensive raw materials, the biocompatibility of the final products, the easy pathway to synthesize particles, as well as the facile modulation of the drug release profile are advantages of great significance for the use of polyurethanes for the transmembrane transfer of the antiherpetic agent. [1]

A multi-analytical approach involving nitrogen porosimetry, small angle neutron and X-ray scattering, FT-IR and nuclear magnetic resonance spectroscopies, X-ray diffraction, thermal analysis and electron microscopy was used to study organically modified silica-based xerogels obtained through the sol–gel process. The combined use of structural characterization methods allowed us to determine the relation between the cavity dimensions, the synthesis pH value and the grade of methyl substitution. The effect of the structural properties on the controlled Captopril release efficiency has also been tested. This knowledge facilitates tailoring the pore network for specific usage in biological/medical applications. [2]

*Hydration of aerogels studied by SANS*

The importance of exploring the mechanism of hydration and hydration induced structural changes of hydrophilic porous materials and the understanding of the alteration of the macroscopic properties of these materials in relation to both air humidity and aqueous environments has increased in the past few years. As a result of the present work it has been found that the stiffening of the Ca-alginate aerogel (CaAG) is due to the formation of new superstructures in the hydrated backbone. Adopting the results to humid air revealed that the solid backbone and the porous structure of CaAG are not altered significantly even at 100% relative humidity (Fig.1) because the water content of the equilibrated aerogel matrix does not reach its critical hydration level. [3]

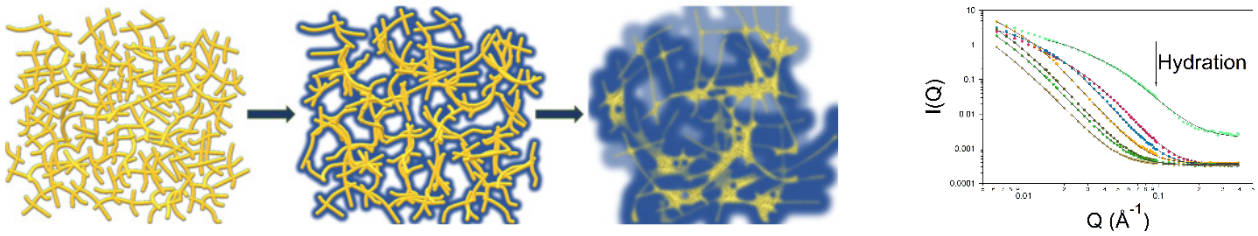


*Figure 1: Scheme of the hydration of CaAG (left side), SANS curves of hydrated CaAG (right side)*

The nanomorphology of native Ca-alginate aerogels and nanoporous polyurea-cross-linked Ca-alginate (X-Ca-alginate) aerogels were investigated using SEM, $N_2$-sorption porosimetry, and contrast variation SANS. Cross-linking of the X-Ca-alginate aerogels with an aliphatic triisocyanate leads to the formation of a dense polyurea layer over the primary nanoparticles. The process leaves the primary Ca-alginate structure undisturbed, while it does affect the structure at the most fundamental level, increasing the primary particle size and reducing the porosity. The different fundamental skeletal nanostructures of X-Ca-alginate aerogels affect not only their material properties but also their potential for application in environmental remediation. [4]

*Blood derived red fluorescent bioconjugates*

The aim of the project was the joining of red fluorescent proteins to liposomes with a natural origin. For this purpose, a detailed description of the protein system is required. Since the binding of protein to the surface of liposomes can be achieved by the addition of salts, the first task was the investigation of the effect of salt on an artificial polyelectrolyte. Detailed Small Angle X-ray Scattering (SAXS) investigations were performed which showed the specific adsorption of inert electrolytes on the surface of macromolecules [5]. Furthermore, the synthesis method of the desired liposomes was also tested with several techniques such as SAXS, FT-IR, circular dichroism (CD), Dynamic Light Scattering (DLS). The results will be submitted to the Journal of Colloids and Interfaces B and Nanomaterials this year.

*Polyester/Graphite Percolating Composite: Structural and Dielectric Analyses*

The structural characterization of a percolating composite of graphite particles with different concentrations in a polyester (PE) matrix was performed [6]. The graphite-PE interface showed surface fractal behaviour. The fractal dimension was the same for all samples. The average pore/crack size was found to be significantly larger when the graphite concentration was above the percolation threshold.

*Photosynthetic membrane systems*

The effect of salt stress in *Euglena gracilis* cells has been studied by the group. Changes in macro-organisation of thylakoid membranes due to salt treatment have been studied by SANS and electron microscopy. It is proposed that the changes in thylakoid membrane organisation, pigment composition and polysaccharides help the adaptation of cells to salt stress [7]. The *Mentha spicata crispa* "Moroccan" cultivar tolerates low salinity levels up to 50 mM NaCl concentrations. Interestingly, in an almost fully dry leaf section, the thylakoid membrane structure was relatively well retained, but, the periodic organisation was partially lost for rooted spearmint treated with 150 mM NaCl [8].

*Nanostructure of functional thin films and membranes*

Due to the inoperative cold neutron beam source during (almost) the entire year, measurement possibilities decreased drastically at the GINA neutron reflectometer. Several scientific groups applied for beam time, but they had to be refused, since the beam intensity without the cold source was about one order of magnitude lower than normal, and not suitable for such complex experiments.

However model planar interfaces between solid electrodes and liquid electrolytes were investigated. These included contrast-variation experiments involving isotopic substitution in the electrolyte and enhancing the sensitivity of the method to probe the structure of thin layers formed on the electrode surface [9]. The structure–function correlations of purified extracellular vesicles in interaction with model membrane systems of variable complex compositions and experiments to spot the role of different membrane phases on the vesicle internalization routes were also studied by neutron reflectometry [10].

*Late Bronze Age hoard from the Velem-Szent Vid hillfort*

The study discusses an unpublished bronze hoard from the famous West Hungarian archaeological site: Velem-Szent Vid (Transdanubia, Vas County). This small Ha B1 assemblage contains a spearhead with remains of the wooden shaft, a sickle, and three different types of ingots. The aim was a comprehensive structural and compositional characterization of the preserved objects from the hoard exclusively by means of non-invasive and non-destructive analytical, structural, and imaging techniques (X-ray Fluorescence Spectroscopy, Prompt Gamma Activation Analysis, Time of Flight – Neutron Diffraction (TOF-ND), Neutron Imaging, X-ray Imaging). The spearhead and the ingots were studied from production to deposition TOF-ND has been used to identify the chalcocite ($Cu_2S$), which points to the possible origin of the raw material or production method (smelting) [11].

*Technological investigations of ancient archaeological pottery*

Further investigations using SANS have been carried out in order to obtain information about ancient pottery making practices. Our projects were focused on developing new methodologies for differentiating between ancient pottery forming techniques and furthermore, to investigate the firing conditions, and especially, the maximum firing temperature of archaeological vessels [12]. During 2021 the SANS measurements were complemented by polarising light optical microscopy and X-ray diffraction. Furthermore, preparations have been made to apply the developed non-destructive SANS methods to an archaeological assemblage from the late Roman fortification of Ságvár and Keszthely, Hungary. The measurements have been postponed due to the pandemic.

*International user program of the Budapest Neutron Centre*

Despite the COVID pandemic, user measurements have been performed on various topics at SANS, GINA, Time of flight (TOF-ND) and Material Test Diffractometer (MTEST) instruments. The following studies have been published in 2021: Small angle neutron scattering study of the nanoscale structure of low-carbon steel after rolling with shear followed by cold drawing [13]; Hybrid silica materials were used for fuchsine-b colour removal from wastewaters [14].

A Time of Flight Small Angle Neutron Scattering (FSANS) instrument mechanical and electronic control system upgrade has been performed. The Yellow Submarine SANS instrument sample environment has also been developed.

## *Remaining work*

The studies on kinase and phosphatase Arabidopsis mutant are still not finished due to the COVID travelling restrictions. Studies on various types of silicagels, on thin films and archaeological ceramics will be continued. The FSANS upgrade will continue with the control and data treatment software development.

## *Related publications*

[1] F. Borcan, A. Len, C.A. Dehelean, Z. Dudás, R. Ghiulai, A. Iftode, R. Racoviceanu, C.M. Soica: *Design and assessment of a polyurethane carrier used for the transmembrane transfer of acyclovir*, Nanomaterials **11(1)**, 51 (2021)

[2] A. Len, G. Paladini, L. Románszki, A. Putz, L. Almásy, K. László, Sz. Bálint, A. Krajnc, M. Kriechbaum, A. Kuncser,J. Kalmár, Z. Dudás: Physicochemical characterization and drug release properties of methyl-substituted silica xerogels made by sol-gel process, Int. J. of Mol. Sci. **22(17)**, 9197 (2021)

[3] A. Forgács, V. Papp, G. Paul, L. Marchese, A. Len, Z. Dudás, I. Fábián, P. Gurikov, J. *Kalmár: Mechanism of Hydration and Hydration Induced Structural Changes of Calcium Alginate Aerogel*, ACS Applied Materials & Interfaces **13(2)**, 2997 (2021)

[4] P. Paraskevopoulou, G. Raptopoulos, A. Len, Z. Dudás, I. Fábián, J. Kalmár: *Fundamental Skeletal Nanostructure of Nanoporous Polymer-Crosslinked Alginate Aerogels and its Relevance to Environmental Remediation*, ACS Applied Nanomaterials (*in press*) (2021)

[5] B. Fehér, I. Varga, J. S. Pedersen *Effect of concentration and ionic strength on the lower critical solution temperature of poly(N-isopropylacrylamide) investigated by small-angle X-ray scattering,* Soft Materials (2021)

[6] R. Belhimria, S. Boukheir, Z. Samir, Z. A. Len, A. Szakál, M. El Hasnaoui, M. ; M. E. Achour, N. Éber, L.C. Costa, A. Oueriagli: *Polyester/Graphite Percolating Composite: Structural and Dielectric Analyses*, J. OF Electronic Materials **50**, 6920 (2021)

[7] S. D. Kanna, I. Domonkos, T. O. Kóbori, Á. Dergez, K. Böde, S. Nagyapáti, O. Zsiros, R. Ünnep, G. Nagy, G. Garab, L. Szilák, K. Solymosi, L. Kovács and B. Ughy: *Salt Stress Induces Paramylon Accumulation and Fine-Tuning of the Macro-Organization of Thylakoid Membranes in Euglena gracilis Cells,* Front. Plant Sci. **12** (2021)

[8] R. Ounoki, F. Ágh, R. Hembrom, R. Ünnep, B. Szögi-Tatár, A. Böszörményi, K. Solymosi: *Salt Stress Affects Plastid Ultrastructure and Photosynthetic Activity but Not the Essential Oil Composition in Spearmint (Mentha spicata L. var. crispa "Moroccan"),* Front Plant Sci. **29(12),** (2021)

[9] F. Perissinotto, V. Rondelli, B. Senigagliesi, Brocca, L. Almásy, L. Bottyán, D.G. Merkel, H. Amenitsch, B. Sartori, K. Pachler et al.: *Structural insights into fusion mechanisms of small extracellular vesicles with model plasma membranes*, Nanoscale **13**, 13158 (2021)

[10] Y.N. Kosiachkin, I.V. Gapon, A.A. Rulev, E.E. Ushakova, D. Merkel, L.A. Bulavin, M.V. Avdeev, D.M. Itkis: *Structural Studies of Electrochemical Interfaces with Liquid Electrolytes Using Neutron Reflectometry: Experimental Aspects*, J. of Surface Investigation: X-ray Synchrotron and Neutron Techniques **15**, 787 (2021)

[11] JB. Tarbay, B. Maróti, Z. Kis, Gy. Káli, L. Szentmiklósi: *Non-destructive analysis of a Late Bronze Age hoard from the Velem-Szent Vid hillfort*, J. of Archaeological Science **127**, 105320 (2021)

[12] A. Len, K. Bajnok, J. Füzi: *Small-Angle Neutron Scattering for Cultural Heritage Studies.* In: S. D'Amico, V. Venuti (eds.): *Handbook of Cultural Heritage Analysis*, Springer International Publishing, 2022 (accepted manuscript)

[13] A. Zavdoveev, A. Len, E. Pashinska: *Small Angle Neutron Scattering Study of Nanoscale Structure of Low-Carbon Steel After Rolling with Shear Followed by Cold Drawing,* Metals and Materials Internationsl **27(3)**, 481 (2021)

[14] I. Fratilescu, Z. Dudás, M. Birdeanu, C. Epuran, D. Anghel, I. Fringu, A. Lascu, A. Len, E. Fagadar-Cosma: *Hybrid silica materials applied for fuchsine B colour removal from wastewaters*, Nanomaterials **11(4)**, 863 (2021)

# ELUCIDATION OF STRUCTURAL ASPECTS OF IRON-BASED MATERIALS VIA MÖSSBAUER SPECTROSCOPY AND OTHER METHODS

*Zoltán Klencsár, Sándor Stichleutner, Károly Lázár*

## *Objective*

We aim to gain insights into the structure and composition of diverse iron-based materials of interest, such as swift heavy ion irradiated FINEMET-type ribbons and $^{57}$Fe thin films, $Nd_{0.6}Sr_{0.4}Fe_xMn_{1-x}O_3$ perovskites, and frozen solutions of iron(III) citrate.

## *Methods*

Besides Mössbauer Spectroscopy (MS) we have also utilized other complementary methods such as magnetization measurements, High-resolution Transmission Electron Microscopy (HRTEM), Scanning Electron Microscopy (SEM), X-ray Diffractometry (XRD), and Electron Magnetic Resonance (EMR) spectroscopy.

## *Results*

$^{57}$Fe transmission and Conversion Electron Mössbauer Spectroscopy (CEMS), as well as XRD, were used to study the effect of swift heavy ion irradiation on stress annealed FINEMET samples with a composition of $Fe_{73.5}Si_{13.5}Nb_3B_9Cu_1$. Changes in the magnetic anisotropy both in the bulk as well as at the surface of the FINEMET alloy ribbons after irradiation by 160 MeV Xe ions with a fluence of $10^{13}$ ion/cm$^2$ were revealed via the decrease in relative areas of the 2$^{nd}$ and 5$^{th}$ lines of the magnetic sextets in the corresponding Mössbauer spectra.

Magnetization measurements were performed on 100 Å thick $^{57}$Fe thin films vacuum deposited onto $SiO_2$/Si wafers and irradiated with 160 MeV Xe ions with a fluence of $5 \cdot 10^{13}$ ion/cm$^2$ to facilitate the identification of the newly formed phases evidenced by $^{57}$Fe CEMS measurements. The magnetization measurements recorded at temperatures of 280 K and 5 K, in external magnetic fields ranging from −5 to +5 T, showed hysteresis loops typical of spin-glass materials, including also those having superparamagnetic behaviour. By correcting for the diamagnetic contribution originating from the substrate, the hysteresis curves match those obtained for sonochemically prepared amorphous iron, thus confirming the existence of the amorphous iron phase detected by Mössbauer spectra in the swift heavy ion irradiated $^{57}$Fe thin films [1,2].

A sample created via an electric explosion of amorphous $Fe_{73.5}Zr_{15.5}B_7Nb_3Cu_1$ (FINEMET-type) ribbons in water was investigated with SEM, HRTEM, and $^{57}$Fe Mössbauer spectroscopy. It was found that the original amorphous state of the ribbons is in part preserved in the resulting samples [3].

The aqueous speciation of $^{57}$Fe enriched iron(III) citrate was studied on frozen solutions using $^{57}$Fe MS and Electron Magnetic Resonance (EMR) spectroscopy. By measuring solutions with a pH = 5.5 at five different Fe:citrate molar ratios ranging from 1:100 to 1:1, the combined application of MS and EMR allowed us to distinguish signals of mononuclear and polynuclear complex species in the samples. The obtained spectra showed the correlation between citric acid concentration and the fraction of iron coordinated as a mononuclear complex. At high Fe:citrate ratios the concentration of the monomer is negligible, but it gradually increases as the ratio is lowered. In the frozen samples, monomers appeared to be the dominant species when the Fe:citrate ratio was lowered to 1:50 and below [4,5].

The effect of iron doping on the structural and magnetic properties of the manganite perovskites $Nd_{0.6}Sr_{0.4}Fe_xMn_{1-x}O_3$ ($0.1 \le x \le 1.0$) was studied by the means of $^{57}$Fe MS, XRD, Transmission Electron Microscopy (TEM), SEM, and FC/ZFC (field-cooled/zero field-cooled) magnetization measurements. As revealed by $^{57}$Fe Mössbauer spectroscopy, iron up to $x = 0.6$ enters this system mainly as high-spin $Fe^{3+}$, substituting $Mn^{3+}$ at the octahedral B sites of the perovskite structure and thereby reducing the $Mn^{3+}$ : $Mn^{4+}$ ratio. The introduction of iron into the system proved to be detrimental to the ferromagnetism associated with $Mn^{3+}$ – $Mn^{4+}$ double exchange, leading to the simultaneous decrease of both the Curie temperature and the magnetization levels. At low iron concentrations this effect may be associated mainly with the depletion of mobile electrons from the Mn-rich regions, given that in contrast with $Mn^{3+}$, $Fe^{3+}$ does not contribute with mobile electrons to maintain double exchange and the associated ferromagnetism in the Mn subsystem. Above $x = 0.6$, the Mössbauer spectra demonstrate the presence of paramagnetic $Fe^{4+}$ ions in the samples at room temperature, which undergo charge disproportionation at lower temperatures, leading to the appearance of $Fe^{5+}$ ionic species at 78 K. Mössbauer spectrum components associated with $Fe^{3+}$ rich antiferromagnetic regions exhibit considerable absorption peak broadening both at 295 K and 78 K, revealing the presence of a multitude of magnetic and electronic states of iron even in these regions [6].

## *Remaining work*

Additional swift heavy ion irradiations of the opposite (wheel) side of the FINEMET ribbons and higher fluences for the 100 Å thick $^{57}$Fe thin films vacuum deposited onto $SiO_2$/Si wafers are in progress to facilitate further changes in magnetic anisotropy and increase the rate of radiation-induced metastable phase formation.

The combined application of $^{57}$Fe MS and EMR methods proved to be particularly effective in the clarification of the origin of different spectral components obtained in the measured spectra of frozen solutions of iron(III) citrate. The same methodology may also be advantageously utilized to perform similar studies on analogous Fe(III) based solutions.

## *Related publications*


[1] E. Kuzmann, K. Nomura, S. Stichleutner, A. Nakanishi, J. Pechousek, L. Machala, Z. Homonnay, V.A. Skuratov, R. Vondrasek, L. Krupa, O. Malina, T. Ingr, S. Kubuki: *Fe-Si oxides and amorphous iron formed in $^{57}$Fe layer vacuum deposited on $SiO_2$/Si due to swift heavy ion irradiation*, Mössbauer Spectroscopy from Magnetic Nanoarchitectures to Environmental Science, 22-26 August, 2021, Atlanta, USA, Abstract ID: 3585606

[2] E. Kuzmann, K. Nomura, S. Stichleutner, A. Nakanishi, J. Pechousek, L. Machala, Z. Homonnay, V.A. Skuratov, T. Ingr, L. Krupa, O. Malina, R. Vondrasek, S. Kubuki: *Nagyenergiájú nehézion besugárzás hatására létrejövő amorf vas és szuperparamágneses Fe-Si oxidok $SiO_2$/Si szubsztrátra párologtatott $^{57}$Fe vékonyrétegben*, Őszi Radiokémiai Napok 2021, 18-20 October, 2021, Balatonszárszó, Hungary, Conf. Program and Book of Abstracts, ISBN 978-615-6018-07-6, p. 16

[3] K. Lázár, L.K. Varga, V. Kovács-Kis, S. Stichleutner, T. Fekete, A. Tegze, Z. Klencsár: *Electric explosion of amorphous iron alloy ribbons in water and glycol*, Mössbauer Spectroscopy from Magnetic Nanoarchitectures to Environmental Science, 22-26 August, 2021, Atlanta, USA, Abstract ID: 3595199

[4] M. Gracheva, Z. Homonnay, Z. Klencsár, K. Kovács: *Spectroscopic studies of iron(III) citrate complexes in aqueous solution*, In: Greculeasa, Simona; Locovei, Claudiu; Kuncser, Victor (eds.) International Conference on the Applications of the Mössbauer Effect - Book of Abstracts ICAME 2021, p. 232. (2021)

[5] M. Gracheva, Z. Klencsár, Z. Homonnay, K. Kovács: *Spectroscopic studies of iron(III) citrate complexes in aqueous solution*, Őszi Radiokémiai Napok 2021, 18-20 October, 2021, Balatonszárszó, Hungary, Conference Program and Book of Abstracts, ISBN 978-615-6018-07-6, pp. 56-61. (2021)

[6] I.Z. Al-Yahmadi, Z. Klencsár, A.M. Gismelseed, F. Al Ma'Mari: *Structural, magnetic and Mössbauer studies of $Nd_{0.6}Sr_{0.4}Fe_xMn_{1-x}O_3$ perovskites, Materials Chemistry and Physics* ***267****, 124619 (2021)*

# SPECTRAL TUNING OF BIOTEMPLATED ZNO PHOTONIC NANOARCHITECTURES FOR PHOTOCATALYTIC APPLICATIONS

*Gábor Piszter, Krisztián Kertész, Gergely Nagy, Zsófia Baji, Zsolt Bálint, Krisztina Frey, Kornél Fél, Tünde Tóth, József Sándor Pap, László Péter Biró*

## Objective

The aim of the project was to investigate the use of various butterfly wings coloured by photonic nanoarchitectures in different spectral ranges for testing the photocatalytic efficiency of the biotemplated, conformal ZnO nanoarchitectures in photocatalytic decomposition of rhodamine B (Rh B) as a model dye.

## Methods

The photonic nanoarchitectures of *Arhopala asopia*, *Hypochrysops polycletus*, *Morpho sulkowskyi*, and *Polyommatus icarus* butterflies were used as biotemplates. Atomic layer deposition (ALD) of 10, 15, and 20 nm thick ZnO layers was carried out at 100 °C growth temperature since the wing samples were thermally sensitive. Scanning and cross-sectional electron microscope images were taken from the resulted biotemplated structures. Optical reflectance measurements were conducted using a fibre optic Avantes system consisting of an AvaSpec-HERO spectrophotometer, a stabilized UV–Vis light source, and an integrating sphere for light collection. The photocatalytic activity was evaluated based on the decomposition of Rh B (15 μM) in its unbuffered solution upon illumination using ultrapure water as solvent. The uncoated and ZnO coated samples were placed vertically in 20 mL of the Rh B solution in a glass cuvette with magnetic stirring. A heat free 300 W Xenon lamp was used for the illumination, while the rate of degradation was followed by an Agilent Cary 60 UV–Vis spectrophotometer equipped with an immersion probe that was placed inside the solution.

## Results

ALD coated butterfly wings exhibited characteristic reflectance spectra as seen in Fig. 1A, and the spectral shift increased with a different degree with the increasing thickness of the deposited ZnO layer (Fig. 1B). For example, for *P. icarus* and *H. polycletus*, the spectral position of the reflectance maximum was shifted 70-80 nm, while for *M. sulkowskyi*, about 50 nm. Therefore, the reflectance spectra could be tuned to overlap with the absorption peak of the Rh B (dashed line in Fig. 1A) which resulted in differences in the photocatalytic decomposition of the test dye. To demonstrate the greater decomposition efficiency of the biotemplated samples over the flat glass samples, the conversion rates of photodecomposition of Rh B over uncoated glass, ZnO coated glass, pristine *M. sulkowskyi* wing and *M. sulkowskyi* wing with 15 nm conformal ZnO coating, are plotted as a function of reaction time (Fig. 1C). The ZnO coating increased the reaction rate in the case of flat glass by a factor of 2.3, and for ZnO coated M. *sulkowskyi* wing as compared with the pristine wing by a factor of almost 2, while the pristine wing exhibited a roughly four-fold increase as compared to the flat glass. The magnitude of the decomposition rate was also proportional with the overlap between the reflectance peak of the biotemplated ZnO nanoarchitecture and the absorption band of Rh B. The results show that biotemplated semiconductor thin films promise enhanced photocatalytic activity which is worth further investigation.

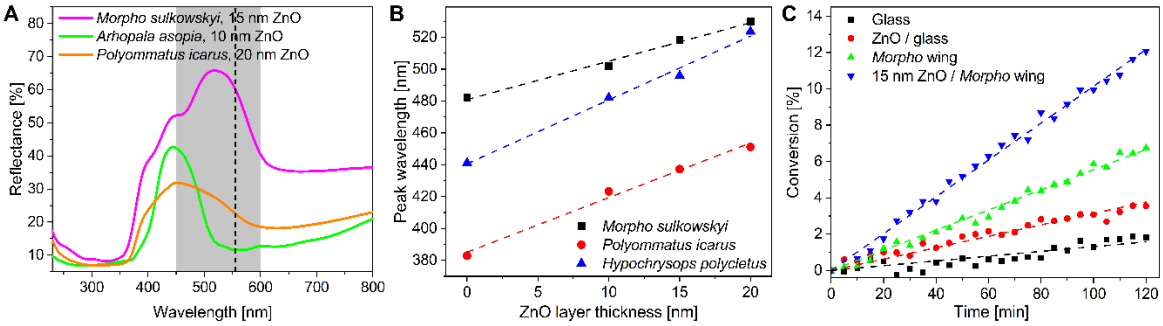


*Figure 1: (A) Reflectance spectra of butterfly wings covered by conformal ZnO thin films. The grey band marks the Rh B absorption range, while the dashed line indicates the absorption maximum. (B) Peak shift of the reflectance spectra of different butterfly wings with the increasing thickness of the deposited ZnO layer. (C) Reaction rate versus time for bare glass, ZnO covered glass, pristine M. sulkowskyi wing, and 15 nm ZnO covered M. sulkowskyi wing.*

## Remaining work

According to our plans, the photocatalytic activity of $TiO_2$-coated biotemplated samples will be explored, similar to what was carried out with ZnO. The outcome of the two sets of experiments will be compared, and the further analysis of the decomposition products will be carried out using Gas Chromatography–Mass Spectrometry (GC-MS). We also plan to test the decomposition efficiency for other dyes.

## Related publication

[1] G. Piszter et al.: S*pectral tuning of biotemplated ZnO photonic nanoarchitectures for photocatalytic applications*, Molecules, under review

# NEUTRON AND X-RAY RADIOGRAPHY AND TOMOGRAPHY AT THE BUDAPEST NEUTRON CENTRE

*Zoltán Kis, László Horváth, László Szentmiklósi*

## *Objective*

We developed and used imaging instrumentation and methodology at the Budapest Neutron Centre (BNC).

## *Methods*

Thermal and cold neutron, as well as X-ray imaging in 2D and 3D, volume rendering, Monte Carlo simulation.

## *Results*

The final design and a detailed CAD assembly of the *neutron beam filter* were completed (*Fig.1 a*), and all parts of the new automatic system were purchased or manufactured. This system will provide computer-controlled beam formation in the thermal, epithermal, and fast energy regime, too. The assembly and first tests of this setup have been started.

We studied an unpublished *bronze hoard* from the famous West Hungarian archaeological site: Velem - Szent Vid [1] using neutron and x-ray imaging. The spearhead and the ingots were studied from production to deposition. Our results suggest that the spearhead was a good quality casting with an extremely low porosity (*Fig.1 b*). The X-ray radiography of a *unique bronze sculpture* (*Fig.1 c*) from the 16th century (one of the three Mors allegories in the world) has shed some light on its manufacturing technique. After the preliminary data analysis, further investigation of the object by neutrons is foreseen.

Using *dynamic neutron radiography,* the inflow of a silicon-based material into an automobile shock absorber was studied with temporal and spatial resolution. It was the first successful attempt to obtain experimental values for the characterization of this dynamic loading process. (*Fig.1 d)*. Using the same methods, we studied the dynamic two-phase flow in a heat-pipe cooling system in the development stage (*Fig.1 e*), which uses a new cooling agent that does not contribute to global warming.

In the foreseeable future, the biological shielding of the measurement stations around the reactor will be reconstructed. *Monte Carlo simulations* of the new shielding design of the RAD station (Static/dynamic thermal-neutron and X-ray imaging station) were carried out to assess its radiation-shielding effectiveness while considering at the same time technical, mechanical, and financial constraints. A series of Monte Carlo N-Particle Transport (MCNP) simulations from conceptual to detailed CAD-based setups were carried out providing data for the final architectural design. The neutron and gamma radiation dose maps were calculated with a 10×10×10 $cm^3$ spatial resolution *(Fig.1 f and g,* respectively*),* and the shielding properties were found to be in line with the applicable legal dose rate limits.

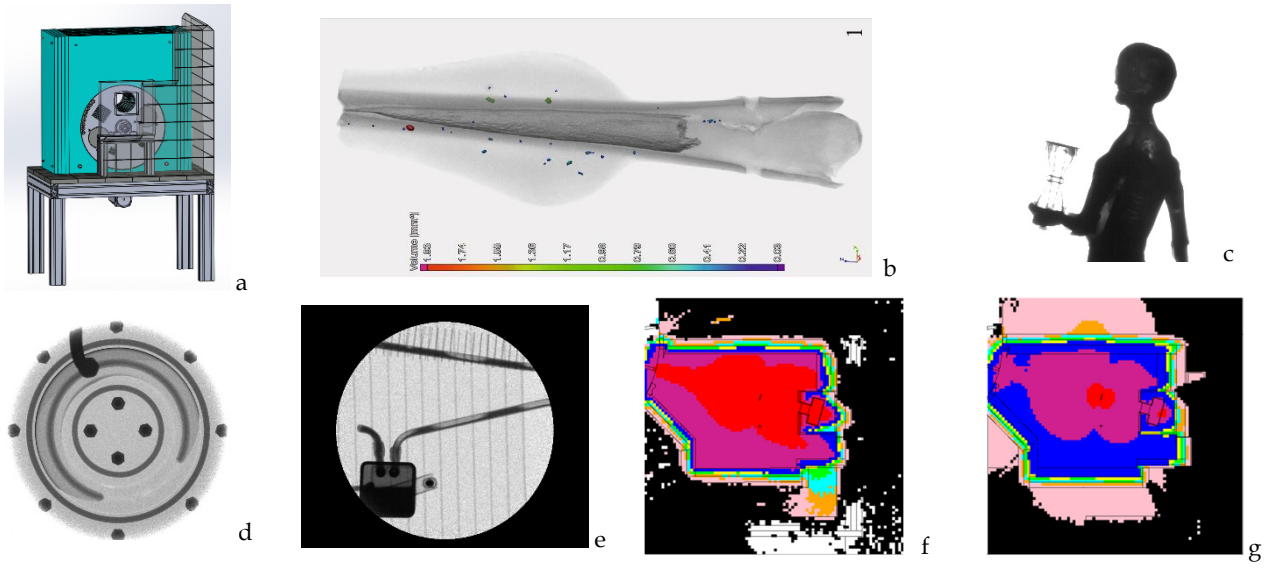


*Figure 1: Neutron and X-ray imaging results: see text for further information*

## *Related publications*

[1] J.G. Tarbay, B. Maróti, Z. Kis, G. Káli, L. Szentmiklósi: *Non-destructive analysis of a Late Bronze Age hoard from the Velem-Szent Vid hillfort.* J. Archaeol. Sci. **127,** 105320 (2021)

[2] D. Molnár, G. Gyarmati, P. Barkóczy, B. Maróti, Z. Kis, C. Bíró, J.G. Tarbay: *Késő bronzkori tokosbalta komplex öntéstechnikai vizsgálata,* Bányászati és Kohászati Lapok Kohászat **2,** 14–19 (2021)

# ALTERNATIVE TESTING METHODS FOR CONCRETE

*Viktória Sugár, Lama Basem A. AlNatour*

## *Objective*

It is necessary to test a concrete structure to determine its quality and ability to serve its designed purpose. Neutron or gamma irradiation of concrete may change its mechanical or structural properties. The estimation of mechanical properties of concrete can be carried out by several methods from destructive, partially destructive and non-destructive test (NDT) methods. Ideally it would be best to use the common (destructive) methods for an irradiated concrete specimen to test mechanical and structural properties of the concrete mix and have results to compare before and after radiation. Since the destructive methods might not be applicable in some cases where the concrete has a large amount of activity, or the concrete is in a structure which cannot be allowed to be destroyed, we will overview other types of either partially or non-destructive methods for the purpose of studying concrete behaviour after exposure to radiation.

## *Methods*

As a literature review, the current study includes the explanation of the following sections and methods: Destructive testing methods and its general concept are briefly explained; partially destructive methods are briefly overviewed with examples; non-destructive methods are properly introduced and thoroughly explored. Visual inspection, the main and most important technique for testing concrete in general is briefly reviewed. A well trained professional would be able to perform this inspection without the need for any further equipment. The half-cell electrical potential method is used to detect the corrosion potential of reinforcing bars in concrete. The Schmidt/rebound hammer test is used to evaluate the surface hardness of concrete. The carbonation depth measurement test is used to determine whether moisture has reached the depth of the reinforcing bars and hence corrosion may be occurring. The permeability test measures the flow of water through the concrete. The Windsor probe test (Penetration resistance) is used to measure the surface hardness and hence the strength of the surface and near surface layers of the concrete. Cover metre testing is used to detect voids in the concrete and the position of stressing ducts. Radiographic testing is used to detect voids in the concrete and the position of stressing ducts. Ultrasonic pulse velocity testing is mainly used to measure the sound velocity of the concrete and hence the compressive strength of the concrete. Impulse radar testing (Ground penetrating radar) is used to detect the position of reinforcing bars or stressing ducts. Infrared thermography is used to detect voids, delamination and other anomalies in concrete and also to detect water entry points in buildings. Resistivity Measurement is one of many techniques which is used to assess the corrosion risk or activity of steel in concrete. A 4 year experimental plan project of the ENDE project is: Comparison between NDT methods; Comparison between destructive and non-destructive methods. The various techniques for measuring the compressive strength and modulus of elasticity were presented from destructive and non-destructive tests on concrete specimens. These are specimen size and testing methods and other tests.

## *Results*

Various NDT methods based on different principles, with their individual merits and limitations have been discussed.

It has been recognized that NDT plays an important role in condition assessment of existing structures, and there has been an urgent need for developing standards for performing NDT methods and for interpretation of NDT results.

A comparison between destructive and non-destructive testing was included in this paper that concluded the following: The difference between the values of resistance obtained by destructive and non-destructive tests decreased considerably at the age of 28 days. Imaging ultrasonic pulse echo methods have the highest potential for progress in the non-destructive evaluation of structural discontinuities in thick and highly reinforced concrete similar to the concrete used in nuclear power plants.

The major advantage of NDT methods has been recognized as their capability to test in situ. A great deal of expertise is required for interpretation of NDT field observations and test results. A combination of different available NDT methods is a better way to assess the structures.

There is an intense need for a standard on the methods of non-destructive testing, with guidelines on testing methods, technologies and technical requirements for each test, and a guidance in terms of the use for each method to meet a certain criteria, and recommendations to assist the user of a specific technology to obtain the results needed to move forward with their work.

NDT provides useful information by revealing hidden or unknown defects, and repair or replacement of reinforced concrete (RC) structures can be planned according to NDT results.

Based on the existing data, various types of deterioration of concrete strength due to neutron irradiation were confirmed.

Before a system of evaluating concrete soundness under irradiation can be applied, further experimental data and scientific background are necessary.

The determination of sample size, mixture proportion, and concrete components are discussed.

The aggregate sizes and material of existing literature are discussed and analysis data are included.

## *Remaining work*

We'll continue the above study, the applicability of the methods in the EK's Reactor should be analyzed.

# THE EFFECT OF THE CHEMICAL COMPOSITION OF CONCRETE ON ITS LONG-TERM PERFORMANCE IN AN IRRADIATED ENVIRONMENT (V4-KOREA RADCON)

*I. Harsányi, Z. Kis, A. Horváth, K. Gméling, V. Szilágyi, L. Szentmiklósi*

## *Objective*

The aim was to recommend raw materials for radiation-resistant, durable concretes with low activation susceptibility, for use in the future nuclear power plant Paks II.

## *Methods*

Elemental composition measurements using Prompt Gamma Activation Analysis (PGAA), Neutron Activation Analysis (NAA), and portable XRF Spectrometer (pXRF). Computer simulations using the MCNP6 and FISPACT codes. Formal data analysis.

## *Results*

1) Material characterization of concrete raw materials for RADCON partners

We determined elemental compositions of limestone- and cement samples for our Slovakian partners, to predict their usefulness for neutron and gamma-ray shielding components in concretes [1]. We also measured the compositions of concrete components, e.g. sand, gravel, numerous additives, and binders originating from Hungarian mines and domestic suppliers [2], which are all candidates for use in hydrate and heavy concrete. The analysed gravels [3] and also the magnetite have relatively high Cobalt contents, which must be considered when using them as shielding-concrete constituents. The Budapest Research Reactor (BRR) was unfortunately not running between March and September 2021 due to the COVID-19 pandemic, technical and human resource issues, and this *vis major* resulted in delays in the experimental work.

(2) Computer simulations to estimate the neutron-activation of concrete

The combination of MCNP6 [4] and the FISPACT [5] computer codes was found to be adequate to create accurate inventories of the radioisotopes induced by neutron irradiation. Realistic input data for these codes were developed for the shielding concrete materials based on the concentrations from PGAA, NAA and pXRF measurements, and hence containing the precursor elements of all the dominant radioisotopes [6]. The calculated simulation results were validated against measured data of neutron irradiation experiments at the BRR. For this purpose, the complete model of the BRR active zone and irradiation sites were created in the MCNP6 code. The energy- and spatial distributions of the neutron field in the No. 17 vertical irradiation position were calculated by MCNP code and transferred to FISPACT code. The activities from the calculations agreed typically within 10% with the experimentally measured activities derived from the NAA irradiations in the No. 17 vertical channel of the BRR.

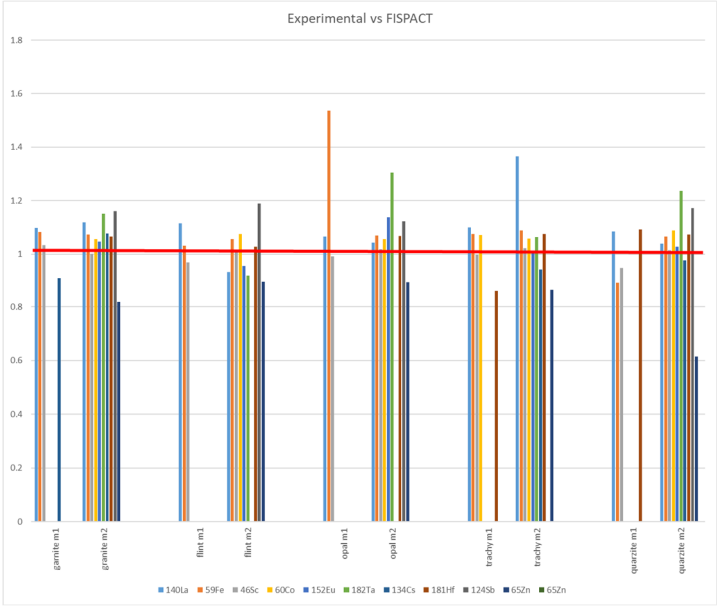


*Figure 1: The ratio of the experimental NAA to the FISPACT-simulated activities of some neutron-induced long-lived radioisotopes in concrete gravel additives, such as Limestone, Opal, Flint, Granite, and Trachybasalt*

Following this benchmarking, the procedure was deemed applicable to calculations related to the Paks II near-vessel concrete components if the neutron flux distribution and the shielding compositions will become known. In addition to the major contributors to the gamma dose rate in concretes, the calculation also accounts for the ground state beta decays without gamma emissions, i.e. invisible to our irradiation experiments.

(3) Concrete pore system characterization by neutron imaging

X-ray Computed Microtomography (XCT), Neutron Computed Tomography (NCT), and Optical Microscopy (OM) were combined to characterize the microstructure of the concrete [7]. The combined NCT/XCT dataset offered the best discrimination between the concrete constituents. The segmented microstructure was finally fed to finite element calculations and the stress and the strain fields of the material were obtained. This research attracted significant attention in the public media, as well as in social media [8].

## *Related publications*


[1] J. Podhorská, M.T. Palou, K. Gméling, V. Szilágyi, I. Harsányi, L. Szentmiklósi: *Experimental Study of Selected Properties of Heavyweight Concrete Based on Analysis of Chemical Composition and Radioactive Elements of its Components,* Solid State Phenomena **321,** 113-118 (2021) Trans Tech Publications Ltd. ISSN: 1662-9779,

[2] https://elkh.org/hirek/az-ek-kutatoi-a-nuklearis-technologiaban-hasznalatos-betonok-nyersanyagait-vizsgaltak-azzal-a-cellal-hogy-csokkenteni-lehessen-az-atomeromuvek-leszerelesenek-koltsegeit/

[3] V. Szilágyi, K. Gméling, S. Józsa, I. Harsányi, L. Szentmiklósi: *Oligomictic alluvial aggregates: petro-mineralogical and geochemical evaluation of sandy gravel formations on the middle course of the Danube (Hungary).* Bulletin of Engineering Geology and the Environment **80,** 5957–5977 (2021)

[4] C.J. Werner, J. Armstrong, F.B. Brown, J.S. Bull, L. Casswell, L.J. Cox, D. Dixon, R.A. Forster, J.T. Goorley, H.G. Hughes, et al: *MCNP User's Manual Code Version 6.2.* Los Alamos Natl. Lab. 2017, 746.

[5] M. Fleming, T. Stainer, M. Gilbert: *The FISPACT-II User Manual*. Oxfordshire: UK Atomic Energy Authority, Culcham Science Centre; 2018.

[6] D. Jóźwiak-Niedźwiedzka, K. Gméling, A. Antolik, K. Dziedzic, M.A. Glinicki: *Assessment of Long-Lived Isotopes in Alkali-Silica Resistant Concrete Designed for Nuclear Installations,* Materials **14,** 4595 (2021)

[7] H.T. Kim, D. F. Tiana Razakamandimby R., V. Szilágyi, Z. Kis, L. Szentmiklósi, M.A. Glinicki, K. Park: *Reconstruction of concrete microstructure using complementarity of X-ray and neutron tomography.* Cement and Concrete Research **148,** (2021)

[8] [https://elkh.org/hirek/az-ek-kutatoinak-reszvetelevel-zajlo-nemzetkozi-egyuttmukodes-kereteben-sikeresen-jellemeztek-betonmintak-mikroszerkezetet-komplementer-rontgen-es-neutrontomografia-segitsegevel/
LENS highlight, 2 radio interviews

# LARGE FACILITY ANALYTICAL STUDIES OF POLISHED AND GROUND STONE ARTEFACTS

*Zsolt Kasztovszky[1], Bálint Péterdi[2], Katalin T. Biró[3], György Szakmány[4], Veronika Szilágyi[1], Katalin Gméling[1], Kata Szilágyi[5], Ildikó Harsányi[1], Dóra Miklós[4], Erika Kereskényi[6], Tamás Sági[4], Levente Illés[1]*

*[1]Centre for Energy Research, [2]Mining and Geological Survey of Hungary, [3]Hungarian National Museum, [4]Eötvös Loránd University, Department of Petrology and Geochemistry, [5]Móra Ferenc Museum, [6]Herman Ottó Museum*

## *Objective*

The project aims to identify the raw material sources of polished and ground stone artefacts in Hungary, delimiting the potential source areas as precisely as possible. Based on our former results, potential sources of some raw material types are located outside Hungary, even outside the Carpathian Basin. The research focuses on a systematic study of finds and raw materials that were not or only partly studied so far, as well as supplementing former results by application of new methods. We will pay special attention to source collected reference materials from the potential raw material sources.

## *Methods*

The unique and irreplaceable archaeological finds will be analysed mostly by non-destructive Prompt-gamma Activation Analysis (PGAA) and "Original Surface" Scanning Electron Microscopy with Energy Dispersive X-Ray microanalysis (OS-SEM-EDX) methods for major components, while Neutron Activation Analysis (NAA) is used to measure the trace elements.

## *Results*

The records of the previously investigated objects were checked and corrected in preparation for registering the items in the database. Due to the prolonged lockdown conditions caused by the COVID19, almost all the tasks connected to travel abroad were cancelled. We have reorganized our tasks and focused on the studies of national collections within the Hungarian border. In addition, due to various reasons, the Budapest Research Reactor's experimental facilities could only be utilized after October 2021, and thus many fewer experiments were realized than we had planned. The following archaeological collections have been chosen and the investigations of them started. 60 stone tools from Gorzsa, made of sand stone, and the corresponding potential raw materials have been analysed by PGAA. With PGAA, the concentrations of the major components and some trace elements (B, Cl, Sm and Gd) are determined. Additionally, their petrography and micromineralogy was studied, and on 21 selected samples, NAA measurements have been performed.

Stone tools from Öcsöd-Kováshalom (Hungarian National Museum (HNM), Eötvös Loránd University (ELTE)), Polgár (ELTE), and Alsónyék (ELKH Archaeological Institute) have been studied and representative samples have been selected for petrographic, SEM-EDX and PGAA analysis. From among these, the collection from Alsónyék comprises around 650 stone axes. Around 30-40 of them were selected for PGAA and 50-60 for SEM-EDX. Due to the COVID19, no fieldtrips to collect geological reference samples were realized in 2021.

## *Remaining work*

In 2022 and 2023, we plan fieldtrips to Slovakia, Little Carpathians (amphibolite- greenschist, contact metabasite), Transylvania (greenschist), Bükk (metavuolcanite), Balaton Highland and Karancs-Medves-Cseres Mts. (basalt), Bohemia, Poland (serpentinite), and Maros region (metadolerite). A revision of previous studies by Hargita Oravecz on the collection of the HNM, as well as measurements of objects from Szegvár-Tűzköves (Koszta József Museum, Szentes) and objects from Százhalombatta are also planned.

## *Related publications*

[1] E. Kereskényi, G. Szakmány, B. Fehér, F. Kristály, I. Harsányi, Z. Kasztovszky, T. M. Tóth: *Archaeometry of greenschist Neolithic polished stone tools from Northeast Hungary*, In: M. Gregáňová, M. Molčan Matejová & V. Šimonová (Eds.): 18th Meeting of the Central European Tectonic Studies Groups. Book of Abstracts. September 22-25, 2021, Terchová, Slovakia, 58-59 (2021)

[2] D. G. Miklós, S. Józsa, G. Szakmány, K. Gméling, F. Horváth, S. Elisabetta: *The origin of the Late Neolithic red sandstone ground stone tools from the tell site of Hódmezővásárhely-Gorzsa (Tisza culture),* Abstract, 51st Meeting of Young Geoscientists, 16-17 p.

[3] Miklós D. G., Szakmány Gy., Józsa S., Horváth F.: *Hódmezővásárhely-Gorzsa késő-neolit (Tisza kultúra) homokköveinek előzetes nehézásvány vizsgálati eredményei,* Absztrakt, 11. Kőkor Kerekasztal, 8-10 p.

[4] Szakmány Gy., Sági T., Józsa S., Szilágyi V., Oláh I., Szilágyi K., Osztás A.: *Előzetes eredmények Alsónyék neolitikus csiszolt kőeszközeinek nyersanyagairól,* Absztrakt, 11. Kőkor Kerekasztal, 19-20 p.

[5] K. Szilágyi: *The implicit assumption of stone tool diversity patterns: exploring economic, social and ritual valuation processes of lithic materials,* 27th Annual Meeting of Association of European Archaeologist, Kiel, Germany, 6-11 September 2021.

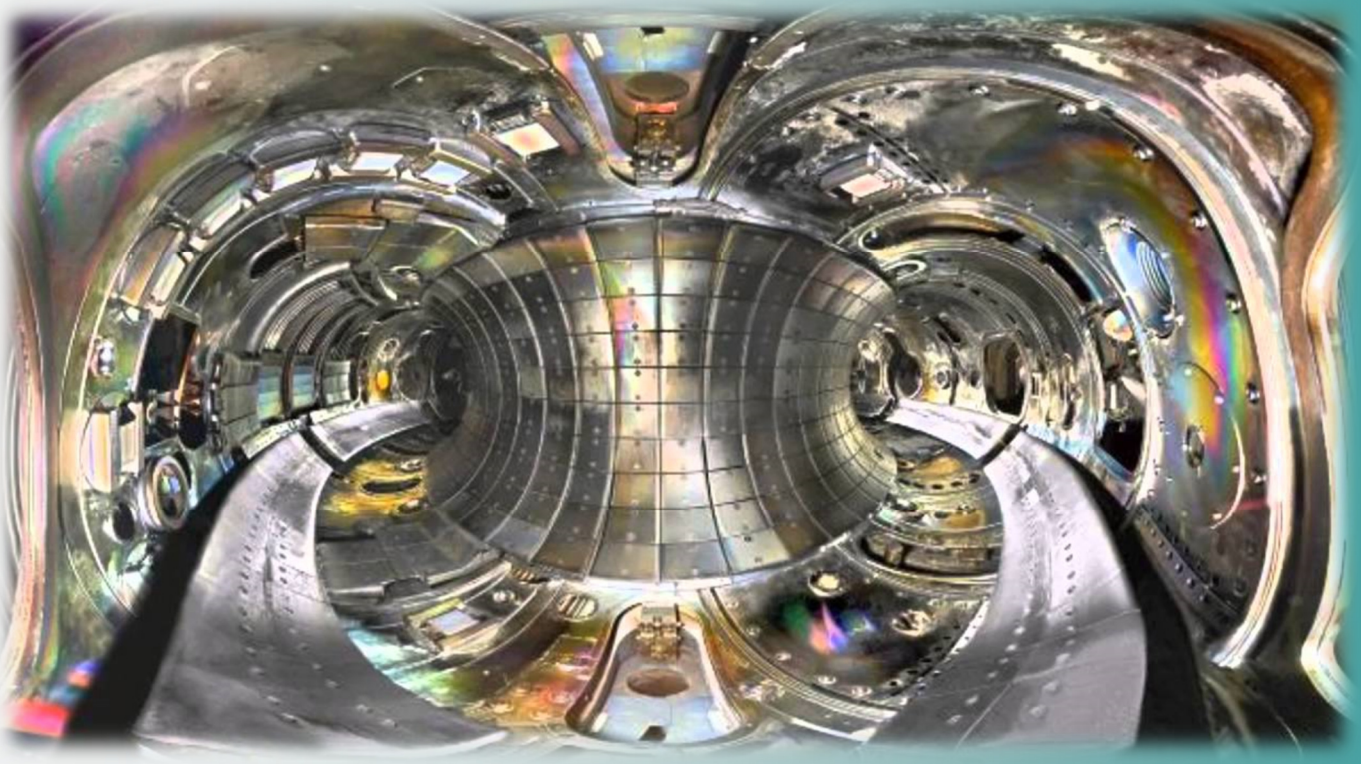

# VI. NULEAR FUSION RESEARCH

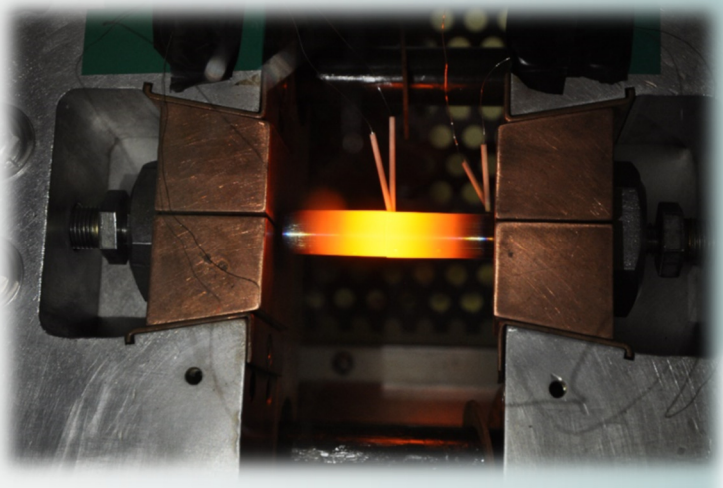

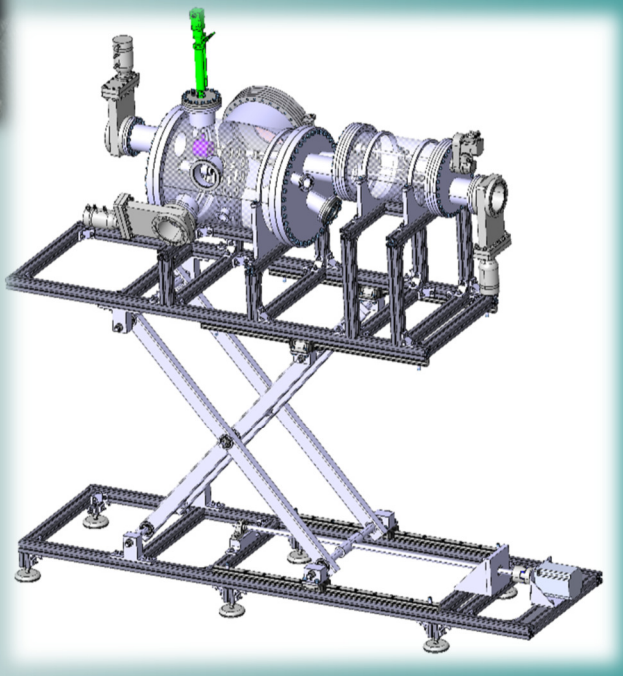

# CONCEPTUAL DESIGN OF THE EU DEMO REACTOR

*Dániel Dunai, Imre Katona, Erik Walcz, Sándor Zoletnik, Jenő Kádi, Miklós Palánkai, Bence Práth*

## *Objective*

One key element of the Eurofusion 2021-25 program is the conceptual design of the demonstration fusion power plant DEMO (DEMOnstration Power Station). The Centre for Energy Research participates in two work packages: remote handling and diagnostics. Remote handling aims at developing the methodology and conceptual design of the robotic maintenance scheme of the device. In this work package, the Fusion Technology Department participated with the development of pipe connection and disconnection technologies while the Fusion Plasma Physics Department contributed with development of the concept of large blanket segment moving devices. In the diagnostic work package, the task coordinator role was given to the Fusion Plasma Physics Department for the visible, infrared and near UV optical diagnostics, and it also contributed to the engineering design of the Fibre Optics Current Sensor (FOCS) diagnostic.

## *Methods*

The conceptual design is done using the Catia engineering design software and it is complemented by analysis using the ANSYS software. The work is performed with international teams where close collaboration is an essential element.

The DEMO diagnostic set is highly restricted compared to present-day research oriented fusion devices. It will contain only those measurement systems which are essential for plasma operation at a given operational point. The radiation environment is also extremely restrictive: no detectors or refractive optical elements are allowed inside the bioshield, and even mirrors can only be installed at the end of long ducts. This situation calls for careful selection of the optical layouts which can survive the environment and still provide the necessary data.

## *Results*

In the DEMO Gate review of 2020, some key problems of the pre-conceptual design were identified, of which the remote maintenance scheme was one of the most difficult. The pre-concept foresaw replacement of large banana shaped blanket segments weighing several 10's of tons from the interior of the vacuum vessel. The access port sizes are very limited and it was found that due to mechanical deformations and loads it is not realistic to remove these large segments. The work of the Fusion Plasma Physics Department focused on devising different alternative segmentation schemes, which reduce the weight and size of the components. Also, the kinematics of the present design was further studied.

In the Fusion Technology Department, several pipe-joining and cutting technologies were studied, focussing on their usefulness in the DEMO environment.

For the breeding blanket, an assessment was made on the service pipe arrangements, and their possible connection and disconnection methods. Two main approaches were considered, the first being an in-bore welding technique, which is a unique application of pipe welding, when pipe joining is done from inside the pipe. To conform to DEMO's Vacuum Handbook, it must be a full penetration weld, which is hard to achieve with increasing thicknesses. Secondly, Mechanical Pipe Connections (MPCs) were investigated. MPCs are well-known in the industry and there are many fusion-related use cases as well. However, locations without direct remote handling access call for new designs and solutions to be devised.

After the evaluation of the existing concepts, laser-arc hybrid welding was deemed to be the most appropriate welding technique. As for the mechanical connections, a flanged design including a central superbolt for preload, and another, inverted union fitting design were selected as the best candidates.

A novel method, the brazing of pipes, was also investigated. The following aspects have been examined: braze filler metal, repeatability and post-braze heat treatment. Two candidates were presented for braze filler metal, both of them already approved for primary torus vacuum boundaries at ITER. Filler metal residue after un-brazing and the required axial separation force were discussed as major questions of repeatability. A new joint configuration is proposed to mitigate the risk of damaging the pipes during disconnection. The recommended heat treatments of 316L and EUROFER 97 had been studied and post-braze heat treatments were proposed for both stainless steels. A forward action plan was recommended which outlines the steps to make large diameter in-bore brazing a qualified joining technique. An experimental study of pipe brazing is confirmed for 2022 or 2023.

In 2021, the technology of the FOCS was reviewed and application examples on the Joint European Torus (JET) and other devices were studied. A detailed engineering design can only be done later, when the overall DEMO design is stabilized.

For the visible/IR/near UV diagnostics the concepts developed until 2020 were reviewed and possible problems which required modifications were considered.

## *Remaining work*

In 2021, the work with DEMO was mostly the preparation for future tasks. The work topics allocated to the Centre for Energy Research will continue as the overall DEMO design matures with the aim of completing the conceptual design in 2025.

# ENGINEERING DESIGN CONTRIBUTION TO DONES PROJECT

*András Zsákai, Tamás Dézsi, Imre Katona, Dénes Oravecz, László Poszovecz*

## *Objective*

An accelerator-based neutron source called Demo-Oriented early NEutron Source (DONES) is being designed as an essential irradiation facility for testing candidate materials for the DEMOnstration Power Station (DEMO) fusion reactor. DONES will generate a neutron flux with a broad energy distribution covering the typical neutron spectrum of a (d-t) fusion reactor. This is achieved by utilizing Li(d,xn) nuclear reactions taking place in a liquid Li target when bombarded by a deuteron beam. The energy of the deuterons (40 MeV) and the current of the accelerator (125 mA) will be tuned to maximize the neutron flux (up to ~ $10^{14} cm^{-2} s^{-1}$) to get irradiation conditions comparable to those in the first wall of a fusion power reactor.

The Fusion Plasma Physics Department is mainly involved in the engineering design of the Material Test Cell of DONES, which is the heart of the DONES facility, because the material testing will take place inside it. Our other contribution is the implementation of a systems engineering approach to the whole project, the identification and management of the overall facility's interfaces, and the participation in the development of the Lithium System and of remote handling equipment and processes.

A Hungarian industry contribution is also connected to the EK work, mainly focusing on the engineering design of the lithium loops, the test cell liner, the design of the HFTM (High Flux Test Module, which contains the material specimens to be irradiated) alignment support and related aspects of remote handling.

## *Methods*

The engineering design of the test cell includes the design of the components using the Computer Aided Three Dimensional Interactive Application (CATIA), which was used to integrate these components into the final complex system. Additionally, the Removable Biological Shielding Blocks (RBSB), made of heavy concrete, required geometrical optimization due to some regions of high level radiation, and fabrication options were also investigated. A complex design analysis based on the application of the RCC-MRx code (French abbreviation for "Design and Construction Rules for Mechanical Components of Nuclear Installations: High Temperature, Research and Fusion Reactors") and finite element analysis has been carried out for the so-called Test Cell Lithium System Interface Cell (TLIC) which is the boundary between the Test Cell and the Lithium System and serves as a primary safety boundary.

The System Engineering work mainly focused on providing the Systems Engineering Management Plan (SEMP) for the project which can serve as a system engineering guideline.

The lithium system development focused on the possible development for a substitute option for the TLIC, and additionally, the remote handling development consisted of working out the possible maintenance procedures for the TLIC.

The industry contribution mainly focused on the engineering design of the test cell liner using RCC-MRx codification, which serves as the main safety boundary and thus can be regarded as a pressure vessel. The High Flux Test Module (HFTM) positioning system has been optimized further, while an investigation has been conducted for the optimization of the TLIC openings due to remote handling needs and the TLIC remote handling equipment has been further developed.

## *Results*

A complex CATIA model has been worked out for the test cell and the latest version was issued for approval. The RBSB layout has been optimized for neutronics needs and further options have been investigated. The TLIC analysis has yielded a suitable design according to RCC-MRx codification. The TLIC remote maintenance procedure has been investigated and several options outlined which considered the needs of maintainable components inside the TLIC, the area available in the TLIC room and the inspection needs due to all interconnecting systems.

A SEMP has been created detailing how the project should be organized in accordance with systems engineering principles.

From the industry contribution, two concepts were previously worked out for the support and alignment of the HFTM, and in 2021, one of the concepts was finally chosen for further development based on the results provided. A complex Finite Element Method Analysis (FEA) on the maintainable test cell liner has been conducted investigating several support options and RCC-MRx design principles were also implemented into the design. The TLIC remote handling equipment has been further developed, giving options for Commercial Off-The-Shelf (COTS) components, too.

## *Remaining work*

The project is ongoing in coming years under the EUROFusion Consortium, and the industrial contribution work is also ongoing.

## *Related publications*

[1] A. Zsákai et al.: *DONES Systems Identification and requirements allocation,* Paper under review, Nucl. Materials and Energy (2021)

[2] I. Katona, M. Tóth, J. Castellanos, F. Arbeiter, T. Dézsi, A. Zsákai, G. Micciche, Y. Qiu, M. Siwek, D. Alonso, C. Melendez, F. Rueda, A. Ibarra: *Preliminary Finite Element Analysis of the Stainless- steel Liner of the Maintainable Test Cell Concept of IFMIF-DONES*, Nucl. Materials and Energy **31,** 101186 (2022)

[3] W. Królas, A. Ibarra, F. Arbeiter, F. Arranz, D. Bernardi, M. Cappelli, J. Castellanos, T. Dézsi, H. Dzitko, P. Favuzza, A. García, J. Gutiérrez, M. Lewitowicz, A. Maj, F. Martin-Fuertes, G. Micciché, A. Muñoz, F.S. Nitti, T. Pinna, I. Podadera, J. Pons, Y. Qiu, R. Román, M. Toth and A. Zsakai: *The IFMIF-DONES fusion oriented neutron source: evolution of the design,* Nucl. Fusion **61,** 125002 (2021)

[4] T. Dézsi, D. Kovács, V. Viktor, A. Zsákai et al.: *Evolution of the design of IFMIF-DONES Test Cell Vacuum Vessel,* Abstract Submission for SOFT conference (2022)

[5] A. Zsákai, T. Dézsi, A. Korossy-Khayll, I. Katoan, E. Kósa et al.: *Integrated design of the vacuum and safety barrier between the Lithium and Test Systems of IFMIF-DONES*, Abstract Submission for SOFT conference (2022)

[6] T. Dézsi, K. Varga, A. Zsákai et al.: *Remote Handling maintenance in IFMIF-DONES: status and future developments,* Abstract Submission (2022)

# PLASMA PHYSICS RESEARCH ON INTERNATIONAL EXPERIMENTS

*Sándor Zoletnik, Gábor Anda, Dániel Dunai, Dániel Réfy, Gábor Kocsis, Tamás Szepesi*

## *Objective*

Magnetic fusion experiments are large experimental devices operated by a few laboratories worldwide. In Europe the Eurofusion consortium coordinates work on 6 major devices. The Fusion Plasma Physics Department participates in work on 4 of them: the Joint European Torus (JET, Culham, UK), the ASDEX Upgrade tokamak (Garching, D), the MAST Upgrade tokamak (Culham, UK) and the Wendelstein 7-X stellarator (Greifswald, Germany). The scientific programs of these devices aim at preparing for the operation of the ITER international fusion experiment and the European Demonstration reactor DEMO. The department also participates in the joint EU-Japan JT-60SA superconductive tokamak experiment which is being commissioned in Naka, Japan and with measurements on the COMPASS tokamak (Prague, CZ) and the TJ-II stellarator (Madrid, SP).

## *Methods*

The contribution of the Fusion Plasma Physics Department to Eurofusion experiments is based on two plasma diagnostic techniques: video camera observations and Beam Emission Spectroscopy (BES). We develop and operate diagnostic systems and perform measurements with them to study plasma physics phenomena relevant for fusion energy production. These are plasma turbulence, pellet injection, plasma instabilities, and the edge density profile. The data are processed using specialized numerical methods and are available to other groups in the Eurofusion community.

For video camera systems we use commercial fast (> 10 kHz) cameras and also the EDICAM devices developed by our department. These detect the edge visible radiation of the plasma from which the plasma shape, edge turbulence and instabilities can be identified. The ablation of solid pellets injected into the plasma can also be observed with our camera systems.

In the BES technique an accelerated (30-100) kV atomic beam is injected into the plasma and its visible radiation is observed by sensitive detector arrays. We use Hydrogen heating beams for plasma turbulence studies and various alkali beams (Li, Na, Rb, Cs) for measuring the plasma edge density profile, turbulence, and potentially, edge plasma currents. The alkali beams are developed in our department. The density profile is calculated from the measured light profile using beam modelling developed by the Budapest University of Technology and Economics (BME).

## *Results*

On the JET tokamak we operate the Lithium beam diagnostic (Li-BES) which measures the edge plasma density profile. The diagnostic was regularly operated whenever requested by the research program. Due to the Covid pandemic, measurements were done remotely from Budapest. The processed density profiles are inserted in the JET processed database and are used by the whole JET community. In 2021, the JET tokamak concentrated on Deuterium-Tritium experiments which have not been done since 2003. As no other present day fusion experiment is capable of operating with Tritium, the data obtained are important for ITER operation preparation. The mitigation of the power exiting the plasma is a key question for preserving the machines integrity during high fusion power deuterium-tritium (DT) operation, and injection of high Z elements into the plasma edge (seeding) is a power mitigation technique being considered for fusion reactors. The Li-BES data has been utilized for the validation of plasma edge seeding simulations [1] in preparation for the D-T operation phase. In case of a future reactor the plasma will have to be operated in H-mode, and to forecast fusion performance, the L-H transition (transition from low to high confinement state) has been investigated at JET with various isotope mixes. The scaling of the L-H transition threshold power with isotope mass has been investigated in dedicated experiments [2]. JET achieved world record fusion energy production and demonstrated that DT plasmas can be operated with somewhat better confinement than pure Deuterium plasmas.

On the MAST Upgrade tokamak, an upgraded BES diagnostic was built in a collaboration between CCFE, University of York and EK in the past years. In 2021, the diagnostic was installed on the tokamak and the first measurements were performed. The diagnostic was operated remotely by EK in the last months of the campaign. The signal levels agree with expectations, but the diagnostic was not optimized for operation. Strong pick-up noise is observed, and the filter transmission still needs to be optimized. Even this limited performance was sufficient to measure fast-particle-driven magnetohydrodynamic (MHD) activity and also the effect of core turbulence was identified. On the ASDEX Upgrade tokamak an 80 keV Caesium beam was installed by our team for testing a new diagnostic concept aiming at measuring the edge plasma current with good time resolution. The same technique has been demonstrated on the COMPASS tokamak in Prague in collaboration with the Czech Institute for Plasma Physics. In 2021, data evaluation procedures were developed for the COMPASS data and the beam quality on the ASDEX Upgrade was improved, which resulted in the first beam detection in the tokamak.

The Wendelstein 7-X superconducting stellarator experiment differs from the above tokamaks due to its complex 3D plasma configuration, the lack of plasma current and the resulting inherent steady-state operation possibility. The Fusion Plasma Physics Department built and operated the 10-camera overview video system and the alkali beam diagnostic. The 1.2b experimental campaign ended in 2018 when both of our diagnostics collected a large amount of data. In 2021, the evaluation of these data continued and revealed statistical properties of edge plasma turbulence (filaments). A new density calculation

method has been developed which allows calculation with about 50 μs time resolution [3]. The edge plasma density profile was provided as a community service when it was specifically requested. State changes at the plasma edge [4] and pellet ablation [5] were studied by the video camera system. This investigation aimed to understand cryogen pellet and Tracer-Encapsulated Solid Pellet (TESPEL) cloud drift. The Wendelstein 7-X device is being upgraded and we are contributing with a new view with the faster camera system and an additional spectroscopy observation optics for the alkali beam diagnostic. Both equipments have been designed, constructed and installed on the stellarator.

The JT-60SA tokamak is also a superconducting experiment, featuring a discharge length about an order of magnitude longer (100 s) than the other tokamaks in the above list. JT-60SA, featuring very high Neutral Beam Injection (NBI) heating power, has been designed to support the operation of ITER by following a complementary research and development program. The Fusion Plasma Physics Department has designed, built and delivered a visible overview camera observation system, based on the EDICAM, for JT-60SA, which was installed in 2020. In 2021, the camera system was ready for operation, waiting for the first plasma discharges. However, the operational campaign had to be cancelled due to an incident with one of the superconducting poloidal field coils. Therefore, our team has focused on software development of the camera, both for controlling and data visualization purposes.

The TJ-II stellarator experiments were conducted in 2020 to investigate the drift of the TESPEL and cryogenic pellet clouds. In 2021 these data were analysed revealing a clear outward drift of the pellet cloud in Electron Cyclotron Resonance Heating (ECRH) heated plasmas, while in NBI heated plasma the drift direction was unclear.

## *Remaining work*

The JET tokamak will operate until 2023, and thus requests have been received for the operation of the lithium beam diagnostic. On the MAST Upgrade, optimization and commissioning of the BES diagnostic is planned bef**o**re the MU-02 campaign in 2022 and the diagnostic is planned to be operated continuously in the next campaign. Commissioning of the upgraded Wendelstein 7-X stellarator will start in September 2022 and the 2.1 campaign in December. Both diagnostics developed by the Fusion Plasma Physics Department will be operated by a team of 4 researchers. The JT-60SA tokamak is also expected to start a new campaign in 2022, during which several members of our team will be present to operate the Edicam system. On the TJ-II stellarator the pellet experiments will continue to clarify the unsolved pellet drift question.

## *Related publications*

[1] P. Chmielewski, …, D.I. Réfy, …, M. Vécsei, …, and the JET Contributors: *TECXY simulations of Ne seeding in JET high power scenarios,* Nuclear Materials and Energy **27,** 100962 (2021), DOI: https://doi.org/10.1016/j.nme.2021.100962

[2] E. Solano, …, D.I. Refy,…: *Recent progress in L–H transition studies at JET: tritium, helium, hydrogen and deuterium*, accepted at Nuclear Fusion, https://iopscience.iop.org/article/10.1088/1741-4326/ac4ed8/meta

[3] M. Vécsei, G. Anda, O. Asztalos, D. Dunai, S. Hegedűs, D. Nagy, M. Otte, G. I. Pokol, S. Zoletnik, and W7-X Team: *Swift evaluation of electron density profiles obtained by the alkali beam emission spectroscopy technique using linearized reconstruction,* Rev. Sci. Instrum. **92,** 113501 (2021)

[4] M. Szűcs, T. Szepesi, Ch. Biedermann, G. Cseh, M. Jakubowski, G. Kocsis, R. König, M. Krause, V. Perseo, A. Puig Sitjes and the W7-X Team: *Experimental confirmation of efficient island divertor operation and successful neoclassical transport optimization in Wendelstein 7-X,* Appl. Sci. **2021,** 1, (2021)

[5] G. Kocsis, N. Tamura, 3, R. Bussiahn, K.J. McCarthy, J. Baldzuhn, C. Biedermann, G. Cseh, H. Damm, P.Kornejew, R. König, N. Panadero, T. Szepesi and the W7-X Team: *Investigation of TESPEL cloud dynamics in Wendelstein 7-X stellarator,* Nucl. Fusion **61,** 016006 (2021)

# SUPPORT LABORATORY FOR THE ITER DISRUPTION MITIGATION SYSTEM

*Sándor Zoletnik, Erik Walcz*

## Objective

ITER is a reactor-scale magnetic fusion experiment under construction by the EU, USA, Russia, Japan, China, South Korea and India in Cadarache, France. It is a tokamak device with a 15 MA plasma current. Tokamaks have a major instability, called disruption, during which the plasma energy is lost to the surrounding surfaces in about a millisecond. Even more dangerous is the possibility that part of the plasma current may be converted to a beam of MeV energy electrons, which may locally deposit energy and cause considerable damage to the device. Since disruptions cannot be completely avoided, Disruption Mitigation Systems (DMS) have been developed in present-day experiments. The original DMS technology planned for the ITER design was Massive Gas Injection (MGI). During the past years, experiments and modelling of MGI have revealed that at the huge volume and current of ITER it would not be effective enough. Therefore, in 2019 the ITER Council decided to replace it with a more recent technology, called Shattered Pellet Injection (SPI). In this method, pellets of solid Hydrogen, Deuterium, Neon and other materials are prepared and accelerated to several hundred m/s velocity with a gas pulse for injection into the ITER vacuum vessel. Close to the plasma, they are shattered on an oblique surface and the resulting solid gas fragments (shards) enter the plasma. These can inject more material in a shorter time than MGI. Although SPI has been demonstrated on present-day devices, ITER requires much larger pellets which have never been produced and shattered before. In order to develop the ITER-scale SPI technology, ITER launched a call for tender for a DMS support laboratory which was won by the Pellet Shattering Test Consortium (PSTC) composed of EK, H-Ion Kft. and VTMT Kft. in 2020. The aim of the laboratory is to produce 19 and 28.5 mm diameter solid Hydrogen, Neon and mixture pellets, launch them and measure how they shatter under various conditions.

## Methods

The equipment of the DMS support laboratory consists of a cryogenic system, which cools a stainless steel pipe (barrel) to about 5 K where the pellet gases desublimate and form the pellet. A special fast, high-pressure valve then injects gas into the barrel and launches the pellet. The pellet flies through multiple gaps in the flight tube, where the propellant gas expands into a large vacuum vessel and the pellet is imaged. Finally, it flies through an approximately 4 m long tube simulating the flight tube in the ITER port cell and shatters on an oblique plate. The resulting fragments are diagnosed in another large vacuum vessel. All components of the system are original designs and constructions of the PSTC consortium.

The project started in November 2020. Firstly modelling codes were developed for pellet acceleration, desublimation and the cryogenics system, followed by the engineering design of the system. The fast propellant valve was a special development based on modelling and bench tests, as no such device is available on the market. The resulting valve can be operated at maximum 150 bar pressure and opens a 20 mm diameter nozzle in 1.5 ms. Construction was strongly affected by delayed component deliveries due to the Covid pandemic, but still the injector could be completed by September 2021.

## Results

After cryogenic and gas system tests the first 19 mm diameter Hydrogen pellets were produced in December 2021. The pellet freezing process was diagnosed by a camera, looking into the barrel which observes light passing through the forming pellet along the barrel. After launch the pellet is photographed by a fast camera. As already expected, desublimation of such large pellets is critical. After trying a few recipes, two Hydrogen pellets could be successfully launched with 800 m/s velocity on 20 December 2021. A photograph of the injector and related equipment is shown in Fig.1 together with one of the first pellets. Meanwhile, components were procured for the shard diagnostic setup, and development and laboratory testing of the shard measurement setup was completed.

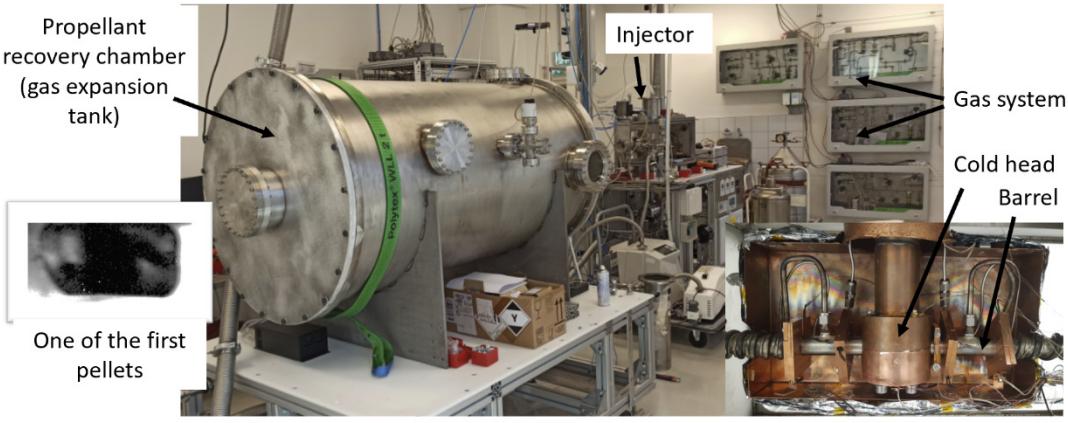


*Figure 1: Photograph of the SPI injector at the time of the first pellet launch and a view into the cryostat. On the left side, the image of one of the first Hydrogen pellets is shown.*

## *Remaining work*

In 2022, the system will be equipped with the 4 m long flight tube, the shattering device and the diagnostic chamber, together with the shard analysis diagnostics. This completes the setup, and systematic measurements will be performed with 19 and 28.5 mm diameter Hydrogen, Neon and mixture pellets. The DMS support laboratory contract is presently signed for 3 years, but it can be extended if ITER needs further tests.

## *Related publication*

[1] S. Zoletnik, M. Vécsei, S. Jachmich: *Modelling of freezing of large cryogenic pellets for the ITER Shattered Pellet Injector,* 47th EPS Conference on Plasma Physics, ECA Vol 54A, P P2.1057 (2021)

# DEVELOPMENT OF REMOTE HANDLING PIPE CUTTING AND WELDING METHODS FOR THE ITER LOWER PORTS

*Miklós Palánkai, Jenő Kádi*

## *Objective*

The objective of the work was to boost the ITER Diagnostics team in the evaluation and establishment of diagnostics systems, providing mechanical engineering design, modelling, analysis and development of mock-ups and prototypes required for design validation, and input to construction work descriptions.

## *Methods*

This work relates to Lower Port Diagnostic systems. These systems are present in 3 lower ports of the ITER machine. The key components of these systems are the diagnostic racks, which are 10.5-ton steel structures housing various diagnostic tenants, and they also contribute to the nuclear shielding of the ITER machine. These racks need to be fed with fluid (water and gas) pipes and electrical cables to actuate subsystems and observe plasma parameters. Being inside the Vacuum Vessel, these racks must be fully Remote Handling (RH) compatible, since no human presence is allowed in this environment.
The main purpose of the work was to further develop the above-described water and gas supplies and electrical services for the racks, in preparation of the Preliminary Design Review (PDR) of the system, and also to contribute to the PDR meeting and the closure of the PDR. The PDR is one of the biggest milestones in the life of the development of a component of the machine.
The work has been divided to six parts as follows:

- Review and development of pipe cutting and welding tools and related tools for the operations,
- Work out pipe and electrical cable routing and attachment systems between feedthroughs and the diagnostic racks,
- Prepare related documents for the design review,
- Work out pipe and electrical cable routing and attachment systems inside the diagnostic racks,
- Work out future mock-up plans for validating concepts,
- Update concepts according to comments the design receives on the PDR.

## *Results*

During the time of the project all the pre-defined goals have been achieved! After reviewing the tools that could be purchased on the market and the others which have been developed for ITER, the preferred ones have been chosen and adapted for the task. One design for the pipe cutting, one for the welding and one alternative design for a mechanical pipe connection have been worked out. Beside the cutting and welding tools, these concepts contain the related support equipment (like pipe manipulators) as well. The routing of the water and gas pipes and electrical cables have been defined and created in all three lower ports. Besides the mechanical designs, mechanical simulations for some of the developed equipment have been made to justify the concept. All concepts have been presented on the PDR.

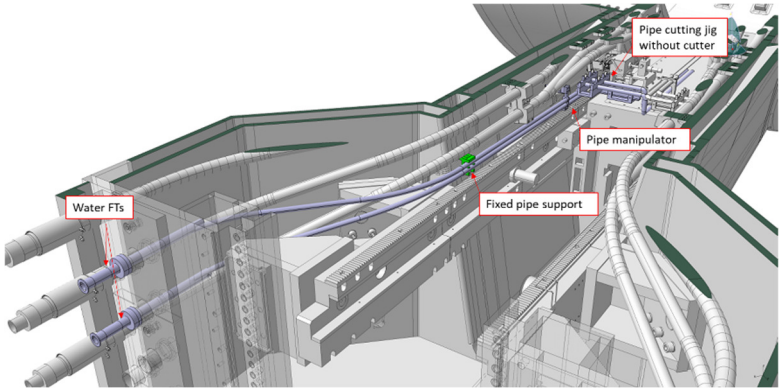


*Figure 1: One of the lower ports area of ITER (section cut of the lower port) – the scene of the developments*

## *Remaining work*

The work has been fully completed on time and approved by the ITER Organization's responsible supervisors; no work remains.

## *Related publications*

All deliverables were uploaded to, and approved on the official document management server of ITER (user.iter.org).

# MATERIALS SCIENCE RESEARCH FOR THE DEMO FUSION REACTOR

*Ildikó Szenthe, Ferenc Gillemot, Márta Horvath, Szilvia Móritz, Balázs Hargitai, Kristóf Andor Csikós, Dávid Cinger*

## *Objective*

The next step in European fusion research after the ITER reactor is the development of the DEMO fusion reactor. In connection with the research on DEMO materials science issues, EK participated in the research activities in 2021 by neutron irradiation of Eurofer97 steel with a fluency resulting in 0.5 dpa (displacements per atom) at 300, 350, 450 and 550 °C; by the further development of a database of research results on Functional Materials (optical and dielectric) and by updating a Handbook of properties of Functional Materials from the results of new research.

## *Methods*

To perform the neutron irradiation of Eurofer97 material specimens, after the elaboration of the research plan, the target holder and the target boxes which contain the specimens, were designed and manufactured. From the block of Eurofer97 material 32 pieces of compact tension specimens were fabricated and coded. The specimens were notched using electrical wire discharge machining and pre-fatigued according to the testing standard. Hardness measurements were also performed, and all data were collected into a database. Six specimens were installed into each target box. For each irradiation temperature a separate target box was prepared. Each box included one set of dosimetry monitor foils (Cu, Fe, Al-Co1%, Nb) to measure the neutron fluence.

The irradiation was performed in an inert gas (Helium-nitrogen mix) atmosphere. Each zone temperature during irradiation was measured by separate thermocouples and controlled by auxiliary electric heating. A PC controlled automatic system regulated the heating and collected the temperature-time data. The irradiation temperature was successfully controlled within a ±10 °C range. Dosimetry monitors were used to measure the fluence. A reactor physics calculation was performed by a simulation of the neutron flux distribution model of the irradiation channel with the target boxes inside the channel, and compared to the measured neutron flux taking into consideration the reactor power history. It resulted in a fitting of the neutron spectrum and a calculation of the resulting dpa parameter.

Another task was to prepare the database of research results on Functional Materials. The properties of aged materials (mainly after neutron and gamma irradiation) were compiled from the yearly reports of the various research groups on the topic. The collected data of the relevant materials including physical properties, such as electrical resistivity, electrical conductivity, permittivity, dielectric strengths, loss of tangent (dissipation factor), and optical properties such as transmission, absorption and reflectance are the most important properties, but the detailed design mechanical and thermal properties may also be used. MS Excel based data collection templates have been developed and filled out. The comments of the research group have been considered and built in. During the development the relevant standards and codes have been considered. The development of the Material Handbook on Functional Materials summarizes the database content at a high level to support the design of DEMO in-vessel components.

## *Results*

Irradiation of 2 x 6 specimens at two temperatures: 300 and 350 °C up to 0.5 dpa (Fe) was finished in March. The target boxes were dismantled; and after the extraction the samples were stored in a hot-cell. The irradiation of the other 2 x 6 specimens at 450 and 550 °C up to 0.5 dpa (Fe) was finished by the end of October. The dosimetry foils' evaluation is ongoing.

The Functional Material database structure had been developed during the previous years for the functional materials. In 2021 additional new and aged properties of optical and dielectrical materials were mainly collected. The Functional Material database and Material Property Handbook were updated and extended with the new data.

## *Remaining work*

To supply baseline data for the elaboration of further testing, the irradiated EUROFER97 material specimens will be tested next year. Further irradiation campaigns will be performed at EK for material qualification purposes. The results of the testing will become part of the updated Material Property Handbook. Further development of the Functional Material Property Handbook and the underlying database are also carried out by EK.

# MICROWAVE PROTON ION SOURCE DEVELOPMENT

*Gábor Anda, Sándor Bató, Balázs Leskó, Dénes Oravecz, András Zsákai*

## *Objective*

The decreasing number of research reactors decreases the number of the available neutron sources. To overcome this problem, accelerator based neutron sources are being developed worldwide. There are many different types of these neutron sources (concerning neutron flux, final beam energy, etc.), but the principle is the same: microwave radiation excited proton/deuterium ion source with a beam current of one to a few hundred mA, beam energy of 30-100keV (it is further accelerated in the second/third stages of acceleration) and beam emittance of below 1 π mm mrad. The development of such a source started at the beginning of 2021.

## *Microwave proton ion source*

The basis of this kind of ion source is a resonant cavity excited by microwave radiation. Protons are extracted electrostatically from this chamber. The basic structure of the EK microwave ion source can be seen in Figure 1.

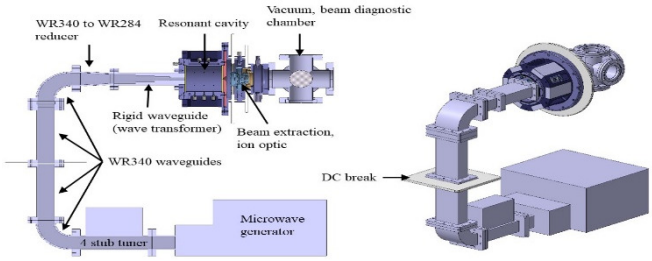


*Figure 1: Basic scheme of the microwave ion sources*

The microwave generator (2.45 GHz) is followed by a stub tuner (for impedance matching). Since the cavity must be at high voltage (35 kV) for extraction the generator is insulated from the cavity via a DC insulator/break in the wave guide. A wave transformer (rigid waveguide) increases the E field of the radiation and leads it into the cavity. The cavity is filled up with hydrogen gas (the flow rate is about 1-5 sccm (standard cubic centimetres per minute)).

To increase the efficiency of hydrogen ionization (and dissociation) the chamber is surrounded by permanent magnets. Six magnet bars surround the chamber axially (electromagnet solutions also exist). The cyclotron frequency of the electrons in an 87.5 mT magnetic field will be equal to the microwave frequency; in this way the electron's energy can be maximized. The magnetic field is designed so that the so-called Electron Cyclotron Resonance (ECR) surface is maximized and positioned at the extraction slit.

The extracted protons are diagnosed in a modified Faraday Cup (FC), see Figure 2. The proton beam hits the base plate (angled ideally at 45 degrees to the beam axis) inside the FC. The top of the FC is open to an infrared camera used to measure the beam spot size and temperature profile. The temperature of the plate will be proportional to the beam flux, i.e. the beam current distribution can be measured with this technique.

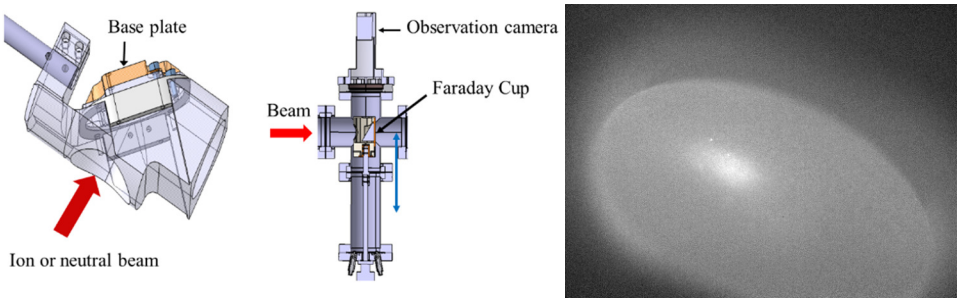


*Figure 2: The modified Faraday Cup (left) and beam spot as seen by the infrared camera (right)*

Up to now ~ 3 mA proton current was extracted from our source.

## *Remaining Work*

The magnetic field still has to be fine-tuned to increase the extracted beam current. In parallel, a measurement method is being developed to distinguish between the $H^+$, $H^{2+}$ and $H^{3+}$ ions extracted from the source.

# DEVELOPMENT OF REMOTE HANDLING PIPE CUTTING AND WELDING METHODS FOR THE ITER LOWER PORTS

*Miklós Palánkai, Jenő Kádi*

## *Objective*

The objective of this work was to assist the International Thermonuclear Experimental Reactor (ITER) Diagnostics team in the evaluation and establishment of diagnostics systems by providing mechanical engineering design, modelling, analysis and development of mock-ups and prototypes required for design validation, and input to construction work descriptions.

## *Methods*

This work relates to the Lower Port Diagnostic systems. These systems are present in three lower ports of the ITER machine. The key components of these systems are the diagnostic racks, which are 10.5-ton steel structures housing various pieces of diagnostic equipment. The racks also contribute to the nuclear shielding performance of the ITER machine. These racks observe plasma parameters and need to be fed with fluids (water and gas pipes) and electrical cables to run the measurement subsystems. Being inside the Vacuum Vessel, these racks are fully Remote Handling (RH) compatible, e.g. human presence isn't allowed in this environment.

The main purpose of the work was to further develop the above-described water and gas supplies and electrical services for the racks, in preparation of the Preliminary Design Review (PDR) of the system, and to contribute to the PDR meeting and the closure of the PDR. PDR is one of the biggest milestones in the life of the development of a component of the machine.

The work was divided into six parts as follows:

- Review and development of pipe cutting and welding tools and related tools for the operations,
- Work out the pipe and electrical cable routing and attachment system between feedthroughs and diagnostic racks,
- Prepare related documents for the design review,
- Work out the pipe and electrical cable routing and attachment system inside the diagnostic racks,
- Work out future mock-up plans for validating of design concepts,
- Update concepts according to comments of the design review.

## *Results*

During the time of the project all the pre-defined goals have been achieved! After reviewing, some of the cutting and welding tools had to be purchased on the market, and others have been developed for ITER. The preferred ones have been chosen and adapted for the task. One design for the pipe cutting, one for the welding and one alternative design for a mechanical pipe connection have been worked out. Beside the cutting and welding tools, these concepts contain the related support equipment (like pipe manipulators) as well. The routing of the water and gas pipes and electrical cables have been defined and created for all three lower ports. Besides the mechanical designs, mechanical simulations for some of the developed equipment have been made to justify the concept. All the concepts have been presented in the design review.

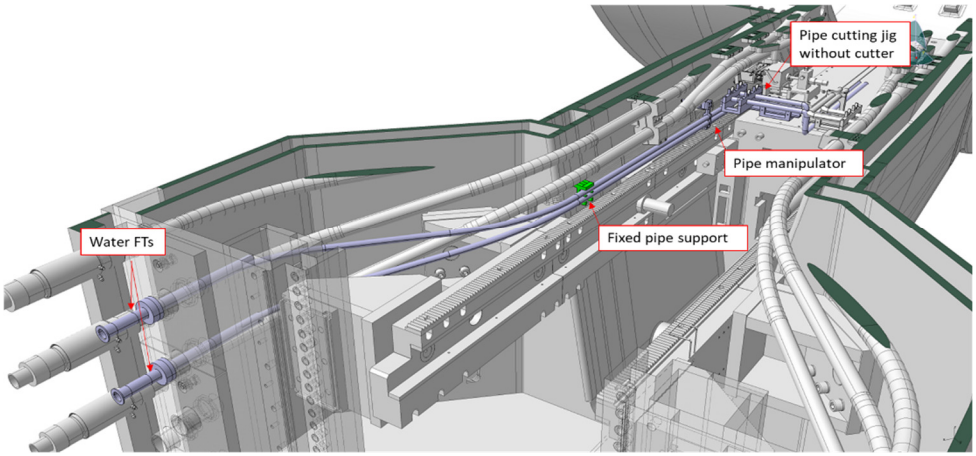


*Figure 1: One of the lower ports' areas of ITER (section cut of the lower port) – the scene of the developments*

## *Related publications*

All deliverables were uploaded to, and approved on the official document management server of ITER (user.iter.org).

# PILOT PROJECT FOR INVESTIGATING THE POSSIBILITIES OF DATA ARCHIVING USING METADATA SCHEMES WITHIN THE FUSION PLASMA PHYSICS LABORATORY

*Gábor Cseh, Miklós Vécsei, Sándor Zoletnik*

## *Objective*

The purpose of this work was to investigate the possibilities in our lab to implement a data archive pilot project and within this project we wanted to find out how we can apply the FAIR (Findable, Accessible, Interoperable, Reusable) metadata principle on our data. This work has been carried out in the framework of a call for tender launched by the HRDA (Hungarian node of the Research Data Alliance). During this work we identified the following subtasks.

1. Create a metadata scheme for our experimental data.
2. Consultation and brainstorming with our colleagues within Eurofusion about the good practices for data archiving and metadata schemes inside the European fusion community.
3. Archive a publication with metadata in the Concorda (Concentrated Cooperation on Research Data) database.

## *Metadata scheme*

After extensive consultation with our colleague at the Institute for Computer Science and Control, we defined a metadata scheme concept with the format of the Harvard Dataverse database (which is technically a specifically formatted Excel file), which can be immediately imported in any derivation of the software package, including the Hungarian Concorda database. We took into account that not all of our metadata needs to be publicly accessible to clearly define any desirable unique piece of our data. Too much (and possibly redundant) metadata would be confusing for the searching process. We defined metadata schemes for our Event-Detection Intelligent CAMera (EDICAM) system as well as the Alkali Metal Beam system.

## *Consultation with the Eurofusion colleagues*

By consulting with the Eurofusion colleagues on how to implement the FAIR principles specifically for our data as the Fusion Plasma Physics Laboratory in the Centre for Energy Research, it turned out that we can meaningfully contribute to the searchable part of FAIR, since the legal rights of the data taken needs to be clarified inside the community first. However, we did exactly that by defining our own metadata scheme.

There is an initiative to use the International Thermonuclear Experimental Reactor (ITER) Integrated Modelling and Analysis Suite (IMAS), which is a common place for many fusion devices across Europe to create a common metadata scheme. This scheme is called the IMAS Data Dictionary (IMAS DD), which contains not only the links to fusion data chunks, but also contains metadata. Some of the records are called Interface Data Structure (IDS), which are entry points to the IMAS DD and can be used by regular users. We agreed that our metadata scheme defined in the Harvard Dataverse style could be integrated in the long run into the IMAS DD in the form of an IDS, so we could introduce our data to the wider fusion community in this way.

## *Archiving a published paper*

We successfully registered to the Concorda database, created the necessary datasets inside Concorda (some, but not all of them were already created), which are the following: CONCORDA → Eötvös Loránd Research Network (ELKH) → Centre for Energy Research → Fusion Plasma Physics Department → Papers. The title of the archived (and published) paper is "*Multi-diagnostic analysis of plasma filaments in the island divertor*". It was already available in the MTMT database (Hungarian Scientific Bibliography Database) and now it is available in CONCORDA as well.

## *Remaining work*

This project has been completed.

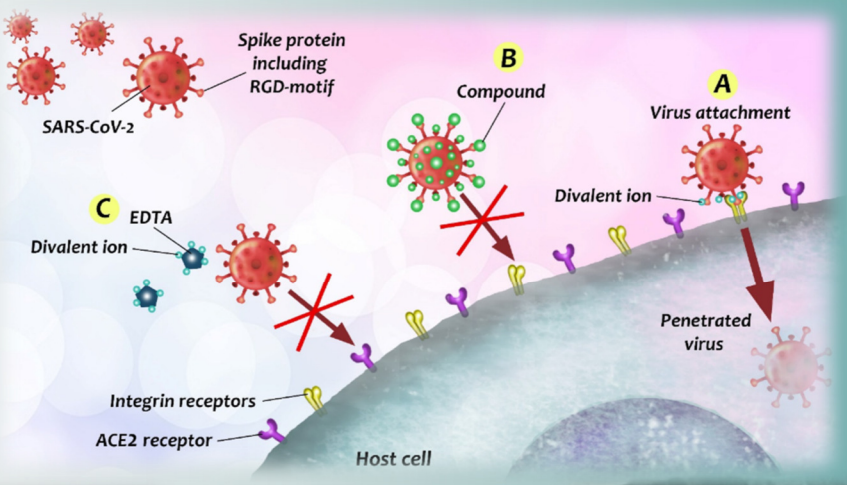



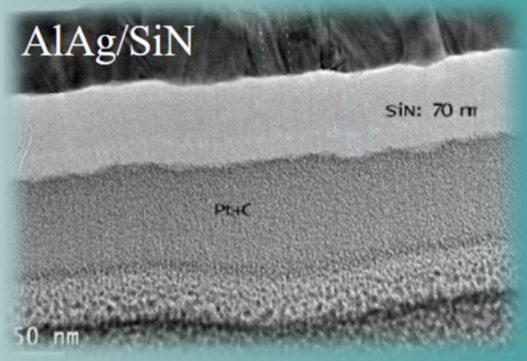


# VII. RESEARCH AND DEVELOPMENT IN INSTITUTE OF TECHNICAL PHYSICS AND MATERIAL SCIENCES

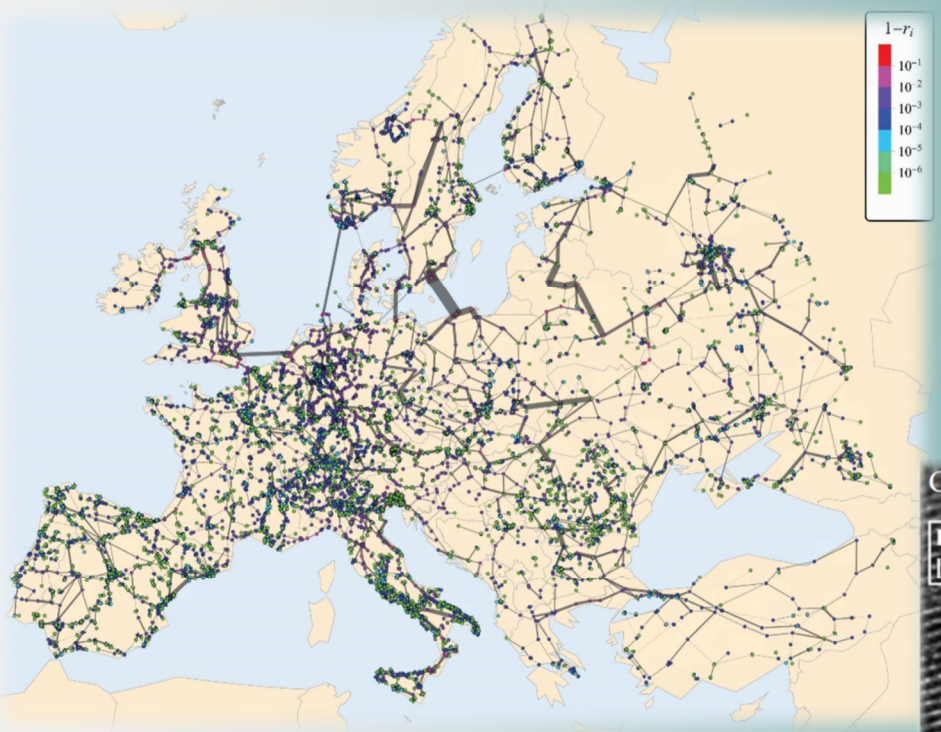


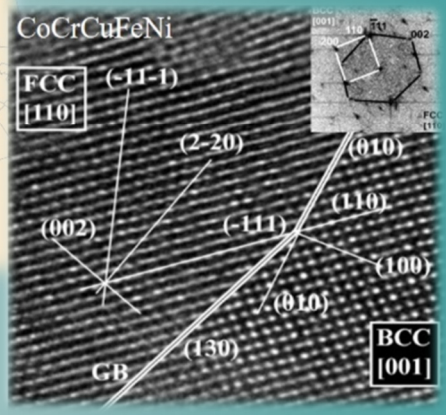

# THE COMPOSITION AND STRUCTURE OF THE UBIQUITOUS HYDROCARBON CONTAMINATION ON VAN DER WAALS MATERIALS

*Lendület LP2017-9, Élvonal OTKA KKP138144, H2020-SGA-FET-GRAPHENE-2019-881603 Graphene Flagship Core3, OTKA K134258*

*A. Pálinkás, Gy. Kálvin, K. Kandrai, G. Németh (Wigner FKI), Á. Pekker (Wigner FKI), M. Németh (EK EKBI), P. Petrik, L. Tapasztó, P. Nemes-Incze*

Layered (van der Waals) materials have gained special interest in the last decade because many of them can be exfoliated down to single unit cell thickness. As the thickness decreases, surface effects become more pronounced; hence, both environmental adsorbates and substrates can substantially influence their properties.

Here we show that a self-organized monolayer of molecules adsorbed from the environment often forms on the surface of van der Waals materials exposed to ambient air for several hours. The molecules self-organize into parallel stripes with 5 +/- 1 nm periodicity on several distinct vdW material surfaces (graphite, hBN, $MoS_2$). The presence of molecules self-assembled into stripes has previously been identified by AFM measurements through the observation of distinct friction domains. However, the molecules forming such stripes have not been identified, since their atomic structure could not be resolved by AFM (contact or tapping mode). We were able to resolve the atomic structure of the molecules forming the self-assembled layer by low-temperature STM measurements on graphite, revealing the inner structure of the stripes: their arrangement, precise length and the atomic periodicity of the individual molecules.

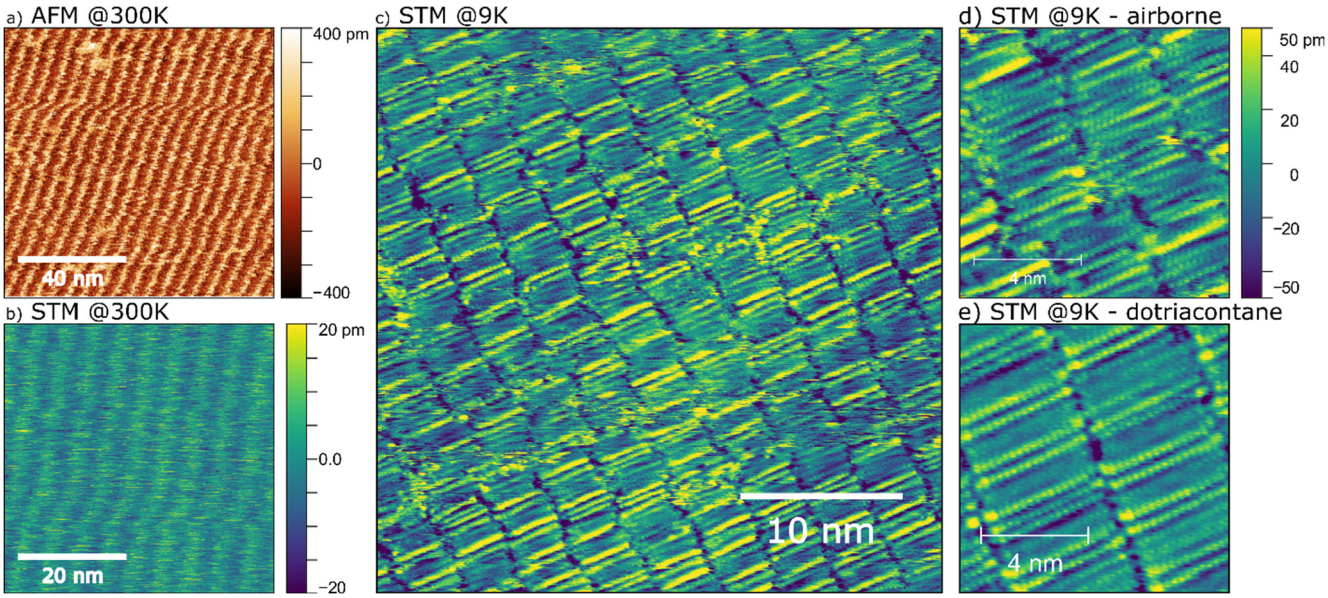


*Figure 1: (a) AFM image of the stripe structure on the surface of graphite b) STM image of the stripes on graphite at 300 K (c-d) Low-temperature STM images revealing the inner structure of the stripes, and the individual molecules self-organized on graphite (e) STM image of vapor deposited dotriacontane ($C_{32}H_{66}$) on graphite revealing rectangular-centered structure.*

The low-temperature topographic STM measurements revealed that the self-assembled monolayer adsorbed from the air consists of long-chain molecules of 20-24 atoms. Such molecules are self-organized into an incommensurate orthorhombic structure. In STM images no signs of any additional functional groups (e.g., -OH, -COOH, -O-, -SH,), have been observed. To further investigate this, we have performed grazing-angle IR-spectroscopy and XPS-measurements, in collaboration. Such measurements did not reveal any signature of functional groups, the obtained spectra were fully consistent with that of the alkyl backbone. From these findings, we can conclude that the airborne monolayer consists of mid-length (20-24 carbon atoms), saturated, linear hydrocarbons, most likely simple alkanes. To support this, we have also performed low temperature STM measurements on vapor-deposited dotriacontane ($C_{32}H_{66}$) on graphite (Fig. 1.e) and found a close similarity with the structure of the monolayer formed during ambient exposure, except for the larger chain length in the $C_{32}H_{66}$ case.

The self-organized monolayer of molecules can be accountable for the domain-like friction anisotropy observed on various surfaces. Fig. 2.a shows an AFM topography map on a graphene (on h-BN), where three domains of different molecule stripe orientation can be recognized, matching the armchair direction of the underlying graphene lattice. The lateral force signal (Fig.

2.b) on the same area reveal three distinct friction domains. We showed that not only airborne monolayer of molecules on vdW-materials, but a vapor-deposited monolayer of dotriacontane ($C_{32}H_{66}$) on HOPG can show similar friction anisotropy.

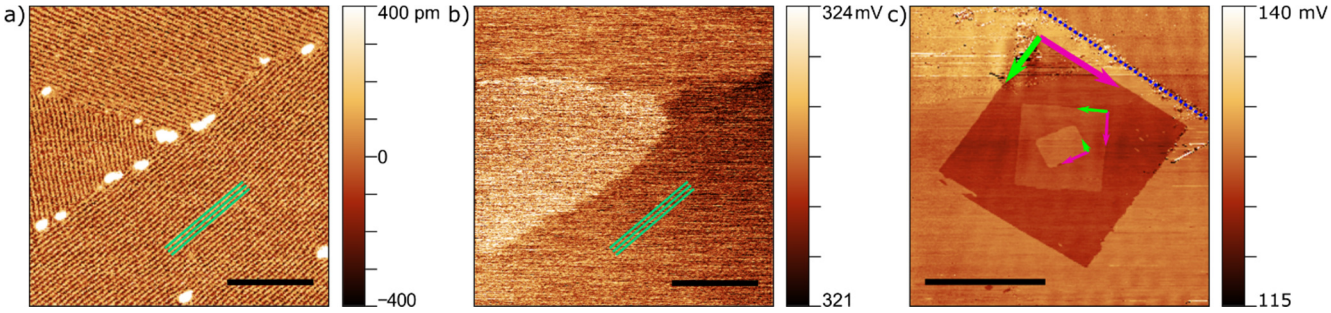


*Figure 2: (a) PeakForce AFM topography map on graphene/hBN shows three distinct domains of stripe orientations. (b) Three distinct friction domains on the same area we measured by contact AFM. (c) The friction force map on a thick hBN crystal after the molecules reorganized by the scanning AFM tip. The fast scan direction (pink arrow) rotated by 60° respect to a zigzag crystal edge (blue dotted line) for the successive "drawing" steps.*

STM measurements indicate that the molecules lie parallel to the zigzag axis of the substrate. We found that the local orientation of the molecular layer can be on purpose switched between the three distinct zigzag directions through repeated scans along the desired direction (mechanical interaction) in contact mode AFM. As a demonstration, we defined three distinct friction domains by three successive rectangular AFM scans (edge length: 15, 7, 3.5 µm) reorienting the molecular arrangement and thus the friction domain structure (Fig. 2.c).

The ubiquitous hydrocarbon chains observed here play a role in the surface chemistry, adsorption, wetting etc. characteristics of 2D materials. Furthermore, the robust and complete saturation of the basal plane, from extremely low concentrations in air might open new routes for designing filters for long chain alkanes.

# DIRECTLY IMAGING VISIBLE-FREQUENCY GRAPHENE PLASMONS BY SNOM IN NANOCORRUGATED GRAPHENE SHEETS

*Élvonal OTKA KKP138144, 680263-NanoFab2D-ERC-2015-STG, H2020-SGA-FET-GRAPHENE-2019-881603 Graphene Flagship Core3, Lendület LP2017-9, OTKA K132869*

*G. Dobrik, P. Nemes-Incze, P. Süle, P. Vancsó, G. Piszter, L. Henrard (Univ. Namur), L. Tapasztó*

We have shown that engineering strong nanoscale corrugations into the atomic structure of graphene, enables the edge-free lateral confinement of graphene plasmons into sub-5nm corrugations, scaling up their resonance frequency from native THz, into the commercially relevant visible range. Visible-frequency graphene plasmons, facilitate orders of magnitude stronger Raman enhancements than previously achieved with graphene, allowing the detection of molecules well below part per trillion level sensitivity, and high selectivity. SERS substrates based on nanocorrugated graphene offer a series of practical advantages over conventional nanoparticle films, such as simpler and cheaper fabrication, better reproducibility, and highly improved environmental stability, up to several months.

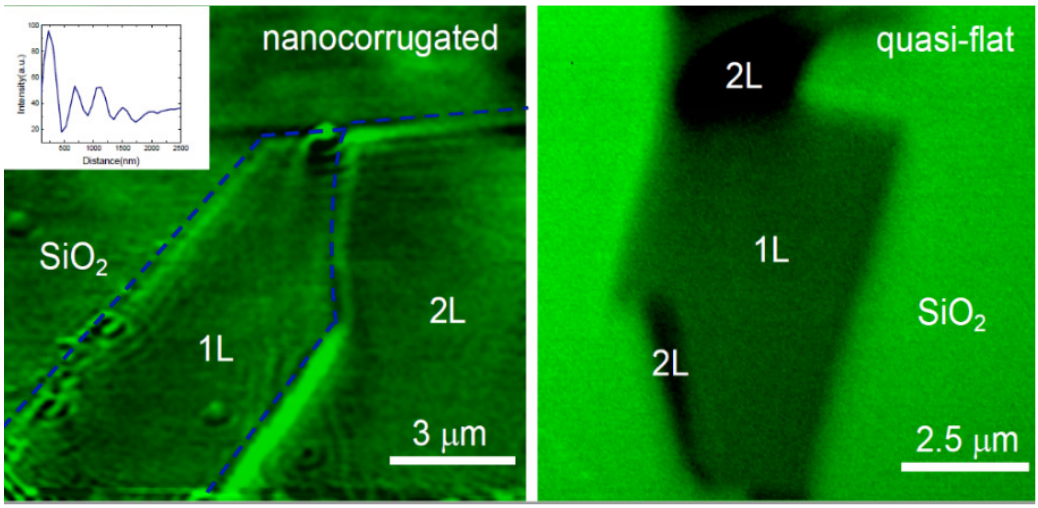


*Figure 1: a) SNOM image (λ= 488nm) of nanocorrugated graphene revealing clear interference maxima and oscillations in the proximity of edges (marked by dashed lines) and defects. Inset shows a line cut perpendicular to the graphene edge. b) SNOM image of quasi-flat graphene recorded under the same conditions, showing no interference patterns.*

Given its significance and the wide range of potential applications, exploring and understanding the detailed properties of visible graphene plasmons is of paramount importance. The most important step in this direction is directly confirming their presence in nanocorrugated graphene. Graphene plasmons in the IR frequency range have previously been detected by Scanning Near-field Optical Microscopy (SNOM), through imaging the interference patterns of the plasmons launched from the apex of a metallic AFM tip with the propagating graphene plasmons reflected from graphene edges and structural defects of the graphene sheet. However, such a technique can only detect propagating plasmon modes, why in our system we were primarily expecting visible plasmons localized into the nanocorrugations.

Our SNOM measurements reveal clear interference maxima in the proximity of edges, as well as fainter ~ 400 nm oscillations inward from edges and defects (Fig. 1.). The observed patterns are highly similar to the SNOM images of plasmon interference patterns on doped quasi-flat graphene at IR frequencies. However, in our case the interference patterns are observed at visible frequencies in nanocorrugated graphene, while quasi-flat graphene samples imaged under the very same conditions show no signs of plasmon interference (Fig. 1.b). Detecting interference patterns, clearly indicates the presence of propagating visible plasmons in nanocorrugated graphene. This is a surprising finding, since localized plasmons were primarily expected. However, localized and propagating plasmons are not mutually exclusive. It has been theoretically predicted and experimentally confirmed that when separated nanostructures, hosting localized plasmons, are located in the close vicinity of each other ($< \lambda_{exc.}$), their interaction can give rise to propagating plasmon modes. In nanocorrugated graphene the corrugations are typically located at least an order of magnitude closer than the excitation wavelength, enabling the interaction of localized plasmons to give rise to propagating modes, observed in our SNOM measurements. Furthermore, in such systems, the dispersion of transversal propagating modes crosses the light line, enabling the existence of plasmon wavelengths larger than the excitation wavelength. This can account for the oscillations of about 400 nm observed in SNOM images.

We have also performed confocal microscopy measurements with the same excitation wavelength. Fig. 2 shows the comparison of the same nanocorrugated graphene flake imaged by AFM, Confocal Microscopy and SNOM.

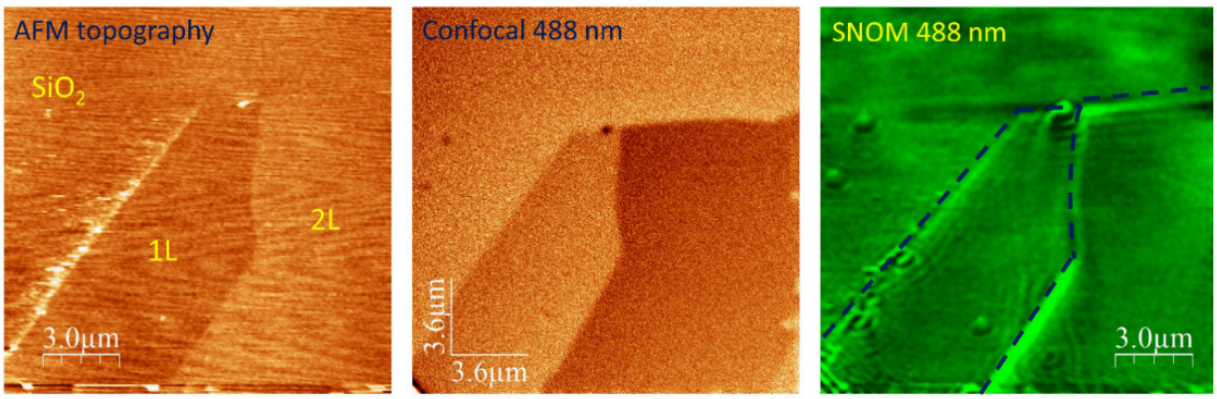


*Figure 2: Confocal ($\lambda_{ex}$= 488 nm) and SNOM ($\lambda_{ex}$ = 488 nm) images of the same nanocorrugated graphene sample*

In contrast to SNOM images, confocal images show no interference patterns on nanocorrugated samples, while using the same excitation laser in both cases. The reason for this is the difficulty of coupling in light into the graphene (to excite the plasmons). While in the case of the evanescent modes of the SNOM tip, this coupling is possible, in the case of far-field propagating light modes the momentum out-of-plane vs. in-plane momentum mismatch preclude the coupling of light into the graphene, and hence the excitation of graphene plasmons. The results have been published in Nature Nanotechnology.

# UNFOLDING THE TOPOLOGICAL PHASE DIAGRAM OF $ZrTe_5$ USING BUBBLE

***Lendület LP2017-9/2017, H2020-SGA-FET-GRAPHENE-2019-881603 Graphene Flagship Core3***

*Z. Tajkov, D. Nagy (ELTE), K. Kandrai, L. Oroszlány (ELTE), J. Koltai (ELTE), Zs.E. Horváth, P. Vancsó, L. Tapasztó, P.Nemes-Incze*

The paradigm of topological phases has permeated much of contemporary condensed matter physics [1]. This fundamentally new way of classifying systems according to global topological properties rather than a local order parameter yielded a deeper understanding of a host of peculiarly robust phenomena. At the heart of these phenomena lies bulk-boundary correspondence, which guarantees robust states localized at the perimeter of the topological materials.

Three-dimensional time reversal symmetric topological band insulators are classified into "strong" (STI) and "weak" (WTI) according to the nature of their surface states. The surface states of the STI are topologically protected from localization, while this does not hold for the WTI [2]. These phases are separated by a metallic, conducting Dirac or Weyl semimetal phase. To change the indices, it is necessary to close and reopen the bandgap through of the metallic phases.

Among the transition-metal pentatellurides, $ZrTe_5$ is an excellent material to investigate the topological phase transitions. This material has been widely studied because it has numerous exotic and therefore interesting physical properties. In the literature of this peculiar crystal, it is well-known that the topological nature of the bulk $ZrTe_5$ has not been unambiguously identified [3]. In our contribution we aimed to investigate the characteristics of the crystal using state-of-the-art experimental STM techniques and computer modelling on a sample of bulk $ZrTe_5$ that hosts bubble on the substrate. The unique strain pattern of the bubble makes possible the tuning of the originally strong topological insulating phase of the crystal into a metallic phase at the perimeter of the bubble. This transition can be observed using STM measurements (see Fig 1.b). The halo of the bubble of this highly anisotropic material only presents at one side of the bubble, where the crystallographic orientation matches the Te-Te chains direction. In the perpendicular direction there is no observable phase transition.

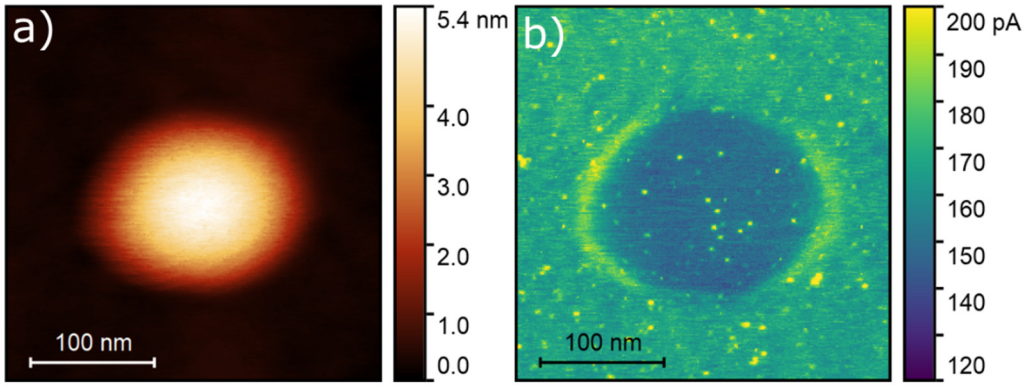


*Figure 1: a) STS topography image of the bubble. b) STM measurements of the same area. The perimeter of the bubble is a high density of states area, indicating a metallic phase. The halo shows a dependency of direction.*

To understand this behaviour, we first must establish a proper description of the elasticity tensor of the material. For this reason, we determined the elasticity tensor elements using density functional theory (DFT) calculations, as the free energy obtained from DFT of a mechanically distorted crystal is a function of the strain pattern of the distortion. This method gave us the total elasticity tensor of the material. Using the data, by numerically solving the three-dimensional equation of motion by the finite element method (FEM), implemented in the COMSOL package, we were able to determine the strain pattern of the bubble. This procedure has allowed us to explain the observed features without the necessity of any phenomenological-based semiphysical, or fitting parameters.

We obtained the electronic properties by DFT of a distorted crystal using the strain pattern that we determined from the FEM method at the two semi-axes of the bubble. The *ab initio* results are in excellent agreement with the measurements. At the major semi-axes point DFT predicts that the band gap is closed, hence the density of states increases. On the contrary at the vicinity of the minor semi-axes the *ab initio* analysis shows a small topologically strong band gap, therefore the density of states remains low.

Establishing the equilibrium state of the crystal we can map the topological phase diagram of the crystal using *ab intio* methods. Fig 2 shows the contour map of the size of the bandgap under different mechanical strain. The horizontal (vertical) axes indicate the strain (in %) along the in plane (van der Waals) lattice directions obtained by DFT. At every point a sign has been assigned to the gap as the topological invariants were calculated. Positive (negative) sign indicates weak topological (strong topological) insulating phase. The phase diagram shows three main domains. Around the equilibrium the system is a STI (1),

and it can be tuned to the WTI phase (3). Between the two insulating phases there is a moderate conducting phase (2). The black tentative line in the conducting phase shows where the Dirac cones in the gamma point touch each other.

This procedure was also tested with a fundamentally different DFT code and the outcome was found to be in perfect agreement with the previous results. Our results will help to clear out some of the controversies about the material and provides a full, experimentally tested, and precise elasticity tensor.

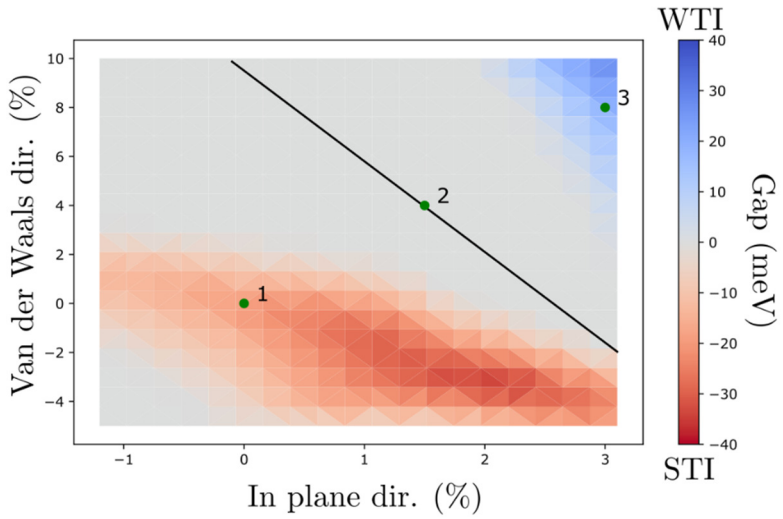


*Figure 2: The phase diagram of the electronic structure of the crystal under mechanical strain. The three main domains are marked by numbers. (1) is STI, (2) is metallic and the black tentative line indicates that the Dirac cones touch each other at the gamma point and (3) is WTI.*

## *Related publications*

[1] J. Asbóth, et al.: *A Short Course on Topological Insulators,* Springer, LNP, 919, (2016)

[2] R. Zohar, et al.: *Strong side of weak topological insulators,* Phys. Rev. B**. 86,** 045102, (2012)

[3] B. Monserrat, et al.: *Unravelling the topology of $ZrTe_5$ by changing temperature*, Phys. Rev. Research **1,** 033181 (2019)

# TUNING THE NANOSCALE RIPPLING OF GRAPHENE WITH PEGYLATED GOLD NANOPARTICLES AND ION IRRADIATION

*OTKA K119532, OTKA FK128327, OTKA K134258*

*Z. Osváth, D. Zámbó, A. Sulyok, A. Pálinkás, A. Deák*

Ripples and wrinkles can highly affect the electronic and optical properties of graphene. The spatially varying strain associated with nanoscale ripples can tune the band structure of graphene through strain-induced pseudo gauge fields. Nanoscale corrugations can also enhance the chemical activity and functionalization of graphene. The controlled realization of nanoscale ripples in graphene has been of high interest in the last decade. However, inducing periodic nanoscale rippling in two dimensions and large areas are still challenging. In this work we present a new method combining gold nanoparticles, strain engineering and ion irradiation for the realization of periodically rippled graphene. The effect of irradiation on the graphene cover layer was revealed by Scanning Tunneling Microscopy (STM), Tunneling Spectroscopy (STS), and Raman spectroscopy.

Gold nanoparticles of 16 nm in diameter were synthesized by seed-mediated, wet-chemical approach, and thiol-terminated polyethylene glycol (mPEG-SH) molecules were grafted onto their surface. High-density monolayers of the PEGylated gold nanoparticles were successfully prepared on Si substrates by the Langmuir-Blodgett technique. Achieving fully ordered state of such small nanoparticles is difficult, nanoparticle voids frequently occur on large scale. These voids appear as dark-contrasted areas on both Scanning Electron Microscopy (SEM) and Atomic Force Microscopy (AFM) images (Fig. 1). The gold nanoparticles were closely spaced in ordered clusters with an average interparticle distance of 18 nm.

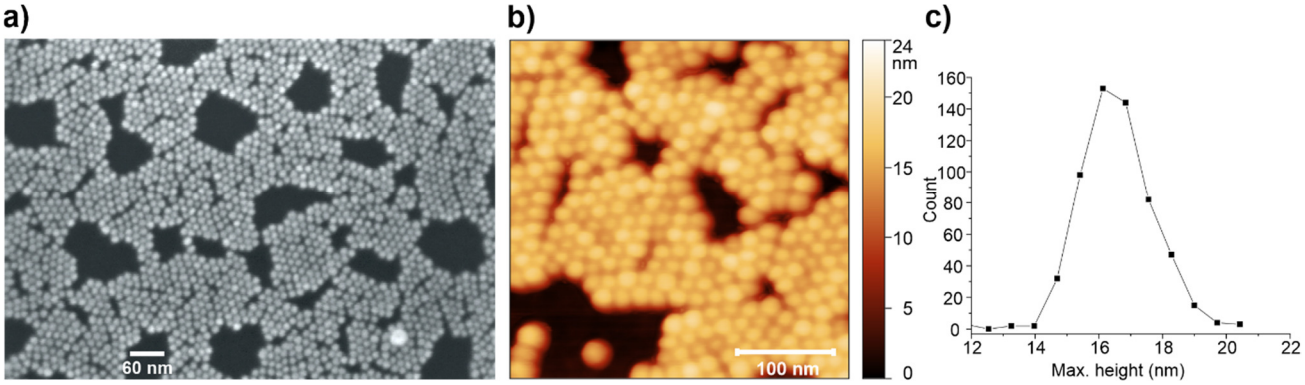


*Figure 1: SEM (a) and AFM (b) images of the prepared gold nanoparticle monolayer. The height distribution of 589 nanoparticles measured by AFM is shown in c).*

Graphene grown by chemical vapour deposition was transferred onto the nanoparticle monolayer. In order to fine-tune the nanoscale rippling of graphene, point defects were introduced by $Ar^+$ ion beam of 1 keV, with fluence of $\approx 10^{12}$ ions/cm$^2$, achieved by 20 sec irradiation. The structure of graphene transferred onto the PEGylated gold nanoparticle monolayer can be observed in Fig. 2.a, which shows the STM image of a completely graphene-covered area. The top of nanoparticles (closely spaced brighter spots), as well as nanoparticle voids (dark-contrasted regions) are both observed through the graphene layer. STM investigations performed after irradiation revealed that the rippling of graphene changed significantly (Fig. 2.b).

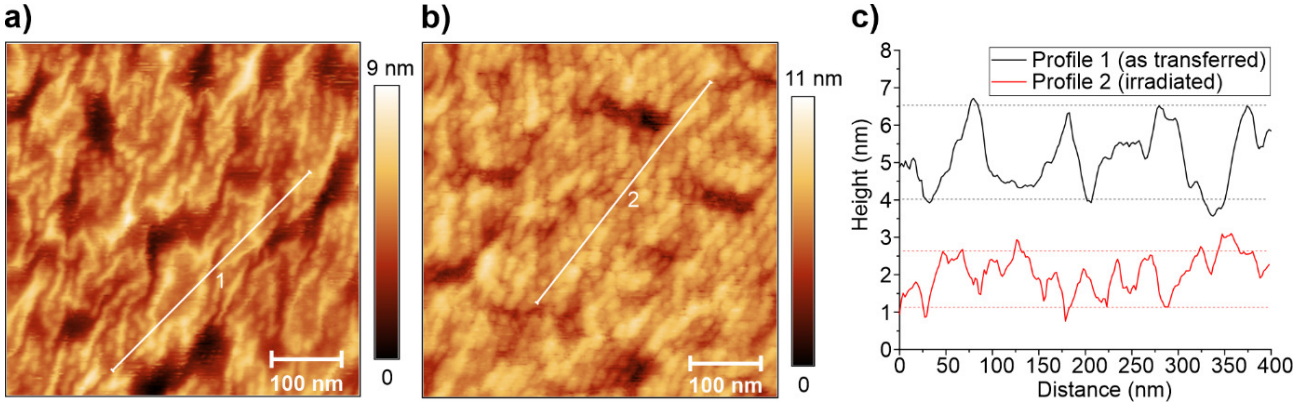


*Figure 2: (a) STM image of graphene as transferred onto the gold nanoparticle monolayer. (b) STM image of graphene supported by nanoparticle monolayer, after ion irradiation. (c) The height profiles corresponding to line section 1 in a) (black line) and line section 2 in b) (red line). Horizontal dotted lines are guides for the eye denoting typical rippling amplitudes. Tunneling parameters: U = 0.5 V, I = 0.5 nA.*

Elongated ripples disappeared, and the typical amplitude of out-of-plane deformations decreased from 2.5 nm to 1.5 nm (Fig. 2.c). A rippling wavelength of around 30 nm can also be identified (Fig. 2.c, height profile no. 2). Although this period is larger than the one of the underlying Au nanoparticles (NPs), it can be considered as a regular, periodic deformation, characterizing the entire irradiated graphene.

Atomic resolution STM measurements revealed hillock-like protrusions, associated with the irradiation-induced point defects, as shown in Figs. 3.a and 3.b (height profile no. 2). As a comparison, the atomic lattice of intact graphene is also resolved (height profile no. 1).

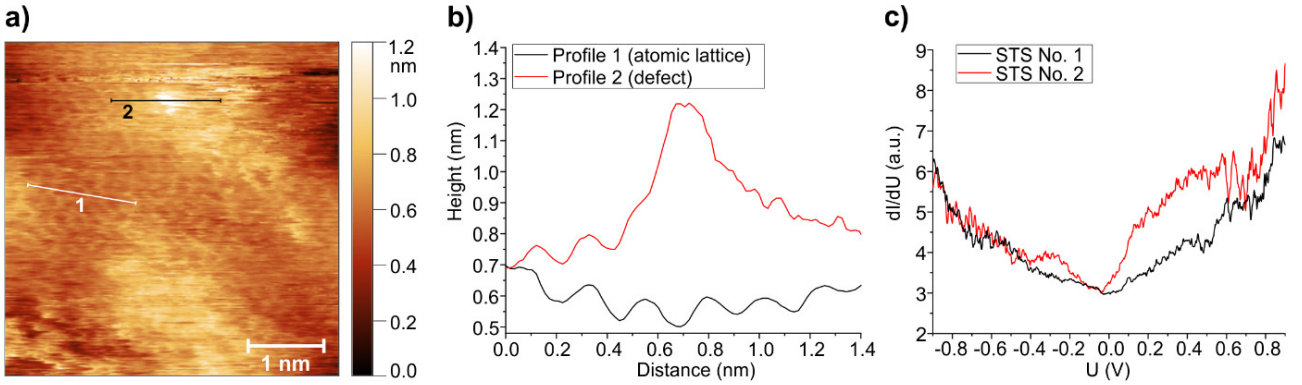


*Figure 3: (a) High resolution STM image of the irradiated graphene shown in Fig. 2b. The height profiles corresponding to unperturbed atomic lattice (section 1) and irradiation-induced point defect (section 2) are shown in (b). (c) STS spectra measured on intact graphene area (black) as well as on graphene area with irradiation-induced defect (red).*

Local dI/dU spectra obtained from STS measurements show increased density of states at a defect site (Fig. 3.c, red line) for positive bias voltages (U), which is the main cause of hillock formation: an apparent increase of height during constant current STM imaging.

## *Related publication*

[1] Z. Osváth, D. Zámbó, A. Sulyok, A. Pálinkás, A. Deák: *Tuning the nanoscale rippling of graphene with PEGylated gold nanoparticles and ion irradiation,* Carbon Trends **5,** 100080 (2021)

# CONCORDANCE OF THE SPECTRAL PROPERTIES OF DORSAL WING SCALES WITH THE PHYLOGEOGRAPHIC STRUCTURE OF EUROPEAN MALE POLYOMMATUS ICARUS BUTTERFLIES

*G. Piszter, K. Kertész, G. Sramkó, V. Krízsik, Zs. Bálint, L. P. Biró*

The wings of butterflies exhibit a richness of colours and patterns unrivalled in the living world. Many of these colors are efficiently used and optimized in sexual communication. These colours may be generated by selective light absorption on pigments, by selective light reflection on photonic nanoarchitectures, or by a combination of the two.

The males of more than 80% of the Lycaenidae species belonging to the tribe Polyommatini exhibit structural coloration on their dorsal wing surfaces. These species-specific colours are produced by the cellular self-assembly of chitin/air nanocomposites. The spectral position of the reflectance maximum of such photonic nanoarchitectures depends on the nanoscale geometric dimensions of the elements building up the nanostructure. Our previous work showed that the coloration of male *Polyommatus icarus* butterflies in the Western and Eastern Palearctic exhibits a characteristic spectral difference. Here, we investigated the coloration and the *de novo* developed DNA microsatellites of 80 *P. icarus* specimens from Europe from four sampling locations, spanning a distance of 1600 km.

The reflectance data for the four dorsal wing surfaces of all male *P. icarus* measured in the present study were used to generate the statistical presentation of the peak wavelength in Fig. 1.A. The averaged spectra of the four sampling sites (TZ: Taizé, France; EF: Érd-1, Hungary; EP: Érd-2 Hungary; EB: Baraţcoş, Romania) are shown in Fig. 1.B. One may observe from both kinds of representations that the colour of the butterflies originating from the four sampling sites show only minor deviations from each other but differs characteristically from the coloration of Asian males investigated previously (Fig. 1.C). The excellent concordance of the coloration from Southern France through Hungary to the Carpathian Mountains in Romania is attributed to similar photonic nanoarchitectures being self-assembled individually in each dorsal wing cover scale in all male specimens investigated.

The chitin building up these species-specific photonic nanoarchitectures is deposited in protein-based molds, self-assembled in a process governed by the DNA of the scale producing cell. The observed spectral similarity within Europe and the difference from the Asian samples, which must originate from difference in photonic nanoarchitectures, may be an indication of subtle divergence that can only be traced by fast-evolving DNA regions. As a first step in the investigation of this hypothesis, we investigated microsatellites – also called Single Sequence Repeats (SSRs) – of European male *P. icarus* butterflies. As SSRs are known to have exceptionally high mutation rate, these are good choice for tracing genetic variability of natural populations.

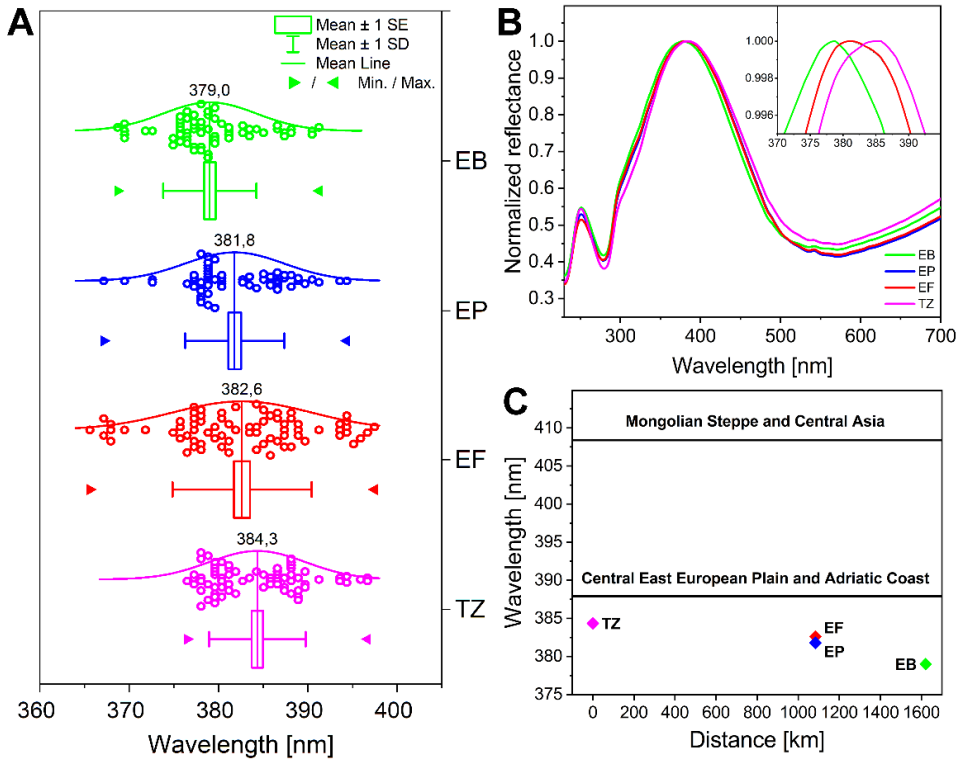


*Figure 1: (A) Box plots of the spectral position of the blue reflectance maximum of male P. icarus butterflies. (**B**) Averaged spectra of the specimens from the four sampling sites. (**C**) The coloured diamonds show the spectral position of averaged reflectance maxima measured now, while the lines stand for the averages of European and Asian samples investigated previously.*

Altogether, we successfully genotyped 79 individuals of *P. icarus* for ten, *de novo* developed species-specific microsatellite loci from four populations representing three geographically distinct groups (France, Hungary, Romania).

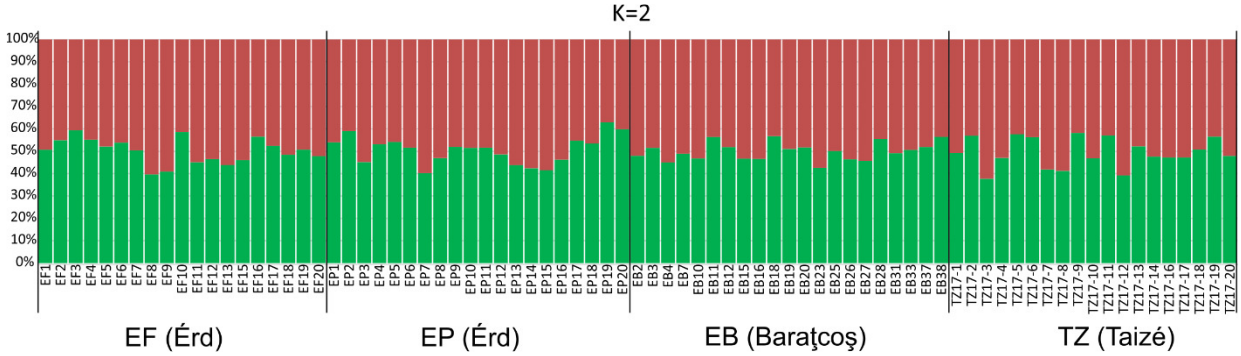


*Figure 2: A posteriori assignment of the studied Polyommatus icarus individuals into two genetic clusters that is the most likely number of clusters in our genetic dataset.*

Population genetic differentiation was found to be exceptionally low between the four populations analyzed, as it can be seen (Fig. 2.), showing remarkably good concordance between the spectral properties of the blue sexual signalling colour (coincident within 5 nm in the four sampling sites) and the population genetic structure as revealed by 10 microsatellites for the *P. icarus* species.

# MULTI-INSTRUMENTAL TECHNIQUES FOR EVALUATING BUTTERFLY STRUCTURAL COLOURS: A CASE STUDY ON POLYOMMATUS BELLARGUS

*K. Kertész, Zs. Bálint, G. Piszter, Z. E. Horváth, L. P. Biró*

Colour is an important communication channel for day-flying butterflies. Chemical (pigmentary) coloration is often supplemented by physical colour generated by photonic nanostructures. These nanoarchitectures (characteristic for a given species) exhibit wavelength ranges in which light propagation is forbidden. The photonic nanoarchitectures are located in the lumen of the wing scales and are developed individually by each scale during metamorphosis. This self-assembly process is governed by the genes in the nucleus of the scale producing cell. It is crucial to establish well-defined measurement methods for the unambiguous characterization and comparison of colours generated in such a complex manner. Owing to the intricate architecture ordered at multiple levels (from centimetres to tens of nanometres), the precise quantitative determination of butterfly wing coloration is not trivial. We present an overview of several optical spectroscopy measurement methods and illustrated techniques for processing the obtained data, using the species *Polyommatus bellargus* as a test case, the males of which exhibit a variation in their blue structural colour that is easily recognizable to the naked eye (Fig. 1.A).

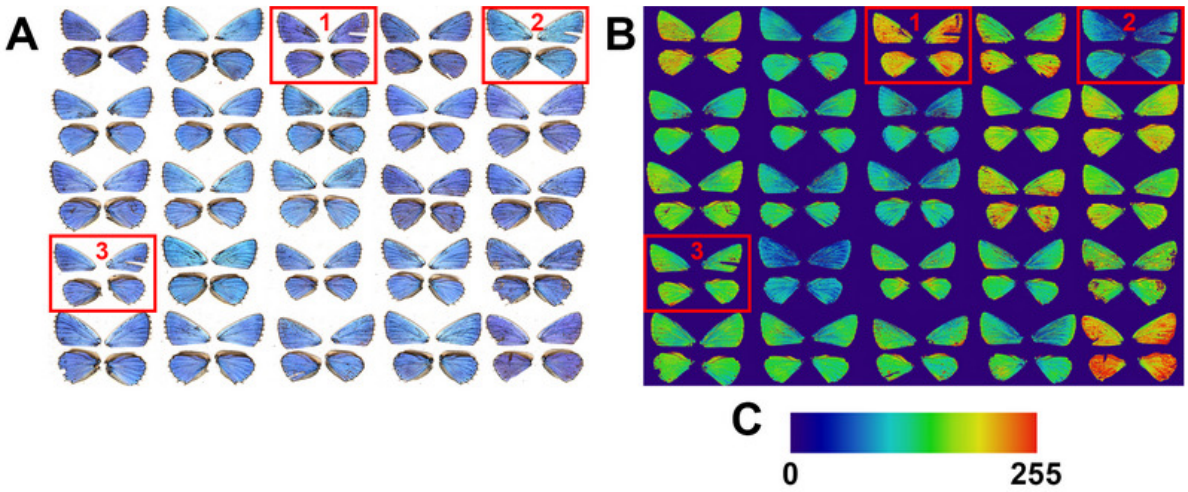


*Figure 1: Photographs and image analysis of 25 Polyommatus bellargus specimens. (**A**) Unprocessed photographs of the four detached wings of the specimens showing dorsal wing surfaces acquired under identical conditions. (**B**) False-colour image of the hue channel of wings shown in (**A**). (**C**) Colour bar showing the colours associated to hue values of 0-255.*

In previous studies, colour characterization was often conducted using one or only a small number of measurement methods and sometimes using only just one or several samples. This may have led to important properties and aspects of intraspecific variation being overlooked. Therefore, the use of multiple techniques to determine the structural and spectral properties of complex objects could be very advantageous.

When investigating the light reflected from a butterfly wing, one may frequently face the question of how to accomplish nondestructive analysis, as these samples are often rare or unique in museum collections. A fast and simple approach is to consider the wing as a flat surface. Starting from the nondestructive optical methods ending with fully destructive electron microscopy, we present an overview of the multi-instrumental analysis of male specimens of the butterfly *Polyommatus bellargus* and demonstrate the possibilities of a detailed characterization of biological structural colours. This allows the reader to assess which is the most useful combination of test methods in terms of sample availability, vulnerability, and desired accuracy. In our test species the hue of the blue colour varies from violet to turquoise, which can be qualitatively analyzed using the photographs (Fig. 1.B) while a more precise differentiation is possible by using various spectroscopy setups. Adding microcopy techniques, the final aim is in the understanding of the relationship between biology and physics via exploring the phenomenon that results from this variation of blue colours and how this colour variance is generated on the nanostructure level.

The properties of the different methods in Table 1 cover aspects worth to consider before planning optical or structural measurements. Not all methods are necessary, the correct selection is governed by the available time, the sample properties, and the required depth of the analysis. Nondestructive and faster methods often provide less precise results than slower and more labor-intensive, destructive ones. In the case of the presented test species, *P. bellargus*, we found the origin of the wing colour differences in the scale nanostructure level which resulted in variation of the blue structural colour. This in turn is tentatively associated with the unusually large genetic drift reported for this species in the literature.

*Table 1: Overview of the discussed materials science methods for a detailed characterization of biological structural colours*

| Method | Speed | Interpretability | Acquisition size | Instrument cost | Sample preparation |
|---|---|---|---|---|---|
| Photograph analysis | fast | easy | > cm | low | nondestructive |
| Normal incidence spectral measurement | fast | easy | ~ 1 mm | medium | nondestructive |
| Integrating sphere spectral measurement | slower | easy | 6 mm | medium | wing removal, preferably flat sample |
| Spectrum fitting | slower | mathematical model is needed before application | - | - | - |
| Hyperspectral measurement | slow | postprocessing is needed | > cm | higher | nondestructive |
| Spectrogoniometer | slow | postprocessing is needed | ~ 5 mm | higher | wing removal |
| Single scale microspectrometry | slow | easy | < 100 µm | higher | wing scale removal |
| SEM | slow | easy | < cm | high | destructive |
| TEM | slow | easy | < 10 µm | high | destructive |

# NON-DESTRUCTIVE EVALUATION (NDE) SYSTEM FOR THE INSPECTION OF OPERATION-INDUCED MATERIAL DEGRADATION IN NUCLEAR POWER PLANTS

## *EU H2020 755330 NOMAD*

*A. Gasparics, G. Vértesy and I. Borsos*

The Long-Term Operation (LTO) of existing Nuclear Power Plants (NPPs) has already been accepted in many countries as a strategic objective to ensure adequate supply of electricity over the coming decades. In order to estimate the remaining useful lifetime of NPP components, LTO requires reliable tools. The objective of NOMAD project is the development, demonstration and validation of a Non-Destructive Evaluation (NDE) tool for the local and volumetric characterization of the embrittlement in operational Reactor Pressure Vessels (RPVs).

In order to address these objectives, developed NDE tools were tested on Charpy geometry samples, which ones represent the material properties, and on cladded material block type specimen which ones emulates the real application. The MFA contributes to the NOMAD project with own micromagnetic testing method: so called Magnetic Adaptive Testing (MAT). MAT is a recently developed method for nondestructive characterization of ferromagnetic materials which is based on systematic measurement and evaluation of minor magnetic hysteresis loops.

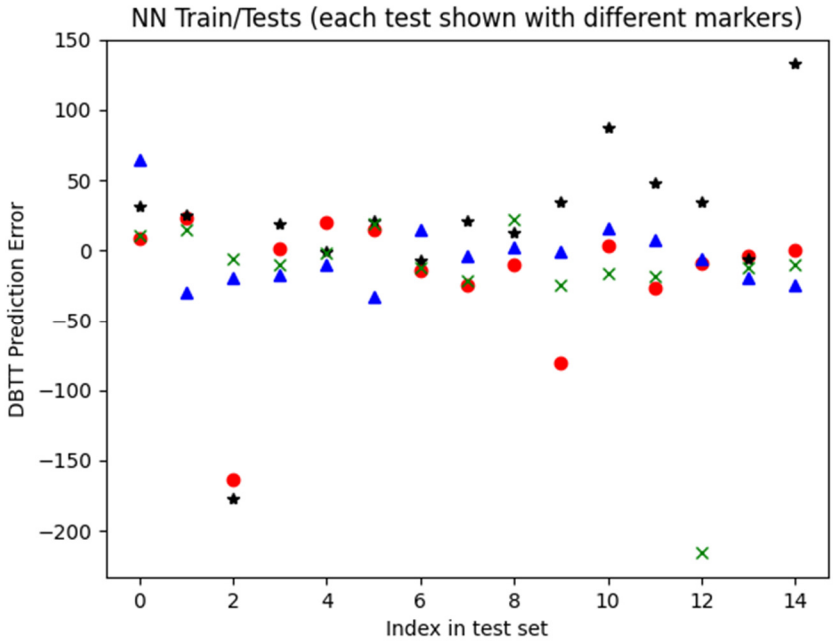


*Figure 1: Example of the Neural Network Regression results on 15 test elements with index of 0…14. The key parameters of the studied structure: 1st Layer width: 128; Depth: 3; Dropout factor: 0.4, Epoch: 10.000*

MAT measurements were performed on reactor steel material before and after neutron irradiation and the nondestructively determined magnetic parameters were compared with the destructively measured Ductile-to-Brittle Transition Temperature (DBTT) values and with other available mechanical test results, such as the Upper Shelf Energy, Vicker Hardness and Yield strength were provided by Belgian Nuclear Research Centre (SCK•CEN). Within the framework of the project five different electro-magnetic, electric and acoustic non-destructive measurement techniques were applied on the common specimen set and their results are processed and evaluated individually. A common data-base has been established on the outcomes of the individual non-destructive, as well as, of the destructive test results in order to evaluate the performances of the different NDE methods, but also to be able to recognize their possible synergies.

Our team performed Neural Network (NN) based analysis on the established common data base of all output values of the five different NDE methods are obtained on all specimens were measured in the hot cell campaigns, as well as, previously to the irradiation. The determination of the DBTT was targeted, and the achieve resolution of the combined methods was studied. Also the applicability of the NN system was studied by using different configuration and structures and their results were compared. The results are quite encouraging: the real and successful application demands to be able to distinguish unambiguously 50° of DBTT shift, and the NN could provide better resolution. However, some outlying elements were observed (Fig. 1). On one hand, this problem can be related to the extraordinary low number of train set elements, that makes hardly applicable any statistical approach. Nevertheless, these outliers were studied further by a Bagging – Bootstrap aggregation method developed by Leo Breimann (1994), so called 'Ensemble machine learning' technique. Each of the dataset

elements was excluded, the NN was trained for the rest in the same predefined way. Than the excluded element was predicted by the NN. The training with randomly selected train sets, and the testing of the excluded element was repeated 20 times (Fig. 2.). Following that, the results were averaged. This way, at the very end, all performance of the NN for all elements could be compared (Fig. 3.).

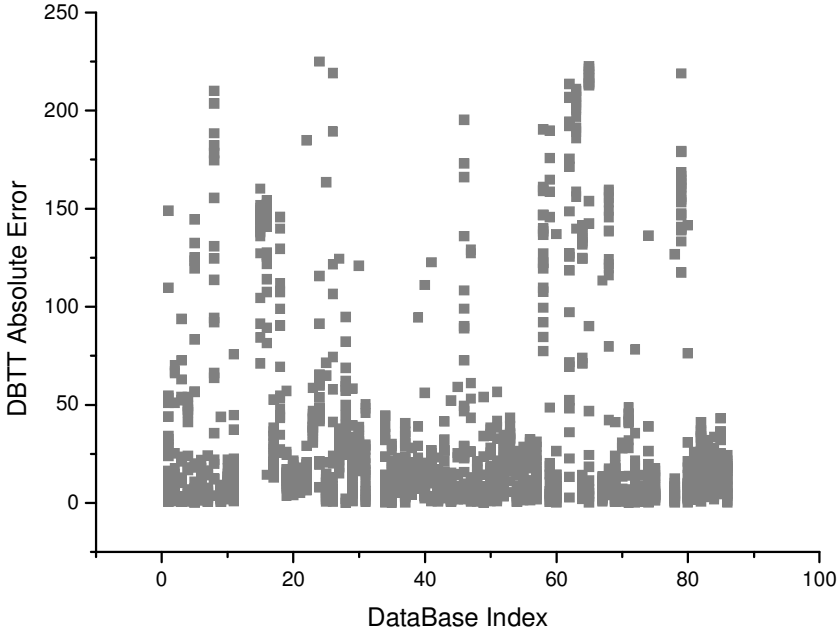


*Figure 2: NN performance (in all test runs) in case of each database element*

By excluding the worst 9 elements of the dataset (out of 89) as outliers the error of prediction was improved significantly. Without database reduction, the prediction error was found ~34°C on average. The exclusion reduced this average error below the margin, as: ~22°C.

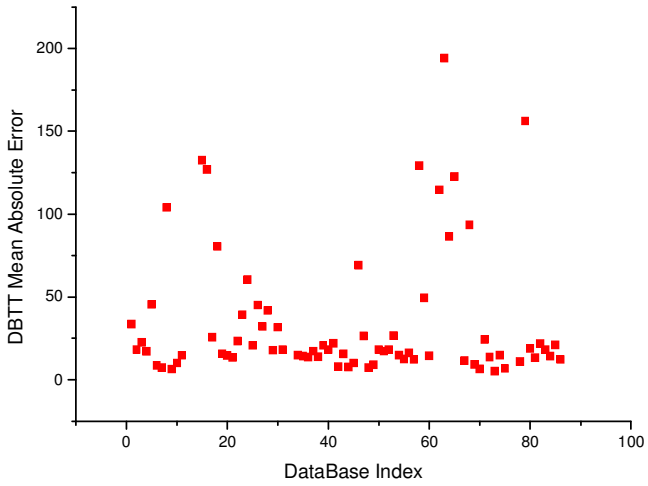


*Figure 3: NN performance (average of errors) in case of each database element*

The possible interpretation of the observed outliers is that the NN technique can be applied for data interpolation only, since it cannot classify those values are outside of the teaching sample range. The outliers represent measurements on the border of the ranges, so by excluding them from the train set, the data range is reduced as well. By excluding these outliers, the NN approach could provide sufficient resolution of the DBTT prediction, i.e. ~22°C that is below the need of the possible application (i.e. 25°C).

The most important NOMAD specimens from application point of view are the irradiated bocks. These were measured in the third hotcell campaign (HCC3) by the MAT method. The Data-analysis of the HCC3 MAT measurements could provide promising outcome for the prediction of the base material degradation that measured though the cladding. Considering the applied neutron fluence values, which were the so called 'independent' parameter of our evaluation, systematic function between the evaluated data and the independent parameter could be found with reasonable errors (Fig. 4).

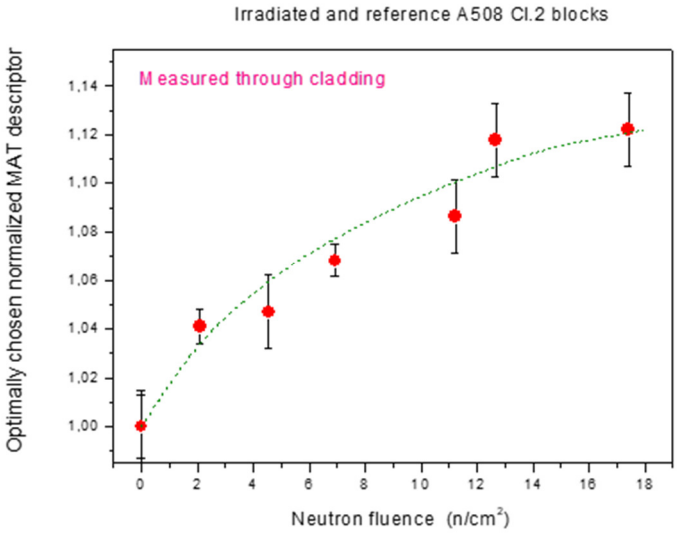


*Figure 4: MAT results obtained on block type specimens through the cladding as a function of the neutron irradiation fluence values*

The importance of this outcome is that there is an application potential of the MAT method for inspecting the nuclear reactor vessel from inside, through the cladding. This has particular importance, since the easiest direction for testing the reactor vessel wall is measure it from inside, i.e. through the cladding on it. We should note, that the very limited sample set does not allow the statistical validation of any method. Also, the inhomogeneity of the tested samples are necessary to study further more.

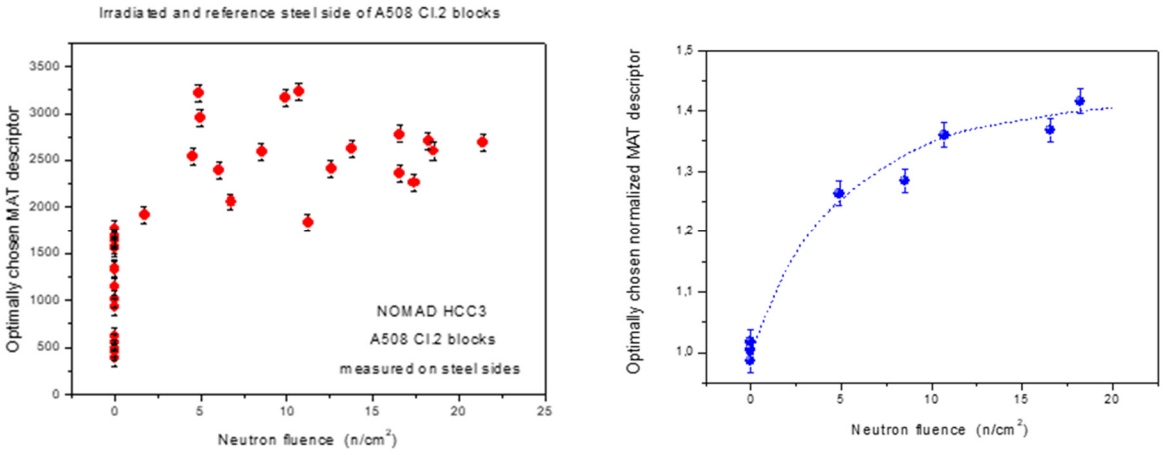


*a)* *b)*

*Figure 5: Preselection of magnetically similar base material samples reduces the scattering a) MAT results on all samples, b) MAT results on the preselected samples*

The MAT method makes also possible the preselection of the experimental results, that means excluding the outliers before(!) the MAT evaluation process on the base of the acquired raw data, practically even in real time with the measurements. The reasons for the outlying probe responses can be various: the magnetic coupling problem, surface contamination or can be also originated from the material inhomogeneity. Unfortunately, this cannot be studied within the framework of the NOMAD project on its merit. However, by using the above mentioned preselection (if the dimension of the dataset makes it possible) it can reduce dramatically the MAT prediction error (Fig. 5.). Therefore, this is also an argument for the MAT applicability [1-3].

## *Related publications*

[1] M. Rabung, M. Kopp, A. Gasparics, G. Vértesy, I. Szenthe, I. Uytdenhouwen, K. Szielasko: *Micromagnetic Characterization of Operation-Induced Damage in Charpy Specimens of RPV Steels,* Applied Sciences-Basel **11:(7),** 2917 (2021) IF: 2,679

[2] G. Vértesy, A. Gasparics, I. Szenthe, M. M.elanie, R. Kopp, J.M. Griffin: *Analysis of Magnetic Nondestructive Measurement Methods for Determination of the Degradation of Reactor Pressure Vessel Steel* Materials **14:(18),** 5256, 15 p. (2021) IF: 3,623

[3] G. Vértesy, A. Gasparics, I. Szenthe, I. Uytdenhouwen: *Interpretation of Nondestructive Magnetic Measurements on Irradiated Reactor Steel Material,* Applied Sciences-Basel **11:(8),** 3650, 13 (2021) IF: 2,679

# CLUSTERING AND SPECTROSCOPY OF NANOPARTICLES

*OTKA FK 128327, OTKA KH 129578*

*D. P. Szekrényes, Zs. Zolnai, D. Zámbó, A. Deák*

In the framework of our running projects we investigate the surface modification and self-assembly of nanoparticles that have engineered surface ligand layers. For the studies we employ plasmonic nanoparticles of different shape and size that are wet-chemically synthesised in our lab. Our research efforts make use of the localised surface plasmon resonance changes that occur when the surrounding of plasmonic nanoparticles is modified. This modification can stem from changes in the composition and distribution of the molecular capping layer of the colloidal particles, or the presence of another particle due to clustering or aggregation. In addition to well-established ensemble characterization methods, like solvent based visible-light extinction spectroscopy and dynamic light scattering, we heavily rely on single-nanoparticle microspectroscopy, that allows a more detailed and fundamental investigation of the optical properties of the nanoparticles and their structures.

The clustering of PEGylated nanoparticles was investigated at the ensemble and single particle level. The aim of this research project is to study the colloidal stabilization properties of surface grafted Polyethylene Glycol (PEG) chains. Two types of gold nanospheres were prepared: one features permanent positive surface charge due to covalently bound MTAB ((11-Mercaptoundecyl)-N,N,N-trimethylammonium bromide), the other has a negative surface charge (citrate, MUA or PEG-COOH coating). The Electric Double Layer (EDL) interaction dominated attractive interaction between these two species leads to heteroaggregation in the bulk liquid phase, and the resulting plasmon shift can be followed by conventional extinction spectroscopy (Fig. 1.a), confirming the affinity of the two particle types. For the PEG-COOH no significant shift is observed, but still, heteroaggregation takes place when the MTAB coated particle is fixed on a substrate and the PEG-COOH coated particle is allowed to assemble on it for several hours (Fig. 1.b). It was found that not only dimers, but larger clusters (up to heptamers) are also formed. All particle assemblies indicate a 2D (in-plane) arrangement of the particles that might be attributed to the relatively weak coordination of the assembling particles and the consequent rearrangement upon drying under the action of immersion type capillary forces. Current efforts target the optimisation of the surface charges and PEG chain length to obtain a better control over the resulting cluster size and structure.

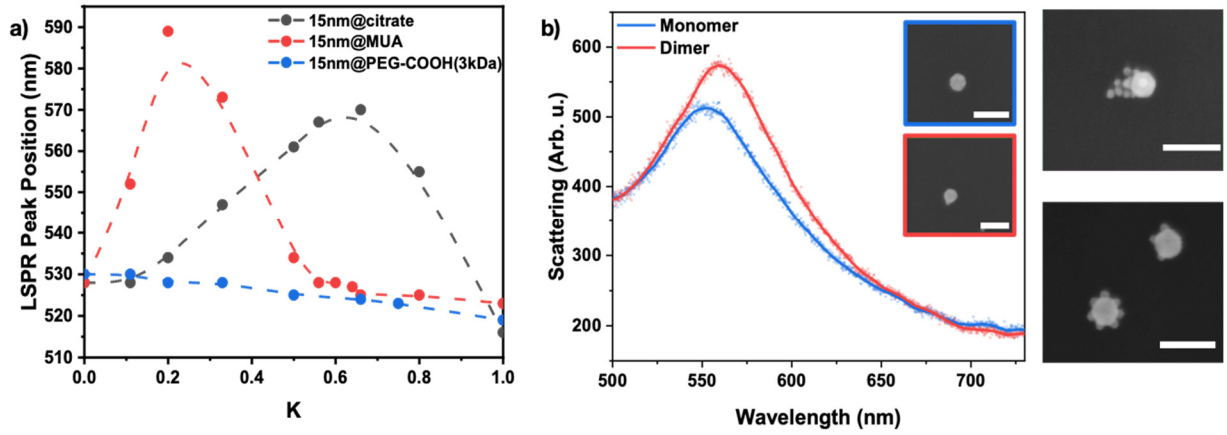


*Figure 1: a) Shift of the surface plasmon resonance as a function of the ratio of MTAB modified, positively charged 49 nm particles with 15 nm nanospheres. b) Single particle spectrum and structure of heteroclusters created at the solid/liquid interface.*

Another focus of our research activity is related to the controlled surface chemical patch formation of plasmonic nanoparticles. The engineered surface modification can allow the fabrication of complex nanoparticle assemblies and provide the background for applications in biology and optoelectronic fields. We employ gold nanoprisms and use two different thiol ligands, namely cysteamine and thiolated PEG (mPEG-SH) to create the molecular patches. Our strategy is based on the different accessibility of the particles' surface having low and high curvature regions. In these regions the original capping ligand layer has different packing density, allowing to create molecular patches first at the tips and edges of the nanoprisms – provided the ligand concentration is kept low enough. As shown in Figure 2.a, the dipole plasmon mode blueshifts over time as cysteamine is added to the system as a consequence of the decreasing effective refractive index in the optical near-field around the tips and edges.

From these measurements alone the site selective accumulation of the short chain thiols cannot be determined unambiguously. Hence we perform additional single particle spectroscopy studies and rely on the chemical interface damping related plasmon linewidth broadening as an additional indictor to assess the total amount of molecules accumulated at the particles' interface. At the present stage it was successfully verified that the scattering spectra of the individual patchy particles' can be fitted with Lorentzian oscillator model, where the contribution of the interband transition is taken into account (Figure 2.b). This enables to study in situ in a flow cell arrangement the molecule adsorption on individual nanoprisms based on the Chemical Interface Damping (CID) induced resonance peak broadening.

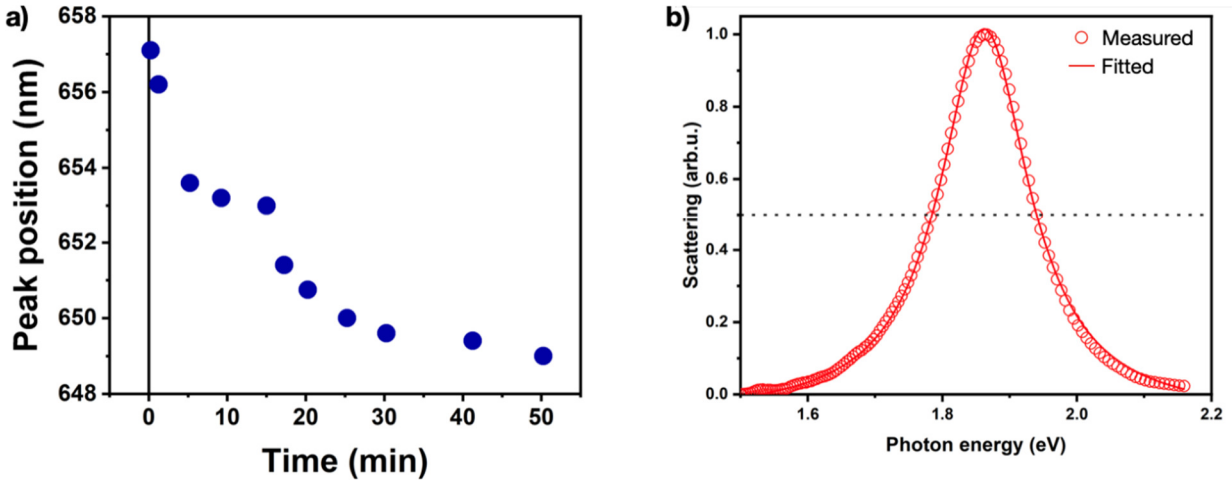


*Figure 2: a) Shift of the dipolar plasmon resonance wavelength as a function of time when cysteamine ($5\times10^{-2}$ mM) is added to gold nanoprisms (average edge length ca. 65 nm). b) Measured and fitted single particle scattering spectrum of a patchy gold nanoprism. The interband transition contributes with 40 meV to the resonance width for the given particle.*

# CAPILLARY BRIDGE PROBE METHOD ON HYDROPHOBIC SURFACES: LIQUID BRIDGES WITHOUT NECK OR HAUNCH

***OTKA FK 128901***

*N. Nagy*

The developed indirect Capillary Bridge Probe method combines the accuracy of the Wilhelmy method and the general usability of the sessile drop method without their limitations. The method is based on the use of a liquid bridge as a probe: the capillary bridge of the test liquid is stretched between the base of a cylinder and the investigated surface under equilibrium conditions. The advancing contact angle on the sample can be measured during the slow (quasi-static) decrease of the bridge length. The receding contact angle is determined during the retraction of the cylinder. The contact angle is calculated from Delaunay's analytical solution, while the three necessary parameters are the measured capillary force ($F_c$), the radius of neck or haunch ($r_0$), and the radius of the contact line ($r_s$) on the investigated surface. The latter two parameters are obtained from the automated analysis of the captured image of the liquid bridge. The radius of the upper contact line ($r_c$) is constant since it pins on the rim of the cylinder.

The evaluation of full measurement cycles on hydrophobic surfaces is difficult, because several measured state of a water liquid bridge e.g. on a Polytetrafluoroethylene (PTFE) surface do not contain the neck or haunch region, as it is shown in Fig. 1. Therefore, one necessary parameter, the neck/haunch radius is unknown. How can be these measurements evaluated?

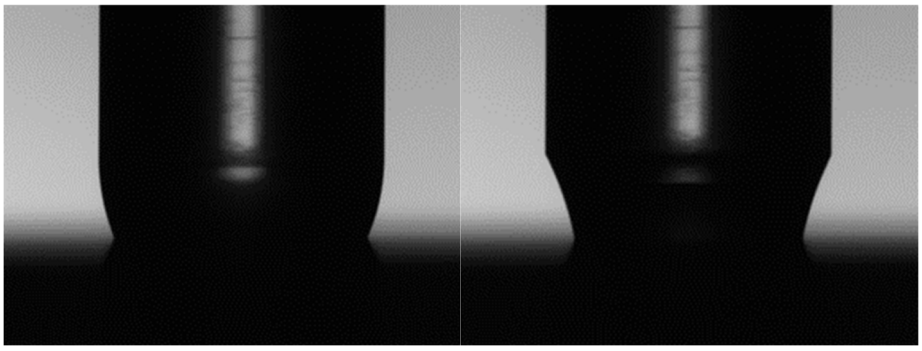

*Figure 1: Water liquid bridges without the haunch (left) and the neck (right) region, captured on a PTFE surface.*

Four different subcases can be identified to solve this problem: neck or haunch is missing and the upper or the lower part of the bridge is observable. These four cases can be seen in Fig. 2.

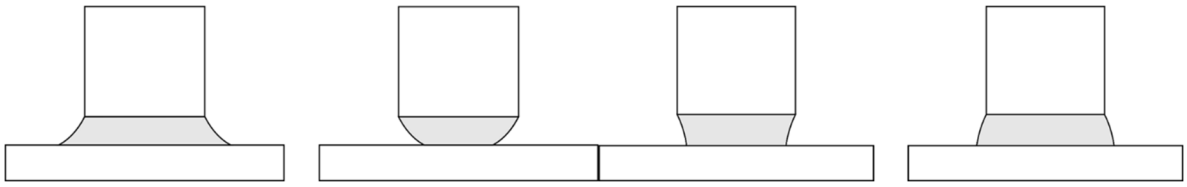

*Figure 2: Four different subcases of capillary bridges without neck or haunch.*

The two schematics to the left represent the lower part, while the two other show upper part of a liquid bridge. If we see the lower part, the surface radius ($r_s$) can be measured. Let's complete the shape of the bridge with the missing part so that let the upper contact radius match the radius of the cylinder (see Fig. 3)!

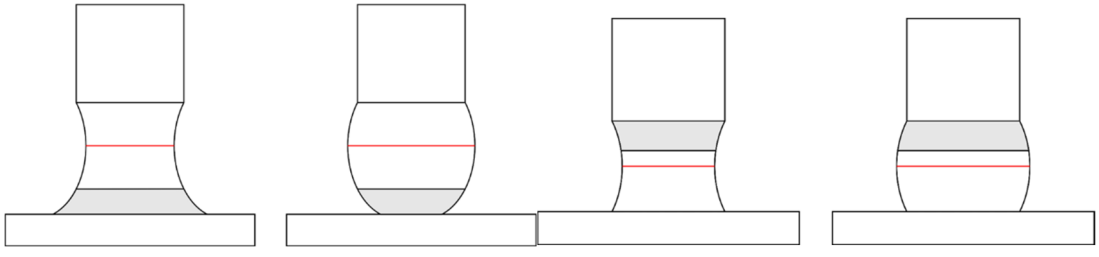

*Figure 3: Completing the shape of capillary bridges with the missing part.*

The resulted liquid bridge has the same radius, curvature, and capillary force as the real one has because of the constant mean curvature of the Plateau-surfaces. Polynomial fitting of the contour results an estimated contact angle on the investigated surface by derivation. According to this value, a contact angle range can be defined, thereby the potential liquid bridges can be found in the previously calculated look-up tables! Finally, the most appropriate capillary bridge with one definite $r_0$ is chosen according to the position of the lower contact points. Therefore, all parameters (including volume and surface area) can be calculated analytically.

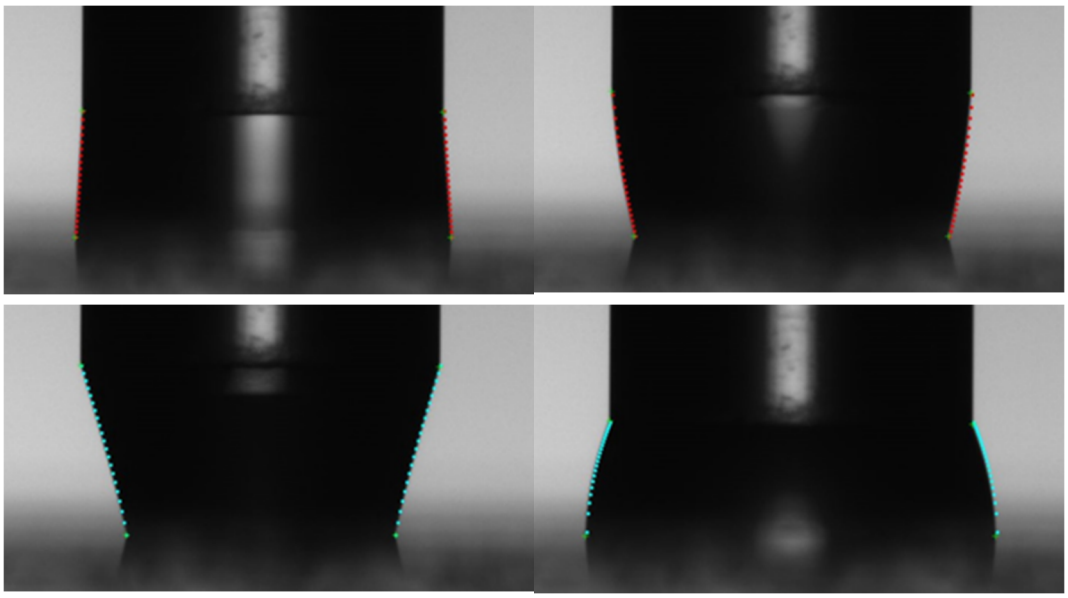

*Figure 4: Evaluated images of a water capillary bridge formed on a Zeonex-coated surface during one measurement cycle. The order of images follows the previous order of different subcases, not the measured sequence.*

In those cases when the upper part appears, the problem seems to be more complicated because the surface radius is also unknown. In this situation, the solution is to find a symmetric liquid bridge, i.e. where the surface radius is equal to the radius of the cylinder! The capillary force of the completed bridge is identical to the force of the real liquid bridge due to their constant mean curvature. Due to the symmetry, the contact angle on the rim of the cylinder is equal to that which is formed on the imaginary surface. From this point, the procedure is similar to the previous cases: the polynomial fit helps to find a contact angle range and the position of the (real) contact points chooses the right nech/haunch radius of the capillary bridge. Now, we have all three input parameters to calculate every parameter of the real, original liquid bridge: contact angle on the sample surface, length, volume, area, etc. A water liquid bridge streched between the cylinder and a Zeonex-coated surface forms all of the four different subcases during one measurement cycle. Fig. 4 shows evaluated examples of these equlibrium states. The order of images in Fig. 4 follows the previous order of different subcases, not the measured sequence.

# NOBLE METAL NANOROD CRYOAEROGELS AS NOVEL ELECTROCATALYSTS

*D. Zámbó*

Properties of nanoparticle building blocks can be retained and novel functionalities arise if they are assembled into functional nanostructures. One of the novel candidates of this materials class is the nanocrystal gel structures, which overcome the limitations emerging in case of practical applications of colloidally dispersed nanoparticles. The potential preparation methods of modern nanocrystal gels can be classified into two main families: the chemical and physical approaches. While the former includes the destabilization of the nanoparticle solutions via chemical triggers, so-called cryoaerogels are a novel class of physically gelated structures, including three main steps: concentration of the solution, flash-freezing and freeze drying of the frozen nanostructure to achieve air-filled pores and thus, aerogel structures. These gels (xerogels, aerogels and cryoaerogels) can revolutionize the application of these nanomaterials in sensorics, photo(electro)catalysis and energy harvesting.

Whilst plasmonic nanoparticles with small sizes and quasi-spherical shape have already been employed as cryoaerogel building blocks, larger plasmonic noble metal nanorods suffered from the limitation of synthetic procedures, stability of concentrated nanorod solutions and their relatively weaker catalytic activity compared to their spherical counterparts.

In this study, we demonstrated the fabrication of solid-supported cryoaerogel electrodes based on gold and silver nanorods via overcoming the above-mentioned limitations. Additionally, a proof-of-concept of electrocatalytically active nanorod cryoaerogels was presented. These porous cryogel networks are of great interest in direct liquid fuel cell-related application, such as ethanol oxidation reaction as well as electrochemical redox and glucose sensing. [1]

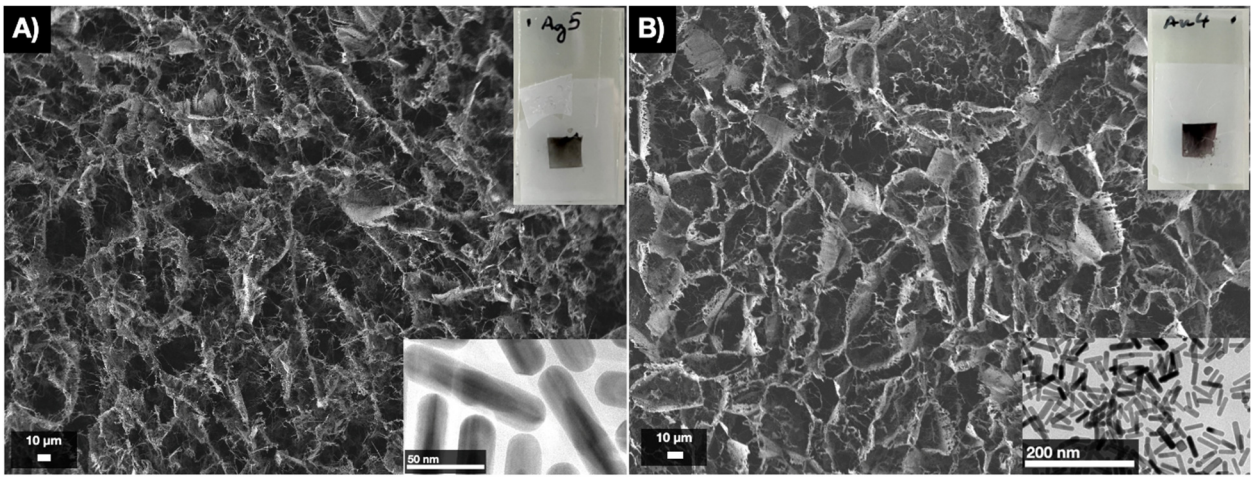


*Figure 1: SEM images of cryoaerogel-coated ITO electrodes consisting of Ag@Au nanorods (A) and Au nanorods (B). Insets show the physical appearance of the electrodes (upper right corners) and the TEM images of the colloidal building blocks (lower right corners).*

This work includes the upscaled colloidal synthesis of the noble metal nanorods, the modification of their surface with a conductive polymer shell (PEDOT:PSS), their concentration up to 5-9 g/L and the fabrication procedure of the cryoaerogel-coated ITO substrates.

It was found, that the cryoaerogels increase the overall conductivity of the ITO electrodes and facilitates their use as electrocatalysts due to the availability of the nanorods' active sites upon assembling the building blocks into porous macrostructures. Thus, electrochemical test reactions were performed to study the oxidation and reduction of the noble metal surfaces, their activity in redox couple reactions ($[Fe(CN)_6]^{4+}/[Fe(CN)_6]^{3+}$), ethanol oxidation reaction and glucose sensing.

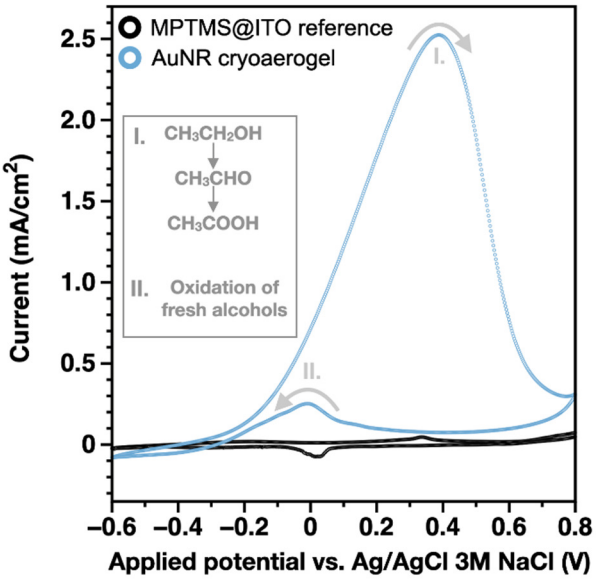


*Figure 2: Performance of the Au nanorod cryoaerogel electrode (blue) and the pure ITO substrate (black) in ethanol oxidation reaction in the presence of KOH.*

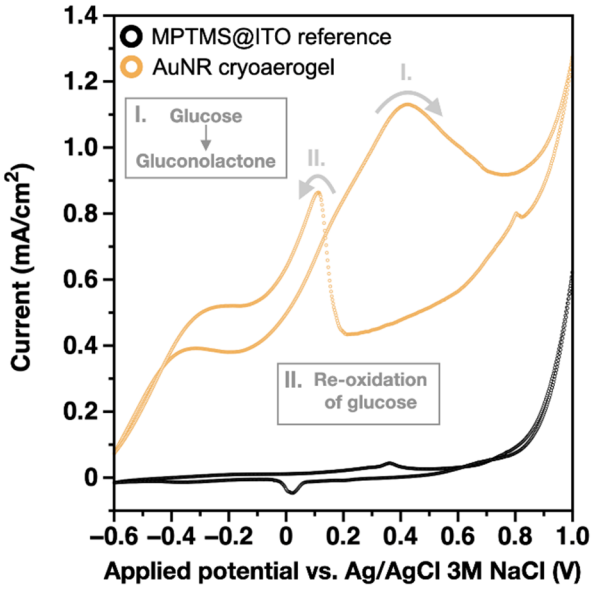


*Figure 3: Performance of the Au nanorod cryoaerogel electrode (orange) and the pure ITO substrate (black) in redox D-glucose sensing reaction in the presence of KOH.*

Cryoaerogelation is a promising technique to prepare nanoparticle-based porous macrostructures without using a chemical trigger for the assembly. The hierarchical porosity allows the electrolyte to rehydrate the gel structure and reach the catalytically active surface sites of the nanoscopic building blocks.

## *Related publication*

[1] D. Zámbó, P. Rusch, F. Lübkemann, N. C. Bigall: *Noble-Metal Nanorod Cryoaerogels with Electrocatalytically Active Surface Sites,* Acs Applied Materials & Interfaces **13:(48),** 57774–57785 (2021) https://doi.org/10.1021/acsami.1c16424

# INVESTIGATIONS OF PLASMONS IN NANOCORRUGATED CVD GRAPHENE BY SPECTROSCOPIC ELLIPSOMETRY AT VISIBLE-FREQUENCIES

*G. Dobrik, P. Nemes-Incze, B. Majerus, P. Süle, P. Vancsó, G.Piszter, M. Menyhárd, B. Kalas, P. Petrik, L. Henrard, L. Tapasztó*

$\Psi$ and $\Delta$ spectra of nanocorrugated CVD graphene transferred onto $SiO_2$/Si substrate were measured using a Woollam M-2000DI rotating compensator Spectroscopic Ellipsometer (SE) at angles of incident 65° and 70° [1]. The surface of the sample was large enough to avoid focusing and the corresponding depolarization effects [2].

The optical model consists of a Si substrate, an interface layer between the thermal oxide and the Si wafer, the thermal oxide layer, an interface layer between the graphene and the $SiO_2$ layer, and the graphene layers (both quasi-flat and nano-corrugated) with a fixed thickness value of 0.34 nm. The reference dielectric function of the silicon substrate was imported from [3], while the oxide and graphene layers were modelled by the Cauchy dispersion fitting the nondispersive and the $\lambda^{-2}$ terms of the Cauchy polynomial and using two Lorentz oscillators, respectively. The wavelength ($\lambda$) range of 400-850 nm was used in the evaluations. We also set the same thickness for the flat graphene and corrugated graphene layers for an easier comparison.

We found the best fit for the $SiO_2$ layer of 303.3 nm (nominally 300 nm), and interface layer of 3 nm thickness. This latter is in good agreement with the values between 2 - 4 nm found in [4]. Once all the thicknesses and dispersions were determined, the refractive indices ($n$) and extinction coefficients ($k$) of the quasi-flat graphene layer was calculated by fixing all the parameters in the model allowing only $n$ and $k$ of the graphene layer to be fitted "point-by-point" for all the wavelengths independently. This method is useful for the accurate and model-independent determination of dispersion [5].

SE investigations revealed a substantially increased extinction in nanocorrugated graphene, for wavelengths above 700 nm, compared to the nearly constant extinction of quasi-flat sheet [5] (Fig. 1). The refraction index also displays unconventional behaviour in the nanocorrugated samples. While $n$ has a nearly constant value between 3 and 4 in the quasi-flat graphene (Fig. 1.b), its value progressively decreases down to 1.5 in the nanocorrugated sample starting from wavelengths above 600 nm (Fig. 1.a). A similar behaviour (increasing extinction, decreasing refraction index) has been observed in graphene by broadband spectroscopic ellipsometry in the UV range, when approaching the wavelengths corresponding to the interband ($\pi$) graphene plasmon [6].

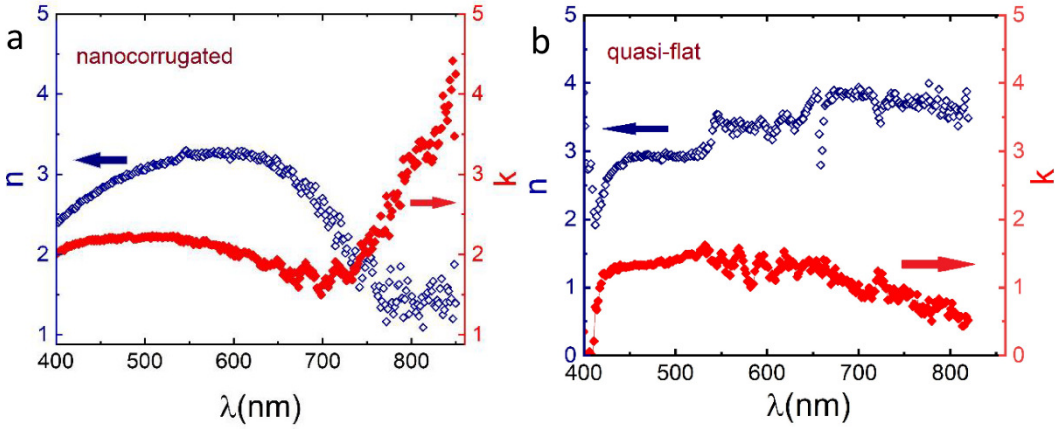


*Figure 1: SE on nanocorrugated CVD graphene sheets (a) reveals plasmonic activity through the drop of the refractive index and increase of the extinction coefficient at visible wavelengths, compared to quasi-flat CVD graphene samples (b).*

## *Related publications*

[1] G. Dobrik, P. Nemes-Incze, B. Majérus, P. Süle, P. Vancsó, G. Piszter, M. Menyhárd, B. Kalas, P. Petrik, L. Henrard, L. Tapasztó: *Large-area nanoengineering of graphene corrugations for visible-frequency graphene plasmons,* Nat. Nanotechnol. (2021) https://doi.org/10.1038/s41565-021-01007-x.

[2] Z. Pápa, et al.: *Spectroscopic ellipsometric investigation of graphene and thin carbon films from the point of view of depolarization effects,* Appl. Surf. Sci. **421**, 714–721 (2017) doi:10.1016/j.apsusc.2016.11.231

[3] W. Paulson, et al.: *Ellipsometric determination of optical constants for silicon and thermally grown silicon dioxide via a multi-sample, multi-wavelength, multi-angle investigation,* J. Appl. Phys. **83,** 3323–3336 (2002) doi:10.1063/1.367101

[4] V.G. Kravets, et al.: *Spectroscopic ellipsometry of graphene and an exciton-shifted van Hove peak in absorption*, Phys. Rev. B **81,** 155413 (2010)

[5] E. Agocs, et al.: *Approaches to calculate the dielectric function of ZnO around the band gap,* in: Thin Solid Films, 684–688. (2014) doi:10.1016/j.tsf.2014.03.028

[6] Li, W., et al.: *Broadband optical properties of graphene by spectroscopic ellipsometry.* Carbon **99,** 348 (2016)

# OXIDATION OF ZR AT MEDIUM TEMPERATURES – CONCORDANT ELEMENT OF THE GROWTH KINETICS

*OTKA K131515*

*A. Romanenko, E. Agócs, Z. Hózer, P. Petrik, and M. Serényi*

We report on the growth of $ZrO_2$ films upon the gradual thermal annealing of Zr in the temperature range of 500-700 K. The Zr samples were annealed in an isolated quartz tube shown in Fig. 1.A. Argon and $Ar/O_2$ gas mixtures with $O_2$ content of ~0, 1.25, 5 and 20 % were flowed at atmospheric pressure. The thickness of the oxide was monitored by in-situ Spectroscopic Ellipsometry (SE) with temporal and thickness resolutions of a few seconds and a few nanometres, respectively (Fig. 1.B). A remarkable feature of the process was that the growth of the oxide can be terminated immediately when decreasing the temperature by a few K shown in Fig. 2. This suggests that, in addition to the driving force, a built-in control adjusts the final thickness determined only by the temperature in sync with the formation and growth of the dense oxide films.

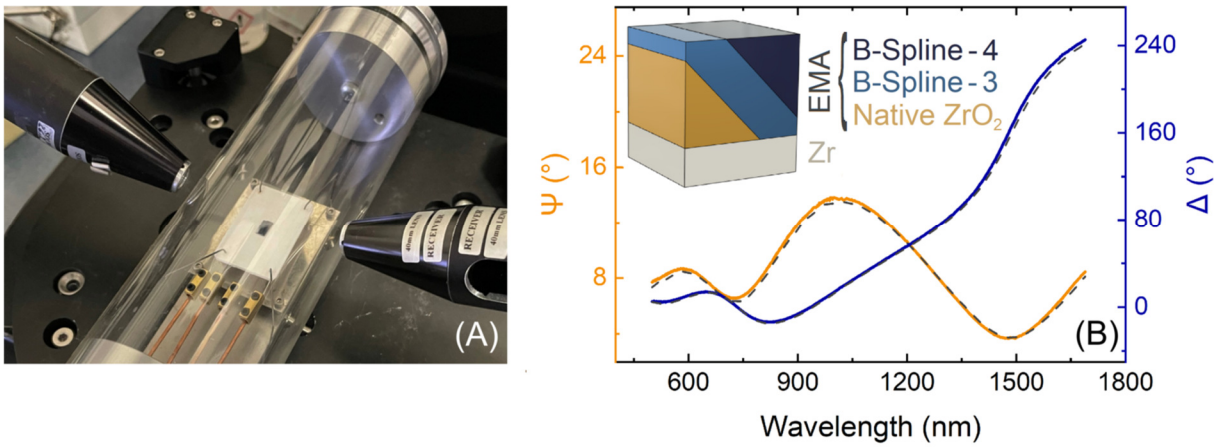


*Figure 1: (A) The heat cell constructed for multiple-angle SE measurements in controlled ambient temperature. (B) Typical measured (solid lines) and fitted (dashed lines) SE spectra on the sample oxidized at 700 K for 18000 s and the optical model used for the evaluation of the SE spectra.*

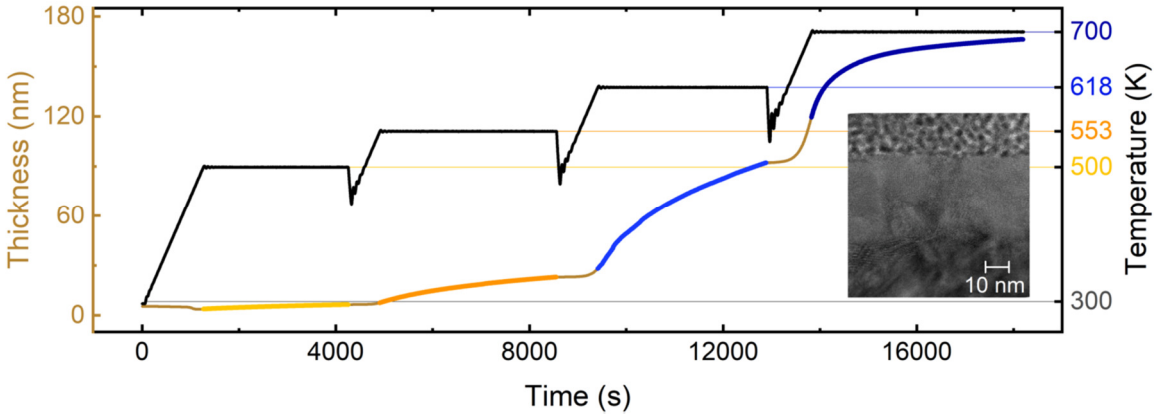


*Figure 2: Steps of thickness increase as a function of time under the influence of the increasing temperature values. The TEM image in the inset shows a typical oxide layer grown for 3600 s at the temperature of 553 K.*

A simple phenomenological model was developed that attempts to relate the parameters of the transport properties of the atomic oxygen to the results of kinetics measured by ellipsometry in a thickness range from a few nanometres to a few hundred nanometres. We apply the roughly simplified form of the Fick II. diffusion law to express the time dependence of the gradient of the $O^-$ anion flux ($J$):

$$J_d(x) - J = c_O \frac{dx}{dt} \qquad (1)$$

where x and $c_o$ denote the thickness of the oxide layer and the oxygen concentration, respectively. Using the formalisms used in the physics of semiconductors, we can solve this differential equation and we obtain for the time dependence:

$$t = -\alpha x - \alpha\delta \cdot ln\left(1 - \frac{x}{\delta}\right) \qquad (2)$$

where δ and α denotes the final thickness of the oxide layer and the growth rate, respectively. A comparison of this equation and the measurements is shown in Fig. 3.

The equations postulate that the oxide thickness approaches a value determined by temperature. The resulting oxide is stoichiometric when the growth occurs in an oxygen-rich environment. Stoichiometry is temporarily impaired in an oxygen-deficient environment, but if the heat treatment time is long enough for $\alpha \cdot \delta$, it becomes complete by the excess oxygen present in the final stage of the process. The driving force introduced into our phenomenological model based on ellipsometric measurements determines the kinetics of growth in a consistent and concordant way.

We focused on an alloy that is relevant in the nuclear power plant technology, and do not discuss the composition-dependent oxidation properties. The material we use in this study is sufficient for the demonstration of the proposed oxidation model. A greater knowledge of the oxidation process in this regime is of primary importance in many applications including nuclear technology and microelectronics. [1]

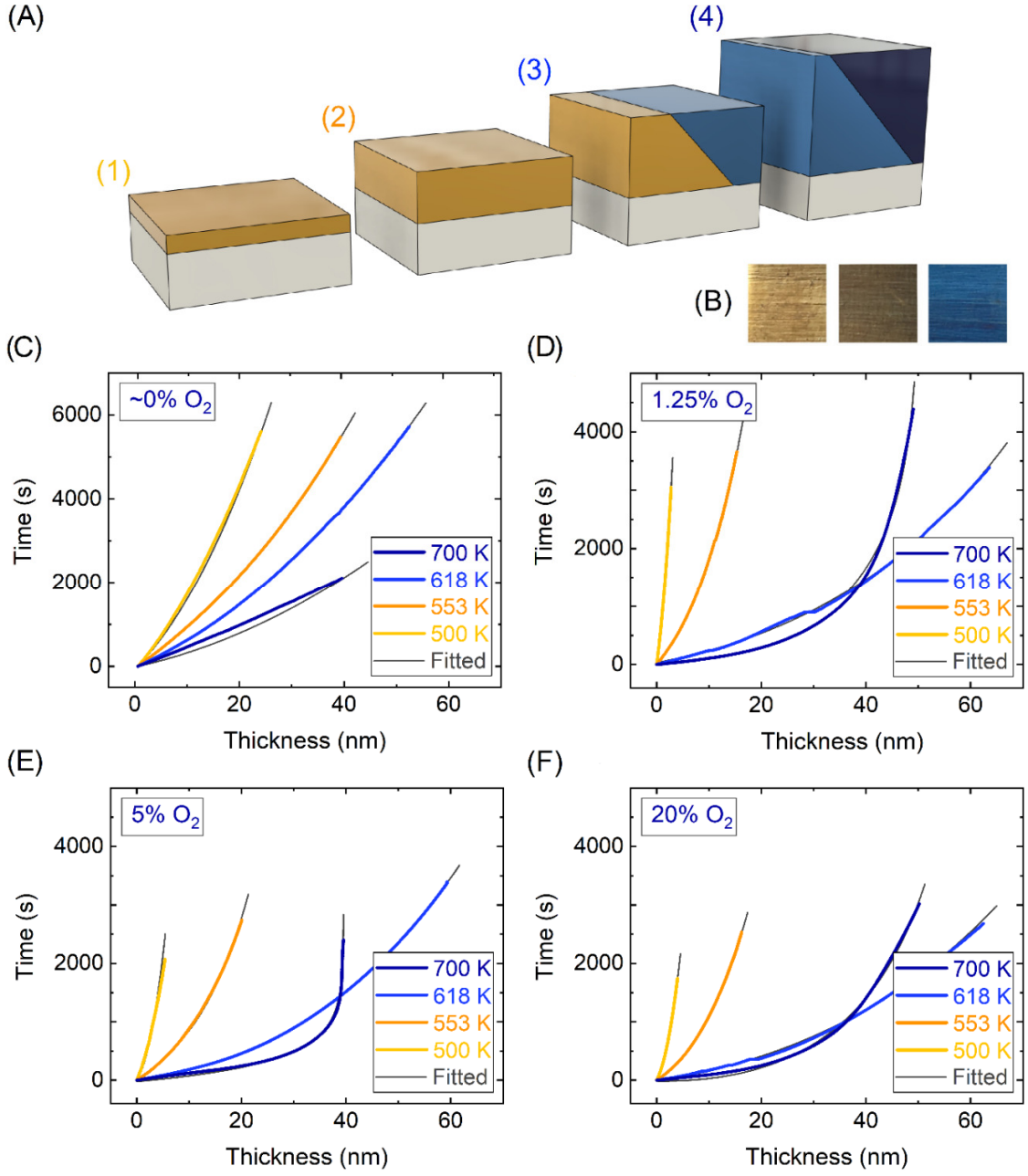


*Figure 3: (A) Optical models at different stages (1-4) of the oxidation process. (B) Photographs of 2 x 2-cm² E125 alloy samples to demonstrate the change of colour due to the different thicknesses of the oxides grown at various $O_2$/Ar ratios. (C-F) Time versus thickness for different $O_2$ concentrations at different temperatures, determined from the optical model shown in (A). The solid dark-grey lines show the curves fitted using Eq. (2).*

## *Related publication*

[1] A. Romanenko, E. Agócs, Z. Hózer, P. Petrik, M. Serényi: *Concordant element of the oxidation kinetics – Interpretation of ellipsometric measurements on Zr,* Applied Surface Science, **573,** 151543 (2022) ISSN 0169-4332, https://doi.org/10.1016/j.apsusc.2021.151543

# FLAGELLIN-BASED ELECTROCHEMICAL SENSING LAYER FOR NICKEL AND ARSENIC DETECTION

*M-ERA.NET OTKA NN117849 and K131515, BIONANO_GINOP-2.3.2-15-2016-00017*

*Z. Lábadi, M. Fried, P. Petrik*

Regular monitoring of heavy metal concentrations in water sources is essential due to their severe health effects. Our goal was to develop a rapidly responding, sensitive and stable sensing layer for the detection of arsenic and nickel.

Flagellin-based proteins were designed and prepared at the University of Pannonia capable of forming stable filament structures with high surface binding site densities. The D3 domain of Salmonella typhimurium flagellin was replaced with arsenic-binding peptide motif of different bacterial ArsR transcriptional repressor factors. As-binding fibres were immobilized on the surface of a gold electrode and used as a working electrode in Cyclic Voltammetry (CV) experiments. Fig. 1 shows the scheme of the process.

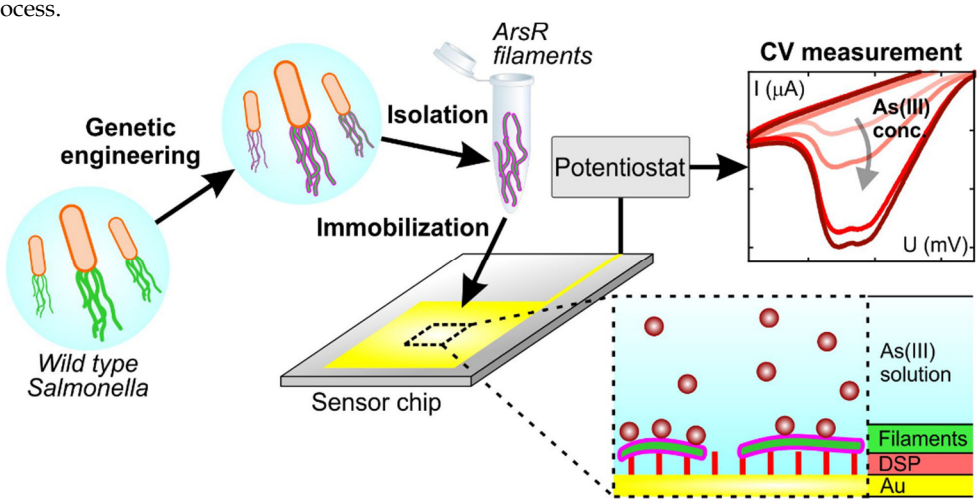


*Figure 1: Schematic workflow of the production of genetically engineered flagellar filaments, their deposition on the gold working electrode surface and CV measurements on As containing samples*

In order to form a stable and dense layer of flagellar nanotubes on the gold surface, thiol-based covalent immobilization chemistry was applied. The dynamics of the filament layer formation on a gold layer was monitored by in situ spectroscopic ellipsometry in the Kretschmann configuration, as shown in Fig. 2.

Fig. 3 summarizes the cyclic voltammetry results obtained on the protein-based sensor layers in the presence of arsenic. Set of CV curves were measured in the presence of As(III) on wild type flagellar nanotubes (A) as well as on FliC-ArsR9 As-binding flagellar nanotubes before (B) and after (C) storage and regeneration. Subfigure (D) shows the areas for FliC-ArsR9 filament cathodic peaks after first use and after regeneration (calculated by averaging four measurements) as a function of the As(III) concentration. Up to 20 times the Maximum Allowable Concentration (MAC), this setup may be suitable for quantitative determination of the concentration of arsenic. Based on the CV results obtained after dimercaptosuccinic acid (DMSA) treatment, it can be stated that the sensor layer is stable and partially regenerable.

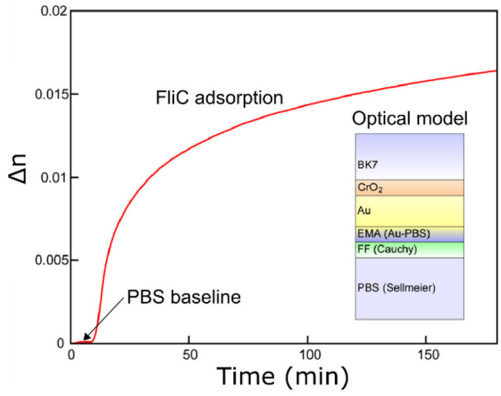


*Figure 2: Change in the refractive index (Δn) near to the surface of a dithiobis(succimidyl propionate) (DSP)-functionalized gold layer caused by the adsorption of flagellar filaments from their 0.5 mg/mL suspension. The kinetic curve was recorded by in situ spectroscopic ellipsometry. The inset shows the optical model used for data evaluation.*

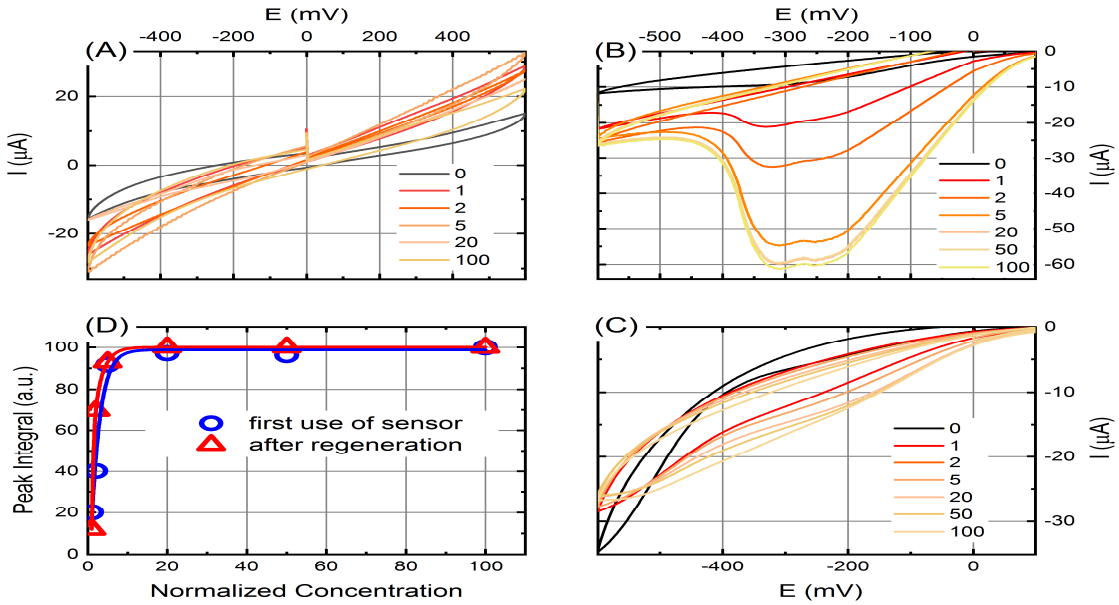


*Figure 3: Cyclic voltammetry on the protein-based sensor layers. Wild type flagellar nanotubes (A), As-binding flagellar nanotubes before (B) and after (C) storage and regeneration. Subfigure (D) shows anodic peak sizes.*

Further experiments were carried out on different protein layers containing Ni binding motifs. Application of stripping voltammetry methods (i.e. accumulation of the Ni ions at the sensor surface by delayed potential cycle) showed that the sensor layer is capable of semi-quantitative detection of Ni ions in concentrations below the health limit. Furthermore, we also showed that the sensing experiments can be repeated in natural water samples instead of model buffer solutions, and the presence of Fe, Cu and Zn ions does not affect the Ni sensitivity of the sensors. Based on these results, it can be concluded that the stable arsenic-binding flagellin variant can be used as a rapidly responding, sensitive, but simple sensing layer in a field device for the MAC-level detection of heavy metals in natural waters [1].

## *Related publication*

[1] H. Jankovics; P. Szekér, É. Tóth, B. Kakasi, Z. Lábadi, A. Saftics, B. Kalas, M. Fried, P. Petrik, F. Vonderviszt: *Flagellin-based electrochemical sensing layer for arsenic detection in water,* Scientific Reports **11:(1),** 3497 (2021)

# MAKYOH TOPOGRAPHY AND RELATED METHODS

*Ferenc Riesz*

Makyoh topography is an optical tool for the qualitative flatness testing of specular surfaces, based on the defocused detection of a collimated light beam reflected from the tested surface (Fig. 1). By inserting a square grid into the path of the illuminated beam, the height map can be calculated by integrating the gradients obtained from the distortion of the grid's reflected image (quantitative extension).

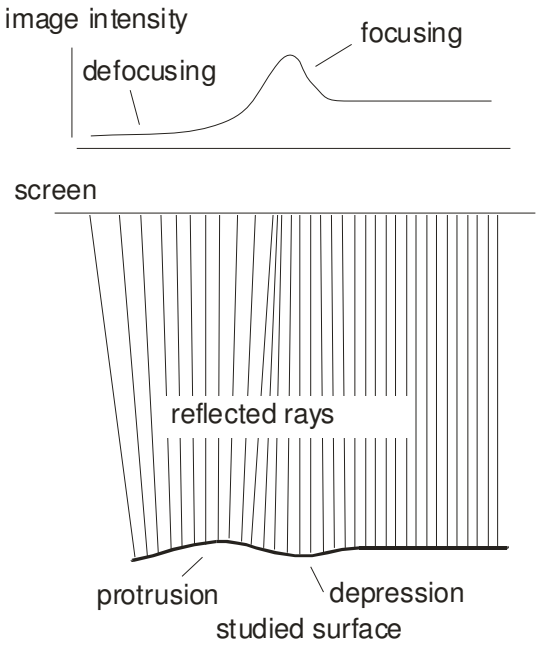


*Figure 1: The scheme of Makyoh-topography*

In the past year, activities were concentrated mostly on methodology.

It was shown earlier that utilizing the existing Makyoh setup under certain geometrical conditions, a schlieren-like measurement can be realized where the imaging lens' aperture plays the role of the schlieren knife edge, or with some modifications, a traditional knife edge can be inserted while maintaining the original Makyoh imaging scenery as well. This leads to a useful tool complementing the traditional Makyoh scheme. Efforts were made to find optimum working conditions.

An approach to the modelling of Makyoh imaging is to utilize the mirror backside relief rather than the front side as the input data. The back relief is transferred to the front convoluted with a Gauss curve (or similar). The construction of a mathematical model using the geometrical model developed earlier (J. Riesz, Phys D, 33 (2000) 3033) within the framework of this approach is under way.

The swirl defects in *p*-type Si wafers were further studied using Makyoh topography and the schlieren-like method. The interpretation of the high amount of data collected is in progress.

# CALIBRATION PROCEDURE TO IMPROVE THE ACCURACY OF SAED IN ABERRATION CORRECTED THEMIS

***OTKA K125100, VEKOP-2.3.3-15-2016-00002***

*Zs. Czigány, V. Kovácsné Kis*

The aim of this work is to demonstrate that fine tuning of experimental and evaluation parameters can improve the accuracy and reproducibility of Selected Area Electron Diffraction (SAED) close to that of conventional laboratory X-Ray Diffraction (XRD) equipment. Among diffraction techniques used for structure investigation (including crystal structure determination, defect structure, grain size, and texture) electron diffraction excels with its locality, however, its accuracy and reproducibility are generally considered to be lower than that of XRD. A conservative estimate, according to the famous handbook by Williams and Carter (2009), for the accuracy and reproducibility of interplanar (d) spacing determination from electron diffraction is 1-3% without internal standard. The primary reason for this degree of uncertainty is that a focused diffraction pattern can be achieved by different combination of specimen height, illumination conditions and diffraction focus giving rise to different Camera Length (CL) values and widths of diffraction rings. This can be improved by application of standard acquisition parameters to achieve of reproducible TEM settings. At our department Lábár et al. (2012) elaborated a calibration procedure and achieved 0.3% accuracy. Higher accuracy (~0.1%) can only achieved by application of internal standard. Since systematic study of the effect of these parameters on the data is missing, similar estimates apply for the error of camera length in a recent aberration corrected transmission electron microscopes. State-of-the-art aberration corrected microscopes have an order of magnitude better acceleration voltage and lens current stability compared to conventional TEMs, which implies an order of magnitude better reproducibility and accuracy in electron diffraction. Besides the stability of acceleration voltage and lens currents, Field Emission Gun (FEG) electron sources provide a coherent electron beam with typical energy spread of 0.7eV which also decrease the instrumental broadening.

We performed our study in a Themis (Thermo Fisher) TEM with Cs correction in the imaging system (spatial resolution in HRTEM mode 0.8Å), operated at 200kV and equipped with Schottky FEG having an energy spread of ~0.7eV. SAED patterns were recorded by a 4kx4k Ceta camera using Velox software (Thermo Fischer). The diffraction patterns were exported in 16 bit tiff format and 1D diffraction profiles, containing intensity distribution as function of scattering angle, were obtained using Process diffraction software. The software allows visual fit and refinement of centre of the pattern (X, Y), eccentricity (ε) and its angle (α) together with calibration of camera length. By careful control of specimen height and illumination conditions (by monitoring lens currents) it was possible to reach a session to session reproducibility better than $3x10^{-4}$ for camera length.

Refinements of the centre of the diffraction pattern and corrections for lens distortions (ellipticity of rings) allowed for determining the ring diameters with an accuracy of $10^{-3}$. For determination of the ellipticity parameters by visualization of the intensity distribution an ideal calibration specimen is composed of nanocrystalline grains free of texture and produce narrow diffraction rings. For this purpose, we deposited a polycrystalline Cu layer on TEM grid coated with nanocrystalline graphene. The achieved accuracy of $10^{-3}$ for lattice spacing measurement without internal standard is compatible with that of XRD, and reduction of instrumental broadening due to the elaborated evaluation procedure allows for separation of close reflections and provides more reliable ring width and thus improved input parameters for further nanostructure analysis as demonstrated on dental enamel bioapatite Fig. 1. [1].

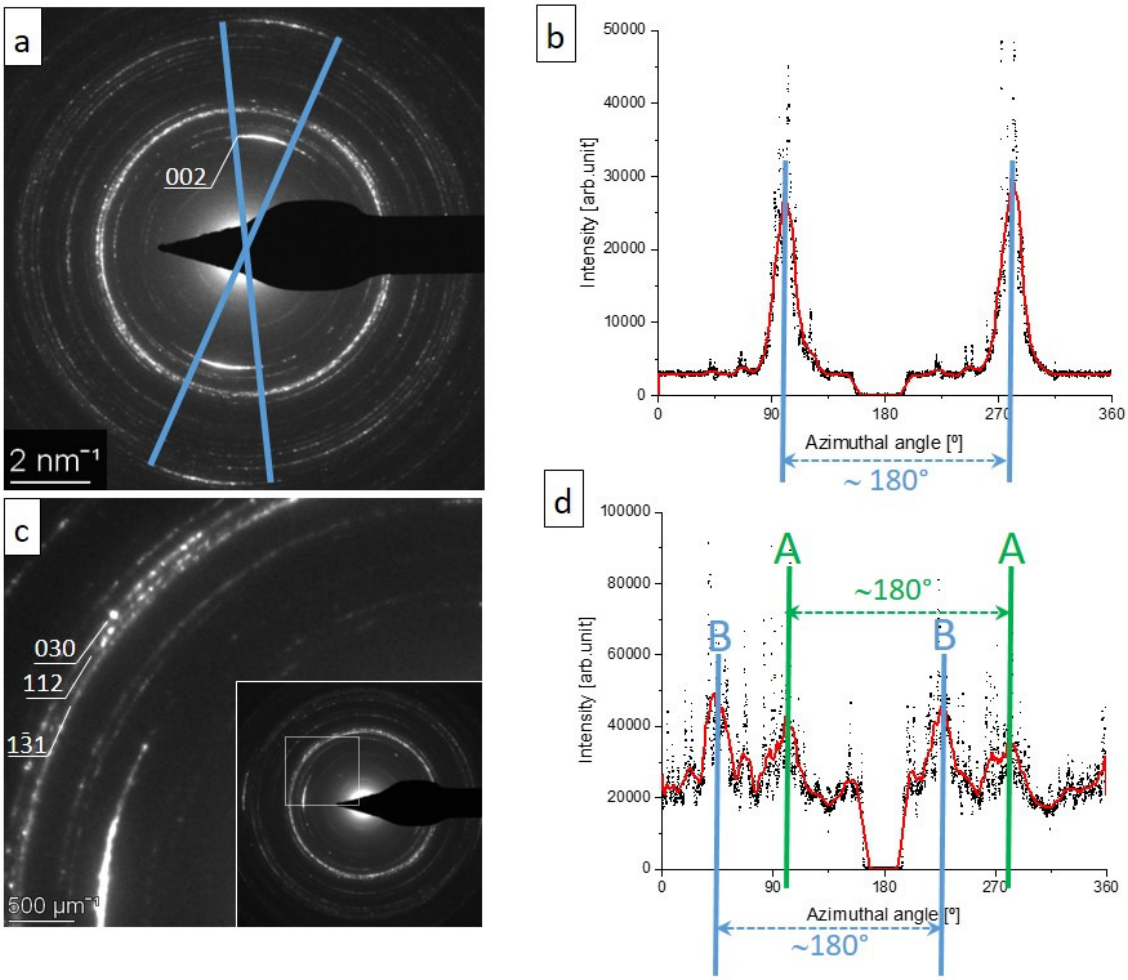


*Figure 1: (a) A typical SAED pattern of dental enamel cross section showing strong [001] texture. (b) Azimuthally integrated intensity profile of 002 reflections in a 15-pixel wide ring. (c) 030 diffraction ring can be resolved (separated from 112), and (d) azimuthal intensity profile of the 030 reflections obtained after integration in an 8-pixel wide ring shows two sets of crystallite population A and B separated by approximately 45°.*

## *Related publication*

[1] Z. Czigány and V. Kovács Kis: *Calibration procedure to improve the accuracy of SAED in aberration corrected TEM,* Microscopy and Microanalysis, submitted

# DIFFMAP: PHASE MAPS AND ORIENTATION MAPS FROM 4D-ED PATTERN SET

*VEKOP-2.3.3-15-2016-00002*

*J. L. Lábár*

Many new Scanning Transmission Electron Microscopes (STEM) can record four-dimensional diffraction (4D-ED) information in addition to the usual Bright Field (BF), Dark Field (DF) and High Angle Annular Dark Field (HAADF) imaging modes. 4D-ED information is collected in the form of a large number of 2D electron diffraction patterns, one pattern per location, each corresponding to a pixel of the 2D HAADF image. Although individual scientific solutions exist in the literature to mine information out of such 4D-ED pattern sets, the manufacturers of the STEMs do not offer commercial programs to solve the problem. Available commercial solutions also need additional hardware elements and use an optical camera to photograph the screen of the (S)TEM to record the diffraction patterns. Here we present a free, stand-alone program that does not require any additional hardware and runs under the Windows operating system. The diffraction patterns can be recorded with the native camera of the TEM controlled by the STEM software independently from our program. The new program processes such data sets (using TIF files as input) to produce phase maps and orientation maps for nanocrystalline samples. Since the diffraction patterns in TIF format can be recorded with STEMs from different manufacturers, our solution is available to many microscopists irrespective to the make of their instrument.

The examples here were recorded on a Titan Themis G2 200 STEM using a 4kx4k CETA 16 CMOS camera (both Thermo Fisher Scientific, Waltham, MA, USA) controlled by the TIA program (FEI, Eindhoven, The Netherlands). The data collection was done in microprobe STEM mode, which means that a fine parallel nanobeam (NB) was scanned over a rectangular area while recording a NB electron diffraction at each pixel. A TEM lamella was cut by focused $Ga^+$ ion beam (FIB) from the same multiphase sample, but from a different location than which was published in [1].

The procedures in DiffMap are based on the solutions originally coded in an unpublished version of the ProcessDiffraction program [2, 3], as cited in publications, where it was already used [1] before it was revamped for publication of the program itself.

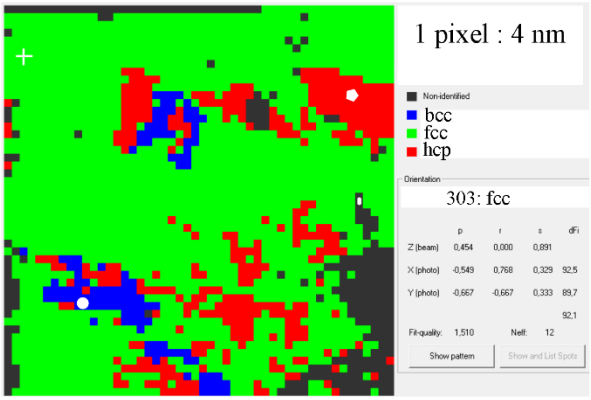


*Figure 1: Phase map from a nanocrystalline Co-Cr-Fe-Ni sample. Pixel size is 4 nm.*

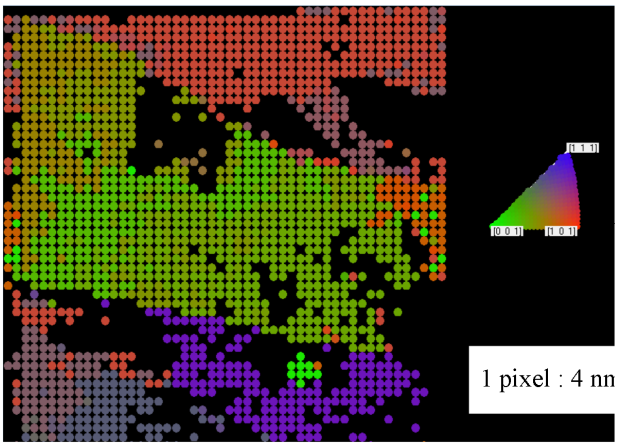


*Figure 2: Orientation map for the fcc phase in the sample as seen from the beam direction (Z-direction in the Lab-system). Pixel size is 4 nm.*

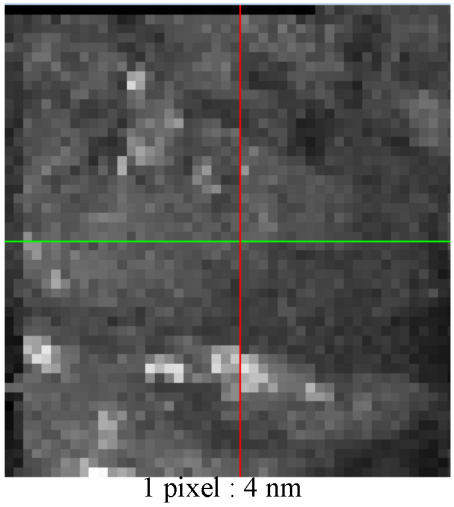


*Figure 3: Fit-quality map. Pixel size is 4 nm.*

The program operates in two, logically distinct steps. First, the several thousand NBD patterns are compared to a set of simulated patterns to calculate, which fits the measured the best. Patterns are simulated for each crystal structure (phase) that can be present in the sample for each symmetrically independent orientations (the rest of orientations are automatically provided by the symmetry operations of the crystal). The results of the matching are stored in a result file. In the second step phase map (Fig. 1), orientation maps (Fig. 2) and quality map (Fig. 3) are created from this results file. Additionally, the original patterns can be consolidated into virtual BF and virtual DF images, by collecting information only from the pre-selected parts of the diffraction patterns.

As a means for optional cross-checking the original data and the correctness of the identification, any measured diffraction pattern can be loaded by double-clicking on a pixel in the phase map. An example of an indexed diffr. pattern is in Fig. 4.

The graphical user interphase is easy to use and the program is available free from https://public.ek-cer.hu/~labar/DiffMap.htm.

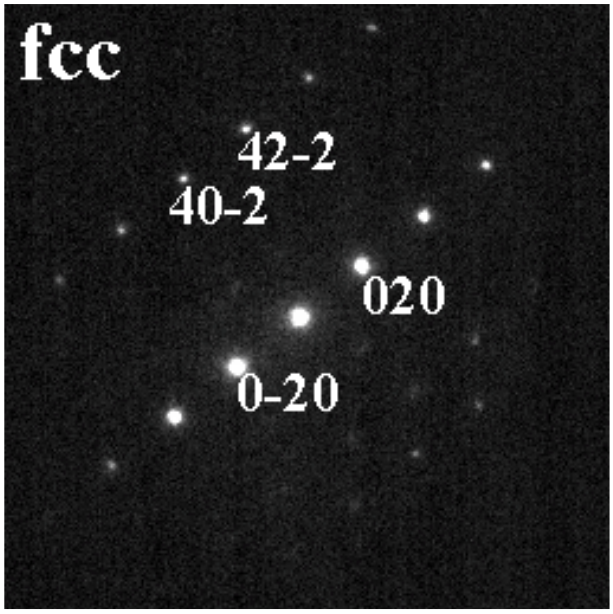


*Figure 4: Example for an indexed diffraction pattern*

The experimental part of this research was supported by VEKOP-2.3.3-15-2016-00002 of the European Structural and Investment Funds. The sample is kindly provided by Johann Michler, László Pethő and Péter Nagy at EMPA Swiss Federal Laboratories for Materials Science and Technology, Laboratory for Mechanics of Materials and Nanostructures, Thun, Switzerland. The author is indebted to Noémi Szász for the preparation of the FIB lamella.

## *Related publications*

[1] P. Nagy, N. Rohbeck, Z. Hegedűs, J. Michler, L. Pethö, J.L. Lábár, J. Gubicza: *Microstructure, Hardness, and Elasti Modulus of a Multibeam-Sputtered Nanocrystalline Co-Cr-Fe-Ni Compositional Complex Alloy Film,* Materials **14,** 3357 (2021) https://doi.org/10.3390/ma14123357

[2] J.L. Lábár: *Consistent indexing of a (set of) single crystal SAED pattern(s) with the ProcessDiffraction program,* Ultramicroscopy **103,** 237–249 (2005)

[3] J.L. Lábár: *Electron diffraction based analysis of phase fractions and texture in nanocrystalline thin films I-III.,* Microanal. **14,** 287–295 (2008), Microsc. Microanal. **15,** 20–29 (2009), Microsc. Microanal. **18,** 406–420 (2012)

# APPLICATION OF INTERNAL STANDARD FOR THE IN-SITU TEM INVESTIGATION OF SOLID PHASE TRANSFORMATIONS AND REACTIONS

## *OTKA NN112156*

*K. Hajagos-Nagy, F. Misják, Gy. Radnóczi*

In an in-situ experiment paying attention to a few aspects/steps can make the measurement procedure and the evaluation of results more effective. However, these are hard to find in the literature. Our goal was to give a description that can facilitate the in-situ investigation of phase transformations and reactions at high temperatures. The steps are demonstrated on amorphous Cu-Mn/C thin films focusing on phase identification in a multicomponent system. Cu-Mn films are of recent technological interest due to their potential application as barrier layers in interconnect structures. Mapping the Cu-Mn-C-O system may help their integration with low-κ dielectrics (eg. SiOCH) [2].

CuMn/C films were in-situ annealed and examined by TEM in a Philips CM-20 electron microscope operated at 200 kV. The temperature range of in-situ annealing was 20-600°C. Separate samples were used in microscope and diffraction mode to be able to follow the initial area of observation during in-situ annealing. The phase compositions of the films were evaluated from SAED patterns using the Process Diffraction program [1].

The amorphous Cu-Mn films crystallized at 300°C into Cu(Mn) and α-Mn-based solisolutions. The lattice parameter of the Cu(Mn) solid solution changed throughout the temperature interval of 300-600°C. At 400°C new phases appeared accompanied with disappearance of the α-Mn-based solid solution. To identify the new phases and to examine the changes in solid solutions we applied the method of internal standard. This method allows calibrating the camera constant for each annealing step and to increase the accuracy of the lattice parameter values by approximately one order of magnitude [3]. MnO was chosen as an internal standard because MnO is present in the whole temperature range of annealing, most of its diffraction maxima can be easily separated from other phases and it produces stable and well defined diffraction rings without the risk of contamination. By separating the effect of thermal expansion and changes in solute concentration, the composition of the Cu(Mn) solid solution in the temperature range of 300-600°C was calculated. To identify the new phases that appear at 400°C, a list of candidate phases was made by comparing the probability of formation of all phases in the Cu-Mn-C-O multicomponent system. Phase identification confirmed the candidate phases: $Mn_{23}C_6$ and $Mn_5C_2$ carbides were present in the temperature range of 400-500°C, and $Mn_5C_2$ and $Mn_7C_3$ carbides from 500°C to 600°C which formed through the reaction of the Cu-Mn film and the C substrate. The presented example can serve as a guideline for the in-situ investigation of phase transformations and reactions at high temperatures.

## *Related publications*

[1] J.L. Lábár: *Consistent indexing of a (set of) single crystal SAED pattern(s) with the ProcessDiffraction program*, Ultramicroscopy **103,** 237–249 (2005)

[2] K. H. Nagy, & F. Misják: *In-situ transmission electron microscopy study of thermal stability and carbide formation in amorphous Cu-Mn/C films for interconnect application,* J. Phys. Chem. Solids **121,** 312–318 (2018)

[3] V. Kovács Kis, Z. Czigány, T. Németh: *Nanostructural investigation of slightly altered rhyolitic volcanic glass,* Mater. Charact. **127,** 121–128 (2017)

# EVALUATION OF AES DEPTH PROFILES WITH SERIOUS ARTEFACTS IN C/W MULTILAYERS

*A. S. Rácz, Zs. Fogarassy, M. Menyhárd*

Tungsten-carbide (WC) is often used as protective coating due to its high hardness and chemical resistivity. In our work we produced WC by means of ion irradiation by irradiating a C/W multilayer structure by noble gases. Due to irradiation at the interfaces ion mixing happened and carbide was formed, as well. The produced carbide was detected by Auger Electron Spectroscopy (AES) and the component in-depth distribution was determined by depth profiling. In the case of a non-irradiated sample we observed that during depth profiling the applied argon ions induced mixing and carbide compound was formed at the interfaces.

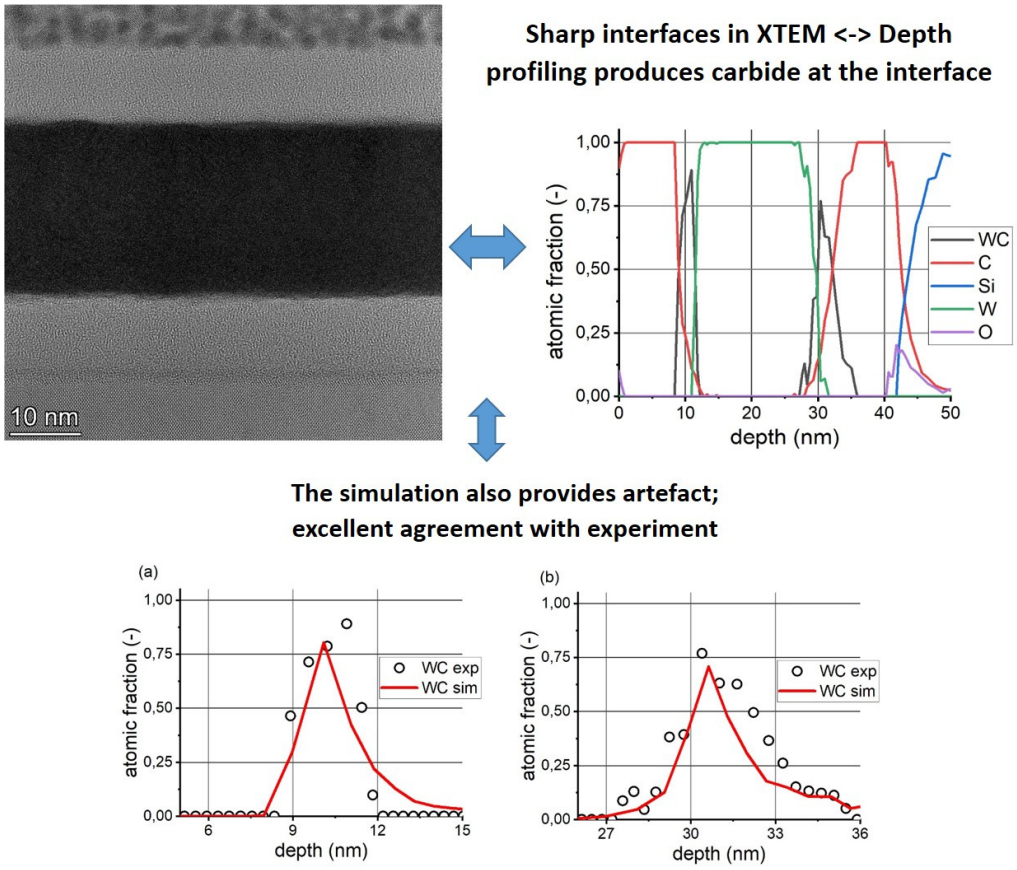


*Figure 1: XTEM, AES and TRIDYN simulation results for a non-irradiated C/W/C/Si substrate multilayer structure*

This was modelled by the TRIDYN simulation which helped us to determine the carbide artefact production of AES depth profiling (Fig. 1.). The simulation was used for reconstructing the real depth profile of ion-irradiated samples. We have shown that the artfact production can be neglected in the case of highly mixed (high carbide content) samples [1].

## *Related publication*

[1] A.S. Racz, Z. Fogarassy, P. Panjan, M. Menyhard: *Evaluation of AES depth profiles with serious artefacts in C/W multilayers,* Applied Surface Science **582**, 152385 (2022)

# MICROSTRUCTURE AND OPTICAL PROPERTIES OF COMPOSITION SPREAD YTiO THIN FILMS

***OTKA K129009***

*D. Olasz, V. Kovácsné Kis, P. Petrik, B. Kalas, Gy. Sáfrán*

Materials with perovskite structures are receiving increasing attention in semiconductor research. They have a chemical formula $ABX_3$, where 'A' and 'B' are cations and X is an anion that bonds to both. A number of elements can be combined to form perovskite structures showing a wide variety of physical, optical, and electrical properties. Perovskite solar cells can be manufactured by simple, additive deposition techniques, like printing, for a fraction of the cost and energy compared to traditional silicon technology.

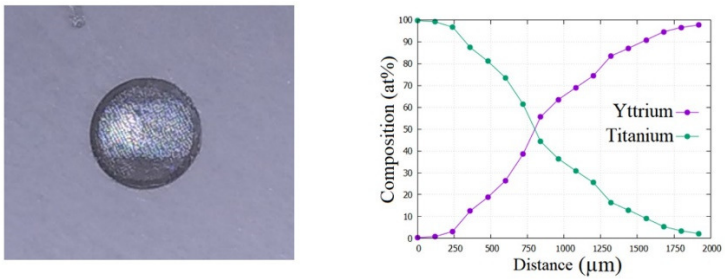


*Figure 1: A combinatorial YTiO sample on a TEM grid and its EDS diagram representing concentration of the cations as a function of distance along the layer. O-concentration values are shown in Fig. 2.*

Recently, the photoconversion efficiency of perovskite solar cells has exceeded 25%, close to that of silicon (27%). From the large family of perovskites, we aimed to produce and characterize the Y-Ti-O system. Thin composition spread samples were deposited on both carbon coated TEM grids and Si slabs by reactive DC magnetron sputtering of yttrium and titanium in $\mathbf{3} * \mathbf{10^{-3}}\ \boldsymbol{mbar}$ Ar gas with $\mathbf{1} * \mathbf{10^{-4}}\ \boldsymbol{mbar}$ $O_2$ inlet. Using microcombinatory [1, 2] we could produce and examine the oxides of the cations in the whole $Y_xTi_{1-x}$ (x=0…1) concentration range in a single sample (Fig. 1). The microstructure as a function of composition was determined by TEM and SAED: at high Y or Ti concentrations crystalline, while in between an amorphous structure was found (Fig. 2).

The radial intensity distribution curves of SAED-s evaluated with ProcessDiffraction software [3] are shown in Fig. 3 for the whole $Y_xTi_{1-x}$ -oxide composition range. At the Ti surplus side of the sample, rocksalt-type cubic TiO structure (space group: $Fm\bar{3}m$, $\boldsymbol{a = 4.1766}$ Å) was formed and the intensity of its characteristic peaks decreases with the increase of Y concentration. Between Y/Ti/O 14/28/58 and 28/8/64 at% compositions only diffuse peaks are present, characteristic for amorphous structure. With a further increase of the Y content, at 33/5/62 at% composition, the peaks of the $Y_2O_3$ crystalline phase appears, showing $Fm\bar{3}m$ space group, cubic ($\boldsymbol{a = 5.2644}$ Å), $CaF_2$ type structure. At even higher Y concentration (33/5/62) additional small peaks appear representing a $Mn_2O_3$ bixbyite-type cubic structure of $Y_2O_3$ (space group: $Ia\bar{3}$, $\boldsymbol{a = 10.5981}$ Å). It has a lattice constant twice as large as the one mentioned above, and its formation is related to the arrangement of O-vacancies.

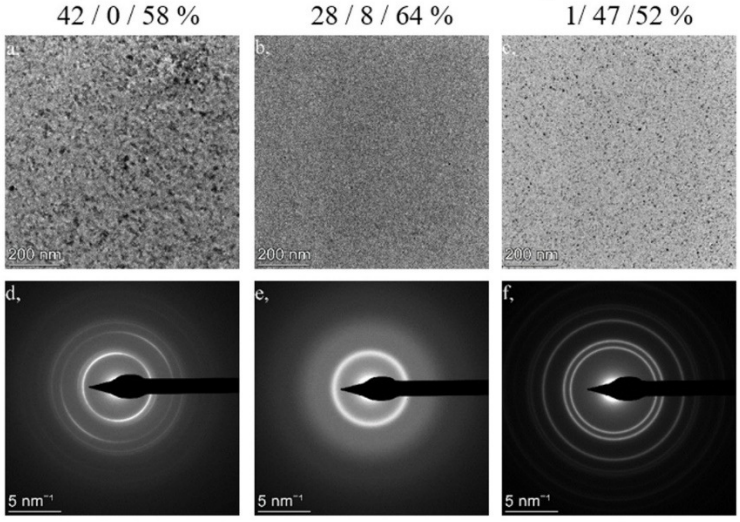


*Figure 2: (a, b, c): BF TEM image of selected Y/Ti/O (at%) compositions (d, e, f) the corresponding SAED patterns. Sharp rings (d, f) show polycrystalline, while diffuse rings (e) represent amorphous structure*

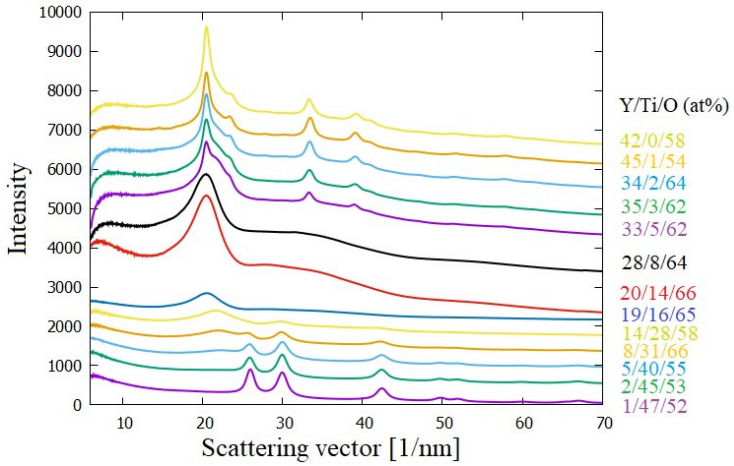


*Figure 3: Radial intensity distribution curves of SAED as a function of layer composition (curves are shifted along the intensity axis)*

The optical properties of the composition spread layer deposited on a Si slab were determined by Spectroscopic Ellipsometry (SE) during in situ heat treatment up to 600°C. A colour map of the measured data is shown in Fig. 4 showing the composition and temperature of the phase transitions and the potential regions where perovskite structure is found. The SE colour map can be used, in future studies, to select the thermal treatment parameters of combinatorial TEM samples to generate and characterize the perovskite structure in the Y-Ti-O system.

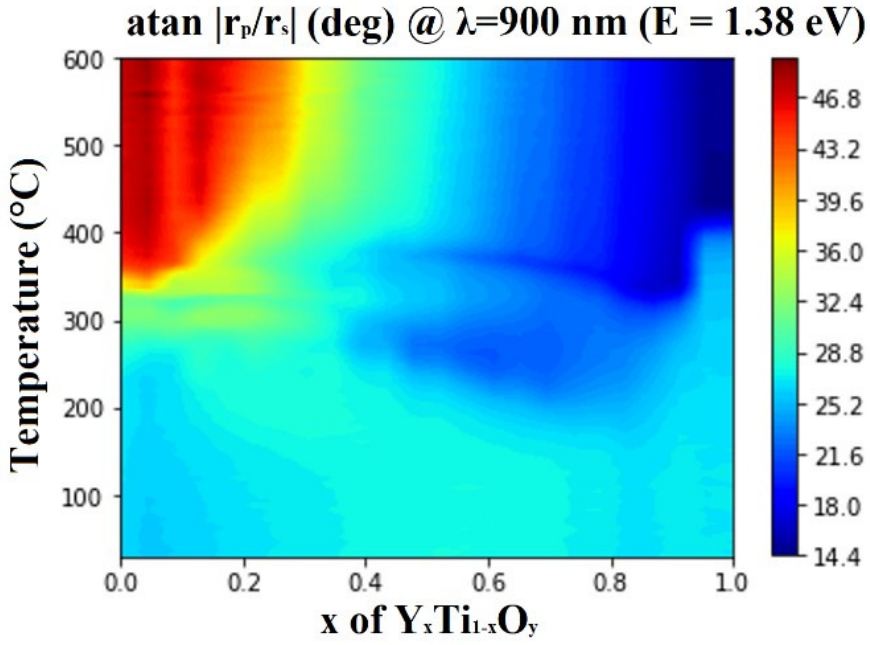


*Figure 4:* $\boldsymbol{atan}\left|\frac{r_p}{r_s}\right|$ *map as the function of temperature and composition in the case of a microcombinatorial YTiO sample deposited on a 10x25 mm² Si slab. Separated regions imply morphological and phase transitions.*

## *Related publications*

[1] G. Sáfrán: *One-sample concept" micro-combinatory for high throughput TEM of binary films,* Ultramicroscopy **187,** 50-55 (2018)

[2] J.L. Lábár: *Electron Diffraction Based Analysis of Phase Fractions and Texture in Nanocrystalline Thin Films, Part I: Principles,* Microsc. Microanal. **14:(4),** 287-295 (2008)

[3] S. H. Chen, C. Carter, Z. Elgat, L R, Zheng, and J. W. Mayer: *The structure of $Ni_5Si_2$ formed in Ni-Si thin film lateral diffusion couples,* J. Appl. Phys. **62:(4),** 1189-1194 (1987)

# IN- AND EX-SITU STUDY OF NICKEL SILICIDE FORMATION IN THIN FILMS

*E. Dódony, I. Dódony (ELTE), Gy. Z. Radnóczi, Gy. Sáfrán*

Due to their excellent physical and electrical properties nickel silicide layers have become one of the most promising components of microelectronics devices. To date, the mechanisms and reaction pathways of Ni-silicide formation remain unexplored, as the outcome depends on a wide range of experimental parameters (temperature, layer thickness, microstructure etc.). [1- 3].

We studied in- and ex-situ the formation of nickel-silicides below 1073K in the solid state reactions between thin amorphous silicon (a-Si) layers and the supporting nickel TEM micro-grids. This unique experimental setup allowed us to reveal the sequentially forming phases of nickel-silicides, in lateral arrangement, by High Resolution TEM (HRTEM) and Selected Area Electron Diffraction (SAED). During heat treatments at 860K and 973K we identified, almost all known silicide phases in reaction Zone 1 and 2 shown by Fig. 1 together with the Ni grid-bar at the lower right corner. The first reaction product observed was α-$NiSi_2$ that was continuously present in Zone 1, at the reaction front advancing in the a-Si layer. (Fig. 1). The HRTEM image in Fig. 2.a shows α-$NiSi_2$ in [110] orientation. Planar defects - stacking faults and micro-twins- are recognized both in the image and in the Fourier transform inset. While the average width of zone 1 remained constant, the width of zone 2 increased continuously during the reaction. Zone 2 is dominated by $Ni_{31}Si_{12}$. Fig. 2 represents HRTEM image of [100] oriented γ-$Ni_{31}Si_{12}$ full of planar defects. Besides $Ni_{31}Si_{12}$ we identified further phases in Zone 2. They followed a tendency of increasing Ni content towards the Ni-grid bar as follows: NiSi, ε-$Ni_3Si_2$, δ-$Ni_2Si$, β1-$Ni_3Si$, β2-$Ni_3Si$. Together with these phases of Zone 2, the $Ni_{31}Si_{12}$ phase was abundant.

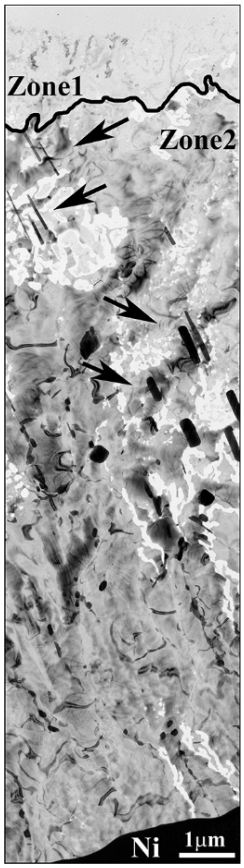


*Figure 1: Bright field TEM image depicts reaction Zone 1 and 2 formed as a result of solid state reaction between Ni grid and a-Si layer. Arrows show whiskers protruding from the thin layer.*

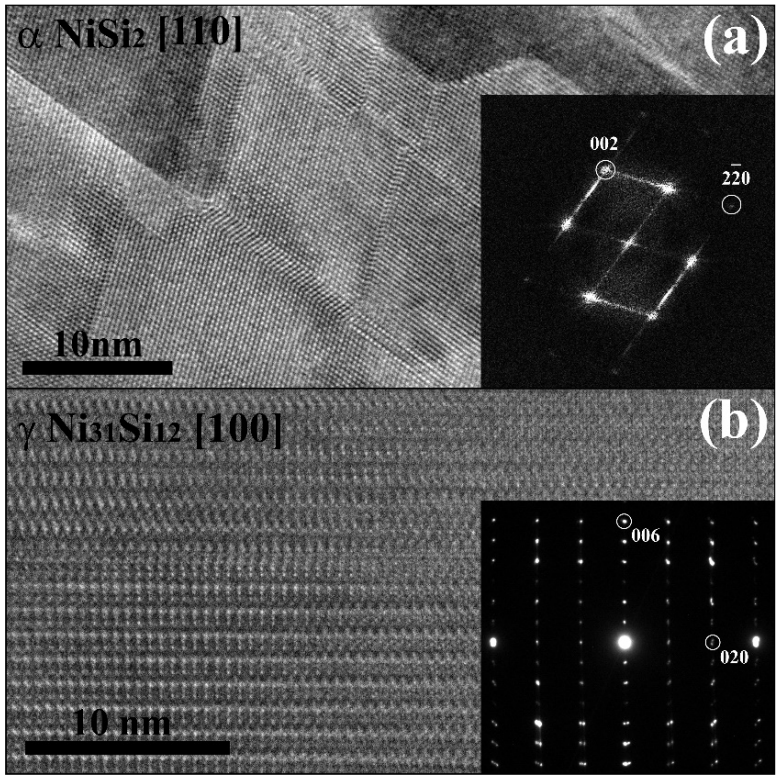


*Figure 2: HRTEM image of (a) $NiSi_2$, the typical phase of Zone 1, showing planar defects, stacking faults and micro twins depicted by the image and the FFT inset, (b) the dominant γ-($Ni_{31}Si_{12}$) phase of Zone 2 and its SEAD showing [100] orientation*

During the heat treatment elongated protrusions, whiskers (shown by arrows in Fig. 2) were ejected preceded by an intense diffraction contrast change in the parent crystal, suggesting the accumulation of compressive stress. It was found that whisker and its parent grain consist of the same phase. As the reaction progresses and the parent grain transforms into a phase with a higher Ni concentration, whisker undergoes the same transformation (NiSi → $Ni_3Si_2$ → $Ni_2Si$ → $Ni_3Si$). This explains the coexistence of whiskers of different phases. It is to mention that whisker formation in the solid-state reaction of Ni and Si was first observed in our experiments.

In conclusion, because of their excellent physical and chemical properties, phase variability, as well as their applicability in microelectronics, the present results on Ni-silicide could be of both scientific and technological importance. However, to get a complete picture of the formation of silicides as thin films and whiskers in the Ni-Si system, further detailed studies are needed.

## *Related publications*

[1] S. H. Chen, C. Carter, Z. Elgat, L R. Zheng, and J. W. Mayer: *The structure of $Ni_5Si_2$ formed in Ni-Si thin film lateral diffusion couples,* J. Appl. Phys. **62:(4),** 1189-1194 (1987)

[2] B. Bokhonov and M. Korchagin: *In-situ investigation of the formation of nickel silicides during interaction of single-crystalline and amorphous silicon with nickel,* Journal of Alloys and Compounds **319**, 187–195 (2001)

[3] F. Nemouchi, D. Mangelinck, J.L. Lábár, M. Putero, C. Bergman and P. Gas: *A comparative study of nickel silicides and nickel germanides: Phase formation and kinetics,* Microelectronic Engineering **83,** 2101–2106 (2006)

# APPLICATION OF MICROCOMBINATORIAL LAYER STRUCTURE FOR TUNEABLE ALAG/SIN BIOSENSORS

*Gy. Sáfrán, B. Kalas, M. Serényi, P. Petrik*

In a collaboration of the MFA Thin Film Physics Department (VRF) and the Photonics Laboratory (FL), we have developed a wide detection range Surface Plasmon Resonance (SPR) AlAg/SiN layer biosensor for various liquids and proteins. The complex geometry so-called Kretschmann-Raether (KR) arrangement [2] of the SPR sensors was used to achieve energy and momentum conservation during the interaction between incident light and surface plasmons propagating on the semi-infinite metal surface (Fig. 1).

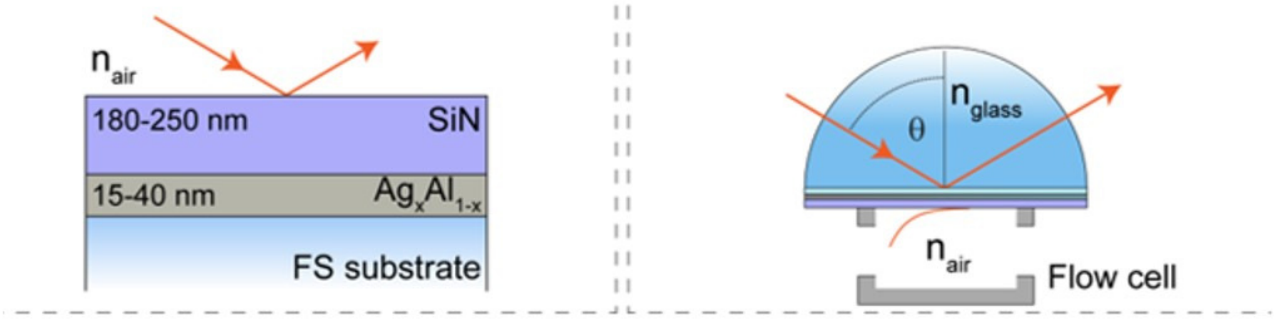


*Figure 1: SE measurement of a variable thickness $Ag_xAl_{1-x}$/SiN sensor in (a) simple (from sample-side) and (b) Kretschmann-Raether arrangement*

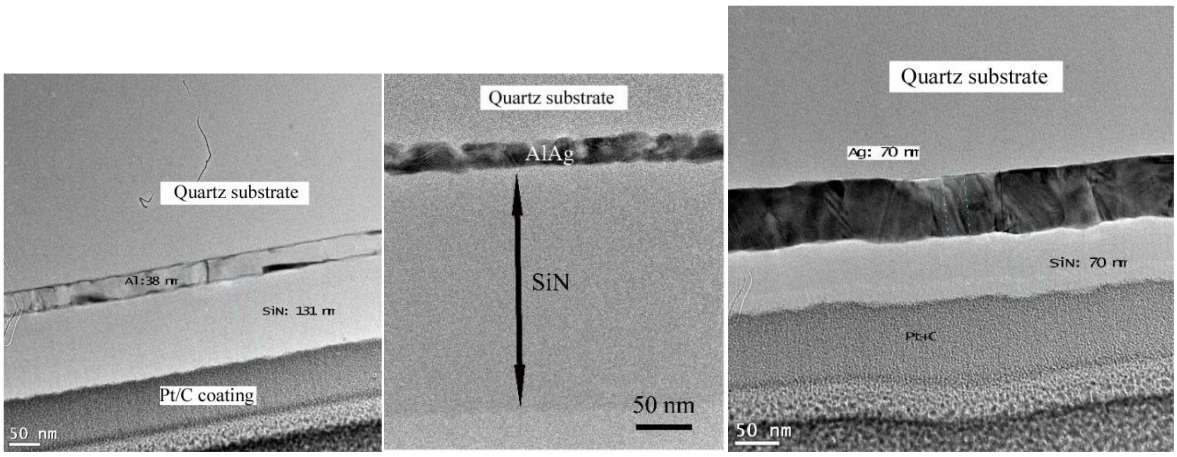


*Figure 2: XTEM images of Al end, centre and Ag end of a sensor prepared at a stage of sensor development. (left: Al: 38nm, SiN: 130nm, middle: Ag: 27nm, SiN: 220nm, right: Ag: 70nm, SiN: 70nm)*

The microcombinatorial technique [1, 3-6], was used to fabricate an $Al_{1-x}Ag_x$ /SiN layered system sensor on quartz substrate with variable properties along the length of sample. This allows the plasmonic frequency to be tuned as a function of the illumination position for spectral ellipsometry measurements. The thickness of pure Ag, on the basis of optical model calculations, is estimated in the range of 40-50 nm that is considered optimal for plasmonic applications, while for pure Al, due to its high optical absorption, a lower thickness is preferred. The thickness of the Ag-Al layer was specified as 40 nm on the Ag side and, with a continuous transition of composition and thickness, 15 nm on the Al side. Thus, as the Ag-Al composition changes along the sample, the thickness of the layer also changes. The layer was deposited from Ag and Al sources on a 25×10 mm² quartz substrate by DC magnetron sputtering through a 0.5 mm wide slot passing over the substrate. The maximum power applied to the Ag and Al targets was 150 W and 330 W, respectively. The variable composition and thickness were achieved by synchronized computer power control using stepper motor slot motion. The resonances in the KR alignment could also be easily tuned by applying an additional RF-sputtered SiN layer of gradient thickness. Diagrams in Fig. 2 are based on FIB TEM cross-sections of the two ends and the middle of the sensor covered with SiN of different composition and thickness show that the geometry is as designed.

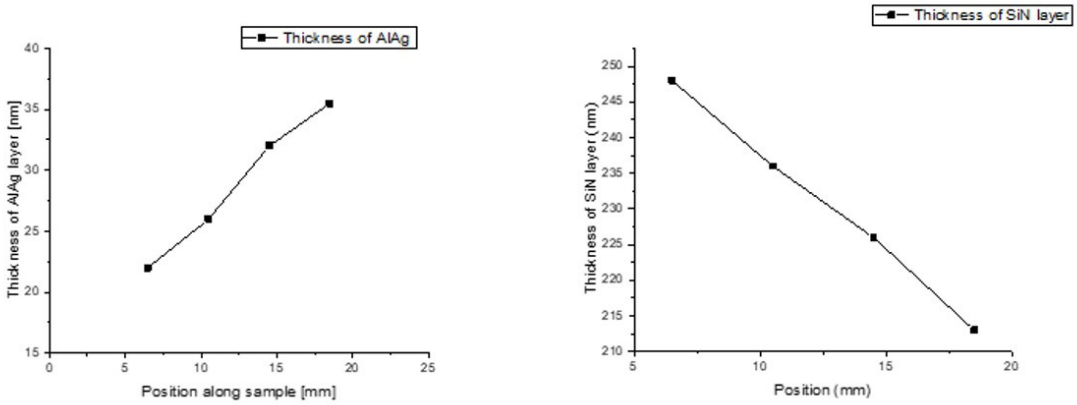


*Figure 3: AlAg and SiN layer thicknesses at selected positions of a sensor revealed by FIB-TEM measurements*

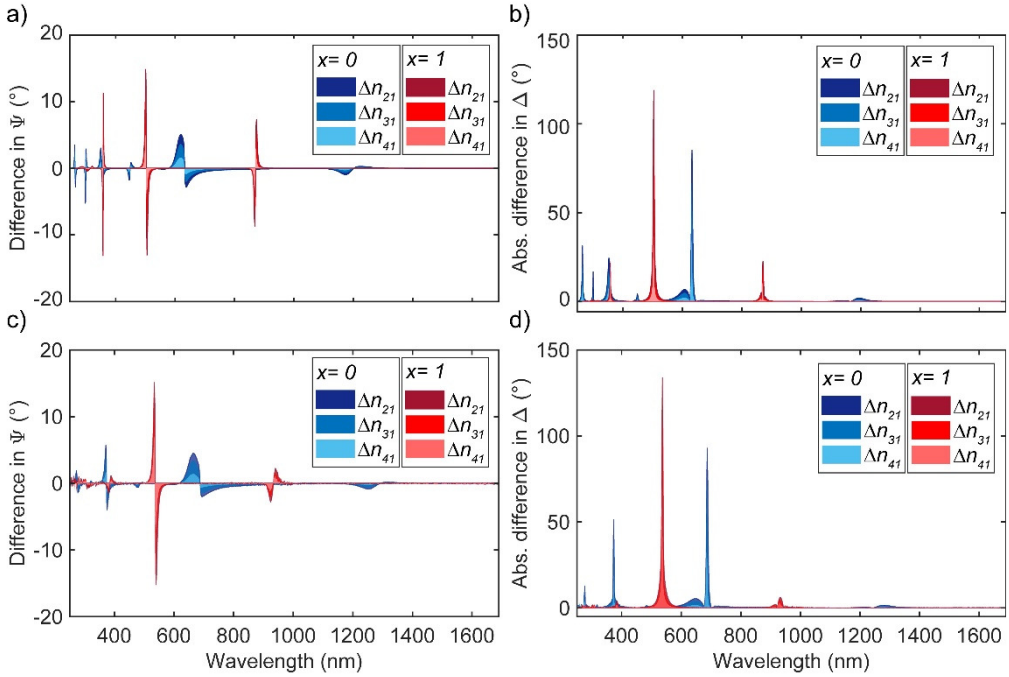


*Figure 4: Difference of simulated (a, b) and measured (c, d) Ψ and Δ spectra at compositions $x = 0$ and 1 for various DI water-isopropanol solution ambient. $\Delta nj1$ denotes the refractive index difference at $\lambda = 632$ nm ($j = 2, 3, 4$)*

The operation and tunability of the sensor in water and isopropanol test medium is demonstrated in Fig. 4 using the spectral ellipsometer with the difference spectra of the Ψ and Δ angles measured at both ends of the sample. A detailed discussion can be found in the PhD thesis of Benjamin Kalas [7].

## *Related publications*

[1] G. Sáfrán: *Theory of the spatial resolution of (scanning) transmission electron microscopy in liquid water or ice layers,* Ultramicroscopy **187,** 50-55 (2018)

[2] E. Kretschmann and H. Raether: *Radiative Decay of Nonradiative Surface Plasmons Excited by Light,* Zeitschrift für Naturforschung **A 23.4**, 615–617 (1968), issn: 1865-7109

[3] G. Sáfrán: *A micro-combinatorial TEM method for phase mapping of thin two-component films,* Hung. Patent No. P 15, 00500 (2015)

[4] G. Sáfrán, J. Szívós, M. Németh, A. Horváth, In: Ágnes, Kittel; Béla, Pécz (szerk.) 12th MCM 2015 Budapest, Magyarország : Akadémiai Kiadó, 559-560, 2 p. (2015)

[5] Q. Chinh Nguyen, G. Sáfrán: H*igh strength of ultrafine-grained Al–Mg films and the relevance of the modified Hall–Petch-type relationship,* MRS COMMUNICATIONS, 4 p. (2019)

[6] B. Kalas, Zs. Zolnai, G. Sáfrán, M. Serényi, E. Agocs,T . Lohner, A. Nemeth, N Q.Khánh, M. Fried, P.Petrik: *Micro-combinatorial sampling of the optical properties of hydrogenated amorphous $Si_{1-x}Ge_x$ for the entire range of compositions towards a database for optoelectronics,* Scientific Reports **10,** 19266 (2020)

[7] Kalas György Benjamin, PhD Thesis

# COMBINATORIAL CATALYSIS; DEVELOPMENT OF BIMETALLIC NI-IN CATALYSTS FOR THE DRY REFORMING OF METHANE WITH CARBON DIOXIDE

*A. Horváth, M. Németh, A. Beck, G. Nagy, M. Serényi, G. Sáfrán*

As a joint initiative of the Thin Film Physics Department (VRF) of the MFA and the Laboratory of Surface Chemistry and Catalysis (FKKL) and in the framework of bilateral Italian and Egyptian MTA grants, the microcombinatorial TEM method was applied for the first time in catalyst research. The catalytic system is the $SiO_x$-supported nickel-indium catalyst of FKKL, which has been investigated in the so-called dry reforming reaction of methane with $CO_2$ ($CH_4+CO_2 \leftrightarrow 2CO+2H_2$) for several years with considerable success [4-6] in environmentally conscious methane conversions: (1) $CO_2$ reactants to obtain synthesis gas ($CH_4+CO_2 \leftrightarrow 2CO+2H_2$), the aim here is to avoid deactivating carbonization of our NiIn catalyst [1] and (2) pyrolysis to obtain pure $H_2$ without $CO_2$ emissions ($CH_4 \leftrightarrow C+2H_2$), the opposite aim here is to increase the carbon deposition propensity of our NiMo catalyst. In the reforming reaction, the harmful carbonization of the catalyst is strongly inhibited due to the indium component, however, the effect of the Ni-In ratio has not yet been studied in detail. Our first $SiO_2$-supported catalyst had a Ni/In=3 composition, but indium may have a beneficial effect even at low concentrations e.g. Ni/In=24. The micro-combinatorial method developed at VRF allows the linear variation of the thickness of a component or the composition within one sample deposited by DC or RF magnetron sputtering. [1, 2-3].

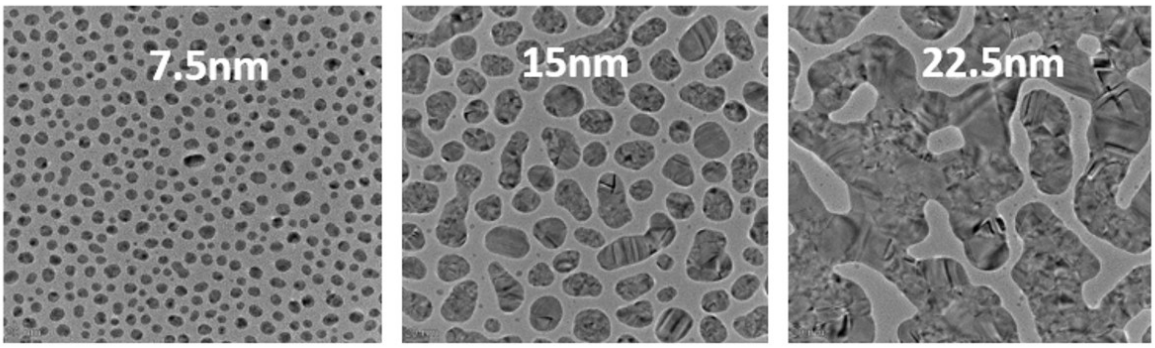


*Figure 1: Morphology of variable layer thickness revealed by combinatorial TEM*

This way we investigated the thickness dependence of size and morphology of pure nickel (Fig. 1.) on a variety of substrates e.g. C, $SiO_2$, $Al_2O_3$. The samples of varying thickness were subjected to oxidation and reduction according to the standard catalyst pre-treatment. HRTEM, STEM-EDS and SEM-EDS measurements were performed to monitor the structural and morphological changes, so we optimised the size and distribution of the particles so that they do not aggregate during heat treatments.

The Ni catalyst layer optimised in the investigated range shows well-separated 5-20 nm grains after standard oxidation-reduction treatment (Fig. 2). The HR-TEM image clearly shows carbon deposit of 3-4 graphite planes (d=3.3 Å) built onto Ni grains, which originates from the bare or $SiO_x$-capped C-support. It is detrimental to the catalyst activity, therefore, in future, the use of the SiN/SiOx support is considered.

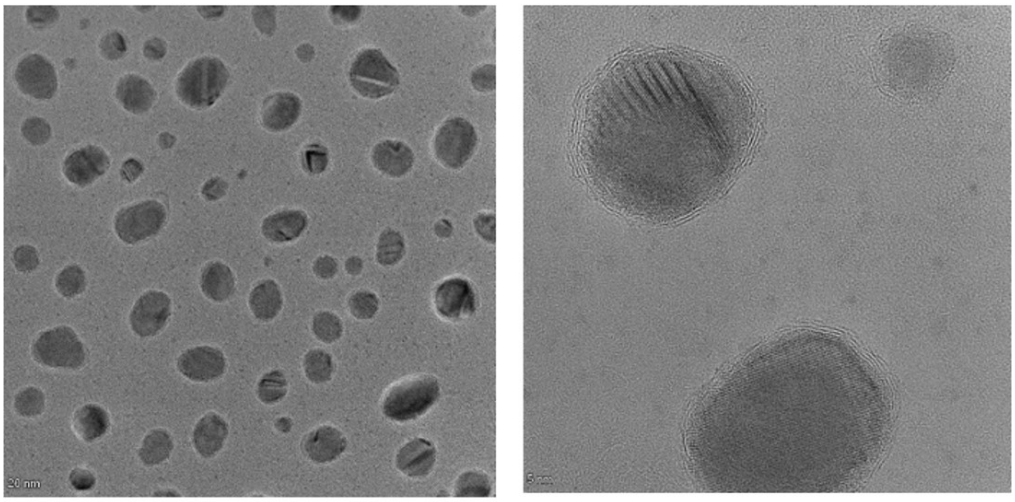

*Figure 2: TEM of 5~20 nm size Ni catalyst grains on C/$SiO_x$ support after standard oxidation-reduction treatment. The HR-TEM image shows the carbon deposit on the Ni grains consisting of 3-4 graphite planes (d=3.3 Å).*

In subsequent experiments, we will add the catalyst in a controlled way, with indium, up to Ni/In=3 ratio, creating a regular concentration variation between the two endpoints of the sample. This will be followed by reacting the samples in a methane stream at various temperatures. Based on our experience, the Ni or NiIn particles are expected to exhibit different levels of carbon deposition depending on the local composition. TEM microstructural studies of the resulting carbon nanotubes, graphitic or amorphous carbon forms provide important information on the expected behaviour, efficiency and self-cleaning ability of a given Ni-In composition in methane dry reforming and thus allow to select the best performing Ni-In compositions. In a third step, nanoparticles with optimal Ni-In composition and morphological-structural properties are prepared by classical wet chemistry and tested under real catalytic conditions in a flow-through system (FKKL). The experience gained can also be used for the optimization of further two-component material systems, e.g. Ni-Mo. The use of the single-sample combinatorial method in catalysis development is new in the literature. The results of ongoing research will be used in the development of energy-efficient, low-temperature stable catalysts that convert methane and carbon dioxide into useful synthesis gases.

## *Related publications*

[1] G. Sáfrán: *Theory of the spatial resolution of (scanning) transmission electron microscopy in liquid water or ice layers,* Ultramicroscopy **187,** 50-55 (2018)

[2] G. Sáfrán: *A micro-combinatorial TEM method for phase mapping of thin two-component films,* Hung. Patent No. P 15, 00500 (2015)

[3] G. Sáfrán, J. Szívós, M. Németh, A. Horváth: In: Ágnes, Kittel; Béla, Pécz (szerk.) 12th MCM 2015 Budapest, Magyarország : Akadémiai Kiadó, (2015) pp. 559-560, 2 p.

[4] J. Károlyi, M. Németh, C. Evangelisti, G. Sáfrán, Z. Schay, A. Horváth and F. Somodi: *Carbon dioxide reforming of methane over Ni-In/$SiO_2$ catalyst without coke formation,* Journal of Industrial and Engineering Chemistry **58,** 189 (2018)

[5] M. Németh, G. Sáfrán, A. Horváth, F. Somodi: *Hindered methane decomposition on a coke-resistant Ni-In/$SiO_2$ dry reforming catalyst,* Catalysis Communications **118,** 56 (2019)

[6] M. Németh, F. Somodi and A. Horváth: *Interaction between CO and a Coke-Resistant NiIn/$SiO_2$ Methane Dry Reforming Catalyst: A DRIFTS and CO Pulse Study,* Journal of Physical Chemistry C, DOI: 10.1021/acs.jpcc.9b06839, (2019)

# THE GROWTH OF A MULTI-PRINCIPAL ELEMENT (COCRFEMNNI) OXYNITRIDE FILM BY DIRECT CURRENT MAGNETRON SPUTTERING USING AIR AS REACTIVE GAS

***OTKA NN112156***

*Gy. Radnóczi, R. Dedoncker (Ghent University), Gy.Z. Radnóczi, Zs. Czigány, A. Sulyok, V. Kovács-Kis (MFA, University of Pannonia), D. Depla (Ghent University)*

Multi-Principal Element Alloys (MPEAs) are a class of alloys that are composed of several elements in near-equimolar concentrations. The field of MPEAs was discovered about 15 years ago but still holds many interesting features. Against the intuitive expectation, some of these compositionally complex alloys have a simple crystallographic structure such as a face centred (fcc) or body centred cubic (bcc) structure with the constituent elements randomly distributed over the lattice positions [1-2] When some specific requirements are reached, these materials can also be labelled high entropy alloys. These materials received already much interest due to their excellent mechanical behaviour as bulk material, but in thin film form many aspects remain undiscovered. Especially, research on compound thin films based on MPEAs holds a vast uncharted territory.

From literature and previous studies, it became clear that nitrides and oxides of alloys consisting of 4-5 components show the same remarkable structures when they are deposited by magnetron sputtering. In the case of the CoCrCuFeNi alloy, the addition of nitrogen or oxygen to the discharge resulted in the same B1 (NaCl) structure. This intriguing similarity triggers the interesting fundamental question whether this behaviour can be extended to a mixture of oxygen and nitrogen, and how both gases influence the structure formation during film growth.

In this paper, a detailed atomic level structural analysis of CoCrFeMnNi oxynitride thin films is performed. The goal is to get insight into the atomistic processes, responsible for the growth mechanism and the morphological development of the film structure.

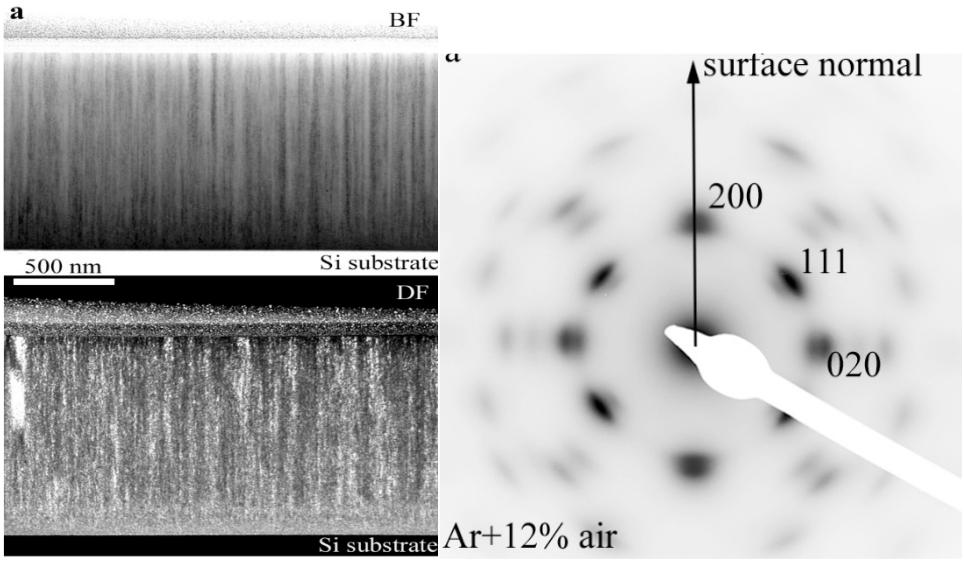


*Figure 1: (a) Cross section Bright Field (BF) and Dark Field (DF) TEM images of film, grown in Ar+12% air sputtering gas. (b) Selected area electron diffraction (Ø1 μm area) of the film shown in a). The strong reflections belong to metallic CoCrFeMnNi alloy, the internal weak reflections belong to the CoCrFeMnNi-oxynitride compound.*

CoCrFeMnNi films were grown by DC magnetron sputtering using Ar+air as sputtering gas. A background pressure of less than $4\times10^{-4}$ Pa was achieved by the combination of a rotary pump and a turbomolecular pump. A CoCrFeMnNi powder target was used according to a procedure described in [2]. At a total pressure of 0.5 Pa the fractional flow rate of air was varied between 0-50 vol.%. The samples were deposited at room temperature on a Si [100] substrate with a native oxide. The growth rate was around 1.5 nm/s and the thickness of the grown layers varied between 1 and 2 mm.

Addition of 4–50% air to Ar in sputtering gas during deposition of CoCrFeMnNi alloy thin films resulted in a change of the phase state of growing film. At 12 % and 20 % of air in sputtering gas a 〈100〉 preferred orientation fcc CoCrFeMnNi alloy, doped with oxygen and nitrogen develops, which is stochastically intermixed with a B1 oxynitride nano-phase. The B1 oxynitride nano-phase is embedded epitaxially into the fcc CoCrFeMnNi alloy.

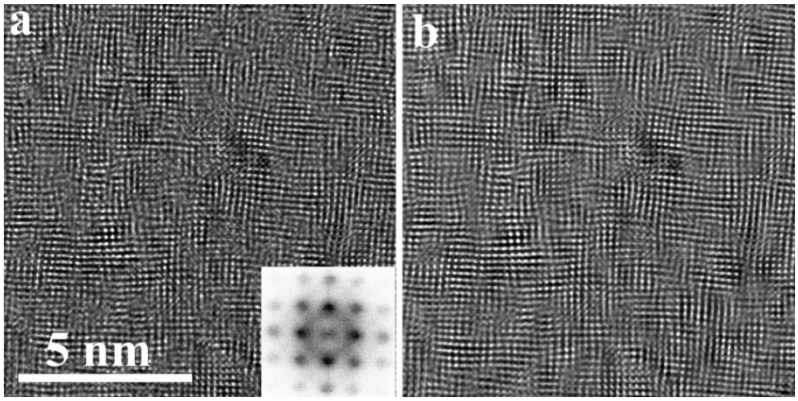


*Figure 2: High resolution image of the film grown in Ar+12% air sputtering gas and its FFT diffraction pattern (a), and the filtered image of the same area created by the 200 type reflections (b).*

At and above 30% of air a B1 phase CoCrFeMnNi-oxynitride forms with ⟨100⟩ preferred orientation. Oxygen is preferentially incorporated into the growing structures, while nitrogen content is inferior. The ⟨100⟩ preferred orientation is the result of selected nucleation (12 and 20% air) or competing growth (30 and 50% of air) of the developing crystals. All films produce broad Bragg peaks and a strong diffuse scattering which can be attributed to the nanoscale stochastic and/or partly ordered (rigid unit mode and ordered fcc) CoCrFeMnNi metal or CoCrFeMnNi-oxynitride lattice. The stochastic and ordered nano-structures are thought to be the result of spinodal processes taking place already during the growth process of the originally homogeneous structure. These kinds of structures and processes can be quite general in MPEA alloys and compounds.

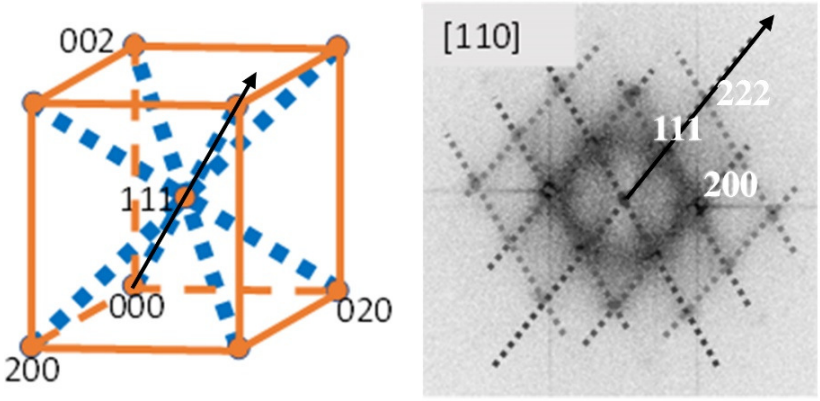


*Figure 3: The reciprocal unit cell of the fcc crystal with infinite rods (dotted lines) in ⟨111⟩ directions, due to the planar disorder on {111} planes in the lattice (left) and their geometry in an {110*} reciprocal lattice plane of 30% air sample (right). The dotted lines correspond to linear streaks in the diffraction pattern.*

## *Related publications*

[1] G. Radnóczi, R. Dedoncker, G.Z. Radnóczi, Zs. Czigány, A. Sulyok, V. Kovács-Kis, D. Depla: *The growth of a multi-principal element (CoCrFeMnNi) oxynitride film by direct current magnetron sputtering using air as reactive gas,* Surface & Coatings Technology **421,** 127433 (2021) https://doi.org/10.1016/j.surfcoat.2021.127433

[2] D. Depla: *High entropy alloy thin films deposited by magnetron sputtering of powder targets,* Thin Solid Films **580,** 71–76 (2015) https://doi.org/10.1016/j. tsf.2015.02.070

# BIORESORBABLE AND BIOCOMPATIBLE BIOACTIVE ION-DOPED, CARBONATED HYDROXYAPATITE LOADED BIOPOLYMER COMPOSITES

## *OTKA PD131934*

*M. Furkó*

The aim of this research work is to develop bioactive ion-doped bioceramic – biopolymer composite coatings onto implant materials. The ion-doped, carbonated hydroxyapatite (cHAp) powders were prepared by wet chemical precipitation using different calcium and phosphorus sources and co-precipitating with different bioactive ions such as Mg, Sr, Zn along with the base CaP. The micro and nanostructure of base cHAp powders were studied with regard to the post treatment after precipitation.

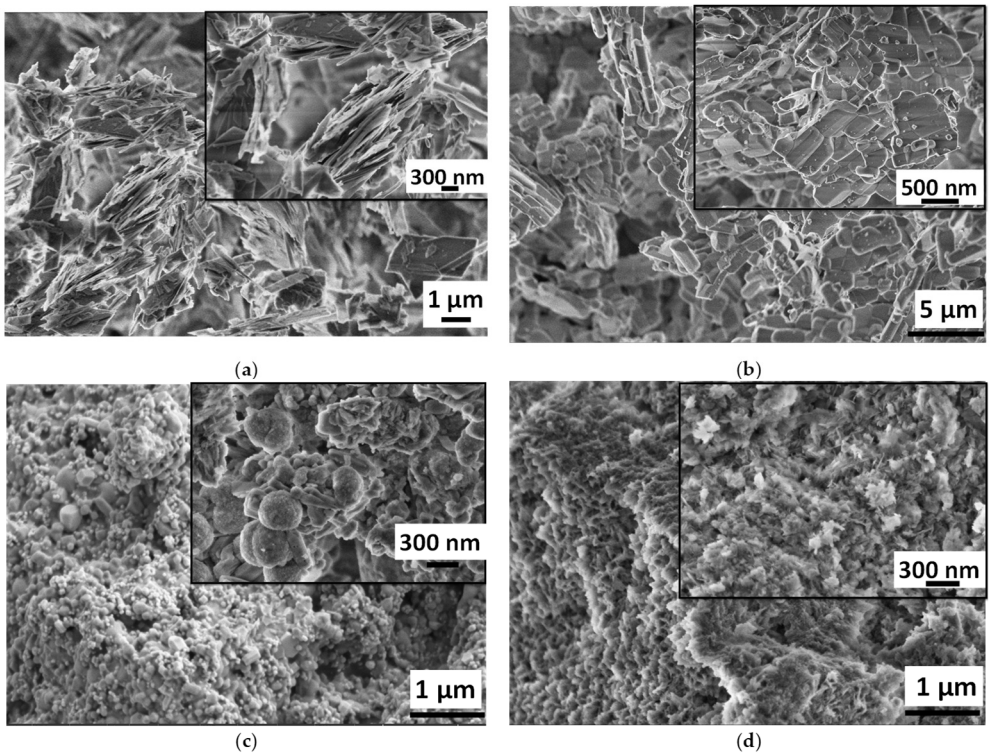


*Figure 1: SEM images of calcium phosphate particles (a) as-prepared by wet chemical precipitation (sample CaP1): magnification 20kX, inset 50kX (b) CaP1 sample heat treated at 650 °C for 5 hours (sample CaP2): magnification 10kX, inset 20kX (c) CaP1 sample heat treated at 900 °C for 5 hours (sample HAp1): magnification 20kX, inset 100kX and (d) CaP1 sample alkaline treated in $Na_2CO_3$ solution for 24 hours (sample HAP2): magnification 50kX, inset 100kX.*

Fig. 1 clearly demonstrates the difference in morphology of CaP powders prepared and treated in different ways. The as-prepared powder using Ca acetate as precursor has particles in the shape of large, thin plates in several micrometre sizes. These plates tended to be oriented parallelly (Fig. 2.a). This type of morphology is characteristic of the monetite phase. After heat treatment, the morphology of particles changed noticeably. Keeping the sample at 650 °C for 5 hours resulted in long, rod-shaped particles and smaller cubes attached together as well as large agglomerated blocks. This change in morphology can be attributed to the phase transformation to calcium pyrophosphate. Effect of ionic substitution: the addition of different bioactive ions into the starting solution has also changed the morphology of the precipitated powders. The substituting ions were also deposited in the form of low soluble phosphate precipitates along with different CaP phases. The forms and sizes of particles were very diverse, the powders contained large plate-like, rod-like grains in 0.5 – 5 µm sizes and small, needle-like particles as well as agglomerated spherical and flake-like particles. The elemental distribution of substituting elements was homogeneous within the CaP matrix according to the SEM elemental mapping.

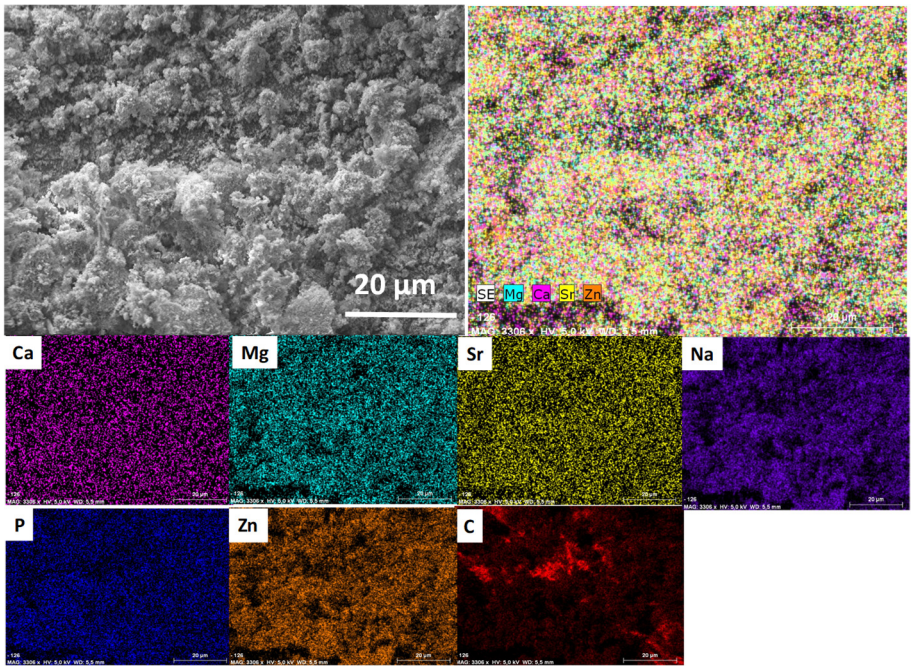


*Figure 2: SEM image and elemental mapping on ionic doped CaP powder prepared from Ca gluconate precursor.*

CaP/biopolymer (Cellulose acetate, CA) composites were prepared by electrospinning technique. The bioactive ions were added to the base CaP suspension in the form of their chloride salts. The incorporation of added ions occurred during the co-precipitation with CaP phases. The suspension was mixed with biopolimer solution in appropriate concentrations and ratio in ethanol media. The fiber generation was performed by electrospinning apparatus, using high voltage difference between the two electrodes (needle and collector). According to SEM analyses, the CaP particles (white agglomerates, nodules) were sufficiently incorporated between the polymer fibers. The particles of HAp2 sample are attached to the CA fibres as clusters and the cover is discontinuous. In other words, the ceramic particles are incorporated into a mat of interwoven fibres. However, it can also be observed that the huge difference between the diameters of individual fibres, compared to pure CA fibres, lowered (between 100 and 400 nm) which can be attributed to the dispersed cHAp particles and the increased viscosity of suspension.

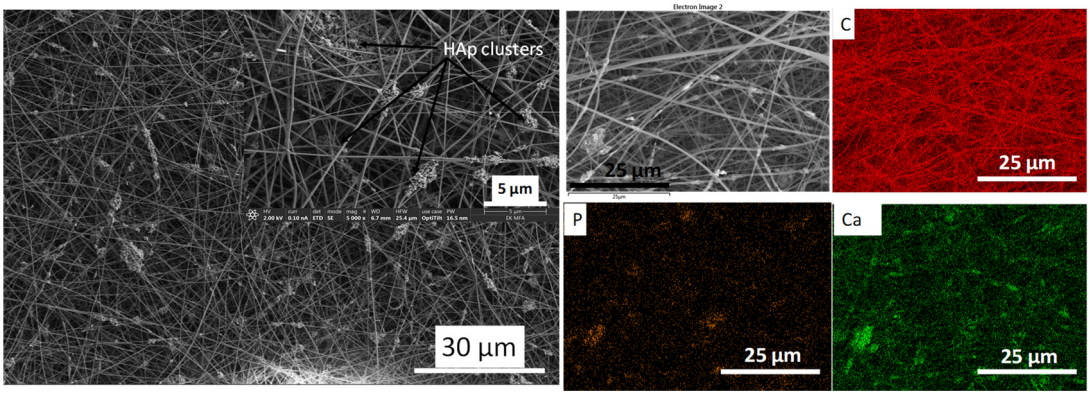


*Figure 3: SEM images on cHAp loaded cellulose acetate as well as the corresponding elemental mapping*

# $Al_2O_3$-AlN Composite and AlON Ceramic Development Using the Powder Technology

***NKFIH NNE***

*K. Balázsi, M. Furkó, V. Varga, S. Gurbán, F. Cinar (ITU), Cs. Balázsi*

Aluminium nitride (AlN) is an alternative refractory ceramic material being used in various range of applications such as optics, electronics and computer circuits for its unique thermal and electrical properties. It has a really high degree of thermal stability and wear resistance while exhibiting a low density. The aim of our work was the preparation of cheap $Al_2O_3$-AlN composites and transparent AlON by eco-friendly technology. Currently commercially available AlON materials show a larger grain size. The development of new methods to control the nano-grain size can improve the material´s properties. The most promising techniques for ceramic aluminium based preparation are the Hot Isostatic Pressing (HIP) or Spark Plasma Sintering (SPS). The currently available and used techniques are still all expensive, as well as being energy and time consuming. We intend to develop an eco-friendly preparation method (Fig. 1) of $Al_2O_3$-AlN and AlON in which we develop a novel way to reduce the temperature and/or time thus requiring lower energy.

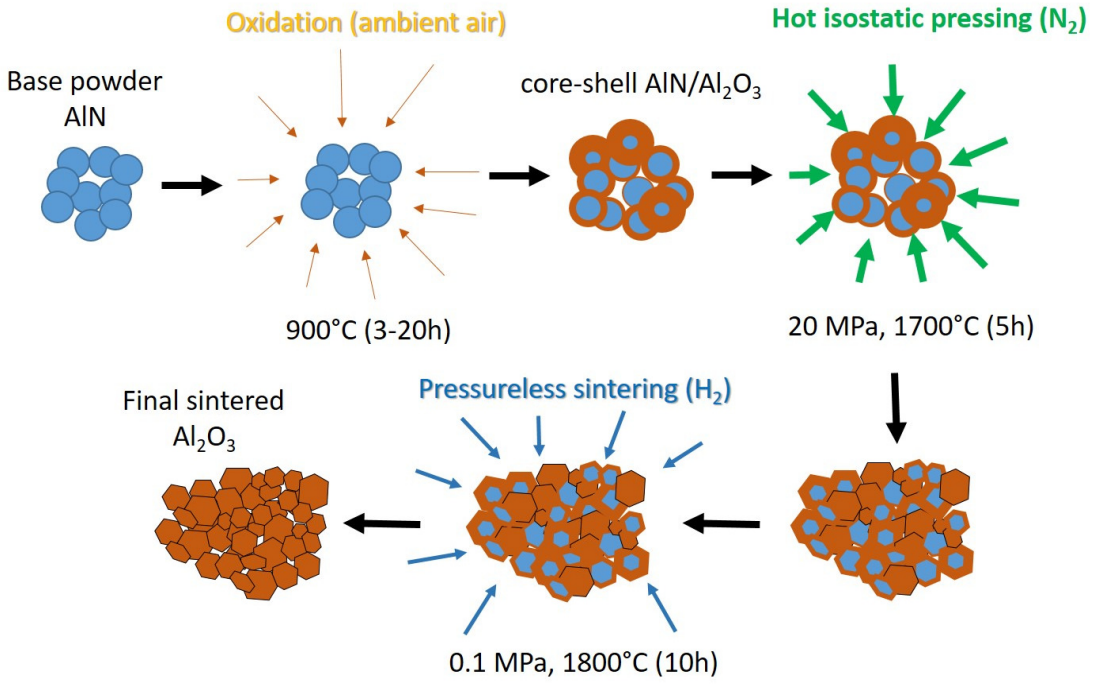


*Figure 1: Schematic view of preparation method*

The effect of the pressureless post-sintering in hydrogen atmosphere on the structural and mechanical properties of the hot isostatic pressed $Al_2O_3$ prepared by oxidized AlN powder has been studied. The micrometer size AlN powder has been oxidized in ambient air at 900° C for different times (3, 6, 10 and 20 hours) and sintered by HIP at 1700°C, 20 MPa nitrogen atmosphere for 5h. Pressureless Sintering (PS) has been applied for all HIP sintered samples in $H_2$ gas at 1800° C for 10 hours. It has been shown that the oxidation caused a core-shell AlN/$Al_2O_3$ structure and the amount of $Al_2O_3$ increased with increasing of the oxidation time of the AlN powder. For the first time, the green samples obtained from oxidized AlN powder have been successfully sintered first by HIP followed by post-sintering by PS under hydrogen without adding any sintering additives.

All post-sintered samples exhibited the main α-$Al_2O_3$ phase. The metastable oxide phases of $Al_2O_3$ have not been present in the post-sintered samples owing to the high temperatures involved in the processing. Sintering in $H_2$ caused the full transformation of AlN to α-$Al_2O_3$ phase and their better densification. Therefore, the hardness values of post-sintered samples have been increased to 17-18 GPa having apparent densities between 3.11 and 3.39 g/cm3 [1].

## *Related publication*

*[1]* D. Varanasi, M. Furkó, K. Balázsi, C. Balázsi: *Processing of $Al_2O_3$-AlN Ceramics and their Structural, Mechanical, and Tribological Characterization,* Materials **14,** 6055 (2021) https://doi.org/10.3390/ma14206055

# POROUS SANDWICH CERAMIC OF LAYERED SILICON NITRIDE-ZIRCONIA COMPOSITE WITH VARIOUS MULTILAYERED GRAPHENE CONTENT

***FLAG-ERA "Ceranea", OTKA NN127723***

*K. Balázsi, M. Furkó, Zs. Fogarassy, V. Varga, Z. Liao (IKTS), J. Dusza (IMR SAS), E. Zschech (IKTS), Cs. Balázsi*

Development of the graphene-filled ceramic sandwiches that deliver materials with enhanced properties and functionalities was a part of the "Graphene Flagship" „CERANEA" project as a part of FLAG-ERA Joint Transnational Call 2017 for graphene supported by the European Commission.

The silicon nitride ($Si_3N_4$) is the widely used high-temperature ceramic material (up to 1500 °C). Due to its extreme high hardness and toughness in a wide range of temperatures, potential applications include reciprocating engine components, turbo chargers, bearings, metal cutting and shaping tools as well as hot metal handling. Silicon nitride has better mechanical properties at high temperatures compared to most metals, and its low Coefficient of Thermal Expansion (CTE) results in a higher thermal shock resistance than for most ceramic materials. These ceramics can be prepared in different forms, sintered bulk or layered. Multilayer Ceramic Composites (MCC) consist of two ceramic materials. These ceramics are consisting of insoluble parts in each other and sequentially piled in a symmetric manner. In this work, we are firstly produced the gradient-structured $Si_3N_4$ ceramics with few layers' graphene by attritor milling and hot isostatic pressing (Fig. 1.).

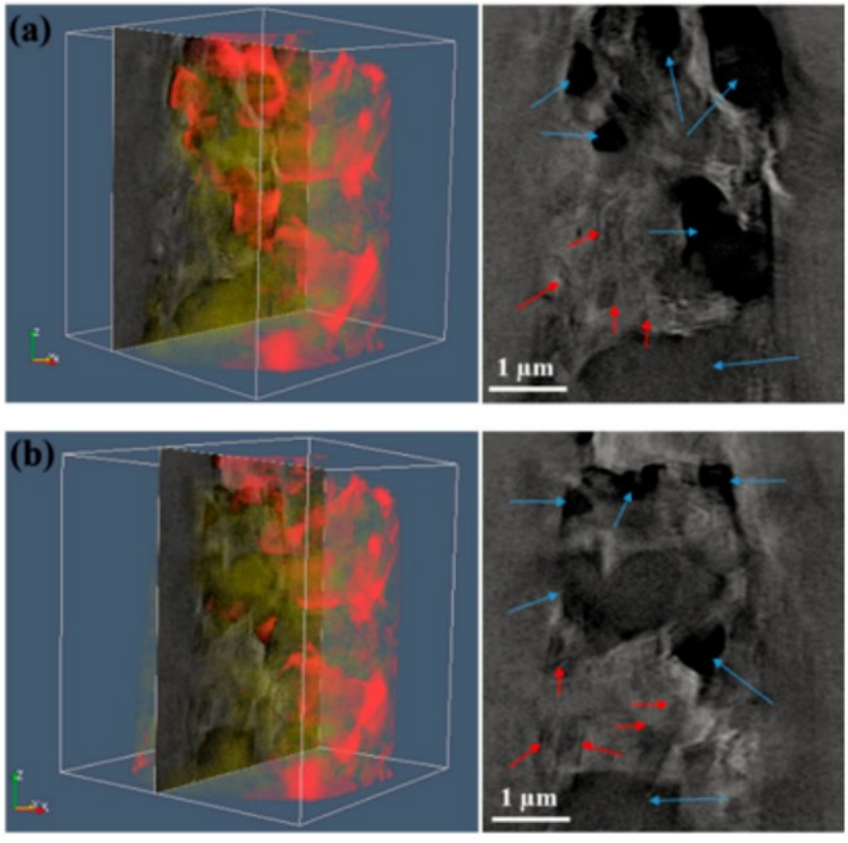


*Figure 1: Image of the multi-layered ceramic composite with different graphene content. Extracted slices from a volumetric reconstruction of the composite with 30 wt.% multilayer graphene (MLG) by synchrotron-based nano-X-ray Computed Tomography (XCT). $ZrO_2$ phases are indicated by blue arrows, $Si_3N_4$ phases are indicated by red arrows*

The porosity of the samples increased by around two times with increasing of the Multilayer Graphene Content (MLG) content. The density values were lower for samples with high MLG content owing to their very porous microstructure. The mechanical test confirmed that sandwich structure with combination of 5-30-5 wt% MLG layers showed 2 or 3 times better properties than structure with 30-5-30 wt% MLG. The main effect on mechanical properties had the layer with 30 wt% MLG with porosity of ~66% and high $\alpha/\beta$-$Si_3N_4$ ratio of sintered ceramic matrix. [1-3]

## *Related publications*

[1] Z. Liao, Y. Standke, J. Gluch, K. Balázsi, O. Pathak, S. Höhn, M. Herrmann, S. Werner, J. Dusza, C. Balázsi, et al.: *Microstructure and Fracture Mechanism Investigation of Porous Silicon Nitride-Zirconia-Graphene Composite Using Multi-Scale and In-Situ Microscopy,* Nanomaterials **11,** 285 (2021) https://doi.org/10.3390/nano11020285

[2] K. Balázsi, M. Furkó, Z. Liao, J. Gluch, D. Medved, R. Sedlák, J. Dusza, E. Zschech, C. Balázsi: *Porous sandwich ceramic of layered silicon nitride-zirconia composite with various multilayered graphene content,* Journal of Alloys and Compounds **832,** 154984 (2020)

[3] K. Balázsi, M. Furkó, Z. Liao, Z. Fogarassy, D. Medved, E. Zschech, J. Dusza, C. Balázsi: *Graphene added multilayer ceramic sandwich (GMCS) composites: Structure, preparation and properties,* Journal of the European Ceramic Society **40:(4),** 4792-4798 (2020)

# OPTIMIZATION OF POST VACUUM ANNEALED V THIN FILMS

*Sloven bilateral 2019-2.1.11-TÉT-2020-00189, Bolyai fellowship, ÚNKP Postdoctoral fellowship*

*Gy. Molnár, Zs. Baji, L. Pósa, L. Illés, J. Volk, G. Drazic (National Institute of Chemistry, Slovenia), A. K. Surca (National Institute of Chemistry, Slovenia)*

The oxidation of vanadium thin films is a promising method for the production of vanadium dioxide ($VO_2$) layers. $VO_2$ has been extensively studied for decades, because of its semiconductor (insulator) – metal transition at about 68°C. This is a first order phase transition accompanied by structural transformation from low-temperature monoclinic to high-temperature tetragonal phase. Besides the structural and electronic properties, the optical features change remarkably between the two phases. $VO_2$ has possible applications for microelectronics including memory and switching devices and for optical shutters and thermochromic smart windows.

Earlier, we studied the oxidation of vanadium film in atmospheric pressure air at different temperatures and time and found a rational fabrication method for the production of low switching temperature $VO_2$ [1]. Recently, we have been trying to enhance the electrical and structural features of the vanadium dioxide films by reducing the pressure of the oxidizing ambient and optimize the time and temperature of the oxidation process.

Thermally oxidized Si wafers were applied as substrates. 100 nm thick vanadium films were evaporated from vanadium ingots using an electron gun. The post deposition heat treatments were carried out in a computer-controlled tube furnace in air at $1.0x10^{-1}$ mbar pressure. The annealing temperature varied between 400 and 480 °C and the annealing times were between 2 and 270 minutes. According to our measurements, the samples annealed at 400°C, for 270 minutes, in $1x10^{-1}$ mbar pressure air have the best electrical properties.

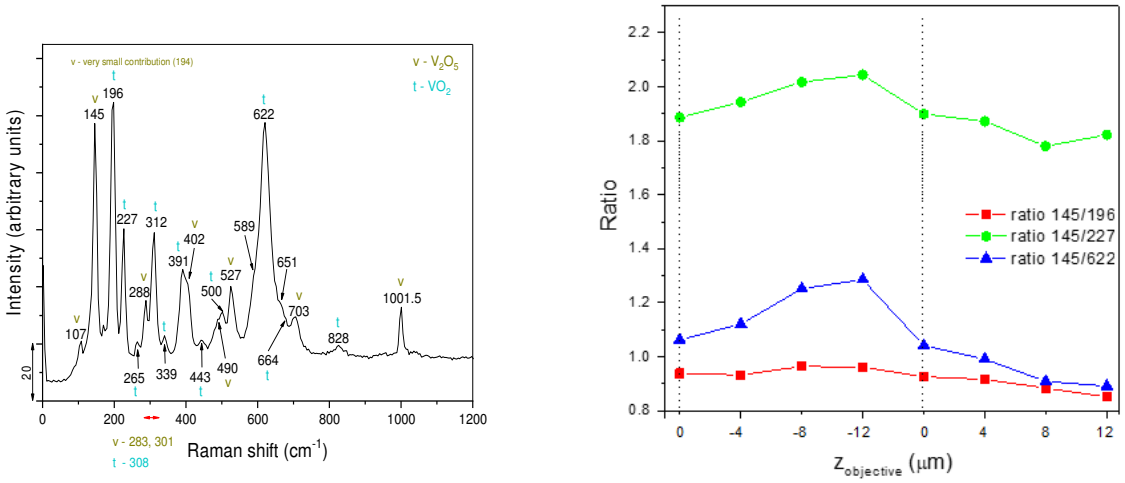


*Figure 1: Raman spectrum of V-oxide film on silicon wafer (left) Ratios of $V_2O_5$ (145)/$VO_2$ bands of Raman spectra taken at various z-axis positions of objective (right).*

The prepared films were analysed with electron energy loss spectroscopy and Raman spectroscopy. It is clear from both measurements that the film is pure vanadium-oxide with only two phases present: $VO_2$ and $V_2O_5$ (Fig. 1). Fig. 2 shows the TEM image with the corresponding EELS spectra. The spectra of the topmost 50 nm of the layer show only the presence of $VO_2$ (spectra 1 and 2 in Fig. 1). The lower ~150 nm of the film consists of $V_2O_5$, as clearly shown by a characteristic shoulder of the L peak of V marked in spectra 3-5 in Fig. 2.

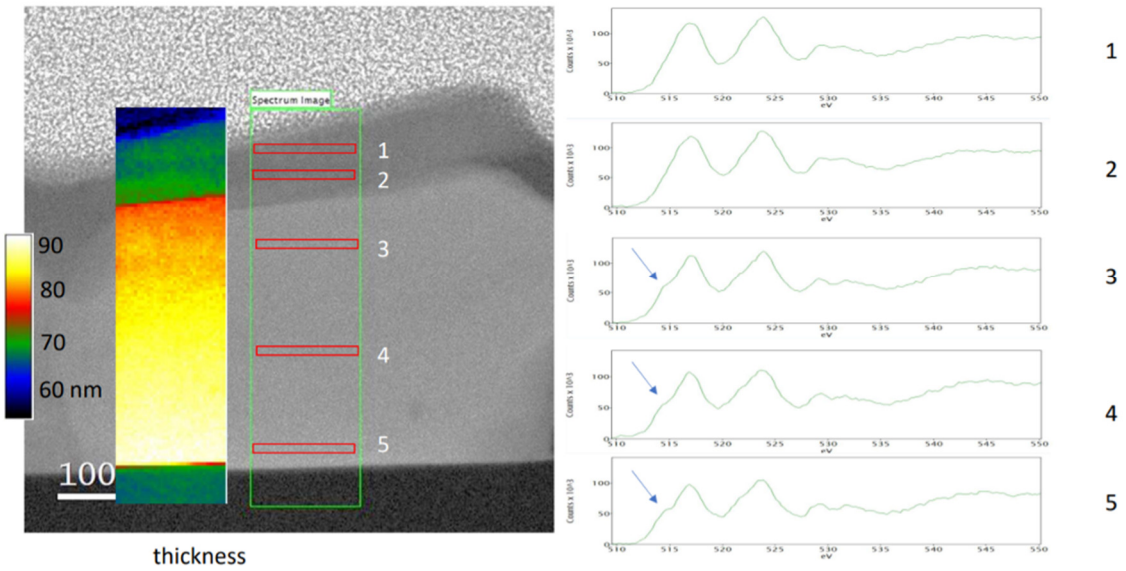


*Figure 2: EELS spectra from different depths of the $VO_x$ layer*

The Raman spectrum of V-oxide film clearly shows that both vanadium oxides ($VO_2$ and $V_2O_5$) are present. The most intense band of $V_2O_5$ is 145 $cm^{-1}$ and the most characteristic one is 1001 $cm^{-1}$. Also the band at 527 $cm^{-1}$ belongs to solely $V_2O_5$. In other bands $V_2O_5$ is accompanied with $VO_2$. Raman spectra were also measured by moving the objective to sample different parts of the film along z-axis and the intensities of the most representative bands (145 $cm^{-1}$ for $V_2O_5$, and 196, 227 and 622 $cm^{-1}$ for $VO_2$) were measured and the ratios calculated. Fig. 1 shows the increase in the value of these ratios when the objective was directed more in-depth of the film. When the objective was directed upwards from the middle of the films, the opposite, the decrease of the ratios was noted, which shows that there is more $V_2O_5$ more in-depth and more $VO_2$ towards the surface, which agrees with the findings of TEM measurements.

According to these results, only the topmost 50 nm of the layer was $VO_2$. Nevertheless, the temperature dependent electrical measurements showed excellent switching properties. As Fig. 3 shows, there is a three orders of magnitude change in the resistance at the transition temperature reported in the literature. The hysteresis width is around 10–13°C, which is also a good value for polycrystalline $VO_2$ thin films.

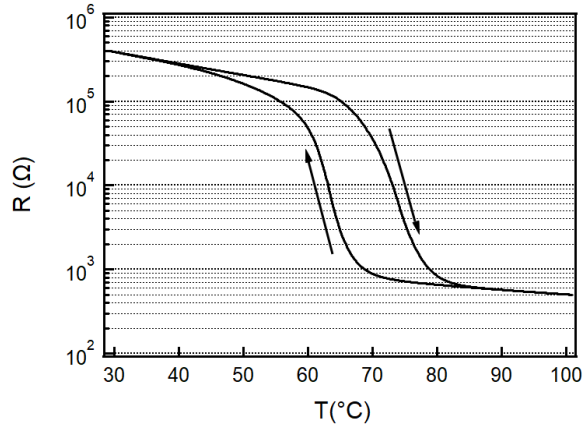


*Figure 2: The temperature dependent resistance curve of the $VO_x$ film*

## *Related publication*

[1] Zs. Baji, Zs. Fogarassy, A. Sulyok, P. Petrik: *Atomic layer deposition of $HfS_2$ from tetrakis(dimethylamino)hafnium,* submitted to JVSTA

# ATOMIC LAYER DEPOSITION OF $HfS_2$ FROM TETRAKIS(DIMETHYLAMINO)HAFNIUM

***OTKA FK139075***

*Zs. Baji, Zs. Fogarassy, A. Sulyok, P. Petrik*

2D materials with sizable bandgaps, such as Transition Metal Dichalcogenides (TMD) have been in the focus of research, as they lack the drawback of the absence of an intrinsic band gap in graphene. $HfS_2$ is a less examined member of the TMD family, with most properties only theoretically predicted, and few reliable ways to synthesize. According to calculations, $HfS_2$ may have an ultrahigh room-temperature electron mobility and sheet current density, combined with a high chemical stability and reasonable bandgap, therefore it could be a very promising material for the transistors, photocatalysts and photodetectors of the future.

$HfS_2$ films can be prepared by mechanical or chemical exfoliation, or chemical vapour deposition but so far, no reliable preparation of $HfS_2$ layers on wafer sized surfaces has been found, although it would be extremely important for later applications. The atomic layer deposition of $HfS_2$ has not yet been explored, there are so far only a handful of papers describing the ALD of $HfS_2$ films using different precursors, but these layers were non-uniform and rough.

In this work, the use of the percursor tetrakis-dimethylamino-hafnium (TDMAH) was explored. Successful deposition with the use of $H_2S$ as a reagent was performed between 200°C and 400°C. The growth rates were the following: 0.07nm/cycle at 200 °C, 0,08nm/cycle at 300°C and 0.06nm/cycle at 400 °C. The wafer scale uniformity of the films was determined by spectroscopic ellipsometry (SE), and the thickness was found uniform within ±1 nm on a 4" wafer size, which corresponds to a relative standard deviation of 2.5%. This is an excellent result previously not reported in the preparation of $HfS_2$ layers. The atomic layer deposition of $HfO_2$ from the same precursor always has a CVD like component, and the deposition of uniform films is not straightforward, it requires a precise tuning of the parameters and long pulsing and purging times. In the light of this, it is surprising that the Atomic Layer Deposition (ALD) of $HfS_2$ provides such high-quality layers, and it may be attributed to the higher reactivity of $H_2S$.

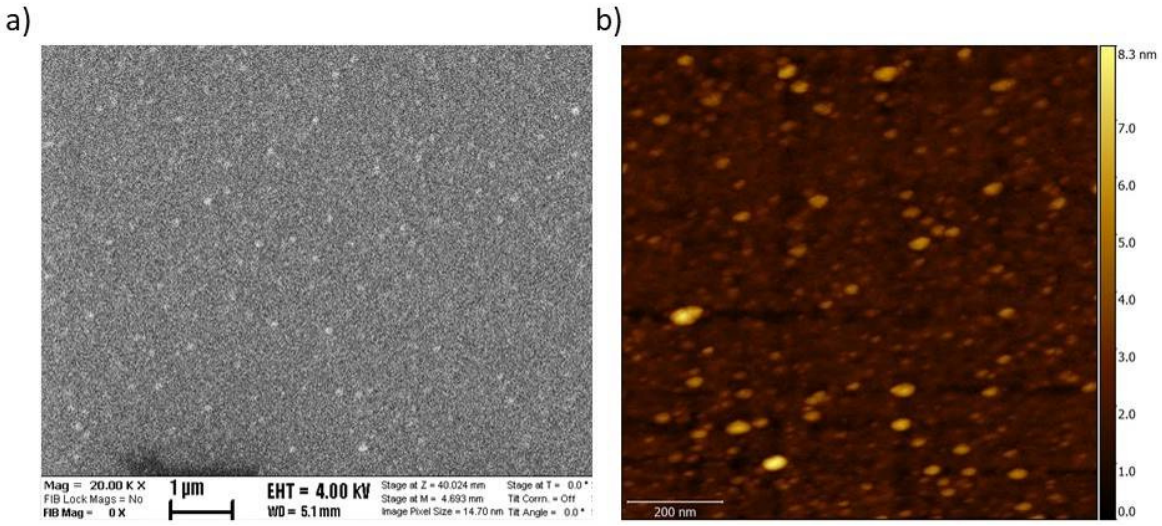


*Figure 1: $HfS_2$ films deposited at 300°C on Si(a), and on sapphire (b)*

The morphology of the layers was investigated with SEM and AFM. According to these, the films are not smooth at an atomic level, they have a slightly granular surface structure with typical grain sizes between 60-100 nm. However, all the layers are very smooth with RMS roughness below 9 nm in the case of silicon substrates, and 1 nm on sapphire (Fig. 1).

The composition of the deposited layers was determined by TEM EDS and XPS. Both methods showed that the films were mostly $HfS_2$, but the presence of $HfO_2$ was also detected, which can be attributed to the presence of some background oxygen in the deposition chamber. TEM analysis also proved that the films were amorphous, but after an annealing at 400°C, crystalline $HfS_2$ layers could be obtained, as shown by the FFT analysis of the film (Fig. 2.b.). The layer consists of crystalline 2D films stacked upon each other with an average distance of 0.59 nm between them.

After thicker films an ultra-thin layer was also synthesized. For this purpose, 10 ALD cycles were performed, with 0.3 s long TDMAH pulses followed by the closure of the ALD reactor for 1.5 s, then the evacuation of the reaction chamber is closed for 6 s to ensure enough time for the precursors to chemisorb to the surface and react with one another (picoflow mode). This method ensured that this ultra-thin film is also continuous and uniform. The thickness of the resulting thin film was measured by AFM (after etching a step with buffered oxide etchant in the layer), and it was found to be 3 nm. This means that the resulting film was about 5-6 monolayers thick. (Fig. 2.c.)

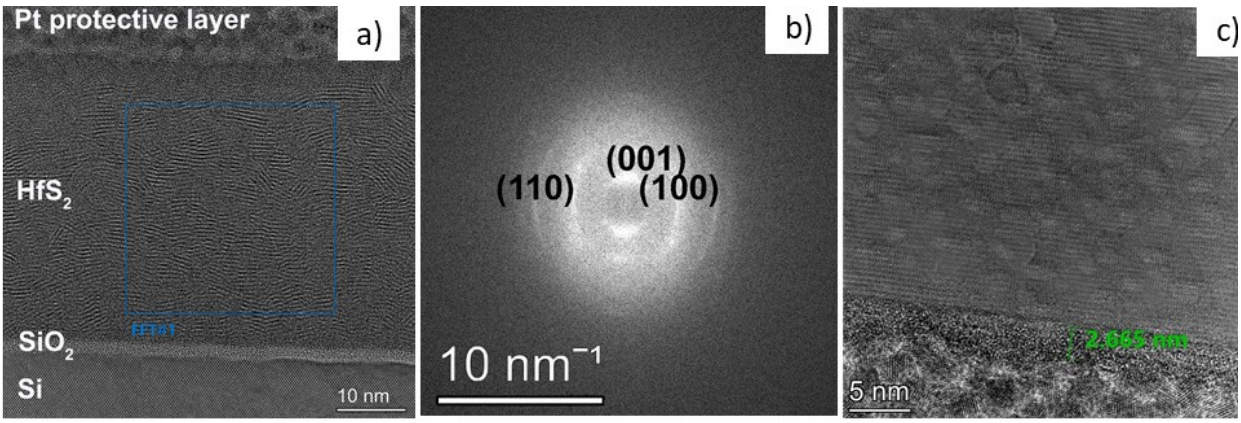


*Figure 2: HRTEM image of the film deposited on sapphire (at 300°C, annealed) (a), the FFT image of the same film (b) and the ultra-thin layer (c)*

The dielectric function spectra of the as deposited films on Si measured by SE also reveal an amorphous structure. The SE measurements showed high-quality, dense, compact, and homogeneous layers with a thickness of ≈40 nm. The optical band gaps of the layers were also calculated from the SE data. The gap of the film deposited at 200°C was 2.2eV, that of the film deposited at 300°C was higher, 3.3eV.

The film deposited at 400°C showed no definable band gap as measured by SE, instead appeared to present dielectric properties. This suggested a $HfO_2$-like behaviour, and implied that the layer may be partly or completely oxidized, therefore, this film was further investigated and the XPS measurement also proved that this film was oxidized, and according to electrical measurement was an excellent insulator. The method proved to be a promising way to prepare this promising TMD material [1].

## *Related publication*

[1] Zs. Baji, Zs. Fogarassy, A. Sulyok, P. Petrik: *Atomic layer deposition of $HfS_2$ from tetrakis(dimethylamino)hafnium,* submitted to JVSTA

# PULSE DC DEPOSITED ALSCN ALLOYS FOR PIEZOELECTRIC MEMS DEVICES

*NVKP_16-1-2016-0018 "KoFAH"*

*N. Q. Khánh, B. Oyunbolor, L. Illés, and J. Volk*

For application of thin piezoelectric nitride film in sensors and energy harvesters, piezoelectric coefficient is the key feature. It can be improved by alloying nitride with scandium, but the result depends strongly on the parameters of given deposition system. We have studied the effect of pulse DC reactive ion sputtering system (VAKSIS – MiDAS) parameters on the properties of scandium nitride film for optimalization of the co-sputtering process.

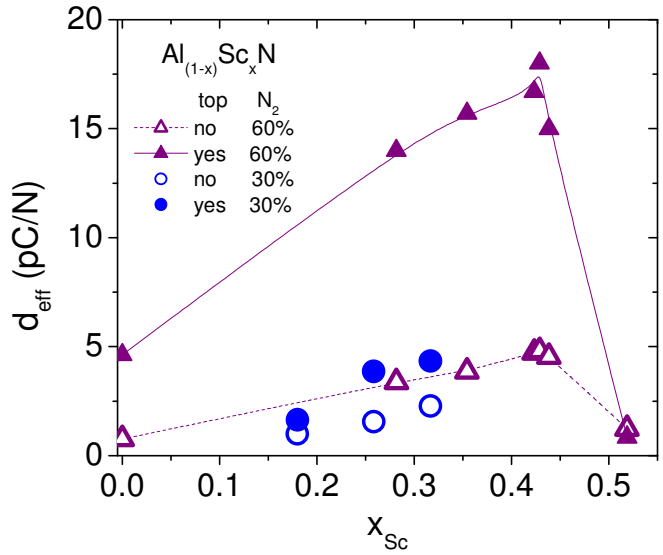


*Figure 1: $d_{33eff}$ measured by piezometer as a function of Sc concentration on $Al_{(1-x)}Sc_xN$ nitride layers deposited using different $N_2/(N_2+Ar)$ gas ratio.*

Fig. 1 shows the benefit of alloying nitride with scandium, where the absolute values of piezoelectric coefficient ($d_{33}$) measured by Berlincourt method (Piezotester, PM-300) are shown as a function of x, i.e. Sc atomic concentration. Up to x~0.45, the higher Sc concentration, the higher the measured piezoelectric coefficient. Afterwards, $d_{33}$ approaches zero at x~0.51. $d_{33}$ measured using top electrode is significantly higher, than that measured on bare nitride. The reason may be that the top electrode keeps the nitride surface clean from ambient, hence excluding the effect of surface contamination on the transport of the generated charge between nitride surface and the measuring head, thus gives data close to the real values. One can also observe in Fig. 1, that the efficiency Sc alloying depends on gas ratio. Deposition using 60% $N_2$ gas ratio (triangles) results in better improvement of $d_{33}$ than with 30% $N_2$ (circles). Besides, nitride surface is smoother for higher $N_2$ gas ratio.

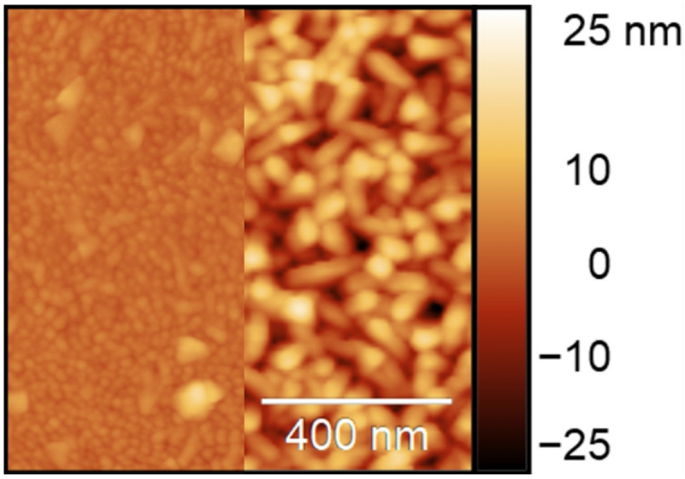


*Figure 2: AFM images of Al(1-18)Sc18N nitride layers deposited at 1.5 mTorr (left), and 3 mTorr (right)*

The most important parameter is the process gas pressure. As shown by AFM images in Fig. 2, only 1.5 mTorr difference in gas pressure resulted in much smoother surface, i.e. 1.7 nm, and 6.8 nm rms for 1.5 and 3 mTorr, respectively. The $d_{33}$ measured by the piezotester is well improved for lower pressure, namely 9.9 pC/N compared to 1.8 pC/N. Because our system works with relatively long target-to-substrate distance (TSD), low gas pressure is needed for adequate mean free path of the sputtered particles to achieve good crystal. We note that using too high $N_2$ (>80%) gas ratio and low pressure may lead to instability of plasma, and low deposition rate.

# SUBSTRATE EFFECTS ON THE INTENSITY AND RADIATIVE DAMPING OF GOLD NANOPARTICLE PLASMON RESONANCE

*OTKA FK128327*

*Zs. Zolnai, D. P. Szekrényes, D. Zámbó, A. Deák*

In general, the far-field scattering intensity of plasmonic Gold Nanoparticles (GNP) is important factor in different applications like nanosensorics and Surface Enhanced Raman Scattering (SERS). Note, besides non-radiative surface damping and chemical interface damping, to date less attention was paid to the radiative damping of Surface Plasmon Resonance (SPR), despite the fact that it may have significant contribution to the overall damping (Γ), and it is related to the far-field scattering intensity of plasmonic GNPs. In this work we investigate the scattering intensity related radiative damping ($\Gamma_{rad}$) of SPR of individual Gold Nanorods (GNR) and Nanospheres (GNS) supported by substrates to reveal the effect of the environment on $\Gamma_{rad}$ and scattering intensity. Fig. 1.a shows dark-field optical scattering spectra of an individual GNR deposited on glass vs. the normalized power of exciting light ($P_{exc}$). The derived Γ and $\Gamma_{rad}$ are also shown in Fig. 1.b No change (within 1 meV) in $\Gamma_{rad}$ can be observed for different power levels. This can be understood as $\Gamma_{rad}$ is related to the rate of energy transferred to radiated power through far-field electromagnetic scattering ($P_{sc}$) emitted by the GNP which supports plasmons with oscillator energy $E_{pl} = \hbar\omega_{pl}$, where $\omega_{pl}$ is the plasmon resonance frequency. $\Gamma_{rad}$ [$s^{-1}$] can be defined as:

$$\Gamma_{rad} = P_{sc}/E_{pl} \quad (1)$$

Since both $P_{sc}$ and $E_{pl}$ depend linearly on $P_{exc}$, $\Gamma_{rad}$ will not change by varying the excitation power, as it is shown in Fig 1. On the other hand, for a GNP embedded, i.e., in a transparent medium, the particle will sense an effective dielectric constant $\varepsilon_{eff}$ [1]. In this case the relation between $\Gamma_{rad}$ and the cross-sections for optical scattering ($\sigma_{scatt}$) and absorption ($\sigma_{abs}$) of the GNP can be computed as [2]:

$$\Gamma_{rad}/\Gamma = \sigma_{scatt}/\sigma_{ext} = 1/[1+(\sigma_{abs}/\sigma_{scatt})] \quad (2)$$

where Γ is overall damping and $\sigma_{ext} = \sigma_{scatt}+\sigma_{abs}$ is the extinction cross-section.

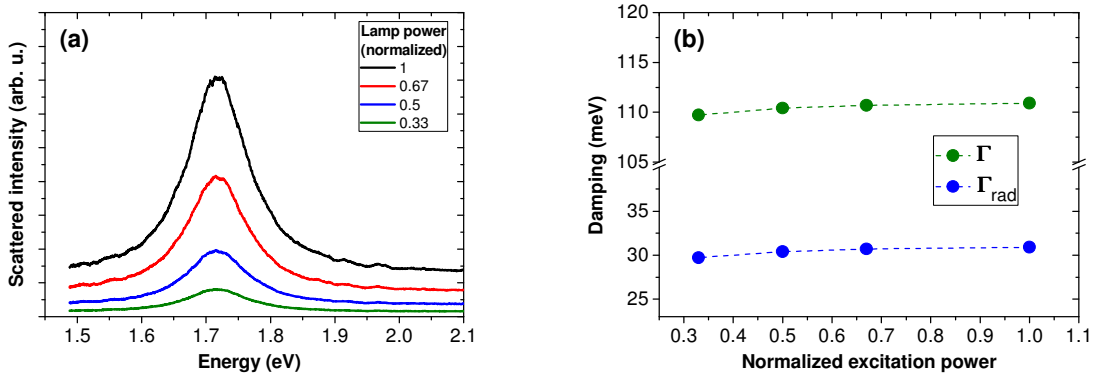


*Figure 1: (a) single particle dark-field scattering spectra of a Gold Nanorod (GNR) measured at different power levels of the light excitation source (normalized power values); (b) derived FWHM (Γ) and radiative damping ($\Gamma_{rad}$) values for the SPR of the same GNR vs. the excitation power.*

Considering that [3]:

$$\sigma_{abs}/\sigma_{scatt} = 6\pi(L^2c^3\omega_b^2\Gamma_{nr})/(\varepsilon_{eff}^{5/2}V\omega_{pl}^2) \quad (3)$$

where L is depolarization factor, c is the speed of light in vacuum, $\omega_b$ is bulk plasmon frequency for gold, while V is the volume of the GNP, and utilizing that the parameters $\Gamma_{nr}$, $\varepsilon_{eff}$, V, and $\omega_{pl}$ can be determined from experimental optical scattering spectra and scanning electron microscopy analysis, one can calculate $\sigma_{abs}/\sigma_{scatt}$, and thus $\Gamma_{rad}$, considering that $\Gamma = \Gamma_{rad} + \Gamma_{nr}$, where $\Gamma_{nr}$ is non-radiative damping (note Γ is the Full width at half maximum (FWHM) of the Lorentzian shaped optical scattering spectrum).

Fig. 2.a shows that for GNSs and GNRs embedded in glass [2] the values of $\Gamma_{rad}/\Gamma$ derived from Eq. (2) and Eq. (3) agree well with those evaluated from $\Gamma_{rad} = \Gamma - \Gamma_{nr} = \Gamma - (\Gamma_b + \Gamma_{ib} + \Gamma_s)$. Here $\Gamma_b$, $\Gamma_{ib}$, and $\Gamma_s$ are the non-radiative bulk, interband, and surface damping terms and they can be calculated according to previous works [1]. When the GNSs and GNRs are deposited on the surface of glass, the ratio $\Gamma_{rad}/\Gamma$ changes significantly for both spherical and elongated particle shape, see Fig. 2.b. Especially for GNRs, better agreement is found when in Eq. (3) a value of $\varepsilon_{eff} = 1$ (air) was considered for the embedding medium and an additional substrate-related correction has been applied for the scattering cross-section.

This correction accounts for the mirror charge effect, induced by the SPR of the GNP in the underlying polarizable substrate.

In case of glass substrate the correction for $\sigma_{scatt}$ is $\sigma'_{scatt} = \sigma_{scatt}(1+\eta)^2$ where $\eta = \pm 0.38$, and + (-) sign holds for a GNS (GNR) with transversally (longitudinally) polarized SPR related to parallel (antiparallel) polarization in the substrate with respect to the polarization of the GNP. For GNSs and GNRs deposited on glass a correction factor of ~1.9 and ~0.38 applies, respectively, which means opposite effect of the substrate for the two different particle shapes. As Fig. 2.b shows the substrate effect on GNRs is significant and suppresses $\Gamma_{rad}$ and thus the far-field scattering intensity. For GNSs either the increase of $\varepsilon_{eff}$ (due to the proximity of glass) or the mirror charge effect will increase $\Gamma_{rad}$ and the scattering intensity, moreover, their impact seems to be comparable when estimated separately.

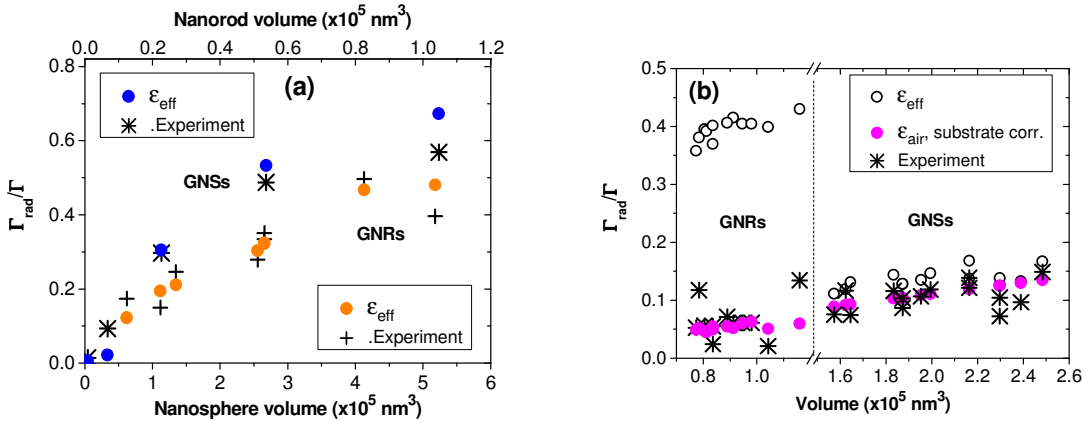


*Figure 2: Ratio of the radiative damping and full damping of the SPR in gold nanospheres and nanorods (a) embedded in a glass layer (data are from [2]) and (b) deposited on the surface of a glass substrate, as a function of the volume of the GNP. Crosses and stars represent experimental values, dots show calculations. In (b) the effect of the substrate is estimated in two different ways, for open dots an effective dielectric constant ($\varepsilon_{eff}$) was considered around GNPs, while for full dots air ambient and mirror charge effect in the underlying substrate have been taken into account.*

Based on the above results we conclude that the presence of a polarizable substrate introduces asymmetric environment around a GNP deposited on it and further work is required to reveal the full effect of different substrates on the scattering intensity and radiative damping of plasmonic GNPs.

## *Related publications*

[1] B. Foerster et al.: *Plasmon damping depends on the chemical nature of the nanoparticle interface,* J. Phys. Chem. C **122,** 19116−19123 (2018)

[2] Carsten Sönnichsen: PhD Thesis, Ludwig Maximilian University, Munich, 2001

[3] Crut et al.: *Optical absorption and scattering spectroscopies of single nano-objects,* Chem. Soc. Rev. **43,** 3921 (2014)

# DEPOSITION OF $^{10}$B THIN FILMS FOR NOVEL NEUTRON DETECTORS

*N. Q. Khánh, L. Illés, P. Petrik, and J. Volk in collaboration with PuliSpace*

$^{10}$B and its compounds ($B_4C$, BN) have been widely used in thermal neutron detection via

$^{10}B(n, \alpha_0)^7Li$: $Q_0$=2.792 MeV

$^{10}B(n, \alpha_1\gamma)^7Li$: $Q_1$=2.310 MeV

reactions, owing to its very large capture cross-section for thermal neutron. When the reaction products ($\alpha$, $^7$Li) are used for neutron detection, single element $^{10}$B is better than its compound, because the particles do not scatter on other elements in compound on the way to detector, thus have higher energy, i.e. higher detection efficiency. However, being semimetal boron target is almost insulator at room temperature, which prevents stable plasma formation near target surface even in pulse DC system.

We have applied the built-in substrate Radio Frequency (RF) unit together with pulse DC input to ignite plasma at the beginning of deposition process, which can be switch off, when the target becomes hot enough, i.e. has sufficient electric conduction on its surface, thus ensuring the stable plasma in pulse DC mode alone. For comparison, the deposition rates of 35nm/h, 97nm/h, and 208 nm/h have been determined by Scanning Electron Microscope (SEM) for pulse DC, RF, and substrate RF ignited pulse DC depositions, respectively, where similar inputs (gas pressure, power) were set.

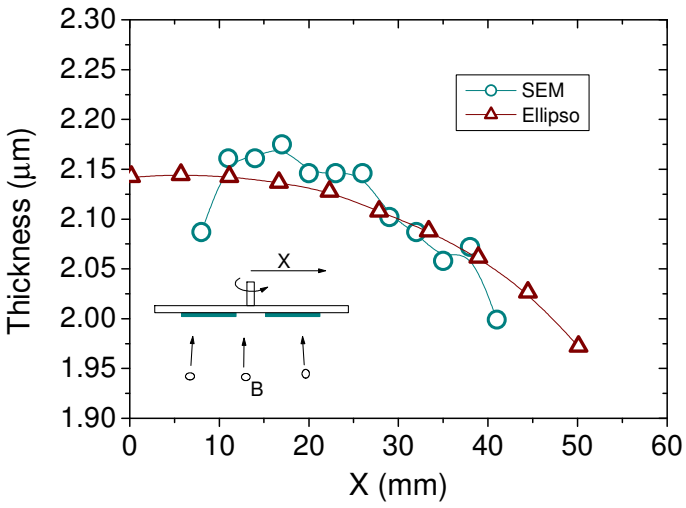


*Figure 1: Boron film thickness measured by Spectroscopic Ellipsometer (triangle) and SEM (circle) across control wafers.*

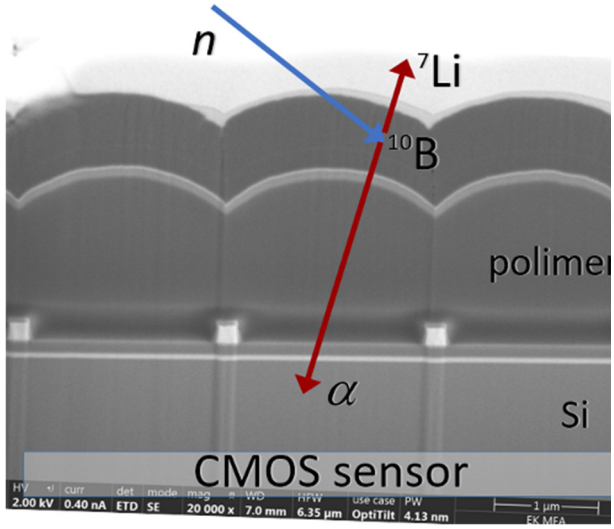


*Figure 2: Cross-section SEM image of CMOS sensor neutron sensitized with boron film. Sketch shows detection principle.*

Enabling pulse DC sputtering of boron target by this manner, the boron film with thickness of ca. 2 µm, i.e. the optimal thickness given by simulation can be deposited in reasonable time. The thickness of boron layer across the control Si substrate was determined by SEM and Spectroscopic Ellipsometer (Fig. 1). The thickness homogeneity over the sensing area is ca. 2.5%.

As an example, applying substrate RF ignited pulse DC sputtering of boron target, we managed to neutron-sensitize a small (10x10x35cm), light weight (0.4 kg) neutron counter developed by PuliSpace Ltd. Fig. 2 shows the cross-section SEM image of the neutron sensing head of the similar device we sensitized with 870 nm boron layer on top.

# VANADIUM-OXIDE BASED MEMRISTIVE SWITCHES

*OTKA K128534, Bolyai fellowship, ÚNKP postdoctoral fellowship*

*L. Pósa, T. N. Török, Gy. Molnár, Sadaf Arjmandabasi, J. Volk, in collaboration with A. Halbritter and Dept. of Physics, BME*

$VO_2$ resistive switches were fabricated by depositing Ti/Au electrodes onto $VO_2$ thin layer. Three different electrode designs were tested, whose geometries are shown in Fig. 1.a-c. The device operation is the same for all types: the $VO_2$ is switched only in a nanogap region, located between the metal electrodes. In the first two cases (Fig 1.a-b) nanogap is defined by electron beam lithography, whereas in the third case, a sub-5nm nanogap is formed subsequently by controlled electromigration of the nanowire. The best device performance was demonstrated by the second electrode design, where a sharp electrode faces with a flat one and the gap size is around 20-30 nm. The device could be switched between its two states more than $2 \cdot 10^5$ times with stable electrical parameters at room temperature. The typical I-V characteristic is shown in Fig. 1.d. Initially the device is in high resistance (OFF) state at zero bias voltage. By increasing the driving voltage, at a threshold bias voltage (set voltage, ≈1.06 V), the $VO_2$ at the nanogap region switches to the metallic state and the current jumps several orders of magnitude.

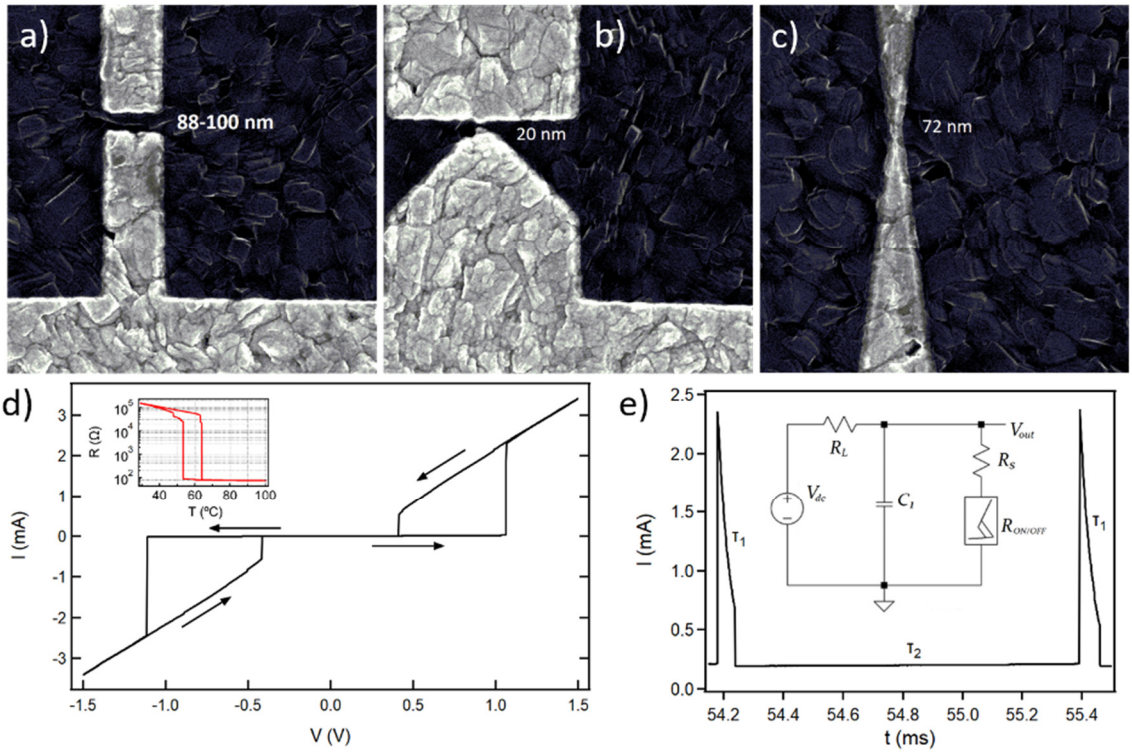


*Figure 1 a-c) SEM micrograph of the metal electrodes (light grey) on the surface of the $VO_2$ thin layer (dark grey). The three different structures mean three different gap size from 100nm to 5nm. d) A representative current-voltage (I-V) characteristic of the volatile $VO_2$ memristor. The arrows indicate the switching directions. The inset shows the resistance of the device versus temperature. e) Waveform of the current flowing through the $VO_2$ device in the oscillator circuit. The phase transitions occur during the sudden current jumps, while during the smooth current increase/decrease the capacitor is charging/discharging. The inset shows the circuit diagram of the oscillator.*

This low resistance (ON) state is preserved until the backward voltage sweep, when the device transforms back to its original high resistance state at the reset voltage level (≈ 0.41V). Due to the unipolar behaviour of the device, the same characteristic is seen at the negative bias polarity with the similar switching parameters. During the I-V measurement a serial resistance of 380 Ω was connected to the electrical circuit to protect the $VO_2$ device from the high current. This serial resistance is seen in the high voltage part of the I-V traces.

The temperature dependent electrical resistance trace of the device (inset of Fig. 1.d) exhibits very sharp phase transitions with larger resistance change than was measured during the layer optimization process. This finding may result from the very small size of the nanogap, it is comparable with the grain size. The first device structure with flat electrodes and 100 nm large gap worked only at elevated temperature (≈60 °C), close to the phase transition temperature, which may result from less efficient Joule-heating and a lower electric field. In case of the third design, we could form the sub-5nm large nanogap, however during the electrical switching the narrow electrodes were too unstable and we could not operate the memristor reproducibly.

Owing to the volatile hysteretic resistive switching behaviour of the $VO_2$ memristor, we can construct astable oscillator by connecting a parallel capacitor ($C_1$) and an external dc voltage source ($V_{dc}$) to the memristor through a load resistor ($R_L$) (Fig 1.e). The current flowing through the device is shown in Fig. 1.e, the state of memristor is periodically altered between the ON state (high current part) and OFF state (low current part). The characteristic time constants ($\tau_1$, $\tau_2$), which belongs to the charging and discharging of the capacitor can be tuned by the external electric elements. These oscillators could be used e.g. in the hardware realization of spiking neural network.

Besides the unipolar spikes, the action potential like signal can also be produced by constructing artificial neuron. The artificial neuron consists of two resistively coupled astable oscillators, each having a d.c. biased active memristor ($X_1$, $X_2$), a parallel capacitor ($C_1$, $C_2$), and a load resistor ($R_{L1}$, $R_{L2}$) (Fig. 2.a). According to the firing characteristic, the neurons can be a tonically or a phasically active neuron. In the former case the neuron fires evenly spaced spikes or burst of spikes when stimulated by a steady dc input. This firing behaviour is demonstrated by a tonic burst signal in Fig. 2.a. The phasically active neurons, on the contrary, fire only a single spike or burst of spikes at the onset of the steady dc input due to transient dynamics and remain quiescent afterwards as the input reaches the steady state. Fig. 2.b shows a rebound spike behaviour in a phasic $VO_2$ neuron. The basic parameters of the generated neural signal, such as period time, number of spikes per period, duration of a spike, voltage offset, etc., can be tuned by the electrical circuit elements (capacitances, resistances, voltage levels). The $VO_2$ arbitrary neurons are promising devices to construct highly efficient brain-machine interfaces.

We simulated the electrical circuit of the artificial neuron by MATLAB using Simulink environment. The $VO_2$ memristor was realized by a two-state switch with hysteresis, controlled by the potential difference between the nodes. The simulation enables us to set the proper resistance, capacitance and voltage values to get the desired output waveform. A simulated physically active neuron is seen in Fig. 2.d, whereas the time dependent energy consumption is shown in the inset. The energy needed to generate single, 40 µs long spike is around 8.2 nJ.

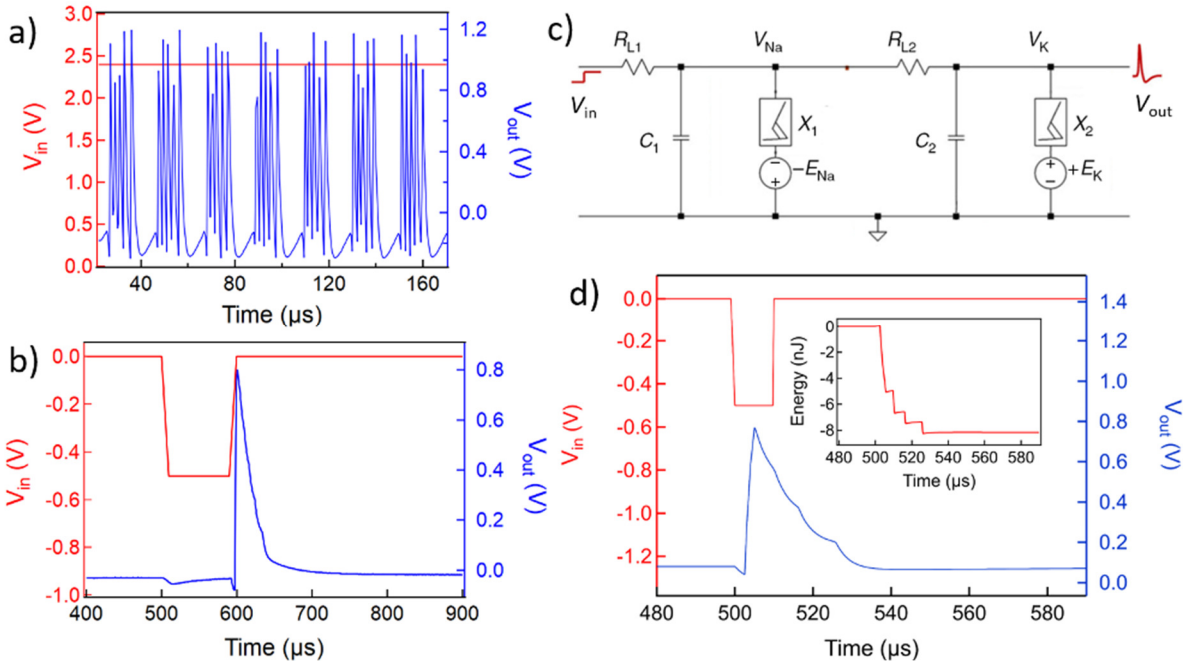


*Figure 2 a) Tonic bursting behaviour in response to the dc input voltage. b) Rebound spike behaviour: the neuron receives and then is released from an inhibitory, negative input, it fires a post-inhibitory (rebound) spike, in response to the release (the rise edge) of the inhibitory input waveform. c) The circuit diagram of the tonically active neuron, which produces the neuronal function, shown in panel a). d) Simulated physically active neuron using MATLAB Simulink software. The inset shows the time dependent energy consumption.*

# ALGAN/GAN HETEROSTRUCTURE BASED FORCE SENSOR

*P. Neumann, J. Radó, J. Ferencz, J. Volk*

GaN, as a piezoelectric wide-bandgap semiconductor, can play an important role in next generation micro- and nanoelectromechanical systems (MEMS, NEMS). It is electrically more resistant in harsh environment and against ionizing radiation than Si, which triggers new applications in space technology. Moreover, epitaxial thin films are already commercially available on Si wafer making it compatible with standard Si MEMS technology.

In this work a novel AlGaN/GaN heterostructure based 3D force sensor (2DEG force sensor) is proposed. The principle of operation is like that of its Si counterpart: a thin membrane is deformed upon applying a loading force on the Si micro-stick formed on the back-side of the membrane. Local strains in four positions of the membrane are measured by semiconductor gauges. By collecting the electrical signals both the magnitude and the direction of the force can be determined. However, in contrast to conventional Si piezoresistive devices, here mechanical strain influences the density of the 2-diementional electron-gas (2DEG) at the AlGaN/GaN interface by changing the magnitude of the discontinuity in the polarization vector between the two layers.

For a side-by-side comparison with our standard Si piezoresistive force sensor, we employed the same device geometry for the 2DEG force sensor. We used a commercial High-Electron Mobility Transistor (HEMT) epilayer stack (GaN(3 nm)/AlGaN (22 nm)/GaN (1,5 um)) grown onto a 4" Si wafer (NTT-AT). During the fabrication process we fabricated four voltage divider bridge circuits on the device side, each having a reference AlGaN/GaN resistors on the bulk and a sensitive one on the top of the membrane (Fig. 1.a). AlGaN/GaN resistors were formed by physical Ar etching from the top down to the semi-insulating GaN layer (mesa structure) and by a subsequent ohmic contact formation. The flexible membrane and the Si microstick are formed by a deep reactive etching (DRIE) step from the backside of the Si wafer. The schematics of the device geometry from both sides and the result of a finite element calculation (Comsol) are shown in Fig. 1.b and 1.c.

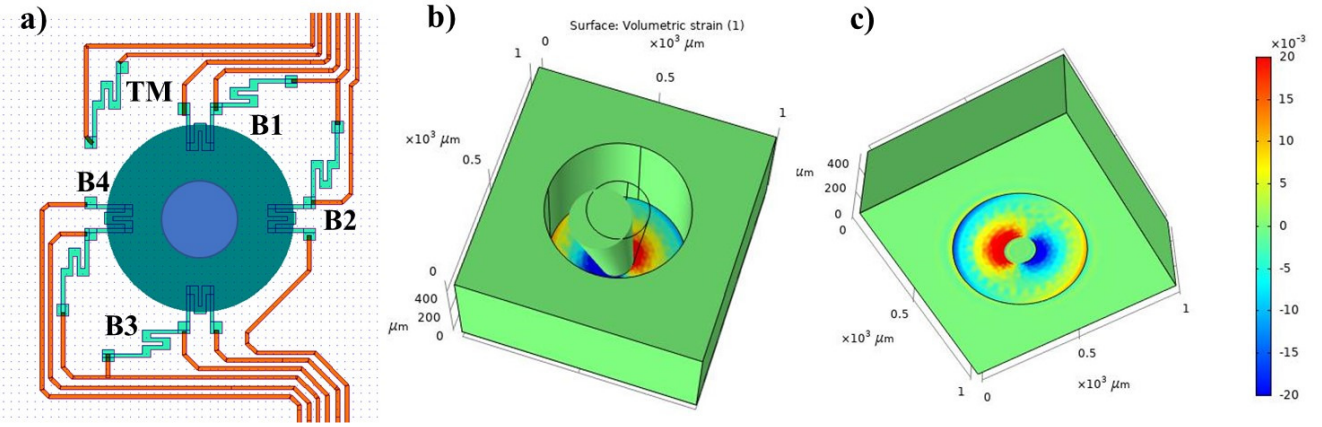


*Figure 1: a) Layout of the AlGaN force sensor from the epilayer side. Each B1-4 voltage divider bridge consists of a strain sensitive 2DEG resistor placed on the membrane (green area) and a reference meander on the bulk. Direction sensitive strain distribution occurs upon pressing the columnar Si stick (blue area). Volumetric strain distribution in the membrane calculated by finite element analysis shown from the backside (b) and from the device side (c) of the chip. By applying a load having lateral force component a significant asymmetric strain builds up in the membrane.*

The characterization of the device was started with a fracture strength test by pressing a sharp metal needle along perpendicularly against the flat top surface of the Si micro-stick. During the test the deflection of the tip position and the applied normal force (Andilog) were recorded (Fig. 2.a). As shown in Fig. 2.b all the tested GaN drumskin membranes had a linear force-displacement curve, the obtained spring constants and fracture strength are in the range of 4,2-5,3 mN/µm and 35-50 mN.

In the next step, the sensitivity of the force sensor on normal force load was investigated. We applied a constant bias of 1V on each bridge and measured the voltage signal between the 2DEG resistors using a matrix switch module (NI PXI). For a better visualization, at the beginning of the measurement a reference voltage was taken for each bridge and only the change as a function of time upon increasing load pulses is shown in Fig. 2.c. The recorded voltage signals gave a fast response (<0.2 s) on the applied load and found to be proportional on that. The relatively high difference in the sensitivity of the bridges can be attributed to the asymmetric device geometry caused by the non-ideal setting of the DRIE system. The 3D loading test of the 2DEG force sensor is still in progress and we also plan to repeat the experiments in the current saturation regime where a higher sensitivity is expected.

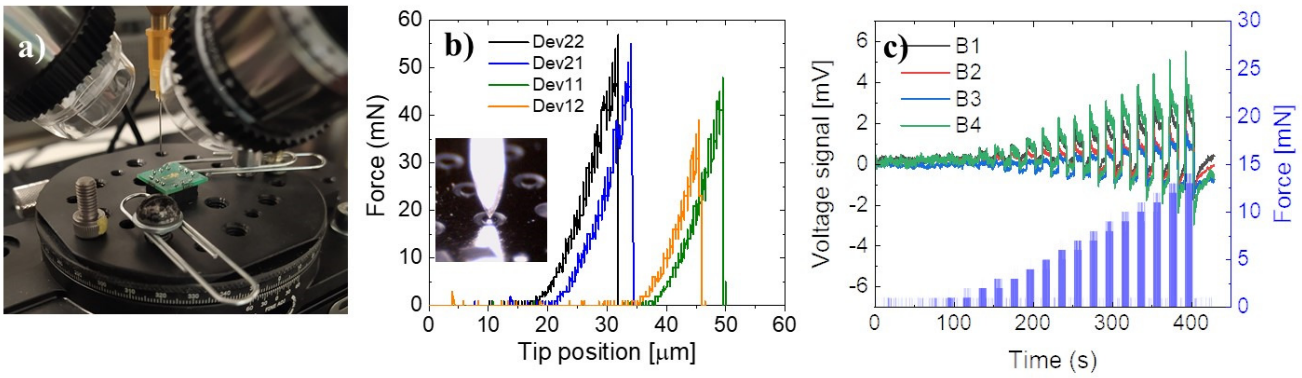


*Figure 2: a) Force sensor testing set-up with the bonded chip (green), perpendicular loading needle mounted on a force gauge (not shown), and USB cameras. b) Force-displacement curves of fracture tests of four devices. Fracture occurs in the range of 35-50 mN. Inset: USB camera image of the needle tip in contact with the force sensor. c) Voltage signals (left axis) of the measuring bridges upon increasing loading force pulses (right axis)*

The 3D loading test of the 2DEG force sensor is still in progress. We also plan to repeat the experiments in the current saturation regime where a higher sensitivity is expected.

# MIDDLE EAR MEMS DETECTORS FOR FULLY IMPLANTABLE COCHLEAR IMPLANTS

*J. Radó, Á. Dacher, Z. Pusztai, J. Volk in collaboration with PTE and SE*

Fully implantable cochlear implants could offer several advantages for patients suffering severe hearing loss. However, the miniaturization, complexity as well as self-powering, signal processing and cochlear multielectrode system are required for such a fully implantable device. Correspondingly, these requirements are to be fulfilled in order to eliminate the use of external unit, i.e. microphone, sound processor, transmitter and battery, which are used in conventional semi-implantable hearing aids. In this work, instead of the direct detection of the sound (microphone), we demonstrate an accelerometer array, which could be mounted on one of the vibration transmitting bones, like anvil (incus), in the middle ear. To reduce the sensor dimensions, the accelerometer array is made with a multi-electrode structure. As a result, more than one frequency can be identified with a single spiral using a simple truth-table based on the phases of the signals (Fig. 1).

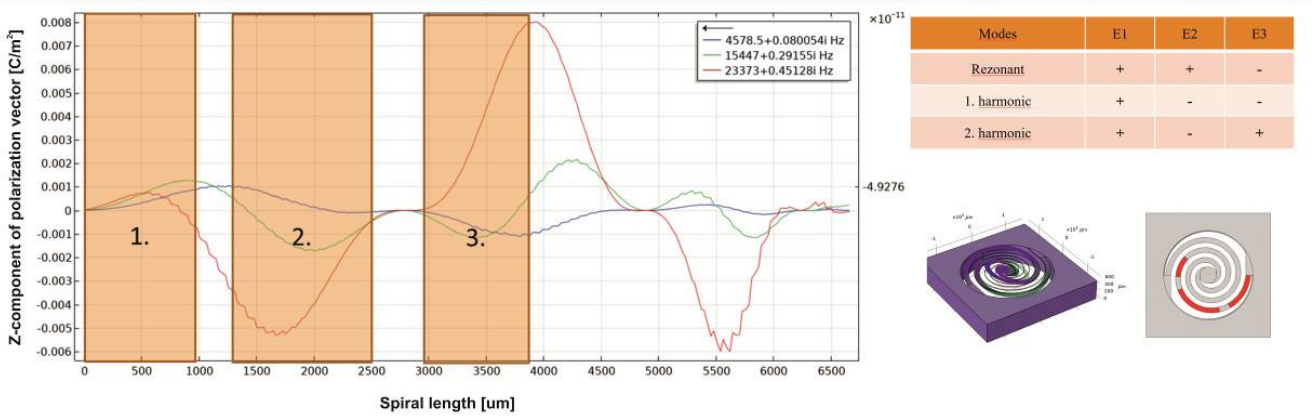


*Figure 1: Z component of the polarization vector along the spiral length (on the left), the truth-table (on the top-right) contained the momentary sign of the signals and the FEM model (on the bottom-right) in which the red bars indicate the position of the electrodes. Every image refers to the same spiral.*

As the dimension and the location of the electrodes are crucial issues for the appropriate operation of the sensor, in 2021 we redesigned the multi-electrode structure based on Comsol Multiphysics FEM calculations. The simulation models were tuned with the results of vibration measurements using a SmarAct PicoScale vibrometer.

***Having*** designed the new layout of the electrode structure, the sensor was fabricated in our cleanroom applying conventional MEMS technology steps (Figure 2). As a continuation of the topic, this year we will validate functionality of the new design with measurements using our vibrometer and minishaker setups.

In parallel, we also started the preliminary animal experimentations in collaboration with University of Pécs Medical School and Semmelweis University. The main goals of the experiments were to practice the implantation process to a mouse cochlea using a 3-contacts cochlear electrode provided by MED-EL Corporation and to test the stimulator electronics and the Auditory Brainstem Response (ABR) measurement system (Fig. 3). In order to reduce ambient noise contamination of the stimulus, we developed an electrically independent stimulator circuit. To ensure synchronization between the stimulus and the ABR signals, the stimulator receives only a trigger signal from the ABR equipment via optical cable. The stimulator generates biphasic nerve-like stimulus to avoid nerve fatigue. The ABR system receives the mouse brain response through a pre-amplifier and records averaged data, repeating the stimulation 800 times. During the data analysis we found that the 1.5V stimulus overrode the ABR pre-amplifier, so the low-level brain signals, which are in the nanovolt range, could not be retrieved from the recorded data. This year, we need to redesign our stimulator so that upon every stimulus onset the recording amplifier is blanked for a few microseconds [1-2].

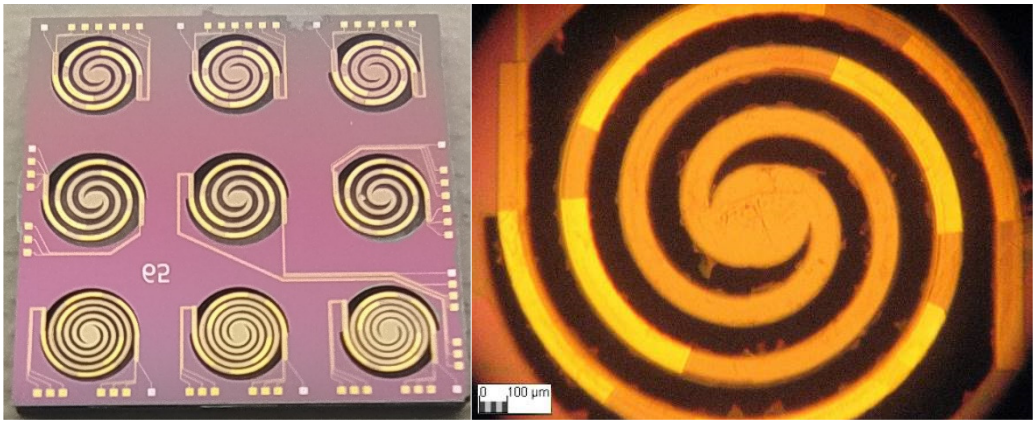


*Figure 2: The completed device with nine single spirals geometrically tuned to different resonant frequencies and harmonics (on the left) and a close view of the central spiral (on the right). The yellow bars indicate the realized gold top electrodes*

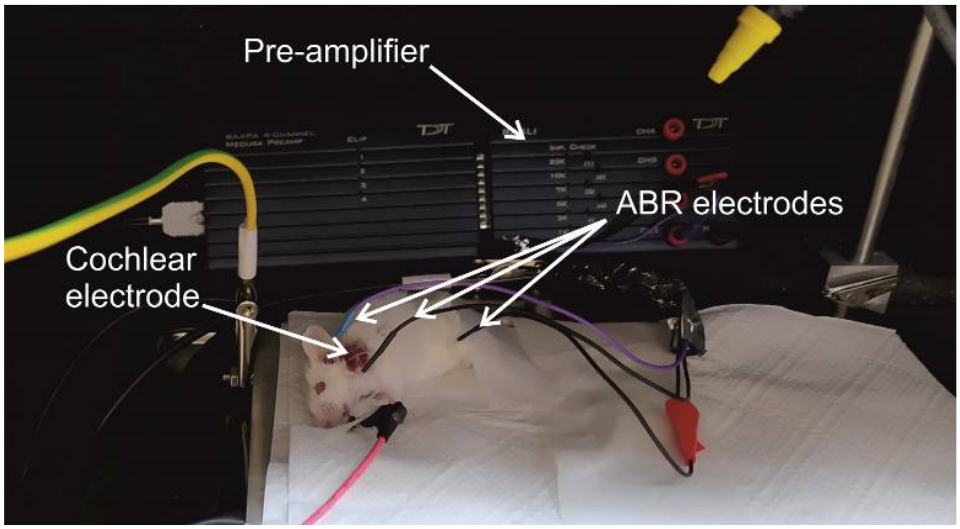


*Figure 3: ABR measurement arrangement. The electrode implantation to the cochlea was carried out under stereomicroscope on an operating table located next to the ABR system. The operating physician was Péter Révész from University of Pécs.*

## *Related publications*

[1] Á. Dacher: *Characterization of piezoelectric cantilevers,* BSc Thesis

[2] Z. Pusztai: *Középfülbe ültethető piezoelektormos MEMS spirálok minősítése (Characterization of piezoelectric MEMS spirals for implantation in the middle ear),* MSc Thesis

# A NOVEL FORCE SENSOR-BASED MEASUREMENT SYSTEM FOR ABNORMAL ROAD SURFACE DETECTION

***NVKP_16-1-2016-0018 "KoFAH"***

*J. Radó, A. Nagy, J. Volk in collaboration with ELTE and SzTAKI*

Besides tire pressure monitoring, intelligent tires can be exploited to analyze tire/road interactions, wheel loading, tread wear, and they can support automotive vehicle applications. In this study we develop a measurement system for intelligent tires including a novel piezoresistive force sensor. In order to protect the sensor from the outer harsh environment and obtain the highest response signals, the inner sidewall was chosen as the embedding location. Based on our previous experience the greatest deformation within the sidewall occurs near the tread, as a result, the sensor was glued there (Fig. 1). To retrieve the data from the sensor built into the inner sidewall of the tire, we developed a readout electronics capable of driving the voltage bridges with 2.5V, conditioning the signals, and transmitting the data wirelessly. The readout electronics was powered by LiPo battery that can be charged from outside the tire with a commercially available RF charging coil. Both electronics and the RF coil were fixed to the tread as a less compliant area of the tire.

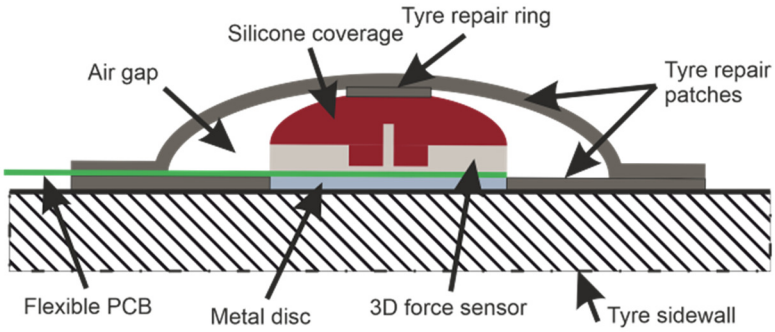


*Figure 1: Schematic of the embedding process. Due to the air gap, the sidewall deformation of the tire can be transmitted to the joystick through the tire repair ring and the flexible silicone coverage*

In order to carry out the dynamic experiments, two test tires were mounted on a Nissan Leaf provided by Institute for Computer Science and Control (SZTAKI). The external receiver electronics were placed in the engine bay of the car as close as possible to the tires to ensure the continuous signal transmission (Fig. 2.). The received signals were transformed according to the CAN BUS protocol of the vehicle for on-board computer processing and data recording. The CAN transformation ensures the synchrony between the tire sensor signals and the other dynamics data, such as accelerations, speed, angular momentum and GPS coordinates.

For the final test, two different, well-separable road surfaces were chosen in Budapest. One, the so-called "normal" surface, was a newly paved, perfect asphalt pavement, while the other, "abnormal" surface, was an old, poor quality concrete road with potholes. We passed through both pavements many times and recorded the signals of the tire sensors along with other dynamic data from the CAN BUS.

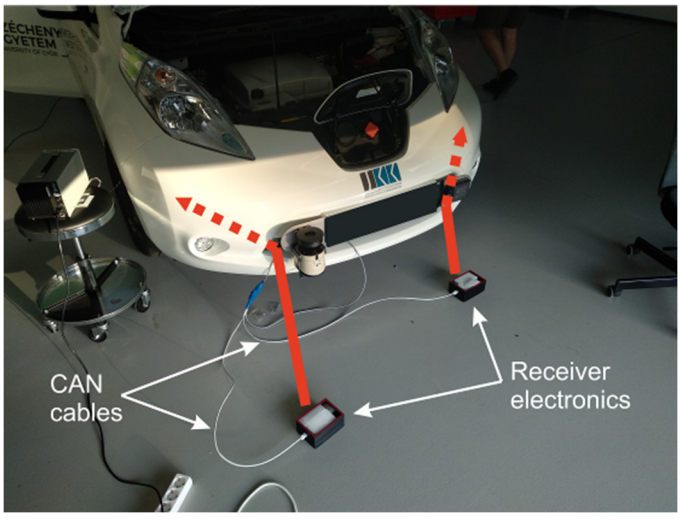


*Figure 2: Off-tire receiver and data conversion electronics. The PCBs were placed in a 3D printed box to protect them from the harsh environment. The red arrows indicate the final position of the electronics*

The output of the sensor was segmented into tire revolution cycles, which were then transformed to a subspace spanned by adaptive Hermite functions. The underlying idea behind this step is to emphasize relevant features of the data which capture the dynamics of the tires. We developed two abnormality detection methods relying on this signal representation. In the first case, the parameters of the applied adaptive transformation were optimized for each sensor output segment separately. The acquired representations were then classified to be normal or abnormal based on an analytic, statistical approach. In the second case, we optimized the parameters of the transformation and the weights of the underlying classifier simultaneously with the help a model driven neural network architecture referred to as a variable projection network (Fig. 3.). Experiments using measurements acquired from the public roads of Budapest show an abnormality detection accuracy of over 97%.

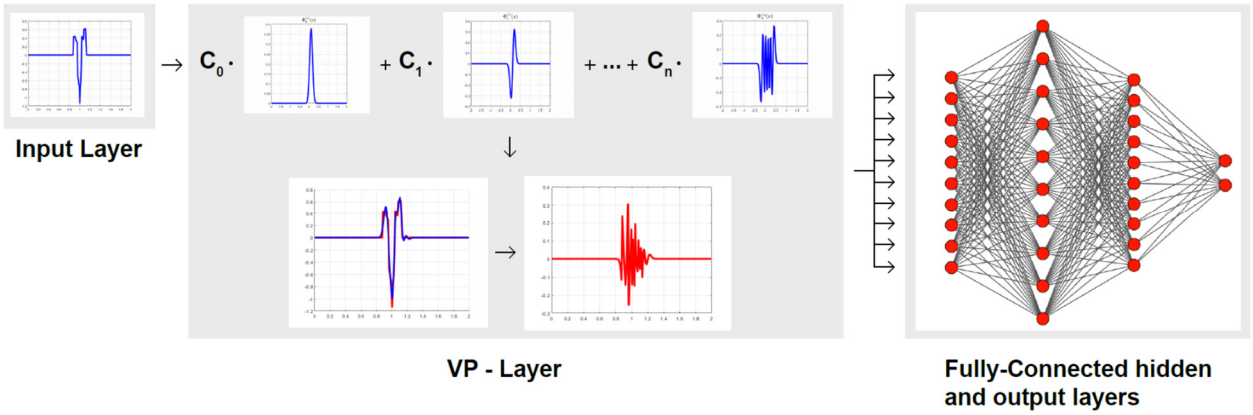


*Figure 3: Variable Projection Network (VPNET) architecture. The first layer implements a variable projection operator (in our case an adaptive Hermite function based residual transformation). The output of this layer is then passed to a neural network. The parameters of the transformation implemented by the variable projection layer are thus trained together with the weights of the underlying classifier.*

# LOW POWER CONSUMPTION-TYPE NANO-SENSORS FOR GAS DETECTION IN HARSH ENVIRONMENT

## *Hungarian-Russian Collaborative Research Program 2017-2.3.4-TéT-RU-2017-00006*

*F. Bíró, I. Bársony, Cs. Dücső*

The ultimate goal of the project is to develop a novel calorimetric gas sensor family what is able to detect $CH_4$, $NH_3$ and CO up to their Lower Explosion Limits (LEL), i.e. 5, 15 and 12,5 %, respectively. The sensors can be operated in harsh environment without any risk of ignition even over LEL concentrations. Apart from the optical and electrochemical approaches and the corresponding systems, there are two viable solutions, both exploit temperature changes and read-out by:

- measuring the temperatures of a heated catalyst surface and a passive reference,
- measuring the temperatures of a filament exposed to gas environment and a perfectly sealed reference heater.

Although the catalytic device is expected to detect lower gas concentration and exhibit better sensitivity, the second, heat-conductivity type device is simpler and still in use in practice. A more sophisticated device applies both sensors, thereby extending the detection range and improves the detection reliability. Another advantage is the commonly used filament or micro-hotplate structure. Therefore, to develop a micro-hotplate meets all the mechanical, electrical and chemical requirements is essential for a reliable and commercialized device.

The basis of the sensor is a newly developed small diameter (150μm) micro-hotplate exhibiting ±1% temperature uniformity on the heated area below 550°C. The stability of the heater is 5000 hours at least at the operation temperature of 530°C, thereby in pulsed mode operation ca. 5 years operation can be achieved. The power dissipation at 500°C is 27mW/1.5V, so the chip can be utilized in portable or wearable devices for personal safety. [1] An alternative, suspended crystalline-Si microheater was also developed to form and test the miniaturised conventional bead-type pellistor.

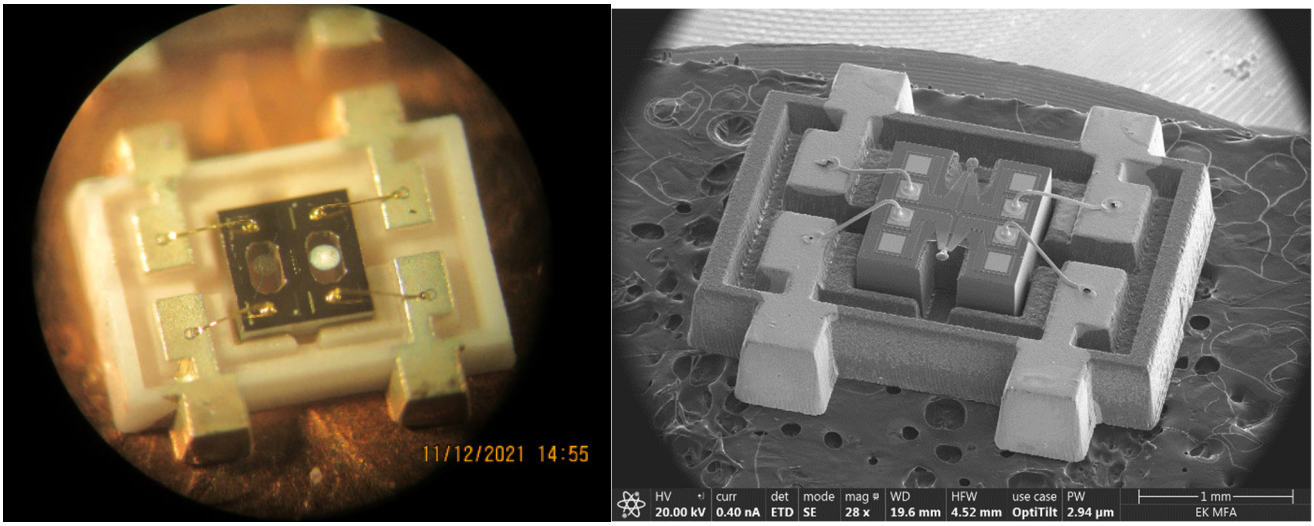


*Figure 1: Gas sensor chips in laser micromilled ceramic headers. Catalyst (black on the optical image) and reference suspensions (white) dropped on hotplates (a) and c-Si filaments (b). The artificially coloured inset shows the shape of the micro-bead. The size of both chips is 1x1 mm².*

The other key element of the development is the Surface Mounted Device (SMD) compatible mechanical encapsulation. The ceramic elements were jointly designed followed by laser milling fabrication at the Russian partner. The catalytic sensors measure the heat generated by the controlled catalytic combustion of the burning/explosive gases. In order to avoid false thermal signals caused by temperature variation, flow and compositional changes (e.g. humidity) of the ambient the sensor consists of two identical heaters; one is covered with chemically active catalyst, whereas the other has a passive cover and serves as a reference (Fig. 1). Although the stability of all the catalysts have been investigated need to be improved to consider them in commercial devices the dynamics of the sensor chips enables the pulsed mode operation (Fig. 2).

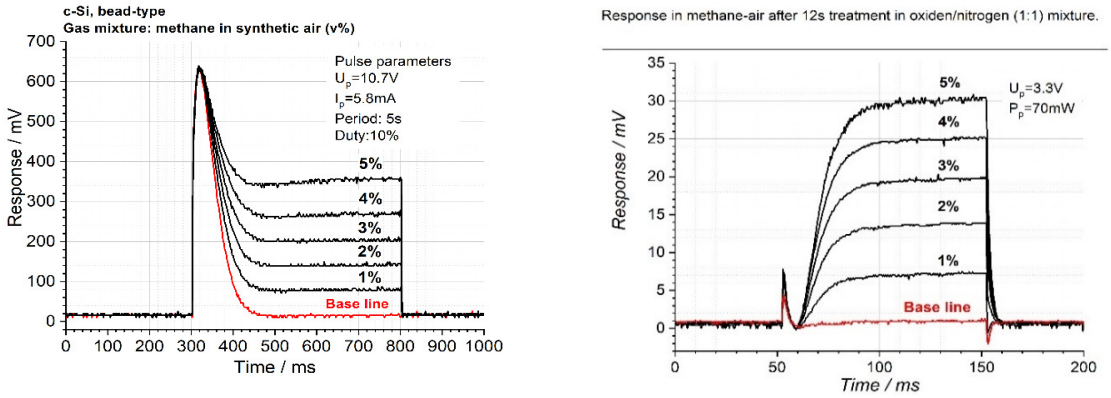


*Figure 2: Responses of freshly prepared pellistors in pulsed mode operation for LEL 20-100% of $CH_4$. The origin of the first peaks is the difference of the heating-up speed of the two elements (active, passive). The bead-type pellistor formed on c-Si microfilament provides stable response after 200ms (left). Reliable signal of the thin film-ALD catalyst covered hotplate is given after 50ms. (right). Apart from the better dynamics the first small peak also indicates the better control of the processing technology.*

In the follow-up activity we plan to elaborate the appropriate material composition of the thin film catalyst to achieve the necessary sensor lifetime required by any commercial device. We hope to build a reliable earth gas sensor with combining the already proven (report 2020) heat conductivity device and this thermocatalytic sensor. Having in hand the **stable heaters** we now focus on other applications.

## *Related publication*

[1] F. Bíró, A. Deák, C. Dücső, Z. Hajnal: *Microheater with uniform surface temperature,* Utility model: U 20 001150, registration number 5279

# DESIGN AND DEVELOPMENT OF A 3D FLEX-TO-RIGID COMPATIBLE FORCE SENSOR

## *H2020-ECSEL-2017-2-783132 "POSITION-II - A pilot line for the next generation of smart catheters and implants", 2018-2.1.6-NEMZ-ECSEL-2018-00001*

*J. Radó, L. Illés, P. Fürjes, Cs. Dücső*

The main objective of the POSITION-II project is the realization of a pilot line for the fabrication of the next generation of smart medical instruments. This second generation of smart medical instruments offers improved performance through better sensors and transducers combined with an improved manufacturability and lower cost. The task of our research group is to develop and demonstrate the applicability of a capacitive force sensor integrable in the tip of an electrophysiological catheter.

The goal of our task was to develop a force sensor structure we can built in the tip head of a catheter. Due to the required function the sensor must have minimum 3 sensing elements. In the first two years we have developed alternative force sensor structures and characterized them in terms of their sensitivity and capability to resolve the loading force components. As described before the best structure utilizes the Philips' CMUT-type surface micromachined capacitor elements arranged in concentric 6 segmented blocks. We also investigated the appropriate coating material and its geometry to get the best force conveying performance. Finally a hemisphere bumpers were formed by moulding the elastomer to cover the capacitor array, then individually glued on the surface. The sensor responses could be dramatically improves if a thin hard coting layer was applied on the elastomer (Fig. 1.).

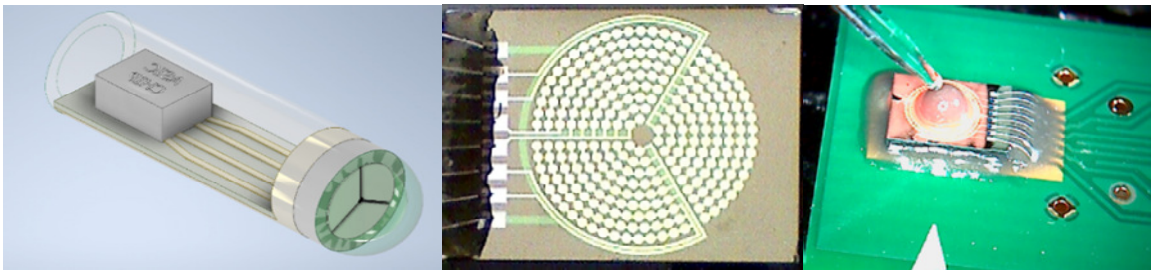

*Figure 1: Concept of the tip head force sensor in the catheter (left). The layout of the six capacitor blocks of the chip contain 42 (inner) and 48 (outer) micromachined capacitances and is covered with force transferring biocompatible elastomer. The chip before encapsulation (middle) and after assembled in the tester (right). The controlled load is applied via a 250µm diameter glass pin.*

In the previous year we determined the sensitivity and demonstrated the 3D resolving functionality by loading the sensor at the centre point from 33 different directions and uniformly increasing the force from 0 N to 500 mN in each case (Fig. 2.). In order to retrieve the loading force and also obtain the load/contact point from the collected data, we applied a deep feed-forward neural network. The neural network consisted 1 input layer, 3 hidden layers and 1 output layer containing different number of neurons. The number of the hidden layers and the neurons were optimized for the force sensor by comparing the root-mean-square errors of each construction. The input and the output layers were determined by the system. The response signals of the six segments provided the six inputs, whereas the three components of the force and the coordinates of the contact point could be obtained as outputs. For training the network, a Levenberg-Marquardt algorithm based back-propagation learning method was employed by using the build-in train function of MATLAB. According to the routine procedure, we split the measurement data into three subsets. The first subset containing 70% of data was the training set, and the remaining 15%-15% of data were used in validation and for testing, respectively.

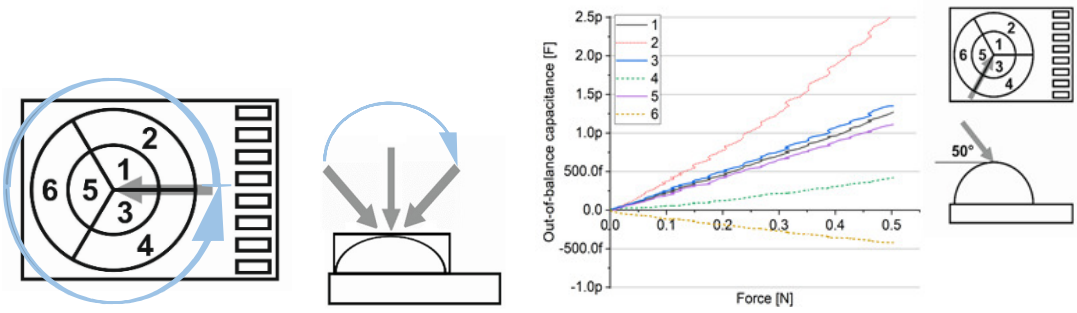


*Figure 2: Representation of the loading directions and the typical responses of the six elements (right).*

In order to examine the contribution of the segments (capacitor blocks) of the outer and the inner rings to the network performance, we made different calculations with different number of network inputs. The network performance was very good for the response signals of the six segments as well as for the three segments of the outer ring. However, the prediction of $F_x$ and $F_y$ components was poor when based on the signals of the inner three segments only. In Fig. 3 the significantly better

performance of the outer 3 elements for the $F_x$ and $F_y$ (tangential) components is clearly seen, as the predicted and calculated values can't be distinguished.

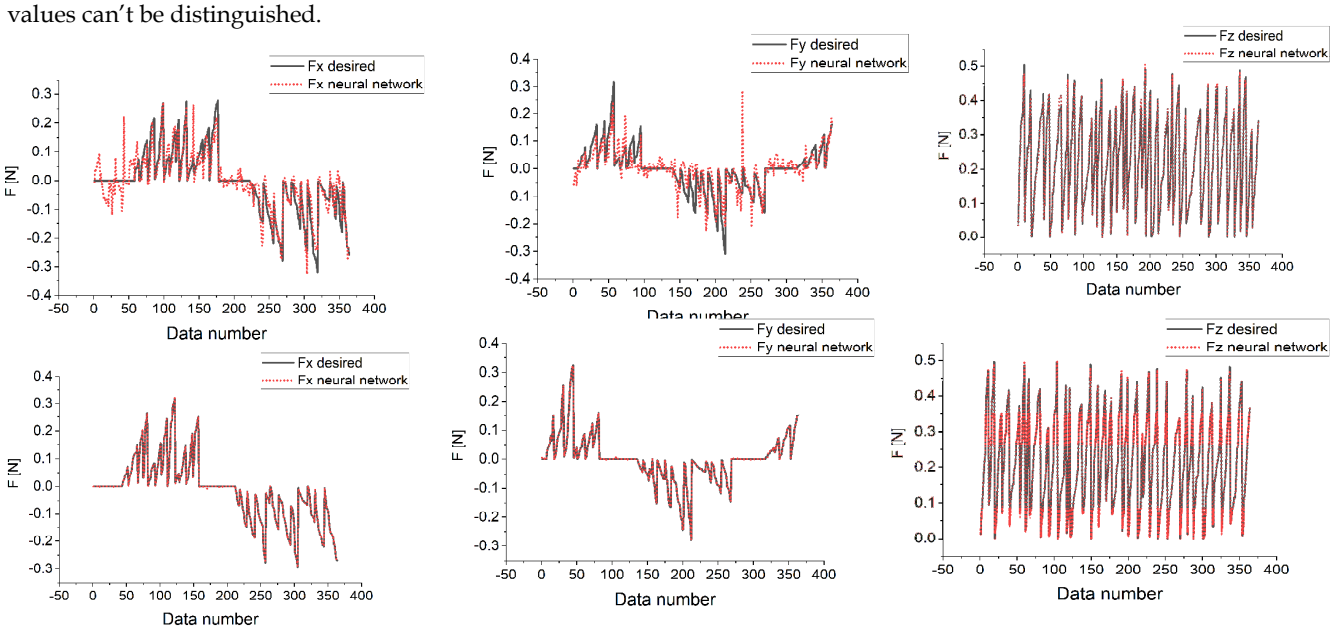


*Figure 3: Estimation of the force components based on response signals of (top row) the inner segments and (bottom row) the outer segments*

Having got an impressive direction dependence in the responses and considering that we have six signals, we also tested whether we can also retrieve the point of application as an additional extra. Parallel with the determination the force vectors, the network performance was also satisfactory in retrieving the position of their contact points. In this case, the RMSE values along the x- and the y-axes were 0.48 and 0.63, respectively. These levels of errors mean that the network estimates the position of the contact points in both directions much more accurately than the characteristic distance between the two neighbouring points we measured for training.

The feasibility of the sensor integration in the catheter tip was demonstrated by the circular shape and the F2R (flex to rigid) compatible processing. The concentric double ring arrangement, and the need for three signals offer the possibility to further reduce the diameter of the circular chip. We have proven the functionality of the 1.6mm diameter chip, but we think that with appropriate design of the chip (i.e. introduction of TSV (through silicon via)) and the electronics, further reduction to 1.2-1.5mm size is also feasible. The sensor sensitivity is in the range of 1-500mN. Training a NN the system can provide accurate and quick information on the contact force.

# POLYMER BASED AUTONOMOUS MICROFLUIDIC SYSTEMS FOR MEDICAL DIAGNOSTICS

## *(Partners: Semmelweis University, Budapest University of Technology and Economics, Aedus Space Ltd.) R&D contract (as subcontractor of 77 Elektronika Ltd.)*

*A. Bányai, P. Hermann, Zs. B. Sík, O. Hakkel, P. Fürjes*

Precise and fast Point of Care (PoC) monitoring of marker molecules or bacteria levels in body fluids or cell culture media could be crucial in effective diagnostics and choosing therapies. Due to the specific tools and novel microtechnology processes the cost-effective, complex but miniaturised analytical systems, such as Lab-on-a-Chip (LoC) and microfluidic devices have become available and applicable for implementing the overall sample analysis from the preparation to the molecular detection. The microfluidic system has to transport the sample and the washing buffer to the active area of the chip meanwhile mix and incubate the sample with the reagents. As the incubation and read-out needs a specified time, precise sample handling and flow control are crucial. The perspective of our work is to develop a polymer based microfluidic cartridge suitable to autonomously controlled sample transport or preparation for integrated bioanalytical device.

To define precise sample flow rates in the microfluidic systems adequate surface modification and macro and microscale structuring of the geometry are crucial. The COP (cyclic-olefin-polymer) material were chosen and modified by specific surface treatment methods, as oxygen plasma treatment, Ar plasma induced polymerisation of Pluronic F127 and PEGMA (Poly(ethylene glycol) methacrylate) layers, dip-coating of BSA (Bovine Serum Albumin). Accordingly the applicability of different surface modification methods were analysed with special consideration of the long term stability of the surface properties as contact angle, roughness, non-specific binding of biomolecules and labelling nanoparticles. The modified surfaces were characterised by surface contact angle measurements, **FTIR (Fourier Transform Infrared Spectroscopy)**, AFM (Atomic Force Microscopy), spectro-ellipsometry. Fig. 1 demonstrates the chemical change of the $O_2$ plasma treated substrates during 12 months' storage: the intensity of the characteristic peaks of hydroxyl groups and carbon-dioxyde molecules indicates the contamination of the surface which is much more moderated in case of low temperature storage with water absorbent.

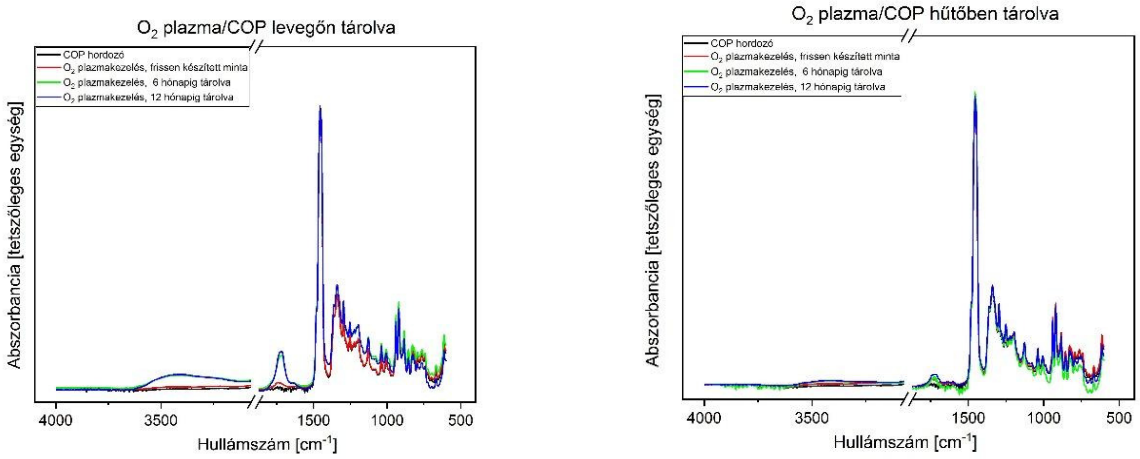


*Figure 1: The ATR FTIR spectra of the uncoated and the $O_2$ plasma treated COP substrates stored at air athmosphere (left) and at 4°C (right) – as prepared and after 6 or 12 months.*

In a previous project (Multiparametric Point of Care development of in vitro diagnostic systems) an autonomous microfluidic system was designed and manufactured for transporting blood or plasma by precisely controlled sample rate. These autonomous sample transport systems were integrated into Point-of-Care Lab-on-a-Chip based diagnostic devices. The developed systems are to be applied for detection cardiovascular diseases in cooperation with 77 Elektronika Ltd. Based on these results we are continuously developing the microfluidics based **Lab-on-a-Chip device** for the specific cardiovascular diagnostic panel. In the actual period the geometry of the microfluidic systems was finalised according to the additional requirements of the optical detection method and the real sample. To step forward the industrial polymer manufacturing technology the injection moulding technology was tested as promising manufacturing solution. The Microsystems Lab developed 3D silicon dry etching technology applicable for structuring mould master for the injection moulding elaborated by Z-Microsystems GmbH. The parameter set for the cryo type deep reactive ion etching was optimised to achieve adequate geometry profiles (Fig. 2.) of the silicon master.

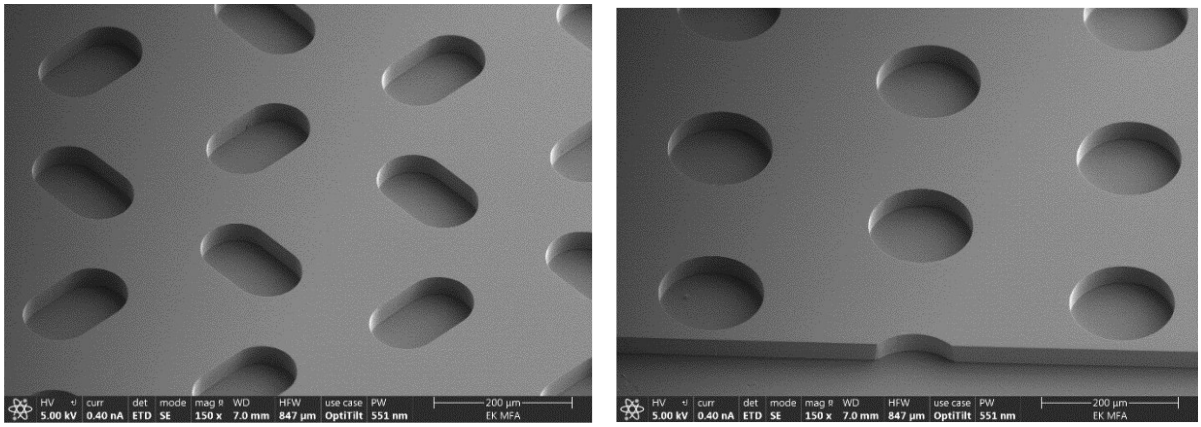


*Figure 2: 3D silicon moulding master fabricated by cryo type deep reactive ion etching for injection moulding of polymer microfluidic cartridges.*

# MICROFLUIDIC SAMPLE PREPARATION SYSTEM FOR RAPID URINE BACTERIA ANALYSIS

## *VEKOP-2.2.1-16-2017-00001 – "Versenyképességi és Kiválósági Együttműködések - Gyors húgyúti baktérium elemző mérőkészülék fejlesztése (Rapid urine bacteria analyzer)"*

*A. Bányai, P. Hermann, Zs. B. Sik, E. L. Tóth, O. Hakkel, P. Fürjes*

In this finished project the main goal was to develop a **single-channel microfluidic cartridge** for certain subtasks of **sample preparation and handling**, which then can be integrated into a measuring instrument. During the optical measurements of bioanalytical tests, the sample handling is solved in an integrated Lab-on-a-Chip cartridge. The cartridge includes transport and filtration of the liquid sample, positioning of bacteria in the detection chamber over the sensing layer, and a microfluidic component for storage of used sample. Accordingly, we focused our attention to develop a **hydrodynamic unit** that is capable of filtering larger elements (>6um) in **urine samples** and positioning permeated bacteria laterally. In order to achieve this goal, we designed and characterized such units. Simultaneously, single-channel cuvettes were made to test the optical system with the sample solution. For the proper passive operation of such device, a bubble-free channel upload had to be provided, by taking account the appropriate setting of the surface properties of the structural materials, and making a special design of the fluidic microstructure. The microfluidic channel was developed by soft lithographic method in PDMS (polydimethylsiloxane) polymer and the raw material was further modified by PDMS-b-PEO copolymer molecules, to ensure the hydrophilic properties of the walls.

For the dielectrophoretic concentration of bacteria, metallization technology was used to develop a high-resolution electrode network on COP polymer film with the thickness of 100 µm. To manage the autofocus function for image processing system, the electrode design were further equipped with an additional pattern. The manufactured microfluidic compartments and COP foils the containing high-resolution gold electrodes were handed over to project partners (77 Elektronika Kft. and SZBK) for further measurements.

Hydrodynamic principle based microfluidic filters and lateral concentrating structures were developed and evaluated by their filtration efficiency for different particle sizes; and by the target loss ratio in the size range of bacteria. After filtering every larger component of the urine sample, the permeated bacteria must be vertically and possibly laterally focused in the detection chamber in order to achieve high trapping efficiency on the functionalized surface. The inertial focusing phenomenon was investigated, which can be used as a passive method for sample preparation and target manipulation in case of particulate suspensions. Asymmetric channel geometry was designed to apply additional inertial forces besides lift forces to promote laterally ordered particles to achieve sheathless focusing or size dependent sorting. The lateral focusing was achieved by a hydrodynamic method and the efficiency of the hydrodynamic focusing depends mainly on the characteristics of the fluidic system and on the particle to channel size ratio. The position of the particle within the flow profile is determined by forces acting on the particle in the fluidic system. The focusing was carried out in an asymmetric microfluidic system with alternating geometric parameters. The evolving hydrodynamic forces were tailored with altered channel parameters (width and height), and different flow rates, to get a better understanding of smaller beads' lateral migration. The behaviour of the microfluidic system were tested by using artificial fluorescent beads with different sizes (diameter of 15.8 µm – 6.08 µm – 1.97 µm beads) and Green Fluorescent Polymer (GFP)-labelled E. coli also. These particles were used to distinguish the focusing position in continuous flow (Fig. 1.), and experimental results were compared to in-silico models for particle movement prediction, made in COMSOL Multiphysics (Fig. 1.). The focusing behaviour of the applied microfluidic system was mainly characterised for particles size in the range close to blood cells and bacterias.

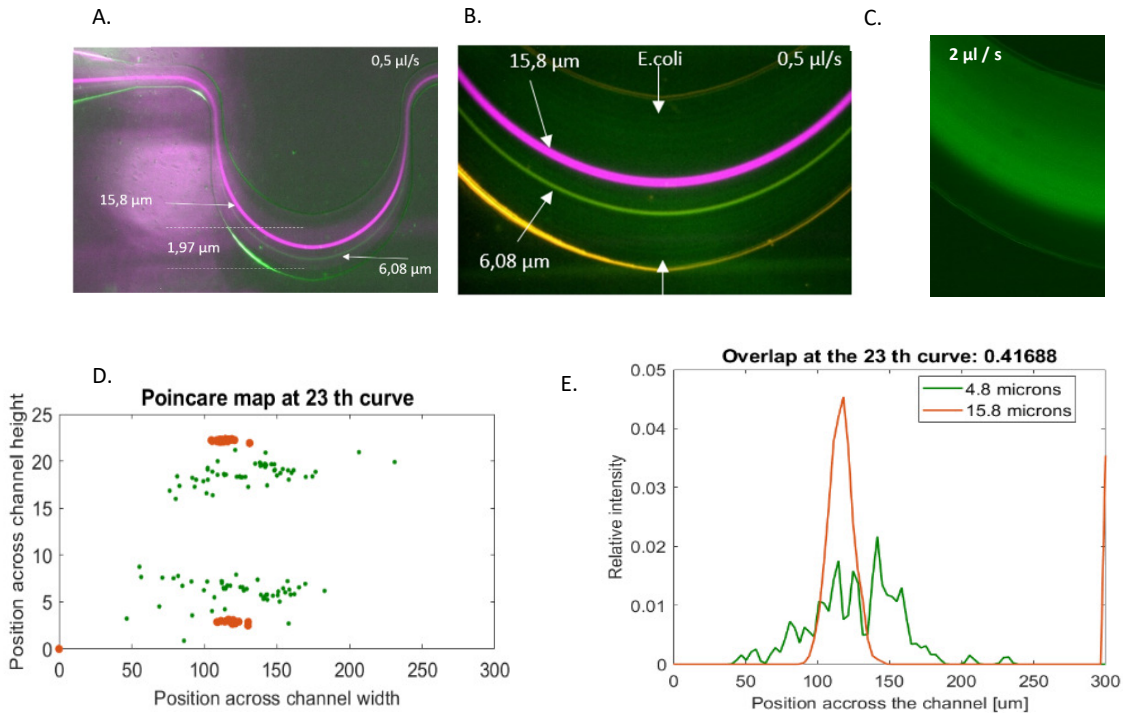


*Figure 1: Lateral focusing of 15.8 and 6.08 µm beads at 0.5 µl/s flow rate and concentration of 1.97 µm beads at the end of the lateral focusing unit (A). E.coli could not be focused in the very same structure (B.), although could be concentrated at decreased channel height (15 µm) and increased flow rate (2 µl/s) (C.). Computational data with the cross sectional distribution of the beads in the channel height (D.) and the lateral distribution of the beads (E.)*

Computational Fluid Dynamics (CFD) simulation was also performed using COMSOL Multiphysics (version 5.3a) to analyse and predict particle movement in the specially designed microchannels. Finite Element Modelling (FEM) is applied to numerically calculate the Navier-Stokes equation considering laminar flow due to the low Reynolds number regime. Particle tracing module was used to calculate particle trajectories in the pre-solved velocity field using spherical particles with two different diameters and properties set to be in correspondence with fluorescently labelled polystyrene beads applied in experimental validation (density: 1055 kg/m3, diameter: 4.8 µm, 15.8 µm). In Fig. 1.C-D the Poincare map represents the calculated positions of the particles at the outer surface of the microfluidic systems, and the lateral distribution function comparable to the fluorescent intensity measurements [1-2].

## *Related publications*

[1] Innováció a labordiagnosztikában, Innotéka, 2021. április, https://www.innoteka.hu/cikk/innovacio_a_labordiagnosztikaban.2239.html

[2] D. Petrovszki, S. Valkai, E. Gora, M. Tanner, A. Bányai, P. Fürjes, A. Dér: *An integrated electro-optical biosensor system for rapid, low-cost detection of bacteria,* Microelectronic Engineering **239,** 111523, 9 p. (2021)

# HIERARCHICALLY COMBINED PERIODIC SERS ACTIVE 3D MICRO- AND NANOSTRUCTURES

*R. Öcsi, Zs. Zolnai, I. Rigó (Wigner FKK), M. Veres (Wigner FKK), O. Hakkel, P. Fürjes*

Raman spectroscopy is finding many applications in biology, life sciences and other areas. Raman scattering is inherently weak, but its sensitivity can be improved by implementing Surface-Enhanced Raman Scattering (SERS). SERS is applied to enhance the Raman signal by several orders of magnitude and significantly improve the sensitivity of the ordinary scattering method. As a result of the electromagnetic enhancement emerging in the vicinity of metallic nanostructures the sensitivity of molecule detection can achieve attomolar concentrations. This highly sensitive detection performance of SERS was utilized for analysing molecules located in the few nanometre distance or immobilised on the surface of nanoparticles trapped in a specially designed microstructure. By means of the effect efficient detection method can be developed for the analysis of low concentration biological samples assuming that sample transport and preparation system is also integrable.

To increase the local field intensity of Raman scattering, gold nanospheres were entrapped in gold coated periodic inverse pyramid structures, being SERS substrates by themselves. The applicability of this complex structure for sensitive molecule detection was proved by comparison of the detected Raman signals with and without particle entrapment. Moreover its relevance in molecular diagnostic was also proposed considering the specific surface functionalisation of the gold nanoparticles.

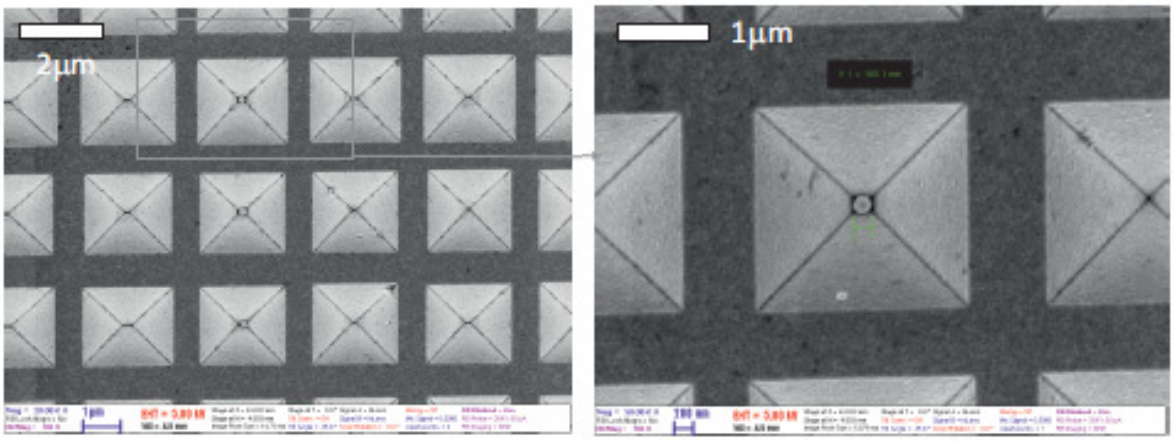


*Figure 1: SEM images of the inverse pyramid SERS substrate with 200 nm GNPs located in some of the voids.*

Silicon was used as substrate material of the inverse pyramids with 150 nm gold coating, and periodically ordered gold nanospheres (with 100 and 200 nm diameter) were placed into the pyramids. A remarkable increase of the surface enhancement has been observed in gold coated micron sized inverse pyramid after placing a gold nanosphere inside it. The amplification of both surface enhanced Raman and fluorescence signals was found to be dependent on the size of the gold nanoparticle, and the enhancement can be two orders of magnitude larger than that of the empty pyramid (Fig. 2.).

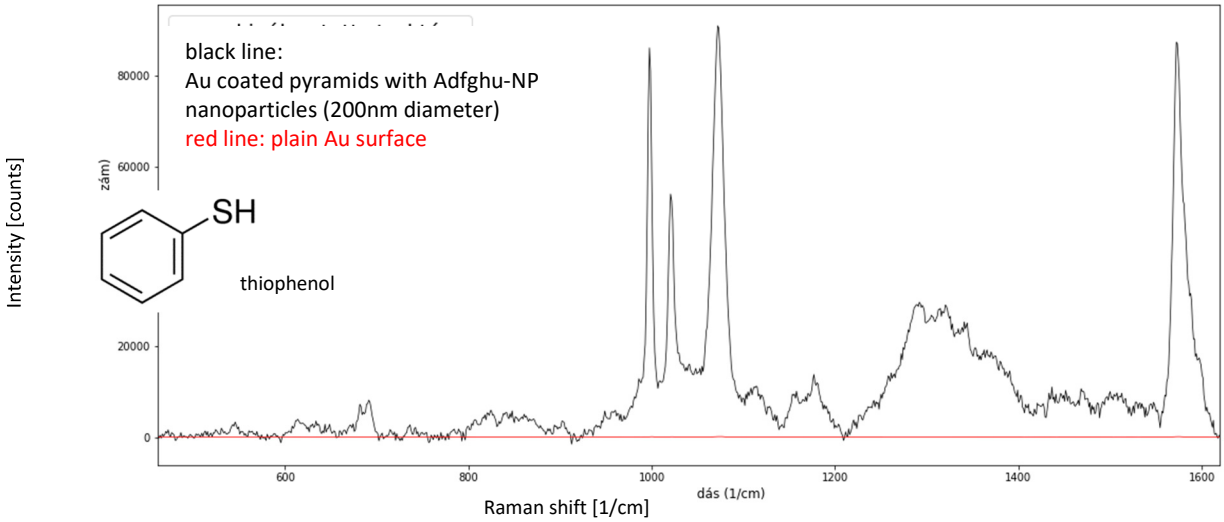


*Figure 2: Surface enhanced Raman spectra of thiophenone solution dripped and dried onto inverse pyramid arrays entrapping an Au NP with diameter of 200nm.*

To understand the analytical performance the near-field intensity distributions of inverse pyramid arrays were studied by FDTD simulations using the Lumerical FDTD Solutions v.8.15.736 software. The origin of the phenomenon was investigated by finite differential time domain simulations that showed that coupling of the electric field occurs when the nanosphere protrudes into the high intensity near-field region of the pyramid. The plasmon-related near-field enhancement was found to be concentrated into the gaps formed around the contact points of the curved sphere and the flat pyramid surface [1].

## *Related publication*

[1] R. Öcsi: *Felületerősített Raman-spektroszkópiára alkalmas chipek fejlesztése sejtanalitikai célokra,* Eötvös Loránd University, OTDK Materials Physics session I. place (supervisors: Zs. Zolnai, P. Fürjes)

# DEVELOPMENT AND SMALL SCALE PRODUCTION OF NEAR INFRARED LEDS AND LED BASED DEVICES AND THEIR SPECTROSCOPIC APPLICATIONS

***Moore4Medical, ECSEL-2019-1-IA -876190 2019-2.1.3-NEMZ_ECSEL-2020-00005***

*F. Bíró, J. Bozorádi, G. Battistig, Cs. Dücső, B. Beiler, Z. Szabó, P. Fürjes*

## *Near infrared LEDs for spectroscopy*

Infrared spectroscopy is a very popular measurement technique especially in food industry, pharmaceutical industry and agriculture for the detection and measurement of organic materials. The -OH, -NH and -CH functional groups found in organic substances can frequently be detected by spectroscopy through absorbance measurements at the resonance wavelength of valence-bond vibrations. The measured wavelengths are 4-2.5µm, while the signal to noise ratio of photon detectors is low due to thermal noise at room temperature. The 1st-3rd harmonic absorption bands are located in the range of the Near Infrared (NIR), where smaller signals can be measured effectively in practice. NIR LEDs have narrow wavelength, therefore they are suitable for measurements at given wavelength. Further advantages of LEDs compared to incandescent lamps are their small dimensions, high efficiency, and low power consumption, which is critical in small handheld devices.

GaInAsP/InP is an ideal material system for the fabrication of double heterostructure devices as the emission wavelength is easily tuneable between 950-1650 nm. As InP has higher bandgap than the lattice-matched GaInAsP active layer the absorption losses inside the device structure can be minimized. In order to tune the emission wavelength of the LED, the composition of the semiconductor light-emitting layer has to be properly set. Our high quality single peak LED chips (1220nm) have a stable market, our business partners are SENOP Oy (Fi) and Anton Paar Ltd. (At).

The purpose of the **LED2Spectro (Knowledge Transfer) project** is to connect the Centre for Energy's Microsystems Lab with the potential application partner Photonic Insights (Germany) who also serves as an interface between the Microsystems Lab and Fraunhofer IZM. Berlin-based company Photonic Insights develops products for advanced quality measurement. Microsystems Lab provides LED based illumination technology that is targeted in the NIR region 950nm to 1650nm. This illumination is an optimal complement for cutting-edge spectrographic sensors. These LEDs can be integrated into the existing spectrographic device created by Photonic Insights. The unique double-wavelength LEDs have the advantage is that emission peaks are stable relative to each other because only one LED driver circuit is needed and both of peaks are generated by the same emission spot. New innovative NIR LED light source is under development which illuminates in the whole NIR spectral range. It could replace the miniature incandescent light sources in the handheld spectroscopic devices. The first solution that will benefit from the cooperation is Photonic Insights' metrology suite which adds value to certain agricultural and water-related use cases due to its price performance ratio.

**Tea quality measurement** is an untapped segment of measurement technology. This is primarily an Asian (China, Sri Lanka, India) agricultural market. In tea quality measurement technology there are so far, two competitors present. One of them offers a stationary, not handheld device with mediocre analytic capabilities, the other offers a mobile-phone-integrated solution, hence handheld; however, the analytical capabilities are low. Optical reflectance measurements in NIR range on wet and dry tea leaves are capable to identify to monitor the drying process of the leaves; optical absorbance measurement in the UV-NIR range helps to investigate the optically detectable target molecules in tea solutions.

Reflectance measurements on tea leaves were carried out simultaneously with mass measurement during the drying process. The known water content vs. reflectance spectra (Fig. 1.a) were analysed by Photonic Insights to identify the most important wavelength lines and develop the calculation method for the moisture measurement. It is possible to distinguish between different types of tea solutions based on the visible and NIR absorbance spectra (Fig. 1.b.). To measure absorbance in UV range further dilution was necessary. The chemical composition of tea is very complex, and it contains, among other things, polyphenols, alkaloids (caffeine, theophylline and theobromine); amino acids (L-theanine); flavanols/tannins; carbohydrates; proteins; chlorophyll and volatile compounds. Photonic Insights has the knowledge base and experience to analyse such a complex data using various analytical methods.

a

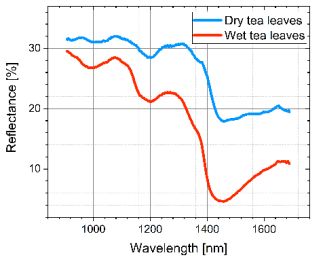


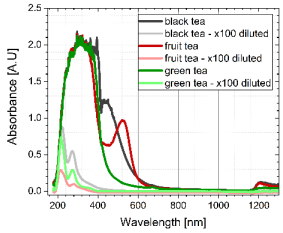


b

*Figure 1: NIR reflectance spectra of wet and dry tea leaves (a) and UV-NIR absorbance spectra of different tea solutions (b)*

## *Marker molecule detection in Organ-on-Chip (OoC) applications*

The 3 year long international Moore 4 Medical project was started in June 2020. The consortium has participants from 12 countries and from around 64 companies and research institutes. The project leader, Phillips Research tries to create the base of new open technology platforms which will accelerate innovations in various medical domains such as implantable devices, organ-on-chip, drug adherence, next generation ultrasound, towards x-ray free surgery and continuous patient monitoring. Our main task is in the field of development organ-on-chip applications, where the collaboration develops a smart multiwell plate system. A smart multiwell plate works as an autonomous system with micropumps, microfluidic infrastructure that provide perfusion, as well as the electronics to drive the micropumps and integrated readout sensors. Another part of the system is a smart multiwell plate lid that can be used in combination with ordinary, as well as the smart multiwell plates. The non-disposable lid contains micropumps and sensors that monitor in situ and in a parallel fashion monitor the medium of cell cultures in incubators.

Our laboratory participates in designing the microfluidic layer of the smart well plate, development flexible sensor module for the smart lid and the **integration of optical NIR spectral sensors**. We intend to develop near IR LED sources and spectroscopic solution for monitoring nutrient composition (e.g. glucose concentration) in microfluidic channels. There is only a small space (~1 $cm^3$) available in the smart well plate for an optical sensor, if we are still intended to construct a modular plug-in module. According to the limited space the miniaturisation and usage microfluidic channels and cuvettes are crucial. The final vision is to construct a modular optical plug-in module integrated with microfluidic sample monitoring system and the measurement has to be restricted to a few specific wavelengths using absorption or fluorescence detection.

For the first period the main goal was to **define system specifications and architecture**. Accordingly the components of the cell culture media and its additives were investigated by measuring their optical characteristics in the 200-2500 nm (UV-VIS-NIR and even in mid infrared) range. Absorbance, transmittance and fluorescence spectra were recorded so far on DMEM/F-12 plus and Vitrolife G1 (plus) solutions, glucose, lactate, glutamine molecules and antibiotics such as penicillin streptomycin, streptomycin sulphate, neomycin sulphate in different concentrations. Other target molecules, various grow factors are also considered. High throughput optical studies were stated by platereader (TECAN Spark) also in the 200-1000 nm range.

- Glucose has only a very small absorption in NIR range in the usual concentration range and has no fluorescence signal.
- Lactate (which indicates the anaerobic glucose consumption) has high absorbance in the UV region and absorbance peaks in the NIR range.

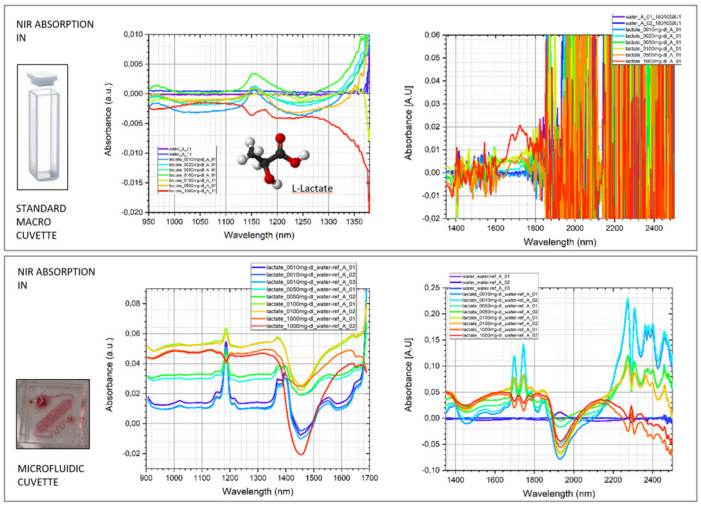


*Figure 2: Spectral characteristics of the lactate in macroscopic (top) and microfluidic environment (bottom) as being a significant marker molecule of OoC applications. The IR light absorption is depressed due to the smaller pathway in microfluidics, and it allows us to measure detailed spectrum.*

For further optical characterisation specific microfluidic cuvettes were designed and manufactured. According to the requirements of low sample volume and autonomous sample transport a specific surface modified PDMS (polydimethylsiloxane) microfluidic cuvette was fabricated by soft lithographic technique. The optical parameters were measured in microfluidic cuvette and compared to the macroscopic case. In microfluidic environment **improved signal-to-noise ratio was achieved due to the suppressed absorption of water** as demonstrated in Fig. 2 in case of Lactate. The top right figure demonstrates the high optical absorption of water in the wavelength range of 1400-2400nm, accordingly the detected signal is low, and the signal-to-noise ratio is low. In contrary in microfluidic environment the effect can be eliminated (see the bottom right figure). To step forward the integration of the optical screening method in smart wellplate system the wellplate compatible microfluidic cuvette was designed including material selection, geometric parameters and fabrication technology in cooperation with Micronit & TUDelft. The possible cuvette materials were characterised optically and COP was chosen. The geometry was defined to be compatible with the fluidic layer of the smart wellplate. Hot embossing and laser welding (in cooperation with Aedus Ltd.) were proposed as industrial scale production compatible technologies.

# DISSOCIATION CONSTANT OF INTEGRIN-RGD BINDING IN LIVE CELLS FROM AUTOMATED MICROPIPETTE AND LABEL-FREE OPTICAL DATA

*LP2012-26/2012 Lendület, OTKA KH126900, OTKA ERC_HU117755, OTKA PD131543, OTKA KKP129936*

*T. Gerecsei, P. Chrenkó, N. Kanyó, B. Péter, A. Bonyár (BME), I. Székács, B. Szabó (ELTE), R. Horváth*

The binding of integrin proteins to peptide sequences such as arginine-glycine-aspartic acid (RGD) is a crucial step in the adhesion process of mammalian cells. While these bonds can be examined between purified proteins and their ligands, live-cell assays are better suited to gain biologically relevant information. Here we apply a computer-controlled micropipette (CCMP) to measure the dissociation constant (Kd) of integrin-RGD-binding. Surface coatings with varying RGD densities were prepared, and the detachment of single cells from these surfaces was measured by applying a local flow inducing hydrodynamic lifting force on the targeted cells in discrete steps. The average behaviour of the populations was then fit according to the chemical law of mass action. To verify the resulting value of Kd2d = (4503 ± 1673) 1/μm², a resonant waveguide grating based biosensor was used, characterizing and fitting the adhesion kinetics of the cell populations. Both methods yielded a Kd within the same range. Furthermore, an analysis of subpopulations was presented, confirming the ability of CCMP to characterize cell adhesion both on single cell and whole population levels (Fig. 1.). The introduced methodologies offer convenient and automated routes to quantify the adhesivity of living cells before their further processing [1].

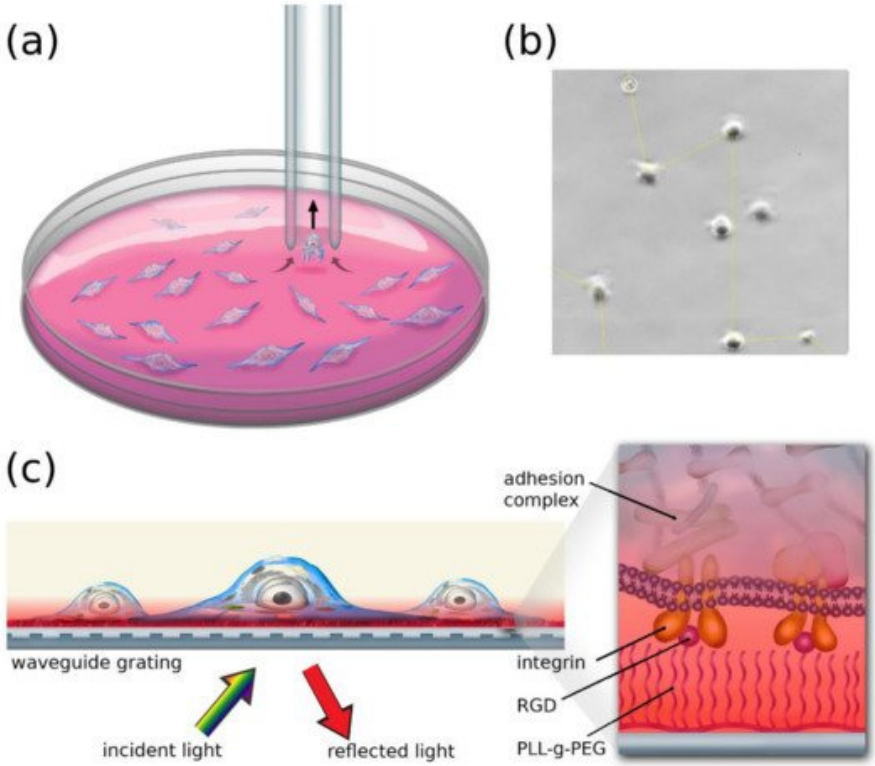


*Figure 1: Illustration of the methods used to measure cell adhesion. (a) The CCMP automatically visits each detected cell and probes them by applying a preset negative pressure. (b) Section of a field of view in a Petri dish containing adhered HeLa cells. (c) Schematic representation of the resonant waveguide-based measurement.*

## *Related publication*

[1] T. Gerecsei, P. Chrenkó, N. Kanyo, B. Péter, A. Bonyár, I. Székács, B. Szabo, R. Horvath: *Dissociation constant of integrin-RGD binding in live cells from automated micropipette and label-free optical data,* Biosensors **11:(2),** 32 (2021)

# DATA EVALUATION FOR SURFACE-SENSITIVE LABEL-FREE METHODS TO OBTAIN REAL-TIME KINETIC AND STRUCTURAL INFORMATION OF THIN FILMS: A PRACTICAL REVIEW WITH RELATED SOFTWARE PACKAGES

*LP2012-26/2012 Lendület, OTKA ERC_HU117755, OTKA KH126900, OTKA KKP129936, OTKA PD131543*

*Saftics, S. Kurunczi, B. Péter, I. Székács, J. J. Ramsden (University of Buckingham), R. Horváth*

Interfacial layers are important in a wide range of applications in biomedicine, biosensing, analytical chemistry and the maritime industries. Given the growing number of applications, analysis of such layers and understanding their behaviour is becoming crucial. Label-free surface sensitive methods are excellent for monitoring the formation kinetics, structure and its evolution of thin layers, even at the nanoscale.

In this paper, we review existing and commercially available label-free techniques and demonstrate how the experimentally obtained data can be utilized to extract kinetic and structural information during and after formation, and any subsequent adsorption/desorption processes. We outline techniques, some traditional and some novel, based on the principles of optical and mechanical transduction. Our special focus is the current possibilities of combining label-free methods, which is a powerful approach to extend the range of detected and deduced parameters. We summarize the most important theoretical considerations for obtaining reliable information from measurements taking place in liquid environments and, hence, with layers in a hydrated state.

A thorough treatment of the various kinetic and structural quantities obtained from evaluation of the raw label-free data are provided. Such quantities include layer thickness, refractive index, optical anisotropy (and molecular orientation derived therefrom), degree of hydration, viscoelasticity, as well as association and dissociation rate constants and occupied area of subsequently adsorbed species. To demonstrate the effect of variations in model conditions on the observed data, simulations of kinetic curves at various model settings are also included. Based on our own extensive experience with Optical Waveguide Lightmode Spectroscopy (OWLS) and the quartz crystal microbalance (QCM), we have developed dedicated software packages for data analysis (Fig. 1.), which are made available to the scientific community alongside this paper [1].

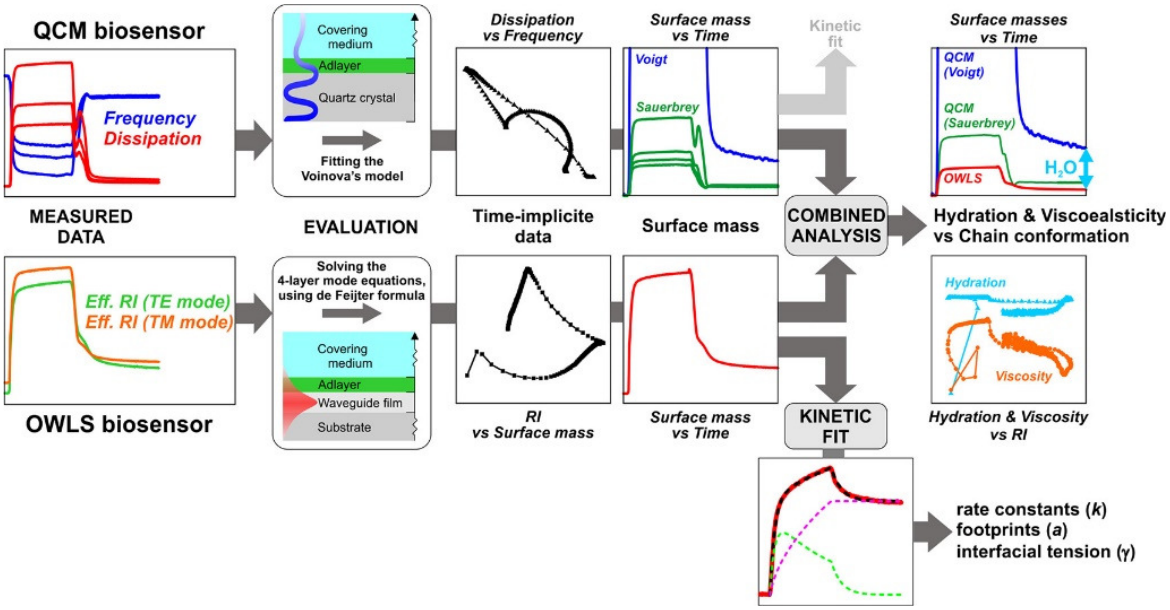


*Figure 1: Simulations of kinetic curves at various model settings are also included in the review article*

## *Related publication*

[1] A. Saftics, S. Kurunczi, B. Peter, I. Szekacs, J. J. Ramsden, R. Horvath: *Data evaluation for surface-sensitive label-free methods to obtain real-time kinetic and structural information of thin films: A practical review with related software packages,* Advances in Colloid and Interface Science **294,** 102431 (2021)

# NANONEWTON SCALE ADHESION FORCE MEASUREMENTS ON BIOTINYLATED MICROBEADS WITH A ROBOTIC MICROPIPETTE

***LP2012-26/2012 Lendület, OTKA PD124559, OTKA PD131543, OTKA ERC_HU117755, OTKA KH126900, OTKA KKP129936***

*R. Ungai-Salánki, B. Csippa (ELTE), T. Gerecsei, B. Péter, R. Horváth, B. Szabó (ELTE)*

Binding force between biomolecules has a crucial role in most biological processes. Receptor-ligand interactions transmit physical forces and signals simultaneously. Previously, we employed a robotic micropipette both in live cell and microbead adhesion studies to explore the adhesion force of biomolecules such as cell surface receptors including specific integrins on immune cells. Here we apply standard computational fluid dynamics simulations to reveal the detailed physical background of the flow generated by the micropipette when probing microbead adhesion on functionalized surfaces. Measuring the aspiration pressure needed to pick up the biotinylated 10 µm beads on avidin coated surfaces and converting it to a hydrodynamic lifting force on the basis of simulations, we found an unbinding force of 12 ± 2 nN, when targeting the beads manually; robotic targeting resulted in 9 ± 4 nN (mean ± SD). We measured and simulated the effect of the targeting offset, when the microbead was out of the axis (off-axis) of the micropipette.

According to the simulations, the higher offset resulted in a higher lifting force acting on the bead. Considering this effect, we could readily correct the impact of the targeting offset to renormalize the experimental data. Horizontal force and torque also appeared in simulations in case of a targeting offset. Surprisingly, simulations show that the lifting force acting on the bead reaches a maximum at a flow rate of ~ 5 µl/s if the targeting offset is not very high (<5 µm). Further increasing the flow rate decreases the lifting force. We attribute this effect to the spherical geometry of the bead. We predict that higher flow rates cannot increase the hydrodynamic lifting force acting on the precisely targeted microbead, setting a fundamental force limit (16 nN in our setup) for manipulating microbeads with a micropipette perpendicular to the supporting surface (Fig. 1.). In order to extend the force range, we propose the offset targeting of microbeads [1]

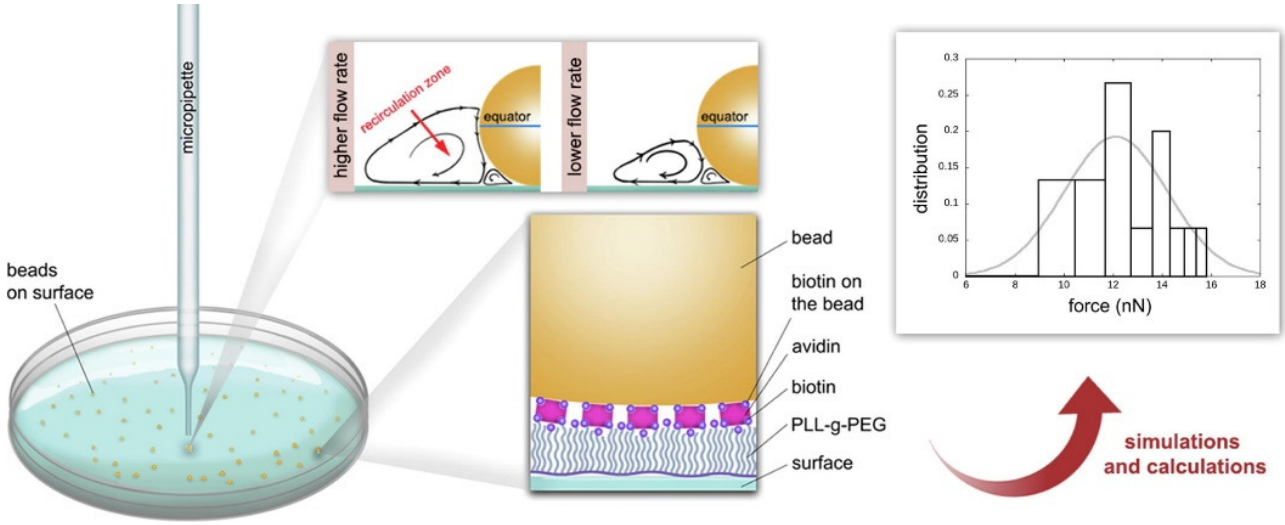


*Figure 1: For measuring the aspiration pressure needed to pick up the biotinylated 10 µm beads on avidin coated surfaces with robotic micropipette.*

## *Related publication*

[1] R. Ungai-Salánki, B. Csippa, T. Gerecsei, B. Péter, R. Horvath, B. Szabó: *Nanonewton scale adhesion force measurements on biotinylated microbeads with a robotic micropipette,* Journal of Colloid and Interface Science **602,** 291-299 (2021)

# NANONEWTON SCALE ADHESION FORCE MEASUREMENTS ON BIOTINYLATED MICROBEADS WITH A ROBOTIC MICROPIPETTE

*LP2012-26/2012 Lendület, OTKA PD124559, OTKA PD131543, OTKA ERC_HU117755, OTKA KH126900, OTKA KKP129936*

*R. Ungai-Salánki, B. Csippa (ELTE), T. Gerecsei, B. Péter, R. Horváth, B. Szabó (ELTE)*

Binding force between biomolecules has a crucial role in most biological processes. Receptor-ligand interactions transmit physical forces and signals simultaneously. Previously, we employed a robotic micropipette both in live cell and microbead adhesion studies to explore the adhesion force of biomolecules such as cell surface receptors including specific integrins on immune cells. Here we apply standard computational fluid dynamics simulations to reveal the detailed physical background of the flow generated by the micropipette when probing microbead adhesion on functionalized surfaces. Measuring the aspiration pressure needed to pick up the biotinylated 10 µm beads on avidin coated surfaces and converting it to a hydrodynamic lifting force on the basis of simulations, we found an unbinding force of 12 ± 2 nN, when targeting the beads manually; robotic targeting resulted in 9 ± 4 nN (mean ± SD). We measured and simulated the effect of the targeting offset, when the microbead was out of the axis (off-axis) of the micropipette.

According to the simulations, the higher offset resulted in a higher lifting force acting on the bead. Considering this effect, we could readily correct the impact of the targeting offset to renormalize the experimental data. Horizontal force and torque also appeared in simulations in case of a targeting offset. Surprisingly, simulations show that the lifting force acting on the bead reaches a maximum at a flow rate of ~ 5 µl/s if the targeting offset is not very high (<5 µm). Further increasing the flow rate decreases the lifting force. We attribute this effect to the spherical geometry of the bead. We predict that higher flow rates cannot increase the hydrodynamic lifting force acting on the precisely targeted microbead, setting a fundamental force limit (16 nN in our setup) for manipulating microbeads with a micropipette perpendicular to the supporting surface (Fig. 1.). In order to extend the force range, we propose the offset targeting of microbeads [1]

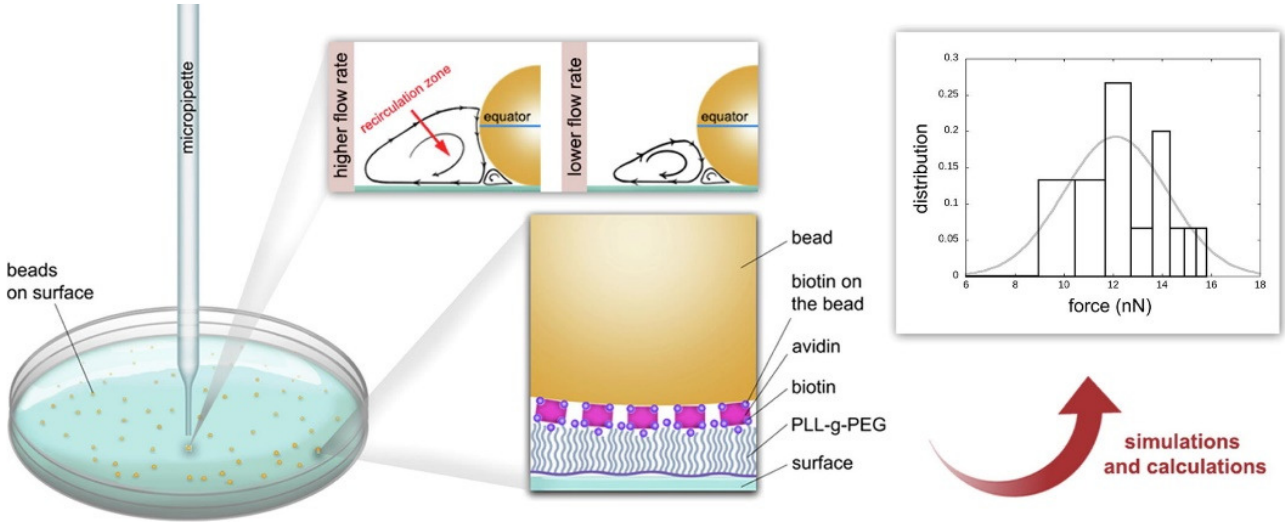


*Figure 1: For measuring the aspiration pressure needed to pick up the biotinylated 10 µm beads on avidin coated surfaces with robotic micropipette.*

## *Related publication*

[1] R. Ungai-Salánki, B. Csippa, T. Gerecsei, B. Péter, R. Horvath, B. Szabó: *Nanonewton scale adhesion force measurements on biotinylated microbeads with a robotic micropipette,* Journal of Colloid and Interface Science **602,** 291-299 (2021)

# DESIGN OF NON-AUTONOMOUS PH OSCILLATORS AND THE EXISTENCE OF CHEMICAL BEAT PHENOMENON IN A NEUTRALIZATION REACTION

*LP2012-26/2012 Lendület, OTKA NN125752, OTKA K131425, OTKA KKP129936, TKP2020 IES, Grant No. BME-IE-NAT*

*H. S. Lawson (BME), G. Holló (BME), N. Német (BME), S. Teraji (KIT, Japan), H. Nakanishi (KIT, Japan), R. Horváth, I. Lagzi (BME)*

The beat in physical systems is a transparent and well-understood phenomenon. It may occur in forced oscillatory systems and as a result of the interference of two waves of slightly different frequencies. However, in chemical systems, the realization of the latter type of the beat phenomenon has been lacking. Here we show that a periodic titration of acid and alkaline solutions with each other using programmable syringe pumps in a continuous stirred-tank reactor exhibits the beat phenomenon in the temporal pH oscillation pattern if the time periods of sinusoidal inflow rates of the reagents are slightly different. Interestingly, the frequency of the chemical beat pattern follows the well-known relationship from physics, namely the frequency of the beat is equal to the absolute value of the difference of the two wave frequencies. Based on our strategy, we can design and engineer non-autonomous pH oscillatory systems, in which the characteristics of the temporal oscillations (amplitude, time period) can easily and precisely be controlled by the experimental conditions such as the inflow rates and feed concentrations (Fig. 1.). The demonstrated phenomena can be exploited in practical applications, we use the non-autonomous pH oscillators to drive the reversible assembly and disassembly of pH-sensitive building blocks (oleic acid and gold nanoparticles), both highly relevant in nanotechnology and biomedical applications [1].

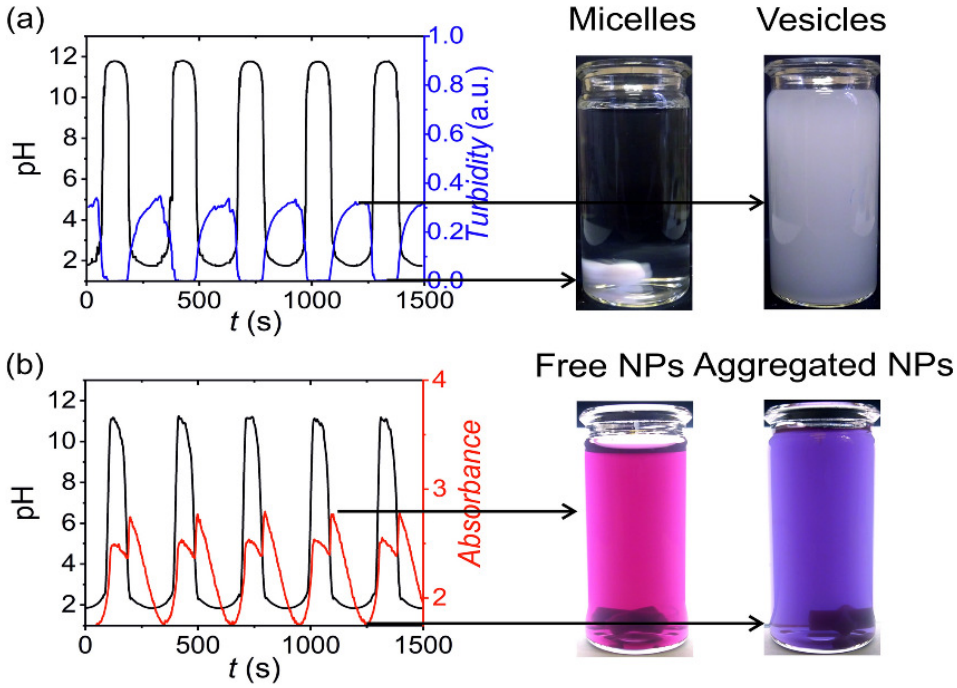


*Figure 1: Reversible transformation of vesicle and micelles (a) and assembly/disassembly of pH-sensitive AuNPs (b) using the non-autonomous pH oscillator.*

## *Related publication*

[1] H. S. Lawson, G. Holló, N. Német, S. Teraji, H. Nakanishi, R. Horvath, I. Lagzi: *Design of non-autonomous pH oscillators and the existence of chemical beat phenomenon in a neutralization reaction,* Scientific Reports **11,** 11011 (2021)

# NEAR CUT-OFF WAVELENGTH OPERATION OF RESONANT WAVEGUIDE GRATING BIOSENSORS

***LP2012-26/2012 Lendület, OTKA ERC_HU117755, OTKA KH126900, OTKA KKP129936, OTKA K132050***

*B.Kovács, F. A. Kraft (Kiel University), Zs. Szabó (PPKE), Y. Nazirizadeh (Byonoy GmbH), M. Gerken (Kiel University), R. Horváth*

Numerical simulations and analytical calculations are performed to support the design of grating-coupled planar optical waveguides for biological sensing. Near cut-off and far from cut-off modes are investigated, and their characteristics and suitability for sensing are compared. The numerical simulations reveal the high sensitivity of the guided mode intensity near the cut-off wavelength for any refractive index change along the waveguide. Consequently, it is sufficient to monitor the intensity change of the near cut-off sensing mode, which leads to a simpler sensor design compared to those setups where the resonant wavelength shift of the guided mode is monitored with high precision. The operating wavelength and the sensitivity of the proposed device can be tuned by varying the geometrical parameters of the corrugated waveguide (Fig. 1.). These results may lead to the development of highly sensitive integrated sensors, which have a simple design and therefore are cost-effective for a wide range of applications. These numerical findings are supported with experimental results, where the cut-off sensing mode was identified [1].

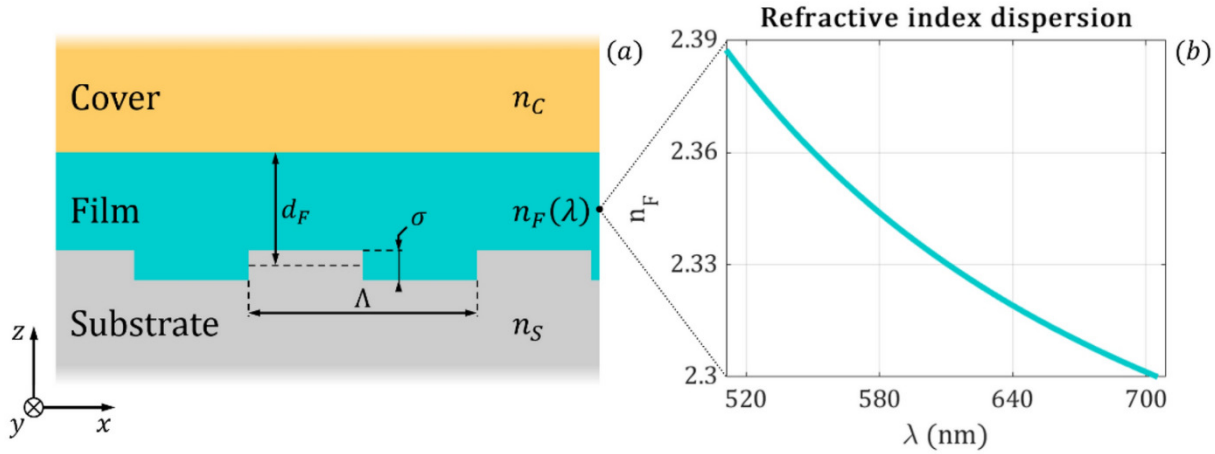


*Figure 1: (a) The cross-section of the modelled corrugated waveguide. The electromagnetic simulations apply Floquet boundary conditions along the x- and y-axis and open boundaries with Floquet ports in the vertical z direction. (b) The frequency dependence of the $Nb_2O_5$ film refractive index.*

## *Related publication*

[1] B. Kovacs, F. A. Kraft, Zs. Szabo, Y. Nazirizadeh, M. Gerken, R. Horvath: *Near cut-off wavelength operation of resonant waveguide grating biosensors,* Scientific Reports **11,** 13091 (2021)

# SINGLE-CELL ADHESION STRENGTH AND CONTACT DENSITY DROPS IN THE M PHASE OF CANCER CELLS

*LP2012-26/2012 Lendület, OTKA PD124559, OTKA ERC_HU117755, OTKA KH126900, OTKA PD131543, OTKA KKP129936*

*R. Ungai-Salánki, E. Haty, T. Gerecsei, B. Francz (CellSorter), B. Béres, M. Sztilkovics, I. Székács, B. Szabó (ELTE), R. Horváth*

The high throughput, cost effective and sensitive quantification of cell adhesion strength at the single-cell level is still a challenging task. The adhesion force between tissue cells and their environment is crucial in all multicellular organisms. Integrins transmit force between the intracellular cytoskeleton and the extracellular matrix. This force is not only a mechanical interaction but a way of signal transduction as well. For instance, adhesion-dependent cells switch to an apoptotic mode in the lack of adhesion forces. Adhesion of tumour cells is a potential therapeutic target, as it is actively modulated during tissue invasion and cell release to the bloodstream resulting in metastasis.

We investigated the integrin-mediated adhesion between cancer cells and their RGD (Arg-Gly-Asp) motif displaying biomimetic substratum using the HeLa cell line transfected by the Fucci fluorescent cell cycle reporter construct. We employed a computer-controlled micropipette and a high spatial resolution label-free resonant waveguide grating-based optical sensor calibrated to adhesion force and energy at the single-cell level (Fig. 1.). We found that the overall adhesion strength of single cancer cells is approximately constant in all phases except the mitotic (M) phase with a significantly lower adhesion. Single-cell evanescent field based biosensor measurements revealed that at the mitotic phase the cell material mass per unit area inside the cell-substratum contact zone is significantly less, too. Importantly, the weaker mitotic adhesion is not simply a direct consequence of the measured smaller contact area. Our results highlight these differences in the mitotic reticular adhesions and confirm that cell adhesion is a promising target of selective cancer drugs as the vast majority of normal, differentiated tissue cells do not enter the M phase and do not divide [1]

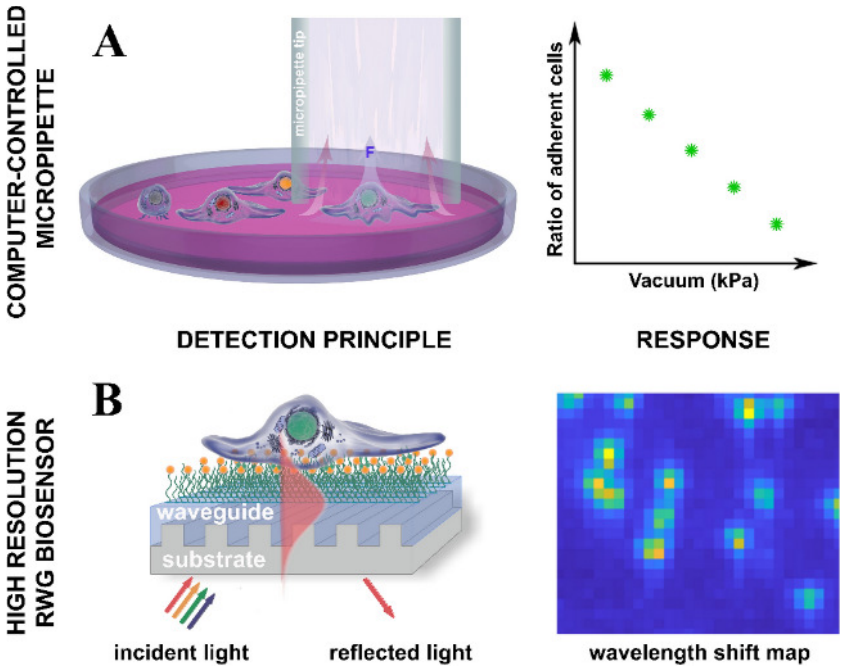


*Figure 1: Schematic representation of the adhesion strength measurements on single cells using a computer-controlled micropipette and the high-resolution Resonant Waveguide Grating (RWG) biosensor (Single-Cell RWG).*

## *Related publication*

[1] R. Ungai-Salánki, E. Haty, T. Gerecsei, B. Francz, B. Béres, M. Sztilkovics, I. Székács, B. Szabó, R. Horvath: *Single-cell adhesion strength and contact density drops in the M phase of cancer cells,* Scientific Reports **11,** 18500 (2021)

# LABEL-FREE TRACKING OF WHOLE-CELL RESPONSE ON RGD FUNCTIONALIZED SURFACES TO VARIED FLOW VELOCITIES GENERATED BY FLUIDIC ROTATION

*LP2012-26/2012 Lendület, OTKA KKP129936, OTKA KH126900, TKP2020 IES, Grant No. BME-IE-BIO*

*K. D. Kovács, M. Novák, Z. Hajnal, Cs. Hős (BME), B. Szabó, I. Székács, Y. Fang (Corning Inc.), A. Bonyár (BME), R. Horváth*

Fluidic flow plays important roles in colloid and interface sciences. Measuring adsorption, aggregation processes and living cell behaviour under a fluidic environment with varied flow velocities in a parallel and high-throughput manner remains to be a challenging task. Here a method is introduced to monitor cell response to well-defined flow with varied velocities over an array of label-free resonant waveguide grating (RWG) based optical biosensors (Fig. 1.). The arrangement consists of a circular well with an array of biosensors at the bottom surface. By rotating the liquid over the biosensor array using a magnetic stirrer bar, flow velocities from zero to a predefined maximum can be easily established over different locations within the biosensor array as characterized in detail by numerical simulations. Cell adhesion and detachment measurements on an Arg-Gly-Asp (RGD) peptide functionalized surface were performed to demonstrate i) measurements at a wide range of simultaneous flow velocities over the same interface; ii) the possibility of parallel measurements at the same flow conditions in one run; and iii) the simple tuning of the employed range of flow velocities. Our setup made it possible to analyze the magnitude and rate of cell detachment at various flow velocities in parallel and determine the critical velocity and force where cells start to detach from the RGD motif displaying biomimetic surface. Furthermore, cellular response to simultaneous mechanical (flow) and chemical stimulation was also investigated using trypsin as a model. This study opens a new possibility to investigate interface phenomena under predefined and conveniently varied flow conditions [1].

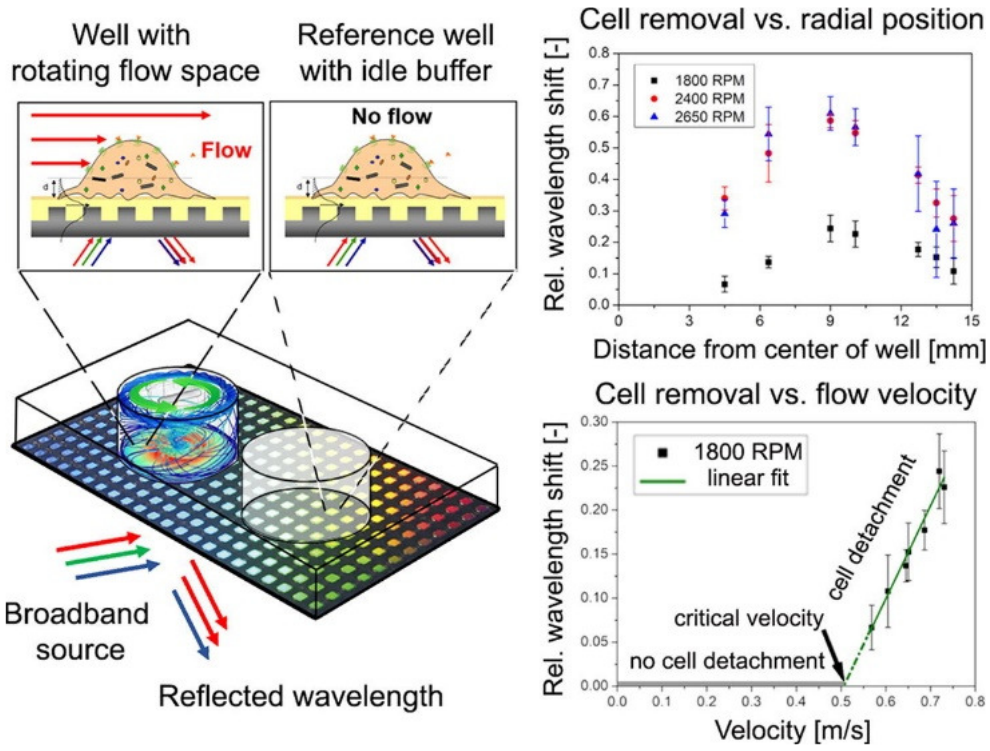


*Figure 1: Illustration of the flow field and cell interactions in the assay and reference wells, respectively*

## *Related publication*

[1] K. D. Kovács, M. Novák, Z. Hajnal, Cs. Hős, B. Szabó, I. Székács, Y. Fang, A. Bonyár, R. Horvath: *Label-free tracking of whole-cell response on RGD functionalized surfaces to varied flow velocities generated by fluidic rotation*, Journal of Colloid and Interface Science **599,** (2021)

# LABEL-FREE REAL-TIME MONITORING OF THE BCR-TRIGGERED ACTIVATION OF PRIMARY HUMAN B CELLS MODULATED BY THE SIMULTANEOUS ENGAGEMENT OF INHIBITORY RECEPTORS

*LP2012-26/2012 Lendület, OTKA ERC_HU117755, OTKA KH126900, OTKA PD 131543, OTKA KKP129936, OTKA K 112011*

*K. Kliment, I. Szekacs, B. Peter, A. Erdei (ELTE), I. Kurucz (ELTE), R. Horvath*

Today, there is an intense demand for lab-on-a-chip and tissue-on-a-chip applications in basic cell biological research and medical diagnostics. A particular challenge is the implementation of advanced biosensor techniques in point-of-care testing utilizing human primary cells. In this study, a resonant waveguide grating (RWG)-based label-free optical biosensor technique has been applied for real-time monitoring of the integrated responses of primary human tonsillar B cells initiated by B cell receptor (BCR) and modified by FcγRIIb and CR1 engagement (Fig. 1.).

The BCR-triggered biosensor responses of resting and activated B cells were revealed to be specific and dose-dependent, in some cases with strong donor dependency. Targeted inhibition of Syk attenuated the label-free biosensor response upon BCR stimulation. Indifferent protein human serum albumin (HSA) did not interfere with the recorded signal to BCR stimulation. Simultaneous engagement of BCR and FcγRIIb modulated the kinetic signal of the cells. Activated and resting B cells exhibited different response profiles upon simultaneous engagement of BCR and CR1. This advanced approach has the potential to decipher interfering signalling events in human B cells, manage differences between activated and resting B cell states, helping to understand the actual integrated response of these immune cells, and could be useful in the point-of-care diagnostic testing on human primary cells [1].

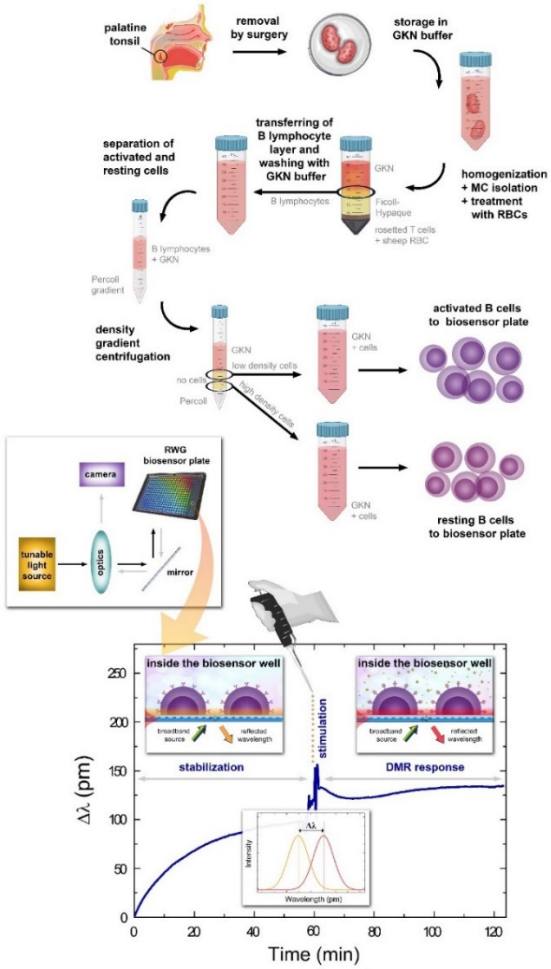


*Figure 1: Schematic overview illustrating the major steps of the biosensor assay: surgery material collection, storage in glucose potassium nutrient (GKN) buffer, mononuclear cells (MC) isolation through rosetting with 2-aminoethylisothiouronium bromide-treated sheep red blood cells (RBCs) by centrifugation over Ficoll-Hypaque solution, with further B cells fractionation on a Percoll gradient. In the end, activated and resting cells were used for the biosensor measurement. The bottom part represents the actual biosensor arrangement and data collection. The schematic readout of the biosensor microplate with incorporated sensor wells and the label-free primary signal (shift in resonant wavelength or deep molecular response) originating from the cells adhering on the surface is also shown.*

## *Related publication*

[1] K. Kliment, I. Szekacs, B. Peter, A. Erdei, I. Kurucz, R Horvath: *Label-free real-time monitoring of the BCR-triggered activation of primary human B cells modulated by the simultaneous engagement of inhibitory receptors,* Biosensors and Bioelectronics **191,** 113469 (2021)

# COOPERATION AND COMPETITION BETWEEN PAIR AND MULTI-PLAYER SOCIAL GAMES IN SPATIAL POPULATIONS

*A. Szolnoki and X. Chen*

The conflict between individual and collective interests is in the heart of every social dilemma established by evolutionary game theory. We cannot avoid these conflicts but sometimes we may choose which interaction framework to use as a battlefield. For instance, some people like to be part of a larger group while other persons prefer to interact in a more personalized, individual way. Both attitudes can be formulated via appropriately chosen traditional games. In particular, the prisoner's dilemma game is based on pair interaction, while the public goods game represents multi-point interactions of group members. To reveal the possible advantage of a certain attitude we extend these models by allowing players not simply to change their strategies but also let them to vary their attitudes for a higher individual income. We show that both attitudes could be the winner at a specific parameter value. Interestingly, however, the subtle interplay between different states may result in a counterintuitive evolutionary outcome where the increase of the multiplication factor of public goods game drives the population to a fully defector state. We point out that the accompanying pattern formation can only be understood via the multipoint or multi-player interactions of different microscopic states where the vicinity of a particular state may influence the relation of two other competitors.

When calculating the payoff of $A_{D,}$ marked by a yellow background, then we sum the payoff elements of four prisoner's dilemma games played with the neighbours. When we calculate the payoff of $O_C$ player, also marked by yellow background, then we should consider the fact that two of its neighbours have "alone" attitude, hence $O_C$ should play prisoner's dilemma game with them. The remaining two neighbours have "together" attitude hence the focal player can play a three-member public goods game with them in the marked $G_0$ group. The focal player also participates in a three-member public goods game of $G_1$ group and in a two-member game of $G_2$ group. For the shake of comparable payoff values we multiply the incomes of public goods games by an α factor. The interactions, where prisoner's dilemma game is used are marked by dashed lines, while the in the case of public goods game they are denoted by solid green (Fig. 1.).

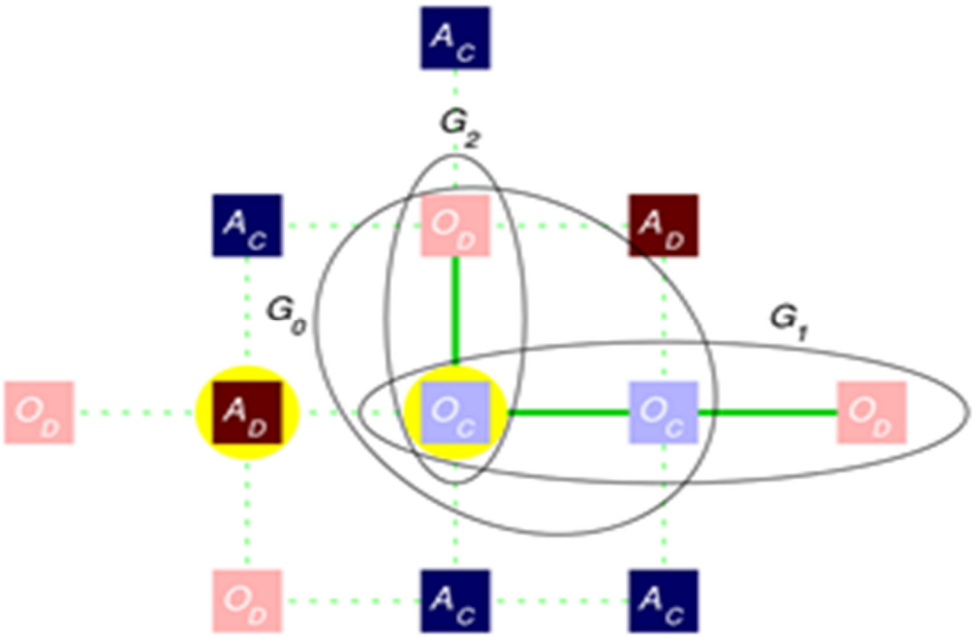


*Figure 1: The competition of "alone" and "together" attitudes.*

On the phase diagram of the four-state model (Fig. 2.) in dependence of the key parameters of basic games r denotes the multiplication factor of the public goods game, while T is the temptation to defect for the prisoner's dilemma game. As expected, at low r values those states which represent pair interactions prevail. As we increase r, however, both attitudes, hence pair and multi-point interactions, coexist. Interestingly, as we support cooperation by increasing r further the system evolves onto a full defection state. Cooperation can only recover for very high r values when the traditional public goods game with multi-point interactions prevail. We may conclude that the freedom to choose alone attitude could be harmful for the vitality of together attitude, but the former could be an escape route in case of harsh conditions.

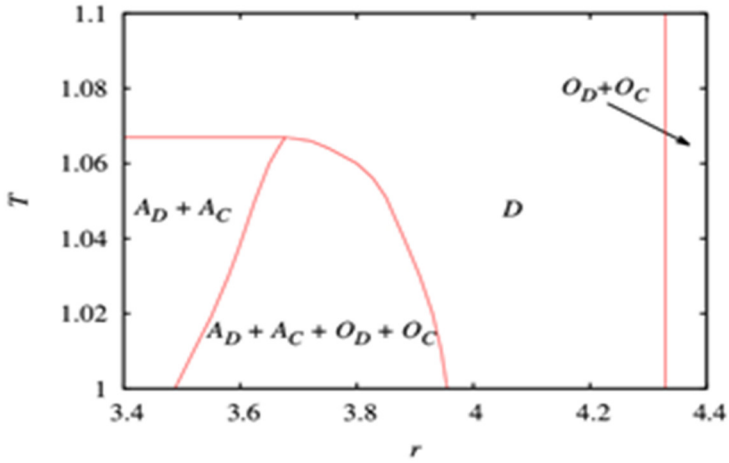


*Figure 2: Phase diagram of the four-state model in dependence of the key parameters of basic games.*

Time evolution of the pattern formation was shown at two representative values of multiplication factor r when T = 1.03. The common prepared initial state is shown in the left side on Fig. 3, where we arranged homogeneous patches of competing states denoted by different colours. Here dark colours mark players having "A" attitude, while light colours denote players with "O" attitude. Furthermore, different shades of red colour mark defector strategies, while various blue colours for cooperator strategies. The legend for the microscopic states are shown in the middle row of the plot. The top row from panels (Fig 3.b-d) illustrates how the initial patchwork evolves at small (r = 3.4) multiplication factor. Here, as white ellipses shown in panel (Fig 3.b), $A_C$ and $O_C$ players can coexist due to the low value of r. Because of the modest temptation value $A_D$ and $A_C$ states can coexist and this mixed phase gradually beat $O_D$ players. This process is marked by a white ellipse in panel (Fig 3.c). In the final state only players with "A" attitude can survive. When r is higher, as shown in the bottom row, $O_C$ beats $A_C$ who gradually diminishes. This is shown by a white ellipse in panel (Fig 3.e). The lonely $O_C$, however, becomes vulnerable against $O_D$ and the previously victorious domains of $O_C$ players gradually shrink. In the absence of other states $A_D$ and $O_D$ would be neutral, but the vicinity of cooperators helps the latter to beat the former defector state. This is shown by a white ellipse in panel (Fig 3.f). Finally, only defector state survives, but a slow voter-like stochastic dynamics will drive the system onto a homogeneous state [1].

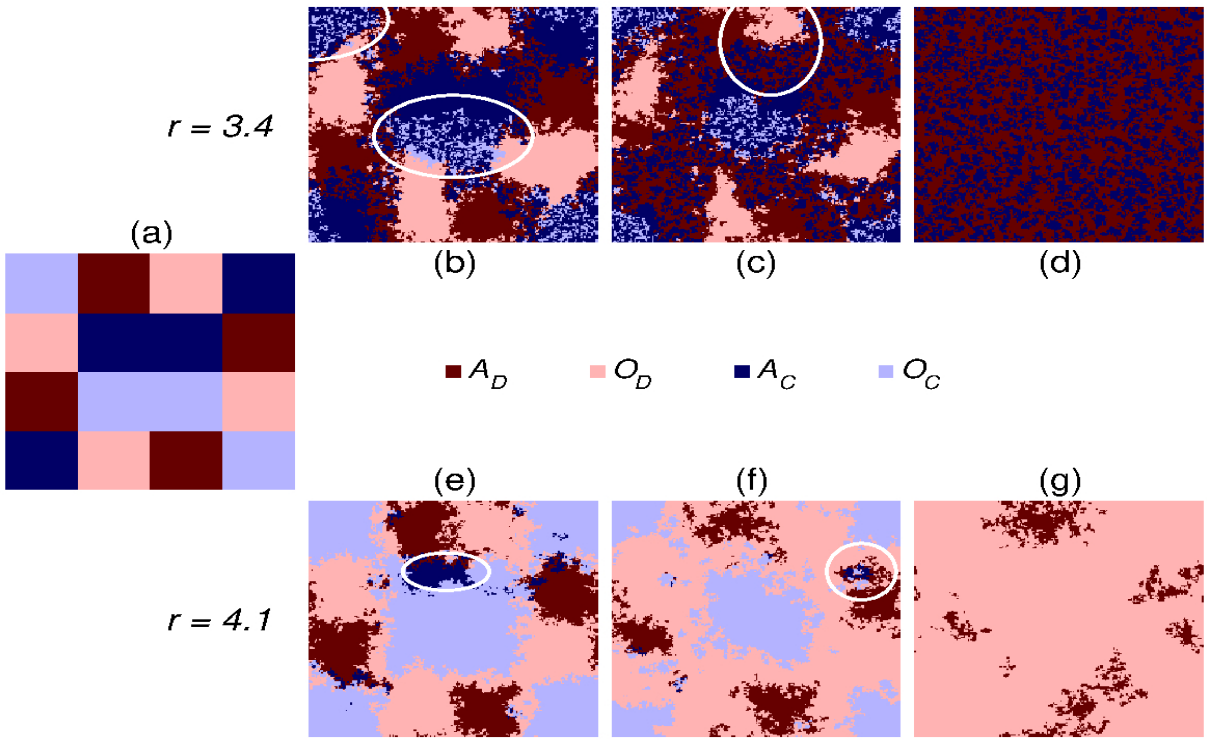


*Figure 3: Time evolution of the pattern formation.*

## *Related publication*

[1] A. Szolnoki, X, Chen: *Cooperation and competition between pair and multi-player social games in spatial populations,* Scientific Reports **11,** 12101 (2021)

# GENERAL FEATURES OF NASH EQUILIBRIA IN COMBINATIONS OF ELEMENTARY INTERACTIONS IN SYMMETRIC TWO-PERSON GAMES

***OTKA PD 138571***

*G. Szabó and B. Király*

One of the key concepts of game theory is the Nash equilibrium, a set of strategy choices from which no unilateral deviations can benefit the players. Nash's theorem states that in a game with a finite number of players who can choose from a finite number of pure strategies there exists, at least in the set of mixed strategies, at least one such equilibrium state. Generally, however, a game can have multiple different Nash equilibria. One such example is the two-person, three-strategy symmetric matrix game described by the dynamical graph shown in Fig. 1. The upper pair of numbers on the nodes of the graph show the strategy choices of the players, while the lower pair indicates the corresponding payoffs, and its directed edges point toward higher payoffs realized during unilateral strategy changes. Pure Nash equilibria, highlighted in yellow, are easily identified in Fig. 1, since these can only have incoming edges attached to them. The game also has a mixed Nash-equilibrium that provides a lower payoff. Games like this may lead to social dilemmas, as they make mutually choosing the "best" equilibrium more difficult for selfish players who do not communicate with each other, which can be circumvented by considering other viewpoints, trust and fraternity. The importance of the problem of choosing from different Nash equilibria is demonstrated by earlier computer studies that proved that the expected number of Nash equilibria increases with the logarithm of the number of strategies when the payoffs are random.

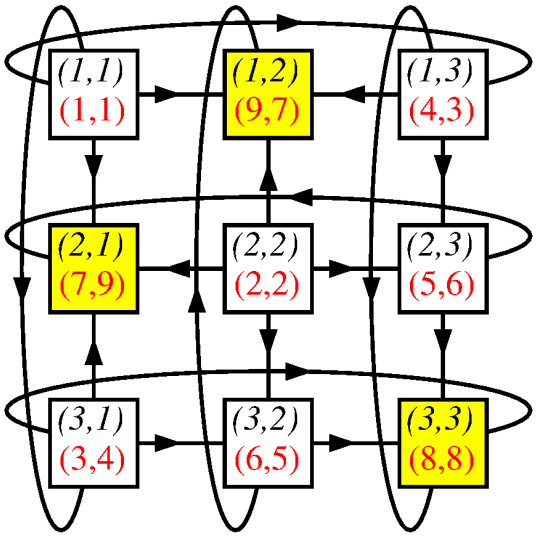


*Figure 1: Two-person, three-strategy symmetric matrix game*

Our research employed direct analytic calculations to analyze the number of Nash equilibria in symmetric matrix games with an arbitrary n number of strategies in light of the decomposition of payoff matrices into four kinds of non-trivial, self-dependent, cross-dependent, coordination and cyclic, elementary interaction types. Our results revealed that in self-dependent games (aside from degenerate cases, in general) there is a single pure Nash equilibrium. Games made up solely of coordination components can have at most n different pure Nash equilibria, and this statement remains true even when beside the coordination component self- and cross-dependent components are also present. An infinite number of mixed Nash equilibria can be observed in certain games composed of appropriate combinations of coordination or cyclic elementary games, which still only constitute a zero-measure subset of all possible games. Purely cross-dependent games also have an infinite number of Nash equilibria, however, adding these or constant components to other games does not change their Nash equilibria. A detailed treatment of our results was published in a game theory special issue of The European Physical Journal B [1].

## *Related publication*

[1] G. Szabó & B. Király: *General features of Nash equilibria in combinations of elementary interactions in symmetric two-person games,* The European Physical Journal B **94,** 102 (2021)

# CRITICAL DYNAMICS, SYNCHRONIZATION AND GRIFFITHS EFFECTS IN BRAIN MODELS

*G. Ódor, G. Deco, J.Kelling*

We have extended the study of the Kuramoto model with additive Gaussian noise running on the KKI-18 large human connectome graph. We determined the dynamical behaviour of this model by solving it numerically in an assumed homeostatic state, below the synchronization crossover point we determined previously. The de-synchronization duration distributions exhibit power-law tails, characterized by the exponent in the range $1.1 < \square t < 2$, overlapping the in vivo human brain activity experiments by Palva et al. We show that these scaling results remain valid, by a transformation of the ultra-slow eigen-frequencies to Gaussian with unit variance. We also compare the connectome results with those obtained on a regular cube with $N = 10^6$ nodes, related to the embedding space, and show that the quenched internal frequencies themselves can cause frustrated synchronization scaling in an extended coupling space [1].

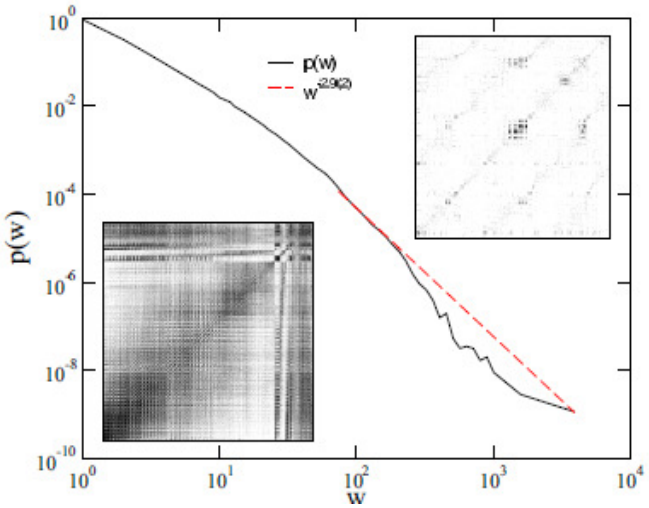


*Figure 1: Weight distribution of the fruit-fly connectome. Right inset: adjacency matrix plot of the fruit-fly connectome. Left inset: full adjacency matrix down sampled with a max pooling kernel of size 10 × 10. Black dots denote connections between presynaptic and postsynaptic neurons. Right inset: zoom-in to the centre of the matrix without down sampling.*

Previous simulation studies on human connectomes suggested that critical dynamics emerge subcritically in the so-called Griffiths phases. Now we investigate this on the largest available exact brain network, the 21662 node fruit-fly connectome, using the Kuramoto synchronization model. As this graph is less heterogeneous, lacking modular structure and exhibit high topological dimension, we expect a difference from the previous results. Indeed, the synchronization transition is mean-field-like and the width of the transition region is larger than that of random graphs, but much smaller than as of the KKI-18 human connectome. This demonstrates the effect of modular structure and dimension on the dynamics, providing a basis for better understanding the complex critical dynamics and consciousness of humans [1-3].

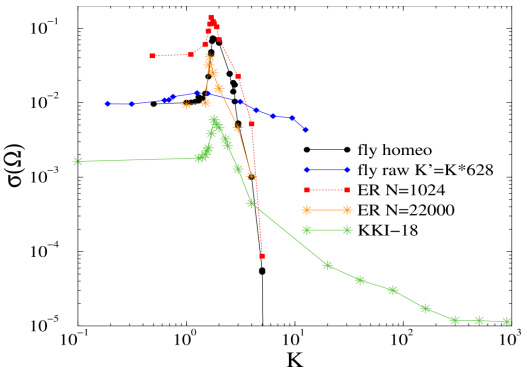


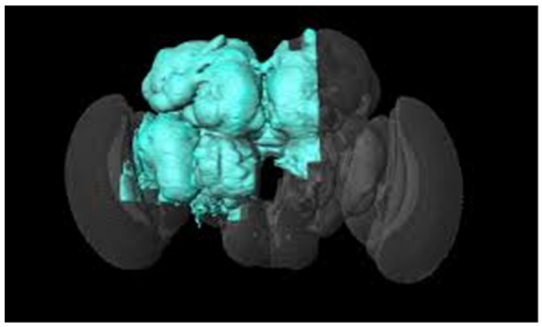

*Figure 2: left: Fluctuations of the frequency entrainment order parameter σ(Ω(t → inf.)) as the function of global coupling K, for different graphs. One can see that the fly results are similar to the random (ER) graph results, while in case of the human connectome KKI-18 an extended region of fluctuations emerge, as in the Griffiths phases. right: image of the fruit-fly brain of which the connectome is used.*

## *Related publications*

[1] G. Ódor, J. Kelling, G. Deco: *The Effect of noise on the synchronization dynamics of the Kuramoto model on a large human connectome graph,* Neurocomputing **461,** 696-704 (2021)

[2] G. Ódor, J. Kelling, M. Gastner, G. Deco: *Modelling on the very large-scale connectome,* Journal of Physics: Complexity **2,** 045002 (2021)

[3] G. Ódor, G. Deco, J. Kelling: *Differences in the critical dynamics underlying the human and fruit-fly connectome,* Physical Review Research **4,** 023057 (2022)

# NONUNIVERSAL POWER-LAW DYNAMICS OF SUSCEPTIBLE INFECTED RECOVERED MODELS ON HIERARCHICAL MODULAR NETWORKS TO MODEL COVID-LIKE EPIDEMICS

*Géza. Ódor, S. Deng*

Power-law (PL) time-dependent infection growth has been reported in many COVID-19 statistics. In simple Susceptible Infected Recovered (SIR) models, the number of infections grows at the outbreak as $I(t) \propto t^{d-1}$ on d-dimensional Euclidean lattices in the endemic phase, or it follows a slower universal PL at the critical point, until finite sizes cause immunity and a crossover to an exponential decay. Heterogeneity may alter the dynamics of spreading models, and spatially inhomogeneous infection rates can cause slower decays, posing a threat of a long recovery from a pandemic. COVID-19 statistics have also provided epidemic size distributions with PL tails in several countries. Here we investigate SIR-like models on hierarchical modular networks, embedded in *2d* lattices with the addition of long-range links (Fig. 1.).

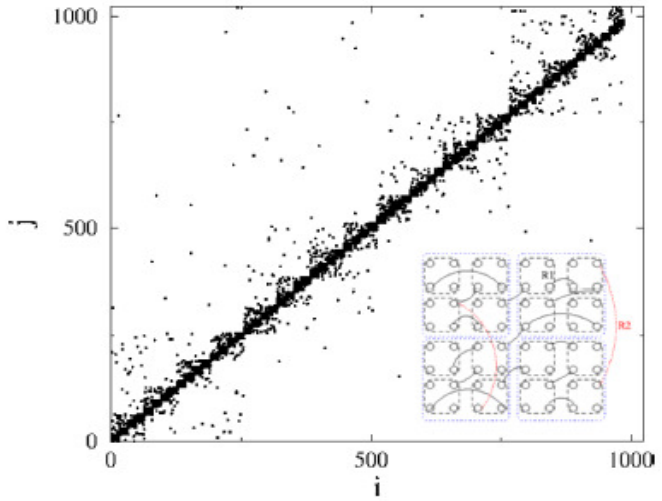


*Figure 1: Plot of the adjacency matrix of an N = 1024 sized sample of the HMN2D graphs, used for the simulations. Black dots denote edges between nodes i and j. The $l_{max}$ = 4-level structure is clearly visible by the blocks near the diagonal. Low density, scattered points away from the diagonal represent long-range links. Inset: scheme of the lowest three levels of a hierarchical, four-block structure of nodes, embedded in 2d space with additional long links. Black solid lines: l = 1 links; red, dashed lines, l = 2 links; l = 0 edges are not shown.*

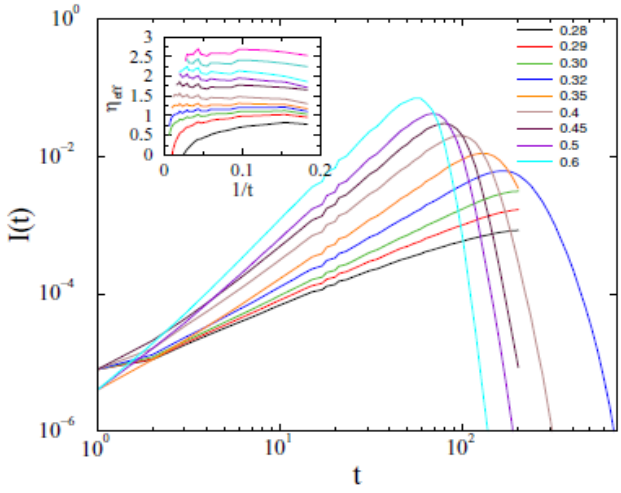


*Figure 2: Density of infected sites in graphs with parameters s=4 and b=1 for infection probabilities λ = 0.28, 0.29, 0.3, 0.32, 0.35, 0.4, 0.45, 0.5, and 0.6 (bottom to top curves). Inset: local slopes of the same curves as well as for λ = 0.7, 0.8. One may think of continuously changing exponents above $\lambda_c$=0.310(5), because short times hinder our ability to see the supercritical point scaling behaviour with the growth exponent η=2.5.*

We show that if the topological dimension of the network is finite, average degree-dependent PL growth of prevalence emerges (see Fig. 2.). Supercritically, the same exponents as those of regular graphs occur, but the topological disorder alters the critical behaviour. This is also true for the epidemic size distributions. Mobility of individuals does not affect the form of the scaling behaviour, except for the *d*=2 lattice, but it increases the magnitude of the epidemic. The addition of a superspreader hot spot also does not change the growth exponent and the exponential decay in the herd immunity regime [1].

## *Related publication*

[1] G. Ódor: *Nonuniversal power-law dynamics of susceptible infected recovered models on hierarchical modular networks,* Phys. Rev. E **103,** 062112 (2021)

# ABBREVIATIONS

| | |
|---|---|
| 4D-ED | Four-Dimensional Electron Diffraction |
| ABR | Auditory Brainstem Response |
| AC | Alternating Current |
| ACE | Area Control Error |
| AEKI | Institute for Atomic Energy Research |
| AES | Auger Electron Spectroscopy |
| AFM | Atomic Force Microscopy |
| AGLAE | Association Générale Laboratoires Analyse Environnement, France |
| ALD | Atomic Layer Deposition |
| ALLEGRO | Experimental Helium Gas Cooled Fast Reactor Developed by the European V4G4 |
| AMS | Accelerator Mass Spectrometry |
| AOP | Advanced Oxidation Processes |
| APC | Aerosol Particle Counter |
| APTES | 3-aminopropyl-triethoxysilane |
| APTMS | 3-aminopropyl-trimethoxysilane |
| ATF-TS | Testing and Simulation for Advanced Technology and Accident Tolerant Fuels |
| ATR | Attenuated Total Reflection |
| ATWS | hypothetical transient without SCRAM |
| BCC | Body Centred Cubic |
| BCF | Boda Claystone Formation |
| BCR | B cell receptor |
| BDD | Boron Doped Diamond |
| BEI | Backscattered Electron Image |
| BF | Bright Field |
| BME | Budapest University of Technology and Economics |
| BNC | Budapest Neutron Centre |
| BOD | Biochemical Oxygen Demand |
| BRR | Budapest Research Reactor |
| BSA | Bovine Serum Albumin |
| BWR | Boiling Water Reactor |
| CA | Cellulose acetate |
| CaAG | Ca-alginate aerogel |
| CARC | Calculations for Atmospheric Release Criteria |
| CCMP | Computer-controlled micropipette |
| CEFR | China Experimental Fast Reactor |
| CEMS | Conversion Electron Mössbauer Spectroscopy CEMS |
| CERIC | Central European Research Infrastructure Consortium |
| CETS | Central European Training School |
| CFD | Computational Fluid Dynamics |
| CFL | Cumulative Fractions of boron Leaching |
| CH | Cultural Heritage |
| CHP | Combined Heat and Power |
| CID | Chemical Interface Damping |
| CL | Camera Length |
| CMOD | Crack Mouth Opening Displacement |
| CMUT | Capacitive Micromachined Ultrasonic Transducer |
| COD | Chemical Oxygen Demand |
| COP | Cyclo-olefin-polymer |
| COTS | Commercial Off-The-Shelf |
| CRP | Coordinated Research Project |

| | |
|---|---|
| CT | Compact Tension |
| CTE | Coefficient of Thermal Expansion |
| CV | Cyclic Voltammetry, Central Vector |
| CVD | Chemical Vapour Deposition |
| DBA | Design Basis Accident |
| DBC | Design Basis Condition |
| DBTT | Ductile-to-Brittle Transition Temperature |
| DC | Drop-Casting, Direct Current |
| DEMO | DEMOnstration Power Station |
| DF | Dark Field |
| DFT | Density Functional Theory |
| DHR | Decay Heat Removal |
| DHZ | Diffusion Hardened Zone |
| DIP | Dip-Coating |
| DLR | German Aerospace Centre |
| DLS | Dynamic Light Scattering |
| DM | Demineralized |
| DMS | Disruption Mitigation Systems |
| DMSA | Dimercaptosuccinic acid |
| DNA | Deoxyribonucleic acid |
| DONES | Demo-Oriented early NEutron Source |
| DPA | Displacement per Atom |
| dpm | difference per mean |
| DRM | Dry Reforming of Methane |
| DRIE | Deep Reactive Etching |
| DRIFTS | Diffuse Reflectance Fourier Transform Infrared Spectroscopy |
| DSCs | Design Safety Calculations |
| DSL | Design Service Lifetime |
| DSO | Distribution System Operator |
| DSP | Dithiobis(succimidyl propionate) |
| DT | Digital Twin |
| EAD | European Active Dosimeter |
| EB | Electron Beam |
| ECR | Equivalent Cladding Reacted, Electron Cyclotron Resonance |
| ED | Electrodeposition |
| EDICAM | Event Detection Intelligent Camera |
| EDL | Electric Double Layer |
| EDS | Energy Dispersive X-ray Spectroscopy |
| EDTA | Ethylenediaminetetraacetic acid |
| EDX | Energy-dispersive X-ray Spectroscopy |
| EELS | Electron Energy Loss Spectroscopy |
| EK | Centre for Energy Research (Hungarian acronym) |
| ELKH | Eötvös Loránd Research Network (Hungarian acronym) |
| ELTE | Eötvös Loránd University, Budapest (Hungarian acronym) |
| EMR | Electron Magnetic Resonance |
| EPR | Electron Paramagnetic Resonance |
| ERO | Earth Return Orbiter |
| ESA | European Space Agency |
| ESIS | European Structural Integrity Society |
| ETDR | Experimental Technology Demonstration Reactor |
| EURAD | European Joint Programme on Radioactive Waste Management |
| F2R | Flex to rigid |
| FAIR | Findable, Accessible, Interoperable, Reusable |

| | |
|---|---|
| FC | Faraday Cup |
| FCC | Face Centred Cubic |
| FDTD | Finite-Difference Time-Domain |
| FE | Finite Element |
| FEG | Field Emission Gun |
| FEM | Finite Element Method |
| FFT | Fast Fourier Transform |
| FIB | Focus Ion Beam |
| FKKL | MFA Laboratory of Surface Chemistry and Catalysis (Hungarian acronym) |
| FL | MFA Photonics Laboratory (Hungarian acronym) |
| FOCS | Fibre Optics Current Sensor |
| FSANS | Focusing Small Angle Neutron Scattering |
| FT-IR | Fourier-transform Infrared Spectroscopy |
| FTO | Fluorine-doped Tin Oxide |
| FWHM | Full width at half maximum |
| GAMS | General Algebraic Modelling System |
| GC | Glassy Carbon, Gas Chromatograph |
| GC-MS | Gas Chromatography–Mass Spectrometry |
| GFP | Green Fluorescent Polymer |
| GFR | Gas-Cooled Fast Reactor |
| GINA | Grazing Incidence Neutron Apparatus |
| GIS | Geographical Information System |
| GKN | Glucose potassium nutrient |
| GM | Geiger–Müller |
| GNP | Gold Nanoparticle |
| GNR | Gold Nanorods |
| GNS | Gold Nanospheres |
| GPS | Global Positioning System |
| GTA | Glutaraldehyde |
| GTN | Gurson-Tvergaard-Needleman |
| GUI | Graphical User Interface |
| GWP | Global Warming Potential |
| HAADF | High-angle Annular Dark-field |
| HEMT | High-Electron Mobility Transistor |
| HER | Hydrogen Evolving Reaction |
| HFTM | High Flux Test Module |
| HIP | Hot Isostatic Pressing |
| HKDI | Hevesy György PhD School of Chemistry |
| HLW | High-level Radioactive Waste |
| HMGU | Helmholtz Zentrum München, Germany |
| HNM | Hungarian National Museum |
| HOPG | Highly Oriented Pyrolytic Graphite |
| HPGe | High-purity Germanium |
| HRDA | Hungarian node of the Research Data Alliance |
| HRGS | High-Resolution Gamma-ray Spectrometry |
| HRTEM | High Resolution Transmission Electron Microscopy |
| HSA | Human Serum Albumin |
| HV | High Voltage |
| IAEA | International Atomic Energy Agency |
| IBANDL | Ion Beam Analysis Nuclear Data Library |
| IBM | Ion-beam Mixing |
| IC | Ion Chromatography |
| ICDs | Interface Control Documents |

| | |
|---|---|
| ICP-MS | Inductively Coupled Plasma Mass Spectrometry |
| ICP-OES | Inductively Coupled Plasma Optical Emission Spectrometry |
| IDA | Internal Dosimeter Array |
| IDS | Interface Data Structure |
| ILW | Intermediate Level Radioactive Waste |
| IMAS | Integrated Modelling and Analysis Suite |
| INAA | Instrumental Neutron Activation Analysis |
| IPNDV | International Partnership for Nuclear Disarmament Verification |
| IR | Infrared, Induced Repair |
| ISS | International Space Station |
| ITER | International Thermonuclear Experimental Reactor |
| ITO | Indium Tin Oxide |
| JAXA | Japan Aerospace Exploration Agency |
| JET | Joint European Torus |
| Kd | Dissociation constant |
| KIKO3DMG | Nodal Reactor Physics Calculation Code Developed in the CER |
| KR | Kretschmann-Raether |
| LED | Light Emitting Diode |
| LEL | Lower Explosion Limit |
| LFC | Load-Frequency Control |
| Li-BES | Lithium Beam Emission Spectroscopy |
| LoC | Lab-on-a-Chip |
| LOCA | Loss of Coolant Accident |
| LSC | Liquid Scintillation Counting |
| LSPSs | Large-Scale Pressure Systems |
| LTO | Long Term Operation |
| LV | Low-Voltage |
| LWR | Light Water Reactor |
| MAC | Maximum Allowable Concentration |
| MAS | Magic Angle Spinning |
| MAT | Magnetic Adaptive Testing |
| MC | Mononuclear Cell |
| MCA | Multi Channel Analyser |
| MCC | Multilayer Ceramic Composite |
| MCM | Monte Carlo Method |
| MCP | Main Coolant Pump |
| MEMS | Microelectromechanical System |
| MEST | Mobile Expert Support Team |
| MFA | Institute of Technical Physics and Materials Science (Hungarian acronym) |
| MGI | Massive Gas Injection |
| MHD | Magnetohydrodynamic |
| MIC | Minimum Inhibitory Concentration |
| MLG | Multi-layered Graphene |
| MCNP | Monte Carlo N-Particle Transport |
| MOX | Mixed Oxide |
| MPCs | Mechanical Pipe Connections |
| MPEAs | Multi-Principal Element Alloys |
| MPTMS | 3-mercaptopropyl-trimethoxysilane |
| MRI | Magnetic Resonance Imaging |
| MS | Mössbauer Spectroscopy |
| MSR | Mars Sample Return |
| MTB | Methylthymol Blue |
| MV | Medium-Voltage |

| | |
|---|---|
| MVM | Hungarian Power Companies |
| NAA | Neutron Activation Analysis |
| NBD | Nano Beam Diffraction |
| NBI | Neutral Beam Injection |
| NCT | Neutron Computed Tomography |
| NDE | Non Destructive Evaluation |
| NEMS | Nanoelectromechanical system |
| NIPS | Neutron-Induced Prompt Gamma-ray Spectroscopy |
| NIR | Near InfraRed |
| NKFIH | National Research, Development and Research Office (Hungarian acronym) |
| NMR | Nuclear Magnetic Resonance |
| NN | Neural Network |
| NOMAD | Non-destructive Evaluation System for the Inspection of Operation-Induced Material Degradation in Nuclear Power Plants (EU H2020 project) |
| NORM | Naturally Occurring Radioactive Materials |
| NP | Nanoparticle |
| NPP | Nuclear Power Plant |
| NR/NT | Neutron Radiography and Tomography |
| NT | Notched Tensile |
| NTI | Nuclear Threat Initiative |
| NUBIKI | Nuclear Safety Research Institute |
| OAH | Hungarian Atomic Energy Authority (Hungarian acronym) |
| ODP | Ozone Depletion Potential |
| OER | Oxygen Evolving Reaction |
| OM | Optical Microscopy |
| OoC | Organ-on-Chip |
| OPC | Optical Particle Counter |
| ORC | Organic Rankine Cycle |
| OSL | Optically Stimulated Luminescence |
| OTKA | Hungarian Scientific Research Fund (Hungarian Acronym) |
| OWLS | Optical Waveguide Lightmode Spectroscopy |
| O&M | Operation and Maintenance |
| Paks NPP | Paks Nuclear Power Plant |
| PAS | Positron Annihilation Spectroscopy |
| PCB | Printed Circuit Board |
| PCI | Pellet-Cladding Interaction |
| PCR | Polymerase Chain Reaction |
| PDMS | Polydimethylsiloxane |
| PDR | Preliminary Design Review |
| PE | Polyester |
| PEG | Polyethylene Glycol |
| PEGMA | Poly(ethylene glycol) methacrylate |
| PFT | Pulmonary Function Test |
| PGAA | Prompt-gamma Neutron Activation Analysis |
| PGAI | Prompt-gamma Activation Imaging |
| PGAI-NT | Prompt-gamma Activation Imaging – Neutron Tomography |
| PHE | Public Health England |
| PhTES | phenyltriethoxysilane |
| PIXE | Particle Induced X ray Emission |
| PL | Power-law |
| PMMA | (Poly)methyl methacrylate |
| PoC | Point of Care |
| POS | Plant Operation State |

| | |
|---|---|
| PPE | Personal Protective Equipment |
| PS | Pressureless Sintering |
| PSA | Probabilistic Safety Assessment |
| PSTC | Pellet Shattering Test Consortium |
| PTFE | Polytetrafluoroethylene |
| PU | Poly-urethane |
| PUMMA | Plutonium Management for More Agility |
| PV | Photovoltaic |
| PVA | Polyvinyl Alcohol |
| pXRF | Portable XRF Spectrometer |
| PWR | Pressurized Water Reactor |
| QCM | Quartz Crystal Microbalance |
| QMS | Quadrupol Mass Spectrometer |
| RBC | Red Blood Cell |
| RBSB | Removable Biological Shielding Blocks |
| RCSM | Radiological Crime Scene Management |
| REEs | Rare Earth Elements |
| RES | Renewable Energy Sources |
| RF | Radio Frequency |
| RGD | Arginine-glycine-aspartic acid (Arg-Gly-Asp) |
| RH | Remote Handling |
| RID | Radioisotope Identification Detectors |
| RMC | Reverse Monte Carlo |
| RMSE | Root Mean Square Error |
| RN | radionuclide |
| RNM | Representative Network Model |
| RPV | Reactor Pressure Vessel |
| RWG | Resonant Waveguide Grating |
| SAED | Selected Area Electron Diffraction |
| SANS | Small Angle Neutron Scattering |
| SAXS | Small Angle X-ray Scattering |
| sccm | standard cubic centimetres per minute |
| SCK•CEN | Belgian Nuclear Research Centre (Centre d'Étude de l'énergie Nucléaire) |
| SCRAM | emergency shutdown of the reactor |
| SDT | Space Dosimetry Telescope |
| SE | Spectroscopic Ellipsometry |
| SEI | Secondary Electron Image |
| SEM | Scanning Electron Microscopy |
| SEM-EDS | Scanning Electron Microscopy with Energy Dispersive Spectroscopy |
| SEM-EDX | Scanning Electron Microscopy with Energy Dispersive X-Ray microanalysis |
| SEMP | Systems Engineering Management Plan |
| SENT | Single Edged Notched Tensile |
| SERS | Surface Enhanced Raman Scattering |
| SFC | Spent Fuel Characterization |
| SGTR | Steam Generator Tube Rupture |
| SI | Structural Integrity |
| SICs | Structural Integrity Calculations |
| SIR | Susceptible Infected Recovered |
| SITON | SImulation TOol for modelling the Nuclear fuel cycle |
| SMD | Surface Mounted Device |
| SMPS | Scanning Mobility Particle Sizer |
| SNOM | Scanning Near-field Optical Microscopy |
| SPI | Shattered Pellet Injection |

| | |
|---|---|
| SPR | Surface Plasmon Resonance |
| SPS | Spark Plasma Sintering |
| SSNTD | Solid-State Nuclear Track detector |
| SSRs | Single Sequence Repeats |
| SURET | SUbchannel REactor Thermohydraulics |
| STI | Strong Topological Insulator |
| STEM | Scanning Transmission Electron Microscope |
| STM | Scanning Tunnelling Microscopy |
| STS | Scanning Tunnelling Spectroscopy |
| SZTAKI | Institute for Computer Science and Control |
| TAL | Technically Allowable Lifetime |
| TDMAH | Tetrakis-dimethylamino-hafnium |
| TEM | Transmission Electron Microscopy |
| TEOS | Tetraethylorthosilicate |
| TESPEL | Tracer-Encapsulated Solid Pellet |
| TÉT | Bilateral Research Program (Hungarian acronym) |
| TFC | Trilateral Flash Cycle |
| TL | Thermoluminescent |
| TLIC | Test Cell Lithium System Interface Cell |
| TMD | Transition Metal Dichalcogenides |
| TOC | Total Organic Carbon |
| TOF | Time-Of-Flight |
| TOF-ND | Time-of-Flight Neutron Diffraction |
| TPR | Temperature Programmed Reduction |
| TRL | Technolgy Readiness Level |
| TSD | Target-to-substrate distance |
| TSO | Transmission System Operator |
| TSV | Through Silicon Via |
| TXRF | Total-reflection X-ray Fluorescence |
| UC | Uranium Carbide |
| UOX | Uranium Oxide |
| UV | Ultraviolet |
| UV-VIS | Ultraviolet-Visible (Spectroscopy) |
| VERONA | VVER On-Line Analysis |
| VI | Virtual Instrument |
| VPNET | Variable Projection Network |
| VRF | MFA Thin Film Physics Department (Hungarian acronym) |
| VTES | vinyltriethoxysilane |
| VVER | Water-Cooled Water-Moderated Energetic Reactor, Russian acronym |
| XANES | X-ray Absorption Near-Edge Structure |
| XCT | X-ray Computed Tomography |
| XPS | X-ray Photoelectron Spectroscopy |
| XRD | X-ray Diffraction |
| μ-XRD | Microscopic X-ray Diffraction |
| XRF | X-ray Fluorescence Analysis |
| μ-XRF | Microscopic X-ray Fluorescence |
| XRS | X-Ray Spectrometry |
| XTEM | Cross-sectional Transmission Electron Microscopy |
| WC | Tungsten-carbide |
| Wigner FK | Wigner Research Centre for Physics |
| WLM | Working Level Month |
| WP | Work Package |
| WTI | Weak Topological Insulator |

# IMPRINT


## Editors

*László Redler*
*Attila R. Imre*

## Lector

*Ferenc Szlávik*
*Jesse Weil*

## Publisher

*Ákos Horváth*
*Tamás Belgya*
*Centre for Energy Research*
*H-1121, Budapest, Konykoly Thege M. út 29-33.*
*Hungary*

## Design

*Anikó Jécsai*
*Tamás Szabolics*

## Picture credits

*Centre for Energy Research*

## Accessibility

*http://www.ek-cer.hu/*


## Contact


*Centre for Energy Research, Eötvös Loránd Research Network*
***Location:*** *KFKI Campus, Budapest Konkoly-Thege Miklós street 29-33., H-1121 Hungary*
***Phone:*** *(+36 1) 395 91 59*
*E-mail adresses: info@ek-cer.hu*


Centre for
Energy Research

Centre for
Energy Research

KFKI Campus, Konkoly-Thege Miklós út 29-33.
Budapest H-1121, Hungary
Phone: +36 1 395 9159
www.ek-cer.hu